Supermassive Black Holes in Active Galaxies

On measuring their mass and influence on circumnuclear PAH features

Jens Juel Jensen

Supervisor: Ass. Prof. Marianne Vestergaard

Dark Cosmology Centre
Niels Bohr Institute
University of Copenhagen

This dissertation is submitted for the degree of
Doctor of Philosophy

March 2018

This thesis is dedicated to my wife and kids.

Acknowledgements

None of this would have been possibly without the help and patience of my family, friends, and co-workers. My first thanks goes to my supervisor Marianne Vestergaard. Your help has been invaluable and you have shown great patience with me. You have allowed me more freedom during this project than I could ever have expected, and I am extremely grateful for that. A warm thanks goes to Sebastian F. Hönig who acted as my co-supervisor, first at Dark, and later in Southampton. Your way of doing research has inspired me, and thank you for making me so welcome during my stay abroad. A thanks to everyone at Dark, administrative and other staff alike, but especially to my fellow PhD students. A deep thanks goes to my friends and family for their support. Finally, I wish to thank my wife Thea and our kids. Without your loving support, none of this would have been possible.

Abstract

Supermassive black holes are found to be ubiquitous in all massive galaxies and their mass is observed to correlate with properties of the host galaxy bulge. Therefore, these black holes are believed to play an important role in galaxy formation and evolution. Most notably so through various feedback mechamisms as the black hole is growing by accreting matter in its phase as an Active Galactic Nucleus (AGN). The amount of possible feedback from the black hole is largely governed by its mass. Accurately measuring masses of black holes in AGN is therefore a crucial part of understanding the physics of AGN and their possible impact on galaxy formation and evolution. Many factors contribute to the uncertainty of the mass estimates in AGN, but studies have shown that the quality of and the way data are measured is important. Specifically, the accuracy to which we can measure broad emission line widths in AGN spectra as a proxy for the velocity of the gas in the Broad Line Region (BLR) has shown to be important. In this work, I aim to provide a comprehensive account of how much the uncertainty on the mass is affected by uncertainties related to measurements of broad emission line widths in AGN spectra. I find that for low data quality and for certain parameterisations of the line width, the impact on the accuracy of the black hole mass can easily be up to 0.5 dex.

In Chapters 2 and 3 I determine the accuracy and precision of four different line width parameters used for black hole mass estimates as a function of spectral S/N. I do so for a sample of objects with spectra representative of the general observed AGN population and covering the broad Hβ, Mg II, and C IV emission lines. I find that the MAD and IPV widths show a higher accuracy and precision than the FWHM and σ_{line} at any given S/N level. In addition, the IPV widths allow us to measure the line width at many fractions of the emission line flux, providing more flexibility and the option of measuring the line shape in a robust way using ratios of different IPV widths. In Chapter 4 I show that narrow absorption negatively affects the accuracy of the four line parameters if it is not accounted for in the spectra. The results in Chapters 2 – 4 can be used to assess realistic uncertainties for mass estimates based on existing spectral data and to plan optimally for future observations. I recommend to aim for S/N $\geq 20\,\mathrm{pixel}^{-1}$ in the continuum and further to have a spectral resolution of $100\,\mathrm{km\,s}^{-1}$ or better in order to be able to account for narrow absorption lines.

The second part of this thesis zooms out further from the central black hole. Spectral mid-IR features from Poly-cyclic Aromatic Hydrocarbon (PAH) molecules are used to infer recent and ongoing star formation around AGN where other more traditional methods typically fail. This method rests upon the assumption that the PAH features are excited exclusively by star formation and not the AGN itself. We test this assumption by using mid-IR high angular resolution spectroscopy for a

sample of nearby AGN. We trace the radial profile of the 11.3 μm PAH feature in each AGN and find that the radial profile for this emission feature is similar amongst the different AGN. This indicates that they are excited by a compact central source and not diffuse star formation. Through comparisons with CLOUDY simulations of an AGN as the excitation source and observations of nuclear star clusters, we find that the most likely explanation for the radial profiles of the 11.3 μm PAH feature is excitation by the AGN. This shows that the 11.3 μm PAH feature probably is contaminated by the AGN within approximately 1 kpc and that care should be taken when using this feature to estimate star formation that close to the active nucleus.

Resume på dansk

Supertunge sorte huller er observeret i alle tunge galakser, og massen af det sorte hul er korreleret med fysiske egenskaber i værtsgalaksens centrale del. Derfor mener man at de sorte huller spiller en vigtig rolle i galaksers dannelse og udvikling, mest prominent i den fase hvor det sorte hul aktivt samler stof og vokser som en aktiv galaksekerne. Mængden af mulig feedback fra det sorte hul er primært styret af det sorte huls masse. Det er derfor nødvendigt at kunne måle massen af sorte huller i aktive galakser nøjatigt for at de kan bruges til at udvide vores forståelse af fysikken i aktive galakser og deres mulige rolle i galaksedannelse og -udvikling. Nøjagtigheden hvormed man kan måle massen af det sorte hul er påvirket af mange faktorer, men tidligere studier har vist at kvalitaten af data og målemetoden man bruger har stor indflydelse. Mere specifikt, så er nøjagtigheden hvormed vi kan måle bredden af emissionslinier i spektre af aktive galaksekerner begrænsende for nøjagtigheden hvormed vi kan måle massen af det sorte hul. I denne afhandling forsøger jeg at give en fyldestgørende oversigt over hvor meget usikkerheden på massen er påvirket af måleusikkerheder på de brede emissionslinjer i spektre af aktive galaksekerner. Jeg finder at for lav datakvalitet og for specifikke parmeteriseringer af liniebredden kan nøjagtigheden på massen være så lav som 0.5 dex eller en faktor 3.

I kapitel 2 og 3 bestemmer jeg nøjagtigheden og præcisionen af fire forskellige parameteriseringer af liniebredden som kan bruges til masseestimater som funktion af spektralt signalstøjforhold (S/N). Det gør jeg for en samling af objekter med spektre som er repræsentative for den observerede polulation af aktive galaksekerner og som dækker de brede Hβ, Mg II og C IV emissionslinjer. Jeg finder at MAD og IPV liniebredderne har højere nøjagtighed og præcision end FWHM og liniedispersionen ved et ethvert givent signalstøjforhold. Jeg finder også at IPV bredderne tilbyder en større fleksibilitet når man skal måle liniebredden end de andre parametre da de kan måles ved enhver ønsket brøkdel af den samlede linieflux. Dette giver også mulighed for at måle linieformen på en robust måde ved at tage forholdet mellem forskellige IPV bredder. I Kapitel 4 viser jeg at smalle absorptionslinier har en negativ påvirkning af nøjagtigheden for alle de fire linieparametre hvis man ikke korrigerer for absorptionen direkte i spektrene. Resultaterne i kapitel 2 - 4 kan bruges til at angive realistiske usikkerheder for liniebredder målt i eksisterende data og til at planlægge fremtidige observationer optimalt. Jeg anbefaler at man planlægger at have $\mathrm{S/N} \geq 20\,\mathrm{pixel}^{-1}$ i spektrene og at man har en spektral opløsning på $100\,\mathrm{km\,s}^{-1}$ eller bedre så man kan korrigere for smalle absorptionslinjer.

Anden del af denne afhandling zoomer yderligere ud fra det sorte hul i centrem af de aktive galaksekerner. Spektrale signaturer der stammer fra Poly-cykliske Aromatiske Hydrokarboner (PAH)

molekyler i det infrarøde område kan bruges til at estimere nylig og igangværende stjernedannelse tæt på aktive galaksekerner hvor mere traditionalle stjernedannelsesindikatorer typisk fejler. Metoden hviler på en antagelse om at PAH molekylerne kun kan exciteres af stjernedannelsen og ikke den aktive galaksekerne selv. Vi tester denne antagelse med infrarød spektraldata med høj rumlig opløsning for en samling af nære galaksekerner. Vi måler den radielle profil af 11.3 μm PAH signaturen i hver enkelt aktiv galaksekerne og finder at profilen ser ens ud for de forskellige aktive galaksekerner. Det indikerer at PAH signaturen er exciteret af en central og kompakt kilde og ikke diffus stjernedannelse. Vi sammenligner vores observationer med CLOUDY simulationer af en aktiv galaksekerne som excitationskilde og med observationer af stjernehobe placeret centralt i galakser. Vi finder at den mest sandsynlige forklaring på de observerede radielle profiler af 11.3 μm PAH signaturen er excitation fra den aktive galaksekerne. Vores resultater viser at 11.3 μm PAH signaturen højst sandsynligt er forurenet af emission fra den aktive galaksekerne inden for $\sim$1 kpc og at man bør udvise stor forsigtighed når man bruger denne signatur til at estimere stjernedannelse så tæt på den aktive galaksekerne.

Table of contents

List of figures

List of tables

Chapter 1

Introduction

One of the big challenges in current astronomy is to understand how galaxies form and evolve. One particular piece of this puzzle is to understand how supermassive black holes, found to be present in all massive galaxies, play a role in the formation and evolution of their host galaxy. Of particular interest is the active phase of these black holes where they accumulate matter and grow to massive sizes of more than a million solar masses.

Young galaxies containing supermassive black holes in the process of growing through accretion of matter are known as Active Galactic Nuclei (AGN). The driving engine behind their large luminosity and their possible impact on their host galaxy through various feedback mechanisms is largely governed by the mass of the central black hole. The accuracy to which we can measure the black hole mass therefore has a direct impact on how well we can hope to understand how massive black holes form, evolve, and interact with their surroundings. The first part of this thesis deals with this issue and aims to improve upon the methods we use for black hole mass estimates in AGN. Specifically, I investigate and quantify how well we can measure emission line widths, used for black hole mass estimates, in AGN spectra and how this affects the accuracy and precision of the resulting mass estimates. This issue is introduced in more detail in § 1.2.

For the second part of the thesis, I zoom out a bit and deal with one particular aspect of the link between the AGN and its host galaxy. In particular, a close link between AGN activity and star formation in its host galaxy bulge has been suggested from both an observational and theoretical point of view. Such a correlation is very difficult to determine because tracing star formation close to AGN is hampered by the strong glare of the nucleus. This issue is introduced in § 1.3. I critically examine one of the most trusted star formation tracers used in AGN to test whether it can be contaminated by emission from the AGN.

This section provides an introduction to the work mentioned above. In § 1.1 I provide a brief introduction to AGN in general, followed by a more thorough introduction to mass estimates of black holes in AGN in § 1.2. I introduce how star formation is traced close to AGN in § 1.3, before I introduce the content of this thesis in § 1.4. Finally, the structure of the thesis is outlined in § 1.5.

1.1 Active Galactic Nuclei

The designation Active Galactic Nuclei covers a range of observational phenomena displaying a wide range of luminosity and emission properties, making it difficult to give a very precise definition of the phenomenon. Most definitions agree on some version of a very compact and highly energetic and luminous source of non-stellar origin in the centre of a galaxy. Some observational properties defining AGN are (e.g., Schmidt, 1969; Peterson, 1997):

- AGN are compact and point like;
- They exhibit strong emission lines;
- They have variable continuum and emission line flux;
- Show evidence for strong emission of non-stellar origin.

Peterson (2008) also lists the following observational properties of AGN: 1) strong X-ray emission; 2) relatively strong radio emission; 3) non-stellar ultraviolet through infrared emission; and 4) broad emission lines throughout the ultraviolet, optical, and infrared, although not all AGN display strong radio emission and broad emission lines. Furthermore, AGN are characterized by emitting over the entire electromagnetic spectrum. Although a subject of long debate, it is now generally accepted that AGN are powered by accretion of matter onto a supermassive black hole. Peterson (2008) has therefore suggested the alternative definition that "active nuclei are those that emit radiation that is fundamentally powered by accretion onto supermassive ($> 10^6 M_\odot$) black holes".

Historically, AGN have been divided into many subclasses according to their observational properties. Seyfert galaxies host a low luminosity AGN, typically in the range 10^{43} – 10^{45} ergs s^{-1}. Seyfert galaxies are nearby and the host galaxy is clearly detectable. Quasars are the high luminosity ($M_V > -23$) and high redshift counterpart of Seyfert galaxies. Their host galaxy is difficult (or impossible; Peng et al., 2006; Kim et al., 2008) to detect, and approximately 5-10% of quasars are strong radio sources.

Seyfert galaxies are divided into two types based on the presence of broad emission lines in their spectra. Type 1 AGN shows two types of emission lines: 1) Narrow emission lines with a width of hundreds of $\mathrm{km\,s^{-1}}$, originating from ionized low density gas emitted at a scale of parsecs from the black hole, and 2) broad emission lines with widths of 10^3–$10^4\,\mathrm{km\,s^{-1}}$, originating from a high density gas at a distance on the order of light days to weeks from the black hole. Type 2 AGN only exhibit the narrow lines in their spectra. There are many other classes of AGN, but it is beyond my scope to go through all of them here.

1.1.1 AGN structure and unification

Despite the many different classes and subtypes of AGN, there exists a general picture of their structure. In its simplest form, this is manifested in the idea of unification which tries to explain the

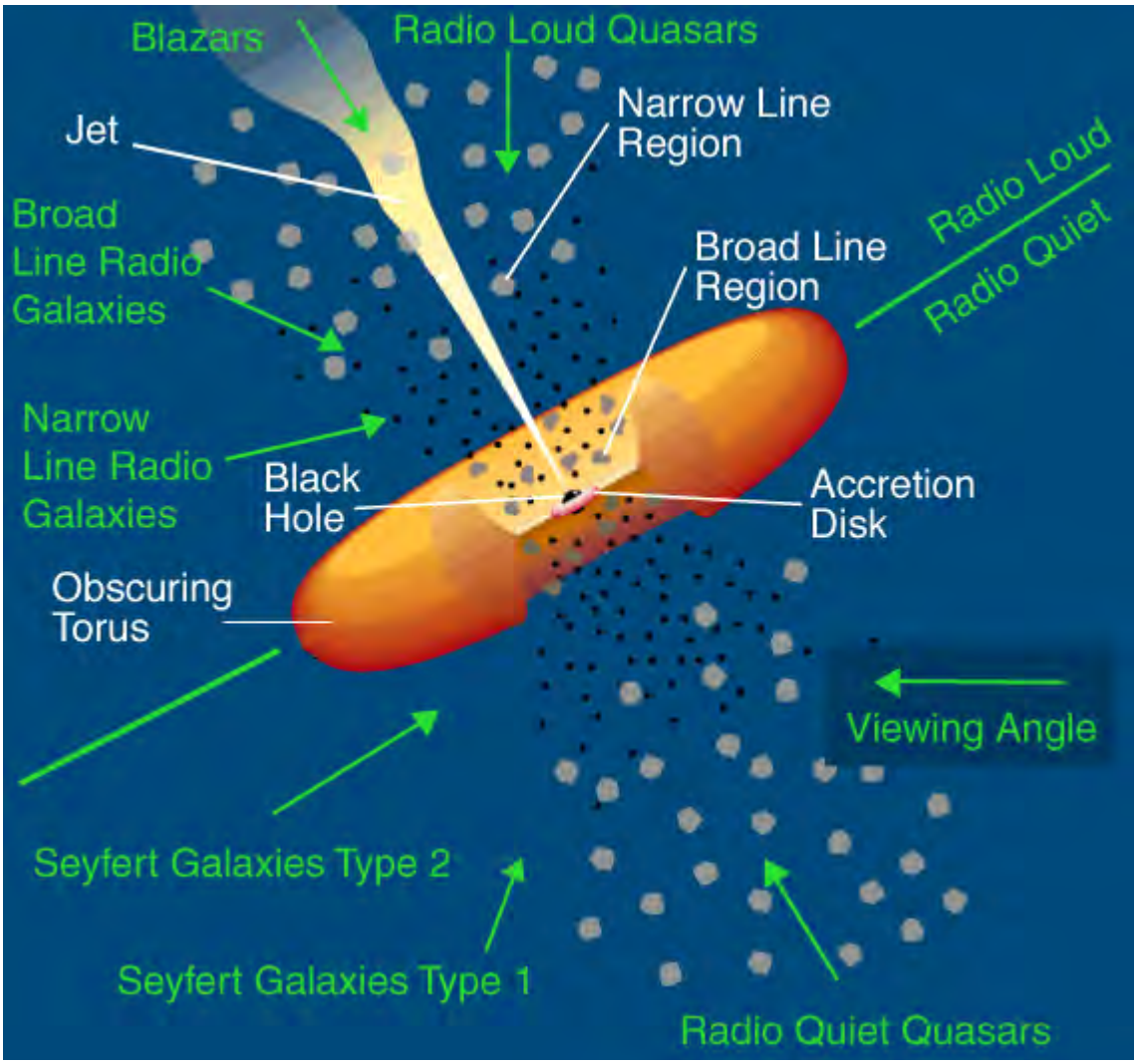

Fig. 1.1 Schematic view of the AGN unification model. Figure adopted from (Urry & Padovani, 1995) and copied from https://www.cta-observatory.ac.uk/?page_id=1196.

difference between the many AGN phenomena by differences in viewing angle (e.g. Antonucci, 1993; Urry & Padovani, 1995; Elvis, 2000; Netzer, 2015). A simplified sketch of the structure of AGN under the unification picture is given in Fig. 1.1.

Within this framework, the central engine of the AGN consists of a supermassive black hole (10^6–$10^{10} M_\odot$) surrounded by an accretion disk formed by matter infalling from the galaxy on its way to the black hole. Surrounding the accretion disk is a region of hot, fast moving, and dense gas which emits the broad emission lines (widths $\geq 10^3$ km s^{-1}) characteristic of Type 1 AGN spectra. The Broad Line Region (BLR) has a size on the order of light days or weeks. Gas in the BLR is almost certainly photoionized by the ultraviolet emission from the accretion disk since it is observed to respond to variations in the continuum luminosity. The electron density of the broad line region gas is probably somewhere around 10^{10} cm^{-3} and forbidden lines are therefore collisionally suppressed

(Peterson, 1997). The temperature of the broad line region is $\sim 10^4$ K which would indicate a thermal broadening along the line of sight $\sim 10\,\mathrm{km\,s^{-1}}$ (Peterson, 1997). Since the broad emission lines are observed to have widths of $10^3\,\mathrm{km\,s^{-1}}$ or more, this indicates that they are not thermally broadened. Instead, it is assumed that their width is due to Doppler broadening because the orbits of the broad line region gas are dominated by the graviational influence of the black hole. This observation and assumption is necessary for black hole mass measurements in AGN based on measuring broad emission line widths (§ 1.2.2 and § 1.2.4). The structure and kinematics of the BLR is poorly known, although significant advances are being made in this field (see § 1.2.2). Surrounding the BLR is a dusty region with an inner boundary marked by the dust sublimation radius. This region is sometimes referred to as the *torus*, although newer studies suggest that the region is circumnuclear and clumpy (e.g., Hönig et al., 2010). The dusty region emits reprocessed continuum emission in the infrared and its inner boundary is possibly a smooth transition from the BLR marked by the dust sublimation radius. Further out is the narrow line region comprised of cool and low density gas from which the narrow emission lines in AGN spectra are emitted. Narrow emission lines have velocities of a few hundred $\mathrm{km\,s^{-1}}$ owing to the fact that they originate in gas far from the central black hole (parsec scale) and therefore experience a significantly smaller graviational potential than the broad emission line gas.

In the unification scheme, the viewing angle determines whether we observe a Type 1 or Type 2 AGN. Type 1 AGN are seen almost face-on such that we have a clear view of the continuum source and the BLR, and therefore the broad emission lines emitted from the latter. Type 2 AGN are seen at larger inclinations and edge on, and the dusty region (torus) surrounding the BLR blocks our view of the central region and therefore the broad emission lines and the AGN continuum.

The idea of unification clearly has its merits as a simple concept that is very useful when trying to compare seemingly very different phenomena. On the other hand, it is a too simplistic picture to explain all the differences between the different AGN types. For example, there is now a growing amount of the so-called *changing look AGN* that changes between being Type 1 and Type 2 AGN (e.g., Denney et al., 2014; LaMassa et al., 2015). Since the viewing angle does not change, some other parameter, such as for example the luminosity, must have an impact on the type of AGN we observe. The luminosity changes in response to changes in the mass accretion rate (Equation 1.12), which again is linked to our understanding of the AGN phenomenon. For example, the black hole at the centre of the Milky Way is not considered to be an AGN even though it accretes matter, but at a very low mass accretion rate.

1.1.2 The central engine

The broad emission lines are observed to vary in luminosity in response to the AGN continuum emission, demonstrating that they most likely are photoionized by emission from the accretion disk. The same response is observed for the narrow emission lines, albeit on much longer timescales (Peterson et al., 2013). This means that the central engine consisting of the black hole and the

accretion disk either directly or indirectly is the source of most of the emission we observe in AGN and therefore an integral part of understanding AGN physics. I therefore briefly outline their important properties that provide the background for the discussions later in this thesis.

The black hole

Black holes are the most compact objects in nature and display the ultimate victory of gravity. In a black hole, matter is in such a compact form that not even light can escape from its event horizon. A black hole has three physical properties: its mass (M_{BH}), its charge (Q), and its spin (a^*). For the discussion here, we will ignore the spin and charge. A non-rotating black hole is called a Schwarzschild black hole. Its size can be defined by its Schwarzschild radius R_S (also called the event horizon)

$$R_S = 2\frac{GM_{BH}}{c^2} \tag{1.1}$$

where G is the gravitational constant and c is the speed of light. A black hole is an object that is smaller than its Schwarzschild radius. The gravitational force from a black hole with mass M_{BH} acting upon a particle with mass m at a distance R is

$$F_{grav} = \frac{GM_{BH}m}{R^2} \ . \tag{1.2}$$

For a particle on a stable circular orbit, the centripetal force ($F_{cent} = (mV^2)/R$) has to balance with the gravitational force from the black hole. As a consequence, the velocity of a test particle on a stable circular orbit can be determined as

$$V_{circ} = \left(\frac{GM_{BH}}{R}\right)^{1/2} \ . \tag{1.3}$$

This means that objects closer to the black hole must have a larger circular velocity than objects farther away because gravity decreases with the distance squared.

A black hole in the centre of a galaxy also has a sphere of influence (R_h). This is the region where the black hole gravitational potential is larger than that of the host galaxy. The sphere of influence of the black hole must be resolved in order to probe the mass of the black hole without any contamination from the mass of the stars. The sphere of influence is defined as (e.g., Gültekin et al., 2009)[1]

$$R_h = \frac{GM_{BH}}{\sigma_*^2} \tag{1.4}$$

where σ_* is the velocity dispersion of the stars in the host galaxy bulge. The gravity, size, and sphere of influence of a black hole depends intimately on its mass. To understand black holes and their impact on their surroundings, it is imperative to determine their masses.

[1]The sphere of influence can also be defined as the radius in which the enclosed mass in stars is half the mass of the black hole.

The accretion disk

As matter is being accreted onto the central black hole, it forms an accretion disk where it can get rid of residual angular momentum through viscous processes (Peterson, 2008). In its simplest form, the accretion disk is considered to be geometrically thin and optically thick and radiates locally as a blackbody (Shakura & Sunyaev, 1973). When matter is accreted, half of its change in potential energy is released as radiation and the other half goes to heating up the gas. The luminosity L is then

$$L = \frac{GM\dot{M}}{2R} = 2\pi R^2 \sigma_{SB} T^4 \tag{1.5}$$

where M is the mass of the object onto which matter is accreted (in this case, the central black hole), $\dot{M}$ is the mass accretion rate, R is the distance from the central object to the gas, σ_{SB} is the Stefan-Boltzmann constant, and T is temperature of the disk. The temperature of the disk can then be estimated as

$$T(R) = \left(\frac{GM\dot{M}}{4\pi R^3 \sigma_{SB}} \right)^{1/4} . \tag{1.6}$$

The peak of the emission is typically around $\sim$1000 Å with a blackbody peak emission temperature of $T \sim 5 \times 10^5$ K. The temperature of the accretion disk at a given radius increase with mass and mass accretion rate, although only slightly as seen from Equation 1.6.

The radiation from the accretion disk will generate a pressure that acts upon the infalling gas. If the system is stable (i.e., the AGN does not immediately disintegrate), the inwards gravitational force must be at least as large as the outwards radiation pressure. Considering the gas to be fully ionized hydrogen, the gravitational force upon an electron-proton pair with masses m_e and m_p, respectively, is

$$F_{grav} = \frac{GM(m_p + m_e)}{R^2} \simeq \frac{GMm_p}{R^2} \tag{1.7}$$

Equating this to the outwards force due to radiation pressure

$$F_{rad} = \sigma_e \frac{L}{4\pi R^2 c} \tag{1.8}$$

where σ_e is the Thompson cross section for a photon to interact with an electron we get

$$\frac{\sigma_e L}{4\pi c R^2} = \frac{GMm_p}{R^2} . \tag{1.9}$$

Solving this for the luminosity L gives

$$L_E = \frac{4\pi G c m_p}{\sigma_e} M \sim 1.26 \times 10^{38} \frac{M}{M_\odot} \text{ ergs s}^{-1} . \tag{1.10}$$

This equation defines the Eddington limit which is the maximum allowed luminosity for a stable and spherically accreting system. There is a fundamental issue related to mass determinations of black holes in AGN arising from the fact that the outwards force due to radiation pressure (Eqn. 1.8) and the

graviational force acting upon a particle (Eqn. 1.7) both depend on the distance from the black hole as R^{-2}. This makes it difficult to separate them from each other and this could possibly lead to too low black hole mass estimates if there is a significant radiation pressure acting upon the gas in the BLR which we use to measure the enclosed mass and thus the black hole mass. This issue is discussed further in § 1.2.2. Another impact of the radiation pressure is that when it is high, it could possibly prevent gas from being accreted to the black hole, thereby having a negative impact on the black hole growth.

From Eqn. 1.10 it is common to define an Eddington mass M_E as

$$M_E = 8 \times 10^5 L_{44}\, M_\odot \tag{1.11}$$

which is the minimum mass required to balance the radiation pressure for a source of luminosity L given in units of 10^{44} ergs s^{-1}, typical of a Seyfert galaxy. This means that for a typical Seyfert galaxy, the black hole should have a minimum mass of $8 \times 10^5 M_\odot$, and for a quasar with a luminosity of 10^{47} ergs s^{-1}, we get $M_{BH} \geq 8 \times 10^8 M_\odot$.

The bolometric luminosity of the accretion disk comes from conversion of mass to energy E. This is done with a certain efficiency η such that the luminosity fueled by accretion of matter is

$$L_{bol} = \frac{dE}{dt} = \eta \dot{M} c^2 \tag{1.12}$$

where c is the speed of light.

1.2 Determination of black hole masses

Supermassive black holes are found to be present in the center of most, if not all, massive galaxies (Kormendy & Richstone, 1995; Magorrian et al., 1998; Ferrarese & Ford, 2005; Kormendy & Ho, 2013), and seem to be a natural part of the galaxy formation and evolution process (e.g., Di Matteo et al., 2005; Hopkins et al., 2007). The mass of the central supermassive black hole is observed to correlate with properties of its host galaxy bulge in both quiescent and active galaxies, such as bulge mass (Magorrian et al., 1998; Wandel, 1999a; Marconi & Hunt, 2003a; Bentz et al., 2009a), luminosity (McLure & Dunlop, 2001; Marconi & Hunt, 2003a; Bentz et al., 2009a; Gültekin et al., 2009), stellar velocity dispersion (σ_*; Ferrarese & Merritt, 2000a; Gebhardt et al., 2000a,b; Ferrarese et al., 2001; Tremaine et al., 2002; Nelson et al., 2004; Onken et al., 2004; Gültekin et al., 2009), and stellar concentration index (Graham et al., 2001; Graham & Driver, 2007; Savorgnan et al., 2013). These correlations are somewhat surprising, considering that the gravitational sphere of influence of the black hole (Eqn. 1.4; typically a few to tens of parsecs) is very small compared to the host galaxy bulge (typically thousands of parsecs) (e.g., Gültekin et al., 2009; Ferrarese & Ford, 2005). Nevertheless, these correlations has led to the idea that the supermassive black hole and its host galaxy co-evolve (see for example Kormendy & Ho (2013) for a discussion of this subject).

In the most simplistic model, either the black hole, the stars, or both, are responsible for some kind of feedback that will regulate the growth of the other component. For example, stellar feedback can be responsible for driving gas to the centre of the galaxy, thereby fuelling the black hole activity. However, stellar feedback can possibly also disrupt the inflow of gas to the central region (e.g., Anglés-Alcázar et al., 2017) and star formation can consume a significant fraction of the available gas mass, thereby limiting the long-term mass supply for black hole growth. On the other hand, feedback from the black hole in the form of for example radio jets can compress gas in the galaxy bulge, thereby triggering star formation, but at the same time it has the potential to heat the same gas and disperse it, halting star formation. The interplay between the star formation and the black hole is therefore expected to be complex (e.g., Anglés-Alcázar et al., 2017).

Several lines of observational evidence supports the idea of AGN feedback. This is observed in the form of quasar disk winds (e.g. Tombesi et al., 2015), molecular outflows from the nucleus (e.g. Aalto et al., 2016; García-Burillo et al., 2016), galactic outflows driven by the AGN (e.g. Wylezalek & Zakamska, 2016), and radio jets and lobes (e.g. Bridle & Perley, 1984). Simulations have also shown that AGN feedback can be powerful enough to shut down star formation (e.g. Di Matteo et al., 2005, 2008), ultimately driving the observed correlations between black hole mass and host galaxy bulge properties. Yet, from an observational point of view, it can be difficult to distinguish whether the AGN or star formation is responsible for a given kind of feedback and to what extent. Also, some studies claim that the observed correlations between black hole mass and host galaxy bulge parameters are driven simply by hierarchical galaxy merging processes (e.g. Peng, 2007; Jahnke & Macciò, 2011) or in the case of the $M_{BH} - \sigma_*$ relationship, by selection effects (Lauer et al., 2007; Batcheldor, 2010). Even if the latter is the case, AGN feedback may still play a role in shaping the exact form of the $M_{BH} - \sigma_*$ relationship (Volonteri & Natarajan, 2009).

One key component of understanding the relationship between the black hole and its host galaxy is to determine the mass of the black hole to a high accuracy. The mass is the most fundamental property of the black hole and it governs most of the physics of the AGN (§ 1.1). Through its gravitational pull, it sets the size, structure, and temperature of the accretion disk, regulates the amount of gas that is accreted onto it, and sets the scale for the energy output from the AGN (§ 1.1). In short, accurately measuring the mass of the central supermassive black hole in AGN is necessary to expand our knowledge of AGN physics and its possible impact on galaxy formation and evolution. Besides this, tracing the black hole population through time helps us to understand how black holes form and grow and allows us to establish possible limits for black hole growth that will also help constrain theoretical models of how massive black holes form and grow (Johnson & Haardt, 2016; Latif & Ferrara, 2016). Below, I will briefly go through some of the techniques that can be used to measure masses of supermassive black holes in the centers of galaxies.

1.2.1 Stellar and gas dynamics

Measurements of black hole masses can be based on stellar or gas dynamical modeling of observed emission and absorption spectra. For these models to work, it is necessary to assume a particular dark matter distribution and a constant mass-to-light (M/L) ratio. Furthermore, the gravitational potential of the galaxy bulge has to be assumed to be axi-symmetric, although this assumption can be relaxed using newer dynamical models based on integral field spectroscopy (e.g. Cappellari et al., 2011). Stellar dynamical models rely on measurements of the line-of-sight velocity of stars at different positions of the host galaxy using stellar absorption lines. For gas dynamical models, the central gas velocity is probed by nebular emission lines instead. Observations of stellar and gas dynamics require spatially resolved long-slit or integral field spectroscopy and can only be applied to relatively nearby galaxies within $\sim$300 Mpc (e.g., Ferrarese & Ford, 2005). These methods can be applied to active and quiescent galaxies alike, but are in practice often difficult to use for most active galaxies owing to the strong nuclear glare. First, in order to minimize the gravitational influence of the host galaxy on the black hole mass measurements, it is necessary to probe the stellar or gas emission lines very close to the galaxy centre. The closer, the more accurate the black hole mass measurement. For AGN, the stellar absorption and gas emission lines are difficult to probe close to the black hole since the strong light from the AGN itself dominates and washes out these features. Another challenge is that only few AGN are nearby enough that the spatial resolution is large enough for our current instruments to resolve the gravitational sphere of influence of the black hole. As a consequence, other techniques have been developed to allow black hole masses to be measured in active galaxies. These are reverberation mapping (§1.2.2) and single-epoch mass estimates (§1.2.4).

1.2.2 Reverberation mapping

A distinct feature of AGN is their intrinsic variability, observed both in the strength of the continuum and the broad emission lines. This particular feature allows for the technique of reverberation mapping (Blandford & McKee, 1982; Peterson, 1993) in order to estimate black hole masses in AGN. In this case, the demand for high spatial resolution, as required by stellar and gas dynamics, is replaced by high temporal resolution instead. The broad emission lines are observed to vary in response to the continuum emission but delayed in time. This time delay (τ) is interpreted as being due to the light travel time of the ionizing continuum photons, originating from the accretion disk, to the BLR gas. The distance from the accretion disk to the BLR, R_{BLR}, can thus be established by measuring this time delay ($R_{BLR} = c \times \tau$).

Reverberation mapping establishes the time delay by cross-correlating a series of observations of the continuum and emission line luminosity with a daily cadence over a campaign lasting from a few weeks to several months. Reverberation mapping thus provides a *responsivity weighted distance* to the BLR gas that responds to continuum variations. There are several techniques for cross-correlating the continuum and emission line light curves, but a discussion of those is beyond the scope of this work.

Two things have to hold true for reverberation mapping to work. First, what we wish to measure is the distance from the black hole to the BLR, but what we actually measure is the distance from from the accretion disk to the BLR. We therefore have to assume that the size of the accretion disk is small compared to the distance to the BLR, although this assumption has been challenged by recent observations of the accretion disk size in NGC 5548 (Edelson et al., 2015; Fausnaugh et al., 2016). Future work will have to address this issue and how it might influence results from reverberation mapping. Second, the reprocessing time in the BLR has to be small compared to the light travel time from the accretion disk to the BLR such that the measured time lag reflects the size of the BLR and not the photoionisation physics in the BLR. This assumption appears to be good (see e.g., Peterson, 1997).

Assuming that the motion of the gas in the BLR is dominated by the gravitational potential of the black hole and that the width of the broad emission lines is due to Doppler broadening, a virial mass of the black hole can be established. If the gas in the BLR is gravitationally bound and moving on isotropic random orbits, then the mass of the black hole (M_{BH}) can be derived using the virial theorem[2]. This is done by combining R_{BLR} with a measure of the gas velocity using the equation

$$M_{BH} = f\frac{\Delta V^2 R_{BLR}}{G} \tag{1.13}$$

where G is the gravitational constant, ΔV is the virial velocity of the BLR gas that responds to continuum variations, and f is a scaling factor that accounts for our ignorance about the inclination, structure, and kinematics of the BLR. The average f-factor is of the order unity, based on comparing the M_{BH}-σ_* relationship for quiescent and active galaxies (Onken et al., 2004; Collin et al., 2006; Woo et al., 2010; Graham et al., 2011; Park et al., 2012; Grier et al., 2013). The exact value of the average f-factor depends on the sample of objects included in the particular study and the specific parameterization used to measure the emission line width.

The velocity dispersion of the gas, ΔV, is measured from the width of the broad emission lines in the variable part of the AGN spectrum (i.e., the rms spectrum). This is the same gas for which the responsivity weighted distance is determined with the reverberation mapping technique by cross-correlating the continuum and emission line variations.

For Equation 1.13 to be valid, it is necessary to assume that the BLR gas is virialized, from which it follows that $R_{BLR} \propto \Delta V^{-2}$. Studies comparing observations of the same object at different epochs or using different emission lines confirm this assumption (Peterson & Wandel, 1999, 2000; Onken & Peterson, 2002; Peterson et al., 2004). There is also a good correspondence between masses measured by reverberation mapping and using stellar and gas dynamics (Onken et al., 2014; Peterson, 2014; Bentz et al., 2016). It is not clear which of these methods that actually give the most accurate black hole masses when used on active galaxies, but it is reassuring that they seem to agree.

[2]The same result can be obtained by equating the centripetal and gravitational force of a test particle in a circular orbit around the black hole as is done in Equation 1.3. This gives $\frac{mV^2}{R} = \frac{GM_{BH}m}{R^2} \Rightarrow M_{BH} = \frac{RV^2}{G}$.

Marconi et al. (2008) have argued for a modification of Equation 1.13 in order to include the possible effect of radiation pressure (Eqn. 1.8) on the dynamics of the BLR gas. If radiation pressure is important, and if it is not accounted for, it would lead to underestimated black hole masses (Krolik, 2001). The role of radiation pressure is difficult to determine since it has a direction and geometrical dilution of $1/r^2$, similar to gravity (Eqn. 1.7). Its influence on black hole mass estimates is debated, but it has been argued that it probably is small, except in high Eddington ratio sources such as Narrow Line Seyfert 1 sources (e.g., Netzer & Marziani, 2010; Peterson, 2014). For the remainder of this work, we will assume that radiation pressure has a negligible effect.

The uncertainty of the reverberation mapping mass measurements is $\sim$0.4 dex, estimated from the scatter of the reverberation based mass estimates around the M_{BH}-σ_* relationship (Onken et al., 2004; Woo et al., 2010). The way to reduce this uncertainty is to establish the f-factor from Equation 1.13 in individual objects by establishing the orientation, geometry, and dynamics of the BLR. Efforts in this direction are ongoing using either dynamical modeling of the BLR (Brewer et al., 2011; Pancoast et al., 2011, 2012, 2014) or velocity-delay maps that measure the time delay as a function of Doppler velocity width across the emission line (Bentz et al., 2010; Grier et al., 2013; Kollatschny et al., 2014; Skielboe et al., 2015).

Bentz & Katz (2015) compiled a database of all the existing reverberating mapping black hole masses. As of now, this database contains mass estimates for 62 AGN, with only two of these at redshifts beyond $z = 0.3$. The fact that only two sources are at $z > 0.3$ is because reverberation mapping of high redshift AGN requires observational campaigns to run over the course of years or even tens of years (Kaspi et al., 2007) which has not been practical for most campaigns this far. There are two reasons for this. First, due to cosmic time dilation, the observed timescale of the variations increase. Furthermore, the size of the accretion disk and BLR, and thereby the timescale for variations, increase with AGN luminosity which means that for high luminosity objects, which are more easily observable at high redshifts, the timescale for variations can increase to several months or years. In addition, the relative amplitude of the variations decrease with luminosity, making them more difficult to detect and the time delays difficult to define and measure for high redshift sources (Kaspi et al., 2007).

This high demand for observing time makes high redshift reverberation mapping impractical in most cases. As a consequence, techniques to estimate black hole masses have been developed based on a single spectrum of an AGN by using the empirical correlation between BLR radius and AGN luminosity (the *R-L* relationship; § 1.2.3). These methods allow for bulk measurements of black hole masses based on for example spectroscopic survey data and are described in § 1.2.4.

1.2.3 The R-L relationship

Reverberation mapping have provided BLR sizes for a large sample of AGN (Bentz & Katz, 2015). This, combined with the corresponding luminosity measurements, have spurred the detection of a tight relationship between the size of the broad line region for the Hβ line, and the optical continuum

luminosity measured at 5100 Å in the AGN rest-frame. This correlation is known as the radius-luminosity, *R-L*, relationship and has the form $R \propto L^{0.5}$ (Kaspi et al., 2000, 2005, 2007; Bentz et al., 2006, 2009b, 2013). The latest version of the relationship spans approximately four orders of magnitude in 5100 Å luminosity and approximately three orders of magnitude in BLR size (Bentz et al., 2013).

Interestingly, a relationship of the form $R \propto L^{1/2}$ can be predicted from simple photo-ionization arguments (see for example Peterson, 1997; Bentz et al., 2013). The line emission from an ionized gas is controlled by the electron number density n and ionization parameter

$$U = \frac{Q(H)}{4\pi R^2 nc} \tag{1.14}$$

where $Q(H)$ is the number of Hydrogen ionizing photons emitted per second from the central source, R is the distance from the ionizing source, and c is the speed of light. Since AGN, to first order, have almost similar emission line ratios and equivalent widths, the product $U \times n$ can be assumed to be the same for all AGN BLRs. If the number of ionizing photons $Q(H)$ is assumed to be proportional to the ionizing AGN luminosity L_{5100}, then we get that $R \propto L^{1/2}$ (see also Kilerci Eser et al., 2015, for a more thorough discussion of this subject). In practice, the ionizing luminosity is mesured as the monochromatic luminosity at 5100 Å. This result, obtained using a rather naïve line of reasoning and a very simplistic view of AGN physics, is in remarkable agreement with slope of the observed relationship.

Dust can possibly play a role in the physical explanation for the $R-L$ relationship by setting the size of the BLR. It has been argued that the dust sublimation marks the outer boundary of the BLR (e.g., Suganuma et al., 2006; Goad et al., 2012), and possibly also the inner edge of the dusty torus of the AGN unification model. If this is true, then an increase in the ionizing photons from the central source will destroy dust grains, causing the outer edge of the BLR to move outwards. Conversely, a decrease in ionizing flux from the central source will move the outer edge of the BLR inwards by allowing more dust grains to form and possibly migrate inwards.

Bentz et al. (2013) find the scatter in the *R-L* relationship for Hβ to be $\sim$0.19 dex, which they further reduce to $\sim$0.13 dex when excluding two objects from the sample for which the measured time delays have low accuracy. Peterson (2010) argue that the intrinsic scatter might be as low as $\sim$0.11 dex. Bentz et al. (2013) also point out that the main source of scatter in the relationship is due to uncertain distances to the AGN host galaxies that do not follow the Hubble flow. Such accurate distance measurements might allow for the scatter to be reduced below 0.11 dex. Use of the UV luminosity will similarly decrease the uncertainty (Kilerci Eser et al., 2015).

In the context of AGN black hole mass measurements in AGN, the *R-L* relationship has proven to be very powerful. Since it allows for an estimate of the BLR radius from a single AGN spectrum, it has enabled the so-called single-epoch mass estimates that estimate the black hole mass using a single AGN spectrum (see § 1.2.4 below). Another interesting consequence is that AGN can be transformed into standard candles by inverting the relationship and use reverberation mapping to measure the BLR

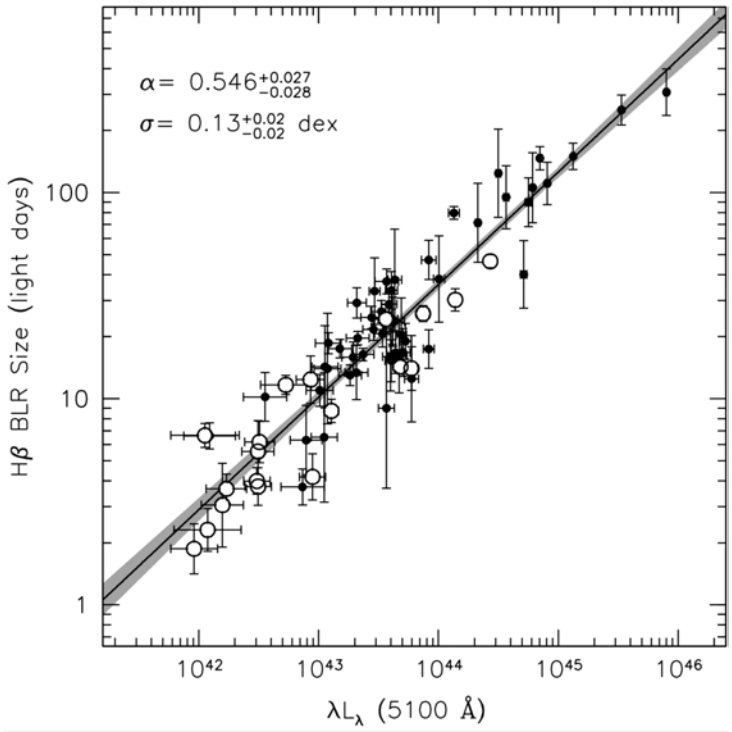

Fig. 1.2 Hβ BLR radius vs. the 5100 Å AGN luminosity. The solid line is the best fit to the data and the gray-scale region shows the range allowed by the uncertainties on the best fit. Figure from (Bentz et al., 2013).

size and then infer the intrinsic AGN luminosity from this measurement (Watson et al., 2011; Kilerci Eser et al., 2015). This allows distances up to high redshifts to be measured using AGN and provide an alternative method to supernovae as standard candles. In practice, this method is feasible to use up to redshifts $z \sim 4$ as it is difficult to observe suitable emission lines within a reasonable time frame above this redshift (Watson et al., 2011).

To reach high redshifts, *R-L* relationships for UV lines such as Mg II and C IV are important since these emission lines move into the optical regime where most ground based spectral data are available for emission line width measurements. Kaspi et al. (2007) attempted high redshift reverberation mapping for a handful of objects using the C IV line and calibrated a *R-L* relationship using these data. The relationship spans almost eight orders of magnitude in 1350 Å luminosity and has a slope of $\sim$0.5, consistent with the slope for the Hβ relationship within the uncertainties. The scatter in the relationship is $\sim$0.19 dex (Kaspi et al., 2007). Because reverberation mapping of high redshift sources is very expensive in term of observing time, the amount of BLR sizes measured using reverberation mapping of the C IV line remains small[3]. Therefore, the preferred *R-L* luminosity relationship to use for single epoch black hole mass estimates is that for Hβ because it is more well determined and constrained.

1.2.4 Single-epoch mass estimates

The *R-L* relationship allows the size of the BLR to be estimated from a measurement of the AGN continuum luminosity in a single spectrum. Combined with a measure of the BLR gas velocity from a measurement of the broad emission line width in the same spectrum, this allows for the black hole mass to be estimated using Equation 1.13. This technique is called mass scaling relations or single-epoch mass estimates. They are extremely powerful as they allow mass estimates of large samples of objects to be made in a very efficient way and are almost ideally suited for use on large spectroscopic samples of AGN spectra from for example the Sloan Digital Sky Survey (SDSS) Quasar Catalog (Schneider et al., 2010) or the 2dF QSO Redshift Survey (Croom et al., 2004). On the other hand, care has to be taken when using these methods since they are statistical in nature and the uncertainty for an individual AGN therefore can be large.

The mass scaling relationships have been calibrated for the broad Hα and Hβ line in the optical regime and the broad Mg II and C IV line in the UV (e.g., McLure & Jarvis, 2002; Vestergaard, 2002; McLure & Dunlop, 2004; Greene & Ho, 2005b; Kollmeier et al., 2006; Vestergaard & Peterson, 2006; McGill et al., 2008; Vestergaard & Osmer, 2009; Shen & Liu, 2012; Park et al., 2017). Using all of these relationships, single-epoch mass estimates can be made for AGN up to $z \sim 4.5$ using optical spectra from for example the SDSS. The single-epoch relationships are therefore ideally suited to trace the evolution of the black hole population in AGN and its role in galaxy formation and evolution through cosmic time.

[3]This might change in the future if surveys such as The Dark Energy Survey and the Large Synoptic Survey Telescope perform high redshift reverberation mapping.

Since the width of the broad emission line is measured in a single spectrum of the AGN, we have no temporal information on variations in the emission. Therefore, it is not possible to disentangle the contribution to the emission line originating from BLR gas that responds to continuum variations from the constant emission component that does not respond to continuum variations. This is an issue since the BLR size is measured from the variable part of the gas and there is no guarantee that this is co-spatial with the constant component of the gas. As a result, the constant component contaminates our measure of the emission line width. Consequently, the single epoch mass estimates will always be an approximation to the reverberation based masses. Finding a reliable way to measure the emission line width, as I do in this work, is a first step to resolve this issue.

The uncertainty of the single-epoch mass estimates is a factor of $\sim$2.5-3.5 (Vestergaard & Peterson, 2006; Vestergaard & Osmer, 2009). In addition to this, the single-epoch mass estimates are calibrated using the reverberation mapping database which suffers from its own uncertainty of $\sim$0.4 dex. Combined, this gives an absolute statistical uncertainty of a factor $\sim$3.5-4.0 for the single-epoch mass estimates. However, the study of Kelly et al. (2010) strongly indicate that the actual uncertainties are much lower – of order 0.2 dex. It is worth noting that if the single-epoch mass estimates are applied to individual objects, the uncertainty is thought to be as large as an order of magnitude.

1.2.5 Improving the AGN black hole mass estimates

There is a wide variety of factors that contribute to the uncertainty of the single-epoch mass estimates. Here, I will give a very brief overview and more details are given in Chapter 2. Roughly, the sources of uncertainty when using the single-epoch mass estimates include: 1) the intrinsic variability of the AGN, 2) the determination of the BLR size, and 3) the determination of the BLR velocity field.

The continuum and broad line emission in a single snapshot spectrum of an AGN is not contemporaneous in the sense that the observed broad line emission is reprocessed continuum emission from an earlier epoch. This means that the line width of the BLR emission lines that we measure is actually not precisely the one corresponding to the current continuum luminosity. For mass estimates based on a single spectrum of an AGN, this will always be an issue. Fortunately, this effect seems only to add scatter of 0.1 dex or less to the mass estimates (Wilhite et al., 2007; Denney et al., 2009). For higher redshift sources where L is high, the relative variability amplitude is low (Vanden Berk et al., 2004; Kaspi et al., 2007), and the variability timescale is increased, this problem is further reduced.

As the size of the BLR is inferred from the *R-L* relationship, the uncertainty in determining R_{BLR} depends directly on the scatter of the *R-L* relationship. As already outlined in §1.2.3, the scatter of the *R-L* relationship is relatively low ($\sim$0.11-0.13 dex). The contribution to the uncertainty of the black hole mass estimate is further diminished since L only enters the mass calculation to the power of $1/2$ through the *R-L* relationship.

This also means that the main contribution to the uncertainty of the single-epoch mass estimates is that originating from our determination of the BLR velocity field. Since this enters the mass calculation squared, any uncertainty related to this measurement is bound to have a rather large impact

on the final uncertainty of the mass estimate. The issues addressed below can have a negative impact on both reverberation mapping and single-epoch mass estimates as well as any study concerned with measuring gas velocities from emission lines.

We can further break down those factors that impact our ability to get an accurate estimate of the velocity of the BLR gas. First, in order to measure the width of the broad emission line, it has to be isolated from the remaining emission components in the AGN spectrum. The process used for this purpose is referred to as spectral decomposition. The specific choice of spectral decomposition model matters for the final mass estimate. For example, Denney et al. (2009) show that failure to remove the narrow line component for Hβ could lead to significantly biased mass estimates by up to an order of magnitude. Vestergaard et al. (2011) show that using two different decomposition methods can induce a scatter in the measured line widths of $\sim$20% for an average line width even at S/N $\geq 20\,\mathrm{pixel}^{-1}$. The quality of the data is also an issue. For example, Mejía-Restrepo et al. (2016) show that for survey quality data (S/N $\leq 10\,\mathrm{pixel}^{-1}$), the line widths can be biased by up to 0.2 dex because it is difficult to estimate the underlying continuum level with high confidence. The cases mentioned here are just a few examples of how a specific choice of spectral decomposition method and data quality can affect the final mass estimates.

Second, there is a lot of technical difficulties related to measuring the broad emission line width as a proxy for the velocity of the BLR gas. These issues are summarized here and discussed in detail in Chapter 2. When the spectrum has been decomposed, the width of the broad emission line has to be measured. This requires line limits to be imposed in order to constrain the line profile and to avoid including extraneous emission in the line width measurement. This issue is not straightforward and, if done in-correctly, can lead to biases in the line measurements as I address in more detail in Chapter 2. After this, a specific line parameterization must be chosen to represent the width of the broad emission line. The different line parameterizations have different strengths and weaknesses and the specific choice can have a large impact on the accuracy to which the black hole mass can be estimated, especially if the spectral S/N is low as I show in this thesis. In Chapter 2 I introduce the different line parameterizations used in this work and their individual strengths and weaknesses.

Since many studies use data from large spectroscopic surveys for mass estimates in AGN (e.g., Vestergaard, 2004; Vestergaard et al., 2008; Kelly et al., 2010; Shen et al., 2011; Kelly & Shen, 2013; Dai et al., 2014; Schulze et al., 2015), the issue of spectral S/N is of particular interest. In general, and by construct, survey data contain spectra of many objects, but of relatively low spectral quality. For example, the SDSS Data Release 7 Quasar Catalog contains spectra of more than 100,000 AGN, but with a median S/N $< 10\,\mathrm{pixel}^{-1}$ (see Figure 1.3). Such low spectral S/N has already been shown by for example Denney et al. (2009) to impact the accuracy of the final mass estimate. Previous work in this field have focused on only a few objects, a few line parameterizations, or a few S/N ratios. What is missing is therefore a comprehensive comparison of the accuracy and precision of the different line width measures as a function of a wide range of S/N values on a sample of spectra representing the general properties of the observed AGN population. With this in hand, a full comparison of the

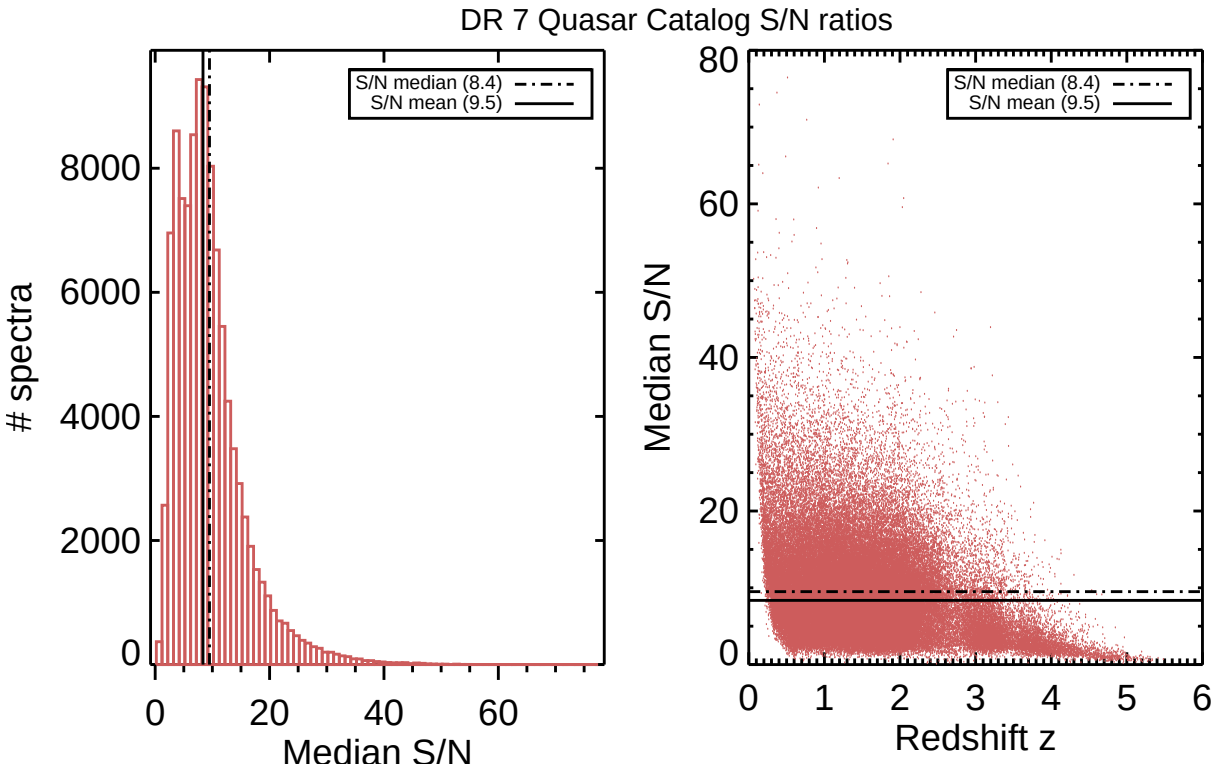

Fig. 1.3 Median S/N of the DR7 Quasar Catalog. Adopted from Jensen (2012).

limitation of each of the line parameters is possible. I present this work in Chapters 2 and 3 for the broad Hβ, Mg II, and C IV lines.

Absorption features are often found imposed upon the broad C IV emission line and are often associated with outflows from the AGN. The absorption features are divided into two categories based on their width. Broad Absorption Lines (BALs) have FWHM $>$ a few 1000 km s^{-1} while Narrow Absorption Lines (NALs) have FWHM $\leq$ 300 km s^{-1}. The narrow C IV absorption lines are detected with an almost even distribution of blueshifts up to 70,000 km s^{-1}, and their equivalent widths are generally below 2 Å and more than half have equivalent widths below 0.2 Å (Perrotta et al., 2016). If these absorption features go unrecognized either due to low spectral resolution, low S/N , or both, they can have a negative effect on the accuracy and precision of the line measurements on which the black hole mass estimates are based. We perform a study of the consequences this can have for mass estimates based on the broad C IV emission line in Chapter 4.

1.3 The potential link between star formation and black hole activity in AGN

1.3.1 Co-evolution between the AGN and star formation in its host galaxy

One outstanding question is the possible co-evolution of the central black hole in an AGN and the star formation in its host galaxy (bulge). In particular, possible feedback mechanism from the black hole and recent and ongoing star formation can regulate and even shut down the black hole growth and/or active star formation. Observations between the mass of the black hole in massive galaxies and properties of its host galaxy support this picture (See § 1.2 above). Several theoretical studies have suggested that black hole feedback can regulate the growth of stars in its host galaxy (e.g., Di Matteo et al., 2005, 2008; Hopkins & Quataert, 2010; King & Pounds, 2015). Observations have also shown that the black hole indeed delivers feedback in many different ways and on many physical scales throughout and beyond its host galaxy (e.g., McNamara & Nulsen, 2012; Tombesi et al., 2015; Aalto et al., 2016; García-Burillo et al., 2016; Wylezalek & Zakamska, 2016). The exact nature and amount of feedback is currently highly debated.

The central black hole is fueled by accretion of gas supplied from gas reservoirs in its host galaxy. Transporting this gas to vicinity of the black hole (sub-pc scale) from the host galaxy (>kpc scale) requires a significant loss of angular momentum (Alexander & Hickox, 2012). Simulations of this process suggests that a circumnuclear disc can be formed where star formation will take place all the way down to a few parsecs from the black hole (Kawakatu & Wada, 2008; Hopkins & Quataert, 2010). Such a star forming circumnuclear disk could be coincident with the dusty torus from the AGN unification model (Antonucci, 1993). Nuclear starbursts are detected in Seyfert 2s and LINERS in UV images (e.g., Heckman et al., 1995; González Delgado et al., 1998; Colina et al., 2002), and simulations by Hopkins & Quataert (2010) suggest that the nuclear star formation and black hole activity is closely linked, especially close to the black hole, albeit with the peak of activity of the black hole delayed in time with respect to the peak of star formation (Hopkins, 2012). This delay is confirmed by observational work in post starburst galaxies (Goto, 2006; Wild et al., 2010) and star formation in AGN (Davies et al., 2007; Ramos Almeida et al., 2013; Esquej et al., 2014).

There are thus several lines of evidence that nuclear star formation and AGN activity are linked, but it is still unclear how and to what extent. One step in moving forward on this issue is to compare the circumnuclear star formation rate with black hole activity in active galaxies. While the black hole activity is fairly simple to determine through observations of the AGN luminosity (§1.1), tracing star formation close to the AGN is more complicated because traditional star formation tracers in the UV and optical are difficult to separate from the strong emission from the AGN itself.

1.3.2 Star formation tracers

Traditional star formation indicators in normal star forming galaxies rely on direct or reprocessed emission from young stars. Combined with stellar synthesis modeling, these observations can then be

used to deduce a star formation history. UV emission, originating from young stars, can be used as a direct tracer of recent and ongoing star formation within the host galaxy of an AGN (Kennicutt, 1998). The strength of the UV emission as a star formation indicator is that it can be used at many different redshifts and that it directly traces stellar emission in quiescent galaxies. In AGN, the UV emission originating from star formation will be mixed with continuum emission from the AGN which makes it less reliable as a star formation indicator. The UV emission is also prone to extinction and the chosen Initial Mass Function (IMF) (Kennicutt, 1998). As the UV emission primarily trace young massive stars, there is a lot of extrapolation involved when determining the slope and normalisation of the IMF from this typically small number of massive stars. Another option is to use reprocessed stellar emission such as Hα and Paα from ionized gas surrounding young massive stars (Kennicutt & Evans, 2012). One issue with Hα is that it is very susceptible to extinction, whereas this is not the case for Paα (Calzetti et al., 2007). Another option is the [Ne II] 12.8 μm emission from HII regions. The advantage of using these emission lines is that they are very sensitive to the amount of stellar light and that they directly trace the population of young stars. On the other hand, they are also sensitive to the IMF, just as UV emission is, and the assumption that all massive star formation is traced by the gas. A common problem for all of these star formation tracers is that they fail close to the AGN where they are hard to detect and measure due to the much stronger AGN emission.

Instead, mid-IR features can be used to trace star formation close to the AGN. In particular, mid-IR features from polycyclic aromatic hydrocarbon (PAH) molecules have shown to be good tracers of nuclear star formation (Peeters et al., 2004; Brandl et al., 2006). There are four prominent PAH features in the mid-IR at 6.2, 7.7, 8.6, and 11.3 μm. Diamond-Stanic & Rieke (2010) find the 11.3 μm to be the most accurate tracer of star formation while the lower wavelength PAH features are found to be suppressed in AGN. Smith et al. (2007) interpretes this as being due to selective destruction of the smallest PAH molecules by radiation from the AGN. The validity of the PAH features as star formation tracers rests on the assumption that they are solely excited by radiation from young O- and B-stars and not the emission from the AGN. From a theoretical point of view, the hard radiation from the AGN should destroy the PAH molecules (Voit, 1992). On the other hand, there are many observations of PAH features close to an AGN (e.g., Siebenmorgen et al., 2004; Tommasin et al., 2010; Esquej et al., 2014) down to scales of less than 10 pc (Alonso-Herrero et al., 2014). In particular, Esquej et al. (2014) and Alonso-Herrero et al. (2014) find that PAH molecules survive in the nuclear regions of AGN and speculate that this might be due to (self)-shielding in dense regions, possibly the dusty torus. In fact, Alonso-Herrero et al. (2014) find the 11.3 μm PAH flux to increase towards the centre when correcting for the strong AGN continuum.

There is thus growing evidence that PAH molecules can survive very close to the AGN. If they indeed do and in concert are excited by the AGN emission, then the assumption that PAH emission traces star formation exclusively has to be relaxed. Investigating this question is the subject of Chapter 5.

1.4 Contents of this thesis

The fundamental motivation for this thesis is to contribute to a better understanding of the AGN phenomenon and its role in galaxy formation and evolution. I tackle two specific pieces of this puzzle.

First, as already laid out in § 1.1 above, the central black hole in the AGN plays a significant role in understanding the AGN physics and the possible feedback the AGN can deliver to its host galaxy. To understand the role of the black hole, we need to know its mass since this is the main property driving the accretion and luminosity of the AGN. Therefore, gaining better black hole mass estimates provides a step forward in determining the physics of AGN and their role in galaxy formation and evolution. To improve on the mass estimates, one of the first steps is to determine how much the uncertainties of the spectral measurements of the BLR velocity field impact the final mass estimates. Additionally, it is important to figure out whether there is a particular parameterization of the line width that gives a more robust determination of the gas velocity. Further, I wish to show the limitations of each line measurement and how this affects the minimum uncertainty of the mass estimate that can be achieved. In particular, the accuracy of current mass estimates is limited by the accuracy to which we can measure broad emission line widths in AGN spectra as a proxy for the velocity field of the gas in the broad line region. Therefore, I focus on mapping, and improving on, the issues concerning this particular step in determining black hole masses.

To cover the evolution in black hole masses and their impact on galaxy formation and evolution, it is important to be able to trace black hole masses up to high redshifts. For this, the broad Hβ, Mg II, and C IV lines are used as they in concert allow black hole masses to be estimated up to redshifts of $\sim$4.7 using optical spectra. One particular issue is that studies of high redshift black hole masses often use survey quality data with low S/N , because that is what is available, which can impact the quality of the results. I map the performance of different line width measures on these three broad emission lines as a function of spectral S/N in order to map which line measures are most accurate and precise and to see if there are any differences between the three emission lines. I map the Hβ and C IV lines in Chapter 2 and the Mg II line in Chapter 3. Another purpose is to identify the specific parameterization of the line width that is most robust to S/N and mild absorption. This issue is addressed in Chapter 4. I find that the most commonly adopted method for line width measurements can lead to mass estimates with a very low accuracy and precision, and in some cases even systematically biased mass estimates. I also find that a less commonly used line measure is to be preferred in terms of both accuracy and precision and that it would be favorable for the community to adopt one single procedure for estimating line widths such that it is easier to compare results between different studies.

In Chapter 5 I focus my attention on another aspect of the AGNs possible role in galaxy formation and evolution. A connection between (nuclear) star formation and AGN activity has been claimed from both an observational and theoretical side. The most popular star formation indicator to use for this investigation is the mid-IR PAH features, based on the assumption that they are solely excited by emission from newly formed stars and not the AGN. Recently, this assumption has been challenged by observations of PAH features very close to AGN (§ 1.3). If the AGN contributes to exciting the PAH

features, then this has to be taken into account when using PAH features as star formation indicators close to AGN.

Chapter 5 contains a study with collaborators lead by me. In this study, we test whether the AGN play a significant role in exciting the observed PAH features. We do so by spatially mapping the distribution of the 11.3 μm PAH feature in a sample of nearby AGN at an unprecedented spatial resolution from $\sim$10 pc to $<$1000 pc. We find that the PAH features follow a radial distribution consistent with a central excitation source. By comparing with CLOUDY models of an AGN as the excitation source, we find that this is a more likely explanation for the observations than for example a nuclear star cluster as the excitation source. Our conclusion is that the AGN probably plays a role in exciting the PAH features in its vicinity and that one therefore should be very careful when estimating star formation based on PAH features within 1000 pc of an AGN.

1.5 Structure of this thesis

The issue of mapping out the accuracy and precision of different emission line width parameters for different broad emission lines is the first subject of this thesis. I deal with the C IV and Hβ lines in Chp. 2 and the Mg II line in Chp. 3. I repeat the study for C IV but include the effect of narrow absorption lines in Chp. 4. The reliability of PAH features as star formation tracers close to an AGN is investigated in Chp. 5. Finally, I present my conclusions in Chp. 6. Importantly, as Chapters 2 and 4 are based on a preliminary study I did as part of my Master's thesis, I highlight the differences between this thesis and that work in Appendix A.

Chapter 2

Hβ and C IV line width measures

This chapter contains the paper (to be submitted):

A large statistical study to investigate a robust method to characterize the velocity field of the broad-line region in Active Galactic Nuclei I: The Hβ λ4861 Å and C IV λ1549 Å emission lines

Jensen, J. J., and Vestergaard, M., to be submitted to MNRAS

2.1 Abstract

Accurate measurements of masses of supermassive black holes in Active Galactic Nuclei (AGN) are important for cosmological studies and to understand the physics of AGN. Currently, the accuracy of such mass estimates is limited by the accuracy and precision to which we can measure broad emission line widths in AGN spectra. We determine the accuracy and precision of four different line parameters used to measure broad emission line widths in AGN spectra as a function of spectral noise. We use these results to compare the line parameters to determine which one will give the most accurate mass estimates for a given spectral quality.

The Mean Absolute Deviation (MAD) relative to the median velocity and the Inter-Percentile Velocity (IPV) width have the highest accuracy and precision of any of the line parameters investigated. In addition, the IPV widths provide the ability to measure the emission line width to a high accuracy and precision at many fractions of the emission line flux, enabling a lot of flexibility when parameterising the emission line width, and the line shape.

Our results can be used as a look-up table to obtain the actual uncertainties associated with line measurements in existing data as well as for optimal preparation of future emission line studies.

2.2 Introduction

Measuring masses of supermassive black holes, believed to be present in the centres of all massive, if not all, galaxies (Kormendy & Richstone, 1995; Magorrian et al., 1998; Kormendy & Gebhardt, 2001),

is important for understanding galaxy formation and evolution. The mass of the central black hole has been shown to correlate with properties of the host galaxy such as the bulge mass (e.g., Magorrian et al., 1998; Wandel, 1999a; Marconi & Hunt, 2003a), bulge stellar velocity dispersion (e.g., Ferrarese & Merritt, 2000a; Gebhardt et al., 2000a,b; Ferrarese et al., 2001; Tremaine et al., 2002; Nelson et al., 2004; Onken et al., 2004; Gültekin et al., 2009), concentration index (e.g., Graham et al., 2001; Graham & Driver, 2007; Savorgnan et al., 2013), and luminosity (e.g., McLure & Dunlop, 2001; Marconi & Hunt, 2003a; Bentz et al., 2009a; Gültekin et al., 2009), not only for quiescent galaxies but also for active galactic nuclei (AGN; e.g., Wandel, 1999a; Ferrarese et al., 2001; McLure & Dunlop, 2001; Nelson et al., 2004; Onken et al., 2004; Bentz et al., 2009a). This has been taken as indication that the black hole and the stellar component somehow affect and regulate the growth of each other with the result that they co-evolve. For example, as stars form and later die, the interstellar medium is heated and redistributed. This may send gas to the center, fueling the black hole but can possibly also disrupt an existing central gas inflow (e.g., Anglés-Alcázar et al., 2017). Yet, the accreting black hole is capable of generating powerful radiation, jets, and other outflows such as winds (e.g., Fabian, 2012; McNamara & Nulsen, 2012; Veilleux et al., 2013) that, on one hand, can compress gas via shocks to trigger star formation and, on the other hand, can heat and disperse the gas in the interstellar medium, thereby limiting or even entirely shutting down star formation. Observational evidences for AGN feedback exist in the form of quasar disk winds (Tombesi et al., 2015), molecular outflows from the nucleus (e.g., Aalto et al., 2016; García-Burillo et al., 2016), galactic outflows driven by the AGN (e.g., Wylezalek & Zakamska, 2016, and references therein), and radio jets and lobes, which relocate and heat the X-ray cooling intercluster gas of cooling-flow clusters, creating the spectacular X-ray cavities in the intracluster medium (e.g., Dunn & Fabian, 2008; McNamara & Nulsen, 2012). We note that it can be difficult in some cases to distinguish whether the radiative feedback is powered by the AGN or by stellar processes; the latter is in some cases observed to be stronger than the AGN feedback (e.g., Diamond-Stanic et al., 2012; Geach et al., 2014; Sell et al., 2014).

Theoretical considerations show that the radiative energy released by the AGN is several orders of magnitude larger than the binding energy of the bulge (Fabian, 2012), making AGN feedback a viable mechanism for shutting down star formation. This feedback can affect the physical properties of the host galaxy, provided that the energy emitted by the AGN can be transferred to the gas in the host galaxy bulge through, for example, a radiatively driven wind (e.g. Silk & Rees, 1998; Fabian, 1999; King, 2003; King & Pounds, 2003; Proga & Waters, 2015). Simulations have shown that these feedback mechanisms can be powerful enough to halt both star formation and AGN growth (e.g. Di Matteo et al., 2005, 2008; Hopkins & Quataert, 2010; King & Pounds, 2015) and to drive the observed correlations between the black hole mass and host galaxy bulge properties. On the other hand, some works argue that the black hole−host galaxy relationships can be explained simply as a result of hierarchical merging of galaxies and their black holes (e.g., Peng, 2007; Jahnke & Macciò, 2011). It is also argued that the relationship between black hole mass and host galaxy velocity dispersion (the M-σ relationship) and its evolution over time is a result of selection effects (e.g., Lauer et al., 2007; Batcheldor, 2010). Even if AGN feedback is not the driver of the observed black hole – host galaxy

relationships, it may still play a role in shaping its exact form (i.e., its slope and scatter) by regulating its black hole growth through radiative feedback (e.g. Volonteri & Natarajan, 2009).

The mass is the most fundamental property of the black hole and it governs the physics of the AGN, from its attraction of gas in the galaxy from which it can feed, to setting the scale of the energy output of the AGN when it converts the rest mass of the fuel to energy. In addition, the black hole mass controls the accretion and luminosity of the AGN, thereby controlling the amount of possible radiative feedback, and the size, structure, and temperature of the accretion disk (e.g., Peterson, 1997). Therefore, obtaining a robust and high accuracy measurement of the mass of the central black hole is crucial for our deeper understanding of not only the possible black hole impact on its galaxy but also of AGN physics itself.

2.2.1 Black hole mass measurement methods

We have two primary methods to establish the mass of a black hole in an AGN. Reverberation mapping (RM), which is primarily used in the local Universe, and the so-called single-epoch mass estimates. The latter is a scaling relation that is easily applied to objects beyond the local Universe.

One distinct property of AGN is their strong variability. This is observed in the continuum emission, originating from the accretion disk surrounding the black hole, but also in the strength of the broad emission lines, originating from dense regions of gas in the broad line region. The variability in the broad emission lines is observed to correlate with that of the continuum, but with a certain time delay, or *lag*. Within our current understanding of AGN physics, the broad line emission is continuum emission reprocessed by the broad line region gas, and the observed time lag corresponds to the light travel time from the accretion disk to the broad line region.

Reverberation mapping (Blandford & McKee, 1982; Peterson, 1993), provides an estimate of the response-weighted size, R_{BLR}, of the broad line region by measuring the time delay between continuum and emission-line variations when observing the same object repeatedly (e.g., nightly) over an extended period of the order of several weeks to a few months for nearby objects. The virial mass, M_{BH}, can be calculated as

$$M_{BH} = f\frac{R_{BLR}\,(\Delta V)^2}{G}, \tag{2.1}$$

where ΔV is the virial velocity of the broad line region gas that responds to continuum variations, G is the gravitional constant, and f is a dimensionless scaling factor accounting for the unknown inclination, structure, and kinematics of the broad line region. The virial velocity ΔV is measured as the width of the broad emission lines in the variable part of the spectrum (i.e., the RMS spectrum), probing the same gas that is used to estimate the size of the broad line region. Onken et al. (2004) estimate the average f-factor to be 5.5 by assuming that the M-σ relationship for AGN is similar to the one for quiescent galaxies. This is a reasonable assumption since the RM AGN have relatively low Eddington luminosity ratios (Peterson et al., 2004), indicating low accretion rates. In this case, their black holes will not grow significantly in the future and should thus on average be consistent

with the mass distribution among quiescent galaxies. Later studies have also found values for the average f-factor of the order unity (Onken et al., 2004; Collin et al., 2006; Woo et al., 2010; Graham et al., 2011; Park et al., 2012; Grier et al., 2013), but where the exact value depends on the sample of objects under study and on the specific parameterisation used to measure the emission line width. Recent work by Shankar et al. (2016) show that the local M-σ relationship might be systematically biased because only galaxies for which the black hole sphere of influence is resolved are selected and this effectively selects galaxies hosting the largest black holes only. When accounting for this effect, Shankar et al. (2016) find an average f-factor of $\sim$1, bringing the M-σ relationships for active and quiescent galaxies in complete agreement without a separate scaling for the former.

Equation 2.1 relies on the assumption that the BLR gas is virialized. This has now been confirmed by several studies that find $R_{BLR} \propto V^{-2}$ when observing the same object at different epochs or using different emission lines (Peterson & Wandel, 1999, 2000; Onken & Peterson, 2002; Peterson et al., 2004). It is also reassuring that black hole masses measured by RM and stellar or gas dynamics, respectively, agree reasonably well (Onken et al., 2014; Peterson, 2014; Bentz et al., 2016).

Beyond the local universe, reverberation mapping is often impractical because the timescale for variations increase with AGN luminosity[1] and the cosmic time dilation due to the expansion of the Universe. Kaspi et al. (2007) performed RM for $2 \leq z \leq 3$ sources and found that timescales of $\sim$10-15 years were necessary to establish the Hβ BLR size. For sources at redshifts higher than $z \sim 0.3$ it is therefore more convenient to use single-epoch (hereafter SE) mass scaling relationships to *estimate* a black hole mass. Given a single spectrum, R_{BLR} is estimated from a single measurement of the monochromatic luminosity through the observed radius-luminosity (R-L) relationship between the broad line region size and the nuclear continuum luminosity of the AGN (Kaspi et al., 2000, 2005, 2007; Bentz et al., 2006, 2009b, 2013). The virial velocity ΔV is estimated from the same spectrum as R_{BLR} by measuring the broad emission line width. The ΔV measurement is thus approximative since it, in addition to the broad line region gas that is varying (represented in the rms spectrum), also includes a contribution from the non-responsive gas and potentially gas with non-virial motion in the broad line region. In spite of being an approximation, the method works remarkably well and produce mass estimates that are within af factor $\sim$2.5-3.5 of the RM masses (Vestergaard & Peterson, 2006). The SE mass scaling relations have enabled SMBH mass estimates (e.g., Vestergaard, 2004; Vestergaard et al., 2008; Kelly et al., 2010; Shen et al., 2011; Kelly & Shen, 2013; Dai et al., 2014; Schulze et al., 2015) for large samples of AGN from spectroscopic surveys like the Sloan Digital Sky Survey (SDSS; York et al., 2000). The SE mass scaling relationships have been developed for use on the Hα and Hβ line in the restframe optical regime and the Mg II and C IV lines in the UV (e.g., McLure & Jarvis, 2002; Vestergaard, 2002; McLure & Dunlop, 2004; Greene & Ho, 2005b; Kollmeier et al., 2006; Vestergaard & Peterson, 2006; McGill et al., 2008; Vestergaard & Osmer, 2009; Shen & Liu, 2012; Park et al., 2017).

[1] As the size of the BLR scale with luminosity (Bentz et al., 2013), so does the variability timescale of the broad emission lines originating in the BLR.

2.2.2 Uncertainties in black hole mass estimates

The statistical uncertainty in the SE mass estimates is of the order ∼0.4 dex (Vestergaard & Peterson, 2006; Vestergaard & Osmer, 2009). This uncertainty only accounts for how well the SE masses reproduce the RM masses to which they are calibrated. The absolute uncertainty of the RM massses themselves is ∼0.4 dex, as estimated from the scatter of the reverberation based mass estimates around the M-σ relation (Onken et al., 2004; Woo et al., 2010). To reduce the uncertainty in the RM masses, the geometry, kinematics, and inclination of the broad line region of each object have to be established. This can be done using velocity-delay maps that provide some information on the structure and kinematics of the broad line region by measuring the time-delay as a function of Doppler velocity width across the emission line (e.g., Grier et al., 2013; Kollatschny et al., 2014; Skielboe et al., 2015) or by dynamical modeling of the gas in the broad line region (e.g., Brewer et al., 2011; Pancoast et al., 2011, 2012, 2014).

Three primary factors contribute to the uncertainty of the SE mass estimates: 1) the intrinsic variability of the AGN; 2) the AGN luminosity used to estimate R_{BLR} through the R-L relationship; and 3) establishing ΔV from profiles that contain an unknown emission contribution from non-responsive and non-virial gas in addition to the virialized gas in the broad line region. The intrinsic variability of AGN, combined with the light travel time from the accretion disk to the broad line region, adds scatter to the SE masses since the emission responsible for ionizing the broad line region gas emitting the broad emission lines was emitted from the accretion disk at an earlier time than the continuum luminosity measured in the same spectrum. This effect adds scatter of ∼0.1 dex or less (Wilhite et al., 2007; Denney et al., 2009). The effect of variability is further diminished for high-redshift luminous AGN for which the relative variability amplitude is lower (e.g., Vanden Berk et al., 2004; Kaspi et al., 2007) and occur on longer time scales.

The contribution to the uncertainty of the SE black hole mass estimate from the R-L relationship is very low for two reasons. First, the scatter in the R-L relationship is as low as 0.13 dex (Bentz et al., 2013) or even as low as 0.11 dex (Peterson, 2010) when using only the highest quality data. But, the scatter may be lower yet, as the uncertain distances of the nearest galaxies that do not follow the Hubble flow contribute significantly to the scatter, especially at lower luminosities (Bentz et al., 2013). Second, the uncertainty of the measured AGN luminosity enters the mass calculation in Eqn. 2.1 as $L^{1/2}$ through the R-L relationship which means that its contribution to the uncertainty of the final mass estimate is further reduced. On the contrary, ΔV enters the mass calculation squared in Eqn. 2.1 and is subject to several sources of uncertainty that are discussed next.

Roughly speaking, there are three sources of uncertainty when estimating the velocity field of the broad line region, ΔV, from a single AGN spectrum. First, how well can the broad emission line component of which we wish to measure the emission line width be isolated? Second, when the emission line is isolated, how well can the line width then be parameterized (i.e., what are the limitations of the specific measurement method used)? Third, how well does the measured line width in an SE spectrum represent the true velocity field ΔV of the variable part of the BLR emission? The

latter is a topic that we are currently investigating, but our focus in this paper will be on determining the limitations of the different line width parameterizations. Before turning to that, we will briefly discuss the impact of spectral decomposition of AGN spectra next (i.e., item one above).

A spectral decomposition method has to account for the different components in the AGN spectrum in order to separate them and, for the purpose here, isolate the broad emission lines. In AGN spectra, this generally means that the host galaxy emission, the nuclear continuum of the AGN, the different broad and narrow emission line components, absorption features, iron emission, a Balmer continuum, and other relevant spectral components have to be modelled (for details on the spectral decomposition methods used in this study, see § 2.6). Vestergaard et al. (2011) show that the specific decomposition method used can introduce a scatter of $\sim$1000 km s^{-1} ($\sim$20% assuming a representative line width of 5000 km s^{-1} in broad line AGN) in the measured line widths at S/N $\geq$ 20 pixel^{-1} by comparing line width measurements using two different spectral decomposition methods from Vestergaard et al. (2008) and Shen et al. (2011) on the exact same dataset. Mejía-Restrepo et al. (2016) show that the measured line widths can be biased by up to 0.2 dex when using survey quality data (e.g., SDSS) because the low data quality (S/N $<$ 10 pixel^{-1}) makes it difficult to establish the level of the nuclear AGN continuum model underlying the broad emission lines. Denney et al. (2009) demonstrate that failure to remove the narrow line components from the emission line can lead to a mass estimate that is offset by an order of magnitude. These studies do not represent an exhaustive list, but simply serve to illustrate some of the ways the specific spectral decomposition method that is used can affect the measured line widths and thereby the black hole mass estimates. The aim in the current work is not to develop and compare different spectral decomposition methods, but instead to implement a robust decomposition method that works in an automated way. This allows us to focus on the limitations of the actual line width measurement for a given isolated emission line profile.

2.2.3 Measuring line profile widths

If we are to make significant improvements in the black hole mass estimates we need to understand the systematic and random uncertainties of each line width parameter since these will dominate the uncertainty of the SE mass estimates. We note though, that as the RM masses also depend on a measure of the line width, they will also benefit from our investigation here. This is in fact true for any quantity that rely on a line width measurement.

To measure the line width, the extent of the line in the spectrum first has to be constrained by placing line limits on each side of it. The purpose of the line limits is to exclude extraneous emission from the line width measurement while at the same time to avoid truncating the wings of the emission line. We present and discuss several methods to do this in § 2.7.

Second, a specific line width parameterization must be chosen. These are presented and discussed in more detail in § 2.3. Traditionally, the full width at half maximum (FWHM) or the line dispersion (σ_{line}) have been used (e.g., Peterson et al., 2004; Rafiee & Hall, 2011; Shen et al., 2011; Denney et al., 2016). Each of these parameterizations have their own merits and limitations. For example, the

FWHM is expected to be straight-forward to measure and robust to blending in the line wings, but sensitive to noise, especially in the line peak. The line dispersion is, on the other hand, expected to be more robust to spectral noise than FWHM (Peterson et al., 2004), but very susceptible to blending in the line wings (e.g., Denney et al., 2009; Rafiee & Hall, 2011). As a consequence, the use of the Mean Absolute Deviation from the median velocity (MAD; e.g., Denney et al., 2016) and the Inter-Percentile Velocity (IPV; e.g., Whittle, 1985; Fine et al., 2008, 2010) widths have been explored as alternatives. It is not clear which of these four alternatives is the most robust and representative measure of ΔV.

Many studies use spectra from large spectroscopic surveys to estimate SE black hole masses (e.g., Vestergaard et al., 2008; Shen et al., 2011). By construct, these data are often of relatively low spectral quality since the focus of these surveys is more on data quantity rather than quality for individual objects. For example, the SDSS Data Release 7 (DR7) Quasar Catalog (Schneider et al., 2010) has a median S/N $< 10\,\mathrm{pixel}^{-1}$, but contains spectra of more than 100,000 quasars. We therefore focus our work on how robust the aforementioned line width measures are to spectral noise.

Denney et al. (2009) use spectra of two different AGN to illustrate how the FWHM and σ_{line} can induce biases and add scatter in the SE mass estimates for data with S/N $\leq 20\,\mathrm{pixel}^{-1}$. Later, Denney et al. (2016) show how the MAD parameterisation is more robust to S/N than FWHM and σ_{line}. Fine et al. (2010) degrade high S/N C IV spectra from the SDSS Data Release 5 Quasar Catalog (77,429 spectra, $1.5<z<3.3$, $R\sim165\,\mathrm{km\,s}^{-1}$, average S/N $\sim 13\,\mathrm{pixel}^{-1}$) and 2dF spectra (31830 spectra, $1.6<z<3.3$, $R\sim465\,\mathrm{km\,s}^{-1}$, average S/N $\sim 5.5\,\mathrm{pixel}^{-1}$) to a third of their original S/N level in order to map the dispersion in measured IPV widths as a function of S/N . They find that above S/N ~ 3 Å $^{-1}$, the IPV50 width is unbiased and accurate within $\sim$20%. A clear limitation of this study is that the spectra are degraded to 1/3 of their original S/N level, irrespective of whether this is $7\,\mathrm{pixel}^{-1}$ or $75\,\mathrm{pixel}^{-1}$. This means that the resulting line width error will be underestimated for those spectra with an intrinsically low S/N level. Another limitation is that they only investigate two S/N levels for each spectum (i.e., the original S/N level and 1/3 of this). Nevertheless, these studies have been important in pointing out some of the limitations of the different line width measures with increasing spectral noise. Here, we aim at comparing all of the four mentioned line width measures in a systematic and statistical manner using a sample of spectra that represent the general properties of the observed AGN population.

One commonly used approach to mitigate the negative effects of spectral noise is to measure the line widths on a functional model of the emission line instead of directly on the data (see e.g., Fine et al., 2010; Rafiee & Hall, 2011; Shen et al., 2011; Denney et al., 2016). This approach can lead to more precise, but unfortunately also biased mass estimates when using the FWHM and σ_{line} (Denney et al., 2009). Therefore, we also investigate whether this approach can in fact improve the mass estimates for our sample of spectra. We describe our approach to testing the robustness of the different line width parameters next.

2.2.4 Our approach

We aim at testing the robustness of four different line width parameters on a sample of degraded versions of high quality (S/N $\geq 30\,\mathrm{pixel}^{-1}$) spectra representative of the observed AGN population. The goal is to establish which parameter provides the most robust estimate of the broad emission line width with increasing spectral noise. Our approach is to degrade individual high quality spectra (hereafter *original spectra*) to a range of S/N levels and compare the line width parameters measured on these degraded spectra with those measured in the original spectra. We subject the degraded spectra and the original spectra, respectively, to the same procedure. Namely, we first perform an automated spectral decompsition (§ 2.6) in order to model the different spectral components, enabling us to isolate the broad emission line profile of relevance for our study. Second, we place line limits on each side of the extracted emission line profile (§ 2.7) in order to constrain its extent in the spectrum, and finally, we measure a suite of different line parameters on the isolated line profile. We measure the line width parameters directly on the data and on a functional model of the data, respectively, to test if the latter approach is an effective way to mitigate spectral noise. For the comparison to be meaningful, each spectrum is treated as if it is unique. This means that all spectra, degraded as well as original, goes through all the steps outlined before we measure the line width parameters.

Denney (2012) show that determining the shape of the broad emission line can be important to accurately calibrate SE masses based on the C IV line. Traditionally, the FWHM/σ_{line} ratio has been used for this purpose. As this shape measure will inherit any limitations of the FWHM and σ_{line} measurements, we compare it with ratios of IPV widths as an alternative measure of the line shape. This is done in § 2.10.

An obvious requirement for a mass estimate is that it stays constant at different epochs as the AGN changes luminosity (i.e., accretion state). We subject the four different line width measures to this test in § 2.11.2 using over 20 years of reverberation mapping data of NGC 5548, similar to the tests performed by Collin et al. (2006) for FWHM and σ_{line}.

SE mass estimates have been calibrated for the broad Hα, Hβ, Mg II, and C IV emission lines, respectively. The Hβ line is especially important since much more reverberation mapping data exist for this line, and consequently, the calibration of the SE mass scale for all other lines is tied to the Hβ mass estimates. Optical spectra, as available in for example the SDSS, allow us to obtain SE mass estimates using the Hβ line for AGN residing at redshift up to ∼0.7. At higher redshifts, the Mg II ($0.4 \leq z \leq 2.2$) and C IV ($1.5 \leq z \leq 4.8$) emission lines are shifted into the optical regime. As a result, all three lines are important for our ability to obtain SE mass estimates based on optical spectra. In this paper, we focus on the Hβ and C IV lines. We will address SE mass estimates using the Mg II line in future work (J.J. Jensen & M. Vestergaard, 2018b, in preparation).

The paper is structured as follows: In § 2.3 we introduce the four different line width parameters that we study. We present our database of Hβ and C IV emission line spectra in § 2.4. We outline the statistical method of our analysis in § 2.5 and describe our spectral decomposition method in § 2.6. In § 2.7 we introduce five different line limits and test which are best suited to constrain the wavelength

range over which the line width parameters are measured. We present our results for the Hβ and C IV spectra in § 2.8 and 2.9, respectively. We compare different methods to measure the line shape in § 2.10 and test the robustness of each line width parameter with varying AGN luminosity in § 2.11.2. Finally, we discuss our results and give our conclusions in § 2.11 and § 2.12, respectively.

2.3 Line width parameters

We investigate four different line width measures with the purpose of quantifying their accuracy and precision as a function of spectral quality; namely the full-width-at-half-maximum (FWHM, § 2.3.1), the line dispersion (σ_{line}, § 2.3.2), the Mean Absolute Deviation from the median velocity (MAD; § 2.3.3), and the Inter-Percentile Velocity width (IPV width, § 2.3.4), described in the following.

2.3.1 The Full Width at Half Maximum

As the name states, the FWHM is the width measured at half the peak intensity of the line. We measure the FWHM using the method presented by Peterson et al. (2004) because it works for both single- *and* double-peaked profiles. With this method, the peak intensity of the profile is measured as the maximum flux density value of the line. This makes the peak intensity and its position, and thus the FWHM, sensitive to spectral noise. Other common methods adopted in the literature to measure the peak intensity include: 1) the average flux density value of the line in a narrow region near the expected wavelength of the line peak; 2) the centroid of the line (i.e. the flux weighted mean position) measured for flux densities above $\sim 75\%$ of the peak intensity; 3) the maximum flux density value of a smoothed version of the line profile; and 4) the maximum flux density value of a functional model of the line. This ambiguity in defining the peak intensity of the line profile illustrates an inherent problem connected to measuring the FWHM on real data that contain noise. The FWHM of an emission line is therefore not a uniquely defined parameterisation of the line width until the measurement method is specified. However, at that point the FWHM is relatively straightforward to measure and is therefore the most common line width parameterisation used for black hole mass estimation in the literature (e.g., Peterson & Wandel, 1999; Wandel, 1999b; McLure & Jarvis, 2002; Vestergaard, 2002; Vestergaard & Peterson, 2006; Woo & Urry, 2002; Shen et al., 2008; Vestergaard & Osmer, 2009; Kelly et al., 2010; Shen et al., 2011). Because the FWHM only depends on measurements of the peak intensity and the half peak intensity wavelengths, it should be relatively robust to emission contamination (i.e., blending) in the line wings. On the other hand, it is expected to be sensitive to both noise and absorption near the line peak and the half-peak intensity positions, respectively. In addition, the FWHM will be somewhat sensitive to the continuum placement since this will affect the measured peak flux.

2.3.2 The line dispersion

The line dispersion, σ_{line}, is the second central moment of the line, defined as:

$$\sigma_{line}^2 = \langle \lambda^2 \rangle - \langle \lambda \rangle^2 = \frac{\int \lambda^2 F(\lambda) d\lambda}{\int F(\lambda) d\lambda} - \left[\frac{\int \lambda F(\lambda) d\lambda}{\int F(\lambda) d\lambda} \right]^2 \tag{2.2}$$

where $F(\lambda)$ is the flux density of the emission line as a function of wavelength λ. We measure the line dispersion by a simple numerical calculation of equation (2.2) between the line limits (see § 2.7). Based on its definition, the line dispersion is larger for lines with relatively more flux in the line wings. This indicates that blending in the line wings can adversely affect the measured value of the line dispersion. An advantage of the line dispersion is that it is well defined for arbitrary (i.e., single- or multi-peaked) line profiles and it is relatively unaffected by narrow emission and absorption line contamination due to its integral nature, in contrast to the FWHM. In addition, the line dispersion is more accurate for low-contrast lines (i.e. low EW), and it has lower relative uncertainties than the FWHM (Peterson et al., 2004).

2.3.3 The Mean Absolute Deviation

The mean[2] absolute deviation (MAD) from the median velocity is defined as (Press et al., 2007):

$$\mathrm{MAD} = \frac{\int |\lambda - \lambda_{\mathrm{med}}| F(\lambda) d\lambda}{\int F(\lambda) d\lambda} \tag{2.3}$$

where λ_{med} is the flux-weighted median of the line profile. We measure the MAD simply by a numerical calculation of equation 2.3 between the line limits. Like σ_{line}, the MAD is an integral measure of the line width and therefore expected to be robust to spectral noise. In addition, since the MAD only weights the flux with the distance to the median of the line to the first order, it is not expected to be as sensitive to noise or flux in the line wings as σ_{line}.

2.3.4 The Inter-Percentile Velocity width

The Inter-Percentile Velocity (Whittle, 1985) width defines line parameters based on the integrated line flux. From the Inter-Percentile markers a and b, positioned at wavelengths for which a given fraction of the total integrated flux of the emission line is contained in the line wings, the Inter-Percentile Velocity at $Y\%$ of the integrated line flux is defined as

$$\mathrm{IPV(Y\%)} = (a+b)\ km\ s^{-1} \tag{2.4}$$

where Y can be any percentage level between 0% and 100% (Whittle, 1985). The parameter scheme and the markers are illustrated in Figure 1 of Whittle (1985). This parameter scheme can be used to

[2]For easier comparison we use the same definition of the MAD as Denney et al. (2016) as opposed to using the *median* absolute deviation.

characterise the line profile from the base of the profile (low Y percentage level) to the line core (high Y percentage level). We note that characterisations of the line profile at all percentage levels carry information on the profile wings as the integration used to locate the position of the inter-percentile markers always runs inward from the line limit. Whittle (1985) determine the position of an inter-percentile marker by integrating the line flux starting from the blue line limit. We determine its position by integrating the line flux inwards from *each* of the blue and red line limits and then use the average of these two marker positions. This approach improves the accuracy and precision of the measured IPV widths slightly.

Due to its integral nature, we also expect the IPV width to be less affected by spectral noise and the spectral resolution than the FWHM (Whittle, 1985). But, similar to the line dispersion and the MAD, the IPV width will be sensitive to line blending in the wings.

2.3.5 Correcting for spectral resolution

Due to the finite spectral resolution of the spectrograph used to obtain the data, any line width we measure is a convolution of the intrinsic (i.e., emitted) line width with the instrumental profile. We correct for the instrumental broadening of the line profile by assuming a Gaussian shape for the instrumental profile and using the equation (e.g., Peterson et al., 2004)

$$\Delta V_{obs}^2 \approx \Delta V_{true}^2 + \Delta V_{res}^2 \tag{2.5}$$

where ΔV_{obs} is the measured line width, ΔV_{true} is the intrinsic width of the emission line before it was broadened by the instrumental profile, and ΔV_{res} is the width of the instrumental profile (i.e. the spectral resolution). The width, ΔV, can be measured as the FWHM, the line dispersion or the IPV width. We calculate the IPV(Y) width of the assumed Gaussian resolution element with the relation $\mathrm{IPV(Y)}_{res} = \mathrm{Q(Y)} \times \mathrm{FWHM}_{res}$, where $\mathrm{Q(Y)} = \mathrm{IPV(Y)}_{Gauss}/\mathrm{FWHM}_{Gauss}$ is a value that relates the IPV(Y) width and the FWHM of a Gaussian distribution. For convenience, we tabulate Q(Y) values for percentage levels between 1% and 99% in Table B.1 in Appendix B. For example, $\mathrm{Q(Y} = 24\%) \approx 1$ means that the IPV(Y=24%) width is equal to the FWHM for a Gaussian profile. For percentages lower (greater) than Y=24%, the Q(Y) value is larger (smaller) than 1 because the IPV width is larger (smaller) than the FWHM of a Gaussian profile.

2.3.6 Line width uncertainty from continuum level determination

The intensity of the continuum emission underlying the emission line influences the measured line flux and the peak flux density of the line, and consequently the line width parameters we measure. For this reason it is pertinent that we quantify the impact of the uncertainty in the continuum level setting on the line width parameters. We calculate this continuum uncertainty as the rms of the flux density around the spectral decomposition model (§ 2.6) in the continuum windows at 1445 Å – 1455 Å and 1690 Å – 1700 Å for the C IV spectra, and the continuum region between 5600 Å and 5700 Å for

the Hβ spectra. We then determine the highest (lowest) plausible continuum level as the best fit continuum level plus (minus) the continuum rms and remeasure the line widths relative to each of these three continuum levels (i.e. best, best$+1\sigma_{\rm cont}$, and best$-1\sigma_{\rm cont}$). We expect this procedure to yield a conservative estimate of the line width uncertainty as the best$+1\sigma_{\rm cont}$ and best$-1\sigma_{\rm cont}$ continuum levels represent the most extreme levels of the continuum within its uncertainty. We will later, in § 2.8, investigate whether this method is a reasonable, or a too conservative, estimate of the line width uncertainty.

2.4 Data and samples

The ideal sample to use for our investigations of how robust each of the line widths are, is one that covers the observed properties of the general AGN population. With this in mind, we impose the following criteria when selecting the data for our study:

1. Each spectrum covers, for a given source redshift, either the Hβ or the C IV emission line;

2. The sample spectra cover a wide range in emission line properties, characterised by three primary parameters: 1) the FWHM emission line width, 2) the emission line strength, i.e., the emission line equivalent width (EW), and 3) the emission line shape, characterised by the FWHM/σ_{line} ratio. We choose these parameters as they are often readily available in the literature for large data sets like e.g. the SDSS;

3. We avoid broad absorption line quasars because the absorption troughs can adversely affect the line width measurements by changing the line shape. We include some spectra with narrow absorption lines, i.e. lines with FWHM less than a few hundred $\rm km\,s^{-1}$. To ensure that these absorption lines do not affect the profile characterisations, we linearly interpolate across each absorption feature using the five pixels in the local continuum on either side of and closest to the absorption line. We add the same level of noise to the interpolated spectral regions as we measure in the spectral continuum (§ 2.5). Several examples of this procedure are shown in Figure 2.2;

4. The signal-to-noise (S/N) level of each spectrum exceeds 30 $\rm pixel^{-1}$ in the continuum. It is measured in a specified continuum region as the median ratio of the observed flux density to the noise spectrum. If the noise spectrum is unavailable, the average flux density level relative to the root-mean-square (rms) around this average level is adopted instead (§ 2.5). The high spectral data quality ensures that we can measure the line width parameters with high confidence and degrade the spectra to a wide range of S/N ratios (§ 2.5.1).

Based on these criteria, we select 63 spectra for our sample. In the following we refer to these as the *original* spectra to distinguish them from the S/N degraded spectra, discussed in § 2.5.1. Two of the Hβ spectra in our sample have S/N lower than our data quality cut of 30 $\rm pixel^{-1}$ (see Table 2.1),

namely J101027.53+413239.0 (S/N $\sim 18\,\mathrm{pixel}^{-1}$) and J113330.30+105223.3 (S/N $\sim 26\,\mathrm{pixel}^{-1}$). We specifically checked that these two spectra do not affect our overall results. If anything, due to their lower intrinsic S/N level, we will underestimate the errors on the line widths in the S/N degraded versions of these particular spectra, which means that they will not enforce any stronger conclusions than for the rest of the sample.

2.4.1 The Hβ spectral database

Our database consists of 29 AGN spectra containing the broad Hβ emission line (Figure 2.1). Six of these are radio-loud quasars selected from Vestergaard (2003) and observed with the X-Shooter spectrograph mounted on the European Southern Observatory (ESO) Very Large Telescope (VLT) at the Paranal Observatory in Chile. The X-Shooter spectra cover the observed wavelength range from 3000 Å to 2.5 μm, divided into three arms: near-infrared (NIR; spectral resolution $R = \lambda/\Delta\lambda = 5600$), visible (VIS; $R = 8800$), and ultra-violet (UVB; $R = 5100$). There is a total of 15 objects in the full X-Shooter sample, but only for six of them is the Hβ emission line suited for our analysis. The remaining are either strongly affected by telluric absorption or have too low S/N . Details on the X-Shooter spectra are given in Appendix E.

The remaining 23 spectra are selected from the SDSS DR7 Quasar Catalog (Schneider et al., 2010). The SDSS spectra cover observed wavelengths from $\sim$3800 Å $-$9200 Å with a spectral resolution of $R \approx 2000$, corresponding to $R \approx 150$ km s^{-1}. In our sample, 17 SDSS spectra are single-epoch spectra of individual quasars while the remaining six are composites of a larger number of AGN spectra from the SDSS DR7 quasar catalog, each binned according to the FWHM as measured by Shen et al. (2011). The composite spectra are constructed in the following way, as will be described in Stephan Frank et al. (in prep), following a similar procedure as described by Frank & Péroux (2010) and Pieri et al. (2014). First, the spectra are binned according to their FWHM, ignoring any objects flagged as broad absorption line quasars. Then, each spectrum in a given FWHM bin is de-reddened according to the extinction maps of Schlegel et al. (1998) and then shifted to the restframe wavelength, conserving the log-wavelength pixel scale of the SDSS spectra. After normalising each spectrum by the flux at 5200 Å, the mean in each pixel of all spectra is used as the composite spectrum. In constructing this mean (i.e., composite) spectrum for a given wavelength bin, we apply two different cuts to avoid obvious bad pixels: a) we discard all pixels with a flux density below zero or above 100 (note that since the spectra are normalised at 5200 Å a flux density value above 100 clearly is an outlier), and 2) of the remaining distribution of pixel flux density values, we discard the top and bottom 3% in order to minimise outliers affecting the mean. The error on the composite at each pixel is derived by calculating the standard deviation of the flux in a sample of $\pm$20 pixels from the central pixel. We find that simply using the standard deviation of the flux densities going into each pixel underestimates the actual error, probably because we apply the 3% outlier cut as described above. Finally, each composite spectrum is rebinned to a linear wavelength scale with a pixel size of 0.2 Å. The emission line properties for our sample of high S/N Hβ spectra are summarised in Table 2.1.

Table 2.1 Spectral properties of the Hβ database

Source	Redshift z	S/N[a]	EW[b]	Line shape[c]	FWHM[d]	σ_{line} [e]	MAD[f]	IPV(50%)[g]	Ref.
(1)	(2)	(3)	(4)	(5)	(6)	(7)	(8)	(9)	
Composite A	...	75	55	0.60	1720	2862	1490	1651	1
Composite B	...	83	77	1.10	3458	3143	1997	2663	1
Composite C	...	70	76	1.44	4808	3339	2257	3250	1
Composite D	...	60	78	1.57	5791	3682	2526	3672	1
Composite E	...	50	75	1.80	6535	3638	2651	4149	1
Composite F	...	36	74	1.98	8065	4063	3108	4998	1
Q1705+0152	2.5750	74	92	0.34	2262	6624	7761	2662	2
Q1542+0417	2.1820	64	79	2.63	3385	1286	1938	3160	2
Q1402-0116	2.5150	48	74	1.35	3773	2805	2135	3411	2
Q0038-0159	1.6700	69	98	1.16	6289	5406	6669	4473	2
Q1554-2020	1.9450	90	108	1.06	6522	6147	4254	5285	2
Q1311-2700	2.1950	47	88	2.72	8230	3023	2589	4519	2
J145108.76+270926.9	0.0645	66	35	0.34	1013	2952	1407	1335	3
J171131.30+333543.3	0.4693	32	73	0.69	1741	2506	1437	1615	3
J112108.58+535121.0	0.1029	52	71	0.69	2261	3271	2044	2238	3
J074948.26+345444.0	0.1318	74	58	0.94	2405	2551	1475	2017	3
J032213.89+005513.4	0.1849	75	113	0.79	2544	3223	1988	2321	3
J093527.09+261709.6	0.1222	65	138	1.71	3604	2107	1605	2583	3
J210001.24-071136.3	0.5997	38	81	1.25	3882	3105	2055	2940	3
J123022.17+662154.6	0.1843	59	115	1.35	4391	3258	2337	3393	3
J101027.52+413239.0	0.6124	18	98	0.99	4406	4435	3057	3918	3
J164258.80+394836.9	0.5935	51	6	1.69	4481	2645	1674	2553	3
J094715.56+631716.4	0.4873	48	103	1.78	6277	3523	2700	4286	3
J080452.73+212050.2	0.1242	55	100	1.97	6818	3462	2497	3944	3
J040148.98-054056.5	0.5702	31	67	2.83	7913	2796	2442	4379	3
J002444.12+003221.2	0.4024	44	104	1.97	8614	4372	3349	5411	3
J113330.30+105223.3	0.5101	26	66	2.16	10171	4704	3765	6303	3
J170441.38+604430.5	0.3716	73	51	1.98	10614	5372	4320	7363	3
J083225.34+370736.2	0.0919	54	119	2.51	14262	5677	4593	7909	3

Note. — SDSS spectra cover ∼3800 – 9200Å in the observed wavelength frame with a spectral resolution of $R = \lambda/\Delta\lambda \approx 2000$, where $\Delta\lambda$ is the width of the spectral resolution element at wavelength λ. This corresponds to a velocity width of a spectral resolution element of $\Delta v = c \cdot \Delta\lambda/\lambda \approx 150\,\mathrm{km\,s^{-1}}$, where c is the speed of light. The SDSS composite spectra all have data from > 100 SDSS spectra in each pixel at rest-frame wavelengths between 4000Å and 6000Å where we perform the spectral decomposition (§ 2.6.1).

Note. — [(a)]Signal-to-noise ratio, S/N, measured in a specified continuum region either as the median ratio of the flux density relative to the noise spectrum or as the average flux density relative to the root-mean-square (rms) around this mean flux density if a noise spectrum is unavailable (§ 2.5); [(b)]Rest-frame equivalent width; [(c)]Emission line shape, parameterised as FWHM/σ_{line}.; [(d)]Full Width at Half Maximum of the emission line as defined in § 2.3; [(e)]Line dispersion of the emission line flux density, the second moment of the flux distribution, defined in equation 2.2; [(f)]The Mean Absolute Deviation from the median velocity, defined in equation 2.3; [(g)]The Inter-Percentile Velocity width of the emission line at 50% of the line flux, as defined in equation 2.4.

(1) Stephan Frank et al. 2018, in prep; (2) This work; (3) Schneider et al. (2010).

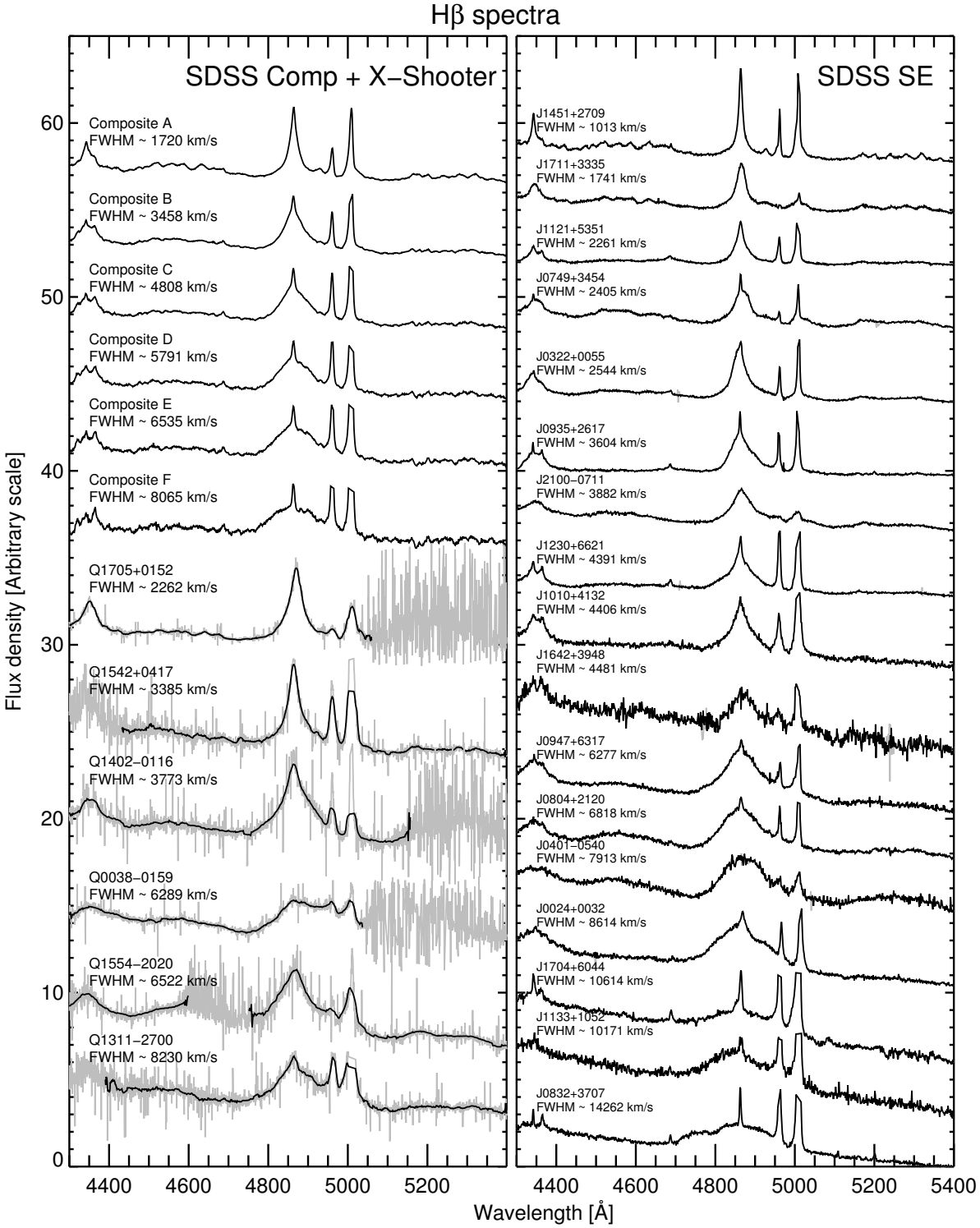

Fig. 2.1 The 29 spectra forming our sample of high S/N Hβ spectra. Only the spectral range near the Hβ emission line is shown. The spectra are shifted in the vertical direction and placed on an arbitrary flux density scale. The narrow [O III] emission lines are truncated for display purposes. For the X-Shooter spectra we show the original spectra rebinned by a factor of two in gray while the versions we perform our line width measurements on are those rebinned by a factor of 6 (Q1705+0152, Q1542+0417, Q0038-0159, and Q1311-2700) or 10 (Q1402-0116 and Q1554-2020) in the NIR arm and shown in black.

We choose our spectra to cover the observed spectral properties of the AGN population. Specifically, we wish to cover as much as possible of the observed parameter space in terms of the strength and width of the Hβ line. For this purpose, we adopt the observed properties of the SDSS quasars as a guide to the intrinsic properties of the AGN population. We specifically compare the spectral measurements of our sample with the subset of quasars used to study the luminosity and black hole mass functions of the DR3 quasar catalog (Richards et al., 2006; Vestergaard et al., 2008) and the DR7 quasar catalog (Shen et al., 2011), respectively. The 5% – 95% percentiles of the parameter distributions observed in these studies cover: (a) FWHM: ∼1750 km s^{-1} to 10000 km s^{-1}; (b) EW: 24 Å to 152 Å; and (c) FWHM/σ_{line}: 0.91 to 2.87. As seen from Table 2.1, our Hβ spectra cover almost the full range of this parameter space. However, we have sparse coverage of emission lines with low and high EW (only two spectra with EW $\leq$ 35 Å and none with EW >138 Å). We do not consider this an issue because the vast majority (∼ 90%) of the AGN spectra in the SDSS (Vestergaard et al., 2008; Shen et al., 2011) have observed emission line parameters covered by our sample.

2.4.2 The C IV spectral database

Five of our 34 C IV spectra are composite spectra (generated in a similar fashion as explained for the Hβ composite spectra in § 2.4.1) and 12 are single–epoch spectra from the SDSS, similar to those described for the Hβ sample. The remainder of the C IV database consists of four mean spectra of objects selected from the reverberation mapping sample of local AGNs (Peterson et al., 2004) and 13 X-Shooter spectra, similar to those described for Hβ. See Appendix E for details on the X-Shooter spectra. The emission line properties are summarised in Table 2.2, and the spectra are shown in Figure 2.2. For the AGNs in the SDSS quasar catalog, the 5% – 95% percentile ranges of the observed C IV line parameters (Vestergaard et al., 2008; Shen et al., 2011) are: (a) FWHM: ∼2050 km s^{-1} to 9600 km s^{-1}; (b) EW: 14 Å to 94 Å; and (c) FWHM/σ_{line}: 0.84 to 2.44. Our sample covers the entirety of this parameter space and is therefore representative of the observed C IV emission line parameters of the general AGN population as quoted above.

2.5 Statistical methods and analysis

One of the main goals of this study is to assess the adverse effects spectral noise may have on our ability to recover the emission line parameters as intrinsically emitted by the AGN. We achieve this by comparing line widths measured on the high S/N spectra in our sample with line widths measured on artificially degraded versions of the same high S/N spectra. We estimate the S/N ratio in the continuum using the error spectrum to measure the noise; if an error spectrum is unavailable, which is the case for the mean spectra based on monitoring data, we instead use the rms of the flux density around the continuum level as an estimate of the noise. The rms of the flux density only provides an upper limit on the noise as real spectral features will enhance the measured rms above that of the true flux uncertainty. However, the method works well for low quality spectra where the rms in the

Table 2.2 Spectral properties of the C IV database

Source	Redshift z	S/N	EW	Line shape	FWHM	σ_{line}	MAD	IPV(50%)	Ref.
(1)	(2)	(3)	(4)	(5)	(6)	(7)	(8)	(9)	
Composite A[a]	...	32	43	0.83	2640	3184	2223	2909	1
Composite B[a]	...	33	44	1.07	3920	3659	2618	3608	1
Composite C[a]	...	46	37	1.30	5004	3857	2810	4039	1
Composite D[a]	...	36	31	1.65	6695	4057	3068	4683	1
Composite E[a]	...	30	27	1.78	8022	4498	3440	5335	1
J111816.94+074558.2	1.7350	37	34	1.39	4620	3333	2530	3882	2
J133335.78+164903.9	2.0885	41	18	1.11	5102	4608	3381	4662	2
J084106.79+031206.8	1.8364	64	17	1.36	5159	3801	2868	4369	2
J100129.64+545438.1	1.7552	39	20	1.22	5201	4256	3174	4839	2
J005021.22+005135.0	2.2341	42	23	1.37	5759	4198	3208	4890	2
J122527.39+223512.9	2.0498	39	25	1.25	5894	4725	3598	5642	2
J005157.24+000354.7	1.9559	39	20	1.81	6503	3584	2668	4272	2
J082450.79+154318.4	1.8739	35	24	1.32	6707	5094	3772	5709	2
J170100.60+641209.3	2.7348	76	20	1.60	6834	4274	3250	5059	2
J142656.18+602550.8	3.1917	50	32	1.79	8080	4509	3436	5319	2
J111800.50+195853.4	1.9356	38	13	3.81	8862	2324	2442	4908	2
J073502.30+265911.5	1.9727	39	18	2.44	10624	4358	3589	6434	2
Fairall 9[b]	0.0470	200	119	0.69	3085	4502	3122	3950	3
NGC 3783[b]	0.0097	200	147	1.00	3131	3129	2221	2983	4
NGC 7469[b]	0.0163	200	78	0.96	3326	3456	2442	3273	5
NGC 5548[c]	0.0172	200	209	0.99	3571	3619	2652	3918	6
Q1542+0417	2.1820	48	35	0.59	1998	3371	2234	2695	7
Q2212-2959	2.7037	45	24	0.67	2350	3515	2200	2550	7
Q1402-0116	2.5150	40	43	0.66	2450	3701	2596	3408	7
Q0106+0119	2.0990	85	21	0.86	3063	3560	2612	3627	7
Q1311-2700	2.1950	35	63	0.88	3510	4005	3036	4555	7
Q1705+0152	2.5750	59	41	1.13	3734	3308	2225	3105	7
Q2150+0522	1.9770	40	45	0.97	3797	3899	2902	4178	7
Q0238+1005	1.8260	30	62	1.11	4193	3788	2770	4020	7
Q0038-0159	1.6700	59	69	1.21	4565	3781	2931	4523	7
Q1554-2020	1.9450	59	29	1.51	4686	3101	2289	3500	7
Q0226-0350	2.0750	54	29	1.20	4705	3918	2812	3961	7
Q1626+1202	1.7900	37	23	1.55	6014	3890	2823	4156	7
Q1442+1011	3.5523	34	22	1.43	6249	4363	3298	5172	7

Note. — See Table 2.1 for column explanations.

Note. — [(a)]The SDSS composite spectra all have data from >150 SDSS spectra in each pixel at rest-frame wavelengths between 1445Å and 1700Å where we perform the spectral decomposition (§ 2.6.2); [(b)]Observed with *IUE/SWP* with a spectral resolution of $\Delta v \approx 1160\,\mathrm{km\,s^{-1}}$. Rest-frame wavelength coverage is 1098Å – 1886Å (Fairall 9), 1138Å – 1951Å (NGC 3783), and 1180Å – 1943Å (NGC 7469); [(c)]Observed with *HST/FOS*, the spectrum covers 1070Å – 2290Å in the wavelength rest-frame with a spectral resolution of $\Delta v \approx 365\,\mathrm{km\,s^{-1}}$.

(1) Stephan Frank et al. 2018, in prep.; (2) Schneider et al. (2010); (3) Rodríguez-Pascual et al. (1997); (4) Reichert et al. (1994); (5) Wanders et al. (1997); (6) Korista et al. (1995); (7) This work.

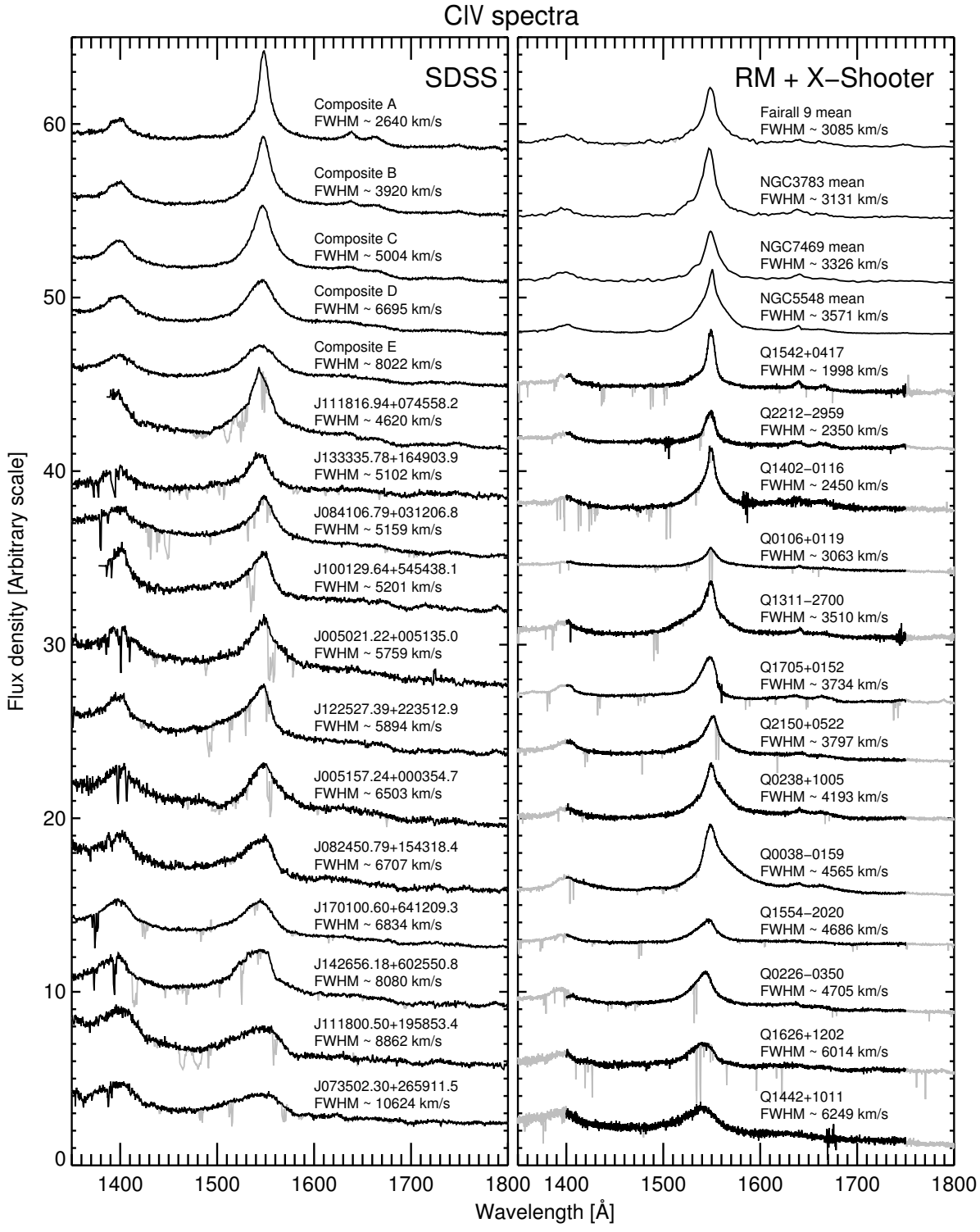

Fig. 2.2 The 34 spectra forming our sample of high S/N C IV spectra. Only the spectral range near the C IV emission line is shown. The spectra are shifted in the vertical direction and placed on an arbitrary flux density scale. The original spectra with narrow absorption lines are shown in gray where relevant.

continuum is dominated by the spectral noise. We use the spectral continuum windows of 1445 Å – 1455 Å and 1690 Å – 1700Å to estimate the S/N level for the C IV spectra and the region between 5600 Å and 5700 Å for the Hβ spectra.

2.5.1 Degradation of spectra

To cover a large range of spectral qualities in our analysis we degrade the high S/N spectra from the original S/N ($> 30\,\mathrm{pixel}^{-1}$) to a range of S/N levels down to S/N $\sim 1\,\mathrm{pixel}^{-1}$. Each degradation is performed by adding a predetermined amount of noise to each pixel of the original high S/N spectrum, where we take into account the S/N level of the original spectrum. We check that all degraded spectra have the desired noise level by measuring their S/N as specified above. We use a Monte Carlo approach to obtain a statistical measure of the accuracy and precision of the line width measures as a function of spectral noise by degrading each original spectrum 500 times to a given S/N level, each time with a different 'seed' for the Gaussian noise distribution.

We show sample degradations in Figure 2.3. Clearly, the added noise has two effects, namely disguising real spectral features and generating fake features. Both effects are unfortunate and the reason that spectral noise cannot be ignored.

2.5.2 Statistical analysis

As the best estimate of the line width at a given S/N level we use the mode of the distributions of the 500 line widths that we measure at that S/N level. The accuracy of the line width is then calculated as the offset between this best estimate and the line width measured on the original high S/N spectrum; the precision is the width of the distribution.

Because the distributions we measure often are highly asymmetric (see Figure 2.9 for an example), we allow for asymmetric errors in the following way. We use the most frequent value (i.e. the mode) to divide the distribution into two parts. Then, 68% of the area enclosed by each of the distributions below or above the mode, respectively, define the error bar. For a Gaussian distribution, for which the mode divides the distribution in two equal halves, this is equivalent to one standard deviation (i.e., 34.1% of the total area or 68.2% of half the area).

We exclude any spectra from our analysis for which the decomposition model (§ 2.6) fails to converge and for which the emission line parameters are impossible to measure due to, for example, a negative line flux in the isolated emission line profile. At S/N $\geq 5\,\mathrm{pixel}^{-1}$, this typically constitutes less than 5% of the spectra, while at S/N < 5 pixel^{-1}, this number can be closer to 10%. The small fraction of spectra that we exclude from further analysis does not affect the main conclusions of this work, but it does highlight the fact that the spectral noise can prevent a credible spectral decomposition.

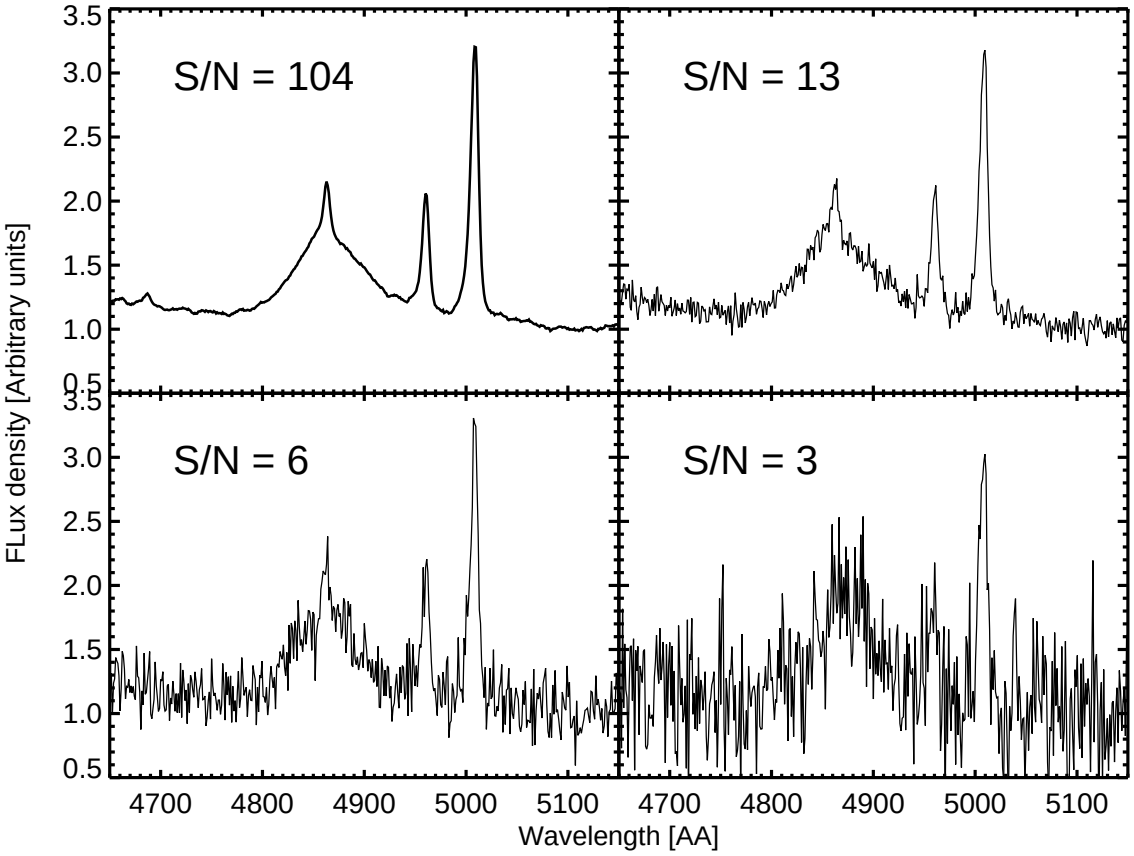

Fig. 2.3 A high S/N Hβ spectrum (upper left corner) degraded to S/N levels of $\sim$ 13, 6, and 3 pixel^{-1}, respectively. The added noise has the effect of disguising real spectral features and creating fake features.

2.6 Deblending spectral features

In order to measure the line parameters it is necessary to first completely isolate the emission line profile. The first step of this process is performed during the decomposition, described in this section, while the second step is to constrain the extent of the line in wavelength space by the use of line limits, described in § 2.7. This is especially important for the integral line parameters (σ_{line}, MAD, and IPV widths) since we need to know over which wavelength range to integrate the flux.

The ideal spectral decomposition is one that provides an accurate description of all spectral features present in the data and is robust to a varying data quality (i.e., S/N and spectral resolution). For the decompositions used in this work, the first criterion is tested in this section on the high S/N spectra that form the original data samples defined in § 2.4. We test the robustness of the spectral decomposition to the S/N level of the data by means of S/N-degraded spectra in § 2.8 and § 2.9 for our Hβ and C IV spectral samples, respectively. In addition, we require the decomposition to be flexible enough that it can be made fully automated as is convenient when there is a need to apply it to large datasets.

Denney et al. (2009) show how the choice of a specific spectral decomposition method profoundly affects the obtainable accuracy and precision of the measured line parameters. Comprehensive and thorough tests of the robustness of existing spectral decomposition methods, of which there are many, is beyond the scope of this study. Instead, we tested a few different approaches using both a *local* and *global* continuum as well as different functional forms (i.e., Gauss and Lorentz profiles) to model the emission lines. We tested these different methods on the spectra in our Hβ and C IV databases and choose the methods described below for the following reasons. First, they were able to successfully model the high S/N spectra, and secondly, they were robust to minor changes in the spectral S/N (changes of $\sim$5 in S/N level).

We use slightly different methods to decompose the Hβ and C IV spectra, outlined in § 2.6.1 and § 2.6.2, respectively. They are *local* decompositions in the sense that they do not cover the entire observed wavelength range, for example between 3800Å – 9200Å available for the SDSS spectra, but they are limited to the 'local' spectral region near the emission line of interest. Measuring line widths on functional fits to the profiles is often considered an effective way to mitigate spectral noise. For our test of the robustness of the line width parameters we therefore determine the profile widths by performing measurements both directly on the data and on functional fits to them.

2.6.1 Spectral decomposition of Hβ spectra

An example of a decomposition of the spectral region around the Hβ emission line is shown in Figure 2.4. The spectral model consists of the following components:

1. A power-law function (dark-brown curve in Figure 2.4), representing the featureless nuclear AGN continuum, defined as $F_\lambda \propto \lambda^\alpha$, where F_λ is the flux density as a function of wavelength λ and α is the power-law slope;

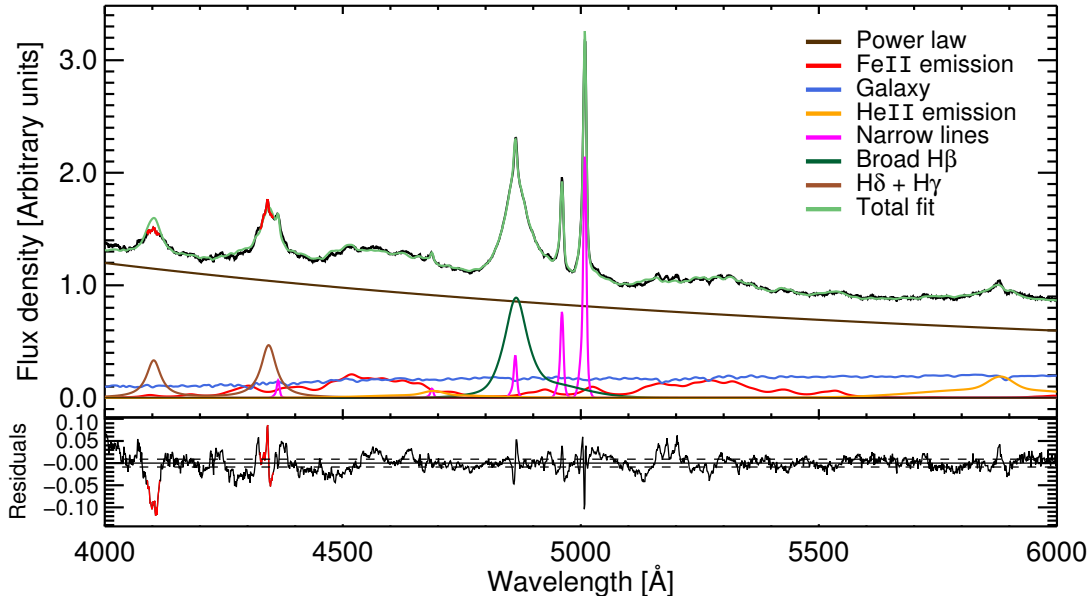

Fig. 2.4 Spectral decomposition of the SDSS Hβ Composite B spectrum with FWHM(Hβ) ∼ 3450 km s^{-1}. Regions around the Hδ λ4102 and Hγ λ4341 lines, shown in red, are masked out. The spectral decomposition model consists of a power-law function to account for the featureless nuclear AGN continuum (dark brown curve), a template of galaxy emission (blue curve), a template of Fe II emission (red curve), and multiple Gaussian and Lorentzian functions to account for the individual narrow and broad emission lines (yellow, magenta, light brown, and green curves). The model of the broad Hβ emission (dark green curve) is at this stage only a temporary placeholder to ensure a good model-fit to the other emission components. The Hβ profile is modelled separately as described in § 2.6.1. Near the Hβ line (∼4600 Å − 5100 Å), the largest residuals are seen around the line center and in the red wing. The dashed lines in the lower diagram show the rms of the flux density measured in the spectral continuum window between 5600 Å − 5700 Å. The broad Hβ profile, after subtracting the contaminating emission of other lines, is shown in Figure 2.5.

2. Iron emission modelled by an empirical template of optical Fe II emission (red curve), extracted from a high-quality spectrum of the Seyfert 1 galaxy I Zw1 (Véron-Cetty et al., 2004). The width and strength of the iron features are allowed to vary during the modelling process;

3. Galaxy emission to account for contaminating stellar light from the AGN host galaxy (blue curve in Figure 2.4). To model this, we use a single template of a 10 Gigayear Bruzual & Charlot (2003) spontaneous stellar population model with a metallicity of $Z = 0.5\,Z_{\odot}$, where $Z_{\odot}$ is the solar metallicity, and allow only the strength of the host galaxy emission to vary. A single host galaxy template is adequate for our analysis because the specific type of host galaxy model adopted does not affect our ability to measure the line width parameters in the 4500 Å – 6000 Å wavelength region. Also, the resolution and nuclear emission contrast present in our data typically does not let us distinguish with confidence between different galaxy types, such as Sa, Sb, S0, or E galaxies, at optical wavelengths around 5000 Å where these galaxy spectra usually have similar spectral slopes. For the SDSS composite spectra, the host galaxy type is not well defined because the stellar light contribution in this case originates from a mixture of different galaxy types, and it is inappropriate to fine tune the model to a specific host galaxy type;

4. The individual emission lines of Hβ, [O III] $\lambda\lambda$4959, 5007, He II λ4686, and He I λ5876 are modelled using multiple Gaussian functions (dark green, magenta, and orange curves, respectively, in Figure 2.4), and the Hδ λ4102 and Hγ λ4341 emission lines are modelled by a single Lorentz function each (brown curves in Figure 2.4), with the width, amplitude and peak velocity shift as free parameters. Experience from previous work (Vestergaard et al., 2008, 2011) has shown that a Lorentz profile is a good match for the profile wings of these lines. The peak of the Hδ λ4102 and Hγ λ4341 lines, respectively, are often difficult to model, so we mask out their central region extending to $\pm 1000\,\mathrm{km\,s^{-1}}$ from each of their line centres. This does not affect our modelling of the Hβ profile and increases the computational speed. Details on the modelling of the individual emission lines are given below.

All emission components are modelled simultaneously in the restframe 4000 Å – 6000 Å spectral window.

The Balmer lines contain contributions from both the broad line region (BLR) and the narrow line region (NLR). However, for black hole mass estimates, we are interested in the velocity of the BLR gas only, because the NLR emission originates from a region located much further from the central engine than the BLR. This is verified by the fact that the NLR emission varies on timescales on the order of years (e.g., Peterson et al., 2013), much longer than the BLR emission variations that takes place on timescales of days to weeks (e.g., Peterson et al., 2004). The fact that forbidden transitions are only observed among the narrow emission lines also corroborate the fact that the physical conditions in the BLR and NLR are different (Peterson, 1997; Osterbrock & Ferland, 2006). For these reasons, it is important that the narrow line contribution to the Hβ emission is subtracted

before we measure the profile width. Failing to do so will result in an underestimation of this width (e.g., Peterson et al., 2004; Denney et al., 2009).

As is common (e.g., Peterson et al., 2004; Bentz et al., 2007, 2009c; Shen et al., 2011), we use the [O III] profile as a template to model the velocity field of the NLR. This is important because the Hβ NLR emission blends strongly with the BLR emission and is thus difficult to model by itself. This is particularly true for Hβ lines with a strong narrow core component (i.e., profiles where the BLR emission itself has a relatively narrow velocity width, such as observed for Narrow Line Seyfert 1 galaxies) where the transition between the NLR and BLR components is smooth and inconspicuous. The [O III] lines and the narrow components of the He II and Hβ lines are therefore modelled with the same width and peak velocity shift, while their individual amplitudes are allowed to vary. We model the [O III] λλ4959, 5007 lines, the narrow components of Hβ and the He II λ4686 line, when present, with two Gaussian functions for each transition. This is necessary since the [O III] lines often show a blue wing (e.g., Heckman et al., 1981; Greene & Ho, 2005a; Komossa et al., 2008) and in some cases even a double peaked profile (e.g., Wang et al., 2009; Liu et al., 2010; Smith et al., 2010).

To allow low S/N profiles to be modelled, we do not hold the [O III] λ4959 / [O III] λ5007 flux ratio constant at the exact value of 1:3 as set by atomic physics. For our 26 high-S/N spectra we obtain a modelled [O III] flux ratio between 0.070 and 0.402 with a median value offset from the theoretical value of 1:3 by 0.01 with a standard deviation of 0.07 relative thereto. Our median value is thus fully consistent with the theoretical value.

We model the broad components of the He II λ4686 and He I λ5876 lines by two Gaussian profiles each (orange curves in Figure 2.4), with the same width and peak velocity shift. The broad Hβ emission is modelled by three Gaussian functions (dark green curve in Figure 2.4) which allow us to reproduce the variety of line shapes observed; notably, if two components suffice, the flux of the last component is zero.

After subtracting the contributions from the NLR, the power-law continuum, the Fe II emission lines, and the galaxy's stellar light to the observed spectra, we obtain an Hβ profile as shown in Figure 2.5. The excess emission (red curve) in the red wing around 4900 Å – 5000 Å is typically present at this stage of our spectral decomposition. It is unclear if this residual is genuine Hβ flux or residual Fe II and [O III] emission due to non-perfect modelling of these rather blended contributions. But, since this emission does not appear to be a natural, redshifted extension of the otherwise smooth and, often, apparently symmetric Hβ profile, we consider it unlikely to be Hβ emission. We therefore employ an extra step of modelling while blocking out the region affected by these residuals in order to eliminate this emission from the narrow-line subtracted Hβ profile (see § 2.6.1). This provides us with an observed Hβ profile, devoid of any contaminating emission, and we can thereafter measure the velocity width of the broad Hβ emission directly on the observed data. In addition, we obtain a functional fit to the broad Hβ profile (described in § 2.6.1) that we will later use to investigate if this approach is effective at mitigating the adverse effect of spectral noise on the accuracy and precision of the line width measures (§ 2.8).

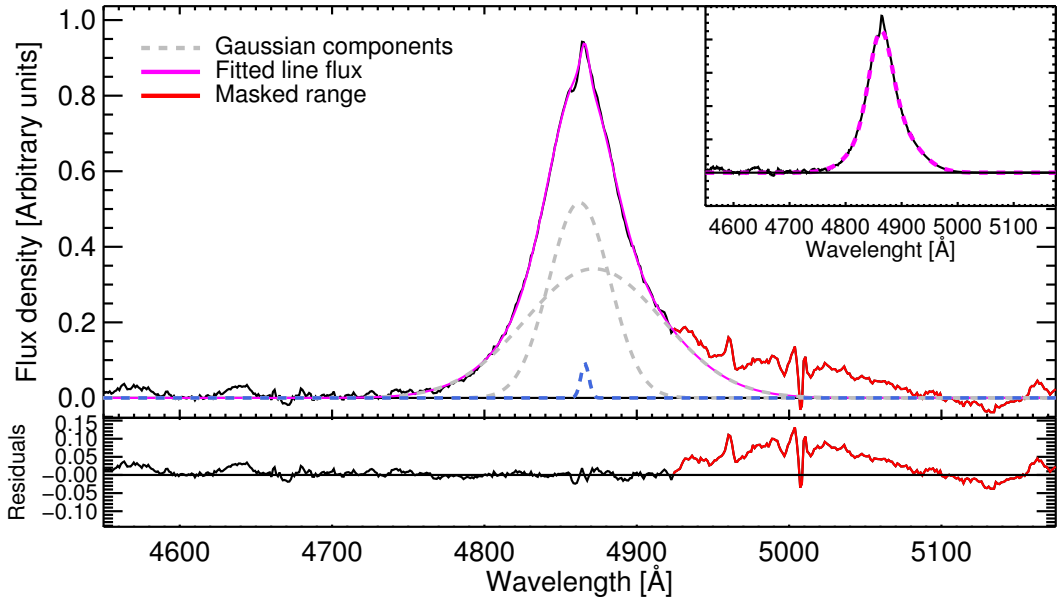

Fig. 2.5 Functional fit (solid magenta curve) to the broad, narrow-line subtracted Hβ profile (solid black curve); spectral regions not used to constrain the model are shown in red. The functional fit provides a smooth extension of the line profile in the red wing of Hβ (shown as the solid black curve in the insert). The three dashed curves indicate the Gaussian components used to model the Hβ profile, but only the two strongest components (grey dashed curves) are retained for the model profile (magenta curve in insert), used in the analysis.

Isolating the observed broad Hβ emission

We remove the contaminating flux in the red Hβ wing (red curve in Figure 2.5) by modelling the narrow-line subtracted Hβ profile with three Gaussian functions (dashed gray and blue lines; Figure 2.5. The profile model (solid purple curve) is constrained by the spectral region from 4600 Å to a position located 3600 km s^{-1} redward of the flux weighted line centroid (measured between 4800 Å and 4922 Å); from a visual inspection of the data we find this to be the position from where the residual flux extends outwards in the line wing. We then replace the observed flux densities (marked in red in Figure 2.5) with the functional model for velocities exceeding 3600 km s^{-1} redward of the line centroid (the black and purple curves are joined at this wavelength). To avoid that one or more of the Gaussian components drift towards the red profile wing, we limit the peak velocity shift of these Gaussian functions to the range $\pm$500 km s^{-1}. This allows for some flexibility in the fitting process, while we avoid assigning the residual flux to the Hβ profile.

As shown in Figure 2.5, our model (magenta curve) reproduces the Hβ profile very well within the spectral fitting window, and the functional fit effectively removes the excess emission in the red wing of Hβ and results in a smooth and clean representation of the Hβ line emission (black curve in insert).

Generating a functional model of the broad Hβ profile

We will later use the functional fittted model, described above, to test if this is an effective way to mitigate the negative effect of spectral noise on the accuracy and precision of the measured line width parameters. To generate the model that we adopt for our analysis, we exclude any of the three Gaussian components with integrated line flux less than 5% of the total line flux and/or components with a line dispersion less than 200 km s^{-1} (comparable to the SDSS spectral resolution element) from the final model of the broad Hβ profile. We do so, because we find such components generally represent residuals present near the line peak after subtraction of the narrow line component. The insert in Figure 2.5 illustrate a model (magenta curve) of a broad Hβ profile after one of the Gaussian components (dashed blue curve) is excluded because it is modelling emission that we regard as residuals from the narrow-line subtraction.

2.6.2 Spectral decomposition of C IV spectra

The decomposition of the C IV spectral region follows the same overall scheme as outlined for the Hβ region with the exception that we do not model the host galaxy contribution. This is mainly due to the fact that most AGN host galaxies (typically of type S0, Sa, Sb, or E; e.g., Bentz et al., 2009b, 2013) have little, if any, significant emission at ultraviolet energies (Kinney et al., 1996). In addition, the SDSS and X-Shooter quasars in our sample, for which the C IV line is observed in the optical or UV region respectively, are high redshift, high luminosity sources, and in this case, the nuclear to host galaxy emission contrast is high (e.g., Kim et al., 2008; Ridgway et al., 2001).

A sample spectral decomposition of a C IV line profile is shown in Figure 2.6. The decomposition includes the following spectral components:

1. A power-law component (dark-purple curve in Figure 2.6) to account for the featureless nuclear AGN continuum;

2. The individual emission lines of N IV λ1486, C IV λ1549, He II λ1640, and the blended emission of [O III] λ1663 and Al II λ1670 are modelled by multiple Gaussian functions with the amplitude, width, and peak velocity shift as free parameters (magenta, dark green, and blue curves, respectively, in Figure 2.6). To model the shape of the N IV and [O III] + Al II lines we use a single Gaussian function for each profile, while we use two and three Gaussian functions for the He II and the C IV lines, respectively;

3. A single Gaussian function (brown curve in Figure 2.6) to account for the emission of unknown physical origin in the so-called red shelf around 1600 Å that can not be accounted for by the models of the He II and [O III] lines (for a discussion on how to deal with this emission, see e.g., Fine et al., 2010; Denney et al., 2013). We also attempted to model this emission using the Fe II UV template extracted from high-quality *HST* spectra of the Seyfert 1 galaxy I Zw1 (Vestergaard & Wilkes, 2001), but found that this gave a poorer description of the high S/N

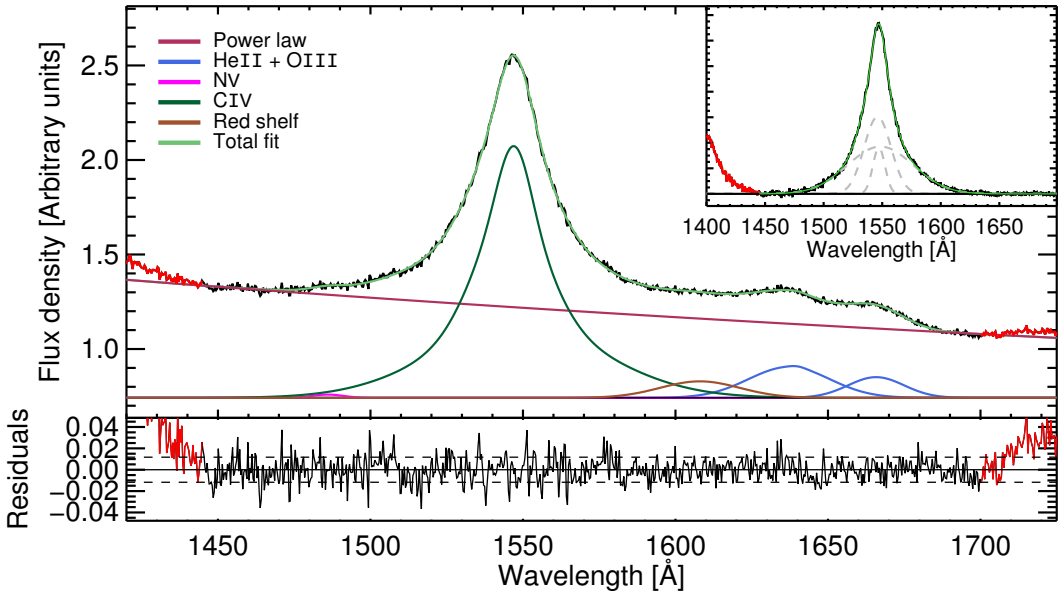

Fig. 2.6 Spectral decomposition of the composite SDSS C IV Composite C spectrum with FWHM(C IV) $\sim 5035\,\mathrm{km\,s^{-1}}$. Regions shown in red are outside the spectral fitting region between 1445 Å – 1700 Å and are not included in the decomposition. The He II, [O III] (blue curves), and red shelf (brown curve) model components reproduce the emission around 1600 Å closely. The insert shows the observed C IV profile (solid black curve), the functional model of the C IV profile (green curve), and the three Gaussian components of the C IV line model (dashed grey curves).

spectra in our C IV sample than the procedure we adopt here. Modelling this emission by a single Gaussian function allows us to effectively isolate the broad C IV emission without assuming any specific physical origin for the emission in the red shelf.

To ensure that the power-law component accurately represents the underlying nuclear continuum, we first model this spectral component alone by fitting to the two spectral continuum windows at 1445 Å – 1455 Å and 1690 Å – 1700 Å. We subtract the modelled power-law continuum before we model the rest of the spectral components.

We note that adopting a one-step spectral decomposition of the full spectral range from 1445 Å to 2200 Å, where all components are modelled simultaneously, does not significantly alter the resulting continuum model or the measured line parameters. However, our two-step modelling process is often up to ten times faster computationally; this is a clear advantage when processing large data sets, as long as the continuum level is well-determined by the continuum windows.

Isolating the broad C IV emission

We obtain the observed C IV profile, devoid of blending line emission, by subtracting the models of the power-law continuum, the red shelf, and of the emission lines of N IV, He II, and [O III] + Al II from the spectrum. The insert in Figure 2.6 shows that our decomposition results in an observed C IV profile (solid black curve) that is smooth and free of blending line emission. We use this C IV profile in § 2.9 to measure the line width parameters directly on the observed data.

Generating a functional model of the C IV profile

We use the sum of the three Gaussian components, defined above in § 2.6.2, to generate a smooth functional model of the C IV profile. In § 2.9 we test if by measuring the line widths on this model, as opposed to the data themselves, can effectively mitigate the effects of spectral noise. The insert in Figure 2.6 shows that our model (green curve), i.e., the sum of the three Gaussian components shown as dashed grey curves, gives a smooth representation of the observed C IV line profile.

2.7 Emission line limits

For an isolated line in a high S/N spectrum the line limits are clearly defined as the wavelength positions from the line centre where the line flux reaches zero intensity. In an observed spectrum with photon-shot noise and additional emission lines that can blend with the wings of the line of interest, the optimal positioning of the line limits is less obvious. The ideal position of the limits is close enough to the line centre to exclude extraneous emission but far enough to avoid truncating the profile. In addition, the ideal limits should be robust to spectral noise.

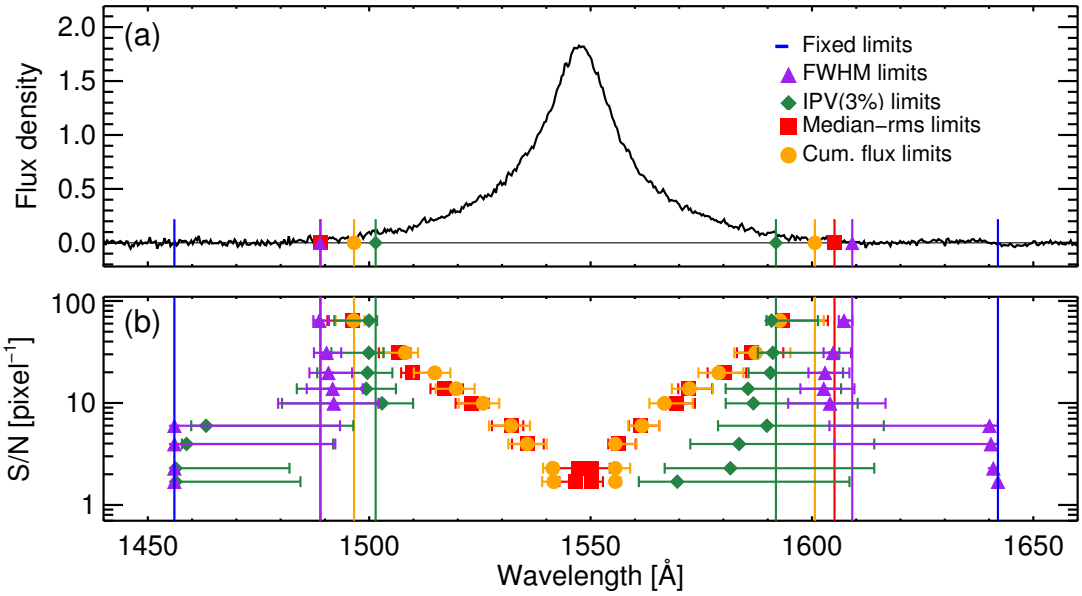

Fig. 2.7 Illustration of the five types of line-wing limits that we test for robustness to the spectral S/N level, here shown measured on the SDSS C IV Composite B spectrum with FWHM(C IV) $\sim 3900\,\mathrm{km\,s^{-1}}$. **Top panel:** The blue and red profile limits of each line-limit method, marked by its own symbol, are shown superimposed on the extracted high S/N emission profile. **Bottom panel:** Data points with error bars show the mode and the standard deviation relative thereto, respectively, of the measured distributions of the line limit positions as a function of spectral S/N level, based on our Monte Carlo analysis described in § 2.5.

We test here the robustness of five methods by which one can define the line limits in an automated manner, suitable for implementation on large data sets. We adopt three suitable methods that we evaluate further in § 2.8 with respect to their influence on the accuracy and precision of the line width measures. The top panel of Figure 2.7 shows the position of five types of line limits on a isolated high S/N C IV profile that we describe in the following.

1. **Fixed limits.** These limits are placed at a fixed distance from the line centre. Then, by definition, they are unaffected by spectral noise. We position these limits (blue vertical lines in Figure 2.7) at a velocity, v_{limit}, of $\pm\,18{,}000\,\mathrm{km\,s^{-1}}$ from the line centre; this corresponds to wavelengths of $\sim$1456 Å and $\sim$1642 Å, respectively, for the C IV profiles, and wavelengths of $\sim$4569 Å and $\sim$5153 Å, respectively, for the Hβ profiles. For a Gaussian profile with FWHM $\leq 14{,}000\,\mathrm{km\,s^{-1}}$, more than 99.7% of the line flux is included between these limits. Using all the high-S/N spectra of our sample we test if the fixed line limits truncate the profiles by varying the wavelength position of the limits between $v_{limit} = 16{,}000\,\mathrm{km\,s^{-1}}$ and $v_{limit} = 20{,}000\,\mathrm{km\,s^{-1}}$ in increments of $500\,\mathrm{km\,s^{-1}}$. We then compare each of the line dispersion, MAD, and IPV(50%) widths measured between these different v_{limit} positions; the FWHM measured in the original high S/N spectra is not affected by a change in line limit position within the range we test here. When we decrease v_{limit} from $18{,}000\,\mathrm{km\,s^{-1}}$ to $16{,}000\,\mathrm{km\,s^{-1}}$ the measured line dispersion, MAD,

and IPV(50%) width generally becomes smaller (at a median decrease of 2.0%, 1.1%, and 0.3%, respectively, for the σ_{line}, MAD, and IPV(50%) widths). This shows that the profiles are generally truncated by line limits below v_{limit}=18,000 km s^{-1}. Conversely, when we increase v_{limit} from 18,000 km s^{-1} to 20,000 km s^{-1}, we do not find a significant increase (<0.5%) in the median line widths we measure. This indicates, that for $v_{limit} > 18{,}000$ km s^{-1}, no significant fraction of the line flux is excluded by the limits. This test also shows that the specific line limit position has a larger effect on the measured line dispersion than on the MAD and IPV(50%) width. This is because the line dispersion depends rather strongly on the flux in the line wings. We refrain from using $v_{limit} > 18{,}000$ km s^{-1} as this increases the risk of including extraneous emission and/or noise in the continuum emission between the limits.

2. **Line limits at $\mathbf{v_{limit}}$ = 3xFWHM.** For an emission line with a Gaussian shape, 99.9% of the line flux is contained within 3xFWHM ($\sim 7\sigma$) of the line centre, while for a Lorentzian line profile with the same FWHM, only 89.5% of the line flux is contained within the same limits. In reality, most observed broad emission lines is a mixture of these two functions with a somewhat Gaussian core and broader Lorentzian wings, and we therefore expect more than 90% of the line flux to be contained within 3xFWHM of the line centre. Therefore, one feasible option is to define the limits to lie at v_{limit} = 3xFWHM (purple vertical lines and triangles in Figure 2.7), where the FWHM is measured between the fixed line limits; the fixed line limits serve as a reasonable reference in this case. We note that for non-Gaussian and/or asymmetric profiles, the profile wings can be truncated, thereby potentially introducing a systematic bias in the measured line width.

3. **Limits at the IPV(3%) width.** We place these limits (green vertical lines and diamonds in Figure 2.7) at the position of the IPV(3%) markers (§ 2.3.4) calculated between the fixed line limits. By definition, these line limits truncate the line by 1.5% of the line flux in each of the profile wings, which may introduce a systematic bias in the measured line widths. The flux excluded by the IPV(3%) line limits results in a median decrease of 14%, 9%, and 4% (with a standard deviation relative thereto of 21%, 15%, and 0.3%), respectively, in the σ_{line}, MAD, and IPV(50%) widths measured on the high S/N spectra in our Hβ and C IV samples, compared to using the fixed line limits. We show later (§ 2.8) that the small fraction of the total line flux excluded by the IPV(3%) limits is insignificant compared to the adverse effect spectral noise has on the accuracy and precision of the measured line width parameters. We have tested similar IPV line limits at smaller percentage levels than 3%, but find that this is the smallest possible fraction of the line flux that we can exclude for these limits to be reasonably robust to spectral noise.

4. **Median-rms limits.** Another option is to establish the line limits at the wavelength positions where the flux density of the line rises above the noise of the underlying continuum emission. We define these limits (red vertical lines and squares in Figure 2.7) as the positions v_{limit} where

the median flux density in a five pixel boxcar exceeds the rms of the continuum emission. We use the pixel closest to the line peak, that fulfills the median-rms criterion, as opposed to the most distant pixel (i.e., the pixel closest to the fixed line limit) because that pixel is more influenced by spectral noise.

5. **Cumulative flux distribution limits.** A way to identify where the line flux rises above the continuum noise is by computing the cumulative flux distribution starting from the fixed line limits, and choosing the wavelength for which the cumulative flux distribution rises above zero. This assumes that the cumulative flux distribution in the continuum will fluctuate around zero, which might not be a reasonable assumption if the spectral decomposition has left residual emission in these spectral regions. We position these limits (orange vertical lines and circles in Figure 2.7) at the wavelength closest to and on either side of the line centre for which the cumulative flux distribution is still below zero.

To test how robust each of the line limits are to spectral noise, we use the same Monte Carlo approach (described in § 2.5.1) that we use to test the robustness of the line width measures (see § 2.8 and § 2.9). This means that we measure the positions of the line limits on artificially degraded versions of all the high-S/N spectra in our Hβ and C IV samples at a range of S/N levels between 1 pixel^{-1} and 50 pixel^{-1} with 500 degraded realisations of each high-S/N spectrum at each S/N level. From the distributions of line limit positions that we measure for each of the line limits at a given S/N level, we then calculate the mode (i.e., the most frequent value) and its uncertainty, taken to be the standard deviation of the distribution on each side of the mode. The bottom panel of Figure 2.7 shows these most frequently used line limit positions and their uncertainties as function of S/N for the artificially degraded versions of the profile shown in the top panel. Hence, figure 2.7 shows the typical response of the five different line limits to increasing spectral noise. The specific numbers discussed in this section only refers to this specific example, but we note that the general conclusions we reach are the same for all the spectra we tested.

The 'median-rms' (red squares) and 'cumulative flux' (orange triangles) line limits are clearly not robust to increasing spectral noise; they approach the line centre and truncate the profile wings as the S/N decreases. This is because the rms around the zero flux density level increases with the noise, as does the probability of the cumulative flux distribution to be negative at a position closer to the line centre. The fixed (blue line), 3xFWHM (purple triangles), and IPV(3%) (green diamonds) line limits are robust: each of them are consistent with their position measured in the high S/N spectrum down to a S/N ~ 10 pixel^{-1}. We note that even at the (relatively) high S/N levels of between ~ 25 pixel^{-1} and 10 pixel^{-1}, the 3xFWHM line limits move closer to the line peak, thereby truncating the line. The increased noise levels cause an overestimation of the peak intensity and thus an underestimation of the FWHM. At S/N < 10 pixel^{-1}, this trend is reversed such that the 3xFWHM limits likely move away from the line peak because the FWHM is overestimated due to noise in the line wings and continuum.

We will focus on the fixed, 3xFWHM, and IPV(3%) line limits as they, in contrast to the median-rms and cumulative flux line limits, do not show a strong sensitivity towards spectral noise. In the

next section we test how these three line limits affect the accuracy and precision of the line width measures as the spectral quality is deteriorated.

2.8 Robustness of the line width parameters: Results for Hβ

Here, we establish the specific line limits and continuum levels that provide the optimal (i.e., most accurate and precise) way to measure each of the four line width parameters and establish their accuracy and precision as a function of S/N. We also demonstrate how the robustness depends on the width (FWHM), strength (EW), and shape (FWHM/σ_{line}) of the original emission line in question. Finally, we consider whether measuring the line width parameters on a functional fit to the line profile, as opposed to directly on the data, is an effective way to mitigate spectral noise. In this section, we focus on the analysis of Hβ and address C IV in § 2.9.

Ultimately, we are interested in how the accuracy and precision of the line parameter affects the accuracy and precision of the black hole mass estimates. We therefore propagate the accuracy and precision of the line width measures to the black hole mass estimates, under the assumption that only the uncertainty of the measured line widths contribute to the uncertainty of the black hole mass, using the formulas

$$\Delta\log(M_{BH}) = 2\log\left(\frac{\Delta V}{\Delta V_{int}}\right) \quad ;accuracy \tag{2.6}$$

$$\sigma^{\pm}_{\log(M_{BH})} = \pm\log\left(1 \pm 2\frac{\sigma^{\pm}_{\Delta V}}{\Delta V}\right) \quad ;precision \tag{2.7}$$

where $\Delta\log(M_{BH})$ is the offset in black hole mass, ΔV and ΔV_{int} are the measured and original line width, respectively, and $\sigma^{\pm}_{\Delta V}$ and $\sigma^{\pm}_{\log(M_{BH})}$ are the positive and negative uncertainty of the measured line width and black hole mass estimate, respectively.

2.8.1 Accuracy and precision of FWHM

In this section we examine the robustness of FWHM when measured directly on the data (FWHM(Hβ; data)). Later (§ 2.8.5) we also examine the FWHM measured on a functional model, but, unless otherwise clearly stated, we always refer to the line parameters measured directly on the data.

Optimal measurement method

The FWHM(Hβ; data) is most robust to spectral noise when measured relative to the best$-1\sigma_{\rm cont}$ continuum level and with either of the fixed, 3xFWHM or IPV(3%) line limits. An example of this is shown in Figure 2.8 for FWHM(Hβ; data) measured on the S/N degraded versions of the SDSS Hβ Composite C spectrum, yet, the conclusions hold for all the spectra in our sample. The best choice of continuum (left panel) and line limits (right panel), respectively, are those that each leads to a measured FWHM(Hβ; data) value near the horisontal black line marking the intrinsic FWHM(Hβ; data) of

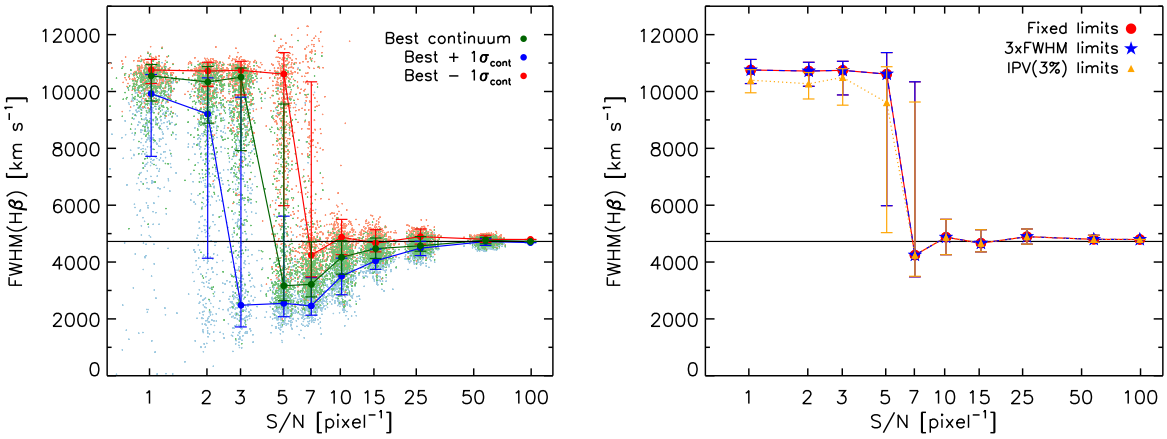

Fig. 2.8 Illustration of the continuum level and line limits that optimise the accuracy and precision of the FWHM(Hβ; data). **Left panel:** The small red, green, and blue dots represent the measured FWHM(Hβ; data) relative to the best$-1\sigma_{\rm cont}$, best, and best$+1\sigma_{\rm cont}$ continuum level, respectively, for each degradation of the original spectrum (in this case the SDSS Hβ Composite C spectrum with a measured FWHM(Hβ; data) $\approx 4800\,{\rm km\,s^{-1}}$). Large dots show the most frequently measured value and its uncertainty at certain S/N levels. The measured FWHM(Hβ; data) is clearly most robust to noise if measured relative to the best$-1\sigma_{\rm cont}$ continuum setting at S/N $\geq 10\,{\rm pixel^{-1}}$. **Right panel:** The figure shows the most frequent value of the FWHM(Hβ; data) measured relative to the best$-1\sigma_{\rm cont}$ continuum level as a function of S/N with fixed (red circles), 3xFWHM (blue stars), and IPV(3%) (orange triangles) line limits. The choice of line limits does not affect the accuracy and precision of the measured FWHM(Hβ; data) in the regime where it can be measured with high accuracy and precision (S/N $\geq 10\,{\rm pixel^{-1}}$; see left panel).

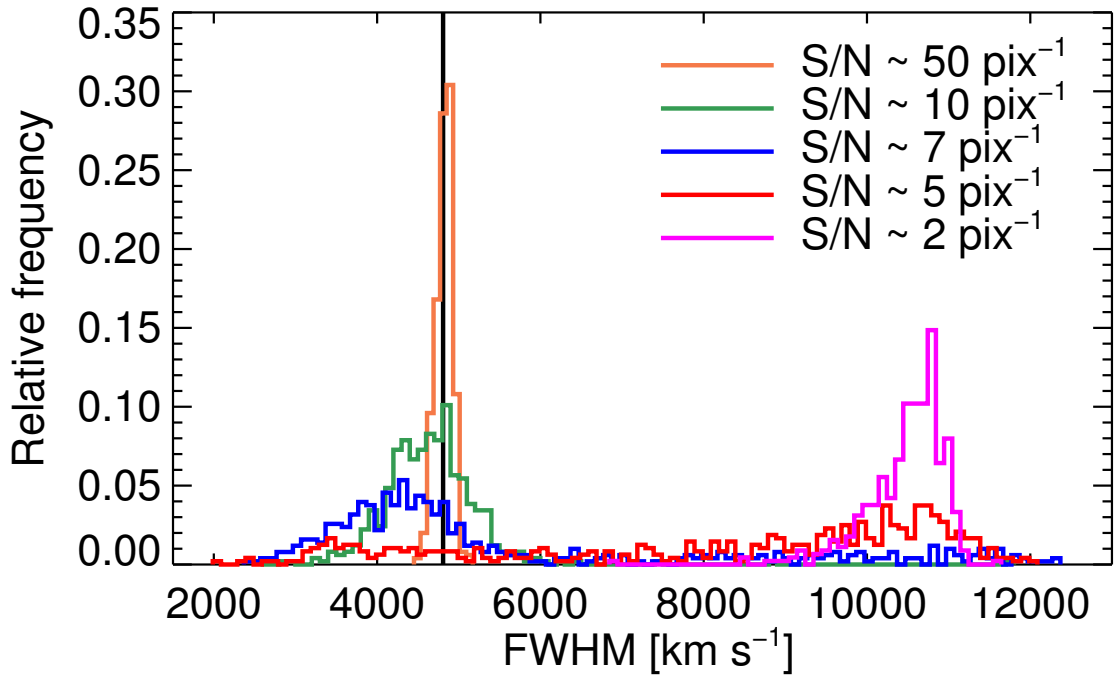

Fig. 2.9 Distributions of the FWHM(Hβ; data) measured directly on the data with fixed line limits and relative to the best$-1\sigma_{\rm cont}$ continuum model for degraded versions of the SDSS Hβ Composite C spectrum with a measured FWHM(Hβ; data) $\sim 4800\,{\rm km\,s^{-1}}$ (solid black line) at S/N levels between $50\,{\rm pixel^{-1}}$ (orange) and $2\,{\rm pixel^{-1}}$ (magenta). Between S/N $\sim 7\,{\rm pixel^{-1}}$ (blue) and S/N $\sim 5\,{\rm pixel^{-1}}$ (red) the FWHM(Hβ; data) transitions from being underestimated due to noise in the line peak to being overestimated due to noise in the line wings and the continuum.

the spectrum. When measured relative to the best continuum setting, the increased noise in the line peak results in an underestimated FWHM (the green symbols deviate from the horisontal line in Fig 2.8). Interestingly, when measured relative to the best$-1\sigma_{\rm cont}$ continuum setting (red symbols), the measured FWHM is robust down to S/N $\sim 10\,{\rm pixel}^{-1}$.

We illustrate how the accuracy and precision of the FWHM is extracted from Figure 2.8 with a few examples. If measured relative to the best (green dots) and best$+1\sigma_{\rm cont}$ (blue dots) continuum level, the FWHM(Hβ; data) is underestimated by 12% and 25% (557 $\,{\rm km\,s^{-1}}$ and $1179\,{\rm km\,s^{-1}}$; 0.11 dex and 0.25 dex in M_{BH}; green and blue curves in the left panel of Figure 2.8), respectively, at S/N $\sim 10\,{\rm pixel}^{-1}$ due to noise in the line peak. At data qualities below S/N $\sim 5\,{\rm pixel}^{-1}$, the FWHM(Hβ; data) can be overestimated by more than 100% ($4800\,{\rm km\,s^{-1}}$; 0.60 dex in M_{BH}; red, green, and blue curves in the left panel of Figure 2.8) because the position of the half intensity wavelengths move away from the line centre due to noise in the line wings and the continuum. This is also seen in Figure 2.9 where the measured FWHM(Hβ; data) predominantly is underestimated due to noise in the line peak at S/N $\sim 7\,{\rm pixel}^{-1}$ (blue histogram) and overestimated due to noise in the line wings and the continuum at S/N $\sim 5\,{\rm pixel}^{-1}$ (red histogram). This latter effect is seen regardless of what reference continuum is used.

Also, FWHM(Hβ; data) measured relative to the best$+1\sigma_{\rm cont}$ and best$-1\sigma_{\rm cont}$ continuum models gives a fairly good estimate of the uncertainty of the FWHM(Hβ; data) measured relative to the best continuum model at S/N $\geq 10\,{\rm pixel}^{-1}$ (the position of the green errorbars is close to the large solid blue and red points, respectively, in the left panel of Figure 2.8). Even though this is true for our entire Hβ sample, we continue to use the uncertainties calculated from our measured distributions of line widths at each S/N level (as described in § 2.5.2) as they do give a more accurate estimate of the uncertainty and can be used to estimate the uncertainty of FWHM(Hβ; data) measured relative to the best$-1\sigma_{\rm cont}$ continuum model, i.e., when it is measured in the most optimal way.

It is interesting to note that when the profile is measured relative to the best$-1\sigma_{\rm cont}$ continuum model, the choice of line limits has no significant effect on the accuracy and precision of the measured FWHM(Hβ; data) as none of the line limits are capable of mitigating the effect of noise in the line peak (Figure 2.8; right panel). Because the IPV(3%) line limits are capable of excluding noise spikes in the continuum surrounding the emission line they improve the accuracy of the measured FWHM(Hβ; data) slightly at S/N $\leq 7\,{\rm pixel}^{-1}$ (orange triangles and curve in right panel of Figure 2.8), but not to a degree that is significant with respect to its uncertainty. The effect of noise is thus more important than the choice of line limits for the robustness of the FWHM(Hβ; data). We therefore choose to measure the FWHM(Hβ; data) between the fixed line limits because they are simplest to implement consistently and provide the same accuracy and precision for the FWHM(Hβ; data) as the 3xFWHM and IPV(3%) line limits.

To summarise, the optimal way to measure FWHM(Hβ; data) is relative to the best$-1\sigma_{\rm cont}$ continuum and between the fixed line limits. From this point forward, unless otherwise noted, this is the method we use to measure the FWHM(Hβ; data).

Results for FWHM(Hβ; data)

We find, that the response of FWHM(Hβ; data) towards decreasing S/N depends on the intrinsic properties of the emission line. Therefore, we discuss the response of FWHM(Hβ; data) in the context of both decreasing S/N and the emission line properties, defined as the line width (FWHM), shape (FWHM/σ_{line}), and strength (EW). The accuracy (left column) and precision (right column) of FWHM(Hβ; data), measured as outlined in the section above, are shown in the top three panel rows in Figure 2.10. In the top, second, and third rows, the results are grouped according to the FWHM(Hβ; data), EW(Hβ; data), and FWHM(Hβ; data)/σ_{line}(Hβ; data), respectively, of the intrinsic spectra in order to clearly show how they depend on the intrinsic properties of the Hβ emission line. The bottom row, pertaining to FWHM(Hβ) measured on a functional model (FWHM(Hβ; funct)) of the broad Hβ emission, is discussed in § 2.8.5.

Panels (a) to (c) of Figure 2.10 show that the accuracy of FWHM(Hβ; data) is well within 20% (0.19 dex in M_{BH}; green, blue, and red shaded areas) for S/N $\geq 25\,\mathrm{pixel}^{-1}$. There is a general tendency to underestimate FWHM(Hβ; data) due to noise in the line peak: all the shaded areas in panels (a) to (c) predominantly lie below the solid black line, marking the FWHM(Hβ; data) measured in the original high S/N spectra. This tendency is strongest for lines with high values of FWHM(Hβ; data) (shaded red area in panel (a)) and high FWHM(Hβ; data)/σ_{line}(Hβ; data) (dashed red area in panel (c)), for which the accuracy quickly drops with decreasing spectral quality; the measured FWHM(Hβ; data) can be underestimated by as much as 38% (0.42 dex in M_{BH}) at S/N $\leq 15\,\mathrm{pixel}^{-1}$. Broad and boxy (high FWHM/σ_{line} values) lines are more sensitive to noise in the line peak and thus there is a high risk that FWHM(Hβ; data) will be underestimated. This trend is more pronounced for these lines than for more narrow (shaded green area in panel (a)) and peaky (shaded green area in panel (c)) lines. Broad and boxy lines are also very susceptible to noise in the line wings and nearby continuum, which increases the risk of overestimating FWHM(Hβ; data). As is clear from Figure 2.10, at S/N $\sim 10\,\mathrm{pixel}^{-1}$, for some broad and boxy lines (shaded red area in panels (a) and (c), respectively), FWHM(Hβ, data) is overestimated by 32% (0.24 dex in M_{BH}) while for other broad and boxy lines it is underestimated by 46% (0.54 dex in M_{BH}). In other words, there is no way of correcting the measured FWHM(Hβ; data) of a broad and boxy emission line at S/N $\leq 10\,\mathrm{pixel}^{-1}$ since it is impossible to know whether the measured FWHM(Hβ; data) is over- or underestimating the intrinsic width of the line.

On a more positive note, if the original emission line is relatively narrow and peaky (shaded green and blue areas in panel a and c, respectively) – roughly corresponding to spectra in our sample with FWHM(Hβ; data) $\leq 6500\,\mathrm{km\,s}^{-1}$ or FWHM(Hβ; data)/σ_{line}(Hβ; data) ≤ 1.8 – then one can expect FWHM(Hβ; data) to be measured to an accuracy within 20% (0.19 dex in M_{BH}) at S/N $\geq 10\,\mathrm{pixel}^{-1}$. Unfortunately, there is no way to establish from data with S/N $< 25\,\mathrm{pixel}^{-1}$ whether the emission line intrinsically has FWHM(Hβ; data) $\leq 6500\,\mathrm{km\,s}^{-1}$ or if it is an intrinsically broader line with a measured width that is underestimated due to spectral noise.

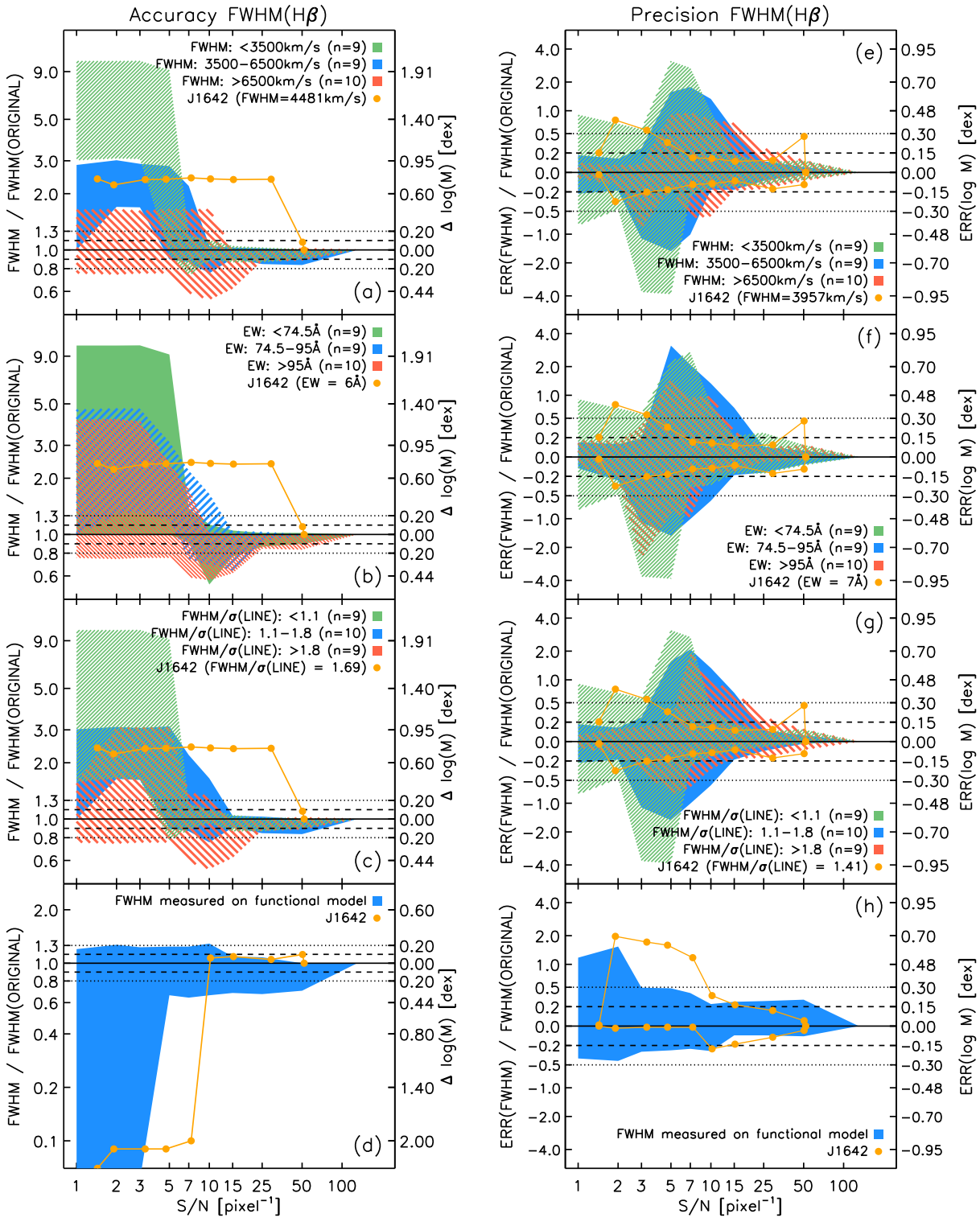

Fig. 2.10 Relative accuracy (left column) and precision (right column) of the FWHM(Hβ) as a function of S/N when measured on all the spectra in our sample of degraded Hβ spectra. A high-accuracy line width will have FWHM/FWHM(ORIGINAL) values very close to unity for all S/N levels (i.e., exhibit a narrow band across a wide x-range at a y-value of $\sim$1.0 in the left panels). For a high-precision line width, the error relative to the line width will likewise hug the reference line at $y = 0$ across a broad range of ... (contd. next page)

(contd.) ... S/N levels in the right hand side panels. Here, the *y*-axis shows the precision as calculated from Equation 2.7 with positive (negative) values representing the uncertainty towards higher (lower) FWHM(Hβ) values. To show how the accuracy and precision of the FWHM(Hβ; data) depends on the characteristics of the emission line, we show the results grouped according to the FWHM(Hβ; data) (top row), the EW(Hβ; data) (second row), and the FWHM(Hβ; data)/σ_{line}(Hβ; data) (third row) as measured on the original high S/N Hβ spectra. The filled area for each group of spectra in each panel shows the span in accuracy (left column) and precision (right column) measured on the Hβ spectra in that group. The legend in each panel shows the grouping criteria and the number of spectra, *n*, in each group. The orange dots connected by solid lines show the accuracy (left column) and precision (right column) in each S/N bin for the spectrum of J164258.80+394836.9, that due to its very low Hβ line strength (EW(Hβ; data) ~ 6 Å) represents a special case, discussed in § 2.8.6. The dashed and dotted horizontal lines in the left column panels mark a relative accuracy of 0.1 dex and 0.20 dex in M_{BH}, respectively, while in the right column they mark a relative precision of 0.15 dex and 0.30 dex in M_{BH}, respectively.

At S/N ≥ 25 pixel^{-1} for which the accuracy is expected to be within 20%, the precision is also expected to be 27% or better (or ≤ 0.19 dex in M_{BH}; shaded areas in panels (e) to (g)). This is almost independent of the intrinsic FWHM(Hβ; data), EW(Hβ; data), or FWHM(Hβ; data)/σ_{line}(Hβ; data) shape parameter values (panels (e), (f), and (g), respectively, in Figure 2.10) of the broad Hβ emission line, although the precision is slightly better for lines with intrinsically low values of FWHM(Hβ; data) and FWHM(Hβ; data)/σ_{line}(Hβ; data) (green and blue areas in panels (e) and (g), respectively, of Figure 2.10). These are the same narrow and peaky lines for which the accuracy is also the highest. At S/N ≤ 5 pixel^{-1}, the precision of the FWHM(Hβ; data) generally improves. This is simply an artefact of FWHM(Hβ; data) always being measured to be the highest possible value allowed within the line limits at these low S/N levels. The increased precision does not suggest that FWHM(Hβ; data) suddenly becomes a trustworthy measure of the line width at low S/N levels. It still has a very low accuracy as evident in panels (a) to (c) of Figure 2.10.

In summary, if FWHM(Hβ; data) is to be measured directly on the data to an accuracy and precision within 20% and 27%, corresponding to 0.19 dex in M_{BH} accuracy and precision, it requires a spectral quality of S/N ≥ 25 pixel^{-1}. At lower S/N, its accuracy and precision drops very quickly. This is especially true for broad and boxy lines that typically have FWHM(Hβ; data) ≥ 6500 km s^{-1} and FWHM(Hβ; data)/σ_{line}(Hβ; data) ≤ 1.8 in which case the effect of spectral noise is the largest.

2.8.2 The line dispersion, σ_{line}(Hβ; data)

Optimal measurement method

In this case, σ_{line}(Hβ; data) is most robust to noise when measured relative to the best continuum model and between the fixed line limits (Figure 2.11). As noted earlier, the optimal choice of continuum level and line limits yield measured σ_{line}(Hβ; data) values that, for a given S/N level, stay close to the horisontal black line in the left panel and to the dashed horisontal line of corresponding

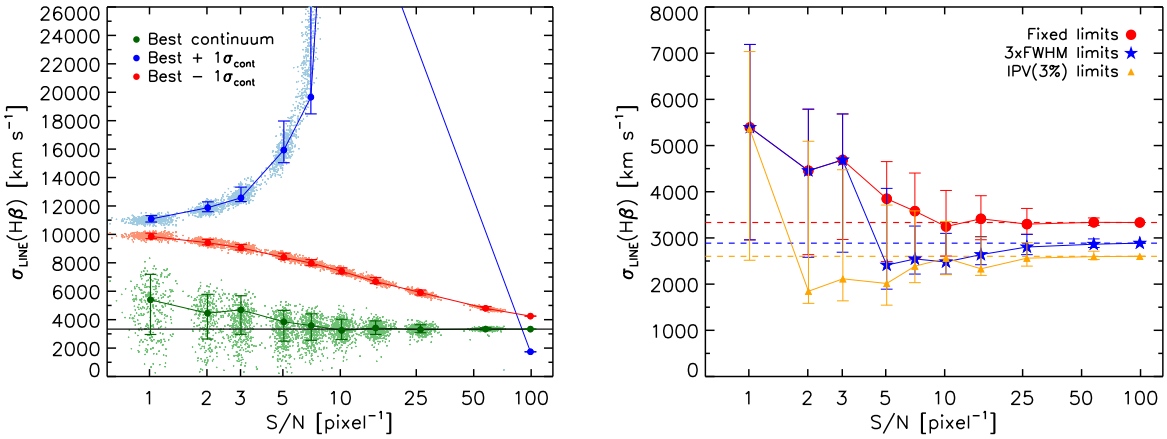

Fig. 2.11 Illustration of the continuum model (left panel) and line limits (right panel) that optimise the accuracy and precision of the σ_{line}(Hβ; data). Symbols and colours are explained in Figure 2.8, except for the dashed lines in the right panel which indicate σ_{line}(Hβ; data) measured in the original SDSS Hβ Composite C spectrum (FWHM(Hβ; data) $\approx 4800\,\mathrm{km\,s^{-1}}$, σ_{line}(Hβ; data) $\approx 3300\,\mathrm{km\,s^{-1}}$) using the fixed (red circles and curve), 3xFWHM (blue stars and curve), and IPV(3%) (orange triangles and curve) line limits. Note that σ_{line}(Hβ; data) is undefined for S/N between 10 pixel^{-1} and 50 pixel^{-1} when measured relative to the best $+1\,\sigma$ continuum level (blue points).

color in the right panel. Contrary to the FWHM, there is no benefit from using another continuum setting than the best-fit one.

We also note, that if measured relative to the best$+1\sigma_{\mathrm{cont}}$ continuum model (blue points in the left panel), σ_{line}(Hβ; data) is undefined at $10\,\mathrm{pixel^{-1}} \leq \mathrm{S/N} \leq 50\,\mathrm{pixel^{-1}}$ because the second term in Equation 2.2 is larger than the first term. It is well-defined again at $\mathrm{S/N} \leq 7\,\mathrm{pixel^{-1}}$, but severely overestimated. This stresses how sensitive the line dispersion is to a robust determination of the underlying continuum level. Notably, because the σ_{line}(Hβ; data) values relative to the best$+1\sigma_{\mathrm{cont}}$ and best$-1\sigma_{\mathrm{cont}}$ continuum levels (blue and red points, respectively) are not contained within the uncertainty of σ_{line}(Hβ; data) relative to the best continuum model (green error-bars), using these continuum levels gives a too conservative estimate of the uncertainty of σ_{line}(Hβ; data) measured relative to the best continuum.

To illustrate exactly how important it is to determine the continuum level accurately, we compare σ_{line} measured on our sample of high quality spectra ($\mathrm{S/N} \geq 30\,\mathrm{pixel^{-1}}$) using the best$+1\sigma_{\mathrm{cont}}$ and best$-1\sigma_{\mathrm{cont}}$ levels compared to the best fit continuum level. We find that using the best$+1\sigma_{\mathrm{cont}}$ (best$-1\sigma_{\mathrm{cont}}$) continuum causes a median underestimation (overestimation) of 37% (31%) compared to using the best fit continuum. This translates to 0.4 and 0.24 dex in M_{BH}, respectively.

For the particular example shown in Figure 2.11 the 3xFWHM and IPV(3%) line limits truncate the wings of the line profile and as a consequence, σ_{line}(Hβ; data) is underestimated. The right panel shows that σ_{line}(Hβ; data) measured in the high S/N spectrum with the 3xFWHM and IPV(3%) line limits is 13% and 22% (0.13 dex and 0.22 dex in M_{BH}; dashed blue and yellow lines in the right panel of Figure 2.11) smaller, respectively, than if measured with the fixed line limits (dashed red line). It

is noteworthy that the truncation of only 1.5% of the line flux in each line wing introduced by the IPV(3%) line limits can cause such a large offset in the measured line dispersion. This illustrates exactly how sensitive σ_{line} is to the flux in the line wings, and as a consequence, also to a robust and accurate decomposition. As a result, to avoid introducing a bias when measuring σ_{line}(Hβ; data), we adopt the fixed line limits as the optimal profile limits. We also note that σ_{line}(Hβ; data) measured between the fixed line limits (red circles in the right panel of Figure 2.11) is more accurate as a function of S/N, i.e., the colored points lie close to the dashed line of the same color, than σ_{line}(Hβ; data) measured with the 3xFWHM (blue stars) or IPV(3%) (yellow triangles) line limits.

To conclude, the optimal way to measure the line dispersion directly on the data is relative to the best continuum model and between the fixed line limits, thereby avoiding profile truncation, which may occur with the other profile limits. This assumes, of course, that the spectral decomposition is accurate and has isolated the line emission correctly.

Results for σ_{line}(Hβ; data)

When measured directly on the data, σ_{line}(Hβ) is more accurate and precise than FWHM(Hβ; data). This is seen by comparing the width of the shaded areas in panels (a) (accuracy) and (e) (precision), respectively, of Figure 2.12 with the corresponding panels in Figure 2.10. As an illustration, the accuracy of σ_{line}(Hβ; data) measured for our entire Hβ sample is within 19% (0.17 dex in M_{BH}; shaded areas in panel (a) of Figure 2.12) at S/N $\geq 10\,\mathrm{pixel}^{-1}$. We show in § 2.8.1 that to obtain an accuracy within ~ 0.19 dex in M_{BH} for FWHM(Hβ; data), a S/N $\geq 25\,\mathrm{pixel}^{-1}$ is required. Increased spectral noise does not appear to impact a systematic over- or underestimation in the measured values of σ_{line}(Hβ; data) at S/N $\geq 10\,\mathrm{pixel}^{-1}$ but only appear to add a wide scatter (e.g., shaded areas in panel (a) in Figure 2.12). Our analysis also shows that for spectra with S/N $\geq 10\,\mathrm{pixel}^{-1}$ in the continuum, the precision of σ_{line}(Hβ; data) is within 50% (or 0.3 dex in M_{BH}; shaded areas in panel (e) of Figure 2.12). However, at S/N $< 10\,\mathrm{pixel}^{-1}$ there is a tendency to systematically overestimate the measured value of σ_{line}(Hβ; data) (shaded areas in panel (a) of Figure 2.10) because the increased spectral noise in the line wings and continuum have an increasingly adverse effect.

Interestingly, we find that for narrow and peaky lines where the accuracy is high for FWHM(Hβ; data), it is low for σ_{line}(Hβ; data) and *vice versa*. This is evident in Figure 2.12 where the shaded green area in panels (a) and (c) representing narrow and peaky lines, respectively, is wider along the y-axis at any S/N level above $5\,\mathrm{pixel}^{-1}$ than the shaded red areas representing broad and boxy lines, respectively. The accuracy of σ_{line}(Hβ; data) is low in this case due to the weak line wings: the wavelength range between the line limit and the line wing – the spectral range where spectral noise has a large effect on the measured σ_{line}(Hβ; data) value – is larger than it is for broader and boxier lines with stronger line wings. That σ_{line}(Hβ; data) is more inaccurate for narrower and peakier lines is in sharp contrast to what we find for FWHM(Hβ) (§ 2.8.1). It is a clear consequence of the fact that the FWHM is very sensitive to noise in the line peak while σ_{line} is more sensitive to noise in the line wings and in the continuum.

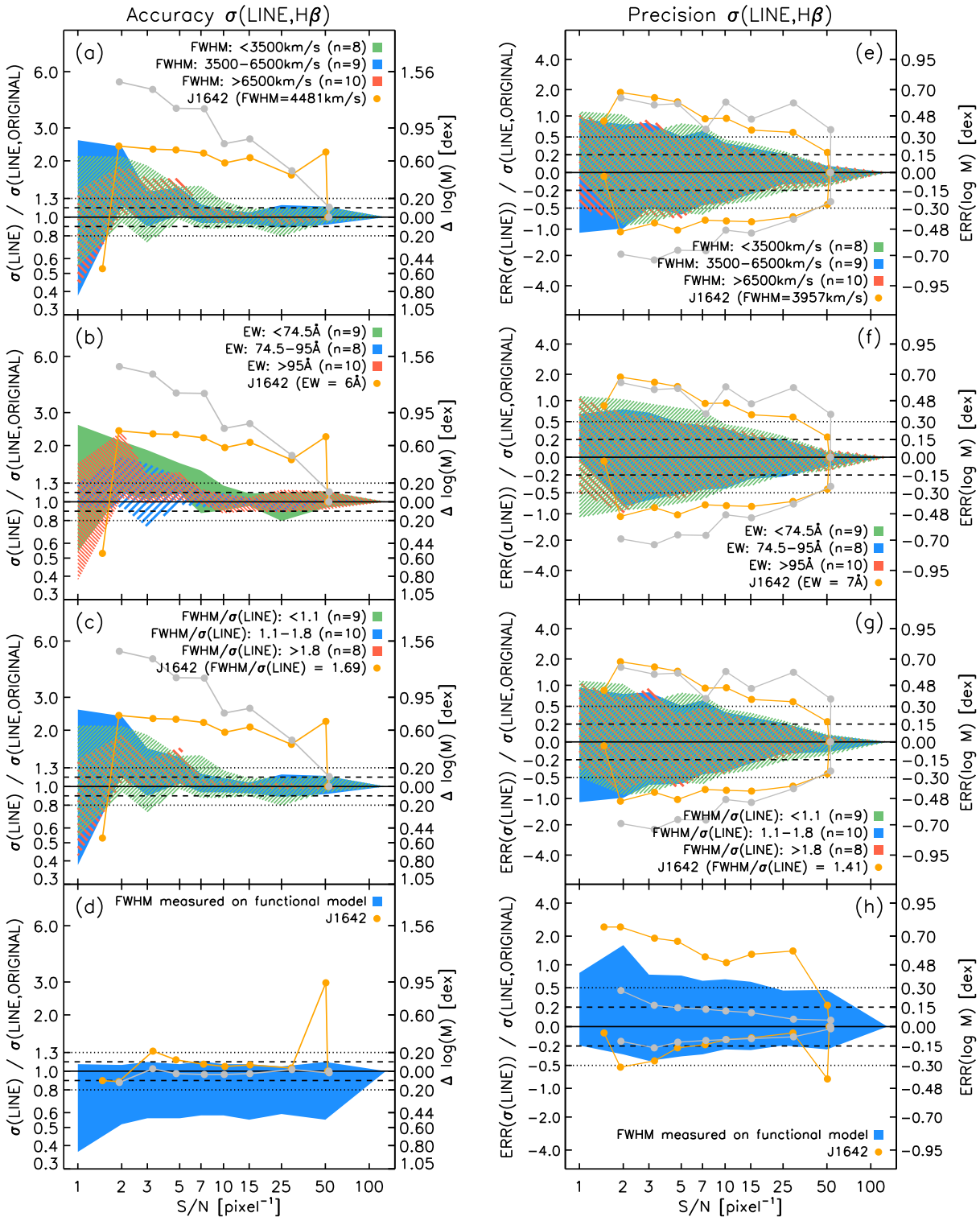

Fig. 2.12 Relative accuracy (left column) and precision (right column) of σ_{line}(Hβ) as a function of S/N when measured on all the spectra in our sample of degraded Hβ spectra. The figure is explained in Figure 2.10. We recall that an accurate line width measure will lie close to the solid horisontal line at $y = 1$ in the left column and a precise line width measure hugs the solid horisontal line at $y = 0$ in the right column. Gray dots connected by lines show results for σ_{line}(Hβ; data) measured on the spectrum of Q1542+0417 and are discussed in § 2.8.6.

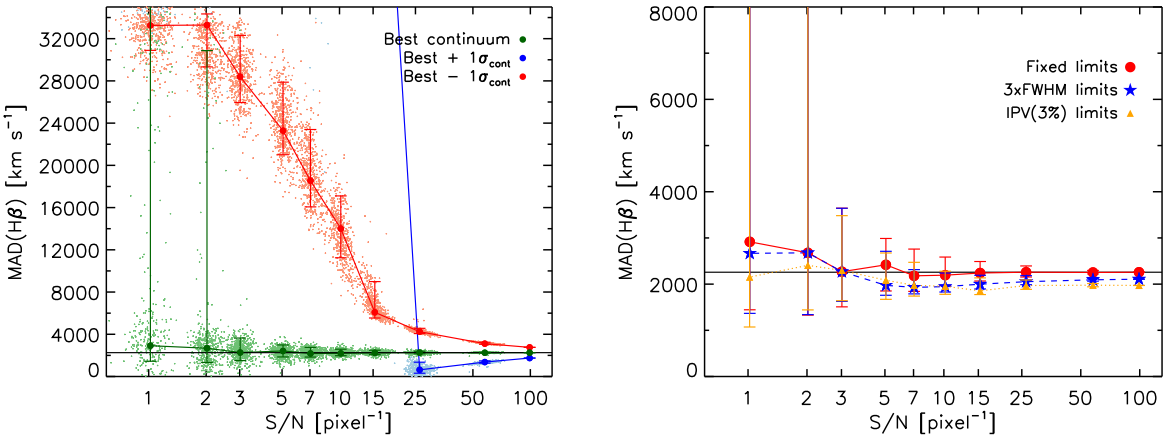

Fig. 2.13 Optimal continuum (left panel) and line limits (right panel) for the MAD(Hβ; data). The example shown here is for the SDSS Hβ Composite C spectrum (MAD(Hβ; data) $\sim 2250\,\mathrm{km\,s^{-1}}$). Symbols and colours are explained in Figure 2.8 and Figure 2.11. Again, we repeat that the best optimal continuum and line limits are those for which the MAD(Hβ) at any S/N level lie close to the horisontal black line marking the intrinsic MAD(Hβ) of the spectrum.

For the same reason, the precision of σ_{line}(Hβ) is slightly better when it is measured on broad emission lines (dashed red area in panels (e) and (g), respectively, of Figure 2.12) than when it is measured on more narrow emission lines (dashed green area in the same panels).

In summary, while we find the accuracy of σ_{line}(Hβ; data) is generally higher than for FWHM(Hβ; data), a S/N $> 25\,\mathrm{pixel^{-1}}$ is required for σ_{line}(Hβ; data) to be measured to an accuracy and precision within 0.1 dex in M_{BH}. With decreasing S/N ratio, both the accuracy and precision decrease such that at S/N $\sim 10\,\mathrm{pixel^{-1}}$ they are within 0.20 dex and 0.30 dex in M_{BH}, respectively. In spectra with S/N $\geq 10\,\mathrm{pixel^{-1}}$ the noise does not appear to introduce any systematic bias in σ_{line}(Hβ; data), but the precision is still low. Because the line dispersion starts to systematically and significantly overstimate the intrinsic value for S/N $< 10\,\mathrm{pixel^{-1}}$ and thereby provide a significantly biased measure of the line width, we argue that the line dispersion should not be measured on data of such low S/N level.

2.8.3 The mean absolute deviation, MAD(Hβ; data)

Optimal measurement method

The MAD(Hβ; data) behave very similar to σ_{line}(Hβ; data). For example, its accuracy and precision depends on the choice of continuum level and line limits, and consequently, it should also be measured between the fixed line limits and relative to the best continuum model. The left panel of Figure 2.13 shows that only relative to the best continuum model (green points) is the MAD(Hβ; data) robust to spectral noise. Using either the best$+1\sigma_{\rm cont}$ or best$-1\sigma_{\rm cont}$ continuum setting the MAD(Hβ; data) will be either under- or overestimated (blue and red points, respectively). We saw the exact same sensitivity towards the continuum level for σ_{line}(Hβ; data), although in that case to a higher degree because σ_{line} is a second order moment of the line. With MAD(Hβ; data) measured in the original

high S/N SDSS Composite C spectrum, M_{BH} is underestimated (overestimated) by 0.22 dex (0.17 dex) using the best$+1\sigma_{\rm cont}$ (best$-1\sigma_{\rm cont}$) continuum, whereas the corresponding numbers using σ_{line}(Hβ) are 0.57 dex and 0.21 dex (see § 2.8.2.)

The accuracy and precision of the MAD(Hβ; data) is best if measured within the fixed line limits (red points in right panel of Figure 2.13). With the 3xFWHM (blue stars) or IPV(3%) (yellow triangles) line limits, the MAD(Hβ; data) is underestimated by 7 and 13% (0.06 and 0.12 dex in M_{BH}) in the original high S/N SDSS Composite C spectrum because the line is truncated by these limits. To avoid introducing any bias in the line width measures due to this effect, we choose to measure MAD(Hβ; data) between the fixed line limits.

In summary, the least biased way to measure MAD(Hβ; data) is to use to best continuum level and the fixed line limits, similar to what we concluded for σ_{line}(Hβ; data) in § 2.8.2.

Results for MAD(Hβ; data)

The MAD(Hβ; data) has an accuracy that is slightly higher than σ_{line}(Hβ; data), which means that it stays within 20% (0.2 dex in M_{BH}) at S/N ≥ 7 pixel^{-1} and with no particular tendency to be biased at these S/N levels. Below these S/N levels MAD(Hβ; data) tends to be overestimated due to noise in the line wings, a trend similar to what we find for σ_{line}(Hβ; data) (§ 2.8.2). Interestingly, the accuracy of MAD(Hβ; data) is not better than that of σ_{line}(Hβ; data) at these low S/N levels although it could be expected to be more robust to noise in the line wings because it only weights the flux density in each spectral bin by its linear distance to the peak of the line, contrary to σ_{line}.

In general, the accuracy of MAD(Hβ; data) is higher for broad, strong, and boxy lines. This is similar to σ_{line}(Hβ; data) and is due to the fact that noise in the line wings and the underlying continuum has a relatively smaller impact on MAD(Hβ; data) for these lines than for more narrow, weak, and peaky lines.

The precision of MAD(Hβ; data) is also similar to that of σ_{line}(Hβ; data). This means that MAD(Hβ; data) has a precision within 35% (0.23 dex in M_{BH}) for S/N ≥ 15 pixel^{-1} compared to 38% (0.25 dex in M_{BH}) for σ_{line}(Hβ; data). Similar to σ_{line}(Hβ; data), the precision is lowest for narrow and peaky lines (green shaded area in panels (e) and (g) in Figure 2.14) where noise in the line wings and on either side of the emission line has the largest impact on the MAD measurement.

In summary, we find that the accuracy and precision of MAD(Hβ; data) is similar to that of σ_{line}(Hβ; data), and to achieve an accuracy within 0.1 dex in M_{BH} using MAD(Hβ; data), a data quality of S/N ≥ 25 pixel^{-1} is necessary. Above S/N ~ 25 pixel^{-1}, the precision of MAD(Hβ; data) is within 27% (0.19 dex in M_{BH}). We find MAD(Hβ; data) to be unbiased for S/N ≥ 3 pixel^{-1} but also that the accuracy and precision decreases with decreasing S/N level. This means that the MAD(Hβ; data) can form basis for unbiased black hole mass estimates down to very low S/N levels, although with a penalty in the form of low accuracy and precision.

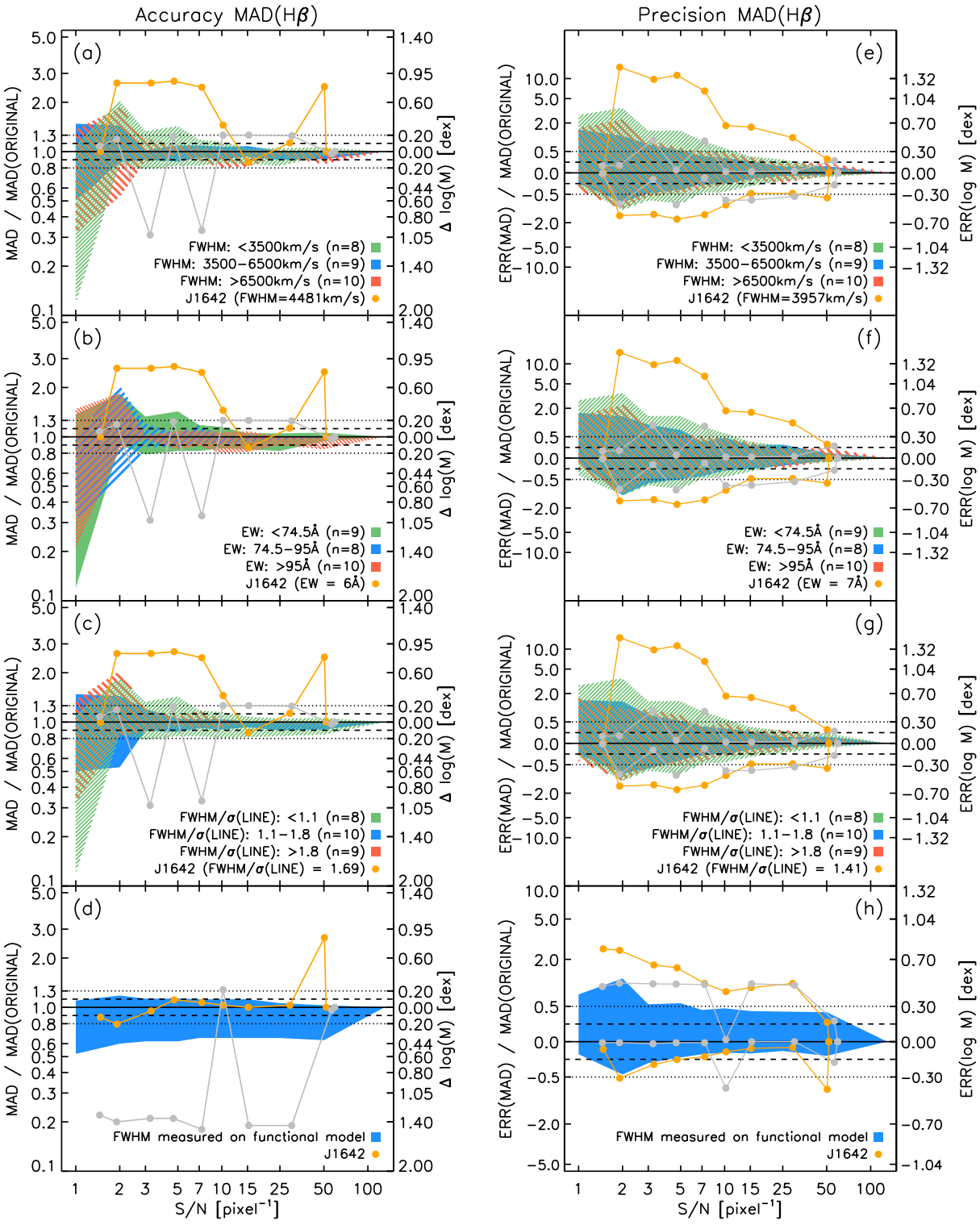

Fig. 2.14 Relative accuracy (left column) and precision (right column) of MAD(Hβ) as a function of S/N when measured on all the spectra in our sample of degraded Hβ spectra. The figure is explained in Figure 2.10. We recall that an accurate line width measure will lie close to the solid horisontal line at $y = 1$ in the left column and a precise line width measure hugs the solid horisontal line at $y = 0$ in the right column. Gray dots connected by lines show results for σ_{line}(Hβ; data) measured on the spectrum of Q1705+0152 and are discussed in § 2.8.6.

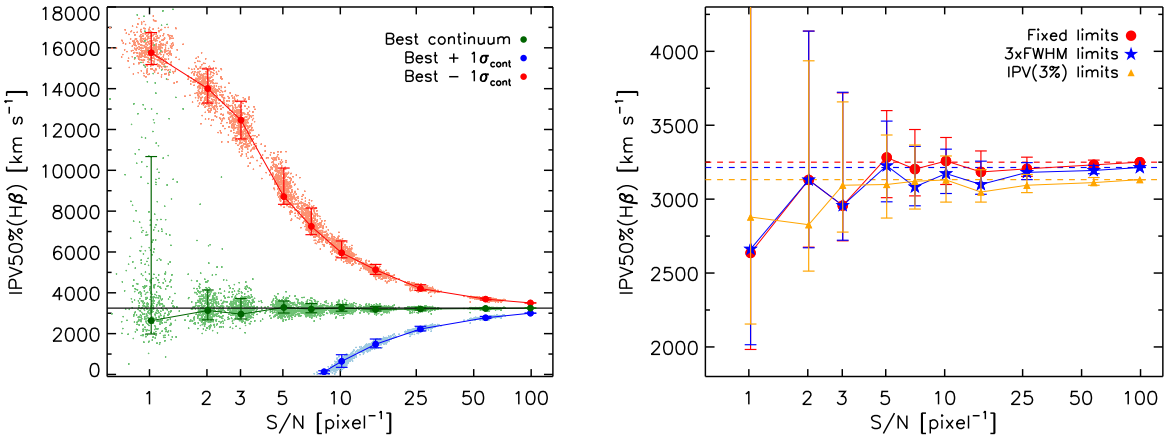

Fig. 2.15 The continuum model (left panel) and line limits (right panel) that optimise the accuracy of the IPV50(Hβ; data) width. The example shown here is for the IPV50(Hβ; data) width measured on the SDSS Hβ Composite C spectrum (FWHM(Hβ; data) $\sim$4800 km s^{-1}, σ_{line}(Hβ; data) $\sim$3300 km s^{-1}, MAD(Hβ; data) $\sim$2250 km s^{-1}, IPV50(Hβ; data) $\sim$3250 km s^{-1}). Symbols and colours are explained in Figure 2.8 and Figure 2.11.

2.8.4 Inter-Percentile Velocity widths, IPV(Y %; data)

We present the accuracy and precision of the IPV widths measured on our entire Hβ sample at a range of percentage levels, Y, from 10% to 90%. For simplicity, we start by considering only the IPV50(Hβ; data) width and expand our results to the full range of IPV widths between IPV10(Hβ; data) and IPV90(Hβ; data) in § 2.8.4.

Optimal measurement method

The optimal way to measure the IPV50(Hβ; data) width is relative to the best continuum model and between the fixed line limits (green points in the left panel and red points in the right panel, respectively, of Figure 2.15). That this is similar to σ_{line}(Hβ; data) and MAD(Hβ; data) (§ 2.8.2 and § 2.8.3, respectively) is expected as they all are integral measures of the line width and therefore rather sensitive to a correct placement of the underlying continuum level. For example, the IPV50(Hβ; data) width measured on the Hβ SDSS Composite C spectrum relative to the best$-1\sigma_{\rm cont}$ continuum is overestimated by 32% (0.33 dex in M_{BH}; large red points in left panel of Figure 2.15) at S/N $\sim$ 25 pixel^{-1}. Also, any line limit that may introduce a truncation of the line profile – e.g., the 3xFWHM and IPV(3%) line limits – can have an adverse effect on the accuracy and precision of the measured IPV width. For our sample of high S/N Hβ spectra we find median offsets of 0.1% and 3.8%, (0.01 dex and 0.03 dex in M_{BH}) with a scatter of 4.7% and 0.5% (0.03 dex and 0.01 dex in M_{BH}) for the IPV50(Hβ; data) width measured between the 3xFWHM and IPV(3%) line limits, respectively, compared to using the fixed line limits. To avoid any such biases and to obtain the highest possible accuracy and precision, the IPV widths should always be measured relative to the best continuum model and between the fixed line limits.

Results for the IPV50(Hβ; data)

The accuracy and precision of the IPV50(Hβ; data) width are shown in Figure 2.16. Compared to FWHM(Hβ; data), σ_{line}(Hβ; data) and MAD(Hβ; data), the IPV50(Hβ; data) width can be measured to a higher accuracy at S/N $\geq 5\,\mathrm{pixel}^{-1}$. This can be seen by comparing the span of the shaded areas in panel (a) of Figures 2.10, 2.12, 2.14, and 2.16, respectively. The precision of the IPV50(Hβ; data) width is also higher than that of FWHM(Hβ; data), σ_{line}(Hβ; data) and MAD(Hβ; data) at S/N $\geq 5\,\mathrm{pixel}^{-1}$ (compare span of shaded areas in panel (e) of the same figures). In particular, the accuracy and precision is within 23% and 133% (0.12 dex and 0.56 dex in M_{BH}; shaded areas in panels (a) and (e) of Figure 2.16), respectively, at S/N $\geq 5\,\mathrm{pixel}^{-1}$. This high accuracy and precision is a consequence of two things. Firstly, the IPV width is, just like σ_{line} and the MAD, an integral measure of the line width and therefore very robust to spectral noise. Secondly, compared to the line dispersion, the IPV width does not weight the flux in each spectral bin with the square of its distance to the line centre and it is therefore less susceptible to noise in the line wings than σ_{line}.

We find that the IPV50(Hβ; data) width measured on broad, strong, and boxy emission lines (shaded red area in panels (a), (b), and (c) in Figure 2.16) is more robust to noise than it is for more narrow, weak, and peaky lines (shaded green areas in the same panels) because the line wings of these narrow, weak, and peaky lines more easily disappear in the noise than they do for the more broad, strong, and boxy lines. Because the line wings disappear in the noise, the IPV50(Hβ; data) width has a strong tendency to be underestimated at S/N $\leq 5\,\mathrm{pixel}^{-1}$ (the shaded areas in panel (a) of Figure 2.16 mostly lie below the solid horisontal line at $y = 1$). The precision of the measured IPV50(Hβ; data) width can also be as low as 1000% (1.32 dex in M_{BH}; shaded green area in panel (e) of Figure 2.16) at these low S/N levels.

To conclude, we find that the IPV50(Hβ; data) width can be measured to a higher accuracy than FWHM(Hβ; data), σ_{line}(Hβ; data), and MAD(Hβ; data). Its precision is higher than that of FWHM(Hβ; data) and similar to that of σ_{line}(Hβ; data) and MAD(Hβ; data). We note that for S/N below $5\,\mathrm{pixel}^{-1}$, the IPV50(Hβ; data) width starts to be biased, underestimating the line width, and the precision can be as low as 1.32 dex in the black hole mass estimate. But, it is worth noting that IPV50(Hβ; data) has a better performance than σ_{line}(Hβ; data) which only was reliable down to S/N $\sim 10\,\mathrm{pixel}^{-1}$.

Results for the other IPV widths

The IPV widths at a range of percentage levels between 10% and 90% are useful for characterising the width of the line profile all the way from its base to its core. And, ratios of these IPV widths provide a way to characterise the line shape, as an alternative to the FWHM/σ_{line} ratio often used. Our results for the IPV20(Hβ; data) and IPV90(Hβ; data) widths are shown in Figure 2.17 and 2.18, respectively, while the results for the remaining percentage levels are shown in Appendix C.

The main result of our analysis is that to achieve an accuracy and precision, respectively, within 0.2 dex in M_{BH} for the IPV widths measured on the data at percentage levels between 20% and 90%, a

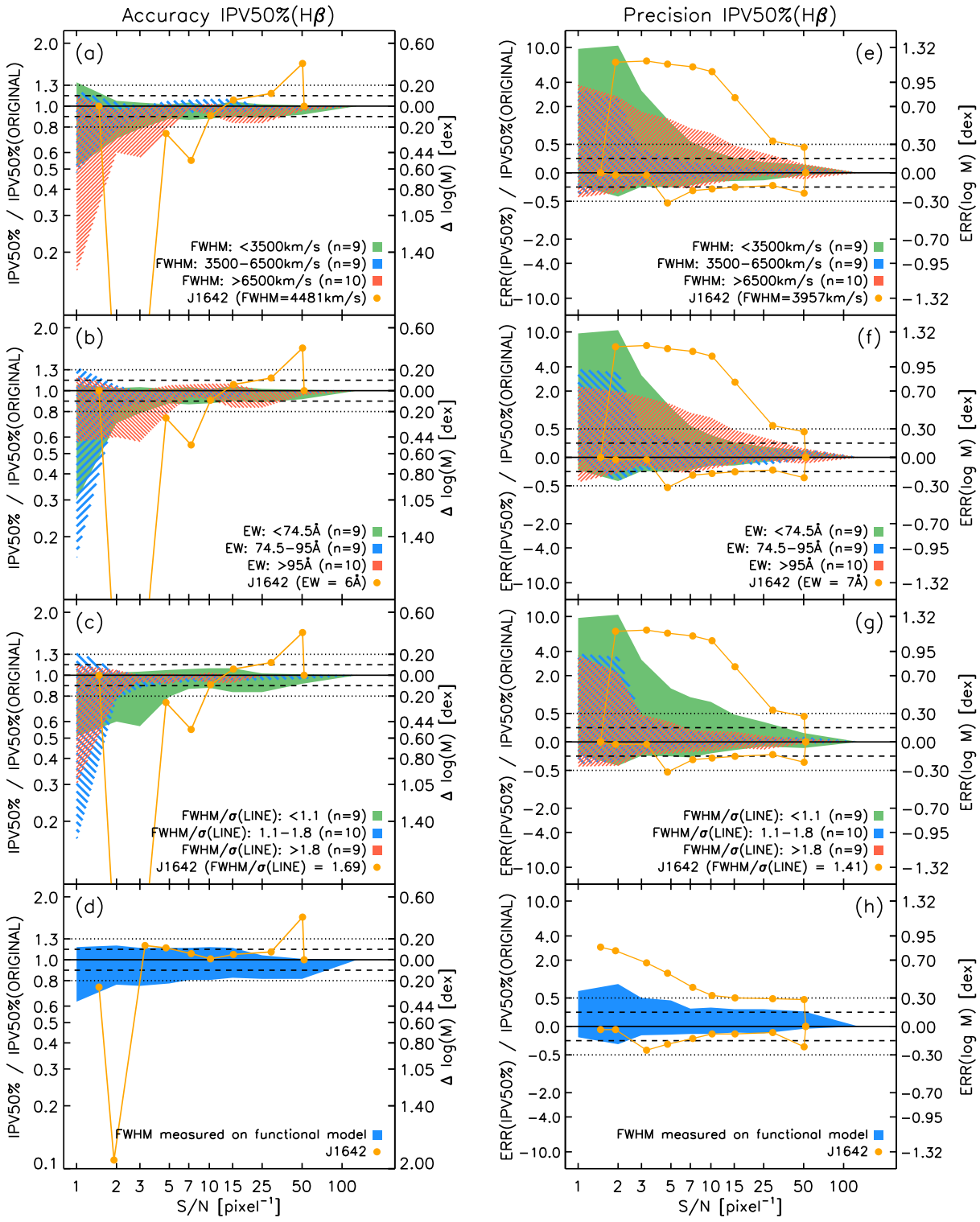

Fig. 2.16 Relative accuracy (left column) and precision (right column) of the IPV50(Hβ; data) width as a function of S/N when measured on all the spectra in our Hβ sample of spectra. A high accuracy and precision is characterised by measurements close to the horisontal line at $y = 1$ (left column) and the horisontal line at $y = 0$ (right column). The figure is explained in Figure 2.10.

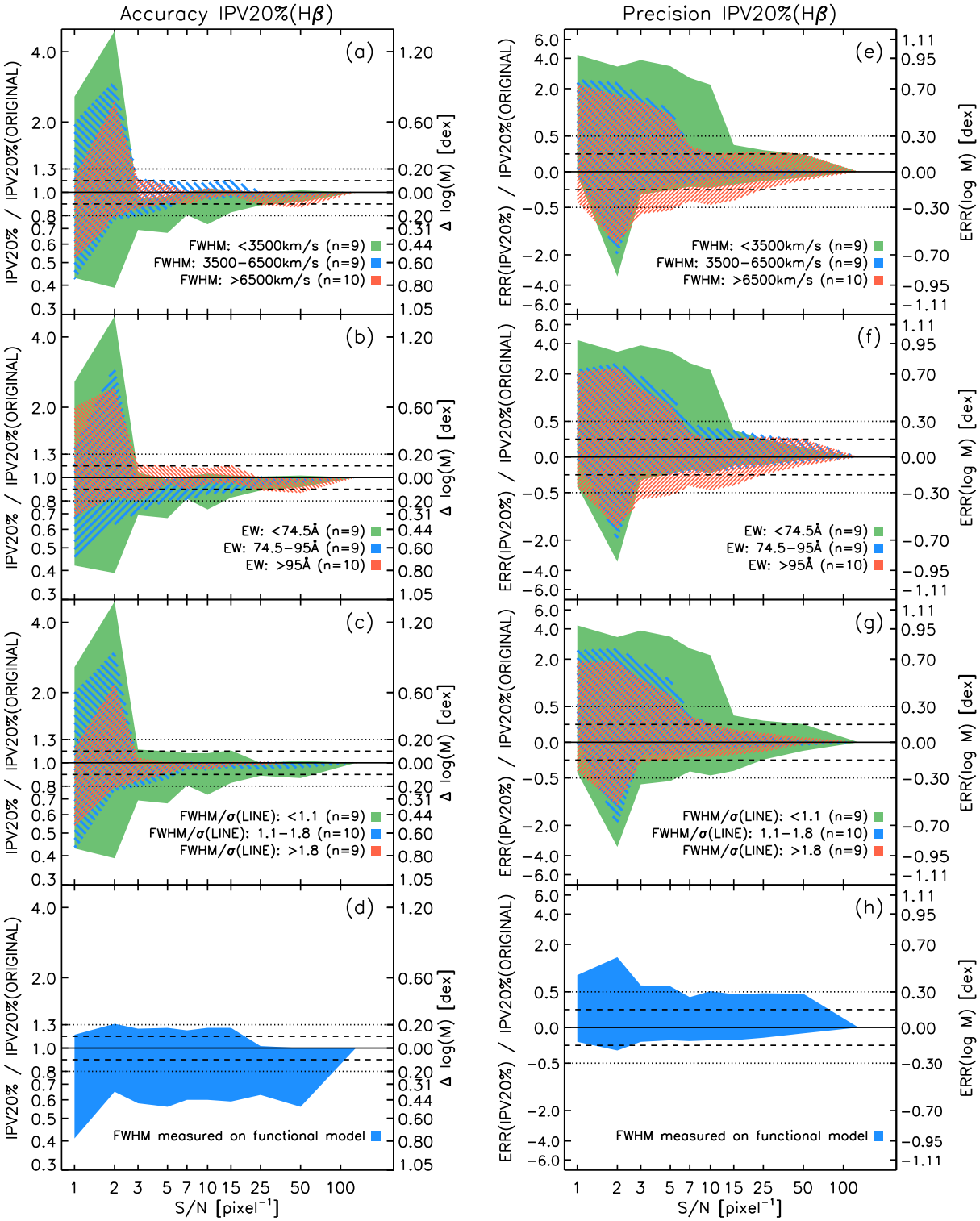

Fig. 2.17 Relative accuracy (left column) and precision (right column) of the IPV20(Hβ; data) width. The figure is explained in Figure 2.10.

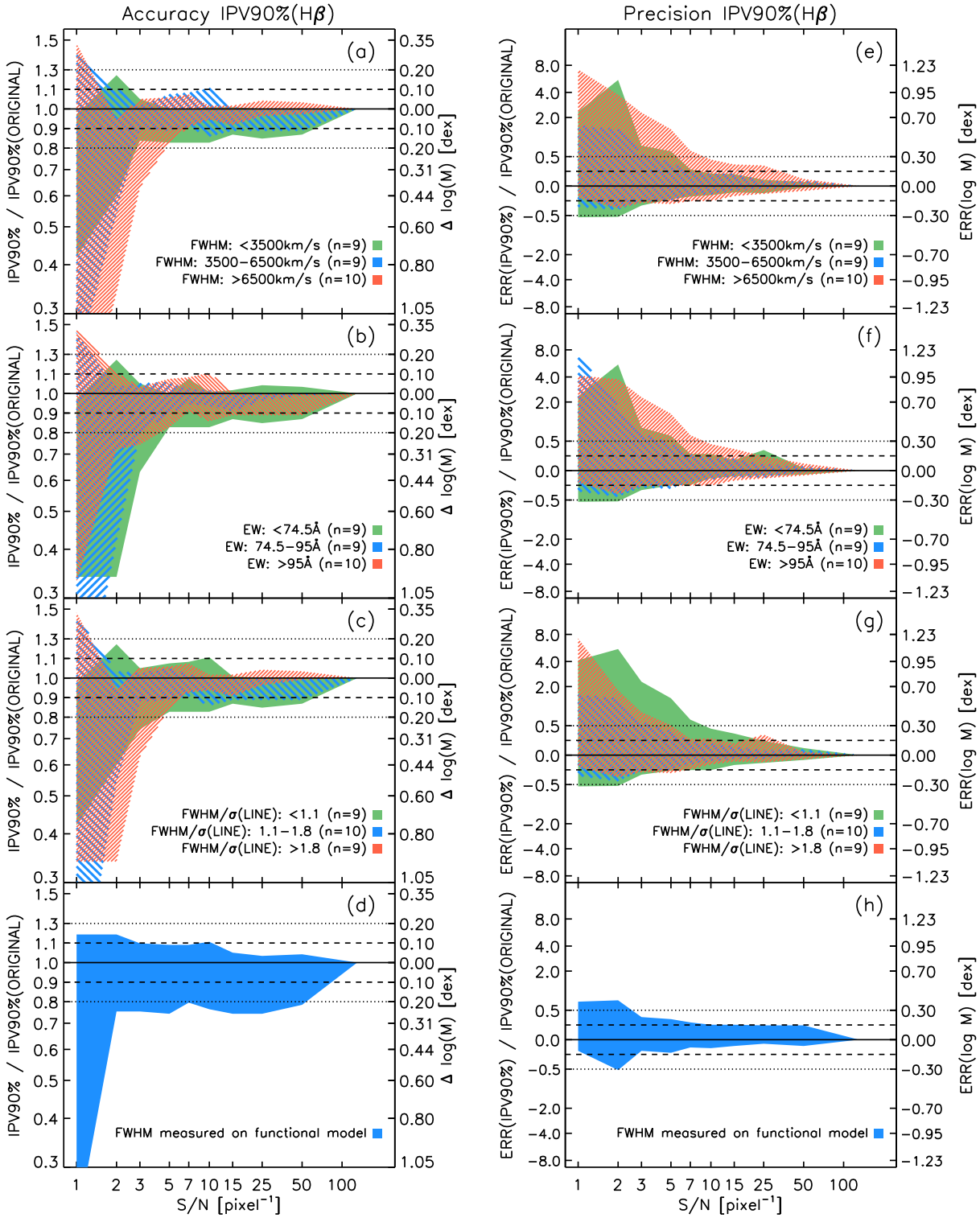

Fig. 2.18 Relative accuracy (left column) and precision (right column) of the IPV90(Hβ; data) width. The figure is explained in Figure 2.10.

data quality of S/N $\geq 10\,\mathrm{pixel}^{-1}$ is required. This is comparable to σ_{line}(Hβ; data) and MAD(Hβ; data) (see § 2.8.2 and § 2.8.3, respectively)). To achieve this accuracy and precision for FWHM(Hβ; data) a S/N $\geq 25\,\mathrm{pixel}^{-1}$ is necessary (see § 2.8.1). We also find the accuracy and precision of the IPV widths at a given S/N level increase with the IPV percentage level, i.e., for a given S/N level, the IPV90(Hβ; data) width can be measured to a higher accuracy and precision than the IPV20(Hβ; data) width for a given emission line. This is because IPV widths at lower percentage levels are more affected by the disappearance of the line wings in the noise. For the same reason, we find the accuracy and precision of the IPV10(Hβ; data) width is very low (see Figure C.1 in Appendix C).

2.8.5 Measurements on a functional model of Hβ

FWHM(Hβ; funct)

Our analysis shows that this approach only helps improve FWHM(Hβ) for data with rather low S/N (i.e., $5\,\mathrm{pixel}^{-1} \leq$ S/N $\leq 10\,\mathrm{pixel}^{-1}$), but still provides rather crude mass estimates with accuracy no better than ∼0.4 dex. For example, in this case FWHM(Hβ; funct) is accurate and precise to within 34% and 48% (0.39 dex and 0.29 dex in M_{BH}), respectively, – a strong improvement over the equivalent values of ∼1000% and 390% (2.0 dex and 0.94 dex in M_{BH}), respectively, when measured on the data.

At higher S/N levels (S/N $\geq 15\,\mathrm{pixel}^{-1}$), the accuracy and precision does not improve significantly with this approach (panels (d) and (h), respectively, in Figure 2.10). In fact, there is a tendency to underestimate FWHM to a larger degree ($\lesssim 30\%$) using this method (compare panel (d) with panels (a)-(c)).

However, the price paid for using FWHM(Hβ; funct) instead of FWHM(Hβ; data) is a systematic bias. We see a median offset of 2.3% (0.02 dex in M_{BH}) with an associated scatter of 9.7% (0.08 dex in M_{BH}) relative to the directly measured FWHM value when on the original high S/N spectra. While a systematic offset can, in principle, be corrected via the calibration of the single-epoch black hole mass scaling relations, the increased scatter introduces an extra uncertainty that propagates into the final uncertainty on the black hole mass estimate.

For this reason, and because the accuracy and precision of FWHM(Hβ; funct) only is better for $5\,\mathrm{pixel}^{-1} \leq$S/N $\leq 10\,\mathrm{pixel}^{-1}$, the FWHM measured directly on high S/N data is therefore the best approach for obtaining mass estimates with the highest accuracy and precision if using FWHM(Hβ) to characterise the line width.

σ_{line}(Hβ; funct) and MAD(Hβ; funct)

We do not find that measuring σ_{line}(Hβ) and MAD(Hβ) on a functional model of the line profile mitigates the adverse effects of spectral noise. Rather, we find that both σ_{line}(Hβ; funct) and MAD(Hβ; funct) have a strong tendency to be biased towards an underestimation of the line width (shaded blue area is predominantly below the horisontal line at $y = 0$ in panel (d) in Figures 2.12 and

2.14, respectively). This is because the wings of the emission line profile, when the noise increases, disappears in the noise and the line peak appears more prominent. Consequently, the functional model will tend to have less flux in the line wings with increasing noise and σ_{line}(Hβ; funct) and MAD(Hβ; funct) are underestimated. Specifically, we find that σ_{line}(Hβ; funct) and MAD(Hβ; funct) are underestimated by at least 50% and 40% (0.60 and 0.44 dex in M_{BH}, respectively) for S/N levels below 50 pixel^{-1}, respectively. In addition, we find no improvement in σ_{line}(Hβ; funct) and MAD(Hβ; funct) compared to σ_{line}(Hβ; data) and MAD(Hβ; data), respectively (compare panels (h) with panel (g) in Figures 2.12 and 2.14, respectively).

Comparing σ_{line}(Hβ; funct) with σ_{line}(Hβ; data) on the original high S/N spectra we find a median offset of 5.7% (0.05 dex in M_{BH}) with a scatter of 35.5% (0.24 dex in M_{BH}). The equivalent numbers for MAD(Hβ) is 3.1 and 9.7% (0.03 and 0.08 dex in M_{BH}, respectively). As noted earlier, the offsets may be mitigated by recalibrating the mass scaling relations, but the scatter will remain and increase the uncertainty in the mass estimate.

In conclusion, σ_{line}(Hβ; funct) and MAD(Hβ; funct) do not represent a viable way to mitigate spectral noise since they have lower accuracy and a strong bias towards too small values compared to σ_{line}(Hβ; data) and MAD(Hβ; data), and, because they show a significant amount of scatter relative to σ_{line}(Hβ) and MAD(Hβ; data) measured directly on the data.

IPV(Hβ; funct)

We note that the precision of the measured IPV widths in some cases can be improved at S/N ≤ 3 pixel^{-1} if measured on a functional model of the profile. At S/N levels higher than this, we see no increase in accuracy compared with IPV(Hβ; data), but we see the same trend of underestimating IPV(Hβ; funct) as we find for σ_{line}(Hβ; funct) and MAD(Hβ; funct), although to a slightly lesser degree. Consequently, IPV(Hβ; funct) is only an effective way to prevent the effect of noise at S/N ≤ 3 pixel^{-1}. In this case, the IPV20% to IPV90% widths each have a median offset and scatter of less than 1% and 4% (0.01 dex and 0.03 dex in M_{BH}) with respect to those measured directly on the data. The uncertainty introduced by the scatter (inherent in using this approach) into the black hole mass estimate is thus very low for the IPV widths.

2.8.6 Special cases

There are a few unusual results that are worth mentioning since they highlight aspects that are important to consider when evaluating the robustness of the line width measures. These issues are illustrated by a couple of special case AGN, discussed next.

J164258.80+394836.9 - a low equivalent width line

This AGN has a very low contrast Hβ line with an equivalent width of only 6Å, and the line is only detected at the 3.9σ level at S/N ~ 25 pixel^{-1}. The consequence is that even at high S/N ($\sim$25 pixel^{-1}), the accuracy and precision of the line widths are low.

For this spectrum, the measured values of all four line width parameters can be overestimated by more than 40% (0.30 dex in M_{BH}) at S/N values between 25 pixel^{-1} and 50 pixel^{-1} (see orange dots and lines in panel (a) of figures 2.10, 2.12, 2.14, and 2.16). The precision at S/N $\sim$ 25 pixel^{-1} is also quite low and only within 50% (0.3 dex in M_{BH}) for all four line widths. Because of the low contrast of the line, the measured FWHM(Hβ) is extremely sensitive to spectral noise in the line peak (§ 2.8.1), and the σ_{line}(Hβ), MAD(Hβ) and IPV(Hβ) widths are all very sensitive to noise in the line wings and in the continuum emission.

This particular Hβ emission line is not representative of the emission lines typically observed in the general AGN population, but it highlights the error inherent when measuring emission line widths of low-contrast emission lines that are close to or below the 3σ detection limit. This is especially an issue for spectra of high-redshift ($z \geq 2$) SDSS quasars that are often noisy with S/N $\leq$ 10 pixel^{-1}.

Q1542+0417 - a boxy profile with weak wings

This profile has quite extended, but weak, wings such that in effect it is a quite narrow, peaky profile with superposed broad and weak wings. This means, that as the noise increases, the apparent signal in the extended wings is also increased which in turn has a huge effect on σ_{line}(Hβ; data).

The σ_{line}(Hβ; data) measurements for Q1542+0417 (gray dots and line in Figure 2.12) have a very strong bias towards too high values with decreasing S/N and is clearly an outlier with respect to the other measurements (hashed areas in same figure). It is also clear that there is a strong trend such that increasing noise leads to a lower accuracy of σ_{line}(Hβ; data) for this particular emission line. Specifically, σ_{line}(Hβ; data) is overestimated by 77% and 280% (0.5 and 1.16 dex in M_{BH}) at S/N $\sim$ 25 and 7 pixel^{-1}, respectively.

While the primary effect is the increased noise, other secondary effects enhanced by the noise also affect σ_{line}(Hβ; data). With a higher noise level, it becomes increasingly difficult to disentangle the spectral components below the wings of the Hβ line (nuclear power-law continuum, iron template, and host galaxy emission template) that are degenerate with the strength of the extended emission line wings. With decreasing S/N , flux is shifted towards the extended line wings in the spectral decomposition process, further enhancing the overestimation of σ_{line}(Hβ; data).

Q1705+0152 - a peaky profile with weak wings

This profile is very peaky with essentially no line wings which means that there is a lot of continuum between the actual line profile and the line limit. In the ideal case, the flux density in this continuum would be pure random noise, but in reality, there is always some structure left. Depending on the specific relation in terms of strength between the spectral components in the decomposition, the structure in the continuum region and the strength of the wings in the emission line profile may vary.

The measurements of MAD(Hβ; data) for Q1705+0152 (gray dots and lines in Figure 2.14) are underestimated by $\sim$70% (1.05 dex in M_{BH}), and are clearly outliers from the rest of the measurements, at S/N $\sim$ 3 and 7 pixel^{-1}. Investigating the results in detail, we find that in practice, the distribution

of MAD(Hβ; data) measurements at any S/N investigated essentially is flat with a tendency to be bimodal with one mode close to the original value and one mode underestimating MAD(Hβ; data) by $\sim$70%. This is a direct consequence of the varying strength between the spectral components in the decomposition and the strength of the wings in the emission line profile.

We also note, that we find a rather broad distribution of σ_{line}(Hβ; data) widths for this particular profile, but always with a small peak near the intrinsic value. Both FWHM(Hβ; data) and IPV(Hβ; data) are unaffected by this issue.

One might argue that the problems in measuring σ_{line}(Hβ; data) and MAD(Hβ; data) for Q1542+0417 and Q1705+0152 are related to the spectral decomposition and not necessarily to these line width parameters. While it is true that the noise primarily affects the robustness of the spectral decomposition, this directly affects σ_{line} and MAD to a higher degree than FWHM and IPV(Hβ; data). In the case of a spectral decomposition which is completely resilient to S/N , the line width parameters may perform more equally; although this particular issue may be difficult to confirm since no spectral decomposition method is perfect.

2.9 Results for C IV

The results for the C IV sample of spectra (§ 2.4.2) generally confirms our results for the Hβ sample (§ 2.8). Specifically, the optimal measurement method, i.e., the optimal continuum level and line limits, are the same as for Hβ. Here, we focus on the main similarities and differences in our findings for C IV and Hβ, respectively.

Figure 2.19 shows the accuracy (left panel) and precision (right panel) of FWHM(C IV; data), σ_{line}(C IV; data), MAD(C IV; data), and IPV50%(C IV; data) (green, blue, cyan, and red shaded areas, respectively). More detailed figures where the accuracy and precision of each line width measure is shown according to the FWHM, EW, and FWHM/σ_{line} ratio of each line can be found in Appendix D. The IPV50%(C IV; data) width has a comparable or higher accuracy and precision than the three other line width characteristics at S/N ≥ 3 pixel^{-1} (compare span of red with other shaded areas in both panels of Figure 2.19). The full range of IPV(C IV) widths at percentages between 20 and 90% also show a better or comparable accuracy and precision than the rest of the line width characterisations for S/N ≥ 3 pixel^{-1} (consult Figures D.5 and D.15 in Appendix D).

Figure 2.20 shows the same trend for the Hβ sample, namely that the IPV50(Hβ; data) width outperforms the remaining line parameters in terms of both accuracy and precision at S/N ≥ 5 pixel^{-1}. We note though, that for a comparable performance for the remaining IPV(Hβ; data) widths, they have to be measured at percentages of $Y \geq 30$% (consult figures in Appendix C).

Interestingly, while we find that the accuracy of each of the line width measures are very similar for the Hβ and C IV sample, the precision is in general somewhat better for the IPV(C IV) and MAD(C IV) than for the IPV(Hβ) and MAD(C IV). We speculate that this is because the continuum level is better constrained for the C IV spectra than for the Hβ spectra where, in the latter case, its

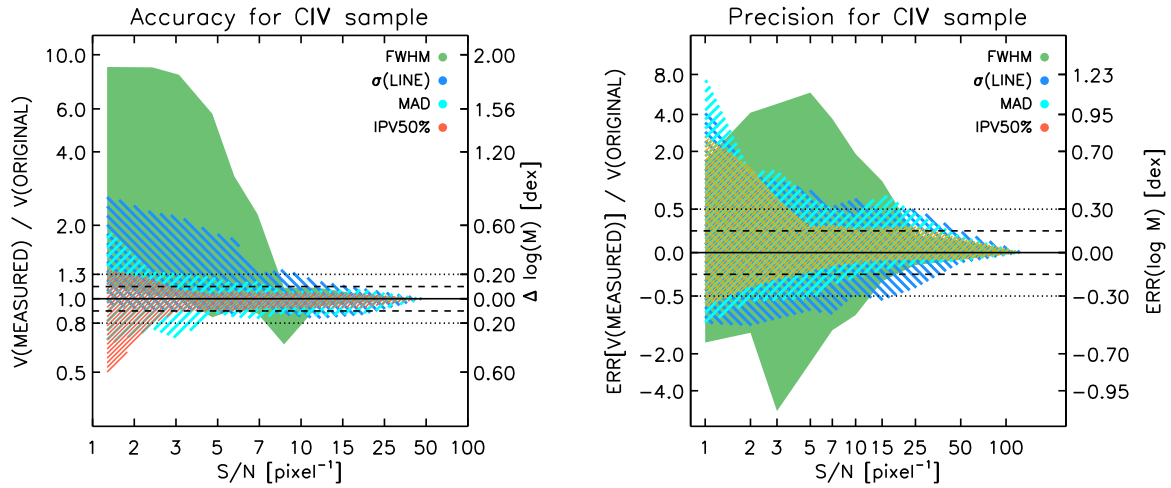

Fig. 2.19 Relative accuracy (left column) and precision (right column) of the four line widths investigated as a function of S/N when measured on all the spectra in our sample of degraded C IV spectra. The full span of measurements for each line width parameter is shown as the shaded areas.

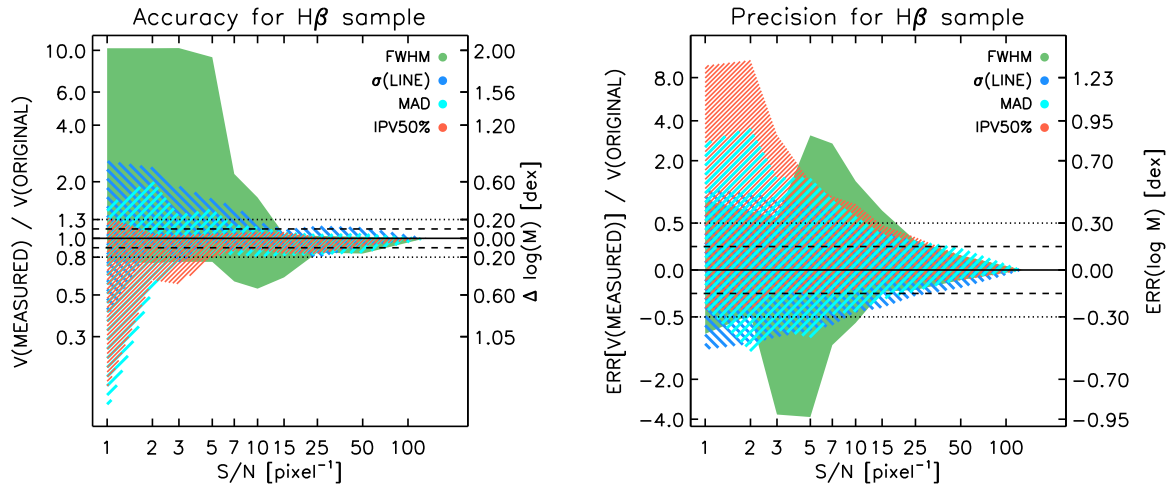

Fig. 2.20 Same as Figure 2.19 but for Hβ.

strength is degenerate with the strength of the host galaxy, Fe II, and Balmer templates. This may be the most likely reason for the scatter in the Hβ line widths compared to the C IV widths.

Finally, measuring the line widths on a functional model of the C IV line profile only increases the accuracy and precision of FWHM(C IV) significantly at S/N ≥ 5 pixel^{-1} while for the other line width characteristics, the accuracy and precision is better when measured directly on the data. Only at S/N < 5 pixel^{-1} do we find an improvement in the accuracy and precision of all the line width characterisations measured on a functional model compared to directly on the data. This is in contrast to Hβ where we found that measuring on a functional model introduced biases in the line widths, most likely related to difficulties with constraining the strength of the Hβ narrow line emission.

We also find a median offset and scatter of less than 0.02 and 0.08 dex in M_{BH}, respectively, between the line widths measured directly on the data and on a functional model on the high S/N C IV spectra. This means that the bias and scatter introduced by use of a functional representation is small compared to the uncertainty of the line width measures at S/N < 5 pixel^{-1} (generally higher than 0.15 dex in M_{BH}). Consequently, measuring the line width on a functional model of the spectra is a viable alternative to directly measured line widths for C IV spectra at S/N < 5 pixel^{-1}.

2.10 Results for line shape parameters

Denney (2012) shows that when calculating the C IV black hole mass estimates, these mass values can be placed in concordance with the Hβ based mass estimates by considering the shape of the line, parameterised as FWHM/σ_{line}. Yong et al. (2016) also argue that the mass estimate uncertainty can be decreased by taking the line shape into account. Both studies indicate the importance of the line shape for the accuracy of black hole mass estimates.

Traditionally, the FWHM/σ_{line} ratio has been used to characterize the line shape (e.g., Collin et al., 2006; Denney, 2012). For values larger (smaller) than $2\sqrt{2\ln 2}\sigma \approx 2.355$ the profile is more stubby (peaky) than a Gaussian profile. Motivated by the demonstrated poor performance of, especially, the FWHM (§ 2.8 and § 2.9), we here compare the robustness of the FWHM/σ_{line} ratio with those of different ratios of IPV widths. Again, we compare the line shapes measured on the degraded spectra with those from the original spectra. In the following, we do not distinguish between the Hβ and C IV spectra because we find that the results do not depend on the specific emission line.

Figure 2.21 shows that as a measure of line shape, ratios of IPV widths (in this particular example the IPV25/IPV60 and IPV35/IPV75 ratios shown in blue and cyan colors, respectively) are superior to the FWHM/σ_{line} ratio (shown in green) both in terms of their accuracy and precision. The main reason for this is simply that the individual IPV widths have higher accuracy and precision than the FWHM and line dispersion. In addition, the scatter in the FWHM/σ_{line} ratio is increased by the fact that the FWHM and σ_{line} in general does not respond to increasing noise in the same manner (i.e., one might be overestimated while the other is underestimated and *vice versa*) and to the same degree. The IPV widths on the other hand always behave similarly which means that the scatter of their ratios will remain low even if the individual IPV widths are subject to a small bias.

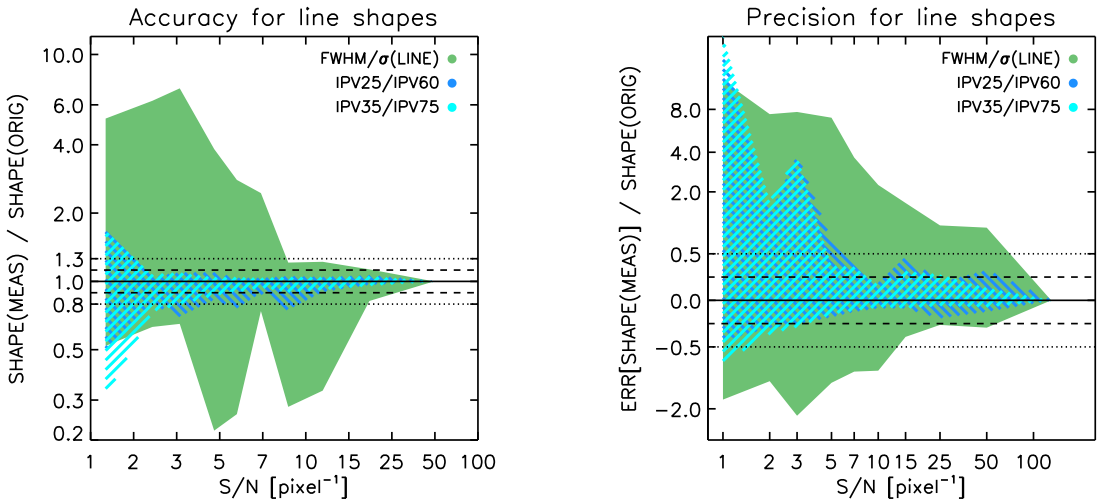

Fig. 2.21 Relative accuracy (left column) and precision (right column) of the FWHM/σ_{line}, IPV25/IPV60, and IPV35/IPV75 ratios for our Hβ and C IV samples combined.

Specifically, the accuracy and precision of the FWHM/σ_{line} ratio can be worse than 20% and 50% (0.2 and 0.3 dex in M_{BH}, respectively) for S/N ≤ 15 pixel^{-1} whereas ratios of IPV widths stay within this level of accuracy and precision for S/N ≥ 5 pixel^{-1}.

Based on our analysis, the results of which are summarized in Figure 2.21, we conclude that the much higher accuracy and precision of the IPV widths, combined with the fact that the combinations of many different IPV widths allows for many different and robust characterisations of the line shape, makes IPV width ratios a superior shape measure compared to the FWHM/σ_{line} ratio. Determining which IPV ratio is optimal for characterizing the line shape with the aim of performing corrections that may be needed for improved mass scaling relations is current work in progress.

2.11 Discussion

Our main focus has been on the robustness towards spectral noise of each of the four line width measures (the FWHM, σ_{line}, MAD, and IPV widths) using AGN spectra containing either the broad Hβ or C IV emission line. Our main result is that the IPV widths measured directly on the data [IPV(data)] offer the most robust and flexible way to measure the emission line width. While the MAD(data) width offers an accuracy and precision grossly similar to the IPV(data) widths, it does not provide the flexibility to parameterise the width of the line at many different levels of the line flux or the option of robustly measuring the line shape. Both can be achieved with the IPV(data) widths.

The discussion is structured as follows. First, we discuss how robust each line width parameter is towards spectral noise and compare the line parameters in this respect. We apply two benchmarks to each of the four line parameters, namely, 1) what is the highest obtainable accuracy, here determined as the accuracy at S/N ~ 50 pixel^{-1}, and 2) what S/N is required to obtain a black hole mass estimate with an accuracy of 0.1 dex or better. Using 0.1 dex is somewhat arbitrary, but it is chosen as an

feasible uncertainty that represents a significant reduction over current uncertainties induced when measuring the commonly used FWHM and σ_{line} widths. Second, we examine how robust each line width parameter is to AGN variability in terms of producing a constant black hole mass. Finally, we discuss the implications of our results and other factors that can influence the accuracy of the mass estimates.

2.11.1 Performance and comparison of the line parameters

FWHM(data) is biased for S/N $\leq$ 25 pixel^{-1}

Since FWHM(data) is extremely sensitive to spectral noise and shows a lower accuracy and precision than the other line parameters at a given S/N level (§ 2.8.1 for Hβ and § 2.9 for C IV), we do not recommend its use on data with S/N < 25 pixel^{-1}. Spectral noise has two effects on FWHM(data). First, FWHM(data) is narrower than expected because the peak density flux of the line is overestimated due to noise spikes in the line peak. This type of bias is also found by Denney et al. (2009). Interestingly, we find that this effect to some degree can be mitigated by measuring the FWHM after adopting the best$-1\sigma_{\rm cont}$ continuum setting (i.e. the best fit continuum model minus an estimate of the continuum flux uncertainty - measured as the 1 sigma scatter of the observed flux density around the best fit continuum model) for S/N ≥ 25 pixel^{-1} (described in § 2.8.1). Second, the FWHM(data) width is artificially increased as the noise increases because the wavelengths marking the half peak flux density move outward from the line centre due to noise spikes in the continuum and line wings (an example is shown in Figure 2.9). In general, the former type of bias (underestimation) takes place at higher S/N than the latter (overestimation) for a given emission line. As a result of these effects, even when accounting for the underestimation by measuring the FWHM relative to the best$-1\sigma_{\rm cont}$ continuum model, we find that FWHM(Hβ; data) can be biased too low by more than 38% (0.42 dex in M_{BH}) for S/N < 25 pixel^{-1} (§ 2.8.1). We therefore do not recommend measuring FWHM(data) for S/N < 25 pixel^{-1}. This is consistent with the result of Denney et al. (2009) although based on their study they recommend a S/N cutoff at 20 pixel^{-1}.

We find the accuracy of the mass estimates based on FWHM(Hβ; data) to be within 0.15 dex at S/N ~ 50 pixel^{-1}, illustrating that a S/N level even higher than this is required for mass estimates that are accurate within 0.1 dex. For C IV we find the accuracy at S/N ~ 50 pixel^{-1} to be $\sim$0.05 dex and that an accuracy of 0.1 dex in the mass estimate can be retained down to S/N ~ 25 pixel^{-1}. As discussed in §2.11.1, this is probably related to the fact that the spectral decomposition for C IV is somewhat more robust than for Hβ, which is surrounded by a larger number of contaminating and blending emission lines, including many more iron transitions (Boroson & Green, 1992; Véron-Cetty et al., 2004; Vestergaard & Wilkes, 2001).

The selective noise sensitivity of the line dispersion

The integral line width parameters [σ_{line}(data), MAD(data), and IPV(data)] are more robust to spectral noise than FWHM(data). Of these, we find σ_{line}(data) to be the most sensitive to noise, because it weights the flux density in each wavelength bin by its squared distance from the line centre (Equation 2.2). For this reason, σ_{line}(data) is extremely sensitive to the placement of the continuum and to any noise or line blending, especially in the line wings and in the continuum on either side of the line. The line dispersion should not be measured on spectra with S/N lower than $\sim$10 pixel^{-1} because it is biased towards too high values (hashed areas in Figure 2.12 panel (a) lie predominantly above the solid black line marking the intrinsic line width). Similarly, Denney et al. (2009) find that σ_{line}(data) is biased and suffer from a low accuracy and precision at these S/N levels when comparing high and low S/N spectra of the Hβ line for two Seyfert 1 AGN at low redshift ($z < 0.1$). Specifically, they degrade the high S/N spectra of those two objects in question and find σ_{line}(data) to be underestimated for S/N < 10 pixel^{-1} because the line wings disappear in the noise, in contrast to the tendency to overestimate σ_{line}(data) that we find. This difference could be related to the differences in spectral decomposition method used in their study and ours. Specifically, they model and subtract the continuum emission without simultaneously modelling the Hβ emission line while we do so in our model. Without specific and detailed knowledge of their method, it is difficult to predict the direct consequences of this difference in spectral decomposition method. Despite this, the underlying issue is the same, namely that the line wings are difficult to recover in low S/N data and that this has a significant effect on the exact recovered value of σ_{line}(data). We show a specific example of this in § 2.8.6 for a boxy line profile with weak wings. In this case, σ_{line}(Hβ; data) suffers from a low accuracy (overestimated by 77% or 0.5 dex in M_{BH} at S/N ~ 25 pixel^{-1}; see gray line in panel (a) of Figure 2.12) because the low contrast wings get artificially enhanced as the noise increases. The effect of spectral noise is surprisingly large and emphasize the need for high S/N spectra to obtain reliable mass estimates.

At S/N ≥ 10 pixel^{-1}, σ_{line}(data) is unbiased and gives an accuracy and precision within 0.2 and 0.3 dex, respectively, when propagated to the black hole mass (illustrated for Hβ in Figure 2.12 and § 2.8.2 and for C IV in Figure 2.19 and § 2.9). Benchmarking σ_{line}(data), we find that the accuracy of the mass estimates is within 0.1 dex at S/N ~ 50 pixel^{-1}. Clearly, this also means that S/N ≥ 50 pixel^{-1} is necessary for mass estimates accurate to within 0.1 dex. For such high accuracy black hole mass estimates, σ_{line}(data) therefore requires just as high S/N as FWHM(data) mentioned above.

The MAD and IPV widths are the most accurate and precise

The performance of the MAD(data) and IPV(Y$\geq$20%; data) widths are in general similar in terms of how high an accuracy and precision that can be achieved at a given S/N level. Specifically, they are both unbiased at S/N ≥ 5 pixel^{-1} and show a higher accuracy and precision than σ_{line}(data) and FWHM(data) (illustrated by the smaller span of the red [IPV(data)] and light blue [MAD(data)] shaded areas compared to the dark blue [σ_{line}(data)] and green [FWHM(data)] ones in Figure 2.20 for

Hβ and Figure 2.19 for C IV). We thus confirm the result in Fine et al. (2010), namely that the IPV50 width is unbiased and accurate within 20% for S/N ≥ 3 Å $^{-1}$, even though they probably underestimate the error in that study, as discussed in § 2.2.3).

Denney et al. (2016) compare C IV line widths measured on single epoch spectra and co-added[3] versions of the same spectra for each of the 482 AGN at redshifts between 1.46 and 4.5 from the SDSS Reverberation Mapping project (R∼2000) in their sample. The single epoch spectra have an average S/N $\sim 5.5\,\mathrm{pixel}^{-1}$, while the co-added spectra have an average S/N $\sim 25.7\,\mathrm{pixel}^{-1}$. From their comparison, Denney et al. (2016) conclude that the MAD(data) has a higher accuracy than the FWHM(data) and σ_{line}(data) line widths, also consistent with our results. Compared to σ_{line}(data), the MAD(data) and IPV(data) widths are more robust to spectral noise because they do not weight pixels far away from the line centre (i.e., in the line wings and the continuum) as strongly. Specifically, we find that black hole mass estimates from both the MAD(data) and IPV(data) widths are accurate and precise to within ∼0.3 and ∼0.5 dex, respectively, for S/N $\geq 5\,\mathrm{pixel}^{-1}$ [this is demonstrated in § 2.8.3 and § 2.8.4 for MAD(Hβ; data) and IPV(Hβ; data), respectively, and § 2.9 for MAD(C IV; data) and IPV(C IV; data)].

Although the performance of the MAD(data) and IPV(data) widths are similar in general, we do show one example where the MAD suffers from a low accuracy (§ 2.8.6). For this line profile, which is peaky and with weak wings, the noise present in the data results in a bimodal distribution of MAD(Hβ; data) widths that at some S/N levels leads to a severe underestimation of ∼70% of MAD(Hβ; data) (gray line in panel (a) of Figure 2.14). The IPV(Hβ; data) width is unaffected by this issue.

Benchmarking the MAD(data) and IPV(Hβ; data) widths, we find that the accuracy of the mass estimates is 0.1 dex at S/N $\sim 50\,\mathrm{pixel}^{-1}$ for both parameters, identical to σ_{line}(data). For the IPV(C IV; data) widths we find an accuracy of the mass estimates between 0.07 dex [IPV20%(C IV; data)] and 0.03 dex [IPV90%(C IV; data)], better than for the rest of the line parameters. This higher performance also means that black hole mass estimates based on IPV(C IV; data) at percentages of y=25% or above are accurate to within 0.1 dex down to S/N $\sim 5\,\mathrm{pixel}^{-1}$, in contrast to the other line parameters where S/N $\sim 50\,\mathrm{pixel}^{-1}$ is required for the same accuracy. We note though, that the penalty of decreasing precision with increasing spectral noise still remains even when the accuracy stays high. For example, at S/N $\sim 5\,\mathrm{pixel}^{-1}$, where the accuracy of mass estimates based on IPV(Y=25%; C IV, data) is within 0.1 dex, the precision of those mass estimates can be as low as ∼0.5 dex (see Figure D.6).

IPV offers more flexibility than MAD

Although the MAD(data) and IPV(data) widths in general have similar accuracy and precision, there are two reasons to favor the IPV(data) widths for black hole mass estimates based on AGN spectra. First, the many fractions of the line flux at which the line width can be measured using the IPV widths

[3]The procedure for combining the individual single epoch spectra to form a high S/N co-added spectrum is as described in Shen et al. (2015)

offers great flexibility in terms of characterising the line width from the base to the core of the line profile. This provides the flexibility to choose the IPV width that most accurately represents the virial velocity that reflects the gravitational field of the black hole. Second, using ratios of different IPV widths allows for a parameterisation of the line shape that is superior to the traditionally used FWHM/σ_{line} ratio (§ 2.10), something that MAD alone cannot do. Denney (2012) compare mean and rms C IV line profiles for seven reverberation mapped sources and show that C IV has a non-variable component of low velocity gas that affects the line widths, and thereby the mass estimates, measured in the mean spectra. No such component is found for the Hβ line. They speculate that this non-variable C IV emission could originate from a broad-line region disk wind or the intermediate-line region, a high-velocity inner extension of the narrow-line region (Denney, 2012). No matter its origin, this non-variable component of the C IV line leads to increased scatter between the Hβ and C IV masses. By using the shape of the line C IV, Denney (2012) show that they can empirically reduce this scatter by approximately a factor of 2 to ∼0.2 dex between the C IV and Hβ masses for the 53 AGN included in their sample. Yong et al. (2016) use the shape of the line to (partially) correct for the unknown inclination of the AGN, removing a tendency for the masses to be overestimated. Gaining an accurate measure of the line shape is therefore most likely important to obtain unbiased black hole mass estimates.

A warning about low equivalent width lines

In § 2.8.6 we investigate a Hβ line profile with an equivalent width of only 6 Å. In the case of such a low contrast line, the FWHM(Hβ; data), σ_{line}(Hβ; data), and MAD(Hβ; data) (see orange lines in panel (a) of Figures 2.10, 2.12, 2.14, respectively) can be offset by more than 100% (0.6 dex in M_{BH}) at S/N ≥ 25 pixel^{-1}. This should be compared to an accuracy that is within 20% (0.19 dex in M_{BH}) for the rest of the sample of Hβ spectra containing higher equivalent width lines. For the IPV50(Hβ; data) width the accuracy is within 40% (0.3 dex in M_{BH}) for the low equivalent width line and 20% (0.19 dex in M_{BH}) for the rest of the sample (see orange line in panel (a) of Figure 2.16) at S/N ≥ 25 pixel^{-1}. While this is indeed an example of a very low contrast line, it clearly illustrates how careful one should be when measuring emission line widths on weak lines in AGN spectra, especially at low S/N levels.

IPV and MAD widths are more precise for C IV than Hβ

We generally find very similar results for the two emission lines Hβ (§ 2.8) and C IV (§ 2.9). Yet, there is a (positive) tendency for MAD(C IV; data) and IPV(C IV; data) to have somewhat higher precision compared to MAD(Hβ; data) and IPV(Hβ; data) (compare the span of hashed blue and red areas, respectively, in the rightmost panels of Figure 2.19 and 2.20, respectively). We speculate that there are two reasons for this. First, the continuum is easier to constrain in the C IV spectra, where it is anchored in two regions free of blending line emission, as opposed to the Hβ spectra, where the local continuum is degenerate with the host galaxy strength, Fe II emission, and the Balmer continuum

emission. Second, the strength of the Hβ narrow line component becomes more difficult to constrain with decreasing noise, thereby adding scatter to the Hβ line width measures.

Functional models bias the line widths

One can measure the line width on a functional model as a means to mitigate the adverse effects of spectral noise. However, our study shows that this only increases the accuracy and precision of the black hole mass estimates at S/N below 5 pixel^{-1} and only if the IPV widths are measured (§ 2.8.5 and § 2.9). This extends the higher robustness of the IPV widths compared to the other line width measures to S/N levels down to $\sim$1 pixel^{-1}. We find FWHM(funct) (i.e. the FWHM measured on a functional model) to be biased by up to 30% (0.30 dex in M_{BH}) at S/N $<$ 50 pixel^{-1} and that its accuracy and precision is only marginally higher than for FWHM(data) at S/N $<$ 10 pixel^{-1} (§ 2.8.5). For σ_{line}, the MAD, and the IPV widths measured on a functional model we find an increase in accuracy and precision for S/N $<$ 5 pixel^{-1} (§ 2.8.5) compared to the directly measured line parameters. But, importantly, at S/N $\geq$ 5 pixel^{-1}, we find that both σ_{line}(Hβ; funct) and MAD(Hβ; funct) suffers from biases that underestimate the line width by $\sim$40-50% (Figure 2.12 and 2.14, respectively), making them unreliable as line width estimators at these S/N levels. Denney et al. (2009) also find that functional models of the broad emission lines can introduce a bias in the black hole mass estimates. Specifically, they compare mass estimates using Gauss-Hermite polynomial fits for two AGN at varying S/N levels with mass estimates using line widths measured directly on the data. They find that for S/N $\leq$ 10 Å $^{-1}$, masses based on Gauss-Hermite polynomial fits can be biased when using the FWHM. Contrary to σ_{line} and MAD, the IPV(funct) widths are unbiased with respect to the IPV(data) widths and can be used on data with S/N $<$ 5 pixel^{-1} in order to get more accurate mass estimates [illustrated in Figure 2.16 for IPV50%(Hβ; funct)]. This further supports our choice of the IPV widths as the preferred line width parameter to use for black hole mass estimates.

Summary on the line width parameters

For emphasis and clarification, we here summarize and re-iterate the main results of our study that have direct implications for the accuracy and precision of black hole mass estimates based on single-epoch spectra. First and foremost, the IPV(data) widths are the preferred line width parameters for data with S/N $\geq$ 5 pixel^{-1} because they have the highest accuracy and precision, yielding unbiased black hole mass estimates with an accuracy and precision within $\sim$0.3 and $\sim$0.5 dex, respectively, at these S/N levels. To get black hole mass estimates with a high accuracay ($<$0.1 dex), a S/N $\geq$ 50 pixel^{-1} is required. This stresses how important it is to acquire high quality data to get high fidelity mass estimates. In addition, the IPV widths offer the flexibility to parameterise the line width at many different levels of the line flux and the line shape using practically any desired ratio of IPV(data) widths. We note that the MAD(data) has an accuracy and precision typically similar to the IPV(data) widths but that it does not offer any flexibility in terms of characterising the line width and shape. However, we highlight one case where the MAD fails in § 2.8.6. For data with S/N $<$ 5 pixel^{-1},

the IPV(funct) widths provide an unbiased and more robust way to measure the line shape than the IPV(data) widths. With this being said, we do advice against using data with such low S/N : other factors than the inherent uncertainty in the line width measure due to spectral noise, such as the lack of ability to robustly decompose the spectrum and to identify absorption lines with high fidelity, will be at play. The impact of these effects is not yet known but will likely be severe in combination with the low data quality. We discuss some of these issues in § 2.11.3 below.

2.11.2 Robustness to AGN variability

So far we have discussed the importance of the line width measures being robust to varying spectral S/N level if they are to be suitable velocity measures to use for black hole mass determinations. There is, in fact, another property that is important. Namely, the line width measures should, in addition, yield consistent mass values as the AGN accretion state, and thus the nuclear luminosity, changes. The test we discuss here is similar to that presented by Collin et al. (2006) for the FWHM and σ_{line}. We determine the black hole mass for several epochs of observations for the same line width measures and the same AGN.

We utilize the monitoring data of NGC 5548 that span a time period of over 20 years (Peterson et al., 2004; Bentz et al., 2007, 2009c; Denney et al., 2010; De Rosa et al., 2015). There are monitoring data for other AGN, but those data sets contain too few epochs – from at most a couple of reverberation mapping campaigns – to be useful for our purpose (Kilerci Eser et al., 2015). The NGC 5548 monitoring data span about an order of magnitude in 5100Å luminosity. This is representative of the typical variability of other reverberation mapped sources, but it does not probe the most extreme variabilities observed (Kilerci Eser et al., 2015). Details on the data and spectral decomposition method is given in Appendix F.

Figure 2.22 shows the virial product

$$VP = \frac{c\tau\Delta V^2}{G} \tag{2.8}$$

(where c is the speed of light, G is the gravitational constant, and τ is the measured time-delay) as a function of 5100Å luminosity for the different line width parameters measured in the mean and rms spectra (filled and open circles, respectively). Table 2.3 lists the mean ($<VP>$) and 1-σ scatter around the mean [$\log(\sigma_{VP})$] of the virial products for each line width measure. The 1-σ scatter in the *VP* is similar for all the line width measures in the mean spectra (column 3 in Table 2.3), ranging from 0.13 dex for the IPV50% width to 0.16 for the FWHM. This rather high scatter is, at least partly, due to the relatively low wavelength coverage, generally 4550 Å to 5200 Å, available in the spectra, which makes it difficult to perform a robust spectral decomposition (Appendix F).

For the rms spectra, the 1-σ scatter is generally slightly larger (column 5 in Table 2.3), but still within 0.20 dex. This larger scatter is most likely an artifact of the lower S/N ratio in the RMS (median S/N $\sim 59 \pm 9$ pixel^{-1}) compared to the mean (median S/N $\sim 119 \pm 18$ pixel^{-1}) spectra.

Table 2.3 Mean and scatter of VP's

	Mean spectra		RMS spectra	
Parameter	$\log < VP >$	$\log \sigma_{VP}$	$\log < VP >$	$\log \sigma_{VP}$
(1)	(2)	(3)	(4)	(5)
VP(FWHM)	8.07	0.16	7.91	0.20
VP(σ_{line})	7.56	0.15	7.29	0.16
VP(MAD)	7.31	0.14	7.06	0.14
VP(IPV50%)	7.70	0.13	7.53	0.15

The virial product calculated from the FWHM is less consistent with a single value than for the other three line width parameters (compare number of filled and open circles in each panel that are consistent with the solid and dashed horisontal lines, respectively, in Figure 2.22).

We also find that all the virial products are correlated with the 5100Å luminosity with a Spearman rank significance $p_s \leq 0.05$ in the mean spectra, indicating that to some degree all the line width measures are sensitive to changing AGN luminosity. The strongest correlation is found for the FWHM virial product (Spearman correlation coefficient $\rho_s = 0.71$); the IPV50%, MAD, and σ_{line} virial products all have $\rho_s \sim 0.65$. Whether this signifies a real correlation or if it simply is an artifact of how difficult it is to correct for the continuum and blending emission is unclear. For example, it is possible to imagine that for low luminosity states, there is a tendency to overestimate the luminosity of the galaxy, which in turn will lead to a lower measured value of FWHM. For high luminosity states, the opposite might be true, leading to a spurious correlation between luminosity and virial products. We stress that these are speculations, but that it is important to consider whether the observed correlations are real or simply a consequence of the shortcomings of the method we use to measure the spectral properties. The correlation strengths are generally weaker and have less significance in the rms than in the mean spectra.

Based on our tests, we can not exclude any of the line width measures as a reliable proxy for the velocity field of the BLR gas since they show similar scatter in the VP and similar correlation strength between the VP and L_{5100}. On the other hand, we find the scatter and correlation strength to be largest for the FWHM which means that the σ_{line}, MAD, and IPV50% widths should be preferred to the FWHM when determining SE mass estimates.

We note that while the data we use for this test is currently the best available, they only represent one object (NGC 5548) which somewhat limits the usefulness of the test. Therefore, it is important that this test be repeated for more objects and high(er) quality data when possible.

2.11.3 Implications of our findings

Consequences for existing and future mass estimates

Our results clearly show that the quality of the data in terms of spectal S/N has a profound impact on the accuracy and precision of the different line width measures and therefore also on the black

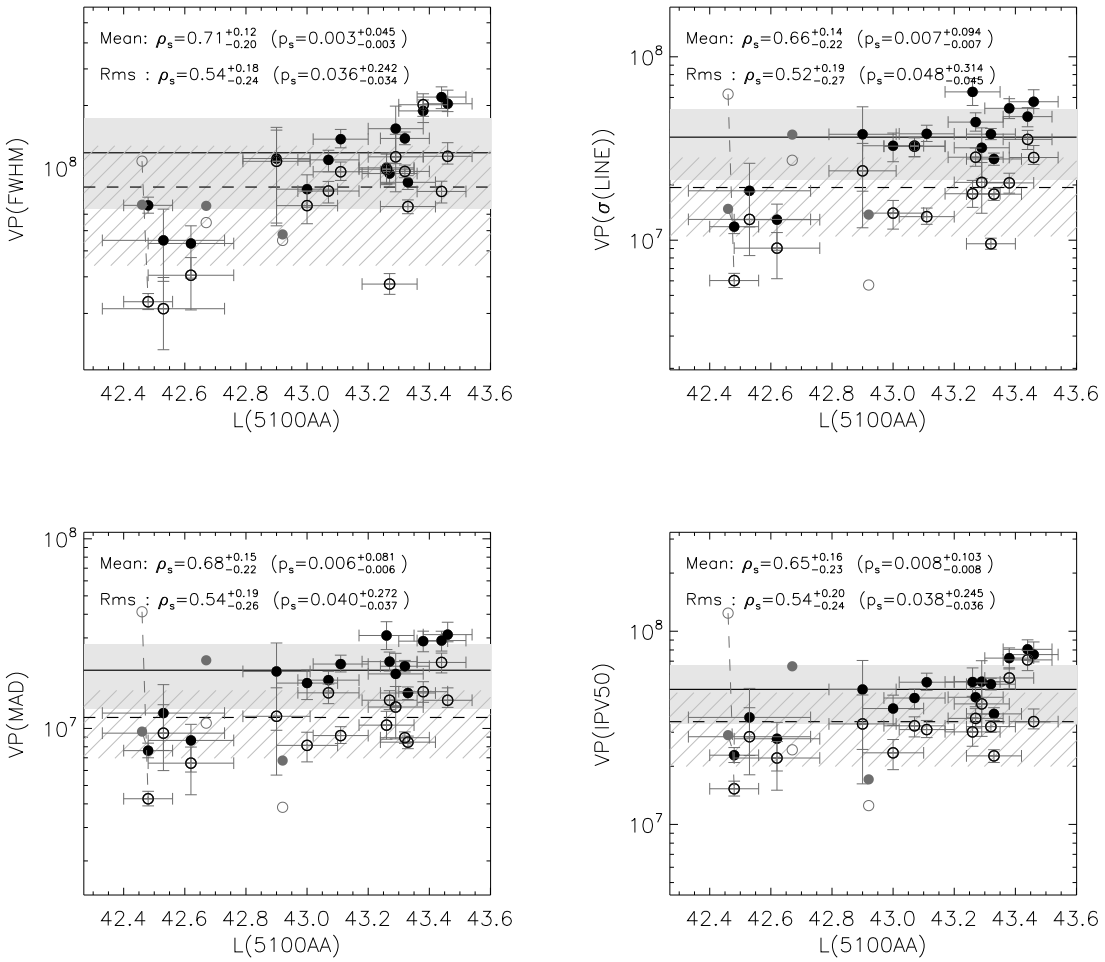

Fig. 2.22 Virial products for the FWHM(Hβ; data) (upper left), σ_{line}(Hβ; data) (upper right), MAD(Hβ; data) (lower left), and IPV50(Hβ; data) (lower right). Filled circles and open circles show the virial product calculated from the line width measured in the mean and rms spectra, respectively, and solid gray and hashed areas show the corresponding 1-σ scatter for the mean and rms based measurements, respectively. Points shown in gray correspond to data from year 12, 19, and to the first half of the year 26 campaign, for which an anomalous response pattern for the broad lines in response to the continuum was observed for the last part of the campaign (De Rosa et al., 2015; Pei et al., 2017), that are excluded from the analysis.

hole mass estimates. This has some immediate consequences for already published results and the use of existing data, but also for the optimal strategy when acquiring new data for black hole mass measurements in AGN.

For already published results and existing data, our findings allow authors to give a more realistic assessment of the uncertainty of the broad emission line width at a given S/N level and for a given emission line profile. Applying a similar way to estimate the uncertainties will make it much easier to compare different studies from different authors on a par. This applies equally well to reverberation mapping studies as well as single epoch mass estimates. In fact, any study using measurments of broad emission line widths in AGN spectra can benefit from assessing their errors using the results presented here.

From a reverberation mapping dataset, the black hole mass can be calculated from either the mean or rms spectrum. The mean spectra have higher S/N than the rms spectra and will therefore yield black hole masses with a higher precision when using a given line measure. On the other hand, the rms spectra yield more accurate black hole masses than the mean spectra because they only represent the part of the BLR gas that is actually varying in response to the changes in continuum luminosity (Peterson et al., 2004). Two factors determine the S/N of a rms spectrum. First, the number of spectra plays a role such that more spectra giver higher S/N . But, just as importantly, the variability amplitude within the observed timeframe determines the amplitude, and thereby also the S/N , of the final rms spectrum. While it is easy to plan for a large number of spectra, there will always be a bit of luck involved in sampling a high enough variability amplitude to get S/N $\geq 50\,\mathrm{pixel}^{-1}$. If we can achieve this S/N level, all line measures should yield black hole masses with an accuracy of $\sim$0.1 dex or better. Measured on the sample of spectra used in the variability analysis of NGC 5548 (§ 2.11.2), the mean spectra have S/N ranging between 60 and 215 pixel^{-1} in the continuum which means that the uncertainty in the mass estimates due to the line width measure should be 0.1 dex or less. The rms spectra on the other hand have S/N ratios ranging between 22 and 87 pixel^{-1} with a significant fraction of the spectra having S/N $\leq 35\,\mathrm{pixel}^{-1}$. In this case, the uncertainties in the mass estimates due to the line width measure can be up to 0.2 dex if using the FWHM or σ_{line}.

Due to the ease at which single-epoch mass estimates can be used, they are commonly used on large spectral surveys of AGN, such as the Sloan Digital Sky Survey York et al. (2000) and the 2dF QSO Redshift Survey Croom et al. (2004). The nature of the designs of such large surveys means that the majority of the spectra have relatively low S/N . To illustrate this issue, Fig. 2.23 shows the distribution of S/N (left panel) and the S/N as a function of redshift (right panel) for quasar spectra in the SDSS Data Release 3 and 7 as measured by Vestergaard et al. (2008) and in this work, respectively. By lowering the S/N cut for these samples from 10 pixel^{-1} (below which σ_{line} is biased) to 5 pixel^{-1} (below which MAD and IPV widths are biased), we roughly double the amount of spectra (from $\sim$6900 to $\sim$13800 and from $\sim$31000 to $\sim$63000 spectra for Data Release 3 and 7, respectively) for which we can reliably estimate a black hole mass. This illustrates the benefit of being able to push the S/N limit by using the MAD(data) and IPV(data) widths instead of FWHM(data) or σ_{line}(data). This is particularly useful to increase the sample size of high redshift AGN spectra that in general

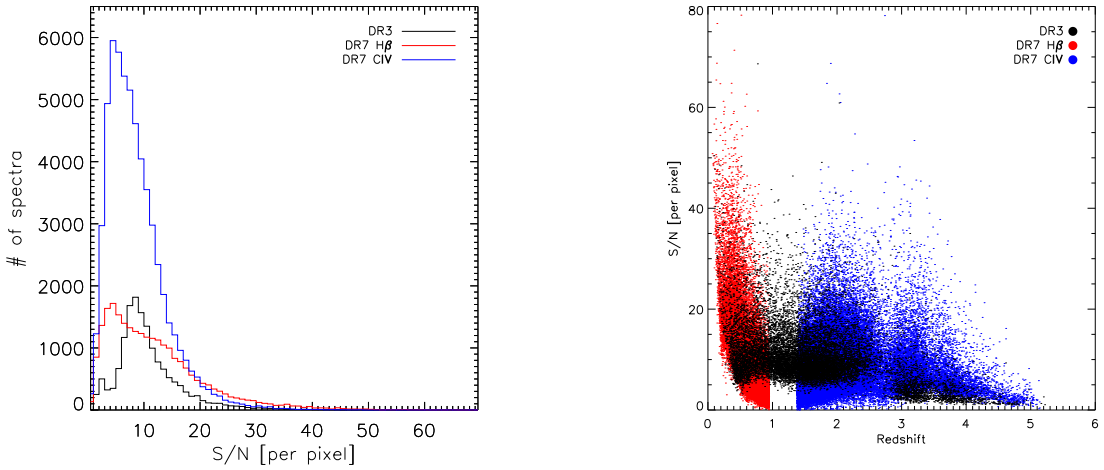

Fig. 2.23 S/N distribution from the SDSS Data Release 3 and 7 quasar spectra. The DR3 data shown here (black points) is the subset used by Richards et al. (2006) to determine the Quasar Luminosity Function and the S/N measurements are from Vestergaard et al. (2008). Various selection criteria have been imposed on this subset, and therefore most of the low S/N data of DR3 is not represented in the figure. The DR7 subset shown here represents all spectra with a C IV (blue points) or Hβ (red points) black hole measurement from Shen et al. (2011).

have the lowest S/N (illustrated in the right panel of Figure 2.23). This figure, combined with our results, also highlights how careful one has to be when working with survey data where spectral data quality often is relatively low due to the observing strategy imposed to maximize the number of targets included in the survey. This is particularly true if working with the C IV line which typically has lower S/N (Figure 2.23) and therefore can lead to more uncertain or even biased mass estimates. This might explain some of the offsets between Hβ and C IV masses found in the literature. A fair comparison requires spectra of high S/N for both Hβ and C IV.

Another way to benchmark the different line parameters against each other is to ask the question: What S/N level is required to obtain a mass estimate with an accuracy of 0.1 dex or better? According to our results, the answer is S/N ≥ 25 pixel^{-1} for FWHM, S/N ≥ 50 pixel^{-1} for σ_{line}, S/N ≥ 50 and 25 pixel^{-1} for the MAD(Hβ; data) and MAD(C IV; data), respectively, and S/N ≥ 50 and 3 pixel^{-1} for the IPV50(Hβ; data) and IPV50%(C IV; data), respectively. In general, a S/N ≥ 25 pixel^{-1} is required for this benchmark, and in many cases, S/N ≥ 50 pixel^{-1} is necessary. Interestingly, the IPV50(Hβ; data) width requires S/N ~ 50 pixel^{-1} for this benchmark, while IPV50%(C IV; data) only requires S/N ~ 3 pixel^{-1}, by far the lowest S/N required for any of the line parameters. Looking into the data for IPV50(Hβ; data), we find that for only two of the spectra is the accuracy worse than 0.1 dex when S/N ≥ 5 pixel^{-1}. This means, that in general, the IPV50(Hβ; data) and the IPV50%(C IV; data) both perform extremely well and provide mass estimates with an accuracy of 0.1 dex or better if S/N ≥ 5 pixel^{-1}.

To summarize: regardless of whether one is estimating a black hole mass from reverberation mapping data or from a single epoch spectrum, we advice that the focus is on the quality of the data (high S/N) instead of the quantity of the data (many objects). For existing data and already published results, we recommend that the error estimates from this work be taken into account when evaluating the results and when comparing different studies.

Notes on the spectral decomposition

Another important issue is the wavelength coverage available in the spectra which affects the fidelity of the spectral decomposition. In turn, this affects the measured line widths and thereby the mass estimates. This issue is particularly important in the context of reverberation mapping masses since historical datasets often have a rather short wavelength coverage around the particular emission line of interest. A specific example is the Hβ spectra observed for NGC 5548 and addressed in §2.11.2 above which only covers 4550 Å to 5200 Å in the wavelength rest frame for most epochs prior to 2010. With such a narrow wavelength coverage, it can be difficult to establish the continuum level below the line as there might not be any line-free continuum windows available in the spectrum. Furthermore, blending can be difficult to establish since it can be hard to distinguish between the underlying continuum and other emission features. For Hβ, it can be a challenge to establish robustly the host galaxy contribution when it is blended with the nuclear continuum and various line emission. This issue is less relevant for the spectral region around the C IV line because the host galaxy contribution is rather weak compared to the AGN continuum emission in the UV (Kinney et al., 1996). All of these issues calls for as large a wavelength coverage as possible. We find that for Hβ, a coverage from $\sim$2000 Å to $\sim$6000 Å is sufficient to robustly distinguish the spectral components from each other. This rather long wavelength coverage is necessary since there are no continuum free windows close to the Hβ line. For C IV we find a spectral coverage from 1445-1700 Å to be sufficient since this includes two contamination free windows at 1445-1455 Å and 1690-1700 Å where the continuum emission can be anchored. In some cases, one can also use windows immediately red of the C III] λ1909 line as additional anchor points for the UV continuum.

Several studies have compared different spectral decomposition methods. For example, Denney et al. (2009) compare a simple prescription using only a local linear continuum below the Hβ line with full spectral decomposition models including a power-law continuum, a host galaxy spectrum, a Fe II pseudo continuum, Balmer continuum emission, and several individual emission lines and with varying Fe II templates and prescriptions for modelling the narrow component of the emission lines. One of the key points of that study is that it is crucial for an accurate mass estimate to model and remove the narrow line contribution to the Hβ line, otherwise the mass estimates may be off by a factor of -1.0 dex for the FWHM and 0.1-0.2 dex for the σ_{line} (Denney et al., 2009). Also, Fine et al. (2010) compare different methods to account for the red shelf of emission of unknown physical origin at $\sim$1600 Å in C IV spectra. They compare methods ranging from simply modelling a local linear continuum below the C IV line to modelling the continuum and several emission components.

They find that the FWHM is relatively robust to the spectral decomposition technique applied, but that the IPV50 width and σ_{line} both change by more than 50% depending on the spectral decomposition method. The issue of choosing a spectral decomposition method clearly has a large impact on the measured value of the line parameters.

A more grave example of the effect of different spectral decomposition methods is given by Vestergaard et al. (2011). Here, the authors compare line widths measured by Vestergaard et al. (2008) and Shen et al. (2011) on a subset of the SDSS DR3 Quasar Catalog. They find that the difference between the FWHM line width measured in those two studies, on the exact same spectra, increase as the S/N decreases. Specifically, for the Hβ, Mg II, and C IV lines that are investigated in this study, Vestergaard et al. (2011) find a scatter between the FWHM measurements of $\sim$1000 km s^{-1} even for a high S/N of $\sim$20 pixel^{-1}. This corresponds to $\sim$20% (or up to $\sim$0.2 dex in M_{BH}) for a typical line width of FWHM$\sim$5,000 km s^{-1}. For S/N levels around 10 pixel^{-1}, the differences in FWHM line width can be as large as 8,000 to 10,000 km s^{-1}, a rather drastic difference.

While testing different spectral decomposition methods is beyond the scope of this work, we make a few observations that are worth mentioning. For example, in order to effectively remove the residuals in the red wing of the broad Hβ line, the observed emission redwards of 4920 Å should be replaced by a functional model of the remaining part of the Hβ line profile extrapolated into the affected region (this procedure is explained in § 2.6.1). This procedure is efficient and robust. We also find, that in order to constrain the normalisation of the nuclear power-law continuum model in the region around C IV, it is necessary to first model and subtract this continuum emission before modelling the rest of the spectral components. This is in contrast to the Hβ region where we model all spectral components simultaneously. The added benefit of using a two-step decomposition for C IV is that it makes the modelling process up to 10 times faster while still obtaining robust results. This has practical implications for studies focused on analyzing large samples with thousands of AGN spectra.

Another issue that can affect the fidelity of the spectral decomposition is the spectral resolution. Our ability to account for blending is directly dependent on the spectral resolution. This is especially true for narrow absorption lines which typically have a width of FWHM$\sim$200 km s^{-1}. To resolve these lines, a minimum spectral resolution of 100 km s^{-1} is necessary. For narrower absorption lines than this, even higher spectral is required. This also means that for example SDSS data that has a spectral resolution of $\sim$70 km s^{-1} only barely resolves narrow absorption lines. In this respect, higher spectral resolution is always desired as a too low spectral resolution hampers our ability to recognize and account for narrow absorption features. The effect of such unrecognized absorption is explored in a forthcoming paper (J.J. Jensen & M. Vestergaard, 2018c, in preparation) where we specifically test the effect of narrow line absorption at varying positions on the C IV line and with different strengths on a sample of different C IV line profiles representative of the observed AGN population.

Clearly, the wavelength coverage, the spectral resolution, and the specific spectral decomposition model applied can affect the shape and strength of the extracted broad emission line profile. In turn, this affects the measured line width such that different spectral decomposition methods can lead to different results, even for the same spectrum (e.g., Denney et al., 2009; Fine et al., 2010; Vestergaard

et al., 2011). In light of this, we recommend that the community move towards a common spectral decomposition strategy such that the work of different authors more easily can be compared. An attempt at finding such a spectral decomposition method is the subject of a forthcoming paper. In the meantime, we recommend the use of the decomposition method applied in this work since this is shown to be robust and its uncertainties for a given S/N level is now known (§ 2.8 and § 2.9).

Next steps

To improve the single-epoch mass estimates based on the results of the current work, we need to recalibrate the mass scaling relations to depend on the IPV widths. However, before this can be done, a few additional studies are necessary: First, a determination of which IPV width most accurately traces the velocity field of the broad line region needs to be determined. Second, a possible shape correction, as suggested necessary by Denney (2012) and Yong et al. (2016) in order to accurately calibrate the black hole masses, based on the IPV widths must be established. Third, the effect of undetected (narrow) absorption features on the emission line must be quantified. Only when these issues are resolved is it meaningful to recalibrate the SE mass estimates based on the IPV widths. We are currently working on resolving these issues.

2.12 Summary and conclusions

To obtain accurate black hole mass estimates in AGN, we need accurate and precise measurements of broad emission line widths in AGN spectra. Our focus here is to investigate the accuracy and precision of four different line width parameters, which can be used for this purpose, as a function of spectral signal-to-noise (S/N). In the process, we also establish the most robust way to measure the line parameters in terms of choosing a set of line limits and a continuum level to constrain the emission line profile. We perform our investigation on a sample of high S/N spectra, containing either the broad Hβ or C IV emission line, and degraded versions of the same spectra. Each original high S/N spectrum is degraded to a range of S/N levels below 50 pixel^{-1} by adding random Gaussian noise. Each spectrum is degraded 500 times to each target S/N level using a different *seed* for the noise distribution each time. We then extract the line width for each of these spectra and use the median and the 1-σ scatter on each side of this median as the representative line width and its uncertainty at that particular S/N level for that particular original spectrum. By comparing this measured line width with the one measured in the original high S/N spectrum, we can establish the accuracy and precision of the line width measure as a function of spectral S/N .

We investigate four different line parameters, namely the full-width-at-half-maximum (FWHM), the line dispersion (σ_{line}), the median absolute deviation (MAD) from the median velocity, and the inter-percentile velocity (IPV) widths. We focus on the line parameters measured directly in the data, but we also investigate whether measuring them on a functional model of the line profile effectively mitigates the negative effects of spectral noise as is commonly assumed in the literature. In addition,

we test how robustly each of the four line parameters provide a black hole mass estimate as the AGN luminosity changes. Our main results are:

- The most optimal way to measure the line parameters directly on the data is to adopt the *fixed line limits*, placed at a distance of $\pm 18\,000\,\mathrm{km\,s^{-1}}$ from the line centre (§ 2.8). This type of line limit at this particular distance ensures that extraneous emission is excluded from the line measurement and at the same time, any significant truncation of the line flux (>1%) is avoided.

- The most optimal continuum setting to adopt for line width measurements is the best fitted one (§ 2.8), except when measuring the FWHM directly on the data (§ 2.8.1). In this case, the best$-1\sigma_{\mathrm{cont}}$ continuum setting should be used in order to mitigate some of the negative effects of spectral noise. Here, best$-1\sigma_{\mathrm{cont}}$ is the best fit continuum model minus an estimate of the continuum flux uncertainty - measured as the 1 sigma scatter of the observed flux density around the best fit continuum model.

- The FWHM measured directly on the data is very susceptible to spectral noise in the line peak and in the line wings, causing its measured value to be under- and overestimated severely. As a consequence of noise in the line peak, FWHM(data) can be underestimated by as much as 38% (0.42 dex in M_{BH}) at S/N $\sim 15\,\mathrm{pixel^{-1}}$ (§2.8.1). For this reason, we caution against measuring it for S/N $< 25\,\mathrm{pixel^{-1}}$. The precision of FWHM that can be achieved at S/N $\sim 25\,\mathrm{pixel^{-1}}$ is ∼25% or ∼0.2 dex in the black hole mass estimate. To achieve an accuracy better than 0.1 dex in the mass estimate, S/N $> 50\,\mathrm{pixel^{-1}}$ is necessary.

- The σ_{line} parameter is more robust to noise than FWHM, but nevertheless it is still affected significantly by spectral noise. This is especially true of noise in or close to the line wings because σ_{line} weights the flux density in each spectral bin by its squared distance from the line centre. For this reason, σ_{line} becomes biased for S/N $< 10\,\mathrm{pixel^{-1}}$ where it tends to be overestimated due to the spectral noise in the line wings. For S/N $\geq 10\,\mathrm{pixel^{-1}}$, σ_{line} achieves an accuracy and precision, respectively, to within ∼30% and ∼50% (∼0.2 dex and ∼0.3 dex in M_{BH}). For a mass estimate with an accuracy of 0.1 dex or better, S/N $\geq 50\,\mathrm{pixel^{-1}}$ is necessary.

- The MAD and IPV widths measured directly on the data are more accurate and precise measures of the line width than the FWHM and σ_{line} at any given S/N level. The MAD and IPV widths are *unbiased* measures of the line width for S/N $\geq 5\,\mathrm{pixel^{-1}}$ and have an accuracy and precision within ∼35% and ∼100% (∼0.3 dex and ∼0.5 dex in M_{BH}), respectively, at this S/N level, and if the IPV widths are measured at a fraction of the line flux of 20% or more. In fact, using the IPV50(Hβ; data) width, mass estimates are accurate to within 0.17 dex for any S/N $\sim 7\,\mathrm{pixel^{-1}}$ or higher, and if the emission line has FWHM<6,500 km s^{-1} or EW<95 Å, the accuracy of the mass estimate is within 0.12 dex. Using the IPV90(Hβ; data) width, the mass estimate accuracy is within 0.20 dex if S/N $\geq 7\,\mathrm{pixel^{-1}}$, and in most cases also within

0.15 dex. The IPV(C IV; data) widths have even higher accuracy. With these, the accuracy of the mass estimate is within 0.1 dex at S/N $\geq 10\,\mathrm{pixel}^{-1}$ for IPV widths at 30% or higher. In fact, for the IPV50%(C IV; data) width, the mass estimates have an accuracy within 0.1 dex for any S/N level above $3\,\mathrm{pixel}^{-1}$. Compared to σ_{line}, the MAD width has a higher accuracy and precision because it only weights the flux density in each wavelength bin by its linear distance from the line centre. The IPV widths do not make any such weighting of the flux by its distance to the line centre but relies on the fractional line flux located in the wings. The MAD widths require S/N $\geq 50\,\mathrm{pixel}^{-1}$ to provide a mass estimate within 0.1 dex.

- In general, we advise against using data with S/N $< 5\,\mathrm{pixel}^{-1}$ in the continuum when using any of line widths for mass estimates. In the case of the FWHM, we advise to use data with a S/N of at least $25\,\mathrm{pixel}^{-1}$ to avoid any systematic biases in the mass estimates. For σ_{line}, we recommend to use data with S/N $\geq 10\,\mathrm{pixel}^{-1}$.

- Combinations of IPV widths provide a more robust way to parameterise the shape of the emission line than any combination of the FWHM, σ_{line}, and MAD line parameters. In particular, ratios of different IPV widths are more robust estimators of the line shape than the traditionally used FWHM/σ_{line} ratio. For example, both the IPV25/IPV60 and IPV35/IPV75 ratios have an accuracy and precision within $\sim$20% and 50% for S/N $\geq 5\,\mathrm{pixel}^{-1}$ compared to $\sim$300% and 700% for the FWHM/σ_{line} ratio (§ 2.10).

- The line widths measured on a functional model, as opposed to directly on the data, in general do not improve the robustness of the line width parameters, contrary to what is commonly assumed in the literature (§ 2.8.5 for Hβ and § 2.9 for C IV). The exception is FWHM(C IV; funct) which is significantly more robust than FWHM(C IV; data). For the remaining line parameters, using a functional model only increase the accuracy and precision if S/N $\leq 3\,\mathrm{pixel}^{-1}$. However, we find evidence that using a functional model in general will lead to biased line width measures. The best example is the σ_{line}(Hβ; funct) and MAD(Hβ; funct) for which the measured value can be underestimated by as much as $\sim$40% ($\sim$0.4 dex in M_{BH}) at S/N $\sim 50\,\mathrm{pixel}^{-1}$ when compared to the intrinsic value. For this reason we do not recommend to measure the line widths on a functional model of the line profile, in order not to introduce any bias in the black hole masses.

- A robust line width measure should at least provide a constant mass estimate despite a varying nuclear luminosity of the central engine. We test all four line width measures using a dataset of NGC 5548 spanning observations over 20 years. We find all four parameters produce a constant black hole mass almost equally well (§ 2.11.2). However, there is a significant scatter observed, caused in part by the short wavelength range of the majority of the available data. The variability observed over the 20 year period for NGC 5548 results in a scatter in the black

hole masses between 0.13 dex and 0.20 dex, depending on what line parameter is used. Further testing on this issue needs to be done for more objects and higher quality data when available.

For the C IV and Hβ emission lines, the most robust and flexible line parameter is thus the IPV widths measured directly on the data. This warrants a new calibration of the black hole mass relations based on the IPV widths. In a parallel paper (J.J. Jensen & M. Vestergaard, 2018b, in preparation) we provide the accuracy and precision of the line parameters measured on the broad Mg II line in AGN spectra. We are also in the process of quantifying the effects of undetected narrow absorption in low S/N C IV spectra on the mass estimates (J.J. Jensen & M. Vestergaard, 2018c, in preparation). Given the significant implications of the uncertainties on the currently used line widths of FWHM and σ_{line} on the accuracy and precision of the single-epoch mass estimates, to move a step further toward improving the mass estimates, we are currently in the process of examining new mass scaling relations based on the results of this work (Vestergaard et al., 2018, in preparation). Finally, we remind the reader that the total error on the mass estimate consists of the squared combination of the accuracy and precision measured here as well as any uncertainty related to the measurement of the broad line region size and the uncertainty related to the calibration of the mass scale.

Acknowledgements

We wish to thank Stephan Frank for contributing with the high S/N SDSS composite spectra of the C IV and Hβ emission lines and Sandra Raimundo for help with processing of X-Shooter spectra. JJJ gratefully acknowledges financial support from the Dark Cosmology Centre. MV gratefully acknowledges support from a FREJA Fellowship granted by the Dean of the Faculty of Natural Sciences at the University of Copenhagen, a Marie Curie International Incoming Fellowship (REA FP7-PEOPLE-2009-IIF; Proposal No 255190; Acronym: 'BHmass') and support from the Danish Council for Independent Research via grant no. DFF 4002-00275. During the preparation of this work the Dark Cosmology Centre was funded by the Danish National Research Foundation.

Chapter 3

Mg II line width measures

This chapter contains the paper:

A large statistical study to investigate a robust method to characterize the velocity field of the broad-line region in Active Galactic Nuclei II: The Mg II $\lambda\lambda$2797, 2802 Å emission lines

Jensen J.J., Vestergaard M., to be submitted to MNRAS

3.1 Abstract

High accuracy mass estimates of supermassive black holes in Active Galactic Nuclei (AGN) are important for cosmological studies and to understand the physics of AGN. In previous work, we have shown that the uncertainties related to measurements of the broad Hβ and C IV emission line widths in AGN spectra can have a significant impact on the accuracy and precision of such mass estimates. In this work, we investigate four different line parameters used for this purpose and compare their accuracy and precision over a range of spectral S/N values to see which one results in the most reliable mass estimates when measured on the broad Mg II emission line.

We find the MAD and IPV widths to be the most robust estimators of the broad Mg II emission line width when compared to the more commonly used FWHM and σ_{line} parameters. The contribution from the IPV line width uncertainty to the uncertainty on the mass estimate is less than $\sim$0.12 dex if S/N $\geq 5\,\mathrm{pixel}^{-1}$. The IPV widths also provide more flexibility when measuring the line width as it can be measured for any fraction of the emission line flux within this scheme. Our results can provide guidelines as to the optimal strategy when planning future emission line studies and on how to assess realistic errors on mass estimates using existing data more accurately.

3.2 Introduction

Active galactic nuclei (AGN) are believed to be powered by accretion of gas onto a central supermassive black hole (Alexander & Hickox, 2012, and references therein). This process releases large amounts of energy in the form of radiation, jets, and winds (e.g., Fabian, 2012; McNamara & Nulsen,

2012; Veilleux et al., 2013). At the same time, strong correlations between the mass of the central black hole and properties of its host galaxy such as bulge mass, stellar velocity dispersion, concentration index, and luminosity have been observed (see e.g. Kormendy & Ho, 2013; King & Pounds, 2015, for a few reviews). This has led to the idea that feedback mechanisms between the black hole and its host galaxy is at play, regulating their individual growth such that they co-evolve. The amount of possible feedback from the AGN is governed by the mass of the black hole as it controls the accretion and luminosity of the AGN (e.g., Peterson, 1997). The mass of the black hole is its most fundamental property, and to determine the physics of the AGN we need to accurately measure the black hole mass. An accurate mass determination is a first step in our quest to advance our understanding of AGN and their role in galaxy formation and evolution.

There are two main methods used to measure the central massive black hole in an AGN. In the local Universe, the primary method is reverberation mapping (Blandford & McKee, 1982; Peterson, 1993). For objects at higher redshifts, single epoch mass scaling relations are easier to apply and therefore more commonly used. The mass scaling relations have been calibrated for use on the Hα, Hβ, Mg II, and C IV lines (see e.g., McLure & Jarvis, 2002; Vestergaard, 2002; McLure & Dunlop, 2004; Greene & Ho, 2005b; Kollmeier et al., 2006; Vestergaard & Peterson, 2006; McGill et al., 2008; Vestergaard & Osmer, 2009; Shen & Liu, 2012; Park et al., 2017).

Both methods rely on measurements of physical characteristics of gas in the broad line region (BLR) in AGN, a dense gaseous region responsible for the broad emission lines that are characteristic of type 1 AGN spectra. To estimate the black hole mass, the velocity of the BLR gas needs to be measured at a certain distance from the centre of the AGN. For reverberation mapping, the gas velocity ΔV is measured from the width of the broad emission lines in the variable part of the spectrum (the RMS spectrum, see e.g., Peterson, 1993). The distance R to the variable gas is established from the observed time lag between the driving continuum emission from the accretion disk and the responding gas in the BLR. For the single epoch mass scaling relations where only a single spectrum is available, the distance R is estimated from the empirical relation between the BLR radius and the AGN luminosity (the *R-L* relation; Bentz et al., 2013) based on a measurement of the monochromatic luminosity in the AGN spectrum. The velocity of the BLR gas ΔV is measured from the width of the broad emission lines in a single spectrum. This spectrum holds information about the combined velocity distribution of both variable and non-variable components of the BLR gas. Assuming that the gas in the broad line region is virialized, an assumption shown to hold true in the cases where it can be tested (Peterson & Wandel, 1999, 2000; Onken & Peterson, 2002; Peterson et al., 2004), the virial black hole mass can be calculated as

$$M = f\frac{R\Delta V^2}{G} \tag{3.1}$$

where M is the virial mass, G is the gravitational constant, and f is a factor of order unity accounting for our ignorance about the inclination, geometry, and structure of the broad line region (Onken et al., 2004; Collin et al., 2006; Woo et al., 2010; Graham et al., 2011; Park et al., 2012; Grier et al., 2013).

The reverberation masses have an uncertainty of ∼0.4 dex (Onken et al., 2004; Woo et al., 2010), and the statistical uncertainty of the single epoch mass estimates constitutes approximately another 0.4 dex (Vestergaard & Peterson, 2006; Vestergaard & Osmer, 2009). The latter uncertainty refers to how well the single epoch mass estimates reproduce the reverberation masses to which they are calibrated. Currently, what limits an improvement of the uncertainty of the black hole mass measurements is the accuracy and precision to which we can measure the emission line width in AGN spectra (Jensen & Vestergaard 2018a; hereafter Paper I). In particular, since single epoch mass estimates are often made from large databases of AGN spectra such as the SDSS Data Release 7 Quasar Catalog where the signal-to-noise (S/N) ratio of the data often is relatively low (typically $\leq$10 pixel^{-1} measured in the continuum), the issue of spectral noise and its adverse effect on the line width measurements is particularly important (Vestergaard et al., 2011). Furthermore, different ways to parameterize the line width is being used among different investigators, leading to confusion when comparing results and their implications. Using spectra of two objects, Denney et al. (2009) show that the two traditionally used line width parameters, the full-width-at-half-maximum (FWHM) and line dispersion (second central moment of the line, σ_{line}) can lead to increasingly biased mass estimates with increasingly low precision as the spectral noise increases. Denney et al. (2016) show similar results for the recently introduced Mean Absolute Deviation from the median velocity (MAD).

In Paper I, we investigate the issue of decreasing S/N for spectra containing either the broad Hβ or C IV line. We examine two samples of high S/N spectra (S/N $\geq$ 30 pixel^{-1} measured in the continuum; unless otherwise stated, S/N ratios are always measured in the continuum), one for Hβ and one for C IV each, where the range of emission line properties are representative of the observed properties of these emission lines in the general AGN population. We investigated four different line width parameters, namely the FWHM, the σ_{line}, the MAD, and the Inter-Percentile Velocity (IPV) widths (Whittle, 1985). More details on the definition of the individual line parameters can be found in Paper I. Using a Monte Carlo approach, where each spectrum in the sample of high S/N spectra was degraded 500 times each to a range of different S/N levels between 1 and 50 pixel^{-1}, we established the accuracy and precision of each of the line widths as a function of spectral S/N , FWHM, Equivalent Width (EW), FWHM/σ_{line} ratio, and specific emission line. The main conclusion of that work is that the most robust and flexible line width parameters are the IPV widths, allowing for mass estimates that are accurate and precise to within 0.2 dex or better if S/N $\geq$ 10 pixel^{-1} when measured directly on the data. In this work, we extend this analysis to the Mg II $\lambda\lambda$ 2797,2802 Å line. The Mg II line is often used for black hole mass estimates in optical spectra where it can be observed in AGN at redshifts of approximately $0.7 < z < 2.2$.

Our approach here is largely similar to that of Paper I, and we refer the reader to that paper for details on the procedure. Here, we highlight the changes to that procedure necessary for Mg II. Briefly, by comparing the line parameters measured on the broad Mg II emission line in the high S/N spectra with those measured on artificially degraded versions of the same spectra, we map the accuracy and precision of each line width measure as a function of spectral quality (i.e., S/N). This allows us to clearly show the pros and cons of each line parameter. Because it is often assumed to be an effective

way to mitigate the effects of increasing spectral noise, we also evaluate whether measuring the line width parameters on a functional model instead of directly on the data leads to a higher accuracy and precision of the line widths, as is often assumed.

The structure of the paper is as follows. In § 3.3 we introduce the sample of high S/N spectra we use as a basis for our analysis. The statistical method is presented in §3.4. The spectral decomposition method we use to extract the broad Mg II line profile from the spectra is presented in § 3.5, and § 3.6 presents the statistical method we use to compare the line width measures and the results of this analysis. Finally, in § 3.7 we discuss the results and in § 3.8 we present our conclusions.

3.3 Data

For the purpose of investigating how robust each of the line widths are, we choose a sample of spectra that cover the general emission line properties of the observed AGN population. We use the subset of quasars used to study the luminosity and black hole mass functions of the DR3 quasar catalog (Richards et al., 2006; Vestergaard et al., 2008) and the DR7 quasar catalog (Shen et al., 2011), respectively, as a guide to the intrinsic properties of the AGN population. Our selection criteria are similar to those in Paper I, namely:

1. Each spectrum covers, for a given source redshift, the Mg II emission line;

2. The sample spectra cover a wide range in emission line properties, characterised by three primary parameters: 1) the FWHM emission line width, 2) the emission line strength, i.e., the emission line equivalent width (EW), and 3) the emission line shape, characterised by the FWHM/σ_{line} ratio. We choose these parameters as they are often readily available in the literature for large data sets like e.g. the SDSS;

3. We avoid broad absorption line quasars because the absorption troughs can adversely affect the line width measurements by changing the line shape. We do include some spectra with narrow absorption lines, i.e., lines with FWHM less than a few hundred $\mathrm{km\,s^{-1}}$. To ensure that these absorption lines do not affect the profile characterisations, we use sigma-clipping to remove them. The sigma-clipping algorithm uses a boxcar of 20 pixels and a 2.5 sigma limit, thereby removing only features that can be considered to be due to absorption (i.e., only features with a negative flux relative to the local continuum is removed). This procedure is efficient at removing narrow absorption lines and only removes a few pixels in each spectrum that can not be considered to be due to narrow absorption but simply are due to spectral noise. Several examples of this procedure are shown in Figure 3.1.

4. The S/N level of each spectrum exceeds $30\,\mathrm{pixel^{-1}}$. The S/N level is measured in the continuum region between 3200–3300 Å in the rest-frame as the median ratio of the observed flux density to the noise spectrum. The high spectral data quality ensures that we can measure the line width parameters with high confidence and degrade the spectra to a wide range of S/N ratios.

Table 3.1 Spectral properties of the Mg II sample

Source	Redshift z	S/N[a]	EW[b]	Line shape[c]	FWHM[f]	σ_{line} [d]	MAD[e]	IPV(50%)[f]	Ref.
(1)	(2)	(3)	(4)	(5)	(6)	(7)	(8)	(9)	
Composite A	...	67	41	2.34	2919	1246	1311	2242	1
Composite B	...	156	59	1.37	4471	3257	2094	2969	1
Composite C	...	107	62	1.55	5388	3482	2331	3371	1
Composite D	...	75	76	1.38	6369	4628	3123	4150	1
Composite E	...	55	90	1.39	7334	5288	3731	5030	1
Composite F	...	40	89	1.56	8972	5768	4279	6083	1
Q1626+1202	1.7900	61	33	0.87	3250	3724	1871	2348	2
Q1554-2020	1.9450	68	31	0.98	4170	4240	2535	3107	2
Q0106+0119	2.0990	40	14	0.96	6433	6700	4614	5196	2
Q2150+0522	1.9770	40	58	1.18	6781	5761	3855	4753	2
Q0038-0159	1.6700	117	66	1.58	8136	5151	3682	5255	2
Q1442+1011	3.5523	44	31	2.08	9194	4425	14206	3228	2
J155304.92+354828.6	0.7219	49	22	1.02	2468	2430	1706	2189	3
J082045.38+130618.9	1.1248	52	27	0.63	3030	4801	2857	2819	3
J100535.24+013445.7	1.0775	54	32	1.22	3295	2700	1849	3090	3
J092542.32+344108.6	1.0667	52	27	1.13	3579	3171	2154	2934	3
J150825.85+201521.2	1.0777	45	56	1.03	4219	4087	2602	3308	3
J094133.68+594811.1	0.9671	62	34	1.16	4269	3695	2452	3238	3
J141301.70+173201.3	1.3022	57	60	1.14	4284	3766	2413	3199	3
J143748.28-014710.7	1.3077	55	51	1.22	5285	4347	2915	3866	3
J150017.58+121036.5	0.7832	50	35	1.19	5650	4758	3167	4183	3
J090824.14+033929.8	1.2609	44	37	3.49	5767	1650	1748	3406	3
J124410.82+172104.5	1.2816	53	18	1.66	5914	3553	2541	3961	3
J074816.97+422509.2	1.1092	58	42	1.23	6096	4962	3407	4659	3
J092756.88+253007.7	1.1945	73	57	1.13	6427	5686	3950	5031	3
J142658.57-002056.4	0.6268	41	84	1.14	6796	5959	4339	5971	3
J212501.20-081328.6	0.6241	44	86	1.56	9100	5815	4443	6977	3

Note. — SDSS spectra cover $\sim$3800 – 9200Å in the observed wavelength frame with a spectral resolution of $R = \lambda/\Delta\lambda \approx 2000$, where $\Delta\lambda$ is the width of the spectral resolution element at wavelength λ. This corresponds to a velocity width of a spectral resolution element of $\Delta v = c \cdot \Delta\lambda/\lambda \approx 150\,\mathrm{km\,s^{-1}}$, where c is the speed of light. The SDSS composite spectra all have data from >100 SDSS spectra in each pixel at rest-frame wavelengths between 2000Å and 4000Å where we perform the spectral decomposition (§ **??**), except for Composite F which has more than 78 SDSS spectra per pixel in the region between 3875 Å and 4000 Å. This does not affect our results.

Note. — [(a)]Signal-to-noise ratio, S/N, measured in a the continuum region between 3200–3300 Å in the wavelength rest-frame as the median ratio of the flux density relative to the noise spectrum; [(b)]Rest-frame equivalent width; [(c)]Emission line shape, parameterised as FWHM/σ_{line}.; [(d)]Line dispersion of the emission line flux density, the second moment of the flux distribution, defined in Paper I; [(e)]; The Mean Absolute Deviation (MAD) from the median velocity, as defined in Paper I; [(f)]; The Inter-Percentile Velocity width of the emission line at 50% of the line flux, as defined in Paper I.

References. — (1) Stephan Frank et al. (2018, in prep.); (2) This work; (3) Schneider et al. (2010).

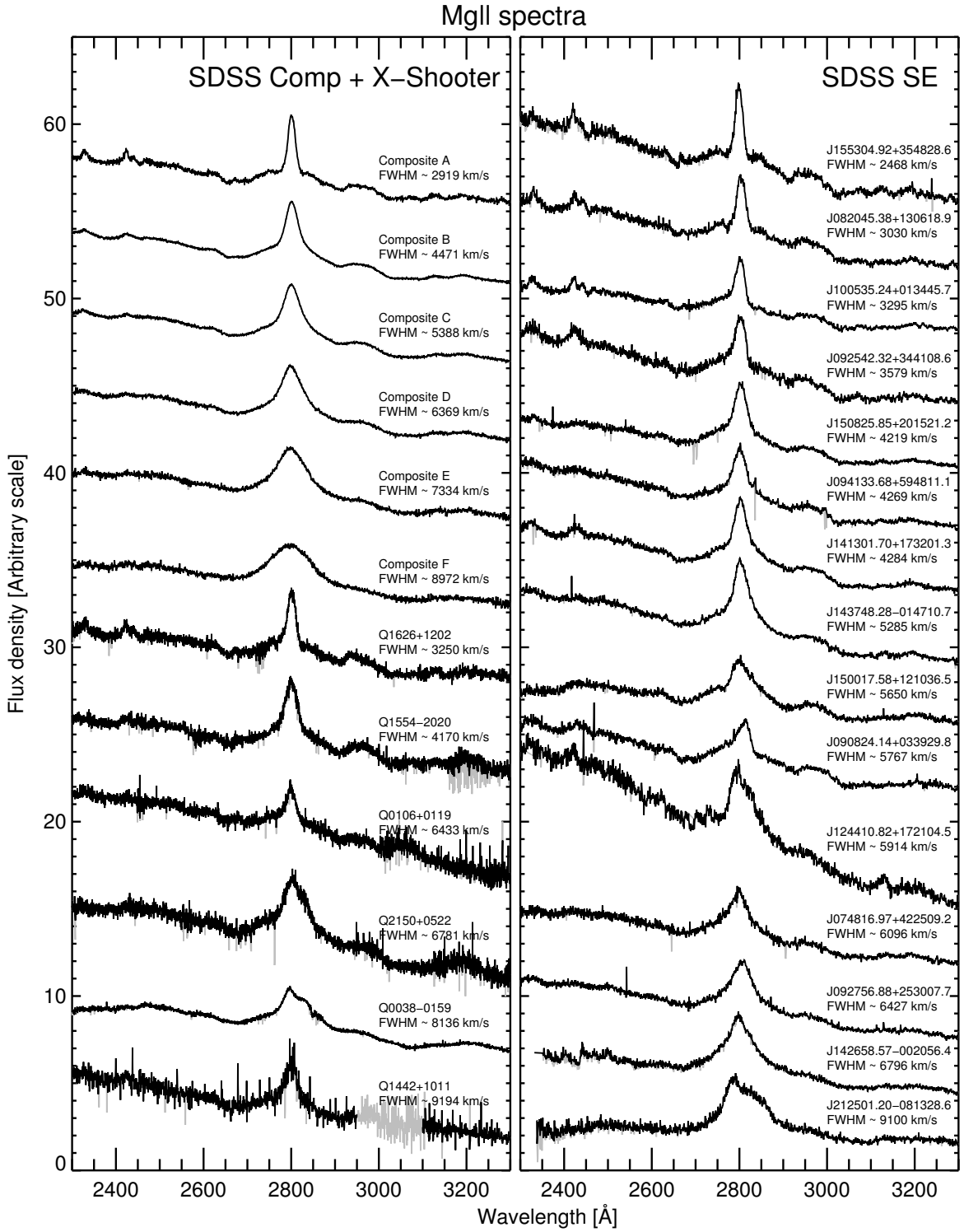

Fig. 3.1 The 27 spectra forming our sample of high S/N Mg II spectra. Only the spectral range near the Mg II emission line is shown. The spectra are shifted in the vertical direction and placed on an arbitrary flux density scale. The original spectra, including narrow absorption lines and spectral regions affected by residuals after removal of telluric lines are shown in gray. The left panel shows the SDSS Composite and X-Shooter spectra. The right panel shows the single epoch SDSS spectra.

Our sample contains 27 spectra. Six are of radio-loud quasars from Vestergaard (2003) and observed with the X-Shooter spectrograph mounted on the European Southern Observatory (ESO) Very Large Telescope (VLT) at the Paranal Observatory in Chile. The other 21 spectra are from the SDSS DR7 Quasar Catalog (Schneider et al., 2010). Fifteen of these are single-epoch spectra of individual quasars while the remaining six are composites of a larger number of AGN spectra from the SDSS DR7 quasar catalog, each binned according to the FWHM as measured by Shen et al. (2011). The composite spectra are constructed as described in Paper I. The emission line properties for our sample of high S/N Mg II spectra are summarised in Table 3.1.

We use the emission line parameters as measured by Vestergaard et al. (2008) and Shen et al. (2011) on the SDSS quasars as a guideline for the general properties of the observed AGN population. The 5% – 95% percentile ranges of the observed Mg II line parameters (Vestergaard et al., 2008; Shen et al., 2011) are: (a) FWHM: $\sim$1950 km s^{-1} to 7500 km s^{-1}; (b) EW: 19 Å to 79 Å; and (c) FWHM/σ_{line}: 1.04 to 2.78. Our sample covers the entirety of this parameter space, except for the narrowest line widths. The narrowest emission line represented in our sample has a FWHM of 2468 km s^{-1}, which is $\sim$500 km s^{-1} wider than the 5% percentile of the SDSS DR7 Quasar catalog. Still, we consider our sample to be representative of the observed Mg II emission line parameters of the general AGN population as quoted above, with the caveat that the narrowest lines are not represented.

3.4 Statistical methods and analysis

The statistical method we use is similar to that of Paper I. Here, we will briefly summarize our method and refer the reader to Paper I for details.

We wish to show the negative effects that spectral noise can have on our ability to recover the emission line parameters as intrinsically emitted by the AGN. For this purpose, we generate a sample of spectra degraded to S/N levels down to $\sim$1 pixel^{-1} for each original spectrum. We degrade the original spectrum 500 times for each target S/N level, each time using a different 'seed' to determine the Gaussian noise that we add to the original spectrum. Therefore, each spectrum at a given S/N level will have a different distribution of spectral noise, having a different effect on the measured line width parameters in each particular spectrum. This allows us to statistically assess the accuracy and precision of each line width parameter at a range of different S/N levels by comparing the line widths measured on the artificially degraded spectra with those measured on the original high S/N spectrum for a given object in our database.

As the best estimate of the line width at a given S/N level we use the mode of the distribution of the 500 line widths that we measure at that S/N level. The accuracy of the line width is then calculated as the offset between this best estimate and the line width measured on the original high S/N spectrum; the precision is measured as outlined below.

We calculate the error (i.e., precision) on the line width in the following way. The mode (i.e. the most frequent value) is used to divide the distribution into two parts. Then, 68% of the area enclosed

by each of the distributions below or above the mode, respectively, define the error bar. For a Gaussian distribution, for which the mode divides the distribution in two equal halves, this is equivalent to one standard deviation (i.e., 34.1% of the total area or 68.2% of half the area).

Ultimately, we are interested in how the accuracy and precision of the line parameter affects the accuracy and precision of the black hole mass estimates. We therefore propagate the accuracy and precision of the line width measures to the black hole mass estimates, under the assumption that only the uncertainty of the measured line widths contribute to the uncertainty of the black hole mass, using the formulas

$$\Delta\log(M_{BH}) = 2\log\left(\frac{\Delta V}{\Delta V_{int}}\right) \qquad ;accuracy \tag{3.2}$$

$$\sigma^{\pm}_{\log(M_{BH})} = \pm\log\left(1 \pm 2\frac{\sigma^{\pm}_{\Delta V}}{\Delta V}\right) \qquad ;precision \tag{3.3}$$

where $\Delta\log(M_{BH})$ is the offset in black hole mass, ΔV and ΔV_{int} are the measured and original line width, respectively, and $\sigma^{\pm}_{\Delta V}$ and $\sigma^{\pm}_{\log(M_{BH})}$ are the positive and negative uncertainty of the measured line width and black hole mass estimate, respectively.

For some of the degraded spectra, the decomposition model (§ 3.5) fails to converge. If this results in for example a negative emission line flux, the line parameters become impossible to measure. We exclude these spectra, which constitute less than 1% of the degraded sample, from our analysis. This small fraction of excluded spectra does not affect any of our conclusions.

3.5 Isolating the Mg II line

To measure the line parameters, we first need to isolate the broad emission line. This is done by a spectral decomposition method which aims at isolating the different spectral features from each other. Ideally, the spectral decomposition gives a full description of all spectral features present and is robust to varying data quality determined by the spectral S/N and resolution. Also, we require that the spectral decomposition can be done in a fully automated way such that it is feasible to implement on large datasets like the SDSS without any need for interaction, as such.

The measured accuracy and precision of the measured line width parameters can be heavily affected by the specific decomposition method chosen (e.g., Denney et al., 2009; Mejía-Restrepo et al., 2016). We do not aim at thoroughly testing different spectral decomposition methods against each other. Rather, we tested a few different approaches and choose our preferred one because it successfully models the high S/N spectra.

The spectral decomposition method we use is *local* in the sense that it only covers the rest frame wavelength range between 2000 – 4000 Å. Such a relatively long wavelength range is necessary to successfully model the underlying Fe II continuum (Vestergaard & Wilkes, 2001). The reason for not using the full observed wavelength range available in e.g. the SDSS spectra between 3800 – 9200 Å is that we wish to test a decomposition that can be used for spectra that only has local wavelength

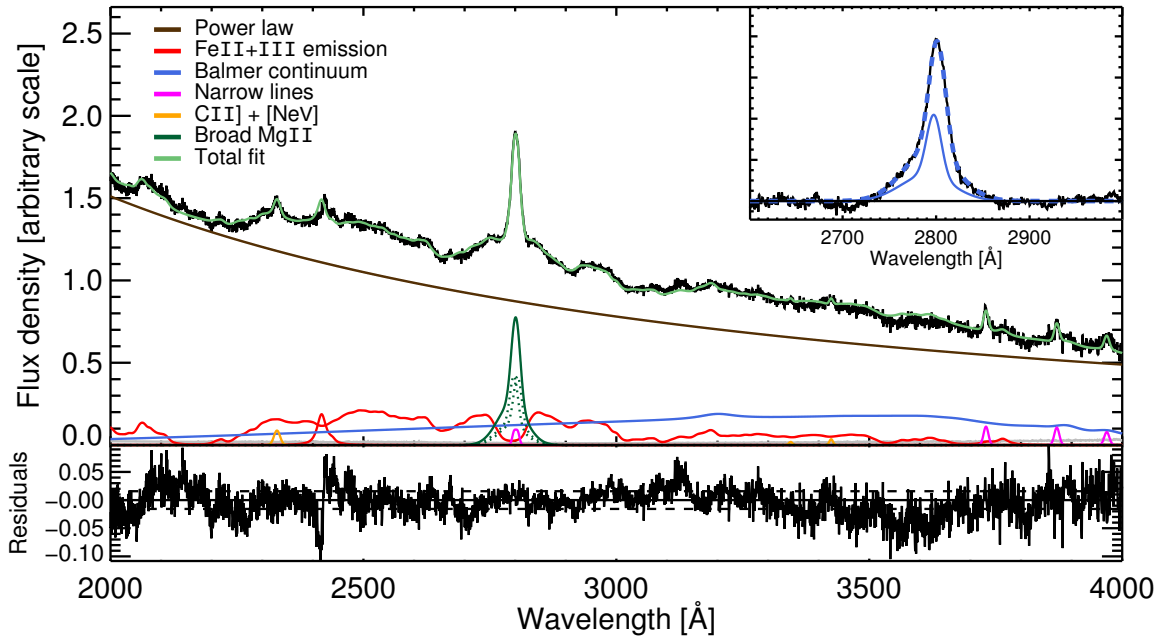

Fig. 3.2 Spectral decomposition of the SDSS Mg II Composite A spectrum with FWHM(Mg II) $\sim 2900\,\mathrm{km\,s^{-1}}$. The spectral decomposition model consists of a power-law function to account for the featureless nuclear AGN continuum (dark brown curve), a template of Balmer continuum emission (blue curve), a template of Fe II and Fe III emission (red curve), and multiple Gaussian functions to account for the individual narrow and broad emission lines (yellow, magenta, and green curves). The dashed green lines show the two individual components of the broad Mg II $\lambda\lambda$2797,2802 Å doublet. The dashed lines in the lower diagram show the rms of the flux density measured in the spectral continuum window between 3200-3300 Å. The inset in the upper right corner shows the extracted broad Mg II profile (black curve) and the full model (dashed blue curve) and one of the Mg II doublet components (solid blue curve).

coverage around the Mg II line. The spectral decomposition is used to isolate the Mg II line from the Fe II pseudocontinuum and extract the broad Mg II emission line profile, and a functional model of it. We use the functional model to test whether this approach is effective at mitigating the negative effects of spectral noise on the line parameters.

An example of the spectral decomposition is shown in Figure 3.2. It is similar to the decomposition methods used for Hβ and C IV in Paper I and consists of the following components:

1. A power-law function (dark brown curve in Figure 3.2), representing the featureless nuclear AGN continuum, defined as $F_\lambda \propto \lambda^\alpha$, where F_λ is the flux density as a function of wavelength λ and α is the power-law slope;

2. Iron emission modelled by an empirical template of UV and optical Fe II and Fe III emission extracted from high-quality HST spectra of the Seyfert 1 galaxy I Zw1 (Vestergaard & Wilkes, 2001). Longward of restframe $\sim$2200 Å, the Fe template contains Fe II emission alone and between $\sim 2000 - 2200$ Å, the template almost exclusively contains Fe III emission (see Figure 3 in Vestergaard & Wilkes, 2001). The Fe III λ2418 Å complex can be hard to model using the same scaling as for the remaining Fe III emission (see Figure 6 of Vestergaard & Wilkes, 2001), so we choose to scale this component separately. In summary, the width and strength of the three Fe emission components (Fe II longward of 2200 Å, Fe III between 2000 and 2200 Å, and a separate component for the Fe III λ2418 Å complex) are allowed to vary, but with the widths tied to each other;

3. Balmer continuum emission modelled by a synthetic spectrum as described in Dietrich et al. (2002) using the method from Grandi (1982);

4. The individual emission lines of Mg II, C II] λ2326, [Ne V] $\lambda\lambda$3345, 3425, [O II] $\lambda\lambda$3726, 3729, and [Ne III] $\lambda\lambda$3869, 3967. The [O II] and [Ne III] components are modelled by a single Gaussian each with the width and peak velocity shift tied to one another. The strength of the individual components is allowed to vary. The C II] and [Ne V] lines are modelled by a single Gaussian function each with the amplitude, width, and peak velocity shift as free parameters. The widths and peak velocity shifts, respectively, of the two [Ne V] components are tied to each other and we fix the [Ne V] λ3345 / [Ne V] λ3425 flux ratio at 0.52 (Cox, 2000). We model the Mg II $\lambda\lambda$2797,2802 emission doublet using two broad components, each consisting of two Gaussian functions (four in total), where each of the amplitudes, widths, and peak velocity shifts are tied between the two Gaussian profiles, respectively. We also model a narrow Mg II doublet, but only if the [O II] lines are present in the spectrum since these serve as a template to constrain the shape of the narrow Mg II doublet. In that case, we tie each of the widths and peak velocity shifts of the narrow Mg II doublet to those of the [O II] lines.

All spectral components are modelled simultaneously in the restframe of the quasar whose spectrum we are analyzing.

For some of the spectra, our decomposition fails to accurately model the region between 3200 Å and 3500 Å in the wavelength restframe. This is most likely due to limitations of the Fe emission template in this region and our ability to accurately constrain the Balmer continuum. Anyhow, since this spectral range is well outside the region we use for line width measurements, this has no effect on the focus of our study.

We extract the broad Mg II line profile by subtracting all other emission components, including the narrow Mg II emission if it is present, from the spectrum. The Mg II line width measured directly on the data is actually the width of the Mg II doublet as we have no possibility of disentangling the two components using only the observed data. This is the most practical approach when measuring the Mg II line width directly on the data. An example of an extracted Mg II line profile is shown in Figure 3.2 as the black curve in the inset.

We also use the model of the Mg II doublet to see if measuring on this instead of directly on the data effectively mitigates the negative effects of spectral noise[1]. The modeled Mg II doublet for the SDSS Mg II Composite A spectrum is shown as the dashed blue curve in the inset of Figure 3.2 along with one of the components shown as the solid blue curve.

3.6 Results

Here, we highlight the most important overall results of our investigation. Many more details can be found by inspecting the figures in this section and in Appendix G. The caption in Figure 3.3 give a detailed account of the content of these figures. Using the FWHM as an example, the three uppermost left panels in Figure 3.3 show the accuracy (Eqn. 3.2) of FWHM(data) grouped according to the line width [FWHM; panel (a)], strength [EW; panel (b)], and line shape [FWHM/σ_{line}; panel (c)]. The three uppermost panels on the right show the same for the precision (Eqn. 3.3) of FWHM(data). In all panels, the horizontal black line indicates the line width measured in the original spectrum (i.e. the baseline).

After extracting the emission line profile (§ 3.5), two steps remain before we can actually measure the line width: constraining the extent of the emission line in the wavelength direction by the use of line limits, and to set the zero flux density level by means of the continuum level below the line. In Paper I we investigated the use of five different line limits and three different continuum levels and their effect on the accuracy and precision of the line parameters. Here, we will use the specific line limits and continuum level that we found give the best performance for each line parameter. Details on the test of different line limits and continuum levels can be found in Paper I.

We measure the line parameters directly on the data using the same method as described in Paper I. Specifically, we measure them between line limits at a fixed distance of $\pm$18,000 km s^{-1} from the

[1] As of now, only one of the Mg II components is included in this analysis.To make a direct comparison between the line widths measured directly on the data and on a functional model, we should instead use both components for our model of the Mg II line. Currently, we are repeating the analysis using the Mg II doublet instead of just one of the Mg II components as discussed here. Our preliminary analysis shows that including both components in the model of the broad Mg II emission line has no impact on the results of this work.

line centre using the best fit continuum model, except for the FWHM, which is measured relative to the best$-1\sigma_{\rm cont}$ continuum in order to mitigate the negative effects of spectral noise. This continuum is the best fit continuum model minus an estimate of the continuum flux uncertainty - measured as the 1 sigma scatter of the observed flux density around the best fit continuum model (see Paper I for details). We also investigate whether the robustness of each line width parameter depends on the width, strength, and shape of the original emission line in question. In §3.6.5 we evaluate whether using a functional model of the line profile for the line width measurements can mitigate the adverse effects of low S/N . Similar to Paper I we propagate the accuracy and precision of each line width parameter to the final black hole mass estimate, using eqns. 3.2 and 3.3, and shown in panels (e)-(h) in Figure 3.3. Finally, we examine the robustness of different shape measures of the Mg II line in §3.6.6.

Our main result confirms what we found for Hβ and C IV in Paper I, namely that using the IPV widths is the most robust and flexible way to measure the emission line width. We now show and discuss the results for each line parameter in turn.

3.6.1 FWHM

The results for the FWHM measured directly on the data, hereafter FWHM(data) are shown in Figure 3.3. The spectral noise affects FWHM(data) in two ways. First, FWHM(data) is underestimated due to noise enhancing the measured peak flux value, thereby pulling the measured half peak flux density wavelengths closer to the line centre. As an example, the FWHM(data) is underestimated by $\sim$20% ($\sim$0.2 dex in M_{BH}) at S/N $\sim 25\,\mathrm{pixel}^{-1}$ [shaded red region in panel (a)]. This is most pronounced for broad, strong, and stubby (high FWHM/σ_{line} ratio) profiles [shaded red regions in panels (a), (b), and (c)] because the effect of peak noise is relatively larger for these lines than for more narrow and peaky lines.

Simultaneously, noise in the line wings and continuum surrounding the line will move the half peak flux density wavelengths away from the line centre such that the value of FWHM(data) is overestimated. This effect has the highest impact on broad, and weak lines [red and green regions in panels (a) and (b), respectively]. As an example, FWHM(data) gets overestimated by $\sim$200% ($\sim$0.95 dex in M_{BH}) at S/N $\sim 25\,\mathrm{pixel}^{-1}$ [red region in panel (a)]. Notice, that at the same S/N level, FWHM(data) can also be underestimated due to peak noise if the line is more strong and stubby, as mentioned above.

As the spectral noise increases to S/N $\leq 10\,\mathrm{pixel}^{-1}$, the effect of noise in the line wings completely dominates and the FWHM(data) is consistently overestimated (all values of FWHM(data) in panels (a), (b), and (c) consistently lie above the solid black line indicating the intrinsic line width). One reason that this effect dominates over that of peak noise is that by measuring FWHM(data) relative to the best$-1\sigma_{\rm cont}$ continuum model, we are able to counterbalance some of the adverse effects of noise in the line peak. In any case, the FWHM(data) measurements suffer from low accuracy ($\sim$200% or $\sim$0.95 dex in M_{BH}) at relatively high S/N levels of $\sim 25\,\mathrm{pixel}^{-1}$.

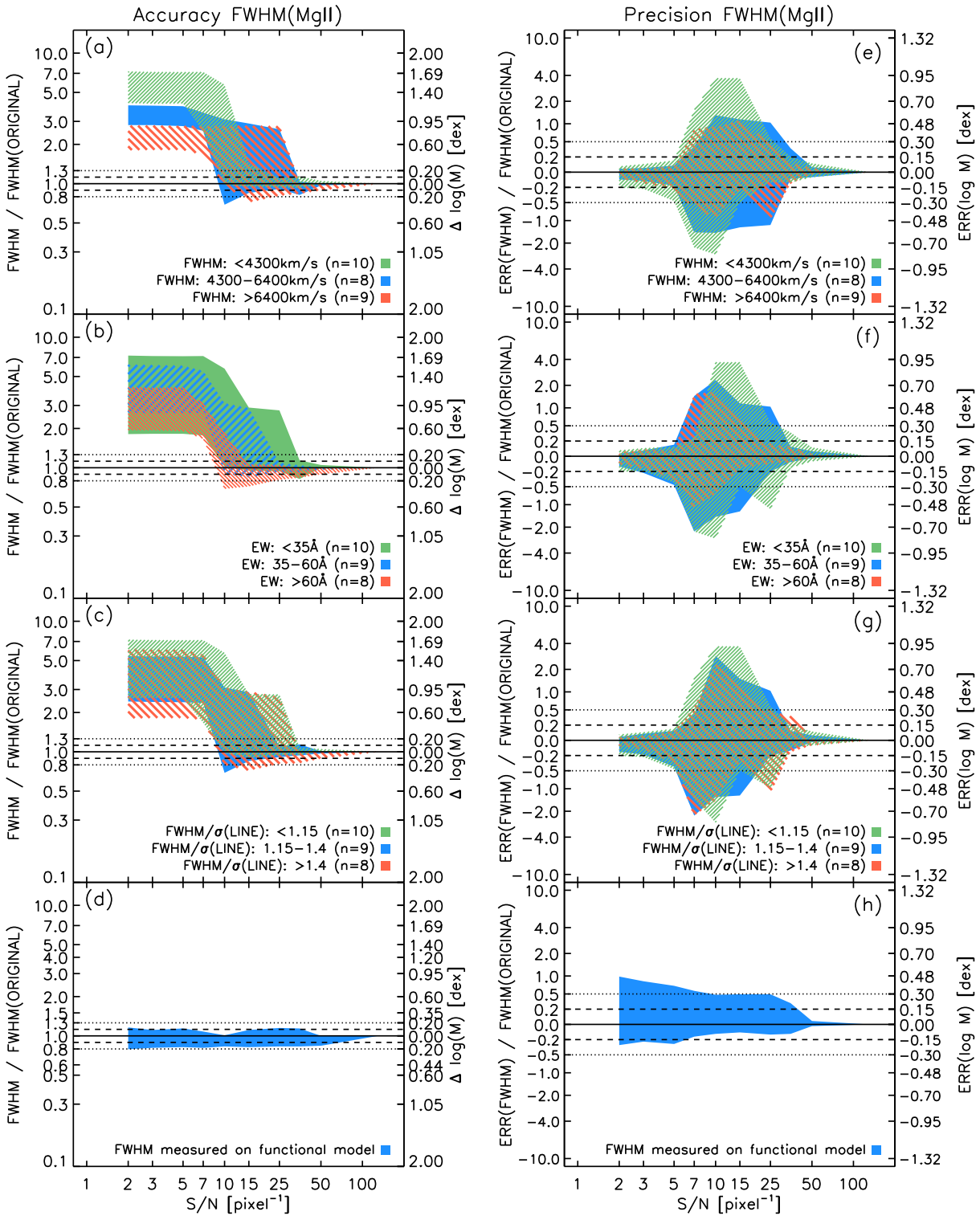

Fig. 3.3 Relative accuracy (left column) and precision (right column) of the FWHM as a function of S/N when measured on all spectra in our sample of degraded Mg II spectra. A high-accuracy line width will have FWHM/FWHM(ORIGINAL) values very close to unity for all S/N levels (i.e., exhibit a narrow band across a wide x-range at a y-value of $\sim$1.0 in the left panels). For a high-precision line width, the error relative to the line width will likewise hug the reference line at $y = 0$ across a broad range of ... (contd. next page)

(contd.) ... S/N levels in the right hand side panels. Here, the *y*-axis shows the precision with positive (negative) values representing the uncertainty towards higher (lower) FWHM values. To show how the accuracy and precision of the FWHM(data) depends on the characteristics of the emission line, we show the results grouped according to the FWHM (top row), the EW (second row), and the FWHM/σ_{line} (third row) as measured on the original high S/N Mg II spectra. The filled area for each group of spectra in each panel shows the span in accuracy (left column) and precision (right column) measured on the Mg II spectra in that group. The legend in each panel shows the grouping criteria and the number of spectra, n, in each group. The dashed and dotted horizontal lines in the left column panels mark a relative accuracy of 0.1 dex and 0.20 dex in M_{BH}, respectively, while in the right column they mark a relative precision of 0.15 dex and 0.30 dex in M_{BH}, respectively.

The precision of FWHM(data) [panels (e), (f), and (g)] decrease with S/N down to S/N $\sim 10\,\mathrm{pixel}^{-1}$ because the increased spectral noise adds scatter to the measurements. Surprisingly, the precision increases again at S/N $\leq 10\,\mathrm{pixel}^{-1}$. This is because the line limits constrain the maximum value that we can measure for FWHM(data). If we look at the accuracy in panel (a), FWHM(data) is consistently overestimated, and the measurements appears to 'flatten' out for S/N $\leq 10\,\mathrm{pixel}^{-1}$. At this point, the effect of noise in the line wings and the continuum around the line completely dominate the measurement, and FWHM(data) is measured as the largest possible value allowed between the line limits. In this case, the precision increases, but the accuracy is still very low.

The results for Mg II are very similar to those we find for Hβ and C IV in Paper I. This confirms the fact that FWHM(data) is very susceptible to spectral noise. In Paper I, we found that using FWHM(Hβ; data) and FWHM(C IV; data) to estimate black hole masses result in an accuracy within 0.2 dex at S/N levels of $\geq 25\,\mathrm{pixel}^{-1}$ and $\geq 15\,\mathrm{pixel}^{-1}$, respectively, somewhat higher accuracy than we have shown here for FWHM(Mg II; data). There are probably two reasons for the Mg II line measurements being of lower accuracy compared to Hβ and C IV. First, the Hβ lines are in general relatively stronger (i.e. have higher EW) than the Mg II lines. This means that the relative effect of the spectral noise is larger for the Mg II lines. Second, isolating the broad emission line is much more complicated for Mg II than for C IV. Several spectral components that are blended and difficult to disentangle around the Mg II line have to be modeled simultaneously, making it difficult to accurately model each individual component. In particular, the relative strengths of the nuclear power-law continuum, the Balmer template, and the strong Fe emission, respectively, below the Mg II line is difficult to constrain. This degeneracy may result in a lower accuracy of FWHM(Mg II; data) compared to FWHM(C IV; data).

3.6.2 The line dispersion

In general, the accuracy and precision of σ_{line} measured directly on the data [σ_{line}(data)] are higher than those of FWHM(data) (one can, for example, compare the span of the shaded regions in panels (a) of Figures 3.3 and 3.4, respectively). This is because σ_{line} is an integral measure of the line width and therefore less sensitive to spectral noise. As an example, the accuracy of σ_{line} is within $\sim$30%

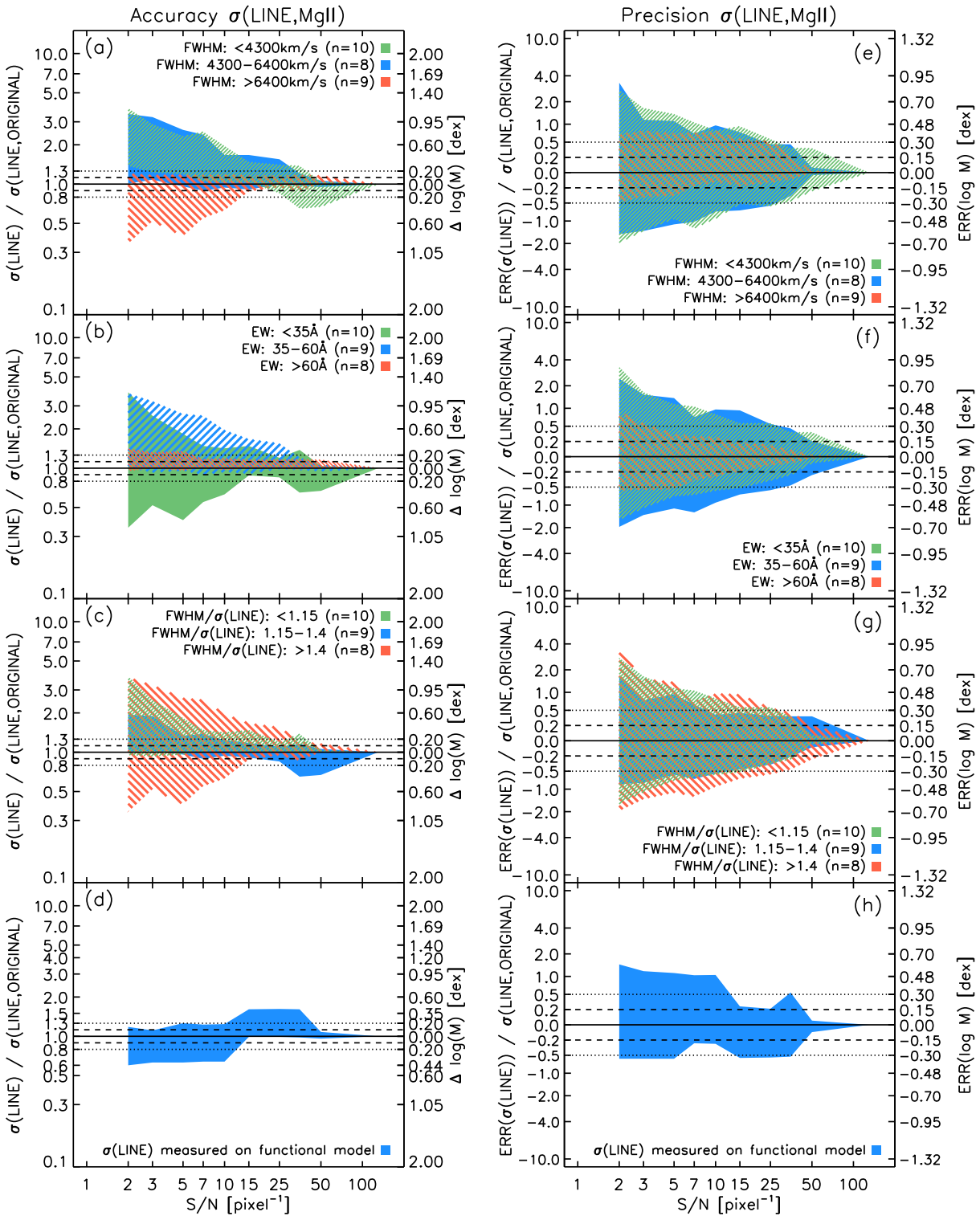

Fig. 3.4 Relative accuracy (left column) and precision (right column) of σ_{line} as a function of S/N when measured on all the spectra in our sample of degraded Mg II spectra. The figure is explained in Figure 3.3

($\sim$0.3 dex in M_{BH}) for S/N $\geq 25\,\mathrm{pixel}^{-1}$, compared to $\sim$200% ($\sim$0.95 dex in M_{BH}) for FWHM(data) at the same S/N levels if the line profile is broad and weak (i.e., the emission line has low EW).

There is a tendency for the measured value of σ_{line}(data) to be systematically overestimated at S/N $\leq 15\,\mathrm{pixel}^{-1}$ when measured on narrow and peaky lines (green shaded regions in panels (a) and (c), respectively, of Figure 3.4 systematically lie above the solid horisontal line indicating the intrinsic line width). This confirms our previous findings for Hβ and C IV (Paper I) that σ_{line}(data) is very sensitive to noise in the continuum surrounding the line and noise in the line wings. In this particular case of narrow and peaky lines with weak wings, the noise causes σ_{line}(data) to be systematically overestimated.

In summary, while we find the accuracy and precision of σ_{line}(data) to be higher than that of FWHM(data) in general, σ_{line}(data) has its own limitations. In particular, it is very sensitive to noise in the line wings and the surrounding continuum, leading to an overestimated value of σ_{line}(data). This is most pronounced for peaky and narrow lines where the line wings are weak and the spectral noise has a relatively larger effect than for more broad lines with stronger line wings. To acquire an unbiased measure of σ_{line}(data), the spectral S/N has to be larger than $15\,\mathrm{pixel}^{-1}$. At these S/N levels, the accuracy and precision of σ_{line}(data) can be expected to be within $\sim$50% ($\sim$0.35 dex in M_{BH}) and $\sim$100% ($\sim$0.48 dex in M_{BH}), respectively.

3.6.3 The mean absolute deviation from the median velocity; MAD

Figure 3.5 shows that the accuracy of the MAD line width is within 30% (0.2 dex in M_{BH}) at S/N $\geq 10\,\mathrm{pixel}^{-1}$ when measured directly on the data [MAD(data)]. In comparison, the accuracy of σ_{line}(data) is only within $\sim$70% ($\sim$0.46 dex in M_{BH}) of the true value at the same S/N levels. The higher accuracy of the MAD(data) compared to σ_{line}(data) is a direct consequence of the fact that MAD(data) does not weight the flux density in each pixel by its squared distance to the line centre, making it less susceptible to noise in the line wings than σ_{line}(data).

The precision of MAD(data) is within $\sim$70% ($\sim$0.38 dex in M_{BH}) at S/N $\geq 10\,\mathrm{pixel}^{-1}$. There is no bias associated with MAD(data) for S/N $\geq 3\,\mathrm{pixel}^{-1}$, but the accuracy and precision both decrease with the S/N level. At S/N $\sim 3\,\mathrm{pixel}^{-1}$, the accuracy and precision of MAD(data) is within 50% and 100% (0.35 and 0.70 dex in M_{BH}, respectively) of the true value. This is similar to what we found for Hβ and C IV in Paper I and confirms that MAD(data) is a more accurate and precise measure of the line width than FWHM(data) and σ_{line}(data).

In summary, the MAD(data) shows a higher accuracy than both FWHM(data) and σ_{line}(data) at any given S/N level above $3\,\mathrm{pixel}^{-1}$. Its precision is higher than that of FWHM(data) and similar to that of σ_{line}(data). Furthermore, the MAD(data) width does not show any tendency to be systematically biased at S/N levels down to $3\,\mathrm{pixel}^{-1}$, making it a very robust line width estimator compared to FWHM(data) and σ_{line}(data) (one can compare the left panels of figures 3.3 and 3.4 to the left panels of figure 3.5).

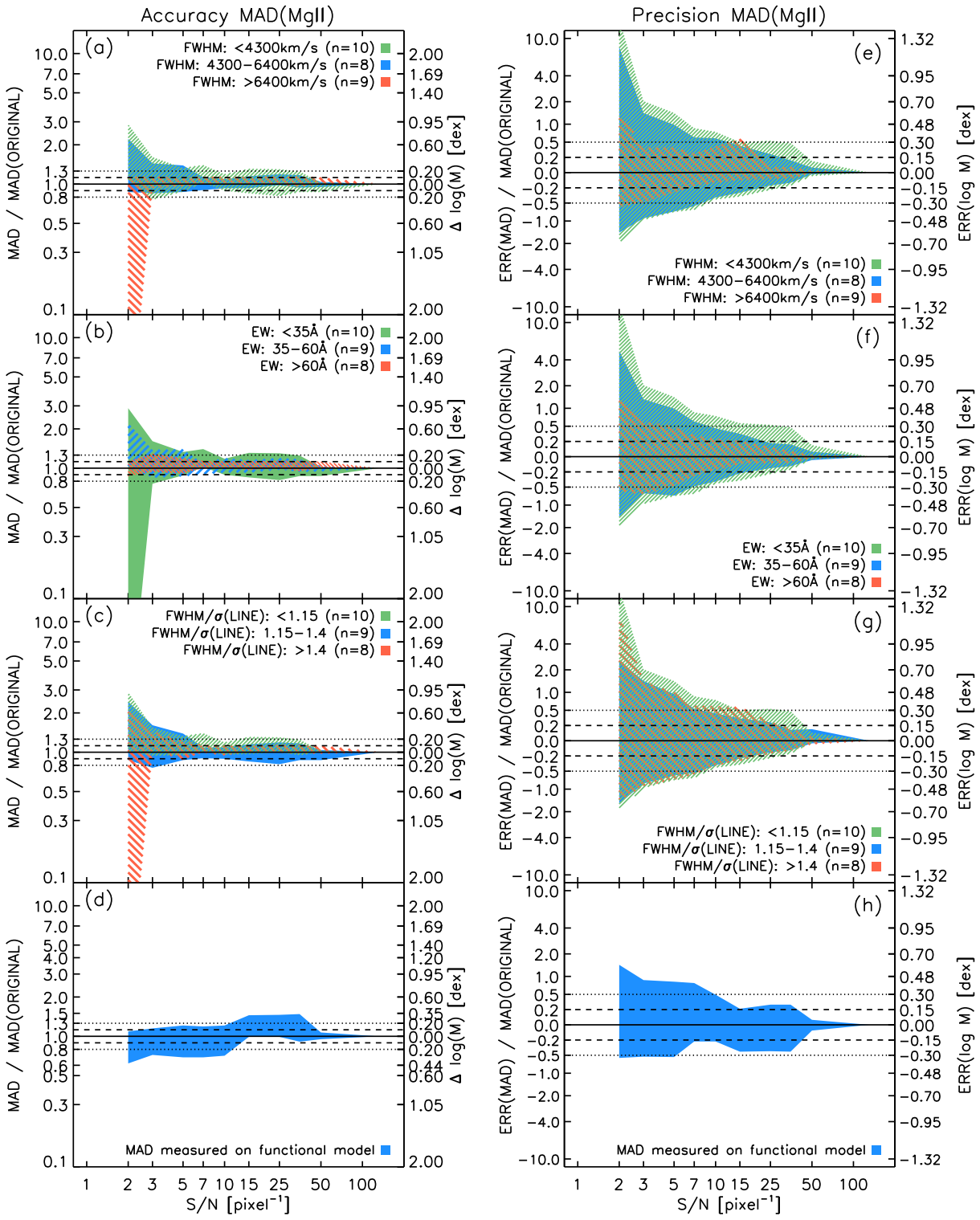

Fig. 3.5 Relative accuracy (left column) and precision (right column) of the MAD width as a function of S/N when measured on all the spectra in our sample of degraded Mg II spectra. The figure is explained in Figure 3.3

3.6.4 The IPV widths

The IPV width can be measured at any fraction of the line flux between 0% and 100%, and we have investigated a range of these values between the IPV10 and IPV90 width. We will start by discussing the IPV50 width measured directly on the data [IPV50(data)], as this IPV width is representative of all the IPV widths. After this, we address the specific performance for all the IPV widths at fractions of the line flux between 10% and 90%.

Compared to FWHM(data), σ_{line}(data), and MAD(data), the IPV50(data) width is the most accurate measure of the line width. Its accuracy stays within 15% (0.12 dex in M_{BH}) for S/N levels of $5\,\mathrm{pixel}^{-1}$ and above (see the span of the shaded regions in panel (a) of Figure 3.6). In comparison, the MAD(data) width – the second most accurate line width parameter – has an accuracy within ∼40% (∼0.3 dex in M_{BH}) for the same S/N range.

The precision of the IPV50(data) width is within 200% (0.70 dex in M_{BH}) at S/N $\geq 5\,\mathrm{pixel}^{-1}$, similar to that of σ_{line}(data) and MAD(data) (compare span of shaded regions in panel (e) of Figures 3.4 and 3.5 with the same panel in Figure 3.6). We also saw this for IPV50(Hβ; data) in Paper I. For this reason, we do not recommend to use IPV50(data) widths at S/N levels below $5\,\mathrm{pixel}^{-1}$.

The high accuracy and precision of the IPV(data) widths emerges for the same reasons as it did for the MAD(data). Namely, the IPV(data) widths are robust to spectral noise because they are integral line measures, just like σ_{line}(data) and MAD(data). In addition, the IPV widths do not weight the flux in each wavelength bin by its linear (MAD) or squared (σ_{line}) distance to the line centre, giving excessive weight to flux in the line wings. This makes the IPV widths significantly more robust to spectral noise, especially if the noise is in the line wings, and thereby more robust line width measures compared with σ_{line} and MAD(data).

Extending our analysis to IPV(data) widths at fractions of the line flux between 10 – 90% (see Figures G.1 – G.11 in Appendix G), we find that any IPV(data) width at a fraction ≥35% of the line flux show a similar or better accuracy and precision than the MAD(data) width. Specifically, the IPV widths measured at fractions of the line flux above 35% are accurate and precise, respectively, to within ∼50% and ∼200% (∼0.35 dex and ∼0.70 dex in M_{BH}) down to S/N $\sim 5\,\mathrm{pixel}^{-1}$. This high accuracy and precision for a large range of IPV(data) widths makes them a very robust and flexible way to parameterise the line width, giving them a significant advantage with respect to the FWHM(data), σ_{line}(data), and MAD(data) widths.

3.6.5 Measuring on a functional model of the Mg II line

For FWHM, both the accuracy and precision is improved significantly when measured on a functional model [FWHM(funct)] instead of directly on the data. Specifically, FWHM(funct) can be measured to an accuracy and precision to within 20% and 100% (0.19 and 0.48 dex in M_{BH}) for S/N $\geq 2\,\mathrm{pixel}^{-1}$ (see span of shaded region in panel (d) and (h) in Figure 3.3). This is a significant improvement compared to FWHM(data) where this accuracy and precision required S/N $\geq 25\,\mathrm{pixel}^{-1}$. There is no strong tendency for FWHM(funct) to be biased (the blue region in panel (d) of Figure 3.3 is almost

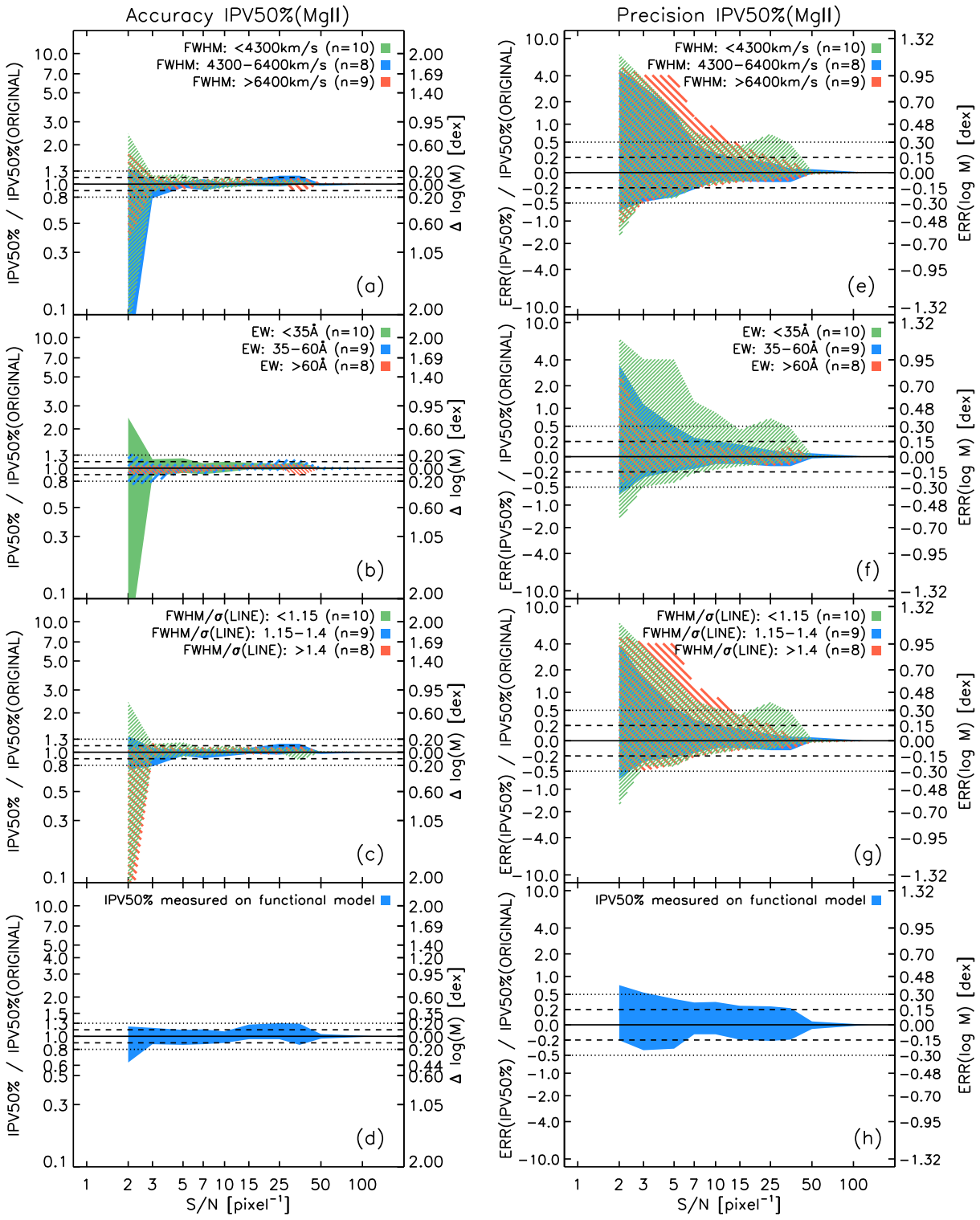

Fig. 3.6 Relative accuracy (left column) and precision (right column) of the IPV50 width as a function of S/N when measured on all the spectra in our sample of degraded Mg II spectra. The figure is explained in Figure 3.3

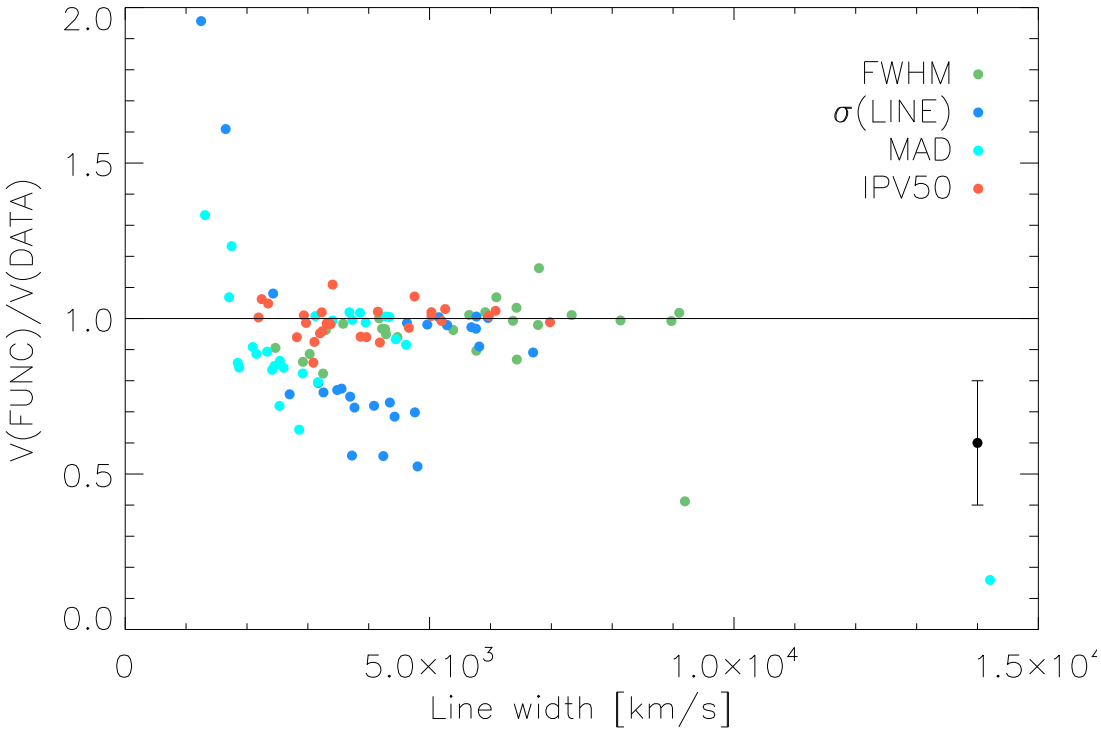

Fig. 3.7 Comparison of the line width parameters measured on a functional model with those measured directly on the data in the high S/N spectra. The typical errorbar is shown in black to the right.

symmetrical around the solid horisontal line indicating the intrinsic line width). This is similar to what we found for C IV in Paper I.

On the other hand, there is no increase in the accuracy of σ_{line}(funct) and MAD(funct) compared to σ_{line}(data) and MAD(data), respectively (compare the shaded regions in panel (d) with panel (c) in Figures 3.4 and 3.5, respectively). There is a slight increase in the precision for both σ_{line} and MAD at S/N $\leq 10\,\mathrm{pixel}^{-1}$. Specifically, the precision improves from $\sim$100% to $\sim$50% for σ_{line}(funct) and MAD(funct) compared to σ_{line}(data) and MAD(data).

For the IPV widths, there is an increase in accuracy at S/N $\leq 3\,\mathrm{pixel}^{-1}$, similar to what we found in Paper I for Hβ and C IV. There is also an increase in precision if S/N $< 10\,\mathrm{pixel}^{-1}$ for the IPV widths. Specifically, the precision of the IPV50 width improves from 100% to $\sim$30% at S/N $\sim 7\,\mathrm{pixel}^{-1}$ when using a functional model instead of measuring directly on the data.

While there is some increase in the accuracy or precision or both for S/N levels below $10\,\mathrm{pixel}^{-1}$ for all four line parameters, we still need to consider whether measuring on a functional model introduces other sources of uncertainty into the black hole mass estimates. In particular, even in the high S/N spectra, there is not necessarily a 1:1 relationship between the directly measured line widths and those measured on a functional model. To quantify this difference, we compare the line widths

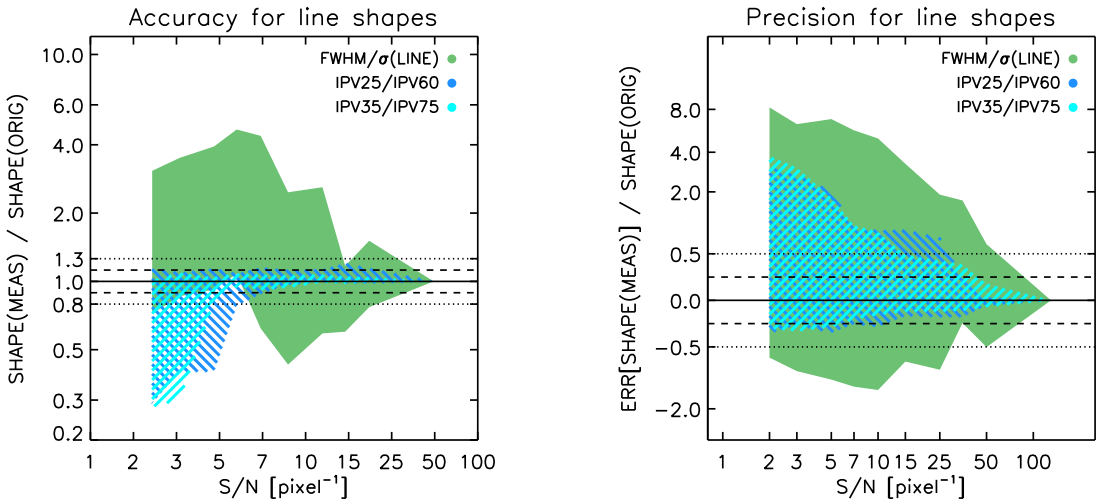

Fig. 3.8 Relative accuracy (left column) and precision (right column) of the FWHM/σ_{line}, IPV25/IPV60, and IPV35/IPV75 ratios measured directly on the data.

measured directly on the original high S/N spectra with those measured on a functional model of the Mg II line in the same spectra (see Figure 3.7). For the FWHM, σ_{line}, and MAD measured directly on the data, we find an offset from those measured on a functional model of 2.2%, 20.7%, and 9.2% (0.02 dex, 0.20 dex, and 0.08 dex in M_{BH}), respectively, with a scatter thereto of 12.9%, 31.5%, and 20.2% (0.09 dex, 0.21 dex, and 0.15 dex in M_{BH}), respectively. The corresponding numbers for the IPV20, IPV50, and IPV90 widths are 1.4%, 0.8%, and 1.8% (0.01 dex, 0.01 dex, and 0.01 dex in M_{BH}), respectively, with a scatter thereto of 10.9%, 5.2%, and 6.0% (0.09 dex, 0.04 dex, and 0.05 dex in M_{BH}), respectively. The offsets can be calibrated, but the scatter remains and adds to the final uncertainty on the black hole mass estimates. In this respect, the largest scatter is added to the mass estimated based on σ_{line}(funct) or the MAD(funct) width.

Taking this into account, we only recommend to measure either the FWHM on a functional model if S/N $< 25\,\mathrm{pixel}^{-1}$ or the IPV width on a functional model if S/N $\leq 3\,\mathrm{pixel}^{-1}$. We advice against using a functional model to measure σ_{line} and MAD as this adds additional scatter to the mass estimates of at least 0.15 dex.

3.6.6 Ratios of IPV widths are the most robust line shape measures

As shown by Collin et al. (2006), Denney (2012) and Yong et al. (2016), accurately correcting for the line shape, traditionally parameterised by the FWHM/σ_{line} ratio, could be important for an accurate calibration of the black hole mass estimate. Motivated by the high accuracy and precision of the IPV(data) widths, we compare the accuracy and precision of the FWHM(data)/σ_{line}(data) ratio with that of different ratios of IPV(data) widths. We did a similar comparison for the Hβ and C IV lines in Paper I.

Figure 3.8 clearly shows that the IPV20/IPV60 and IPV35/IPV75 ratios have a much higher accuracy and precision than the FWHM(data)/σ_{line}(data) ratio (compare the blue regions with the green region in left and right panel). Compared to the true value, the IPV(data) ratios have an accuracy and precision within 20% and ∼80% (0.2 and 0.45 dex in M_{BH}, respectively) for S/N ≥ 7 pixel^{-1}. The corresponding numbers for the FWHM(data)/σ_{line}(data) ratio is 400% and 600% (1.4 and 1.11 dex in M_{BH}, respectively) at the same S/N levels.

The high accuracy and precision of the IPV(data) widths at fractions of the line flux of 35% and above offers a wide range of combinations to parameterise the line shape robustly and with great flexibility. This is in contrast to the FWHM(data)/σ_{line}(data) ratio which suffers from low accuracy and precision. In addition, FWHM/σ_{line} offers no flexibility in parameterising the line shape.

3.7 Discussion

In our current study we have investigated the accuracy and precision of the line parameters measured on the broad Mg II emission line as a function of spectral S/N . Here, we will compare the performance of the line parameters (§ 3.7.1) and discuss the implications our results (§ 3.7.2).

3.7.1 Comparison of the line parameters

Generally, our results confirm the overall results we found for C IV and Hβ in Paper I. Also for the Mg II emission line are the IPV widths the most robust line width estimators with increasing spectral noise. The MAD can provide a similar accuracy and precision at most S/N levels, but it does not offer the option of measuring the line width at different levels of the line flux or the possibility to measure the line shape.

The FWHM (§ 3.6.1) is very susceptible to noise, both in the line peak where it leads to an underestimated value of the measured FWHM and in the line wings where it overestimates the FWHM. This means that the FWHM measured on spectra with S/N lower than 25 pixel^{-1} can be fairly inaccurate. Specifically, we find that already at S/N ~ 25 pixel^{-1}, the FWHM can suffer from an accuracy as low as 200% or 0.95 dex in the black hole mass. The accuracy of the measured FWHM value is lowest for broad and weak (i.e., low equivalent width) lines where the effect of noise in the line wings is largest. These results confirm and mirror our results for the Hβ and C IV line in Paper I.

The line dispersion (§ 3.6.2) shows a higher accuracy and precision than the FWHM, owing to the fact that it is an integral measure of the line width and therefore less susceptible to noise spikes in the spectrum. We find that σ_{line} is unbiased down to S/N levels similar to 15 pixel^{-1} with an accuracy and precision within 0.35 dex and 0.48 dex, respectively, for the resulting mass estimate. On the other hand, σ_{line} weights the flux in each pixel by the square of its distance to the line centre, making it very susceptible to noise in the line wings. As a consequence, σ_{line} is biased towards too high values for S/N ≤ 10 pixel^{-1}. This corroborates our results from Paper I for Hβ and C IV, namely that while σ_{line} in general offers higher accuracy and precision than FWHM, it is so susceptible to noise in especially

the line wings that it is unreliable for S/N levels below approximately $10\,\mathrm{pixel}^{-1}$ with an accuracy within $\sim$0.6 dex in the black hole mass.

Overall, the MAD (§ 3.6.3) shows the same behavior towards spectral noise as σ_{line}, but with a higher accuracy and precision. This is a simple consequence of the fact that the MAD does not excessively weight flux in the wings of the line. Therefore, the MAD is unbiased down to S/N levels of approximately $3\,\mathrm{pixel}^{-1}$. While still unbiased at such low S/N levels, there is a penalty in the form of low accuracy and precision for the MAD as the spectral noise increases. Specifically, while the accuracy of the MAD is within 0.2 dex in the mass estimate for $\mathrm{S/N} \geq 10\,\mathrm{pixel}^{-1}$, it can be as low as $\sim$0.5 dex for $\mathrm{S/N} \sim 3\,\mathrm{pixel}^{-1}$.

The IPV widths (§ 3.6.4) provide the highest accuracy and precision of all the line parameters investigated here. Specifically, any IPV widths measured at a percentage of the line flux of 35% or higher shows an accuracy and precision that is equivalent to, or better, than that of the MAD. Mass estimates based on IPV widths can be expected to be unbiased and to have an accuracy and precision within 0.35 and 0.7 dex, respectively, if $\mathrm{S/N} \geq 5\,\mathrm{pixel}^{-1}$. For $\mathrm{S/N} \sim 15\,\mathrm{pixel}^{-1}$, the IPV widths result in mass estimates with an accuracya and precision within 0.1–0.15 and 0.5 dex, respectively.

Another way to compare the four different line parameters is to see what S/N level that is required to obtain a mass estimate with an accuracy equal to or better than 0.1 dex. This is important to know when preparing studies aimed at measuring high accuracy black hole masses. Although 0.1 dex is a somewhat arbitrary choice, it represents a significant reduction of the current uncertainties in the mass estimates when calculating them from the commonly used FWHM and σ_{line} widths. The FWHM, σ_{line}, and MAD widths all require a S/N of at least $50\,\mathrm{pixel}^{-1}$ to facilitate a mass estimate with an accuracy of 0.1 dex or better. In fact, for σ_{line}, the accuracy of the mass estimate can be as low as $\sim$0.3-0.4 dex at $\mathrm{S/N} \sim 50\,\mathrm{pixel}^{-1}$ (see shaded areas in panel (a) of Figure 3.4). In stark contrast to this, the IPV widths provide mass estimates within $\sim$0.03 dex if $\mathrm{S/N} \sim 50\,\mathrm{pixel}^{-1}$. In fact, mass estimates based on the IPV widths can be expected to have an accuracy within 0.1 dex all the way down to $\mathrm{S/N} \sim 15\,\mathrm{pixel}^{-1}$. For these reasons, we consider the IPV widths the clear winner as the most robust of these line parameters.

We also compare ratios of IPV widths, specifically the IPV20/IPV60 and IPV35/IPV75 ratios, to the more traditionally used FWHM/σ_{line} ratio (§ 3.6.6) as a measure of the line shape (§ 3.6.6). We find that ratios of IPV widths offer a significantly higher accuracy and precision than the FWHM/σ_{line} ratio, and that this result can be achieved for a large range of IPV ratios. This is one more reason that we prefer the IPV line parameter.

Functional models

We also investigate the common assumption that one can effectively mitigate the adverse effects of spectral noise by measuring the line widths on a functional model of the line profile instead of directly on the data (§ 3.6.5). We only recommend this approach on the FWHM if $\mathrm{S/N} < 25\,\mathrm{pixel}^{-1}$ and on the IPV widths if $\mathrm{S/N} \leq 3\,\mathrm{pixel}^{-1}$, since there is no significant improvement in the accuracy and

precision of the σ_{line} or MAD widths by using this method. Another complication is that this method induces additional scatter in the mass estimates compared to measuring the line widths directly in the data. This is because not even in the original high S/N spectra do the line parameters measured on a functional model of the broad emission line correspond to those measured directly on the data. The scatter induced from this fact amount to somewhere between 0.21 dex in the mass estimate for σ_{line} to 0.04 dex in the mass estimate for the IPV50 width. In our analysis of the Hβ and C IV emission lines (in Paper I) we find a similar level of penalty when measuring the line parameters on a functional model instead of directly on the data.

3.7.2 Implications

Our results have consequences for the optimal line measurement to use when estimating black hole masses in AGN. This is true for the strategy one should use when analysing existing data, but also for that applied when acquiring new data for this purpose.

First of all, our results can be used as a way to assess the errors of mass estimates in a uniform way across different studies. This applies both to reverberation mapping studies and those based on single-epoch mass estimates. In fact, it applies to any study aimed at measuring broad-emission line widths in source spectra. For reverberation mapping specifically, this also means that when planning future observing campaigns, the aim should be to have data of such a high quality that a rms spectrum with a S/N of 50 pixel^{-1} can be constructed. This means obtaining a large number of spectra, but also a bit of luck in order to sample a large enough variability amplitude that the amplitude in the rms spectrum is large enough to obtain a sufficiently high S/N . This is the only way to ensure that all the line width parameters can be measured to such a high fidelity that the mass estimates are accurate within 0.1 dex based on the line measurements alone. As already discussed in Paper I, the mean spectra from reverberation mapping typically has S/N ≥ 50 pixel^{-1} such that the resulting mass estimates will have a high accuracy and precision as quoted above. On the other hand, the S/N in the rms spectra can be as low as S/N ~ 20 pixel^{-1} in which case the accuracy of the mass estimate can be 0.2 dex or worse if using the FWHM and 0.4 dex or worse if using σ_{line}.

When dealing with existing survey data, there can be a significant advantage of using the IPV widths instead of the more commonly used FWHM or σ_{line} widths. Such data are often used for single-epoch mass estimates due to the convenience of having a plethora of spectra readily available for measurements. But, most of these spectra have relatively low S/N due to the way the surveys are designed. As an example, lowering the S/N cut from 15 pixel^{-1} (above which σ_{line} is unbiased) to S/N ~ 3 pixel^{-1} (above which the MAD and IPV widths are unbiased), the amount of spectra in the SDSS Data Release 7 Quasar Catalog (Schneider et al., 2010) that can be included in the analysis is increased by a factor of more than five (from $\sim$2,100 to $\sim$11,700 spectra; Paper I). This represents a significant increase in the amount of spectra for which an unbiased mass estimate can be made, simply by using the MAD or IPV widths instead of the FWHM or σ_{line}, with the caveat that the precision is lowered to $\sim$1.0 dex in the mass estimate.

There is an ongoing debate as to the reliability of the Mg II line as a virial mass estimator, based on comparisons with Hβ mass estimates. For example, Onken & Kollmeier (2008) find an Eddington ratio bias when comparing Hβ and Mg II mass estimates from a sample of AGN spectra in the SDSS that covers both the Hβ and Mg II line. On the other hand, Rafiee & Hall (2011) argue that the Mg II line can be an unbiased estimator of the black hole mass, but that this depends on the actual way the line width is measured. One underlying assumption for most of these studies is that masses based on Hβ are the most correct. While this might be true, it is also true that a lot of trust is put in Hβ masses simply because this is the most intensively monitored line in reverberation mapping campaigns. In comparison, only a few attempts have been made at reverberation mapping for the Mg II line (e.g., Metzroth et al., 2006; Cackett et al., 2015; Shen et al., 2016). This means that there is no radius-luminosity relationship established for Mg II, and consequently, the Mg II mass estimates are calibrated to Hβ which adds some uncertainty because it is not clear that the Mg II emission line is emitted from the same radial distance as Hβ (Metzroth et al., 2006; Cackett et al., 2015). Furthermore, the Mg II line has a low responsivity which makes it difficult to use for reverberation mapping (e.g. Goad et al., 1993, Lawther et al. 2018 in prep.). While many issues remain open regarding Mg II mass estimates, one way to move forward is to be able to compare different studies on a par. Adopting a uniform way to measure the line widths and to assess their errors based on the results in this study will present a significant step forward on this endeavor (see also, e.g. Vestergaard et al., 2011).

The spectral decomposition of the Mg II line is always difficult as it is heavily blended with a pseudo continuum of Fe emission superimposed on the nuclear continuum emission, the Balmer continuum emission, and emission from other spectral lines. Our spectral decomposition method applied here appears to be relatively robust, judging from the fact that some of the line parameters can be measured to a high accuracy and precision down to S/N levels similar to 5 pixel^{-1}. But, we do in general find a lower accuracy of the line width parameters when compared with the results obtained for C IV in Paper I. This is most likely a consequence of the fact that the nuclear continuum is much better constrained in the spectral region around C IV for which there is less line blending compared to the spectral region around Mg II (e.g., Vestergaard & Wilkes, 2001). One way to deal with this issue is to obtain as high S/N data as possible, as already advocated in order to increase the reliability of the line width measures. Furthermore, the Fe emission covers a very wide wavelength range all the way from the C IV line at 1549 Å and up to $\sim$6000 Å. Therefore, as large a wavelength coverage as possible is desirable in order to be able to anchor the nuclear continuum properly. There is also ample evidence that the spectral decomposition method adopted can have a large effect on the measured line parameters (e.g., Denney et al., 2009; Fine et al., 2010; Rafiee & Hall, 2011; Vestergaard et al., 2011; Mejía-Restrepo et al., 2016). Therefore, we advise to adopt the spectral decomposition method presented in this study consistently across studies to make results easier to compare on a par.

3.8 Summary and conclusions

Accurate measurements of black hole masses in AGN are important for our understanding of AGN physics and the impact of the AGN on its surroundings. Currently, the limiting factor in improving the accuracy of such mass estimates is the accuracy and precision to which we can actually measure broad emission line widths in AGN spectra as shown in this work and Paper I. In this work, we have investigated the robustness with respect to spectral noise (S/N) of four different line width parameters, commonly used in the literature for black hole mass estimates, measured for the Mg II emission line in AGN spectra. We do this by comparing line widths measured in high S/N spectra with line widths measured in artificially degraded versions of the same spectra. We use a statistical approach where each original high S/N spectrum is degraded to a range of S/N levels, 500 times at each S/N level, each time using a different *seed* for the random noise distribution. This allows us to use the median and 1-σ scatter of the line width distribution at a given S/N level as a measure of the accuracy and precision, respectively, of the line width measure at that particular S/N level. We investigate four line width parameters, namely: the FWHM, the line dispersion (σ_{line}), the Mean Absolute Deviation from the median velocity (MAD), and the Inter-Percentile Velocity (IPV) widths. We focus on the line parameters measured directly on the data, but we also test the assumption that measuring the parameters on a functional model is an effective way to mitigate the adverse effects of spectral noise, as is often assumed. Our main conclusions are the following:

1. The FWHM (§ 3.6.1) measured from the peak line flux density suffers from noise in both the line peak and the line wings, leading to under- and overestimated values, respectively, of the measured FWHM. For example, we find that the FWHM can be overestimated by as much as $\sim$200% (corresponding to 0.95 dex in the black hole mass) already at a high S/N $\sim 25\,\mathrm{pixel}^{-1}$. At the same S/N level, the precision can be as low as $\sim$100% ($\sim$0.5 dex in M_{BH}). For this reason, we strongly advice against measuring the FWHM on data with S/N $< 25\,\mathrm{pixel}^{-1}$.

2. The line dispersion (σ_{line}, § 3.6.2)is more robust to increasing spectral noise than the FHWM. But, since it weights the flux density in each pixel by the square of its distance to the line centre, the σ_{line} is still very susceptible to noise in the wings of the emission line profile. As a result, σ_{line} tends to be systematically overestimated for narrow and peaky lines for spectral S/N $< 15\,\mathrm{pixel}^{-1}$. At this S/N level, σ_{line} has an accuracy and precision, respectively, within $\sim$50% and $\sim$100% ($\sim$0.35 and $\sim$0.48 dex in M_{BH}).

3. The MAD (§ 3.6.3) and IPV widths (§ 3.6.4) are more robust to spectral noise than the FWHM and σ_{line}. The reason is that the MAD does not weight the flux density in each pixel excessively by the square of its distance to the line centre, as σ_{line} does, and that the IPV widths make no such weighing of the flux density at all. As a consequence, the MAD and IPV widths measured at percentages above 35% are unbiased all the way down to S/N $\sim 3\,\mathrm{pixel}^{-1}$. Mass estimates based on the MAD are accurate and precise, respectively, within $\sim$0.3 and $\sim$0.6 dex if S/N $\geq 5\,\mathrm{pixel}^{-1}$. For the IPV widths at 35% or more of the line flux, the corresponding

accuracy and precision is ∼0.35 and ∼0.7 dex, respectively. The IPV50 width results in an accuracy of 0.12 dex or better in the mass estimate if the S/N is 5 pixel^{-1} or higher.

4. We find that in order to achieve a black hole mass estimate with an accuracy of 0.1 dex or better, based on the line measurements alone, the S/N level has to be 50 pixel^{-1} or higher for the FWHM, σ_{line}, and the MAD. In comparison, the IPV widths only require S/N of 15 pixel^{-1} or higher for the same accuracy. This makes the IPV widths a significantly more accurate line measure to use for mass estimates than the other line parameters we have investigated.

5. We find ratios of IPV widths to be a superior measure of the line shape compared to the more traditionally used FWHM/σ_{line} ratio. Specifically, we find that the IPV20/IPV60 and IPV35/IPV75 ratios have an accuracy and precision, respectively, within 20% and 80% for S/N ≥ 7 pixel^{-1} compared to 400% and 600%, respectively, for the FWHM/σ_{line} ratio at the same S/N levels.

6. We do not recommend to measure the line parameters on a functional model instead of directly on the data except in the case of measuring FWHM for S/N ≤ 25 pixel^{-1} or on the IPV widths if S/N ≤ 3 pixel^{-1}. We find no significant improvement in using this method for σ_{line} or the MAD. In addition, we find that this method introduces additional scatter in the mass estimates of up to ∼0.2 dex because even in the high S/N spectra, line widths measured on a functional model not are equal to those measured directly on the data.

Our results for the Mg II line in this work confirm our results obtained for the Hβ and C IV lines in Paper I, and can be used to assess realistic errors for existing data and to plan future observations in the most optimal way. Specifically, we show that the IPV widths measured directly on the data are the most robust and flexible line parameters. As a consequence, the mass scaling relations should be re-calibrated based on IPV widths. This work is the subject of a forthcoming paper (Vestergaard et al., 2018, in preparation). In addition, comparative studies of mass estimates based on for example Hβ and Mg II should be repeated using these new mass calibrations based on the IPV widths. We remind the reader that the final uncertainty on the mass estimates is a combination of the squared sum of the accuracy and precision as presented in this study as well as the statistical uncertainty from the calibration of the mass scale.

Acknowledgements

We wish to thank Stephan Frank for contributing with the high S/N SDSS composite spectra of the Mg II emission line and Sandra Raimundo for help with processing of the X-Shooter spectra. JJJ gratefully acknowledges support from the Dark Cosmology Centre. MV gratefully acknowledges support from the Danish Council for Independent Research via grant no. DFF 4002-00275 during the preparations of this work.

Chapter 4

Effects of narrow absorption on the C IV line width measures

This chapter contains the paper:

A large statistical study to investigate a robust method to characterize the velocity field of the broad-line region in Active Galactic Nuclei III: The effects of narrow absorption lines

Jensen, J.J., Vestergaard, M., to be submitted to MNRAS

4.1 Abstract

Narrow absorption features blueshifted from the broad C IV emission line are common in spectra of Active Galactic Nuclei (AGN) and can affect the accuracy of black hole mass estimates based on measurements of the broad C IV emission line width. We quantify these negative effects for four different line parameters used for black hole mass estimates in AGN. We investigate nine types of narrow absorption features and use a Monte Carlo approach to statistically quantify their negative effects on each of the line parameters as a function of spectral noise down to S/N $\sim 1\,\mathrm{pixel}^{-1}$. We find that the measured value of all four line parameters is adversely affected by the narrow absorption features. The effect is strongest for the line dispersion (σ_{line}), leading to biases up to $>70\%$ for S/N $\sim 25\,\mathrm{pixel}^{-1}$ (when measured in the continuum). For all the line parameters, the negative effect of the absorption increase with its strength. The Full Width at Half Maximum (FWHM) is mostly affected by absorption in the peak of the emission line, while σ_{line} and the Mean Absolute Deviation (MAD) relative to the median velocity are mostly affected by absorption in the wing of the emission line. Our results show that S/N $\geq 25\,\mathrm{pixel}^{-1}$ and a spectral resolution of $100\,\mathrm{km\,s}^{-1}$ or better is needed to identify and correct for the weak narrow absorption lines investigated here such that their negative effect on the measured line parameters is minimized.

4.2 Introduction

Supermassive black holes are observed to be present in most, if not all, massive galaxies (Kormendy & Richstone, 1995; Magorrian et al., 1998; Kormendy & Gebhardt, 2001) and their mass is observed to correlate with properties of the host galaxy bulge both in quiescent (e.g., Magorrian et al., 1998; Wandel, 1999a; Ferrarese & Merritt, 2000a; Ferrarese et al., 2001; Gebhardt et al., 2000a,b; Graham et al., 2001; Graham & Driver, 2007; McLure & Dunlop, 2001; Tremaine et al., 2002; Marconi & Hunt, 2003a; Nelson et al., 2004; Onken et al., 2004; Bentz et al., 2009a; Gültekin et al., 2009; Savorgnan et al., 2013) and active galaxies (e.g., Wandel, 1999a; Ferrarese et al., 2001; McLure & Dunlop, 2001; Nelson et al., 2004; Onken et al., 2004; Bentz et al., 2009a). This indicates that the supermassive black hole and its host galaxy might co-evolve. This has led to the idea of black hole feedback that can regulate the star formation in the host galaxy by triggering it through shocks or by depleting the galaxy of its reservoir of cold gas, ultimately halting star formation and black hole growth alike. Although simulations (e.g., Di Matteo et al., 2005, 2008; Hopkins & Quataert, 2010; King & Pounds, 2015) and observations (e.g., McNamara & Nulsen, 2012; Tombesi et al., 2015; Aalto et al., 2016; García-Burillo et al., 2016; Wylezalek & Zakamska, 2016) of AGN feedback supports this picture, the exact strength and nature of the different feedback mechanisms are currently not well established. To understand these mechanisms, we first need a better understanding of the physics that drives the black hole growth and AGN luminosity. The main physical parameter governing the accretion and luminosity of the AGN, and thereby the possible AGN feedback, is the mass of the central black hole. Accurately measuring masses of supermassive black holes in AGN is therefore crucial for our understanding of the physics of AGN and its role in galaxy formation and evolution.

To address the issue of the accuracy of mass determinations, we have initiated a large statistical study to quantify some of the uncertainties related to black hole mass measurements in AGN (Jensen & Vestergaard 2018a, 2018b; hereafter Paper I and II). In the following, we give an overview of those studies and their relevance for this study where we tackle the specific issue of narrow absorption lines and how they affect the mass measurements. The following section provides an overview of how the black hole mass is measured in AGN and the limitations of these procedures (§ 4.2.1). After this, we introduce the specific issue of measuring broad emission line widths in AGN spectra and the most important results from our previous work in Paper I and II in § 4.2.2. Finally, in § 4.2.3, we introduce the narrow absorption lines that are the subject of this work.

4.2.1 Measurements of black hole masses in AGN

A characteristic of type 1 AGN spectra is the broad emission lines originating from a dense gaseous region appropriately named the Broad Line Region (BLR). By assuming that the gas in the BLR is virialized (an assumption supported by observations in those cases where it can be tested (Peterson & Wandel, 1999, 2000; Onken & Peterson, 2002; Peterson et al., 2004)), the black hole mass can be calculated according to the formula

$$M = f\frac{\Delta V^2 R}{G} \tag{4.1}$$

where M is the virial mass, ΔV is the gas velocity of the BLR, R is the distance from the black hole to the BLR gas, G is the gravitational constant, and f is a factor of order unity accounting for our ignorance about the inclination, geometry, and structure of the broad line region (Onken et al., 2004; Collin et al., 2006; Woo et al., 2010; Graham et al., 2011; Park et al., 2012; Grier et al., 2013). The two most common methods used to estimate black hole masses in AGN are: 1) Reverberation mapping (Blandford & McKee, 1982; Peterson, 1993), primarily used for nearby sources, and 2) single-epoch mass scaling relations (e.g., McLure & Jarvis, 2002; Vestergaard, 2002; McLure & Dunlop, 2004; Greene & Ho, 2005b; Kollmeier et al., 2006; Vestergaard & Peterson, 2006; McGill et al., 2008; Vestergaard & Osmer, 2009; Shen & Liu, 2012; Park et al., 2017) that are more easily applicable to high redshift sources.

When measuring black hole masses using reverberation mapping, ΔV is measured as the width of the broad emission lines in the RMS spectrum (i.e., the variable part of the spectrum, see e.g., Peterson, 1993). The distance to the variable gas R is measured by the observed time lag between the driving continuum emission from the accretion disk and the responding gas in the BLR.

The method of single-epoch mass estimates is based on a single spectrum that provides a snapshot of the emission spectrum at the observed epoch. Whilst there is no information of R in individual spectra, this can be estimated from the continuum luminosity measured in the spectrum. In this case, the method relies on a result of reverberation mapping, namely the empirical relation between R and the continuum luminosity L (the R-L relation; Bentz et al., 2013), where the luminosity of the AGN is estimated from a measurement of the monochromatic luminosity in the AGN spectrum. In a single epoch spectrum, the velocity of the BLR gas ΔV is estimated from the width of the broad emission lines. In a single spectrum, the variable components can not be separated from the non-variable components because the spectrum contains no variability information by itself. Therefore, single-epoch masses are an approximation to reverberation masses where the broad emission line width is measured only in the variable part of the spectrum.

The uncertainty of the masses based on reverberation mapping measurements is approximately 0.4 dex, derived from the scatter in the relationship between the black hole mass and stellar velocity dispersion (the $M-\sigma$-relation) for active and quiescent galaxies (Onken et al., 2004; Woo et al., 2010). The single-epoch mass estimates are calibrated to the reverberation mapping masses and has an additional statistical uncertainty of approximately 0.3-0.4 dex (Vestergaard & Peterson, 2006; Vestergaard & Osmer, 2009). Since Paper I describes the uncertainties associated with single epoch mass estimates in detail, we only provide a very brief overview here. Currently, the limiting factor in reducing the mass uncertainty is the accuracy to which the line width can be measured in AGN spectra (Paper I and II). The two other main sources of uncertainty in the single-epoch mass estimates are the intrinsic variability of the AGN and the scatter of the R-L relationship used to estimate the distance to the BLR gas (Bentz et al., 2013; Kilerci Eser et al., 2015). Each of these factors contribute with $\sim$0.1

dex or less to the single-epoch mass estimates. In Paper I and II we established the uncertainty when measuring the line width as a function of spectral S/N and provide the foundation for the current study of the impact narrow absorption lines on the line width measures. The next section summarizes the conclusions from Paper I and II in order to prepare for the introduction of the current work in § 4.2.3.

4.2.2 Measuring emission line widths

Large samples of AGN spectra from spectroscopic surveys, such as the Sloan Digital Sky Survey (SDSS) and the 2dF quasar survey, are often used for single epoch mass estimates. The advantage of using survey data is that a large number of spectra are readily available for analysis. The disadvantage is that due to the design of such surveys, focusing on quantity rather than quality, the spectral S/N is often relatively low. In Paper I, we mapped the consequence of low spectral S/N on four different line parameters used to measure emission line widths in AGN spectra for the purpose of estimating black hole masses. We did this by analyzing two large samples of high S/N spectra (S/N ≥ 30 pixel^{-1} in the continuum emission), one for Hβ and one for C IV. In each sample of spectra, the range of emission line properties are selected to be representative of the observed properties of these lines in the general observed AGN population. We mapped four different line width parameters, namely the FWHM, the σ_{line}, the MAD, and the Inter-Percentile Velocity (IPV) widths (Whittle, 1985). These parameters are described in greater detail in Paper I. We established the accuracy and precision of each line parameter as a function of spectral S/N by using a Monte Carlo approach where each spectrum in the sample of high S/N spectra was degraded 500 times, each to a range of different S/N levels between 1 and 50 pixel^{-1}. The main conclusion of that work is that the most robust line width parameters are the IPV widths. They facilitate mass estimates that are accurate and precise to within 0.2 dex when measured directly on the data and if S/N ≥ 10 pixel^{-1}. We extend this analysis to include the Mg II $\lambda\lambda$2796,2804 emission line in Paper II which confirms the robustness of the IPV widths. In the current work we focus our attention to the effects of narrow line absorption on the broad emission lines as a function of spectral S/N level and the properties of the absorption feature.

We repeat the study from Paper I for a subset of the sample of C IV spectra with the sole addition of adding narrow line C IV absorption to the high S/N spectra before degrading them and measuring the line widths. We compare line widths measured on the broad C IV emission line in the high S/N spectra with those measured on artificially degraded versions of the same spectra, but with narrow line C IV absorption superimposed. This allows us to determine the accuracy and precision of each line parameter as a function of spectral S/N and the impact of the superimposed absorption on the line parameters. We refer the reader to Paper I for more details on the general procedure. In this study, we will focus on the effects of superimposed narrow line C IV absorption upon a variety of broad C IV emission line profiles. Narrow absorption features are commonly observed around the broad C IV emission line. Furthermore, the broad C IV emission line shows a wider range in profile shapes, compared to the broad Mg II emission line, and we wish to investigate the effect of absorption features on as broad a range of emission line profiles as possible.

4.2.3 Properties of C IV absorption features

The physical properties of the outflows associated with possible AGN feedback can be probed by absorption features detected against the UV/X-ray continuum in AGN spectra. These absorption features are usually divided into two categories: 1) Broad Absorption Lines (BALs) that are broad (FWHM $>$ a few 1,000 km s^{-1}), deep, and smooth, and 2) Narrow Absorption Lines (NALs) that are narrow (FWHM $\leq$ 300 km s^{-1}) and with more sharp profiles. Spectra with line profiles clearly affected by strong absorption features such as BALs should not be used for mass estimates as they can lead to significantly biased results. Especially the NALs are useful for probing the physical properties of outflows since they do not blend together and the individual components of for example the C IV λ1549 Å and Mg II doublets can be discerned. Narrow C IV absorption lines are found to be almost evenly distributed with blueshifts between zero and 70,000 km s^{-1} from the systemic redshift and with equivalent widths (EWs) generally below 2 Å with more than half having EW$<$0.2 Å in the rest-frame of the AGN (e.g., Perrotta et al., 2016). In spectra with low resolution, low signal-to-noise (S/N) spectra, or both, such lines can be hard to detect. Here, we wish to quantify the effect that narrow absorption lines can have on the line width parameters if the absorption is not accounted for.

The structure of the paper is as follows. In § 4.3 the sample of high S/N spectra we use as a basis for our analysis is introduced. § 4.4 describe how we superimpose the absorption features, the statistical analysis method, and the spectral decomposition method we use to extract the broad C IV line profile from the spectra. The results are presented in § 4.5. Finally, in § 4.6 we discuss the results and in § 4.7 we present our conclusions.

4.3 Data

Our goal is to establish the effect that narrow line absorption has on the four different line parameters. For this purpose, we choose a subset of 16 of the high S/N C IV spectra used in Paper I. These spectra are representative of the observed C IV emission line properties of AGN and quasars in terms of line width (FWHM), strength (equivalent width, hereafter EW), and shape (FWHM/σ_{line} ratio) as described in Paper I. Furthermore, these spectra are chosen to have high spectral quality (S/N $\geq$ 30 pixel^{-1}). Specifically, in Paper I, we selected a sample of AGN spectra covering the Hβ or C IV line. These spectra were chosen from the Sloan Digital Sky Survey DR7 Quasar Catalog (Schneider et al., 2010), from reverberation mapping campaigns of local AGNs (Peterson et al., 2004), and from a sample of radio-loud quasars selected from Vestergaard (2003) and observed with the X-Shooter spectrograph mounted on the European Southern Observatory (ESO) Very Large Telescope (VLT) at the Paranal Observatory in Chile. The spectra were chosen to have high spectral quality (S/N $\geq$ 30 pixel^{-1} in the continuum) and cover wide ranges in terms of spectral properties of the C IV line of FWHM: $\sim$2000–10500 km s^{-1}, EW: 13-209Å, and FWHM/σ_{line} ratio: 0.59-3.84, representative of the properties of the observed AGN population. The spectra cover spectral resolutions from $\sim$60 km s^{-1}(X-Shooter

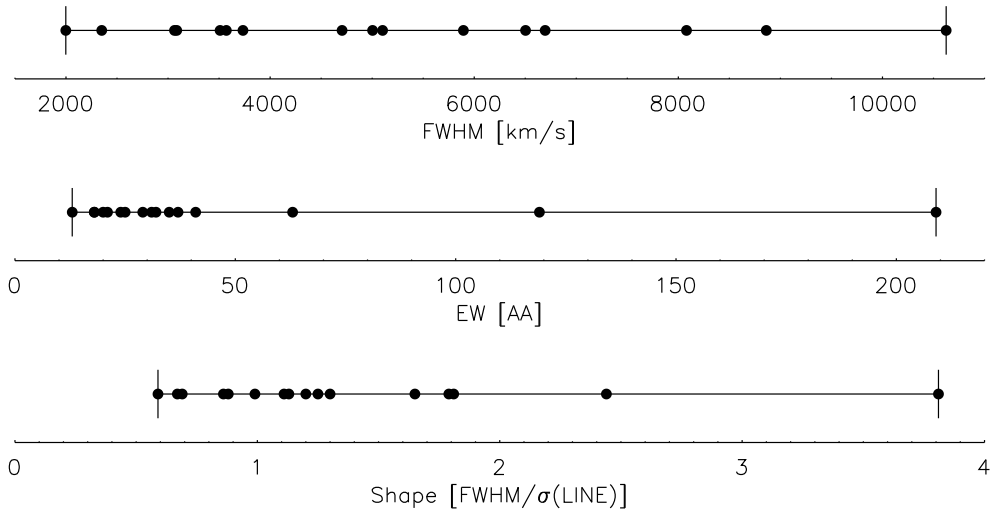

Fig. 4.1 The coverage in FWHM, EW, and FWHM/σ_{line} ratio of the C IV emission line properties of our database. Dots mark spectra included in this work. The vertical lines bracketing these values show the coverage of the high S/N C IV spectra described in Paper I.

spectra) to $\sim$1170 km s^{-1}(reverberation mapping spectra). For details on the sample selection and the spectra, the reader is referred to Paper I.

Figure 4.1 illustrates the distribution of the measured FWHM (top), EW (middle), and FWHM/σ_{line} ratio (bottom) of the spectra in our database. For FWHM, the subset of spectra used in this work covers the same parameter space covered by the sample in Paper I (marked by the two vertical lines) almost uniformly. For the EW and the FWHM/σ_{line} ratio, the distribution is skewed towards smaller values, but this is consistent with the distributions of these two parameters as demonstrated in Paper I. Overall, our subsample is representative of the full sample of high S/N C IV spectra from Paper I. Details on the spectra included in this work and the C IV emission line properties are given in Table 4.1.

Besides spanning a large range in emission line properties, our sample of spectra also covers a range of spectral resolutions from $\sim$60 km s^{-1} for the spectra observed with X-Shooter to $\sim$1160 km s^{-1} for the mean reverberation mapping spectrum of Fairall 9. The difference in spectral resolution can have a profound effect on our ability to detect and account for absorption features. For example, for a typical line width of $\sim$200 km s^{-1} for narrow C IV absorption features, a spectral resolution of $\sim$100 km s^{-1} or better is required in order to fully resolve the absorption lines. This means that if the spectral resolution is lower than this, the features will be smeared out and be harder to account for, possibly leading to biases in the measured line parameters. We return to this issue in § 4.5.1.

Table 4.1 Spectral properties of the C IV database

Source	Redshift z	S/N[a]	EW[b]	Line shape[c]	FWHM	σ_{line} [d]	MAD[e]	IPV(50%)[f]	Ref.
(1)	(2)	(3)	(4)	(5)	(6)	(7)	(8)	(9)	
Composite C[g]	...	46	37	1.30	5004	3857	2810	4039	1
Composite D[g]	...	36	31	1.65	6695	4057	3068	4683	1
J133335.78+164903.9	2.0885	41	18	1.11	5102	4608	3381	4662	2
J122527.39+223512.9	2.0498	39	25	1.25	5894	4725	3598	5642	2
J005157.24+000354.7	1.9559	39	20	1.81	6503	3584	2668	4272	2
J142656.18+602550.8	3.1917	50	32	1.79	8080	4509	3436	5319	2
J111800.50+195853.4	1.9356	38	13	3.81	8862	2324	2442	4908	2
J073502.30+265911.5	1.9727	39	18	2.44	10624	4358	3589	6434	2
Fairall 9[h]	0.0470	200	119	0.69	3085	4502	3122	3950	3
NGC 5548[i]	0.0172	200	209	0.99	3571	3619	2652	3918	4
Q1542+0417	2.1820	48	35	0.59	1998	3371	2234	2695	5
Q2212-2959	2.7037	45	24	0.67	2350	3515	2200	2550	5
Q0106+0119	2.0990	85	21	0.86	3063	3560	2612	3627	5
Q1311-2700	2.1950	35	63	0.88	3510	4005	3036	4555	5
Q1705+0152	2.5750	59	41	1.13	3734	3308	2225	3105	5
Q0226-0350	2.0750	54	29	1.20	4705	3918	2812	3961	5

Note. — [(a)] Signal-to-noise ratio, S/N, measured in the continuum region between 1445-1455Å and 1690-1700Å either as the median ratio of the flux density relative to the noise spectrum or as the average flux density relative to the root-mean-square (rms) around this mean flux density if a noise spectrum is unavailable; [(b)] Rest-frame equivalent width; [(c)] Emission line shape, parameterised as FWHM/σ_{line}; [(d)] Line dispersion of the emission line flux density, the second moment of the flux distribution, defined in Paper I; [(e)] Mean Absolute Deviation from the Median Velocity as defined in Paper I; [(f)] The Inter-Percentile Velocity width of the emission line at 50% of the line flux, as defined in Paper I; [(g)] The SDSS composite spectra all have data from > 150 SDSS spectra in each pixel at rest-frame wavelengths between 1445Å and 1700Å where we perform the spectral decomposition (§ 4.4.3); [(h)] Observed with *IUE/SWP* with a spectral resolution of $\Delta v \approx 1160\,\mathrm{km\,s^{-1}}$. Rest-frame wavelength coverage is 1098Å – 1886Å; [(i)] Observed with *HST/FOS*, the spectrum covers 1070Å – 2290Å in the wavelength rest-frame with a spectral resolution of $\Delta v \approx 365\,\mathrm{km\,s^{-1}}$.

References. — (1) Stephan Frank et al., in prep; (2) Schneider et al. (2010); (3) Rodríguez-Pascual et al. (1997); (4) Korista et al. (1995); (5) This work.

4.4 Method

To prepare the data for our analysis of the combined effect of spectral S/N and narrow line absorption on the measured line parameters, we start out with the subset of high S/N spectra described in § 4.3. Then, we first add narrow line C IV absorption to each spectrum (described in § 4.4.1). Second, we add the effect of the spectral S/N by adding artificial noise to the high S/N spectra for which intervening narrow absorption is superimposed on the profiles (described in §4.4.2). Finally, we extract the broad C IV emission line profile by means of spectral decomposition modeling (§4.4.3) and measure the line parameters on this isolated line profile.

4.4.1 Adding narrow line absorption

We wish to investigate the effect of narrow line C IV absorption at different positions of the line profile and for different strengths of the absorption feature. Therefore, for each original high S/N spectrum in our sample, we generate nine different absorption profiles covering a combination of three different positions on the emission line and three different absorption strengths. We model the narrow C IV absorption doublet by two Gaussian profiles, each with a width of FWHM=200 km s^{-1}. The separation between the two absorption profiles is fixed at 580 km s^{-1} in velocity space, corresponding to positions of 1448 Å and 1551 Å in the wavelength restframe. The relative strength of the two components is fixed at 2:1.

We generate the absorption feature with three different strengths measured as the equivalent width of the sum of the two absorption lines relative to the local continuum. We use values of 0.5 Å, 1.0 Å, and 2.0 Å for the C IV absorption doublet. Perrotta et al. (2016) show that the vast majority (>90%) of C IV absorption systems have equivalent widths <0.5 Å, so in most cases, the observed strength of the absorption will be similar to or have lower strength than this. But, stronger absorption is also observed (e.g., Vestergaard, 2003), and we also wish to probe the effect of such more prominent absorption features. We therefore include absorption features with strengths of 1.0 Å and 2.0 Å, respectively. While not common, such strong absorption is expected to have a profound adverse impact on the accuracy of the measured value of the line parameters if it goes undetected due to low S/N , low spectral resolution, or both.

We position the absorption feature at three different distances from the rest frame wavelength of the broad C IV emission line. We wish to investigate the effect of absorption positioned at the peak of the emission line, in the (far) wing of the emission line, and in between these two positions. Specifically, we blueshift the absorption feature by 10%, 65%, and 140% of the FWHM of the broad C IV emission line that is measured in Paper I on the high S/N spectrum. Absorption in the peak is expected to impact the FWHM by altering the measured value of the peak flux density of the line. On the other hand, absorption in the middle and wing of the emission line profile is not a priori expected to have a large impact on FWHM. The line dispersion depends very strongly on the flux in the wings of the line, and is therefore expected to be heavily affected by absorption in the wing, but not in the peak of the emission line. The MAD is expected to show the same trends as σ_{line}, but to a lesser

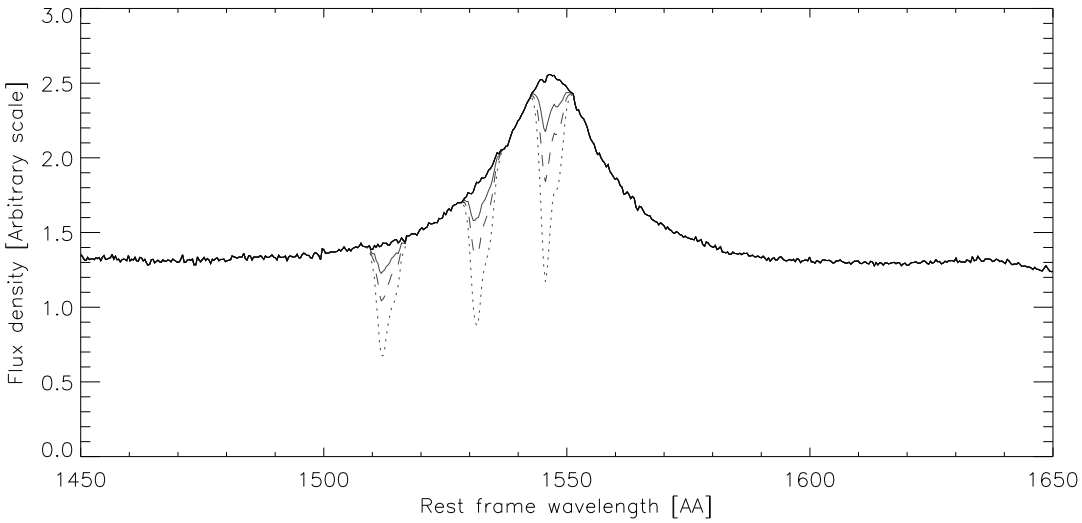

Fig. 4.2 Sample absorption features added to the Composite C spectrum (spectral resolution $R \approx 2000$ equivalent to $\approx$150 km s^{-1}). The absorption feature is shown blueshifted at three distances from the peak of the broad C IV emission line and with three relative strengths with equivalent widths of 0.5 Å (solid gray), 1.0 Å (dashed gray), and 2.0 Å (dotted gray).

degree since it does not weight the flux density by the square of its distance to the line centre. Finally, the IPV widths are expected to be affected by absorption at all positions of the line because they are integral measures of the line profile.

To make our modelled data as realistic as possible, we convolve the absorption feature with the spectral resolution of the data before we add it to the spectrum. As a consequence, the same absorption feature (same relative position and strength) will appear sharper in a spectrum with a high spectral resolution and more smeared out in a low resolution spectrum. An example of the nine versions of the C IV absorption feature added to the Composite C spectrum is shown in Figure 4.2.

4.4.2 Statistical methods and analysis

As described above, for each high S/N spectrum listed in Table 4.1, we create nine high S/N spectra such that each version of the spectrum contains its own unique narrow C IV absorption doublet superimposed on the C IV emission profile. Each of these spectra are then degraded to lower S/N levels following the procedure from Paper I. We briefly describe the procedure here.

Each high S/N spectrum is degraded to a range of S/N levels between 1 and 50 pixel^{-1}. We degrade each spectrum 500 times at each S/N level, using a different seed for the noise distribution each time. As a result, each degraded spectrum is unique and therefore has a unique effect on the measured line width parameters. This allows us to assess the accuracy and precision of each line width parameter in a statistical manner at a given S/N level. We do this by comparing the line widths measured at a specific S/N level with those measured in the original high S/N spectrum. An example

of a spectrum degraded to S/N levels of ∼10, 5, and 2 is shown in Figure 4.3 together with the original high S/N spectrum.

We use the mode of the distribution of line widths as the best estimate of a particular line parameter at a given S/N level. The offset between this value and the line width measured in the original absorption free high S/N spectrum is then used as the accuracy of the given line width measure. We then use the mode to divide the distribution of measured line widths in two. The area enclosed by 68% of the measurements above or below the mode, respectively, is then used as the error bars. These define the precision of the line width measure at that particular S/N level. For a Gaussian distribution, this would correspond to one standard deviation.

Ultimately, we are interested in how the accuracy and precision of the line parameter affects the accuracy and precision of the black hole mass estimates. We therefore propagate the accuracy and precision of the line width measures to the black hole mass estimates, under the assumption that only the uncertainty of the measured line widths contribute to the uncertainty of the black hole mass, using the formulas (Paper I)

$$\Delta\log(M_{BH}) = 2\log\left(\frac{\Delta V}{\Delta V_{int}}\right) \qquad ;accuracy \tag{4.2}$$

$$\sigma^{\pm}_{\log(M_{BH})} = \pm\log\left(1 \pm 2\frac{\sigma^{\pm}_{\Delta V}}{\Delta V}\right) \qquad ;precision \tag{4.3}$$

where $\Delta\log(M_{BH})$ is the offset in black hole mass, ΔV and ΔV_{int} are the measured and original line width, respectively, and $\sigma^{\pm}_{\Delta V}$ and $\sigma^{\pm}_{\log(M_{BH})}$ are the positive and negative uncertainty of the measured line width and black hole mass estimate, respectively.

We exclude a few spectra from our analysis, namely those where the spectral decomposition fails to converge during the modelling process. The fraction of spectra excluded on these grounds is less than 1%, and they have no effect on our analysis or conclusions.

4.4.3 Spectral decomposition

We use the exact same spectral decomposition method as described in Paper I for the C IV line. This model includes the following components:

1. A power-law component to account for the featureless nuclear AGN continuum;

2. Individual emission line components to account for the line emission of N IV λ1486, C IV λ1549, He II λ1640, and the blended emission of [O III] λ1663 and Al II λ1670. Each of these components are modelled by one or more Gaussian functions. Details on the individual components are given in Paper I;

3. A Gaussian function to account for the so-called red shelf of emission around 1600 Å of unknown physical origin. We found in Paper I that a Fe II template was insufficient to describe

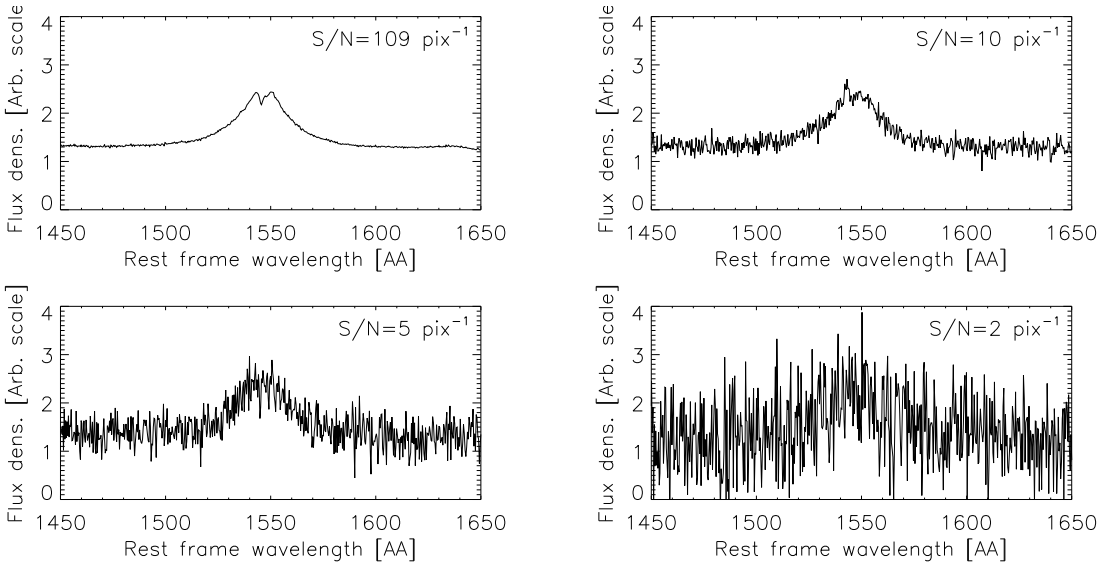

Fig. 4.3 Example of the effect of S/N on the Composite C spectrum with the absorption feature added at the peak of the line with a strength of 0.5 Å. The absorption feature is clearly visible at S/N $\sim 109\,\mathrm{pixel}^{-1}$ (upper left panel), whereas at S/N $\sim 5\,\mathrm{pixel}^{-1}$ (lower left panel) and S/N $\sim 2\,\mathrm{pixel}^{-1}$ (lower right panel), it is indistinguishable from the spectral noise. The interesting case is S/N $\sim 10\,\mathrm{pixel}^{-1}$ (upper right panel) at which point the absorption feature might be recognized. But, due to the spectral noise and without any a priori knowledge about the feature, it might as easily be confused with a odd shaped broad C IV emission line profile or even a narrow emission component of the C IV line.

the feature. For details on the modelling, see Paper I, and for a discussion of how to deal with the 1600 Å emission feature, see for example Fine et al. (2010) or Denney et al. (2013).

The power-law function is modelled first in the continuum windows between 1445-1455 Å and 1690-1700 Å to ensure a proper normalization. After subtraction of this nuclear emission line component, the remaining spectral emission components are modelled simultaneously. We extract the broad C IV emission line profile by subtracting all other spectral components.

Since we wish to show the effect of unrecognized absorption, we make no attempt to correct for it, not even in the high S/N spectra where it is rather easy to recognize. Clearly, the effect of absorption is only relevant if we are unable to account for it, which is probably not the case for high S/N spectra (probably somewhere around S/N $\geq 10\,\mathrm{pixel}^{-1}$ as shown in Figure 4.3). But, our ability to recognize and account for the absorption is also a matter of sufficiently high spectral resolution. Thus, even at high S/N levels, the narrow absorption features might go unrecognized if the spectral resolution is low. Therefore, there is still some value in establishing the effect of narrow absorption features on the measured value of the line parameters at high S/N .

4.5 Results

Intervening absorption lines primarily introduce an offset (bias) in the measured line widths. This means that the absorption has very little effect on the precision of the line measures, compared to what we found without including absorption in Paper I. Therefore, we focus on the accuracy of each line width in this work. Figures showing the accuracy and precision for each line measure and each absorption strength and position are shown in Appendices H–M.

It is not a trivial task to separate the effect of narrow line absorption from that of spectral S/N , and in practice, we need to know the combined effect. Nevertheless, we try to separate them here in order to show the isolated effect of the narrow absorption such that we can compare it with the effect of spectral S/N as already presented in Paper I. Both the combined effect of spectral S/N and absorption and the isolated effect of absorption will therefore be taken into account. Furthermore, for each line parameter, we wish to show the effect of the narrow absorption features strength and position on the broad C IV emission line. For example, some line measures will be highly affected by absorption in the line peak versus absorption in the line wing, and *vice versa*.

Figure 4.4 shows the difference between the line width measured with and without absorption [e.g., ΔFWHM(ABS)], normalised by the intrinsic line width measured in the original high S/N spectrum with no absorption present [FWHM(ORIGINAL)]. Each row shows one of the line parameters: the FWHM, the σ_{line}, the MAD, and the IPV50 width, respectively. In each row, three diagrams are shown. From left to right, these show the effect of absorption placed near the peak (left), between the peak and the wing (middle), and in the line wing (right). Finally, three colored areas are shown in each plot according to the strength of the absorption with green, red, and blue colors corresponding to

an equivalent width of 0.5, 1.0, and 2.0 Å, respectively. The content off the figure will be explained further in the following.

Figure 4.5 is structured in the same way, but here, the accuracy is shown without any attempt to separate the contributions from pure noise and absorption from each other. We will focus on Figure 4.4 to establish the effects of absorption, but will compare with Figure 4.5 in order to evaluate whether the absorption effects are significant compared to the isolated effect of decreasing S/N . The results for each line width parameter will be presented in turn below and we will compare and discuss the results in § 4.6.

4.5.1 FWHM

The narrow C IV absorption doublet has the strongest impact on the FWHM when it is positioned near the peak of the emission line. This can be seen by comparing the span of the shaded areas in the uppermost left panel (absorption placed near the peak of the line) with those in the uppermost right panel (absorption placed in the wing of the line) in Figure 4.4. The offset can be up to $\sim$0.3 dex in the black hole mass (right hand y-axis) when the absorption is placed in the core of the line and S/N $\geq 15\,\mathrm{pixel}^{-1}$. The narrow absorption feature can also result in both under- and overestimated masses (the shaded area is distributed almost evenly around the horisontal line at y=0 marking the line width measured without absorption). By looking at the figures in Appendix H, we can see that for broad and boxy emission lines the measured value of FWHM tends to be underestimated (the red areas in panels (a) and (c) in Figure H.3 are consistently below the solid horisontal line), while for narrow and peaky lines it tends to be overestimated (green areas in panels (a) and (c) in Figure H.3 are consistently above the solid horisontal line).

Although the effect of absorption can be even larger than 0.3 dex in M_{BH} for S/N $\sim 15\,\mathrm{pixel}^{-1}$, we remind the reader that it is not recommended to measure the FWHM on data with S/N $< 25\,\mathrm{pixel}^{-1}$ (as argued in Paper I). Furthermore, at these low S/N levels, the adverse effect of spectral noise dominates over that of the absorption (compare span of shaded areas in top row of Figure 4.4 with corresponding areas in Figure 4.5).

Absorption in the middle and in the wing of the profile has a smaller effect on the FWHM than absorption in the core. At S/N $\geq 25\,\mathrm{pixel}^{-1}$, this can be up to $\sim$0.2 dex and $\sim$0.15 dex in the final mass estimate, respectively (middle and right top panels, respectively, in Figure 4.4), compared to $\sim$0.3 dex for absorption near the peak.

Finally, we find a tendency for the effect of the absorption on the measured FWHM to depend somewhat on the strength of the absorption line. This is most clearly seen by comparing the span of the shaded areas in the uppermost left panel of Figure 4.4 which shows the results for absorption placed near the peak of the emission line. Here, the span (i.e., the offset of the measured FWHM value due to absorption) increases from $\sim$ 0.2 dex to $\sim$0.3 dex as the equivalent width of the absorption line is increased from 0.5 Å (green color) to 2.0 Å (blue color).

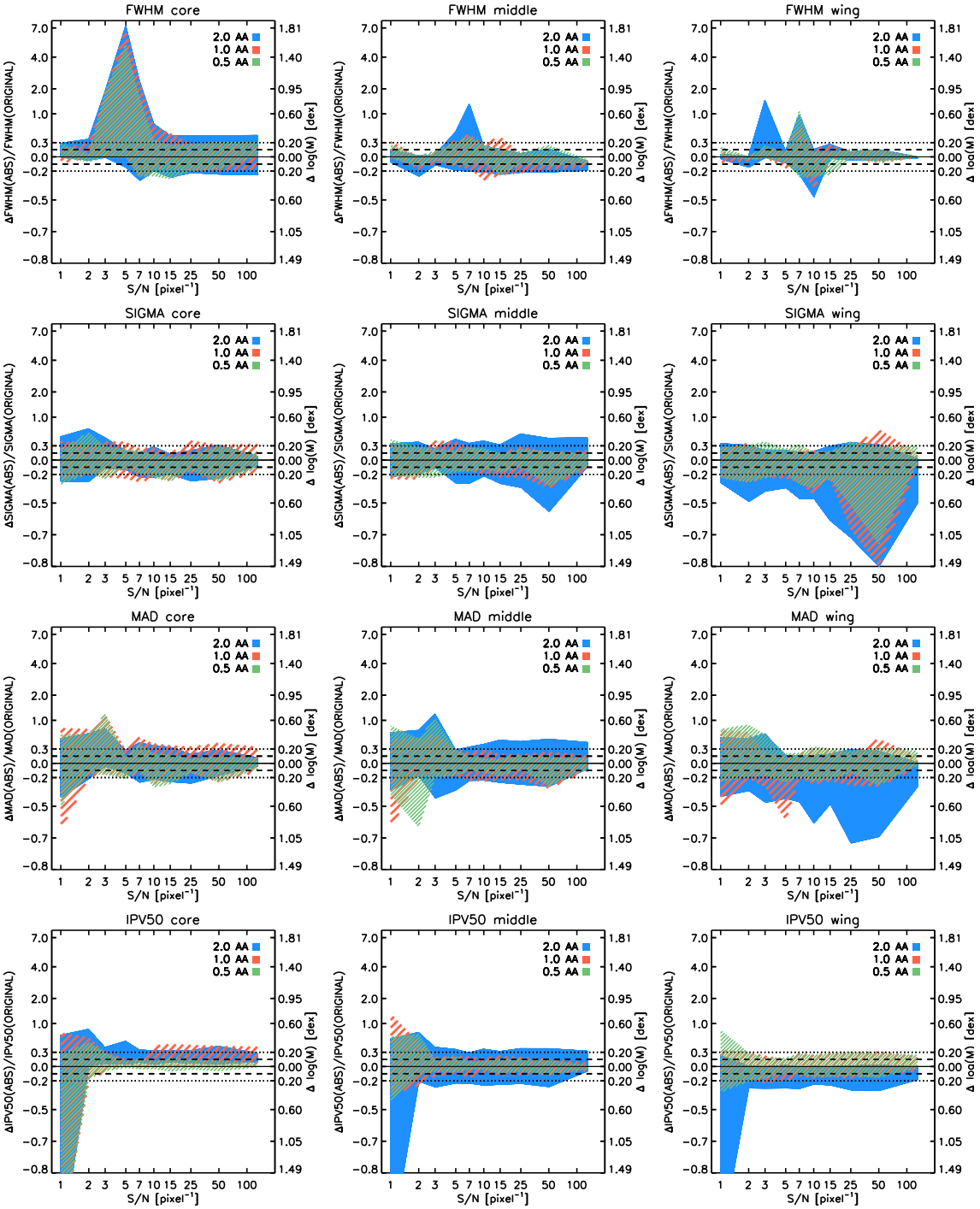

Fig. 4.4 Accuracy of the four line width parameters when narrow line C IV absorption is added. In this figure, the isolated effect of spectral S/N , as established in Paper I, is subtracted such that these results show the effect of the absorption alone. The left y-axis in each panel shows this offset relative to the line width measured in the original high S/N spectrum, and the right y-axis shows this offset propagated to an offset in the resulting black hole mass. From the top, panels in each row show the accuracy of the FWHM, σ_{line}, MAD, and IPV50 width, respectively. Each column shows the blueshift of the absorption lines by 10%, 65%, and 140% of the FWHM of the broad C IV emission line from the left to the right. In each panel, the effect of absorption with an equivalent width of 0.5, 1.0, and 2.0 Å is shown in green, red, and blue, respectively.

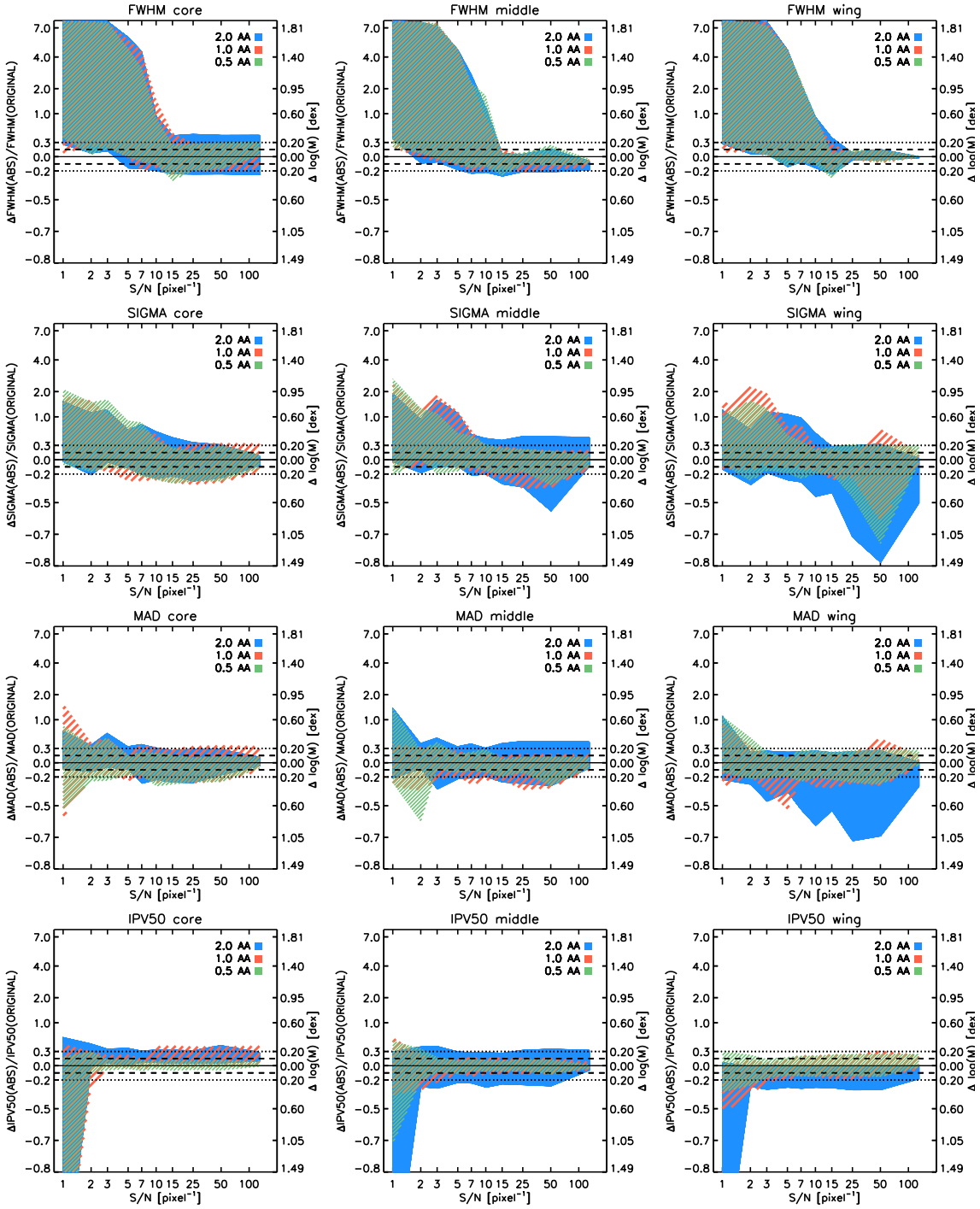

Fig. 4.5 Same as Figure 4.4, but with the effect of spectral S/N included.

It is clear that unrecognized absorption can have a quite strong effect on the measured value of the FWHM, even at S/N ≥ 25 pixel^{-1}. This is especially true if the absorption is placed near the peak of the emission line and if it is strong. On the other hand, one might argue that at such relatively high S/N levels it is simple to account for these unwanted absorption features. But, this is of course only true if the spectral resolution is high enough. The absorption we have superimposed here has a width of FWHM = 200 km s^{-1}, typical of narrow absorption lines in AGN spectra. This can just barely be resolved in for example SDSS spectra which has a spectral resolution of $\sim$70 km s^{-1}. For narrower absorption lines it is unclear whether we could detect it, then it is not certain that we could account for it, even if the S/N was higher than $\sim$25 pixel^{-1}.

4.5.2 The line dispersion - σ_{line}

In general, absorption has a stronger effect on σ_{line} than on FWHM. The reason for this is that σ_{line} is a integral measure of the line width, while the FWHM is not. A very clear example of this is seen by comparing the span of the shaded areas in the rightmost panel in the top row (FWHM) with that in the second row (σ_{line}) of Figure 4.4. For σ_{line}, absorption can cause offsets of up to 1.5 dex in the black hole mass for S/N ≥ 25 pixel^{-1}. For FWHM the offset is less than 0.1 dex in black hole mass for the same S/N levels.

We also find that broad, boxy, and low equivalent width emission lines are more strongly affected by absorption than more narrow, peaky, and high equivalent width lines. This can be seen by comparing the span of the shaded red (broad), green (low EW), and red (boxy) areas in panels (a), (b), and (c), respectively, of Figure I.9 with the green (narrow), red (high EW), and green (peaky) areas in the same panels. There is also a strong tendency for σ_{line} to be underestimated (shaded areas in for example the rightmost panel in the second row of Figure 4.4 predominantly lie below the intrinsic line width marked by the solid black horizontal line) because the absorption effectively removes flux from the integrated line profile on which σ_{line} depends.

Two other trends clearly emerge for σ_{line}. First, the effect of the absorption increase as its strength (i.e., its equivalent width) increases. This is illustrated by the span of the shaded areas in the rightmost panel in the second row of Figure 4.4 that increase from an equivalent width of 0.5 Å (green) to 2.00 Å (blue). A similar effect is visible in the middle panel of the second row in the same figure.

Second, the effect of the absorption gets stronger as it moves from the core towards the wing of the emission line. This is illustrated by the expansion of the shaded areas in the second row of Figure 4.4 as the absorption moves from the peak (leftmost panel) to the wing (rightmost panel). This is a direct consequence of the fact that σ_{line} weights the flux density in each pixel by its distance to the line peak.

While it might be possible to correct for the absorption if S/N ≥ 25 pixel^{-1} and if the spectral resolution is high enough, there is a regime where it might not be possible to correct for the absorption due to low S/N . This will be somewhere below S/N ~ 25 pixel^{-1} and above S/N ~ 10 pixel^{-1}; we do not recommend measuring σ_{line} at S/N < 10 pixel^{-1} since it becomes biased at these low S/N levels

(Paper I). In this case, if one fails or is unable to account for the absorption, it can cause an offset in the black hole mass of up to ∼0.6 dex if the absorption is positioned in the line wing. The effect of absorption on σ_{line} can therefore be quite severe, even at moderate S/N levels.

4.5.3 The MAD

Overall, absorption has the same effect on the MAD as it has on σ_{line}. These results are shown in the third row from the top in Figure 4.4. This means that the adverse effect of the absorption increases with the strength of the absorption and as it moves towards the line wing. But, since the MAD does not excessively weights the flux density in each pixel by its squared distance to the line centre, absorption has a smaller negative impact on the MAD compared to σ_{line}. Absorption in the wing of the emission line can cause the MAD to be underestimated by up to ∼50% (∼0.6 dex in black hole mass) for virtually any S/N level above 3 pixel^{-1} (see span of shaded areas in rightmost panel of third row from the top in Figure 4.4). This is a lot, but still much less than the 1.5 dex in black hole mass we found for σ_{line} for the same absorption strength and position on the line as shown in the panel above.

Similar to σ_{line}, the problems arise in the regime where the S/N is low enough that it can be problematic to account for the absorption. As an example, in Paper I, we find the accuracy of black hole mass estimates based on the MAD to be within 0.15 dex if 5 pixel^{-1} ≤ S/N ≤ 10 pixel^{-1}. In this case, unrecognized absorption adds an offset of 0.6 dex to the black hole mass, which is a significant decrease in the accuracy compared to what can be expected if there is no absorption present.

4.5.4 The IPV widths

We have investigated the effects of absorption on IPV widths ranging from the IPV20 to the IPV90 width. In Figure 4.4 we only show results for the IPV50 width, the results for the IPV20 and IPV90 width are shown in Appendices K and M, respectively. The results for the remaining IPV widths are not shown here, but they are fully consistent with those for the IPV20, IPV50, and IPV90 results presented here.

For the IPV widths, the absorption has some of the same effects as for σ_{line} and MAD. Namely, that as the strength of the absorption increases, so does its negative effect on the measured IPV width.

The effect of the absorption also depends on both the IPV percentage and the position of the absorption on the emission line profile. To illustrate, the IPV20 width is more affected by absorption in the line wing than near the peak (compare span of shaded areas in panel (a) of Figure K.3 with those in panel (a) of Figure K.9). In the former case (absorption in the core), the effect absorption has on the accuracy of the mass estimate is up to ∼0.2 dex at S/N ≥ 5 pixel^{-1}, while in the latter case (absorption in the wing), it is up to ∼0.6 dex at the same S/N levels. The opposite is true for the IPV90 width. In this case, absorption near the peak of the broad C IV emission line profile has the largest negative impact on the accuracy of the mass estimates. Here, absorption in the core of the emission line profile can affect the black hole mass estimate by ∼0.6 dex (see Figure M.3) while absorption in the wing can affect it by ∼0.2 dex (see Figure M.9), both when measured at S/N ≥ 5 pixel^{-1}.

The IPV50 width is mostly affected by absorption in the wing, with offsets up to ∼0.4 dex in the black hole mass estimate if S/N ≥ 5 pixel^{-1} (bottom row in Figure 4.4). As for the MAD, there is thus a S/N range where it is difficult to account for the absorption and where it will have a significant adverse effect on the accuracy of the mass estimate. To illustrate, the decrease in accuracy of the mass estimate due to the absorption for S/N ≥ 5 pixel^{-1} is up to 0.4 dex for the IPV50 width (Figure 4.4), compared to an accuracy of 0.2 dex at the same S/N levels without absorption (Paper I).

4.6 Discussion

We have examined the sensitivity of four different line width parameters, namely the FWHM, σ_{line}, the MAD, and the IPV widths, measured on the broad C IV emission line, towards narrow absorption line features. We tested the sensitivity towards a narrow C IV absorption doublet placed at three different positions on the broad C IV emission line and with three different strengths. In total, nine different absorption features.

Overall, we find that the accuracy of all four line parameters is decreased as a consequence of the absorption, no matter its position or strength. Clearly, this serves as an overall warning to make sure to have sufficient spectral S/N and spectral resolution in order to be able to effectively account for the absorption features prior to the line width measurements. The integral line measures (the σ_{line}, MAD, and IPV widths) are affected more by absorption features than the FWHM because the absorption effectively removes flux from the broad emission line. Therefore, we also find a tendency for these line parameters to be underestimated in the presence of absorption super-positioned on the broad C IV emission line (shaded areas in second, third, and fourth row in Figure 4.4 show a tendency to lie below the solid black line).

We also find that the negative effect of the absorption becomes stronger as the strength of the absorption feature increases. As an example, absorption in the wing of the emission line with a strength of EW$\leq$1.0 Å can cause the MAD to be underestimated by ∼30% at S/N ~ 25 pixel^{-1}, while at the same S/N , if the absorption has a strength of EW=2.0 Å, the MAD can be underestimated by more than 70% (compare span of shaded green and red areas with the blue shaded area in the right panel in the third row from the top in Figure 4.4). This trend is also clear for the σ_{line} and the IPV widths (second and fourth row in Figure 4.4).

We also find that the position of the absorption on the emission line matters. The FWHM is mostly affected by absorption in the peak of the emission line where it affects the measured value of the peak flux density [the span of shaded areas in the top row of Figure 4.4 increase when moving from the right (absorption in the wing) to the left (absorption in the peak)]. On the other hand, the σ_{line} and the MAD are more affected by absorption in the wing since they both weight the flux density in each pixel by its distance to the line peak [span of shaded areas in second and third row in Figure 4.4 increase when moving from the left (absorption in the peak) to the right (absorption in the wing)]. This effect is most pronounced for σ_{line} since it weights the flux by the square of the distance from the line peak. Finally, the IPV widths are affected by the position of the absorption feature differently

depending on whether they measure the line width at the base (low IPV percentage) or the core (high IPV percentage) of the line. Specifically, the IPV20 width is more affected by absorption in the wing of the emission line while the IPV90 width is more affected by absorption in the peak of the emission line.

Especially the σ_{line} and the MAD widths suffer from very large biases (>70% or >1.0 dex in the black hole mass) for relatively large S/N values of 25 pixel^{-1} or higher. In this regime, provided that the spectral resolution is high enough, it should be relatively straightforward to account for the absorption features in order to remove (most) of this bias. But, as the S/N decreases, our ability to account for the absorption also decrease. As a specific example, this probably happens somewhere between S/N $\sim$ 15 pixel^{-1} and S/N $\sim$ 5 pixel^{-1} for the spectrum shown in Figure 4.3. At these S/N levels, the σ_{line} and MAD can be biased by up to $\sim$30% (0.3 dex in M_{BH}), even if the absorption has a strength of only EW=0.5 Å. Absorption can thus give a significant offset in the black hole mass estimates if unaccounted for. It is worth noticing that this offset is smallest for the IPV widths.

Besides simply looking at the spectral S/N level, the spectral resolution has a profound effect for our ability to recognize and account for the narrow absorption features. As the spectral resolution decrease, so does our ability to resolve the absorption features and therefore also our ability to account for them. In this case, even if the spectral S/N is high, the absorption feature might go undetected and can then have a strong negative effect on the accuracy of the measured line parameters.

While the examples presented and discussed in this study can not be considered to be a complete representation of all possible absorption features present in AGN spectra, they do serve as a showcase for the negative effects unrecognized absorption features can have on the measured line parameters. As a general consideration, this leads to the following recommendation when acquiring spectra to use for mass estimates in AGN: The spectral S/N , as well as the spectral resolution, should be high enough that we can account for narrow (FWHM$\sim$200 km s^{-1}) absorption features. In practice, this means a spectral resolution of 100 km s^{-1} or better and a spectral S/N level of 25 pixel^{-1} or better.

4.7 Conclusion

We have reached the following conclusions when investigating the effect of narrow absorption features with three different positions and three different strengths super-positioned on top of the broad C IV emission line for four different line parameters (namely the FWHM, σ_{line}, MAD, and IPV widths) as a function of spectral S/N :

1. All four line parameters are affected by the absorption features if unaccounted for. This leads to biases between 0.1 and 1.5 dex in the resulting mass estimates, depending on which line measure is used and the strength and position of the absorption feature on the broad C IV emission line.

2. The σ_{line}, the MAD, and the IPV widths are more affected by the absorption features than the FWHM because they all rely on the integrated line flux which effectively is decreased by the absorption.

3. In general, the negative effect of the absorption on the measured value of the line parameters increase with absorption strength.

4. The different line parameters are affected to a different degree by absorption super-positioned at different positions on the emission line. For example, the FWHM is mostly affected by absorption in the peak of the emission line where it can change the measured value of the peak flux density. On the other hand, the σ_{line} and MAD widths are more affected by absorption in the line wing since they weight the flux density in each pixel by its distance from the line peak. Finally, IPV widths measuring the width at the base of the line (low IPV percentages) are more affected by absorption in the wing of the emission line compared to the peak, while the opposite is true of IPV widths measured at the core of the line (high IPV percentages). Overall, the IPV widths are less affected by absorption than the other line parameters.

In most cases, a S/N $\geq 15\,\mathrm{pixel}^{-1}$ will be enough to account for the absorption features, provided that the spectral resolution is high enough. But, this also means that high S/N alone not is enough. We therefore recommend to aim for a spectral resolution of $100\,\mathrm{km\,s}^{-1}$ or better, combined with a spectral S/N level of $25\,\mathrm{pixel}^{-1}$ or higher if one aims to obtain a mass estimate with an uncertainty better than $\sim$0.3 dex. Only in this case can we have high enough confidence that the absorption features can be detected and effectively accounted for.

Acknowledgements

We wish to thank Stephan Frank for contributing with the high S/N SDSS composite spectra of the C IV emission line and Sandra Raimundo for help with processing of X-Shooter spectra. JJJ gratefully acknowledges support from the Dark Cosmology Centre. MV gratefully acknowledges support from the Danish Council for Independent Research via grant no. DFF 4002-00275 during the preparations of this work.

Chapter 5

Using PAH features as a star formation tracer in AGN

This chapter contains the paper[1]:

PAH features within a few hundred parsec of active galactic nuclei
Jensen J.J., Hönig S.F., Rakshit S., et al., 2017, MNRAS, 470, 3071–3094

5.1 Abstract

Spectral features from poly-cyclic aromatic hydrocarbon (PAH) molecules observed in the mid-infrared (mid-IR) range are typically used to infer the amount of recent and ongoing star formation on kiloparsec scales around active galactic nuclei (AGN) where more traditional methods fail. This method assumes that the observed PAH features are excited predominantly by star formation. With current ground-based telescopes and the upcoming JWST, much smaller spatial scales can be probed and we aim at testing if this assumption still holds in the range of few tens to few hundreds of parsecs. For that, we spatially map the emitted 11.3 μm PAH surface flux as a function of distance from $0.4-4$ arcsec from the centre in 28 nearby AGN using ground-based high-angular resolution mid-IR spectroscopy. We detect and extract the 11.3 μm PAH feature in 13 AGN. The fluxes within each aperture are scaled to a luminosity-normalised distance from the nucleus to be able to compare intrinsic spatial scales of AGN radiation spanning about 2 orders of magnitude in luminosity. For this, we establish an empirical relation between the absorption-corrected X-ray luminosity and the sublimation radius in these sources. Once normalised, the radial profiles of the emitted PAH surface flux show similar radial slopes, with a power-law index of approximately -1.1, and similar absolute values, consistent within a factor of a few of each other as expected from the uncertainty in the intrinsic scale estimate. We interpret this as evidence that the profiles are caused by a common compact central physical process, either the AGN itself or circumnuclear star formation linked in

[1]This chapter contains the content of that paper as published. No other changes than reformatting has taken place.

strength to the AGN power. A photoionisation-based model of an AGN exciting dense clouds in its environment can reproduce the observed radial slope and confirms that the AGN radiation field is strong enough to explain the observed PAH surface fluxes within $\sim 10-500$ pc of the nucleus. Our results advice caution in the use of PAH emission as a star formation tracer within a kpc around AGN.

5.2 Introduction

Understanding galaxy formation and evolution is a fundamental part of current astronomical research. Observed strong correlations between the mass of the central supermassive black holes (SMBHs), believed to be ubiquitous in all galaxies, and the properties of their host galaxy bulge (Magorrian et al., 1998; Wandel, 1999b; Ferrarese & Merritt, 2000b; Gebhardt et al., 2000a; Ferrarese et al., 2001; McLure & Dunlop, 2001; Marconi & Hunt, 2003b) indicates that some kind of feedback or co-evolution is at play. One piece of this puzzle is to understand the connection between the growth of a SMBH during its phase of active accretion ("active galactic nucleus"; AGN) and the star formation in its host galaxy bulge.

In the standard model of unification, an AGN is fueled by accretion of gas onto a central SMBH (Alexander & Hickox, 2012, and references therein). Within this scenario, the accretion of gas into the central parts of the galaxy will almost certainly lead to nuclear star formation, as indicated by observations and simulations alike (Kawakatu & Wada, 2008; Hopkins & Quataert, 2010). Models by Hopkins (2012) predict a correlation between the star formation rate and the black hole accretion rate. However, the black holes accretion phase is slightly delayed with respect to the peak of star formation. Observational evidence of AGN activity in post-starburst galaxies (Goto, 2006; Wild et al., 2010) and star formation in AGN (Davies et al., 2007; Ramos Almeida et al., 2013; Esquej et al., 2014) supports this picture. Other simulations suggest that most star formation occurs in a circumnuclear ring, which could be coincident with the dusty torus of the AGN unification model (Wada & Norman, 2002; Thompson et al., 2005; Kawakatu & Wada, 2008).

Star formation is traditionally probed by UV emission, Hα, Paα, [Ne II] 12.8 μm, and modelling of stellar populations. However, in the vicinity of AGN, emission from the accretion process contaminates these tracers. Alternatively, emission features in the mid-infrared (mid-IR) provide a powerful tool to test recent and ongoing star formation — most prominent the 6.2, 7.7, 8.6, and 11.3 μm emission complexes. These aromatic features (hereafter PAH), assumed to originate from stretching and bending modes of poly-cyclic aromatic hydrocarbon molecules (Leger & Puget, 1984; Allamandola et al., 1985, 1989; Tielens, 2008), are supposedly excited by UV radiation from young massive O- and B-stars (Roche & Aitken, 1985; Roche et al., 1991). The strength of these features has been shown to be a good tracer of star formation rates due to their strong correlation with the infrared luminosity in pure starbursts (e.g., Peeters et al., 2004; Brandl et al., 2006).

PAH features are surprisingly abundant even in the AGN proximity (e.g., Roche et al., 1991; Clavel et al., 2000; Siebenmorgen et al., 2004; Davies et al., 2007; Smith et al., 2007; Deo et al., 2009; Wu et al., 2009; Diamond-Stanic & Rieke, 2010, 2012; Díaz-Santos et al., 2010; Hönig et al.,

2010; Sales et al., 2010; Tommasin et al., 2010; González-Martín et al., 2013; Alonso-Herrero et al., 2014, 2016; Esquej et al., 2014), although they can be easily destroyed by strong radiation fields (Voit, 1992). On the other hand, PAH features are suppressed in AGN compared to star forming galaxies (Roche et al., 1991; Peeters et al., 2004; Smith et al., 2007), with the caveat that the decrease found in PAH equivalent width can be interpreted as being due to increased dilution from the AGN continuum rather than destruction of the PAH molecules (see for example Esquej et al. (2014) and Alonso-Herrero et al. (2014) for a discussion of this issue). More specifically, Diamond-Stanic & Rieke (2010) find the 11.3 μm feature to be a good tracer of star formation in AGN while the 6.2, 7.7, and 8.6 μm features are too suppressed for this purpose. This relatively larger suppression of PAH features at shorter wavelengths was interpreted as selective destruction of the smallest PAH molecules by the radiation field from the AGN (Smith et al., 2007). On the contrary, the survival of PAH grains in the nuclear regions of AGN may be related to (self-)shielding from the nuclear radiation field in dense regions (e.g., Esquej et al., 2014; Alonso-Herrero et al., 2014).

Most of the previous assessments of PAH in the AGN vicinity assume that the PAH features are exclusively excited by circumnuclear kpc-scaled star formation. In this work, we study the spatially resolved 11.3 μm PAH feature at unprecedented spatial resolution from $\sim$10 pc to $<$1000 pc. A specific focus is put on the question if the AGN may play a significant role in exciting the PAH grains on these small, previously untested spatial scales. While it may be difficult to spectrally disentangle both contributions, we follow the idea of spatially mapping the emitted surface flux of the PAH on scales of few tens of parsec around the AGN and assess the spatial distribution as well as the energy budget. For this, we establish the radial distribution of the 11.3 μm PAH feature from within $\sim 10-1000$ pc around our sample of nearby AGN. We then discuss the observed fluxes, both in physical scaling and AGN-luminosity normalised scales. The results are put into physical context using CLOUDY simulations and a discussion of stellar clusters in two examples. A brief description of the observations and the data is presented in § 5.3 and our method for extracting the 11.3 μm PAH feature is described in § 5.4. In § 5.5 we present a novel relation between the intrinsic X-ray luminosity of an AGN and its dust sublimation radius to be able to compare the same intrinsic scales for AGN with different luminosities. In § 5.6 we present the radial dependence of the PAH features, and we discuss these results in the context of CLOUDY models and PAH excitation by stars in § 5.7. Finally, in § 5.8, we present our conclusions.

5.3 Observations and data

The goal of this paper is to spatially map the emitted 11.3 μm PAH emission in the vicinity of AGN. For this purpose we use archival low-resolution 8–13 μm spectrosopic data from Very Large Telescope (VLT) Spectrometer and Imager for the mid-InfraRed (VISIR; Lagage et al., 2004) observations of a sample of local AGN (Hönig et al., 2010; Burtscher et al., 2013). We supplement these data with new, unpublished observations taken in 2005, 2008, and 2010, which represent VISIR spectra for Circinus, ESO 138-G001, F9, F49, and NGC 1068. Information on these previously unpublished observations

Table 5.1 Previously unpublished data

Object	Obs. ID	RA [h m s]	Dec [° ′ ″]	Obs. Date [YY-MM-DD]	Slit Width [arcsec]	Slit Orientation [°]
NGC 1068	075.B-0163(A)	02 42 40.7	-00 00 48	05-11-18	0.4	356
Circinus	280.B-5068(A)	14 13 09.9	-65 20 21	08-03-14	1.0	315
ESO138-G001	085.B-0251(A)	16 51 20.1	-59 14 05	10-06-27	0.8	320
F9	085.B-0251(B)	01 23 45.8	-58 48 21	10-07-20	0.8	45
F49	085.B-0251(A)	18 36 58.3	-59 24 09	10-09-01	0.8	105

are shown in Table 5.1. For the archival data, a slit width of 0.8 arcsec was used, except for NGC 4507, MCG-3-34-64 and IC5063 observed with a 1.0 arcsec slit, and ESO 323-G77, MCG-6-30-15, IC4329A, NGC 5643 and NGC 5995 observed with a 0.75 arcsec slit. More information on the archival data can be found in the respective sources listed in Table 5.2. The sample represents the highest spatial resolution observations available in the mid-IR and is typical of the local population of AGN. The data reduction and calibration follows the methods and tools outlined in Hönig et al. (2010). This includes the standard ESO pipeline [2] and additional procedures to model and remove a periodic background pattern from the observations. Moreover, flux calibration is carried out on the full 2-dimensional spectrum instead of only an optimised aperture. These ground-based observations achieve angular resolutions of 0.3–0.4 arcsec.

The final sample contains 28 nearby AGN at distances from 4.2 to 248 Mpc (median distance of 45.3 Mpc; see Table 5.2). We supplement these data with absorption-corrected 2–10 keV luminosities compiled by Asmus et al. (2015). These data allow us to estimate the intrinsic strength of the AGN and establish a luminosity independent "intrinsic" scaling for the AGN (see Sect. 5.5). We find a range of 1.3×10^{42} to 4.0×10^{44} erg s^{-1} for our sample, which puts all objects firmly into the Seyfert regime. We note that one of our objects (NGC 7213) is classified as a broad-line LINER (Véron-Cetty & Véron, 2010).

5.4 Extraction of the 11.3 μm PAH feature

Ground-based mid-IR observations of PAH features provide the highest angular resolution. However, they are restricted to the atmospheric N-band window between 8 and 13 μm, which limits the choice of features that can be investigated to the 7.7/8.6 μm complex and the 11.3 μm PAH features. Of these two spectral regions, only the 11.3 μm feature is completely within the spectral range covered by VISIR. Therefore we spatially map the 11.3 μm PAH feature as a proxy for PAH molecules. We reiterate that this feature seems to be the one least suppressed by radiation around AGN (Smith et al., 2007; Diamond-Stanic & Rieke, 2010). For each object, we extract spectra at various distances from the nucleus in steps of 0.4 arcsec and aperture widths of 0.4 arcsec, which corresponds to the typical spatial resolution of the data at this wavelength.

[2] http://www.eso.org/sci/software/pipelines/visir/visir-pipe-recipes.html

Table 5.2 Characteristics of our AGN mid-IR spectroscopic sample

Object	Type[a]	RA [h m s]	Dec [° ′ ″]	z[b]	D_L[c] [Mpc]	Slit ori.[d] [°]	log L_X [e] [erg/s]	r_{sub} [f] [pc]	Ref.[g]	PAH detected
IZw1	S1h	00 53 34.9	+12 41 36	0.0578	269.0	1	43.68 ± 0.17	0.081 ± 0.021	3	yes
F9	S1.2	01 23 45.8	-58 48 21	0.0466	215.0	45	43.99 ± 0.11	0.111 ± 0.025	1	no
NGC 1068	S1h	02 42 40.7	-00 00 48	0.0030	14.4	356	43.64 ± 0.30	0.078 ± 0.036	1	no
NGC 1365	S1.8	03 33 36.4	-36 08 25	0.0051	17.9	303	42.12 ± 0.20	0.017 ± 0.005	3	no
LEDA 17155	S1h	05 21 01.4	-25 21 45	0.0427	196.0	360	44.46 ± 0.40	0.180 ± 0.130	3	yes
NGC 2110	S1h	05 52 11.4	-07 27 22	0.0080	35.9	55	42.67 ± 0.10	0.029 ± 0.005	2	no
ESO 428-G14	S2	07 16 31.2	-29 19 29	0.0063	28.2	60	42.15 ± 0.37	0.017 ± 0.011	2	no
MCG-5-23-16	S1i	09 47 40.1	-30 56 55	0.0095	42.8	50	43.28 ± 0.30	0.054 ± 0.025	2	no
MARK 1239	S1n	09 52 19.1	-01 36 43	0.0211	95.4	320	43.32 ± 0.30	0.056 ± 0.026	3	no
NGC 3227	S1.5	10 23 30.6	+19 51 54	0.0049	22.1	300	42.14 ± 0.21	0.012 ± 0.001	2	yes
NGC 3281	S2	10 31 52.1	-34 51 13	0.0118	52.8	5	43.27 ± 0.37	0.054 ± 0.016	3	no
NGC 3783	S1.5	11 39 01.7	-37 44 19	0.0108	48.4	315	43.24 ± 0.07	0.071 ± 0.004	2	no
NGC 4507	S1h	12 35 36.6	-39 54 33	0.0128	57.5	330	43.21 ± 0.17	0.050 ± 0.030	2	no
ESO 323-G77	S1.2	13 06 26.1	-40 24 53	0.0159	71.8	354	42.76 ± 0.12	0.032 ± 0.004	2	yes
MCG-3-34-64	S1h	13 22 24.4	-16 43 42	0.0176	79.3	315	43.33 ± 0.48	0.057 ± 0.014	2	no
MCG-6-30-15	S1.5	13 35 53.7	-34 17 44	0.0087	38.8	30	42.80 ± 0.14	0.033 ± 0.006	2	yes
IC 4329A	S1.2	13 49 19.2	-30 18 34	0.0170	76.5	120	43.85 ± 0.09	0.130 ± 0.080	2	no
Circinus	S1h	14 13 09.9	-65 20 21	0.0019	4.2	315	42.26 ± 0.28	0.019 ± 0.017	1	yes
NGC 5643	S2	14 32 40.7	-44 10 28	0.0047	20.9	85	42.23 ± 0.38	0.019 ± 0.004	2	yes
NGC 5995	S1.9	15 48 24.9	-13 45 28	0.0257	117.0	60	43.45 ± 0.15	0.064 ± 0.010	2	yes
ESO 138-G001	S2	16 51 20.1	-59 14 05	0.0093	41.8	320	43.31 ± 0.37	0.056 ± 0.023	1	yes
F49	S1h	18 36 58.3	-59 24 09	0.0199	90.1	105	43.34 ± 0.11	0.057 ± 0.036	1	yes
MARK 509	S1.5	20 44 09.7	-10 43 25	0.0335	153.0	315	44.12 ± 0.09	0.125 ± 0.008	2	no
IC 5063	S1h	20 52 02.3	-57 04 08	0.0109	49.1	45	42.86 ± 0.10	0.035 ± 0.008	2	no
NGC 7213	S3b	22 09 16.3	-47 10 00	0.0051	23.0	300	42.19 ± 0.06	0.018 ± 0.011	2	no
NGC 7469	S1.5	23 03 15.6	+08 52 26	0.0151	67.9	315	43.19 ± 0.07	0.041 ± 0.001	2	yes
NGC 7582	S1i	23 18 23.5	-42 22 14	0.0044	23.0	60	42.53 ± 0.38	0.025 ± 0.005	2	yes
NGC 7674	S1h	23 27 56.7	+08 46 45	0.0277	126.0	120	44.02 ± 0.55	0.115 ± 0.025	2	yes

Note. — [a] AGN types from Véron-Cetty & Véron (2010); [b] redshifts from NED; [c] luminosity distance based on CMB reference frame redshifts from NED and $H_0 = 73$ km s^{-1} Mpc^{-1}, $\Omega_{\rm m} = 0.27$, and $\Omega_{\rm vac} = 0.73$; [d] slit orientation; [e] L_X = absorption-corrected 2-10 keV luminosity from Asmus et al. (2015); [f] dust sublimation radius calculated from equation 5.1 in this work, except for IC4329 A (Kishimoto et al., 2011), NGC 3783 (Glass, 1992), and MARK 509, NGC 3227, and NGC 4593 (Koshida et al., 2014); [g] reference for the VISIR spectroscopic data.

References. — (1) This work; (2) Hönig et al. (2010); (3) Burtscher et al. (2013).

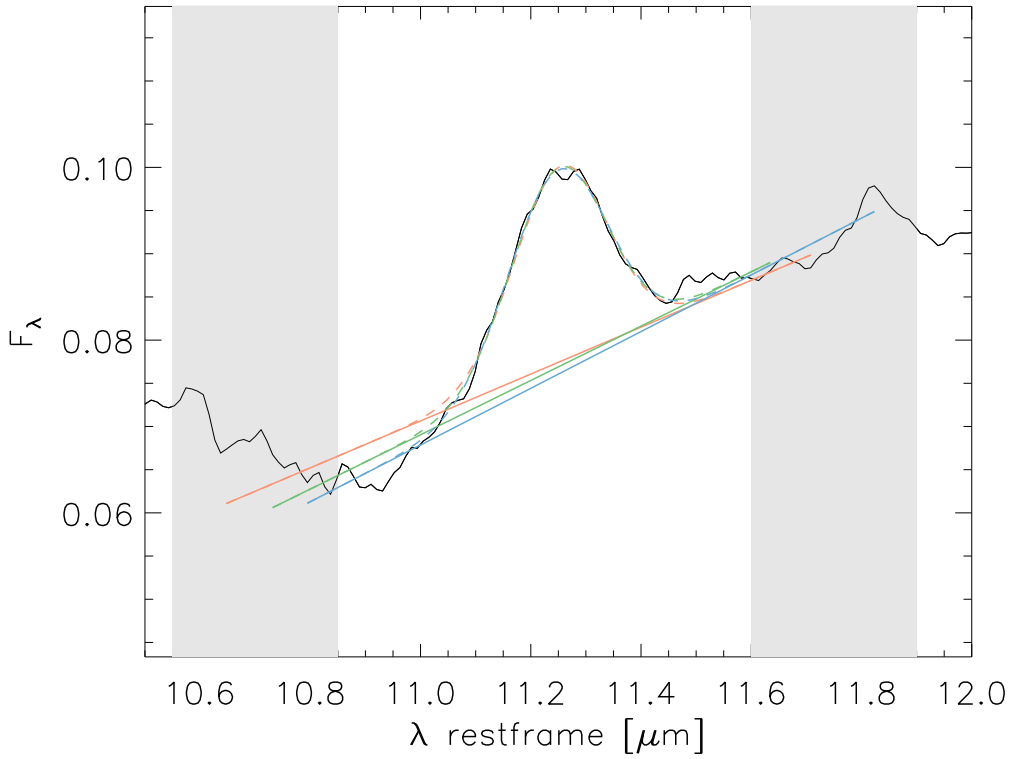

Fig. 5.1 Three examples of fits to the 11.3 μm PAH feature in the spectrum extracted at an offset of 0.4 arcsec from the nucleus in NGC 3227. The shaded gray areas show the spectral regions from which the continuum anchors are drawn. Each fit is shown in its own color with the continuum as the solid line and the Gaussian model as the dashed line.

The emitted PAH flux in each spectrum is calculated from a Gaussian model fit to the continuum-subtracted 11.3 μm emission. We note that other studies have used different functional forms for the PAH emission (e.g., Uchida et al., 2000; Peeters et al., 2002; Smith et al., 2007) but since we are only interested in the strength, not the shape, of the feature, a Gaussian function is sufficient for our purpose[3]. The continuum is modelled by a local linear fit. This fitting routine is repeated 50 times for each spectral extraction by randomly varying the continuum anchors on each side of the PAH feature. Three examples of these Gaussian models are shown in Figure 5.1. Such a Monte-Carlo-based procedure, similar to the one used by Hernán-Caballero & Hatziminaoglou (2011), allows us to include the systematic uncertainty due to the selection of the continuum subtraction into the overall errors of the extracted lines. The continuum anchors are generally drawn from the regions between 10.55–10.85 μm and 11.6–11.9 μm in the rest frame. However, we varied these windows slightly if significant background contamination was present. For each repetition of the fitting routine we manually reject or accept the fit. The mean and standard deviation of all accepted fits for a given extraction is then used as the measured PAH flux and its uncertainty, respectively. In those cases where the signal-to-noise (S/N) ratio of the continuum drops below 1 or where no clear 11.3 μm PAH feature is present, we attempt to measure an upper limit. In a few cases, neither a measurement nor an upper limit can be extracted, simply because the spectrum is completely noise dominated or there is not enough flux in the spectrum.

As a note of caution, we risk underestimating the uncertainty of our fits by biasing the manually accepted fits to those that look similar. If the noise in our manually chosen continuum regions does not represent the true amount of continuum noise we also risk to underestimate the 11.3 μm PAH flux uncertainty. This is especially a concern if the continuum range is narrow, the spectral noise is low, or both. However, given the wide range of continuum shapes and noise levels, in addition to the narrow spectral range of our data, the outlined procedure is the most practical one.

We find PAH features in 13 out of the 28 objects. The PAH luminosity as a function of physical distance from the AGN for these 13 objects is shown in Figure 5.2. This detection rate is similar to what is found in other studies of Seyfert galaxies (e.g., Esquej et al., 2014; Alonso-Herrero et al., 2016). For Circinus and Mark 1239, we do not detect the 11.3 μm PAH feature in the central aperture, but the feature appears at apertures further away from the nucleus. For Circinus, this is consistent with the work by Roche et al. (2006) who found the 11.3 μm PAH feature to be very weak within 2 arcsec of the nucleus.

Figure 5.5 shows upper limits for the 15 AGN where we do not detect the 11.3 μm PAH feature. Most of these are within the region (gray shaded area) where we detect PAH features for the remaining 13 objects in our sample, which means that the PAH features might very well be present in these objects, but that they are too weak for us to detect them. For the few remaining sources, we can only speculate as to why we do not find any 11.3 μm PAH feature. One possibility is that the molecular clouds are not sufficiently self-shielding to protect the PAH molecules from destruction by the hard

[3]It should be noted that the fitting procedure used makes the 11.3 μm feature strengths about half the ones derived with PAHFIT (see Figure 8 and Table 6 in Smith et al., 2007).

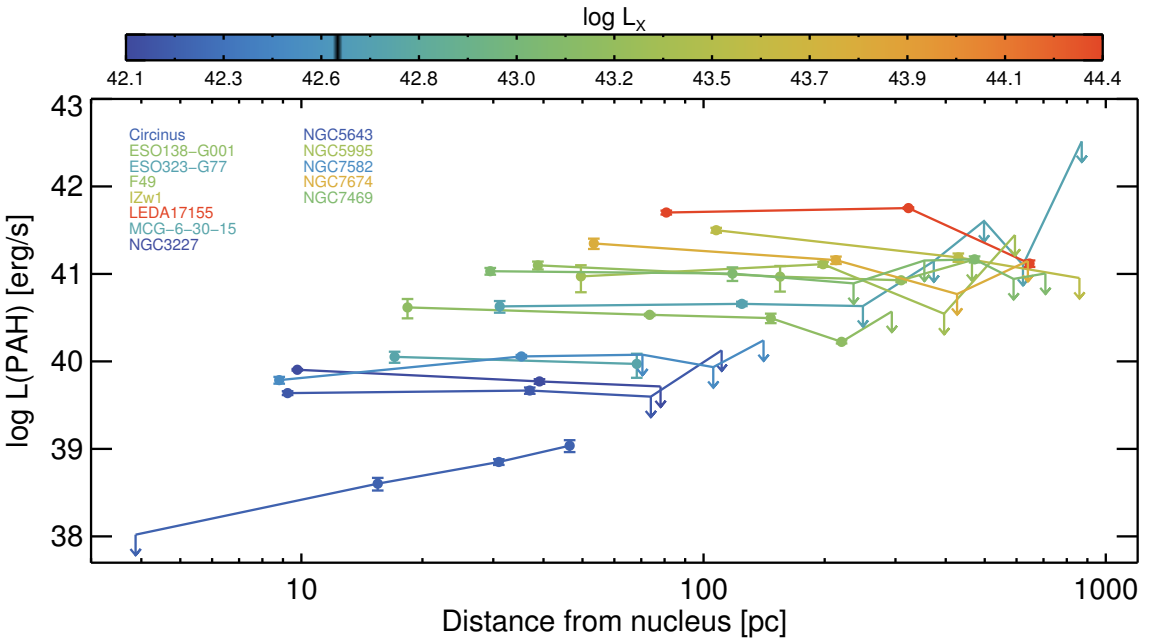

Fig. 5.2 Luminosity of the 11.3 μm PAH feature measured within 0.4 arcsec apertures as a function of physical distance for the 13 AGN in our sample where we detect the feature. Upper limits are shown as downward arrows. Each object is colour coded according to its intrinsic X-ray luminosity L_X listed in Table 5.2.

AGN radiation field. This could be a matter of either not dense enough clouds or too few clouds, meaning a too low covering factor, or both. As an example, work by Mason et al. (2009) shows that modeling the silicate emission of NGC 2110 favors models with only a few clouds along the line of sight, probably not enough to provide sufficient self-shielding for the PAH grains to survive in the vicinity of the AGN. We stress that these suggestions only are speculative and need further investigation in the future.

For fifteen of the objects in our sample, the 11.3 μm PAH feature flux and equivalent width have been measured previously by Esquej et al. (2014) using spectra extracted with aperture sizes between 0.35 and 1.00 arcsec (except for Circinus where they used a 3.7 arcsec aperture). For ESO323-G77, we detect the 11.3 μm PAH feature whereas Esquej et al. (2014) only provide an upper limit. Our measurement is consistent with this upper limit. For two objects, NGC 1068 and Mark 509, Esquej et al. (2014) detect the 11.3 μm PAH feature, whereas we are unable to reliably measure a flux. For these two objects, we find that the contrast between the feature and the underlying continuum in the central aperture is too low for a detection within our extraction process. For the rest of the objects common to both studies, detections and non-detections agree. Figure N.1, Figure N.2, and Figure N.3 in Appendix N show the spectra extracted inside the central 0.4 arcsec aperture for all the objects in our sample.

In Appendix O, we show the emitted surface flux of the 11.3 μm PAH feature and the underlying continuum for the 13 objects where we detect the feature. For all these objects, the emitted continuum

surface flux – originating from the unresolved nuclear source – declines more rapidly than that of the 11.3 μm PAH feature. A similar behaviour was found by Alonso-Herrero et al. (2014) for a few local AGN observed with the Gran Telescopio CANARIAS CanariCam. This means that the PAH features are indeed spatially resolved, at least marginally. However, this also implies that the point spread function (PSF) will affect the radial profiles of the PAH features and needs to be taken into account when modelling/interpreting the results. All the extracted spectra for the 28 objects are made available online[4].

5.5 The $L_X - r_{sub}$ correlation

In our data analysis and discussion, we want to assess if the AGN has any influence on the PAH feature in its vicinity by searching for evidence that the PAH strength in the nucleus is (universally) related to that of the AGN. However, our AGN sample spans a large range in luminosity and distance: the same angular scale corresponds to a different degree of incident AGN flux, since both the physical distance from the AGN and the AGN intrinsic luminosity determine its strength in each of our extraction windows. The difference in physical scales (=pc; as shown in Fig. 5.2) can easily be accounted for by taking into account the physical distances from the AGN for each of our extraction windows in each source. For the differences in incident AGN radiation, we have to further normalise the extractions windows according to a scale that accounts for the $1/r^2$ dilution of radiation. We thus normalise the emission profile by a scale intrinsic to the AGN allowing us to directly compare the objects.

Since the PAH features are supposedly originating from dense molecular and dusty clouds, a convenient choice for such an intrinsic scale is the dust sublimation radius. Unfortunately, only few of the type 1 objects in our sample have measured sublimation radii from near-IR interferometry or reverberation mapping (Glass, 1992; Kishimoto et al., 2009, 2011; Koshida et al., 2014). Moreover, the current empirical relations between AGN optical luminosity and hot dust time lags are only applicable to type 1 AGN, since type 2s suffer from significant obscuration in the optical. Therefore we take a different approach and aim at establishing a relation between an intrinsic AGN luminosity tracer that is unaffected by obscuration and the near-IR time lags. For that we compile a sample of 11 sources that have both near-IR time lag measurements and absorption-corrected 2–10 keV X-ray luminosities (L_X). These are listed in Table 5.3 and the data are visualised in Fig. 5.3. Using X-rays has the advantage that intrinsic X-ray luminosities can be estimated even for highly obscured sources up to the Compton-thick limit, and beyond, if one can robustly model the broadband X-ray spectra (for a discussion of uncertainties in intrinsic X-ray luminosities of Compton-thick AGN, see for example Gandhi et al., 2014, 2015), which allows us to reliably estimate the sublimation radius in optically-obscured type 2 AGN.

We model the data with a power-law of the form $r_{sub} \propto L^{\gamma}$ using the IDL procedure `linmix_err` (Kelly, 2007). The underlying method uses a Bayesian approach to linear regression and accounts

[4]Will be made available on VizieR upon publication

Table 5.3 Objects used to calibrate the $L_X - r_{sub}$ relation

Object	r_{sub} [pc]	$\sigma(r_{sub})$ [pc]	Ref.	log L_X [a]	$\sigma(\log L_X)$ [b] [erg/s]	Ref.
Akn 120	0.1165	0.0147	1	43.90	0.06	4, 5, 6
IC 4329A[c]	0.13	0.08	2	43.85	0.09	7, 8, 9, 6
MARK 509	0.125	0.008	1	44.12	0.09	10, 11, 12
MARK 590	0.0312	0.0023	1	42.98	0.09	13, 14, 15
NGC 3227	0.0122	0.0005	1	42.14	0.21	16, 8, 12, 6
NGC 3783	0.071	0.004	3	43.24	0.07	17, 18, 19, 6
NGC 4051	0.0123	0.0004	1	41.55	0.17	20, 21, 22, 6
NGC 4151	0.0417	0.0006	1	42.52	0.29	18, 23, 24
NGC 4593	0.0365	0.0015	1	42.86	0.31	25, 18, 26, 6
NGC 5548	0.0463	0.0006	1	43.38	0.25	27, 28, 18
NGC 7469	0.0405	0.0012	1	43.19	0.07	29, 17, 18

Note. — [(a)] L_X = absorption-corrected 2-10 keV luminosity from Asmus et al. (2015) with the original references from that work listed in the last column of this table; [(b)] $\sigma(\log L_X)$ = uncertainty on L_X adopted from Asmus et al. (2015); [(c)] we assign an uncertainty of 0.2 dex to r_{sub} for IC4329A based on the scatter in Figure 4 of Kishimoto et al. (2007) between radial size and UV-luminosity and Figure 30 in Suganuma et al. (2006) between time lag (i.e., radial size) and V-band magnitude as quoted by Kishimoto et al. (2011).

References. — (1) Koshida et al. (2014); (2) Kishimoto et al. (2011); (3) Glass (1992); (4) Vasudevan & Fabian (2009); (5) Winter et al. (2012); (6) Winter et al. (2009); (7) Dadina (2007); (8) Brightman & Nandra (2011); (9) Brenneman et al. (2014); (10) Shinozaki et al. (2006); (11) Ponti et al. (2009); (12) Shu et al. (2010); (13) Gallo et al. (2006); (14) Longinotti et al. (2007); (15) Rivers et al. (2012); (16) Markowitz et al. (2009); (17) Nandra et al. (2007); (18) Rivers et al. (2011); (19) Brenneman et al. (2011); (20) King et al. (2011); (21) McHardy et al. (2004); (22) Vaughan et al. (2011); (23) Wang et al. (2010); (24) Lubiński et al. (2010); (25) Horst et al. (2008); (26) Markowitz & Reeves (2009); (27) Andrade-Velázquez et al. (2010); (28) Krongold et al. (2010); (29) Asmus et al. (2015).

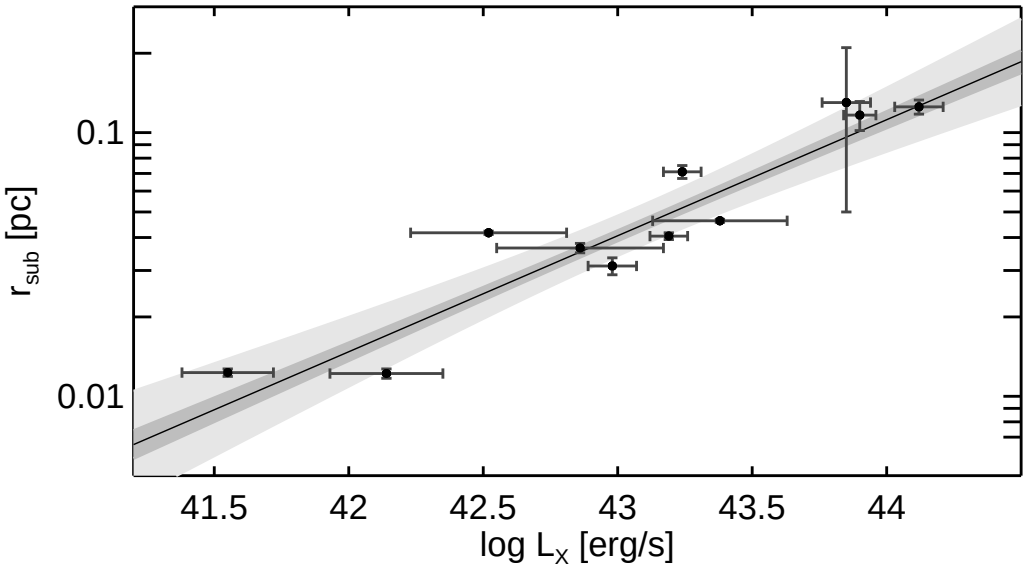

Fig. 5.3 Dust sublimation radius (r_{sub}) as a function of intrinsic 2–10 keV X-ray luminosity (L_X) for the 11 type 1 AGN summarised in Table 5.3. Solid line shows the best power-law fit using `linmix_err`. Shaded areas shows the 68 and 95 per cent confidence intervals, respectively.

for effects of uneven sampling. The data and best-fit linear regression (solid black line) are shown in Figure 5.3. The best-fit model parameters are

$$r_{\rm sub} = (0.0407 \pm 0.0003)\,{\rm pc} \left(\frac{L_{\rm X}}{10^{43}\,{\rm erg/s}} \right)^{0.44\left(^{+0.06}_{-0.07}\right)} \tag{5.1}$$

with a correlation strength measured in terms of the Spearman rank of $\rho_s = 0.97^{+0.02}_{-0.06}$. The power-law slope of $0.44^{+0.06}_{-0.07}$ is consistent with the canonical $1/2$ within the 68 per cent confidence interval (Barvainis, 1987; Suganuma et al., 2006; Kishimoto et al., 2007). Since the relation between X-ray and UV-optical luminosity is observed as non-linear (e.g., Lusso et al., 2010; Marchese et al., 2012), a deviation from $1/2$ may however be expected. The bisector regression of the $L_{\rm disc} - L_{2-10\,{\rm keV}}$ relation of Marchese et al. (2012) implies a $r_{\rm sub} - L_{\rm x}$ power-law index of $\sim 0.42 \pm 0.03$, which is consistent with our measurement.

The luminosity range spanned by the 11 objects in Table 5.3 is almost identical to that of the 28 objects of our main sample. Together with the fact that we use the intrinsic X-ray luminosity, this justifies our use of equation 5.1 to estimate dust sublimation radii for both type 1 and type 2 AGN, at least for objects that are not Compton-thick. We note that some of our sources are Compton-thick but that we consider their L_X measurements to be very reliable as they are shown to lie on the same $L_X - L_{\rm MIR}$ correlation as those sources that are not Compton-thick (Gandhi et al., 2009; Asmus et al., 2015). In addition, detailed broadband X-ray spectroscopy of several of these has found excellent agreement with expectations based upon the correlation (cf. Bauer et al. (2015) for NGC 1068; Arévalo et al. (2014) for Circinus; Annuar et al. (2015) for NGC 5643).

5.6 Results and analysis

5.6.1 Qualitative analysis

In Fig. 5.2, we show the radial dependence of the PAH luminosities, scaled in physical units. As can be seen, the absolute scaling is offset by more than 3 orders of magnitudes. The physical scales of detected fluxes range from 8 pc to 700 pc (i.e. 2 orders of magnitudes), which illustrates the increased spatial resolution of about a factor of 10 as compared to Spitzer IRS observations. Given the large offset in luminosities, it is difficult to make a comparison between the different objects from this plot. In particular, if we are interested in the possible effect of the AGN on the PAHs, we want to make sure that the physical scales and the observed fluxes of all the objects are normalised for the difference in AGN luminosities. Therefore, we normalise the physical scales by an AGN-intrinsic scale – here the dust sublimation radius as defined in section 5.5. We also use the same intrinsic scale to normalise the observed PAH fluxes or luminosities to the emitted surface flux from the respective spatial scale. This way, any given distance from the AGN receives the same radiation field from the AGN in all sources and the emitted radiation can directly be compared among the different objects.

Figure 5.4 shows this renormalised, emitted 11.3 μm PAH surface flux for the 13 objects where we detect this feature. These were calculated from the extracted PAH fluxes and the respective aperture area. The first interesting observation of this renormalisation is that the overall range in observed PAH fluxes is reduced from more than 3 orders of magnitudes in the physical scaling to less than 1 order of magnitude in the AGN-normalised scaling. If the PAH emission would be independent of the AGN, we would not necessarily expect that scaling for the AGN would reduce the scatter in the observed flux normalisations of the sample, unless the star formation closely correlates with the AGN activity in all galaxies. Therefore, the source of PAH excitation must be related to the AGN power, i.e., it could either be a physical process that scales with the AGN power or it could be the AGN itself. We will discuss these scenarios further in section 5.7.

The second interesting observation of this AGN-normalised PAH emission concerns the dependence on distance. In Fig. 5.4, we see that all objects except for Circinus fall into a narrow band where the PAH surface flux decreases with increasing distance from the AGN. This confirms the earlier finding by Alonso-Herrero et al. (2014) for Seyferts and LIRGs. The band only widens at distances larger than $\sim$5,000 r_{sub} (marked by the grey-hatched area), although part of this widening is related to non-detections rather than detections. A prominent example of the change in behaviour at distances $>$5,000 r_{sub} is NGC 7469 (green labelled curve in Figure 5.4). This source has a well known starburst ring at about 2 arcsec distance from the AGN (Genzel et al., 1995; Díaz-Santos et al., 2007), which coincides with this turnover. As such, the turnover in this source indicates that local star formation activity clearly is the dominant contributor to the PAH emission at these radii. We will statistically analyse the scatter in the slopes of all the objects in the next subsection.

Circinus is an outlier both in terms of radial slope as well as absolute PAH surface flux. Tristram et al. (2014) have shown that it has a strong optical depth gradient of $\Delta\tau = 27$ arcsec^{-1} in the mid-IR from the west to the east side of the nucleus on parsec scales. Such a gradient was also found by Roche et al. (2006), albeit with a value of only $\Delta\tau = 0.6$ arcsec^{-1} and on larger scales. Larger scale observations indicate that the eastern side of the galactic disc (Freeman et al., 1977) and a circumnuclear molecular ring (Curran et al., 1998, 1999) are closer to us, so that the obscuration increases towards the nucleus (see also Mezcua et al., 2016). This provides a feasible explanation for the reverse slope we observe for the PAH features in Circinus compared with the rest of our sample. Indeed, we find a slope of the PAH features in Circinus which corresponds to a gradient in the optical depth of $\Delta\tau = 2.5$ arcsec^{-1} at mid-IR wavelengths, in between the two previous measurements. Therefore, we consider Circinus as a special case and leave it out of the following analysis. This leaves us with 12 objects to investigate quantitatively.

5.6.2 Statistical analysis

We want to quantify the slope of the radial dependence of the PAH emission by a model of the form $\log\Sigma_{PAH} = \log\Sigma_{0,\mathrm{PAH}} + \alpha * \log(r_{\mathrm{sub}})$. For that, we first model the emitted PAH fluxes for each object individually and then combine the results to obtain a joint probability distribution function for the

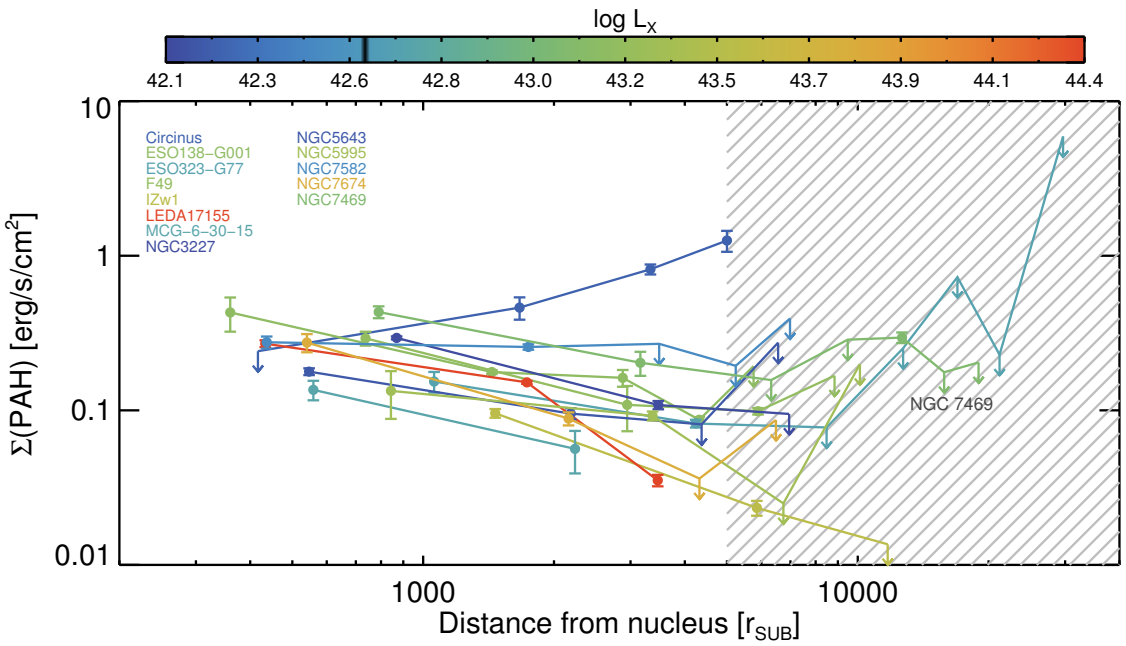

Fig. 5.4 Emitted surface flux of the 11.3 μm PAH feature measured within 0.4 arcsec apertures as a function of sublimation radius for the 13 AGN in our sample where we detect such features. Upper limits are shown as downward arrows. The hashed gray area above 5000 r_{sub} shows where emission associated with star formation starts to become the dominant excitation mechanism for the PAH grains (see § 5.6). Each object is colour coded according to its intrinsic X-ray luminosity L_X.

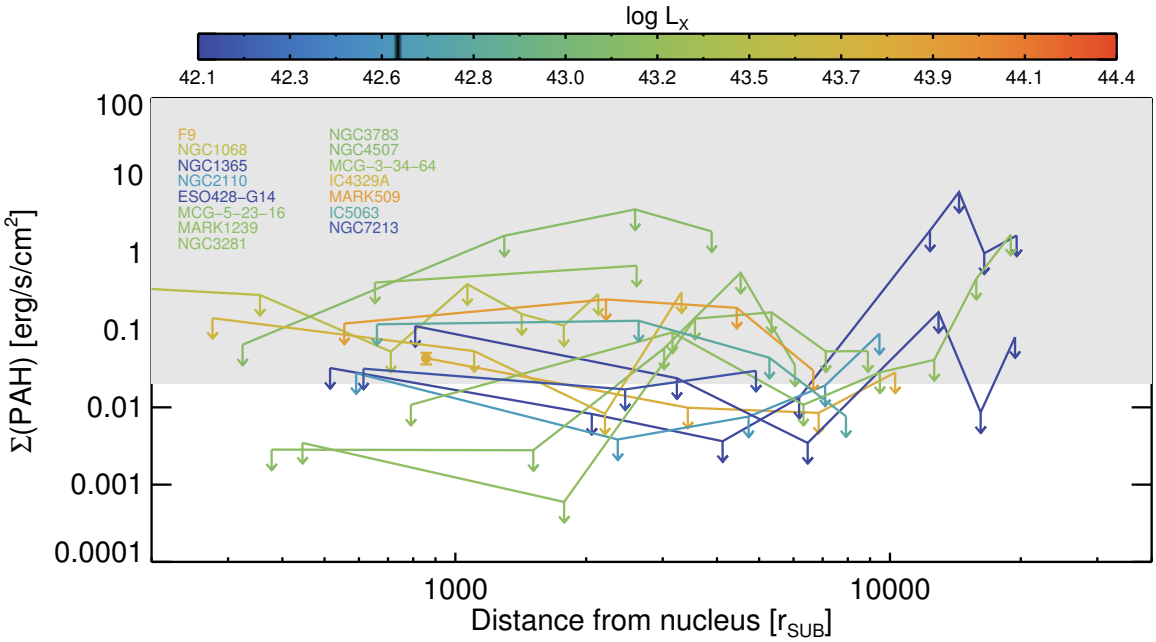

Fig. 5.5 Upper limits for the emitted surface flux of the 11.3 μm PAH feature measured within 0.4 arcsec apertures as a function of sublimation radius (see § 5.5) for the 15 AGN in our sample where we do not detect the feature. The shaded gray area shows where our detections fall (see Figure 5.4) and indicate the detection limit for the 11.3 μm PAH feature. Each object is colour coded according to its intrinsic X-ray luminosity L_X.

Table 5.4 Slope of the r_{sub} vs. Σ_{PAH} relation

$r_{sub,outer}$	$\alpha_{bin=0.01}$ [a]	$\alpha_{bin=0.1}$ [b]	σ_α [c]	$n_{objects}$
3000	$-0.69^{+0.33}_{-0.20}$	$-0.8^{+0.3}_{-0.3}$	0.32	2
5000	$-1.19^{+0.10}_{-0.05}$	$-1.2^{+0.2}_{-0.1}$	0.42	5
6000	$-1.16^{+0.06}_{-0.04}$	$-1.1^{+0.1}_{-0.1}$	0.36	7
7000	$-1.15^{+0.04}_{-0.04}$	$-1.1^{+0.1}_{-0.1}$	0.40	9
10000	$-1.14^{+0.04}_{-0.03}$	$-1.0^{+0.1}_{-0.1}$	0.35	10

Note. — [a] Median slope and $\pm1\sigma$ uncertainty using a bin size of 0.01 for the joint probability distribution; [b] median slope and $\pm1\sigma$ uncertainty using a binsize of 0.1 for the joint probability distribution; [c] scatter of the fitted slopes. For a radial cutoff between 5000 and 7000 r_{sub}, the spearman rank significance for most objects is < -0.8.

power-law slope. Since some objects show changes in the slope at larger radii, we also investigate how selection of an outer cut-off affects the fit. We perform a linear regression in log-log space using radial cut-offs at 3000, 5000, 6000, 7000, and 10,000 r_{sub}, respectively (see Table 5.4). When modelling the PAH emission for each object, we generate 10,000 random realisations of the data using Monte Carlo simulations to account for the measurement uncertainties. We assume all measurements to have normally distributed errors and include the upper limits in the fit by allowing them to take on any value between the measured upper limit and 1 per cent of this value.

Because the point spread function of the observations smears out the signal and distributes flux from smaller to larger radii, we observe a shallower PAH slope than the intrinsic one. To account for this in our fitting process, we convolve the power-law model with a Gaussian function with FWHM = 0.4 arcsec, corresponding to the spatial resolution of the observations. Therefore, the fitted slopes for each object represent the intrinsic dependence, which we will refer to in the following, unless otherwise stated.

We combine the results of the modelling process for each object to get a joint probability distribution function for the power-law slope α. From this distribution we extract the median slope, its 68 per cent confidence interval, and the sample scatter of the fitted slopes. As the resulting probability distribution for the slope depends slightly on how we bin the discrete distributions for α, we calculate results for bin sizes of 0.01 and 0.1, respectively. These joint probability distribution functions are shown in Appendix Fig. P.1. As we require at least three data points to be included within the radial cut-off for each object, the number of objects included in the estimation of the PAH slope increases with radial cut-off. The power-law slopes for each object and each radial cut-off are shown in Table P.1 in Appendix P.

Table 5.4 shows our results for the joint PAH slope using the different radial cut-offs. For radial cut-offs between 5,000 and 10,000 r_{sub}, the slope is similar with a value of approximately -1.1 ± 0.1, independent of the bin size used. For the radial cut-off of 3,000 r_{sub} the slope is very shallow and not consistent with the other cut-offs. However, this cut-off region includes only two objects, which

Table 5.5 Reduced χ^2 statistic for consistency with the single joint slope (second column) and the slope extracted from the CLOUDY models (fourth column). Also listed is the intrinsic scatter in the slopes that needs to be added to receive a reduced $\chi^2_r = 1$ for the joint slope (third column).

$r_{sub,outer}$	χ^2_r joint slope	$\sigma_{\rm int}(\chi^2_r = 1)$	χ^2_r model
3000	0.28	...	1.31
5000	1.08	0.13	0.62
6000	1.74	0.19	0.87
7000	1.76	0.21	0.90
10000	1.66	0.20	1.25

Note. — The number of degrees of freedom are the number of objects as listed in Table 5.4 minus 1.

means that the slope is quite uncertain. Indeed, the slope is still consistent within 1.4σ with all other estimates.

Figure 5.6 shows the individual power-law slopes for the 9 objects within the radial cut-off at 7,000 sublimation radii (solid black circles). We also plot the 68% confidence region of each fitted slope. The joint PAH slope of all 9 objects is shown as a solid black line with the 68% confidence region as a solid gray background.

To judge if a joint slope is a reasonable hypothesis, we test consistency of the individual radial slopes with the nominal joint slope of -1.1. For the different outer cut-offs listed in Table 5.4, we calculate the reduced χ^2_r statistic taking into account the asymmetric errors of the individual slopes and uncertainty in the common slope. The results are shown in Table 5.5. These values may be roughly interpreted as being consistent with *no* joint slope at the $0.5 - 1.7\sigma$ level assuming normally distributed errors. We also test what intrinsic scatter of the population would be required to obtain $\chi^2_r = 1$. These values are listed in the third column of Table 5.5. For comparison, the errors of the individual slopes are given in Appendix Table P.1 and are larger than the required intrinsic scatter. We address expectations for the intrinsic scatter in Sect. 5.7.1.

5.7 Discussion: PAH excitation from a compact central radiation source

The similarity in the relation between PAH surface flux and luminosity-normalised distance from the AGN is not straight-forward to interpret. In a generic scenario where PAH emission only traces star formation, and where star formation and AGN activity are not related, all galaxies should have their own distribution of PAH-emitting gas, depending on the individual star-formation history, without characteristics in common across the sample. Here, we do find a common slope, which would make this scenario unlikely and requires some common physical property to cause the observed radial distribution of the PAH emission.

Since PAH emission is commonly believed to be associated with star formation, one possibility is a common distribution of star formation around the nucleus. This would require a common mechanism

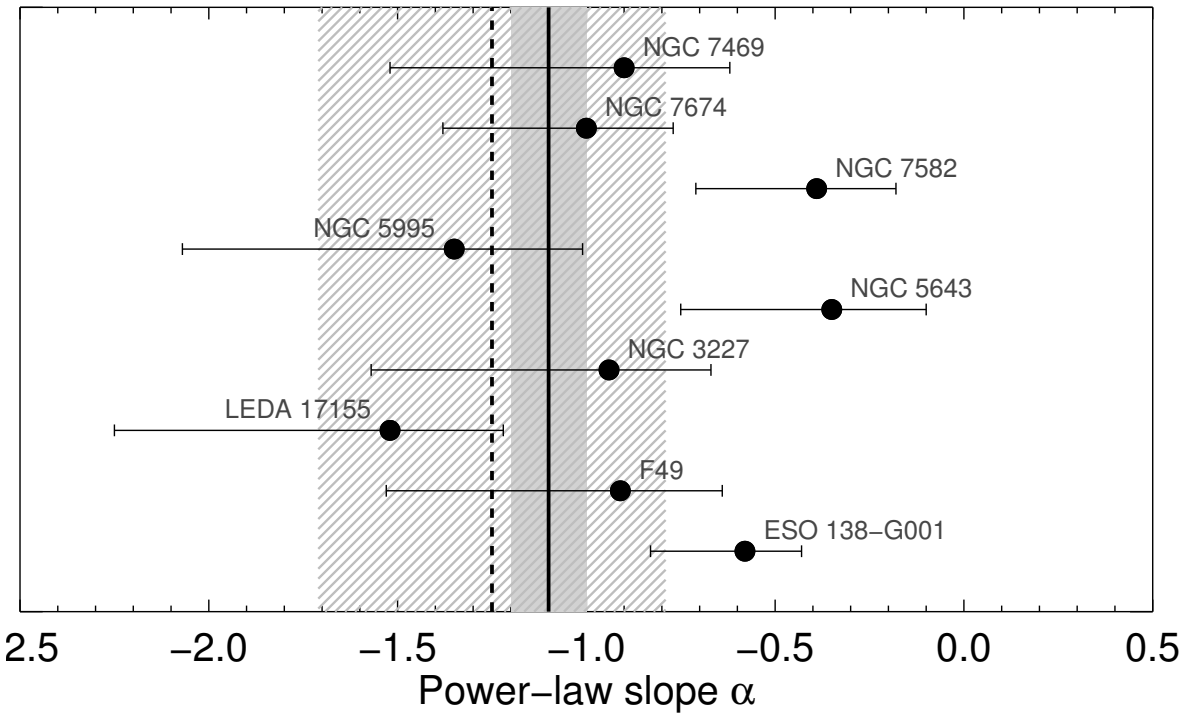

Fig. 5.6 Comparison of individual PAH power-law slopes (filled black circles) and the joint PAH slope (solid black line) and its uncertainty (filled gray area) for a radial cut-off of 7000 r_{sub}. Also shown is the power-law slope fitted to the CLOUDY models of the PAH emission (dashed black line) and its uncertainty (hatched gray area) described in § 5.7.1.

to trigger a universal distance-dependent star formation distribution in the black hole environment, which may be difficult to achieve. On the other hand, we find that the scatter in absolute values of the PAH fluxes reduces overall if we scale with AGN luminosity. Therefore, both the distribution of star formation as well as its strength need tight coupling to the luminosity of the AGN.

An alternative to circumvent the required spatial and energetic relations between AGN and stars is to decouple PAH emission from star formation. This way, it is not necessary to find a physical mechanism that causes a universal radial star formation distribution, but rather a common mechanism for the excitation of PAH emission. Here, we propose that this excitation source should be centrally located and compact with respect to the PAH emission. Under this hypothesis, the main driver for the common radial slope is the r^{-2}-dilution of radiation from the central source of radiation. In principle, this could still lead to different radial slopes: the PAH emission is effectively reprocessed radiation that traces the combination of (diluted) incident radiation and radial distribution of PAH-emitting material. Therefore, the PAH-emitting gas should be fairly uniformly distributed in the central environment, e.g. gas clouds in the ISM. The range in absolute surface flux values, i.e. the relative offsets in Fig. 5.4, is then caused by the volume filling factor of the PAH emitting gas clouds, which can be quite different from object to object. This hypothesis would explain both why we see PAH detections and non-detections among our sample and why those with detections show a common radial slope.

The key questions for this hypothesis are: Is it possible to reproduce the observed slopes? And, does any central radiation source provide enough energy to explain the observed emission? We consider the AGN and a central stellar cluster as the two major viable candidates for the central excitation source. In the following, we will first investigate the AGN by building a CLOUDY model for the proposed scenario and test the slopes and emitted fluxes under the influence of radiation from the AGN. Afterwards, we will discuss the energetic viability of a central stellar cluster as the source of excitation based on observational constraints from two of the objects in our sample.

5.7.1 AGN as the excitation source

We set up a CLOUDY[5] model to test the hypothesis that the AGN acts as a central excitation source for uniformly distributed PAH-emitting gas in the central region. First, we calculate the emission of clouds at a range of distances between approximately 100 and 10 000 r_{sub} from the AGN. The CLOUDY simulations take into account gas and dust physics and were set up to include back-heating effects on each cloud by surrounding clouds. This provides us with distance-dependent source functions $S_\nu(r)$ of the dusty gas clouds. We then combine these source functions to receive the distance-dependent emission from the central region as

$$F_\nu(r)\, dr = f_{\rm fill}\, S_\nu(r)\, r\, dr/(\pi r_{\rm sub}^2), \tag{5.2}$$

[5]Calculations were performed with version C13.1 (March 2013) of CLOUDY, last described by Ferland et al. (2013).

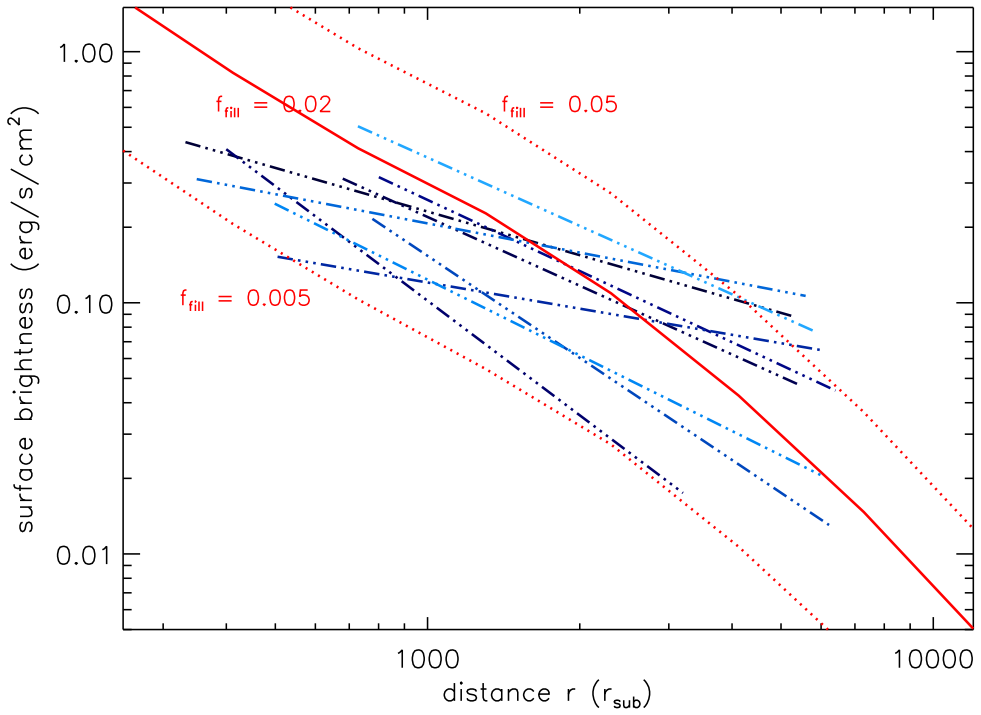

Fig. 5.7 Comparison between power-law models of the observed emitted PAH fluxes (dot-dashed lines) and the CLOUDY models (red solid and dotted lines). The slopes of the power-law models and the CLOUDY models appear very similar.

where $f_{\rm fill}$ is the filling factor, which is the only free parameter in this model. For a comparison to observations, we extract the 11.3 μm PAH flux similar to the observations, i.e. by subtracting the linearly interpolated continuum underneath the observed feature (interpolation anchors are set at 11.11 and 11.63 μm, where the CLOUDY SEDs are continuum only).

In Fig. 5.7, we show the intrinsic PAH emission slopes of the 9 objects included for the cut-off at 7,000 r_{sub} (see section 5.6.2). To avoid crowding, we only plot the best-fit value of the slopes; the 68% confidence regions are shown in Fig. 5.6. Overplotted in Fig. 5.7 are model PAH surface fluxes with a range of model $f_{\rm fill}$ values that bracket these intrinsic slopes. Two lessons can be learned from this comparison: First, the required filling factor $f_{\rm fill}$ in the range of spatial scales covered by the observations is much lower than unity, which implies that the AGN does indeed provide enough energy to excite the observed PAH emission at the observed distances. Indeed, with $f_{\rm fill} \sim 0.01$, only a small number of AGN-heated, PAH-bearing dusty gas clouds are required to account for the observed fluxes. Alternatively, one may interpret the $f_{\rm fill}$ values in a way that only a small fraction of AGN light needs to reach out to these distances to provide enough energy for producing the observed PAH emission.

Second, we see that the model does not show one unique slope but becomes steeper at large distances from the AGN. To compare the model to observations, we extract model PAH fluxes at similar apertures as the observations and linearly fit slopes to these model-extracted fluxes. To account for the different intrinsic spatial scales in the objects, we vary the inner radius using a Monte Carlo scheme, so that the total spatial range from 400 r_{sub} to 7,000 r_{sub} is covered. We recover a model slope of $\alpha_{\rm mod} = -1.25 \pm 0.46$. This slope is fully consistent with the joint slope of $\alpha = -1.1 \pm 0.1$. Similarly to the analysis in Sect. 5.6.2, we also calculate χ^2_r values to quantify consistency of the observed slopes with the model. Here, we take into account the errors of the observations *and* the intrinsic scatter of the model. The resulting χ^2_r statistic is listed in the fourth column of Table 5.5. We find χ^2_r that support the CLOUDY model as a reasonable representation of the data. Indeed, $\chi^2_r < 1$ for the range of outer cut-offs between 3000 and 7000 $r_{\rm sub}$. This is easily understood when considering that the intrinsic scatter of the model slope of 0.46 is larger than the one implied by testing each individual source against the joint slope.

In the models shown in Fig. 5.7, we adopt a Hydrogen column density of $N_H = 10^{23}\,{\rm cm}^{-2}$. This column density provides enough self-shielding within the dusty gas clouds for PAHs to survive. Such column densities can be expected from physical arguments of the state of clumps in the region of the torus (Krolik & Begelman, 1988; Vollmer & Beckert, 2002; Beckert & Duschl, 2004; Hönig & Beckert, 2007; Stern et al., 2014; Namekata et al., 2014). Increasing the column density changes the model emission only marginally.

We would like to point out again that the AGN-excited PAH model we use contains only one free parameter, yet it reproduces the observed slope and is energetically viable. One may consider a slight variation of this model to allow for a slight variation in slopes by making the covering factor distance-dependent. However, this is not the purpose here. We only want to test the general viability of AGN as the heating source of the small-scale circumnuclear environment.

5.7.2 Excitation by nuclear star clusters

A second source of central heating/excitation of the PAH molecules might be radiation from a compact nuclear star cluster (NSC). Here, compact would mean that the bulk of the radiation is originating from scales smaller than the observed and resolved PAH emission. Since NSCs may vary significantly among different galaxies, we assess their viability to produce the observed PAH emission via energy conservation arguments in two galaxies within our sample where observational constraints are available.

NGC 3227. Davies et al. (2006) report a total luminosity of the NSC in NGC 3227 of $L_{\rm NSC}(\text{NGC 3227}) \sim 1 \times 10^{43}$ erg s^{-1} and measured in a 0.8 arcsec aperture. This corresponds to an intrinsic aperture radius of $\sim 3300\, r_{\rm sub}$. In addition, they estimate the AGN luminosity as $L_{\rm AGN}(\text{NGC 3227}) \sim 4 \times 10^{43}$ erg s^{-1}. Thus, we estimate that the stars contribute about 20 per cent to the total radiation field within $\sim 3300\, r_{\rm sub}$ of the nucleus of NGC 3227.

NG 7469. For NGC 7469, we can make a similar assessment. Davies et al. (2007) report a *K*-band luminosity of the stellar component with the same 0.8 arcsec aperture. Given their approximate conversion to bolometric stellar luminosity, we can estimate $L_{\rm NSC}(\text{NGC 7469}) \sim 8 \times 10^{43}$ erg s^{-1} within $\sim 3000\, r_{\rm sub}$. Using the X-ray luminosity of the AGN in Table 5.3 and the bolometric conversion by Marconi et al. (2004), we obtain a bolometric luminosity of the AGN of $L_{\rm AGN}(\text{NGC 7469}) \sim 3 \times 10^{44}$ erg s^{-1}. From that, we estimate a stellar contribution of $\sim$20 per cent to the total radiation field.

In summary, from energy conservation we can conclude that the AGN, compared to stars, does indeed have the potential to provide the photons necessary for excitation of the PAHs. There are two caveats to consider in this respect: From AGN unification, we may expect only about half of the solid angle around the AGN to receive significant UV emission necessary to excite the PAHs. Thus, the actual share of AGN contribution may have to be lowered accordingly. On the other hand, the AGN emits much more UV photons than star formation for a given luminosity given the respective spectral shapes. This effect counters the solid angle effect. While it is not possible to rule out star formation as a significant contributor to the PAH emission, the point that needs to be stressed is that the radiation field of the AGN is very strong on these scales and should be considered at least as likely to excite PAHs as stars from an energy perspective.

We conclude that AGN heating/excitation of PAH-containing dusty gas clouds is a viable option to explain the observed narrow range of PAH surface fluxes and the common radial slopes in our AGN sample with PAH detection below $\sim 7\,000\, r_{sub}$. In reality, we expect that both AGN and NSC contribute to the heating/excitation of the PAHs. Stars will probably dominate at larger distances of $\geq$500 pc, where the AGN radiation field becomes too small. These are the scales where the well-known PAH emission-star formation relations have been established.

Our findings do not contradict previously established relations between the 11.3 μm PAH feature and star formation rates on larger scales in AGN (e.g., Diamond-Stanic & Rieke, 2010, 2012). Using the 11.3 μm PAH feature as a tracer of star formation in AGN relies on two assumptions: 1) that the

feature is not suppressed in AGN, and 2) that the [Ne II] 12.8 μm emission, to which the 11.3 μm PAH star formation estimates are calibrated, is a reliable tracer of star formation in AGN. While the 11.3 μm PAH feature is less suppressed than features at 6.2, 7.7, and 8.6 μm in AGN (Smith et al., 2007; Diamond-Stanic & Rieke, 2010), it is not clear whether it is not suppressed at all. Also, the [Ne II] emission has its own limitations as a star formation tracer in AGN. First, the [Ne II] emission can have a significant contribution from AGN emission (Groves et al., 2006; Meléndez et al., 2008; Pereira-Santaella et al., 2010), which, if not properly accounted for, will lead to overestimated star formation rates. Indeed, a strong Baldwin effect, commonly associated with AGN excitation, has been reported for the [Ne II] (Hönig et al., 2008; Keremedjiev et al., 2009). These points, together with the common radial slopes and energetic viability of the AGN to excite PAH features, should raise caution in adopting the 11.3 μm PAH feature on small scales in circumnuclear environment of AGN. Indeed, a correlation between AGN luminosity and PAH emission on these small scales may be either interpreted in terms of an AGN-star formation relation or as indicative of PAH excitation by the AGN.

5.8 Conclusions

We analyse ground-based mid-IR spectra of the nuclear region of a sample of 28 nearby AGN to study the radial emission profiles of the 11.3 μm PAH feature. The data map the PAH emission on unprecedented small spatial scales below 1 kpc. Out of the 28 objects, we detect PAH features in 13 and establish radial profiles of the emitted surface flux for 12 of the sources. To compare the observations on a distance- and luminosity-independent spatial scale, we normalise the emitted surface flux to the dust sublimation radius of each object. As a result, the incident AGN emission at each normalised (=intrinsic) radius is the same in all objects. The sublimation radii are determined based on a new relation between intrinsic X-ray luminosity and sublimation radius. We conclude:

- We find a clear radial decrease of the emitted PAH surface flux in the inner $\sim$7,000 sublimation radii ($\sim$500 pc) around the AGN. The slope of the profile and its normalisation are essentially universal in all objects when normalised by an AGN-intrinsic scale $\propto L^{1/2}$ (here, the sublimation radius). The normalisation of PAH surface fluxes shows a scatter of less than 1 order of magnitude in AGN-intrinsic scales while the PAH luminosities scatter over more than 3 orders of magnitude otherwise.

- Circinus is an obvious outlier to this trend, which may be related to strong extinction in the nuclear environment.

- By fitting a power-law to the observations of each object, we find a common slope of about -1.1 ± 0.1 when combining the power-law slopes from the individual objects.

- We argue that a compact emission source is required to explain the common slopes and test the AGN and a nuclear star cluster (NSC) as possible sources of PAH heating/excitation. A simple CLOUDY model of reprocessed AGN radiation is able to reproduce the observed slopes and

absolute fluxes. Energy conservation arguments show that the AGN has the potential to provide the radiation field needed to excite PAHs.

- About 50 per cent of the AGN in the total sample have no detection of a 11.3 μm PAH feature in our data. About half of these sources have upper limits that fall within or above our detections, meaning that they may need higher S/N data to reveal the features. The rest seem to have genuinely weak features or lack those.

While there exist well-established relations between the PAH emission and star formation on larger scales, our results require some caution when trying to invoke these relations within tens to hundreds of parsecs of an AGN. The James Webb Space Telescope will allow for mapping the radial profiles on similar scales for a much larges sample of AGN and test our findings. Although previous studies have found the 11.3 μm PAH feature to be most robust around AGN, we would expect a similar behaviour for other PAH features in the mid-IR, but due to the differential suppression of these features, slopes and normalisations of the radial PAH profiles is expected to differ.

Acknowledgments

We thank the anonymous referee for critical and constructive comments that led to significant improvements of the manuscript. The Dark Cosmology Centre is funded by the Danish National Research Foundation. S.F.H. acknowledges support via a Marie Curie International Incoming Fellowship within the 7th EC Framework (PIIF-GA-2013-623804) and the Horizon 2020 ERC Starting Grant *DUST-IN-THE-WIND* (ERC-2015-StG-677117). S.R. thanks Aryabhatta Research Institute of Observational Sciences (ARIES), Nainital, India for providing local support and hospitality during the preparation of this manuscript. A.A.-H. acknowledges financial support from the Spanish Ministry of Economy and Competitiveness through grant AYA2015-64346-C2-1-P. P.G. thanks STFC for support (grant reference ST/J003697/2).

This research has made use of the NASA/IPAC Extragalactic Database (NED) which is operated by JPL, Caltech, under contract with NASA. This research has made use of the VizieR catalogue access tool, CDS, Strasbourg, France. The original description of the VizieR service was published in A&AS 143, 23.

Chapter 6

Conclusions and outlook

For my dissertation I worked on two topics related to AGN. First, I have investigated how broad emission line widths in AGN spectra can be measured in the most optimal way to ensure black hole mass estimates that have a high accuracy and precision. Second, I have critically examined the mid-IR 11.3 μm PAH feature as a star formation tracer in the vicinity of AGN. Here, I present my overall conclusions and provide a brief outlook.

In Chapters 2, 3, and 4 I present an analysis of the accuracy and precision of four different parameters that can be used to determine the width of the broad Hβ, Mg II, and C IV emission lines in AGN spectra. These emission line widths can then used to infer the velocity of the gas in the BLR which in turn is used for black hole mass estimates in AGN. I focus my work on the impact of low spectral S/N (measured in the continuum region of the spectrum) and in the case of the C IV line also the impact of weak and intermediate strength absorption lines. I show that the two most traditionally used line width measures, namely the FWHM and σ_{line}, are the most affected by low spectral S/N . This manifests itself in systematically biased measurements already at S/N ~ 25 pixel^{-1} for FWHM and at S/N ~ 15 pixel^{-1} for σ_{line}. For FWHM, this leads to mass estimates with an accuracy of only 0.95 dex, and for σ_{line}, the accuracy can be as low as 0.35 dex at the beforementioned S/N levels. In comparison, mass estimates based on either the IPV or MAD widths are unbiased down to S/N ~ 5 pixel^{-1}, albeit with decreasing accuracy and precision as the S/N becomes lower. In comparison with the FWHM and σ_{line}, the IPV and MAD widths have a higher accuracy at any given S/N level above 5 pixel^{-1}. Below S/N ~ 5 pixel^{-1}, all line parameters leads to mass estimates with low accuracy (0.5 dex or more). It is also clear from my work that S/N ≥ 50 pixel^{-1} in the continuum typically is necessary for a mass estimate with an accuracy within 0.1 dex, except for the IPV widths where this can be achieved for S/N ≥ 15 pixel^{-1}.

Besides having a high accuracy and precision, the IPV widths are favored for their flexibility. As they can provide a measure of the line width at any percentage of the integrated line flux, they can parameterize the line width with a high accuracy all the way from the base of the line to its core. This also opens up for the possibility of parameterizing the line shape using ratios of different IPV line width fractions. Traditionally, this has been done using the FWHM/σ_{line} ratio, but we find that this

shape parameter has a very low accuracy at any S/N level below 25 pixel^{-1}. There are indications that a shape correction is necessary in order to accurately calibrate the black hole mass relationships in AGN and therefore it is pertinent that we are able to determine this shape accurately and without biases. Ratios of IPV widths will provide that.

Finally, I do not find that measuring the emission line widths on a functional model of the emission line, as opposed to directly on the data, improves the reliability of the mass estimates. Specifically, using a functional model can introduce systematic biases in the measured emission line widths, and I therefore recommend against using this method. Instead, I recommend to only use data with high S/N (>20 pixel^{-1}) and that if existing data with low S/N is used, to adjust the uncertainties of the line width measures according to the results presented here. We also advise to obtain data with a spectral resolution $\sim$100 km s^{-1} or higher such that narrow absorption lines are resolved and can be accounted for. Because if uncorrected, they can have a negative impact on the accuracy of the line width measures.

There are a number of relations that must be re-visited in the future in the light of this work. First, it should be determined which IPV width that gives the most reliable black hole mass estimate as a preparation for a re-calibration of the mass scaling relations based on IPV widths. Part of this work is to check if a shape correction is necessary and to check which ratio of IPV widths might be best suited for this purpose. Studies comparing mass estimates based on different emission lines should also be repeated using IPV widths to check whether differences between mass estimates based on different emission lines persists.

In the second part of the thesis, I examine the mid-IR 11.3 μm PAH feature as a star formation tracer in AGN. I find strong indications that the AGN emission excites the PAH features, contaminating them as pure star formation tracers. It is also clear that data from current instruments are unable to settle this issue as it will require even higher spatial resolution and sensitivity. In the future, this experiment should be repeated using the planned Mid-Infrared Instrument (MIRI) on board of the James Webb Space Telescope (JWST). With its unprecedented spectral resolution, sensitivity, and wavelength coverage it will enable us to draw a more solid conclusion about the validity of the 11.3 μm PAH feature as a star formation tracer. Furthermore, the long wavelength coverage of JWST will enable a comparative study between the different PAH features in the mid-IR and how well they trace star formation in the vicinity of AGN.

Bibliography

Aalto S., et al., 2016, A&A, 590, A73

Alexander D. M., Hickox R. C., 2012, New Astron. Rev., 56, 93

Allamandola L. J., Tielens A. G. G. M., Barker J. R., 1985, ApJ, 290, L25

Allamandola L. J., Tielens A. G. G. M., Barker J. R., 1989, ApJS, 71, 733

Alonso-Herrero A., et al., 2014, MNRAS, 443, 2766

Alonso-Herrero A., et al., 2016, MNRAS, 455, 563

Andrade-Velázquez M., Krongold Y., Elvis M., Nicastro F., Brickhouse N., Binette L., Mathur S., Jiménez-Bailón E., 2010, ApJ, 711, 888

Anglés-Alcázar D., Faucher-Giguère C.-A., Quataert E., Hopkins P. F., Feldmann R., Torrey P., Wetzel A., Kereš D., 2017, MNRAS, 472, L109

Annuar A., et al., 2015, ApJ, 815, 36

Antonucci R., 1993, ARA&A, 31, 473

Arévalo P., et al., 2014, ApJ, 791, 81

Asmus D., Gandhi P., Hönig S. F., Smette A., Duschl W. J., 2015, MNRAS, 454, 766

Barvainis R., 1987, ApJ, 320, 537

Batcheldor D., 2010, ApJ, 711, L108

Bauer F. E., et al., 2015, ApJ, 812, 116

Beckert T., Duschl W. J., 2004, A&A, 426, 445

Bentz M. C., Katz S., 2015, PASP, 127, 67

Bentz M. C., Peterson B. M., Pogge R. W., Vestergaard M., Onken C. A., 2006, ApJ, 644, 133

Bentz M. C., et al., 2007, ApJ, 662, 205

Bentz M. C., Peterson B. M., Pogge R. W., Vestergaard M., 2009a, ApJ, 694, L166

Bentz M. C., Peterson B. M., Netzer H., Pogge R. W., Vestergaard M., 2009b, ApJ, 697, 160

Bentz M. C., et al., 2009c, ApJ, 705, 199

Bentz M. C., et al., 2010, ApJ, 720, L46

Bentz M. C., et al., 2013, ApJ, 767, 149

Bentz M. C., Cackett E. M., Crenshaw D. M., Horne K., Street R., Ou-Yang B., 2016, ApJ, 830, 136

Blandford R. D., McKee C. F., 1982, ApJ, 255, 419

Boroson T. A., Green R. F., 1992, ApJS, 80, 109

Brandl B. R., et al., 2006, ApJ, 653, 1129

Brenneman L. W., et al., 2011, ApJ, 736, 103

Brenneman L. W., et al., 2014, ApJ, 788, 61

Brewer B. J., et al., 2011, ApJ, 733, L33

Bridle A. H., Perley R. A., 1984, ARA&A, 22, 319

Brightman M., Nandra K., 2011, MNRAS, 413, 1206

Bruzual G., Charlot S., 2003, MNRAS, 344, 1000

Burtscher L., et al., 2013, A&A, 558, A149

Cackett E. M., Gültekin K., Bentz M. C., Fausnaugh M. M., Peterson B. M., Troyer J., Vestergaard M., 2015, ApJ, 810, 86

Calzetti D., et al., 2007, ApJ, 666, 870

Cappellari M., et al., 2011, MNRAS, 413, 813

Clavel J., et al., 2000, A&A, 357, 839

Colina L., Gonzalez Delgado R., Mas-Hesse J. M., Leitherer C., 2002, ApJ, 579, 545

Collin S., Kawaguchi T., Peterson B. M., Vestergaard M., 2006, A&A, 456, 75

Cox A. N., 2000, Allen's astrophysical quantities

Croom S. M., Smith R. J., Boyle B. J., Shanks T., Miller L., Outram P. J., Loaring N. S., 2004, MNRAS, 349, 1397

Curran S. J., Johansson L. E. B., Rydbeck G., Booth R. S., 1998, A&A, 338, 863

Curran S. J., Rydbeck G., Johansson L. E. B., Booth R. S., 1999, A&A, 344, 767

Dadina M., 2007, A&A, 461, 1209

Dai Y. S., et al., 2014, ApJ, 791, 113

Davies R. I., et al., 2006, ApJ, 646, 754

Davies R. I., Müller Sánchez F., Genzel R., Tacconi L. J., Hicks E. K. S., Friedrich S., Sternberg A., 2007, ApJ, 671, 1388

De Rosa G., et al., 2015, ApJ, 806, 128

Denney K. D., 2012, ApJ, 759, 44

Denney K. D., Peterson B. M., Dietrich M., Vestergaard M., Bentz M. C., 2009, ApJ, 692, 246

Denney K. D., et al., 2010, ApJ, 721, 715

Denney K. D., Pogge R. W., Assef R. J., Kochanek C. S., Peterson B. M., Vestergaard M., 2013, ApJ, 775, 60

Denney K. D., et al., 2014, ApJ, 796, 134

Denney K. D., et al., 2016, ApJS, 224, 14

Deo R. P., Richards G. T., Crenshaw D. M., Kraemer S. B., 2009, ApJ, 705, 14

Di Matteo T., Springel V., Hernquist L., 2005, Nat, 433, 604

Di Matteo T., Colberg J., Springel V., Hernquist L., Sijacki D., 2008, ApJ, 676, 33

Diamond-Stanic A. M., Rieke G. H., 2010, ApJ, 724, 140

Diamond-Stanic A. M., Rieke G. H., 2012, ApJ, 746, 168

Diamond-Stanic A. M., Moustakas J., Tremonti C. A., Coil A. L., Hickox R. C., Robaina A. R., Rudnick G. H., Sell P. H., 2012, ApJ, 755, L26

Díaz-Santos T., Alonso-Herrero A., Colina L., Ryder S. D., Knapen J. H., 2007, ApJ, 661, 149

Díaz-Santos T., Alonso-Herrero A., Colina L., Packham C., Levenson N. A., Pereira-Santaella M., Roche P. F., Telesco C. M., 2010, ApJ, 711, 328

Dietrich M., Hamann F., Shields J. C., Constantin A., Vestergaard M., Chaffee F., Foltz C. B., Junkkarinen V. T., 2002, ApJ, 581, 912

Dunn R. J. H., Fabian A. C., 2008, MNRAS, 385, 757

Edelson R., et al., 2015, ApJ, 806, 129

Elvis M., 2000, ApJ, 545, 63

Esquej P., et al., 2014, ApJ, 780, 86

Fabian A. C., 1999, MNRAS, 308, L39

Fabian A. C., 2012, ARA&A, 50, 455

Fausnaugh M. M., et al., 2016, ApJ, 821, 56

Ferland G. J., et al., 2013, Rev. Mex. Astron. Astrofis., 49, 137

Ferrarese L., Ford H., 2005, SSR, 116, 523

Ferrarese L., Merritt D., 2000a, ApJ, 539, L9

Ferrarese L., Merritt D., 2000b, ApJ, 539, L9

Ferrarese L., Pogge R. W., Peterson B. M., Merritt D., Wandel A., Joseph C. L., 2001, ApJ, 555, L79

Fine S., et al., 2008, MNRAS, 390, 1413

Fine S., Croom S. M., Bland-Hawthorn J., Pimbblet K. A., Ross N. P., Schneider D. P., Shanks T., 2010, MNRAS, 409, 591

Frank S., Péroux C., 2010, MNRAS, 406, 2235

Freeman K. C., Karlsson B., Lynga G., Burrell J. F., van Woerden H., Goss W. M., Mebold U., 1977, A&A, 55, 445

Freudling W., Romaniello M., Bramich D. M., Ballester P., Forchi V., García-Dabló C. E., Moehler S., Neeser M. J., 2013, A&A, 559, A96

Gallo L. C., Lehmann I., Pietsch W., Boller T., Brinkmann W., Friedrich P., Grupe D., 2006, MNRAS, 365, 688

Gandhi P., Horst H., Smette A., Hönig S., Comastri A., Gilli R., Vignali C., Duschl W., 2009, A&A, 502, 457

Gandhi P., et al., 2014, ApJ, 792, 117

Gandhi P., Yamada S., Ricci C., Asmus D., Mushotzky R. F., Ueda Y., Terashima Y., La Parola V., 2015, MNRAS, 449, 1845

García-Burillo S., et al., 2016, ApJ, 823, L12

Geach J. E., et al., 2014, Nat, 516, 68

Gebhardt K., et al., 2000a, ApJ, 539, L13

Gebhardt K., et al., 2000b, ApJ, 539, L13

Genzel R., Weitzel L., Tacconi-Garman L. E., Blietz M., Cameron M., Krabbe A., Lutz D., Sternberg A., 1995, ApJ, 444, 129

Glass I. S., 1992, MNRAS, 256, 23P

Goad M. R., O'Brien P. T., Gondhalekar P. M., 1993, MNRAS, 263, 149

Goad M. R., Korista K. T., Ruff A. J., 2012, MNRAS, 426, 3086

González Delgado R. M., Heckman T., Leitherer C., Meurer G., Krolik J., Wilson A. S., Kinney A., Koratkar A., 1998, ApJ, 505, 174

González-Martín O., et al., 2013, A&A, 553, A35

Goto T., 2006, MNRAS, 369, 1765

Graham A. W., Driver S. P., 2007, ApJ, 655, 77

Graham A. W., Erwin P., Caon N., Trujillo I., 2001, ApJ, 563, L11

Graham A. W., Onken C. A., Athanassoula E., Combes F., 2011, MNRAS, 412, 2211

Grandi S. A., 1982, ApJ, 255, 25

Greene J. E., Ho L. C., 2005a, ApJ, 627, 721

Greene J. E., Ho L. C., 2005b, ApJ, 630, 122

Grier C. J., et al., 2013, ApJ, 773, 90

Groves B., Dopita M., Sutherland R., 2006, A&A, 458, 405

Gültekin K., et al., 2009, ApJ, 698, 198

Heckman T. M., Miley G. K., van Breugel W. J. M., Butcher H. R., 1981, ApJ, 247, 403

Heckman T., et al., 1995, ApJ, 452, 549

Hernán-Caballero A., Hatziminaoglou E., 2011, MNRAS, 414, 500

Hönig S. F., Beckert T., 2007, MNRAS, 380, 1172

Hönig S. F., Smette A., Beckert T., Horst H., Duschl W., Gandhi P., Kishimoto M., Weigelt G., 2008, A&A, 485, L21

Hönig S. F., Kishimoto M., Gandhi P., Smette A., Asmus D., Duschl W., Polletta M., Weigelt G., 2010, A&A, 515, A23

Hopkins P. F., 2012, MNRAS, 420, L8

Hopkins P. F., Quataert E., 2010, MNRAS, 407, 1529

Hopkins P. F., Bundy K., Hernquist L., Ellis R. S., 2007, ApJ, 659, 976

Horst H., Gandhi P., Smette A., Duschl W. J., 2008, A&A, 479, 389

Jahnke K., Macciò A. V., 2011, ApJ, 734, 92

Jensen J. J., 2012, Master's thesis, Dark Cosmology Centre, Juliane Maries Vej 30, DK-2000 Copenhagen N

Johnson J. L., Haardt F., 2016, PASA, 33, e007

Kaspi S., Smith P. S., Netzer H., Maoz D., Jannuzi B. T., Giveon U., 2000, ApJ, 533, 631

Kaspi S., Maoz D., Netzer H., Peterson B. M., Vestergaard M., Jannuzi B. T., 2005, ApJ, 629, 61

Kaspi S., Brandt W. N., Maoz D., Netzer H., Schneider D. P., Shemmer O., 2007, ApJ, 659, 997

Kausch W., et al., 2015, A&A, 576, A78

Kawakatu N., Wada K., 2008, ApJ, 681, 73

Kelly B. C., 2007, ApJ, 665, 1489

Kelly B. C., Shen Y., 2013, ApJ, 764, 45

Kelly B. C., Vestergaard M., Fan X., Hopkins P., Hernquist L., Siemiginowska A., 2010, ApJ, 719, 1315

Kennicutt Jr. R. C., 1998, ARA&A, 36, 189

Kennicutt R. C., Evans N. J., 2012, ARA&A, 50, 531

Keremedjiev M., Hao L., Charmandaris V., 2009, ApJ, 690, 1105

Kilerci Eser E., Vestergaard M., Peterson B. M., Denney K. D., Bentz M. C., 2015, ApJ, 801, 8

Kim M., Ho L. C., Peng C. Y., Barth A. J., Im M., 2008, ApJS, 179, 283

King A., 2003, ApJ, 596, L27

King A. R., Pounds K. A., 2003, MNRAS, 345, 657

King A., Pounds K., 2015, ARA&A, 53, 115

King A. L., et al., 2011, ApJ, 729, 19

Kinney A. L., Calzetti D., Bohlin R. C., McQuade K., Storchi-Bergmann T., Schmitt H. R., 1996, ApJ, 467, 38

Kishimoto M., Hönig S. F., Beckert T., Weigelt G., 2007, A&A, 476, 713

Kishimoto M., Hönig S. F., Antonucci R., Kotani T., Barvainis R., Tristram K. R. W., Weigelt G., 2009, A&A, 507, L57

Kishimoto M., Hönig S. F., Antonucci R., Barvainis R., Kotani T., Tristram K. R. W., Weigelt G., Levin K., 2011, A&A, 527, A121

Kollatschny W., Ulbrich K., Zetzl M., Kaspi S., Haas M., 2014, A&A, 566, A106

Kollmeier J. A., et al., 2006, ApJ, 648, 128

Komossa S., Xu D., Zhou H., Storchi-Bergmann T., Binette L., 2008, ApJ, 680, 926

Korista K. T., et al., 1995, ApJS, 97, 285

Kormendy J., Gebhardt K., 2001, in Wheeler J. C., Martel H., eds, American Institute of Physics Conference Series Vol. 586, 20th Texas Symposium on relativistic astrophysics. pp 363–381 (arXiv:astro-ph/0105230), doi:10.1063/1.1419581

Kormendy J., Ho L. C., 2013, ARA&A, 51, 511

Kormendy J., Richstone D., 1995, ARA&A, 33, 581

Koshida S., et al., 2014, ApJ, 788, 159

Krolik J. H., 2001, ApJ, 551, 72

Krolik J. H., Begelman M. C., 1988, ApJ, 329, 702

Krongold Y., et al., 2010, ApJ, 710, 360

LaMassa S. M., et al., 2015, ApJ, 800, 144

Lagage P. O., et al., 2004, The Messenger, 117, 12

Latif M. A., Ferrara A., 2016, PASA, 33, e051

Lauer T. R., Tremaine S., Richstone D., Faber S. M., 2007, ApJ, 670, 249

Leger A., Puget J. L., 1984, A&A, 137, L5

Liu X., Shen Y., Strauss M. A., Greene J. E., 2010, ApJ, 708, 427

Longinotti A. L., Bianchi S., Santos-Lleo M., Rodríguez-Pascual P., Guainazzi M., Cardaci M., Pollock A. M. T., 2007, A&A, 470, 73

Lubiński P., Zdziarski A. A., Walter R., Paltani S., Beckmann V., Soldi S., Ferrigno C., Courvoisier T. J.-L., 2010, MNRAS, 408, 1851

Lusso E., et al., 2010, A&A, 512, A34

Magorrian J., et al., 1998, AJ, 115, 2285

Marchese E., Della Ceca R., Caccianiga A., Severgnini P., Corral A., Fanali R., 2012, A&A, 539, A48

Marconi A., Hunt L. K., 2003a, ApJ, 589, L21

Marconi A., Hunt L. K., 2003b, ApJ, 589, L21

Marconi A., Risaliti G., Gilli R., Hunt L. K., Maiolino R., Salvati M., 2004, MNRAS, 351, 169

Marconi A., Axon D. J., Maiolino R., Nagao T., Pastorini G., Pietrini P., Robinson A., Torricelli G., 2008, ApJ, 678, 693

Markowitz A. G., Reeves J. N., 2009, ApJ, 705, 496

Markowitz A., Reeves J. N., George I. M., Braito V., Smith R., Vaughan S., Arévalo P., Tombesi F., 2009, ApJ, 691, 922

Marziani P., Sulentic J. W., Zamanov R., Calvani M., Dultzin-Hacyan D., Bachev R., Zwitter T., 2003, ApJS, 145, 199

Mason R. E., Levenson N. A., Shi Y., Packham C., Gorjian V., Cleary K., Rhee J., Werner M., 2009, ApJ, 693, L136

McGill K. L., Woo J.-H., Treu T., Malkan M. A., 2008, ApJ, 673, 703

McHardy I. M., Papadakis I. E., Uttley P., Page M. J., Mason K. O., 2004, MNRAS, 348, 783

McLure R. J., Dunlop J. S., 2001, MNRAS, 327, 199

McLure R. J., Dunlop J. S., 2004, MNRAS, 352, 1390

McLure R. J., Jarvis M. J., 2002, MNRAS, 337, 109

McNamara B. R., Nulsen P. E. J., 2012, New Journal of Physics, 14, 055023

Mejía-Restrepo J. E., Trakhtenbrot B., Lira P., Netzer H., Capellupo D. M., 2016, MNRAS, 460, 187

Meléndez M., Kraemer S. B., Schmitt H. R., Crenshaw D. M., Deo R. P., Mushotzky R. F., Bruhweiler F. C., 2008, ApJ, 689, 95

Metzroth K. G., Onken C. A., Peterson B. M., 2006, ApJ, 647, 901

Mezcua M., Prieto M. A., Fernández-Ontiveros J. A., Tristram K. R. W., 2016, MNRAS, 457, L94

Modigliani A., et al., 2010, in Observatory Operations: Strategies, Processes, and Systems III. p. 773728, doi:10.1117/12.857211

Namekata D., Umemura M., Hasegawa K., 2014, MNRAS, 443, 2018

Nandra K., O'Neill P. M., George I. M., Reeves J. N., 2007, MNRAS, 382, 194

Nelson C. H., Green R. F., Bower G., Gebhardt K., Weistrop D., 2004, ApJ, 615, 652

Netzer H., 2015, ARA&A, 53, 365

Netzer H., Marziani P., 2010, ApJ, 724, 318

Onken C. A., Kollmeier J. A., 2008, ApJ, 689, L13

Onken C. A., Peterson B. M., 2002, ApJ, 572, 746

Onken C. A., Ferrarese L., Merritt D., Peterson B. M., Pogge R. W., Vestergaard M., Wandel A., 2004, ApJ, 615, 645

Onken C. A., et al., 2014, ApJ, 791, 37

Osterbrock D. E., Ferland G. J., 2006, Astrophysics of gaseous nebulae and active galactic nuclei

Pancoast A., Brewer B. J., Treu T., 2011, ApJ, 730, 139

Pancoast A., et al., 2012, ApJ, 754, 49

Pancoast A., Brewer B. J., Treu T., Park D., Barth A. J., Bentz M. C., Woo J.-H., 2014, MNRAS, 445, 3073

Park D., Kelly B. C., Woo J.-H., Treu T., 2012, ApJS, 203, 6

Park D., Barth A. J., Woo J.-H., Malkan M. A., Treu T., Bennert V. N., Assef R. J., Pancoast A., 2017, ApJ, 839, 93

Peeters E., Hony S., Van Kerckhoven C., Tielens A. G. G. M., Allamandola L. J., Hudgins D. M., Bauschlicher C. W., 2002, A&A, 390, 1089

Peeters E., Spoon H. W. W., Tielens A. G. G. M., 2004, ApJ, 613, 986

Pei L., et al., 2017, ApJ, 837, 131

Peng C. Y., 2007, ApJ, 671, 1098

Peng C. Y., Impey C. D., Rix H.-W., Kochanek C. S., Keeton C. R., Falco E. E., Lehár J., McLeod B. A., 2006, ApJ, 649, 616

Pereira-Santaella M., Diamond-Stanic A. M., Alonso-Herrero A., Rieke G. H., 2010, ApJ, 725, 2270

Perrotta S., et al., 2016, MNRAS, 462, 3285

Peterson B. M., 1993, PASP, 105, 247

Peterson B. M., 1997, An Introduction to Active Galactic Nuclei

Peterson B. M., 2008, New Astron. Rev., 52, 240

Peterson B. M., 2010, in Peterson B. M., Somerville R. S., Storchi-Bergmann T., eds, IAU Symposium Vol. 267, Co-Evolution of Central Black Holes and Galaxies. pp 151–160 (arXiv:1001.3675), doi:10.1017/S1743921310006095

Peterson B. M., 2014, SSR, 183, 253

Peterson B. M., Wandel A., 1999, ApJ, 521, L95

Peterson B. M., Wandel A., 2000, ApJ, 540, L13

Peterson B. M., et al., 2002, ApJ, 581, 197

Peterson B. M., et al., 2004, ApJ, 613, 682

Peterson B. M., et al., 2013, ApJ, 779, 109

Pieri M. M., et al., 2014, MNRAS, 441, 1718

Ponti G., et al., 2009, MNRAS, 394, 1487

Press W. H., Teukolsky S. A., Vetterling W. T., Flannery B. P., 2007, Numerical Recipes 3rd Edition: The Art of Scientific Computing, 3 edn. Cambridge University Press, New York, NY, USA

Proga D., Waters T., 2015, ApJ, 804, 137

Rafiee A., Hall P. B., 2011, MNRAS, 415, 2932

Ramos Almeida C., Rodríguez Espinosa J. M., Acosta-Pulido J. A., Alonso-Herrero A., Pérez García A. M., Rodríguez-Eugenio N., 2013, MNRAS, 429, 3449

Reichert G. A., et al., 1994, ApJ, 425, 582

Richards G. T., et al., 2006, AJ, 131, 2766

Ridgway S. E., Heckman T. M., Calzetti D., Lehnert M., 2001, ApJ, 550, 122

Rivers E., Markowitz A., Rothschild R., 2011, ApJS, 193, 3

Rivers E., Markowitz A., Duro R., Rothschild R., 2012, ApJ, 759, 63

Roche P. F., Aitken D. K., 1985, MNRAS, 213, 789

Roche P. F., Aitken D. K., Smith C. H., Ward M. J., 1991, MNRAS, 248, 606

Roche P. F., Packham C., Telesco C. M., Radomski J. T., Alonso-Herrero A., Aitken D. K., Colina L., Perlman E., 2006, MNRAS, 367, 1689

Rodríguez-Pascual P. M., et al., 1997, ApJS, 110, 9

Sales D. A., Pastoriza M. G., Riffel R., 2010, ApJ, 725, 605

Savorgnan G., Graham A. W., Marconi A., Sani E., Hunt L. K., Vika M., Driver S. P., 2013, MNRAS, 434, 387

Schlegel D. J., Finkbeiner D. P., Davis M., 1998, ApJ, 500, 525

Schmidt M., 1969, ARA&A, 7, 527

Schneider D. P., et al., 2010, AJ, 139, 2360

Schulze A., et al., 2015, MNRAS, 447, 2085

Sell P. H., et al., 2014, MNRAS, 441, 3417

Sergeev S. G., Nazarov S. V., Borman G. A., 2017, MNRAS, 465, 1898

Shakura N. I., Sunyaev R. A., 1973, in Bradt H., Giacconi R., eds, IAU Symposium Vol. 55, X- and Gamma-Ray Astronomy. p. 155

Shankar F., et al., 2016, MNRAS, 460, 3119

Shen Y., Liu X., 2012, ApJ, 753, 125

Shen Y., Greene J. E., Strauss M. A., Richards G. T., Schneider D. P., 2008, ApJ, 680, 169

Shen Y., et al., 2011, ApJS, 194, 45

Shen Y., et al., 2015, ApJS, 216, 4

Shen Y., et al., 2016, ApJ, 818, 30

Shinozaki K., Miyaji T., Ishisaki Y., Ueda Y., Ogasaka Y., 2006, AJ, 131, 2843

Shu X. W., Yaqoob T., Wang J. X., 2010, ApJS, 187, 581

Siebenmorgen R., Krügel E., Spoon H. W. W., 2004, A&A, 414, 123

Silk J., Rees M. J., 1998, A&A, 331, L1

Skielboe A., Pancoast A., Treu T., Park D., Barth A. J., Bentz M. C., 2015, MNRAS, 454, 144

Smette A., et al., 2015, A&A, 576, A77

Smith J. D. T., et al., 2007, ApJ, 656, 770

Smith K. L., Shields G. A., Bonning E. W., McMullen C. C., Rosario D. J., Salviander S., 2010, ApJ, 716, 866

Stern J., Laor A., Baskin A., 2014, MNRAS, 438, 901

Suganuma M., et al., 2006, ApJ, 639, 46

Thompson T. A., Quataert E., Murray N., 2005, ApJ, 630, 167

Tielens A. G. G. M., 2008, ARA&A, 46, 289

Tombesi F., Meléndez M., Veilleux S., Reeves J. N., González-Alfonso E., Reynolds C. S., 2015, Nat, 519, 436

Tommasin S., Spinoglio L., Malkan M. A., Fazio G., 2010, ApJ, 709, 1257

Tremaine S., et al., 2002, ApJ, 574, 740

Tristram K. R. W., Burtscher L., Jaffe W., Meisenheimer K., Hönig S. F., Kishimoto M., Schartmann M., Weigelt G., 2014, A&A, 563, A82

Uchida K. I., Sellgren K., Werner M. W., Houdashelt M. L., 2000, ApJ, 530, 817

Urry C. M., Padovani P., 1995, PASP, 107, 803

Vanden Berk D. E., et al., 2004, ApJ, 601, 692

Vasudevan R. V., Fabian A. C., 2009, MNRAS, 392, 1124

Vaughan S., Uttley P., Pounds K. A., Nandra K., Strohmayer T. E., 2011, MNRAS, 413, 2489

Veilleux S., et al., 2013, ApJ, 776, 27

Vernet J., et al., 2011, A&A, 536, A105

Véron-Cetty M.-P., Véron P., 2010, A&A, 518, A10

Véron-Cetty M.-P., Joly M., Véron P., 2004, A&A, 417, 515

Vestergaard M., 2002, ApJ, 571, 733

Vestergaard M., 2003, ApJ, 599, 116

Vestergaard M., 2004, ApJ, 601, 676

Vestergaard M., Osmer P. S., 2009, ApJ, 699, 800

Vestergaard M., Peterson B. M., 2005, ApJ, 625, 688

Vestergaard M., Peterson B. M., 2006, ApJ, 641, 689

Vestergaard M., Wilkes B. J., 2001, ApJS, 134, 1

Vestergaard M., Fan X., Tremonti C. A., Osmer P. S., Richards G. T., 2008, ApJ, 674, L1

Vestergaard M., Denney K., Fan X., Jensen J. J., Kelly B. C., Osmer P. S., Peterson B. M., Tremonti C. A., 2011, in Narrow-Line Seyfert 1 Galaxies and their Place in the Universe. p. 38

Voit G. M., 1992, MNRAS, 258, 841

Vollmer B., Beckert T., 2002, A&A, 382, 872

Volonteri M., Natarajan P., 2009, MNRAS, 400, 1911

Wada K., Norman C. A., 2002, ApJ, 566, L21

Wandel A., 1999a, ApJ, 519, L39

Wandel A., 1999b, ApJ, 519, L39

Wanders I., et al., 1997, ApJS, 113, 69

Wang J.-M., Chen Y.-M., Hu C., Mao W.-M., Zhang S., Bian W.-H., 2009, ApJ, 705, L76

Wang J., Risaliti G., Fabbiano G., Elvis M., Zezas A., Karovska M., 2010, ApJ, 714, 1497

Watson D., Denney K. D., Vestergaard M., Davis T. M., 2011, ApJ, 740, L49

Whittle M., 1985, MNRAS, 213, 1

Wild V., Heckman T., Charlot S., 2010, MNRAS, 405, 933

Wilhite B. C., Brunner R. J., Schneider D. P., Vanden Berk D. E., 2007, ApJ, 669, 791

Winter L. M., Mushotzky R. F., Reynolds C. S., Tueller J., 2009, ApJ, 690, 1322

Winter L. M., Veilleux S., McKernan B., Kallman T. R., 2012, ApJ, 745, 107

Woo J.-H., Urry C. M., 2002, ApJ, 579, 530

Woo J.-H., et al., 2010, ApJ, 716, 269

Wu Y., Charmandaris V., Huang J., Spinoglio L., Tommasin S., 2009, ApJ, 701, 658

Wylezalek D., Zakamska N. L., 2016, MNRAS, 461, 3724

Yong S. Y., Webster R. L., King A. L., 2016, PASA, 33, e009

York D. G., et al., 2000, AJ, 120, 1579

Appendix A

Difference to Master's thesis work

The investigations in chapters 2, 3 and 4 of this thesis (hereafter referred to as 'this work') are based on a preliminary study I did as part of my masters thesis work (Jensen, 2012). To avoid any confusion, and to make it completely clear how my masters thesis differs from this work, I specifically point out the differences between these two pieces of work here. Very briefly, the work presented in chapters 2, 3 and 4 provide a significantly larger in-depth study compared to my masters thesis work. Specifically, they cover a larger and more representative sample of AGN spectra (18 in masters thesis vs. 90 in this work), they include more line parameters in the investigation, and they test in depth how the accuracy and precision of the line parameters depend on the intrinsic characteristics (i.e., the width, strength, and shape) of a given emission line profile. My masters thesis work served as a preliminary study in order to get a general idea of some of the uncertainties associated with the different line width parameters, so to evaluate if the current study was necessary. As a consequence of expanding the sample size for this work, I had to develop a new spectral decomposition method to facilitate a larger variety in spectral parameters across the sample. For this reason, all of the spectra included in my masters thesis have been completely re-analyzed according to the more detailed and comprehensive analysis in this work. Another important difference is that I analyze each emission line separately in order to highlight the differences between them. In my Master's thesis work, only the Hβ and C IV lines were analyzed and not in a separate fashion.

The specific differences are here given for each major component of the analysis:

1. **Emission lines:** In this work I analyze spectra containing the broad Hβ λ4861Å, Mg II λ2796Å, or C IV λ1549Å emission lines, respectively. In my masters thesis, I only included Hβ and C IV. The Mg II line can be used to estimated black hole masses in optical spectra for redshifts $\sim 0.7 < z < 2.2$. This particular redshift range bridges the redshift ranges covered by the Hβ ($z < 0.8$) and C IV ($1.5 < z < 4.7$) emission lines in observed optical spectra. In concert, these three lines allow us to probe black hole masses in AGN all the way from the local universe up to redshifts of $z \sim$4.7 using optical spectra from for example the Sloan Digital Sky Survey (SDSS).

2. **Sample size:** The total number of high S/N spectra covering the Hβ or C IV line in this work is 63 (29 for Hβ and 34 for C IV), compared to 18 high S/N spectra (9 for each of Hβ and C IV) in my masters thesis. These larger samples of spectra cover a much wider range in terms of the spectral properties observed in the general AGN population (see item 3 below) and the analysis in this work is therefore much more comprehensive than the one in my masters thesis. Furthermore, because the Mg II line is included in this work, this adds another 27 spectra, giving a combined sample size of 90 high S/N spectra. The spectra in my masters thesis were mainly SDSS spectra, either single-epoch or composite spectra, supplemented by four spectra from reverberation mapping campaigns averaged over periods of $\sim$1.5 to 8 months. In this work, I include a higher number of single-epoch SDSS spectra and several spectra of objects observed with X-Shooter, respectively, for all three emission lines. The larger sample size in this work provides a better statistical basis and places my results on a significantly firmer footing compared to my masters thesis.

3. **Line properties:** The spectra used in my masters thesis were chosen to cover a wide range in emission line width as parameterized by the FWHM, roughly covering the range between $\sim$2000 km s^{-1}and 8000 km s^{-1}for the Hβ and C IV lines, respectively. In this work, the spectra are also chosen to cover a wider range in profile properties, namely in terms of the emission line width (FWHM), strength (EW), and shape fo the profile. I adopt the FWHM/σ_{line} ratio as it has been frequently used in the literature for this purpose. The sample of spectra for each emission line in this work roughly covers the 5 – 95% percentiles of the observed emission line parameters observed in the SDSS as parameterized by Vestergaard et al. (2008) and Shen et al. (2011). The wider coverage in terms of the FWHM, EW, and FWHM/σ_{line} ratio for both Hβ and C IV spectra, respectively, in this work, compared to my masters thesis, ensure that our results are applicable to the general population of observed broad AGN emission lines.

4. **Spectral decomposition:** In this work I include a larger number of spectra with more diverse emission line profiles and spectral shapes and features. This made it necessary to revisit my spectral decomposition method for Hβ and C IV spectra necessary in this work. I made several significant upgrades to the procedures for both Hβ and C IV such that the spectral decomposition method was able to accurately model all of the high S/N spectra in my sample. This involved a lot of additional testing of different methods. For example, for Hβ spectra, I added a Lorentzian profile to model the wings of the broad Hδ and Hγ emission lines. For C IV, I replaced the Fe II template from Vestergaard & Wilkes (2001) with a Gaussian function because the template often gave a poor description of the Fe II features on the red side of C IV. Adjusting a spectral decomposition must be done carefully. First, any new component has to improve the spectral decomposition for a given problematic spectrum that motivated its addition. On the other hand, it is equally important that the adding a new component does not make the spectral decomposition worse for other spectra in the sample. Adjusting a spectral decomposition therefore involves a lot of trial and error and consequently takes a lot of time.

For Mg II, I had to develop the decomposition from scratch and test each potential method with the same scrutiny and rigor as I applied to the new spectral decomposition method that I developed for Hβ and C IV.

5. **Line parameters:** In this work, the MAD width is included in the analysis as a line width parameter, motivated by the fact that Denney et al. (2016) found it to be more robust to spectral noise than FWHM and σ_{line}. I implemented the MAD width and analyzed its results as part of this work.

6. **Line limits:** In this work, I re-examined the five types of line limits introduced in my Master's thesis, but here I extend the analysis. In my masters thesis, I placed the fixed line limits at a distance of $\pm$18,000 km s^{-1} from the line centre of the C IV line, and at a distance of 13,000 km s^{-1} and 16,000 km s^{-1} on the blue and red side, respectively, of the Hβ line. On the blue side of the Hβ line, I often found residuals from the spectral decomposition rather close to the line which prevented me from placing the line limit further away. This can for emission lines with a broad base lead to a truncation of the line wing. Owing to the improved spectral decomposition in this work, such problems generally no longer exist around Hβ, or C IV for that matter. This allows me to place the line limits further away from the line centre and thereby avoid to truncate the emission line profile. For this purpose, I perform an extensive test for the optimal position of the fixed line limits as described in Chapter 2. I find the optimal distance, in fact, to be $\pm$18,000 km s^{-1}from the line centre for both the C IV and Hβ line. At this distance, no extraneous emission is included in the line measurement, and the truncation of the line wings is negligible. Although I reach the same conclusion as in my Master's thesis, the extended investigation serves to solidify at higher significance that using the line limits positioned at a fixed distance from the line centre is the best method to use. In contrast to my Master's thesis work, this investigation has found that a placement of $\pm$18,000 km s^{-1}from the line centre is the optimal distance for both the Hβ and C IV line. Furthermore, this work confirms that the placement of the line limits is robust with the new spectral decomposition methods for C IV and Hβ that were implemented for this work.

7. **Depth of analysis:** In my masters thesis, I did not distinguish between the results obtained for Hβ and C IV emission line spectra. I also used a lognormal distribution to describe the line width measurement distributions at each S/N level for each original high S/N spectrum. In this work, I have done a more thorough analysis. First, I have analyzed Hβ and C IV separately, allowing for a comparison and a more accurate assessment of the strengths and weaknesses of the width parameters measured on each of the two lines. This is important since newer studies indicate a difference in how the profile of the two emission lines change as the line become broader (e.g. Denney, 2012). Secondly, in this work, I present the results for each line width parameter in terms of the emission line width, strength, and shape (see Item 3 above). With this information I identify how these line characteristics impact the accuracy and precision of the

line width parameters. Thirdly, in this work, I use a non-parametric description of the line width distribution at a given S/N level. This gives a better extraction of the accuracy and precision from each distribution than forcing a log-normal parameterization as I did in my masters thesis. All of these changes have led to more extensive and accurate results and conclusions in this work compared to my masters thesis.

8. **Variability:** In this work, I include a test of how robust each line width measure is to AGN variability using monitoring data for the Hβ line in NGC 5548. This test is important as the mass of the black hole should remain constant over the timescales observed, and a mass estimator must therefore also give a constant black hole mass as the AGN luminosity varies. This analysis was not a part of my Master's thesis work.

9. **C IV absorption:** In my masters thesis, I did a preliminary study of the effects of narrow line absorption on the measured line parameters for the C IV line. I used the five C IV composite spectra in that work and for each I added five types of narrow line absorption. These covered the core of the profile with two different absorption strengths (EW of 0.6Å and 1.2Å, respectively), in between the core and the wing of the profile with two different absorption strengths (EW of 0.6Å and 1.2Å, respectively), and in the wing of the profile with only one strength (EW of 0.6Å). This resulted in 25 spectra with absorption features. I attempted to automatically correct for the absorption using a flux-clipping method based on the median and standard deviation of the flux in a running boxcar. I investigated the FWHM, σ_{line}, and IPV50 width in that work. In this work (Chapter 4) I revisit this problem. This time I use a sample of 16 high S/N spectra that represent the larger coverage in line properties represented in this work (see Item 3 above). Furthermore, the 16 spectra also cover spectral resolutions ranging from $\sim$60 km s^{-1} (X-Shooter spectra) to $\sim$1150 km s^{-1} (Fairall 9 spectrum), compared to only a single spectral resolution (SDSS data, $R \sim$150 km s^{-1}) in my masters thesis work. The absorption features covered in this work are placed at three different positions of emission line and with three different strengths at each position. This gives a sample of nine high S/N spectra with distinct absorption features for each of the 16 high S/N spectra for a total of 144 absorbed spectra compared to the 25 in my masters thesis work. In this work, I also include all of the IPV widths and not only the IPV50 width as in my masters thesis. Finally, I make no attempt to correct for the absorption features in this work as I wish to show the effect of unrecognized absorption, whether this is due to low spectral S/N or low spectral resolution or a combination of both.

Appendix B

Conversion between IPV widths and FWHM for a Gaussian function[1]

[1] Appendix to Chapter 2.

Table B.1 Conversion between IPV widths at percentage levels from 1% to 99% and the FWHM of a Gaussian profile

Percentage level Y %	Scaling factor Q(Y) $\frac{IPV(Y)}{FWHM}$	Percentage level Y %	Scaling factor Q(Y) $\frac{IPV(Y)}{FWHM}$
1	2.1877	51	0.5596
2	1.9758	52	0.5464
3	1.8431	53	0.5334
4	1.7443	54	0.5205
5	1.6646	55	0.5077
6	1.5974	56	0.4950
7	1.5389	57	0.4825
8	1.4869	58	0.4700
9	1.4400	59	0.4576
10	1.3970	60	0.4454
11	1.3574	61	0.4332
12	1.3205	62	0.4211
13	1.2860	63	0.4091
14	1.2534	64	0.3972
15	1.2226	65	0.3854
16	1.1934	66	0.3736
17	1.1655	67	0.3619
18	1.1387	68	0.3503
19	1.1131	69	0.3388
20	1.0885	70	0.3273
21	1.0647	71	0.3158
22	1.0417	72	0.3044
23	1.0195	73	0.2931
24	0.9980	74	0.2819
25	0.9770	75	0.2706
26	0.9567	76	0.2595
27	0.9369	77	0.2483
28	0.9175	78	0.2372
29	0.8987	79	0.2262
30	0.8803	80	0.2152
31	0.8623	81	0.2042
32	0.8446	82	0.1933
33	0.8273	83	0.1824
34	0.8104	84	0.1715
35	0.7938	85	0.1606
36	0.7774	86	0.1498
37	0.7614	87	0.1390
38	0.7456	88	0.1282
39	0.7301	89	0.1175
40	0.7148	90	0.1067
41	0.6998	91	0.0960
42	0.6849	92	0.0853
43	0.6703	93	0.0746
44	0.6558	94	0.0639
45	0.6416	95	0.0533
46	0.6275	96	0.0426
47	0.6136	97	0.0319
48	0.5999	98	0.0213
49	0.5863	99	0.0106
50	0.5729		

Appendix C

Accuracy and precision of the IPV widths measured for the Hβ line[1]

[1] Appendix to Chapter 2.

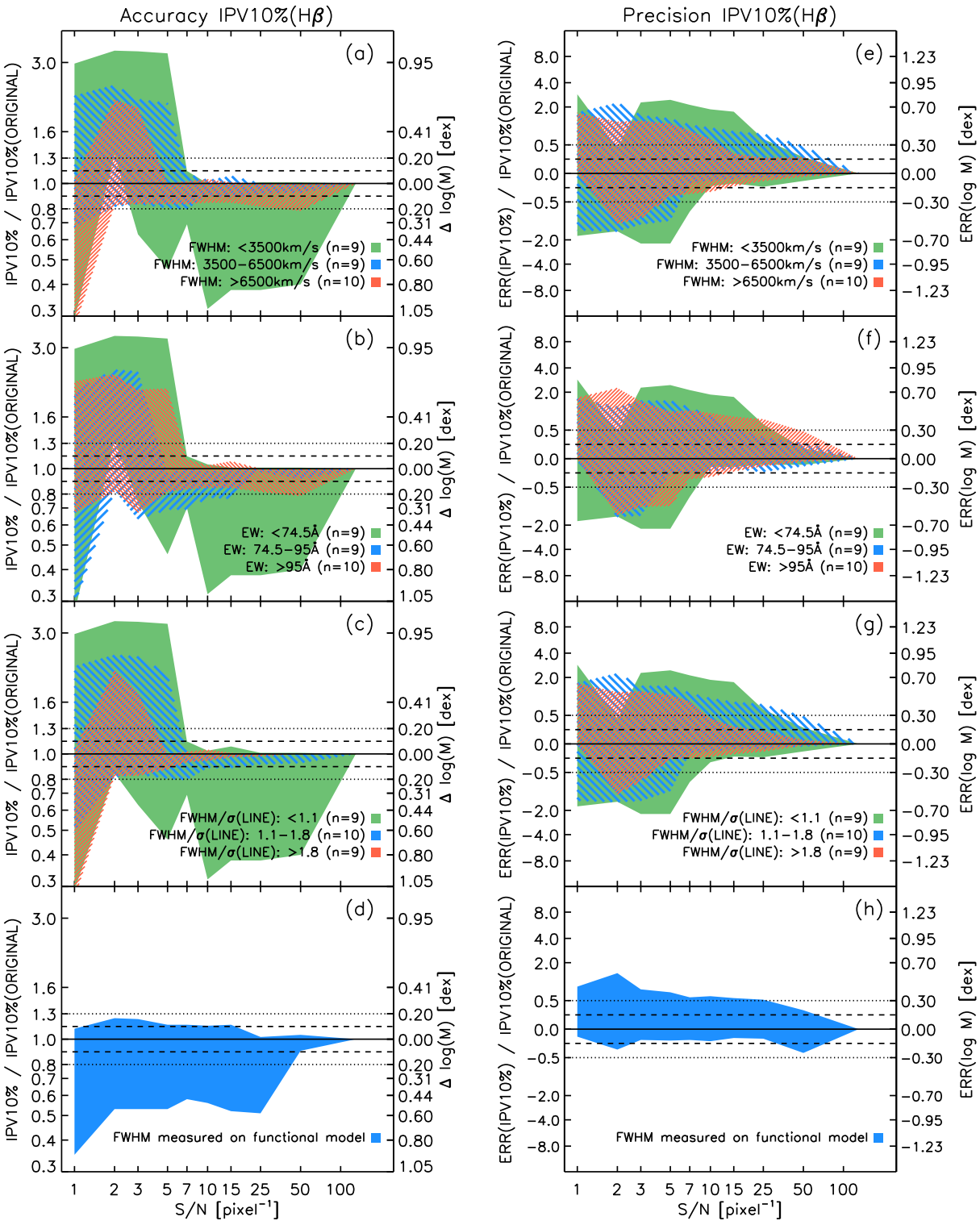

Fig. C.1 Hβ IPV(10%) width.

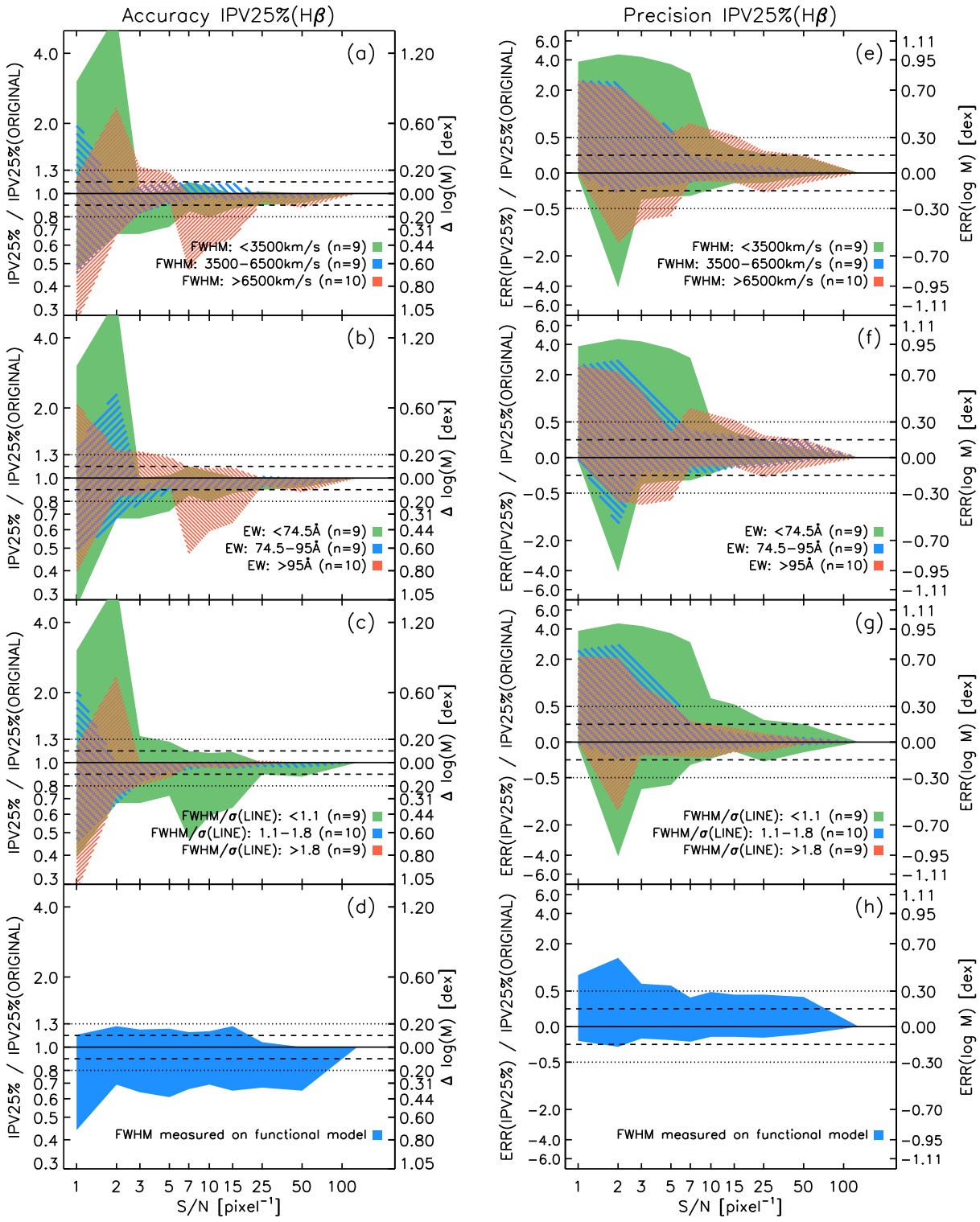

Fig. C.2 Hβ IPV(25%) width.

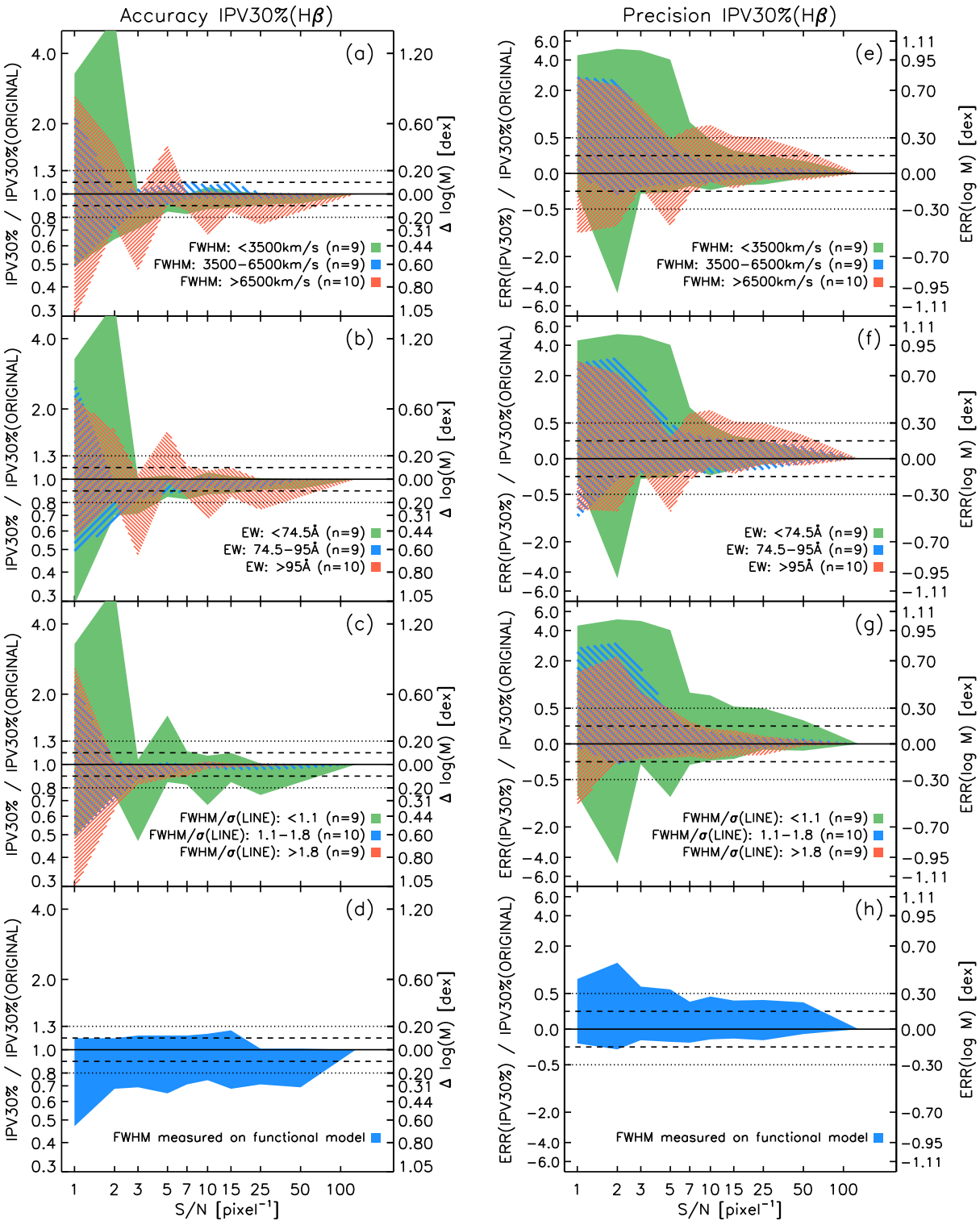

Fig. C.3 Hβ IPV(30%) width.

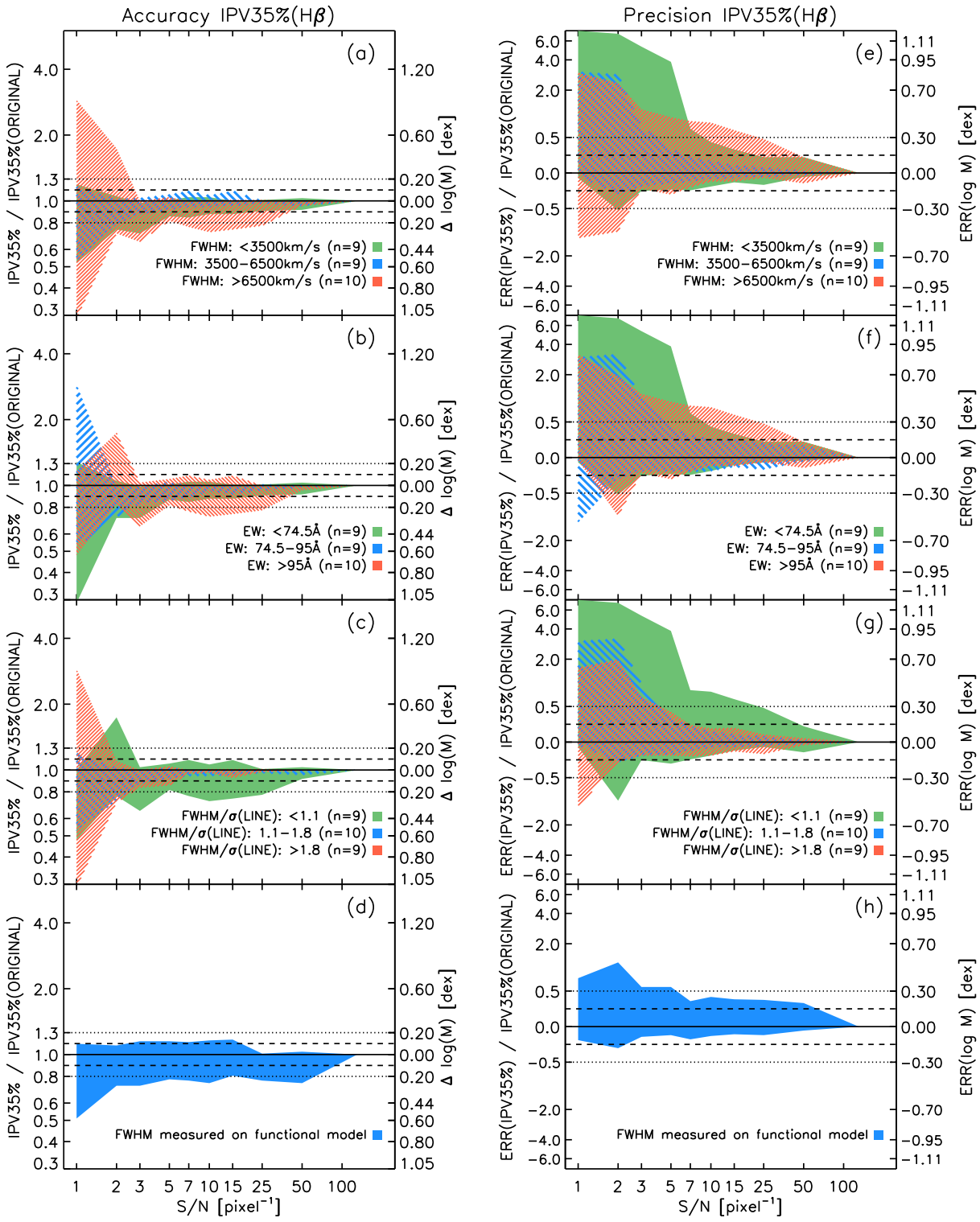

Fig. C.4 Hβ IPV(35%) width.

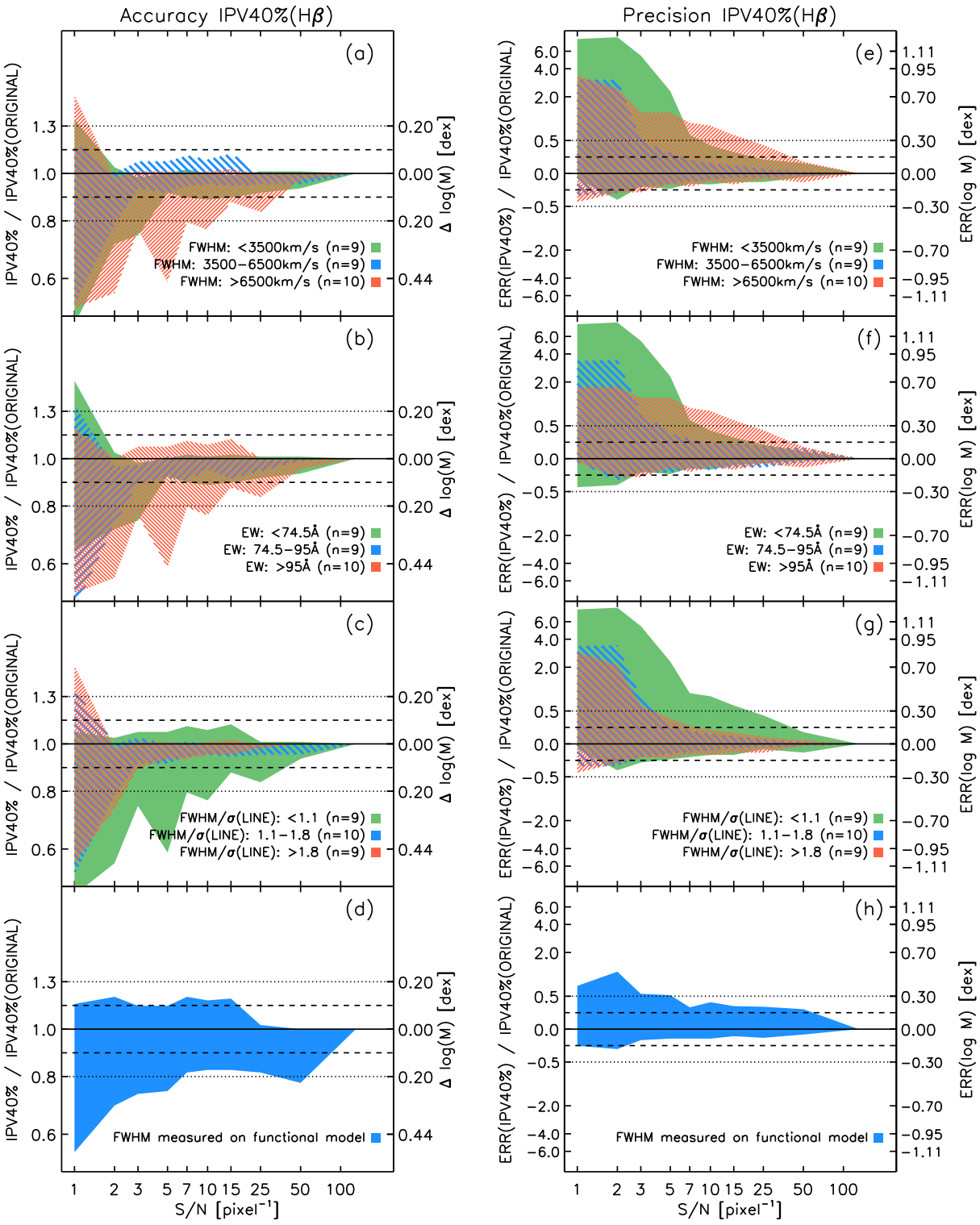

Fig. C.5 Hβ IPV(40%) width.

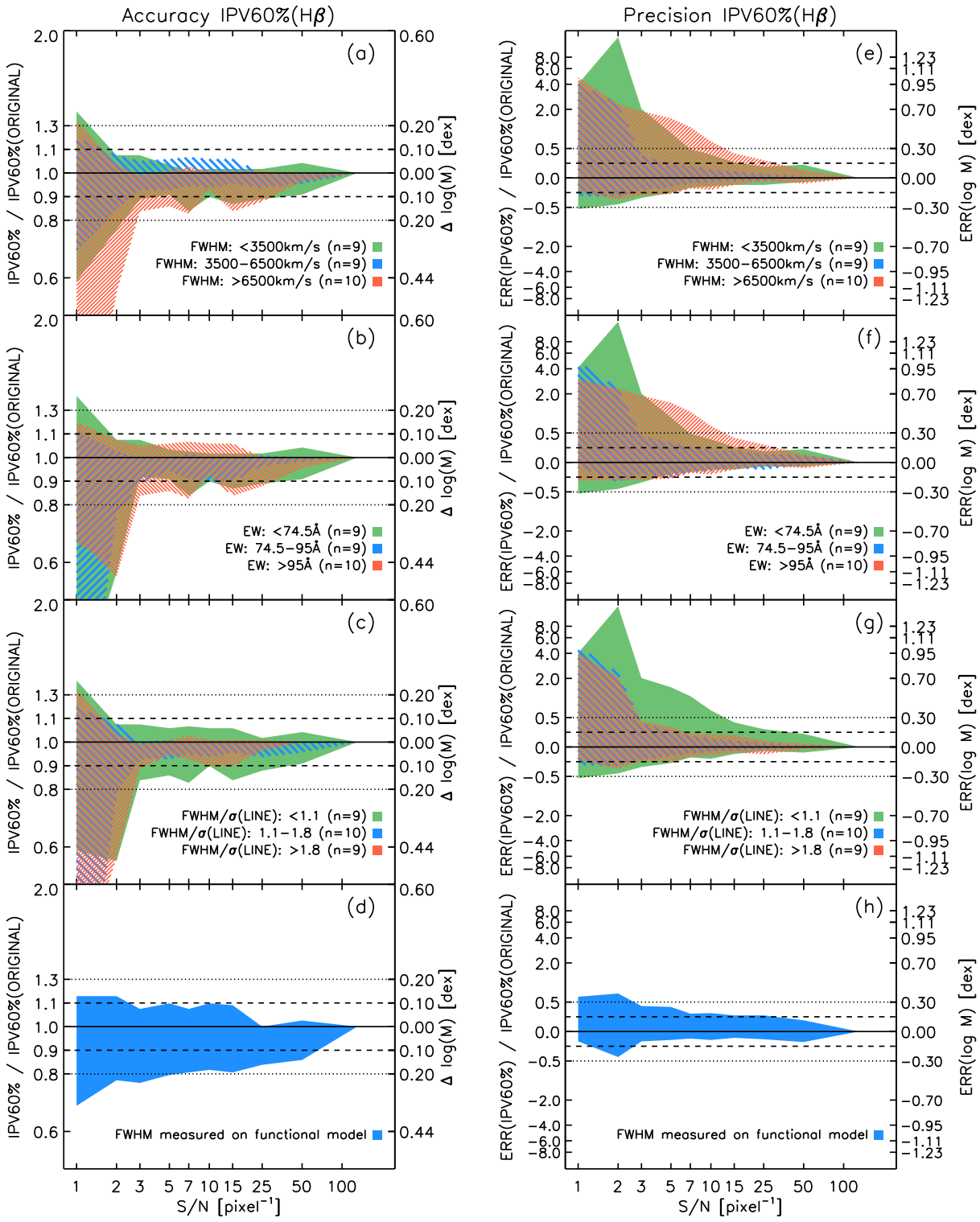

Fig. C.6 Hβ IPV(60%) width.

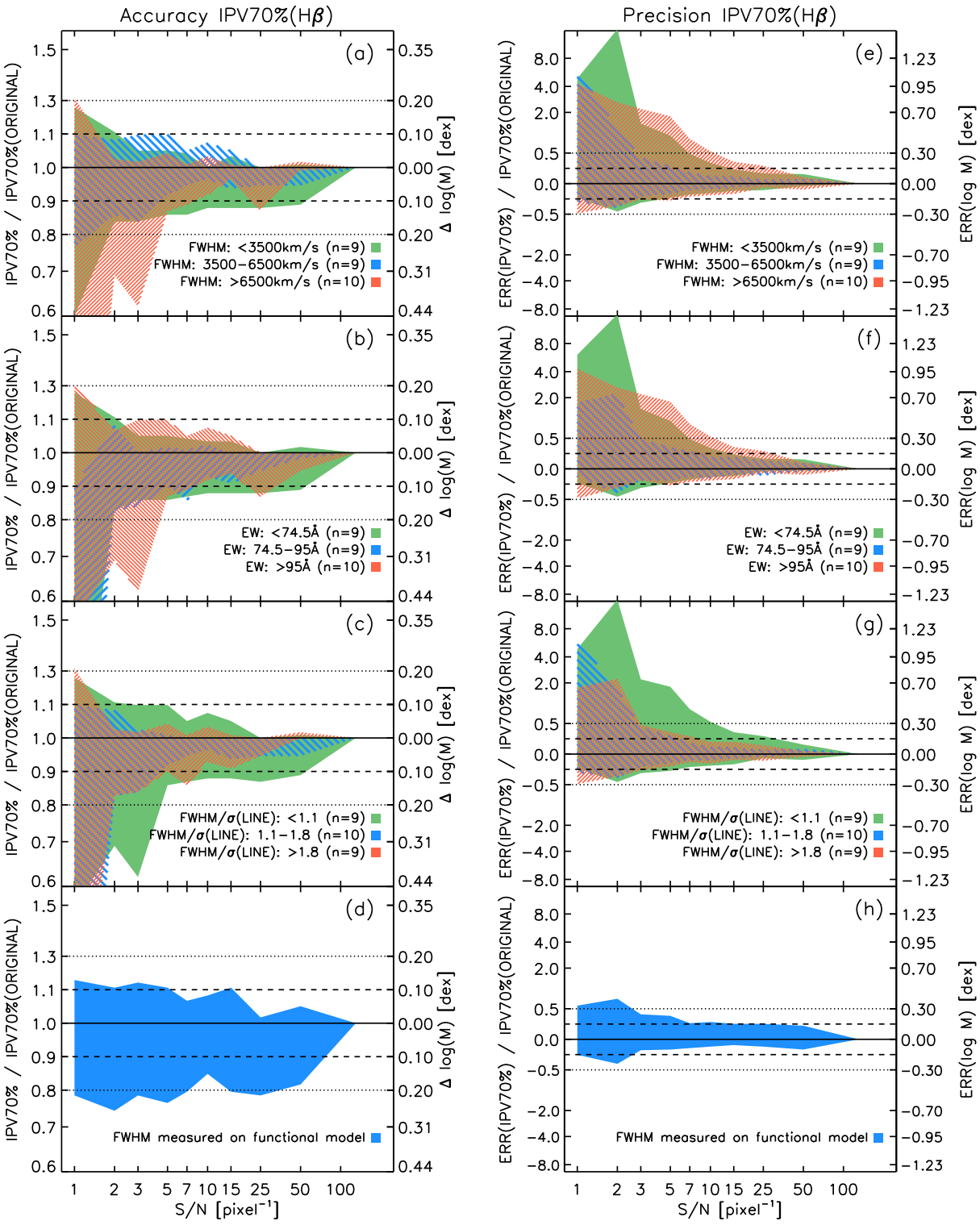

Fig. C.7 Hβ IPV(70%) width.

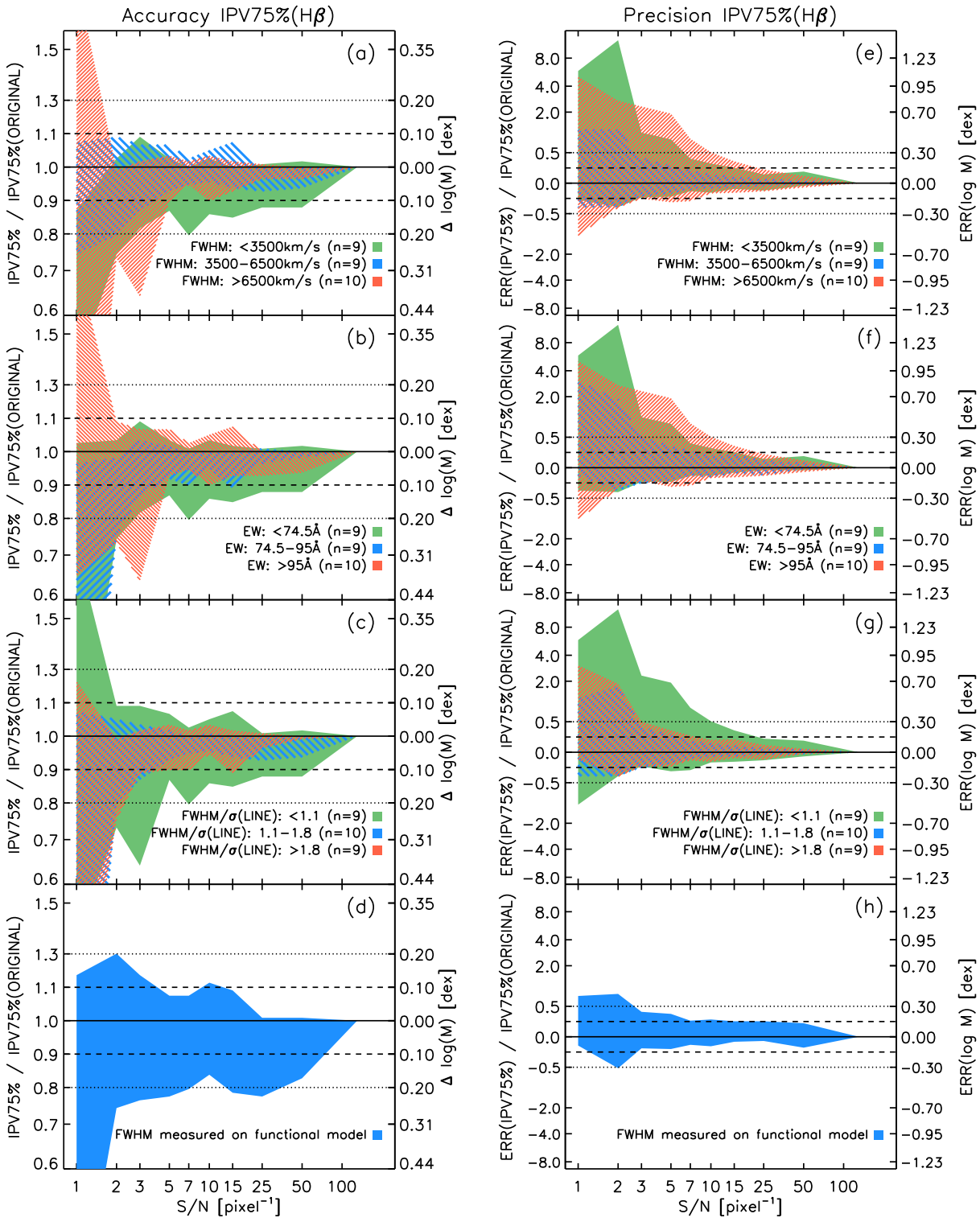

Fig. C.8 Hβ IPV(75%) width.

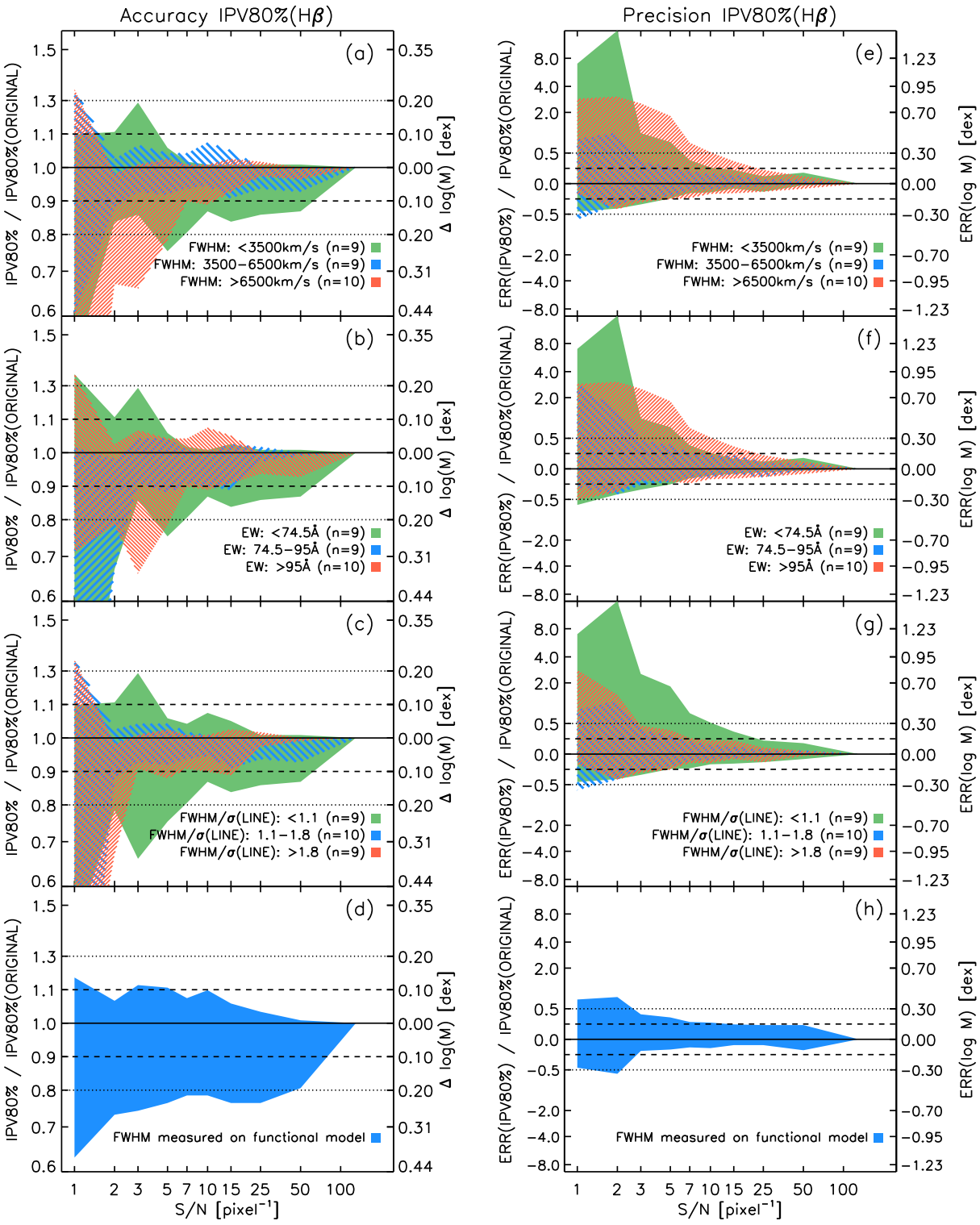

Fig. C.9 Hβ IPV(80%) width.

Appendix D

Accuracy and precision of the line width parameters for the C IV line[1]

[1] Appendix to Chapter 2.

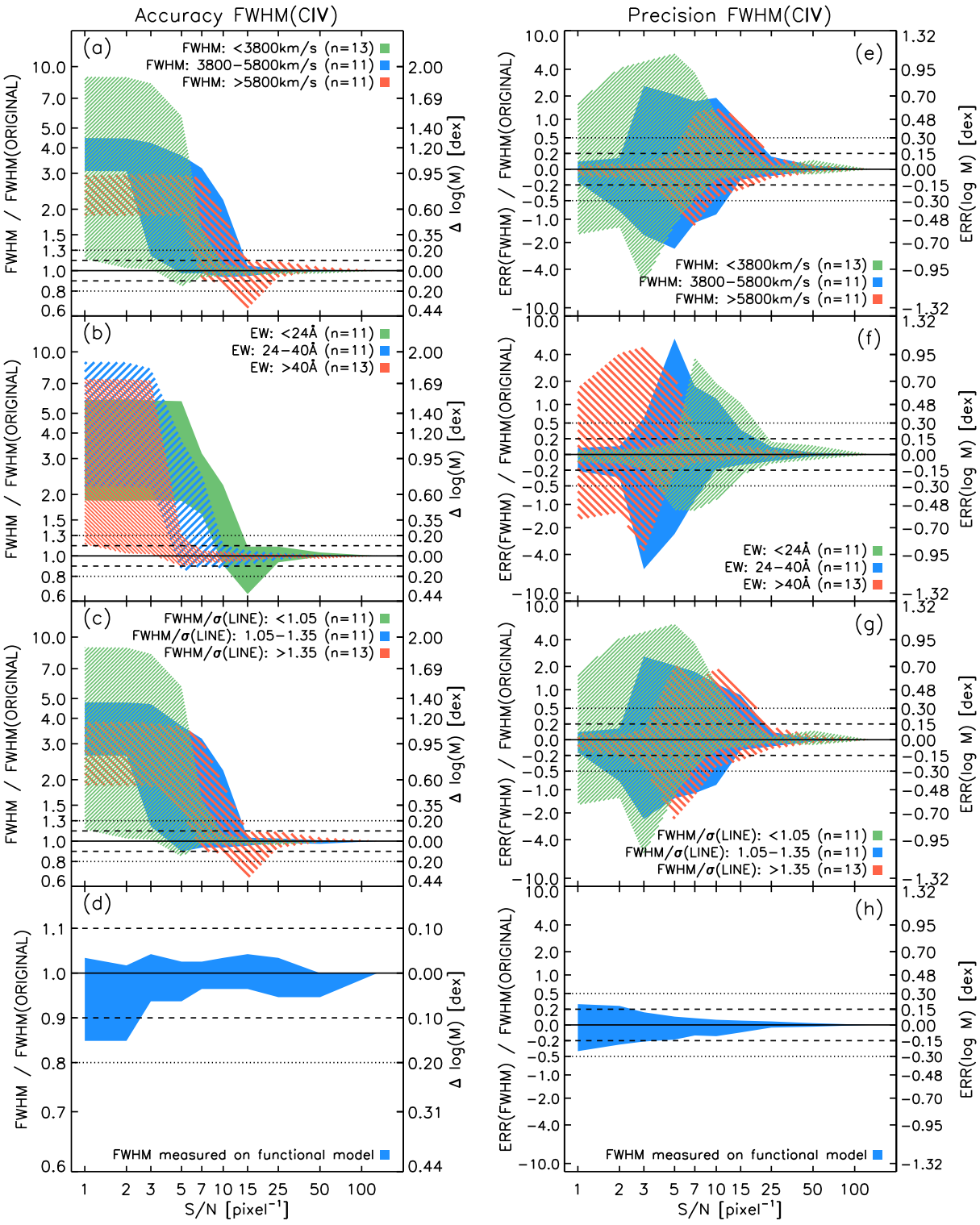

Fig. D.1 Relative accuracy (left column) and precision (right column) of the FWHM(C IV) width as a function of S/N when measured on all the spectra in our sample of degraded C IV spectra. The figure is explained in § 2.8.1.

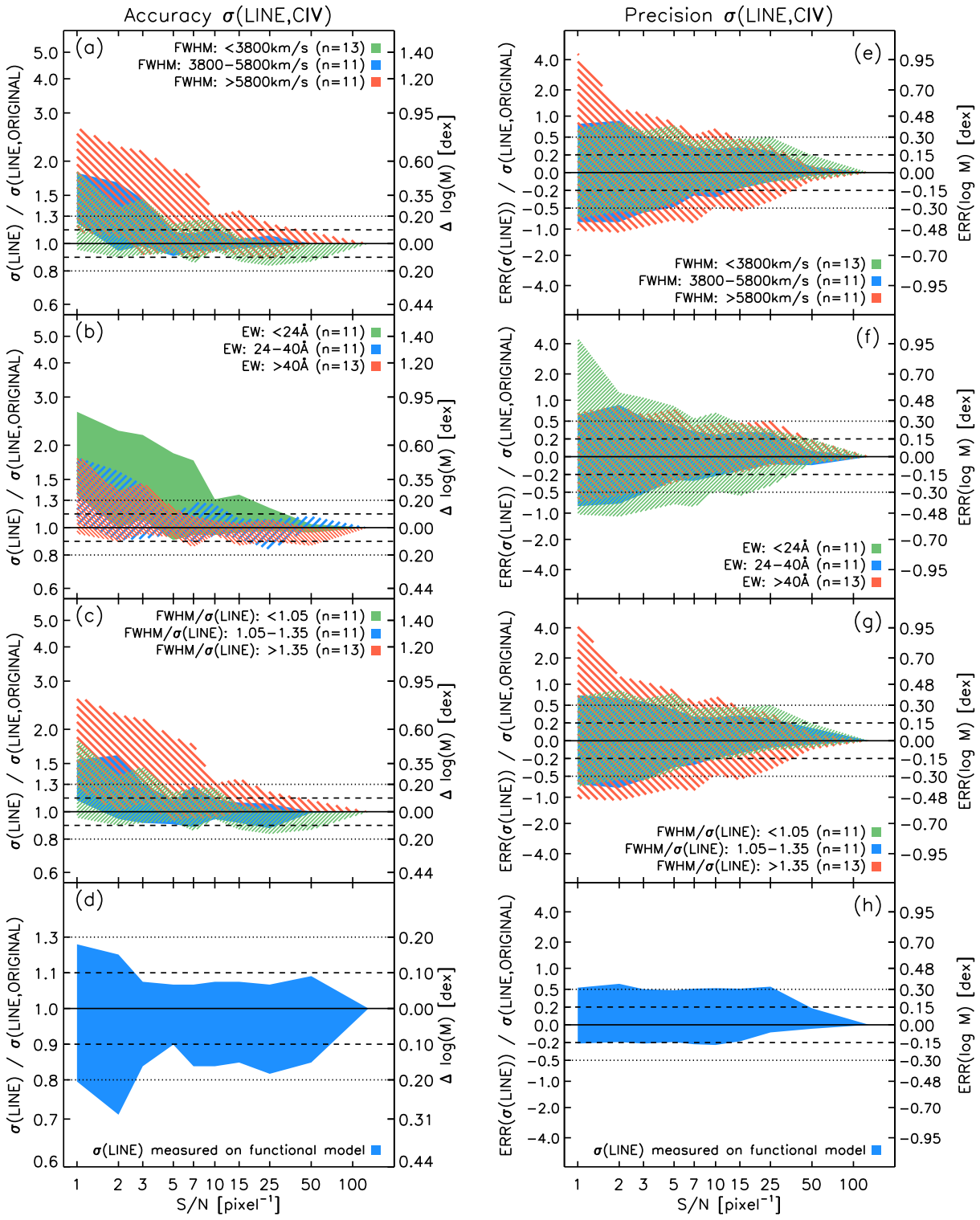

Fig. D.2 Relative accuracy (left column) and precision (right column) of the σ_{line} (C IV) width as a function of S/N when measured on all the spectra in our sample of degraded C IV spectra. The figure is explained in § 2.8.1.

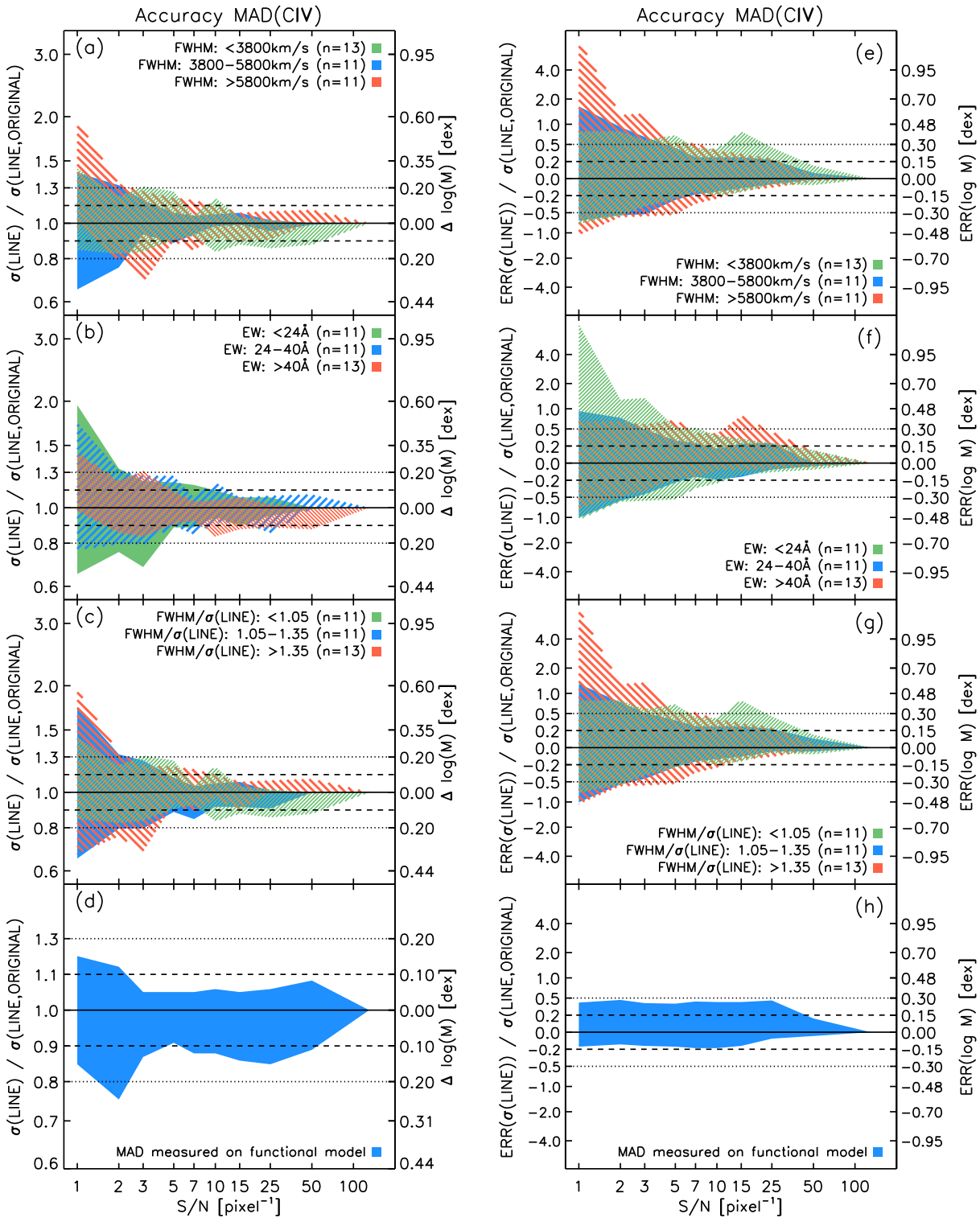

Fig. D.3 Relative accuracy (left column) and precision (right column) of the MAD(C IV) width as a function of S/N when measured on all the spectra in our sample of degraded C IV spectra. The figure is explained in § 2.8.1.

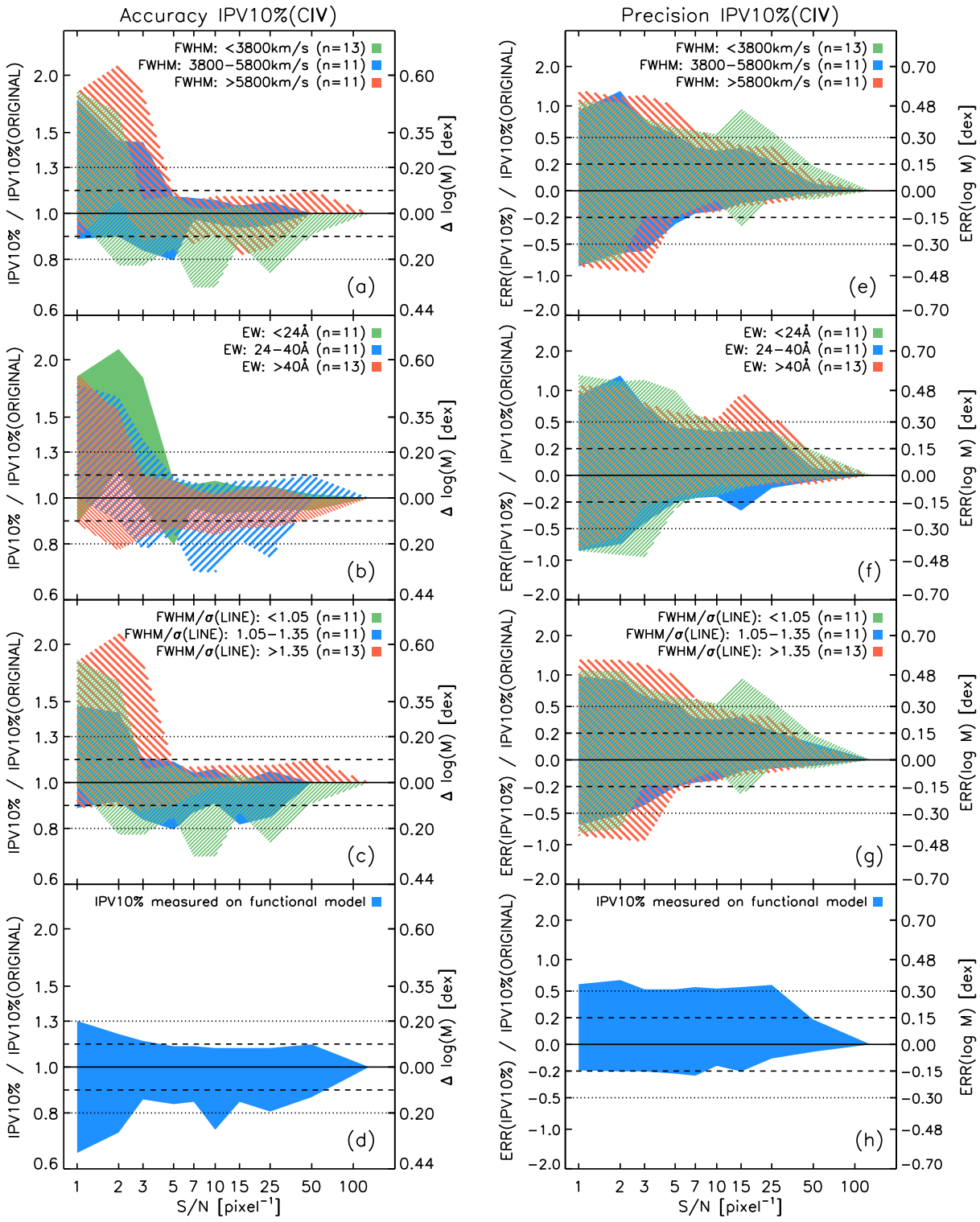

Fig. D.4 C IV IPV(10%) width.

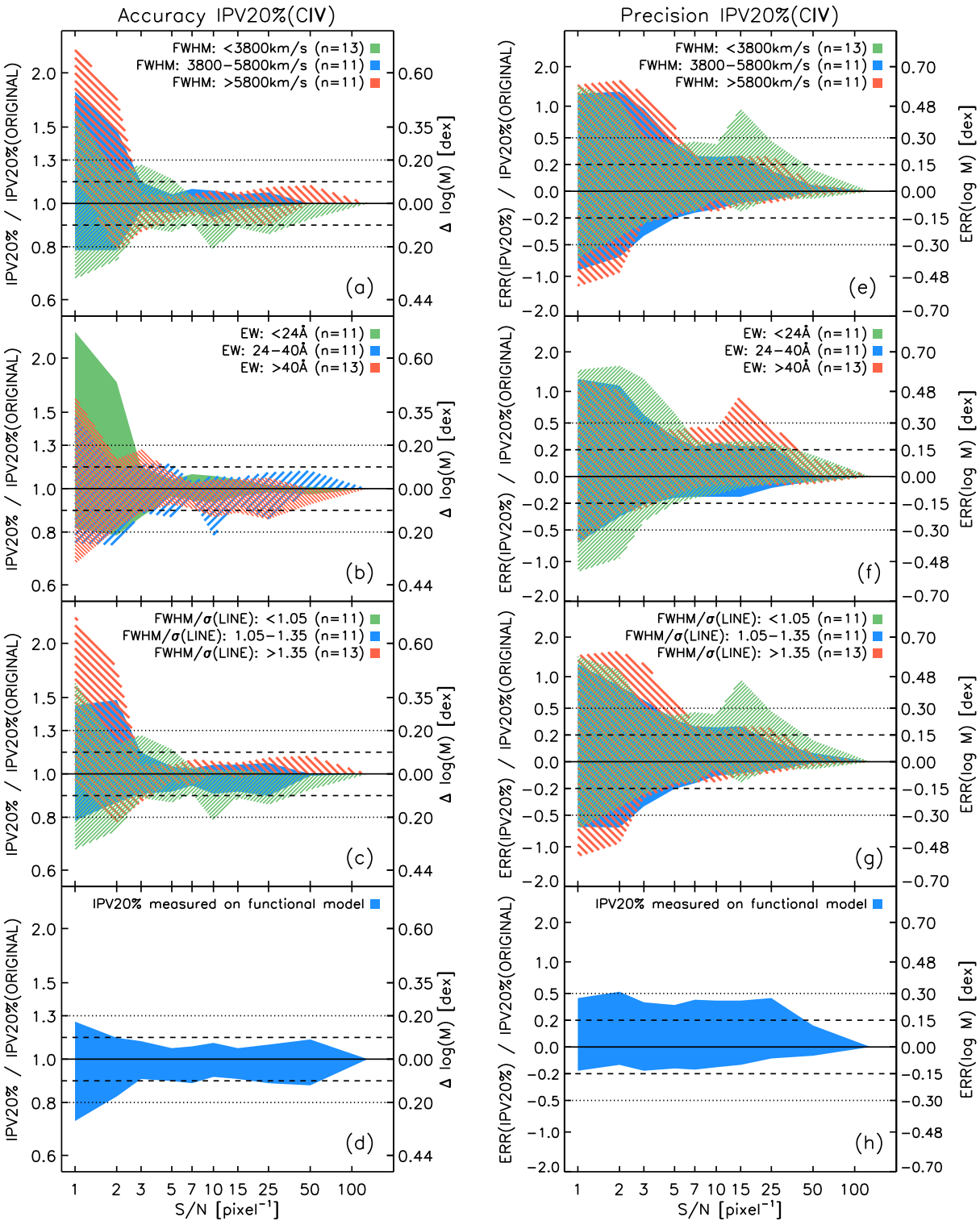

Fig. D.5 C IV IPV(20%) width.

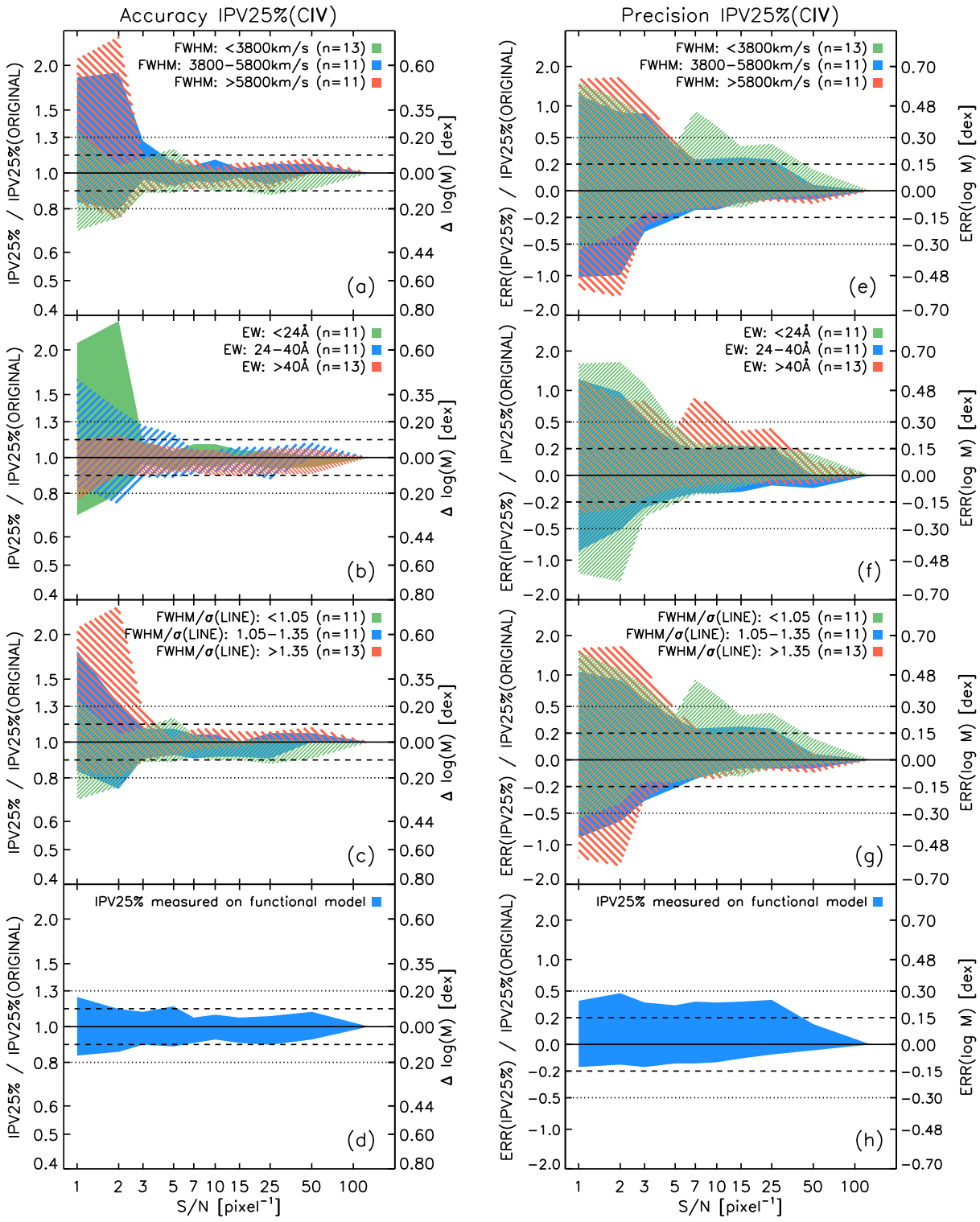

Fig. D.6 C IV IPV(25%) width.

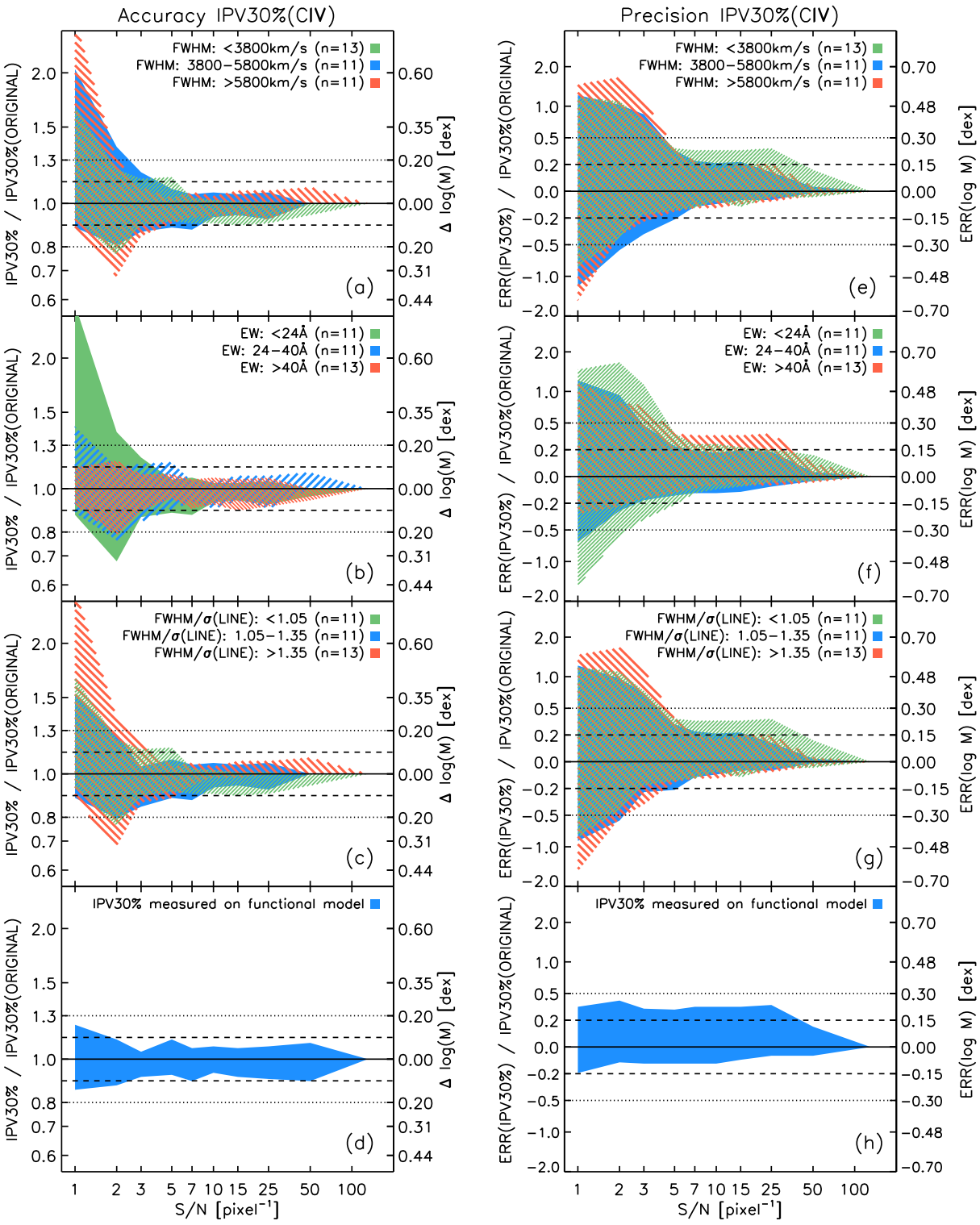

Fig. D.7 C IV IPV(30%) width.

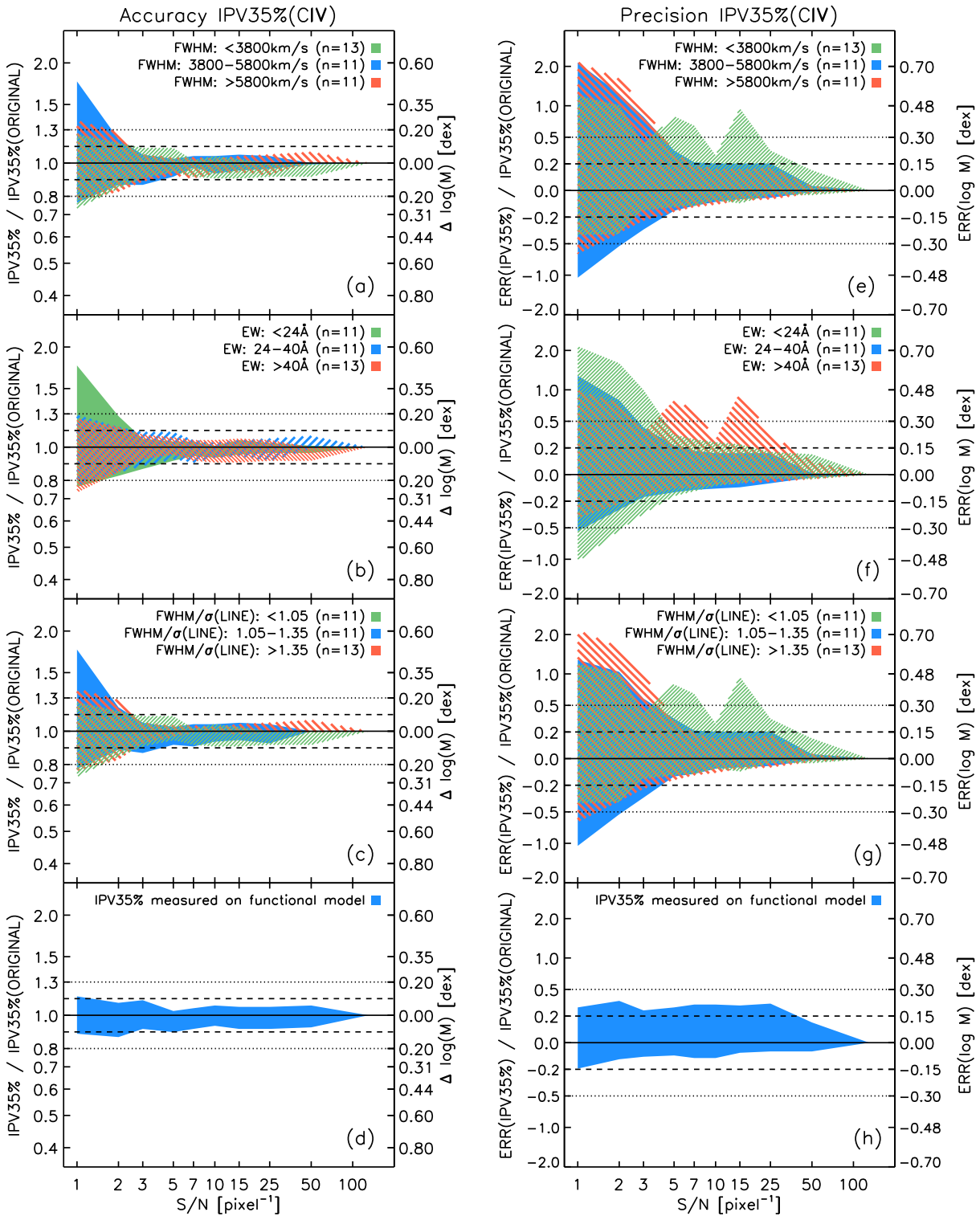

Fig. D.8 C IV IPV(35%) width.

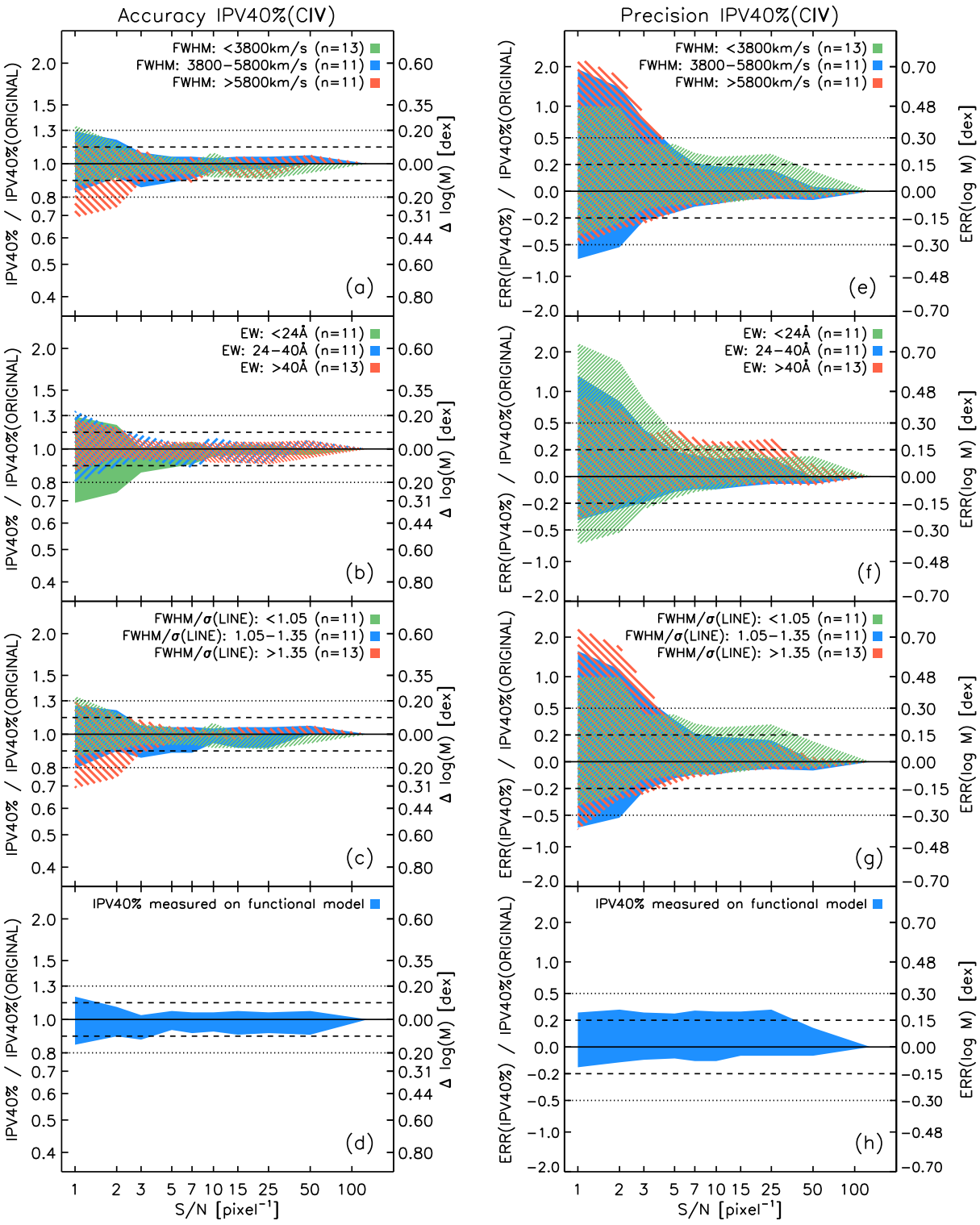

Fig. D.9 C IV IPV(40%) width.

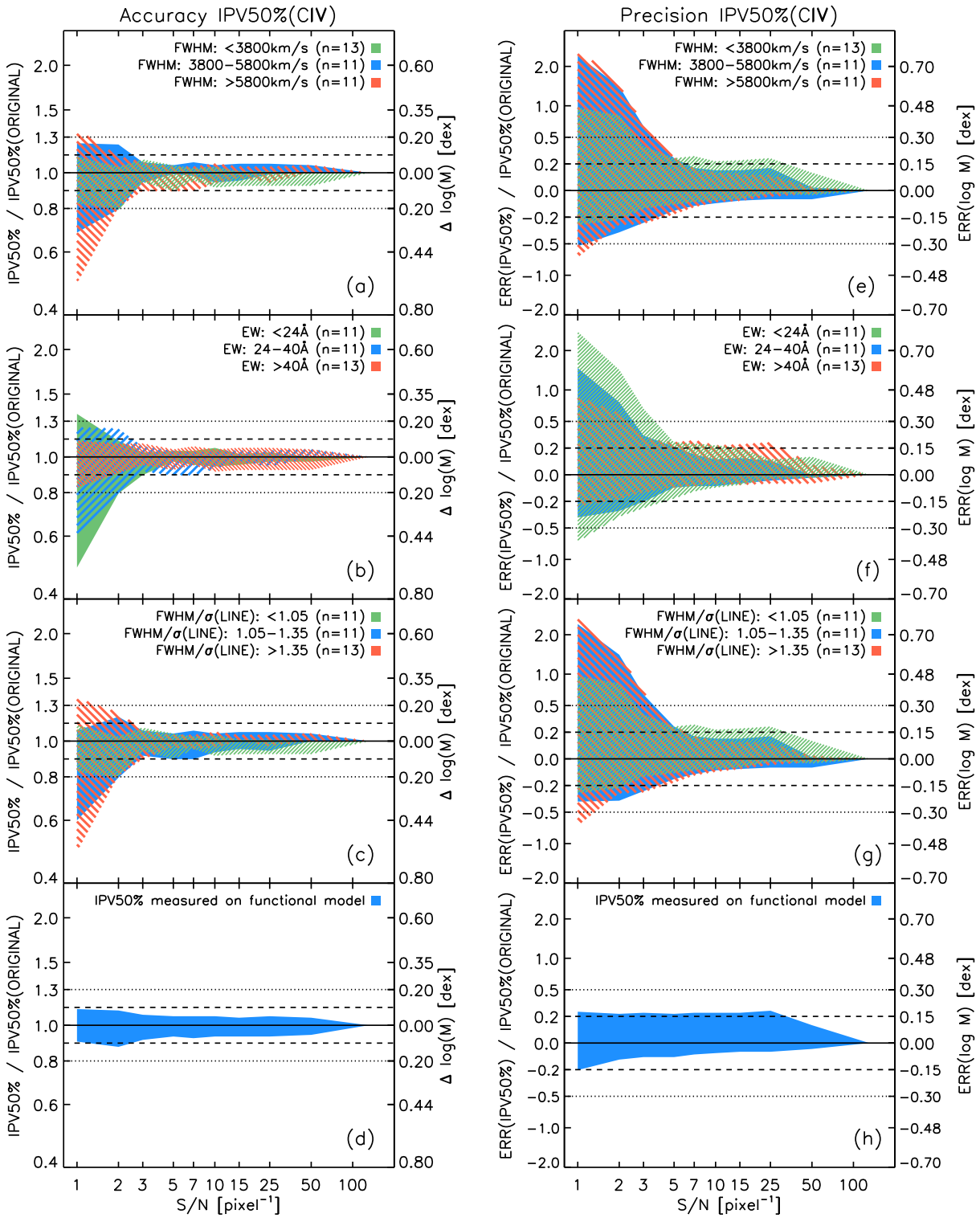

Fig. D.10 C IV IPV(50%) width.

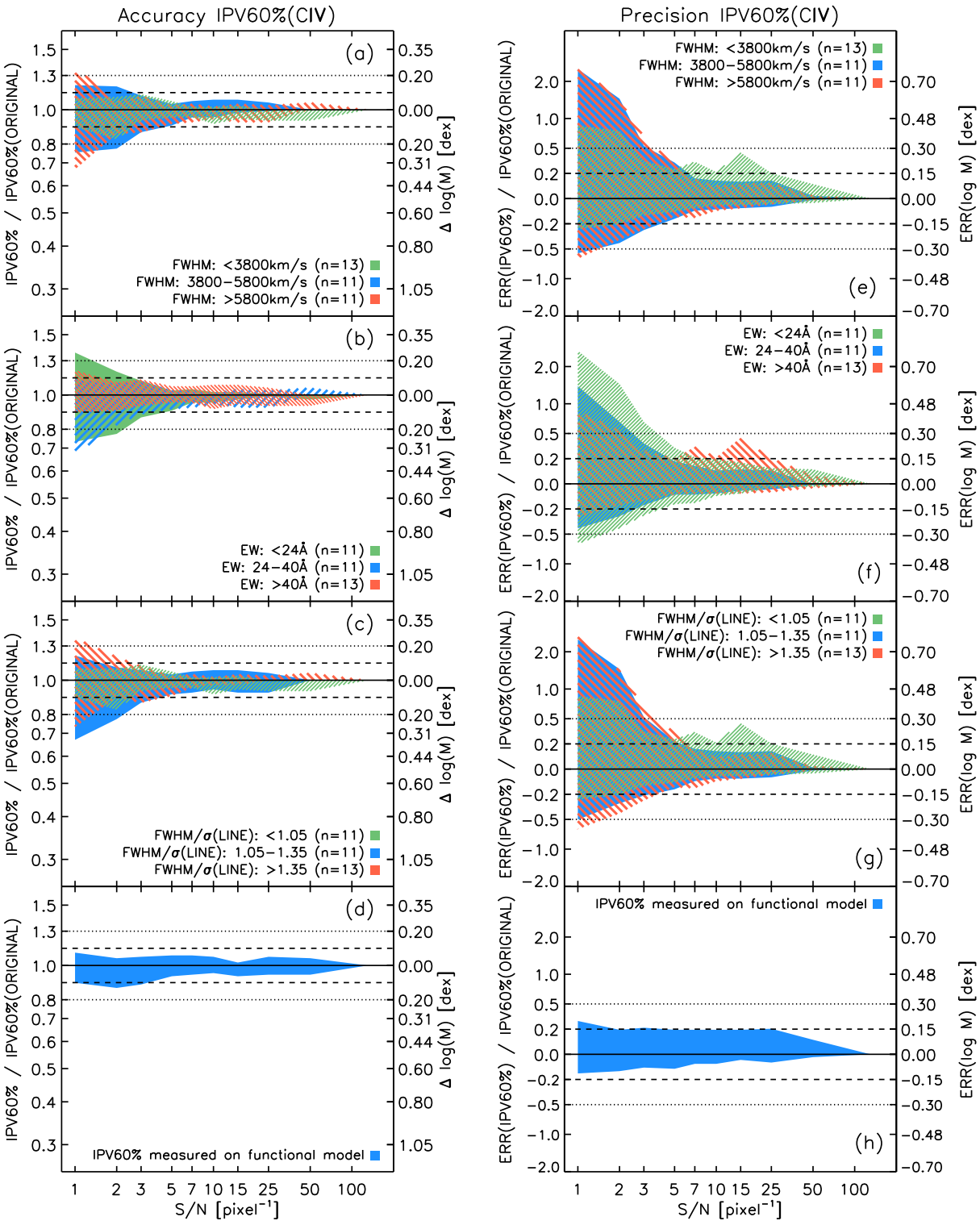

Fig. D.11 C IV IPV(60%) width.

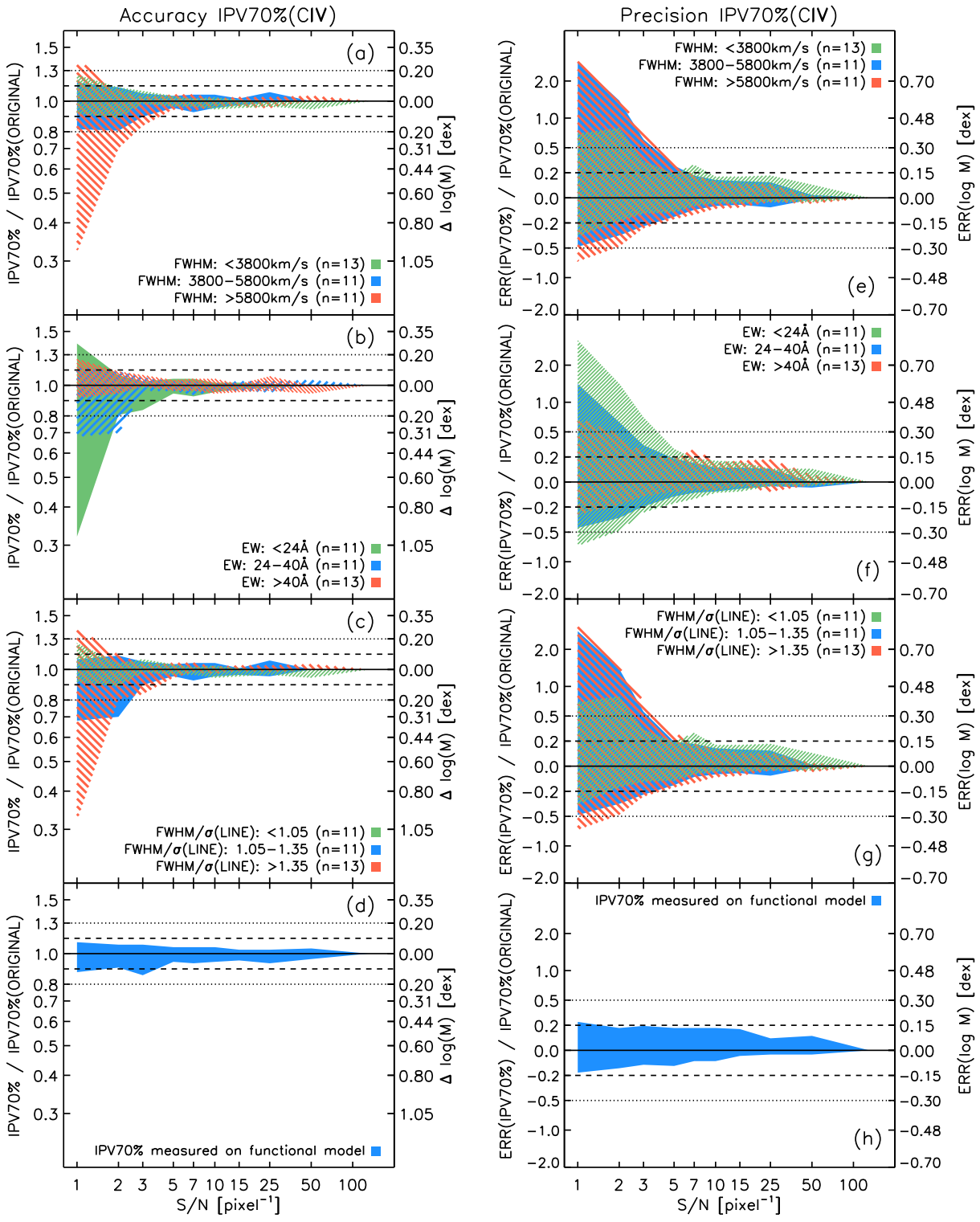

Fig. D.12 C IV IPV(70%) width.

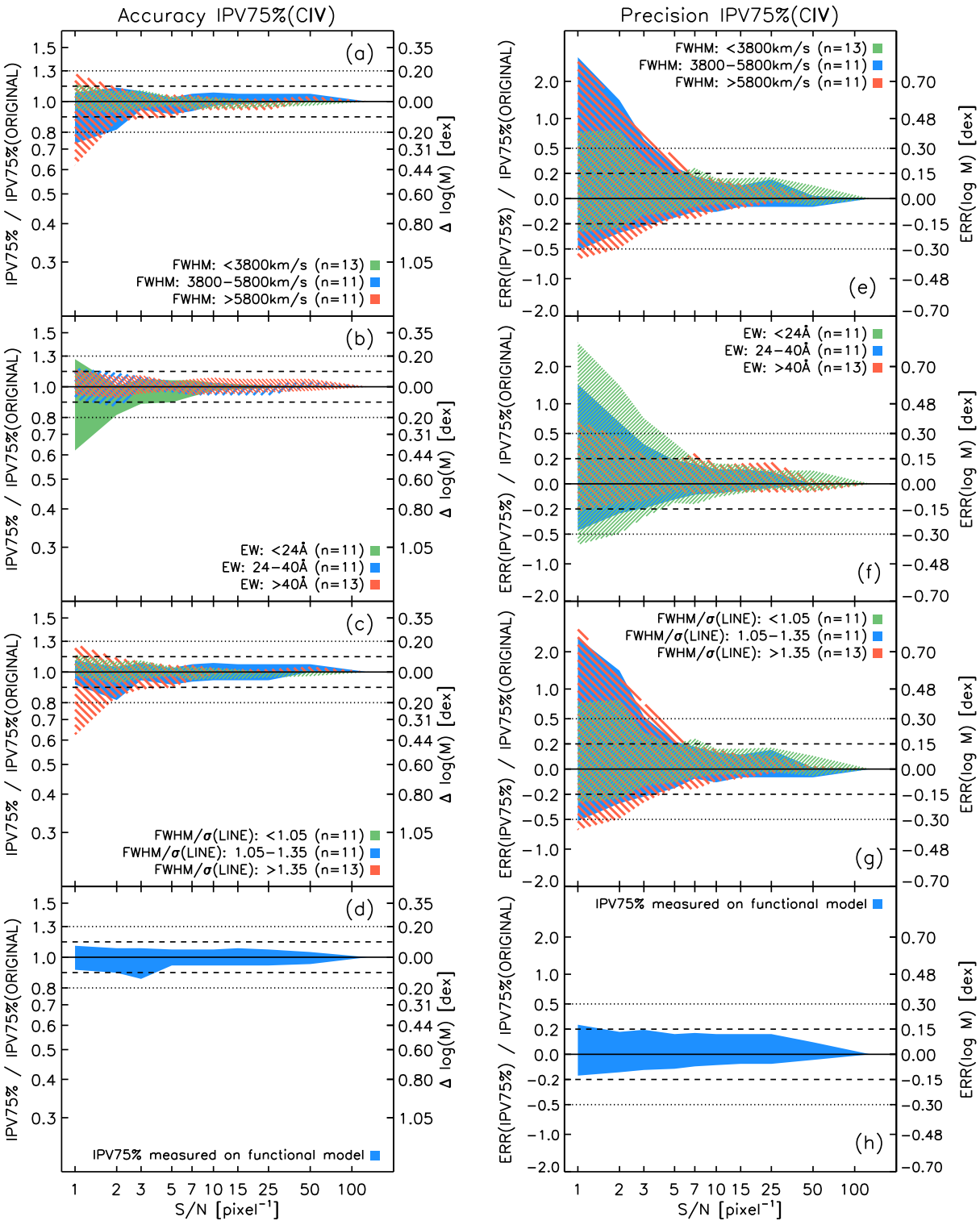

Fig. D.13 C IV IPV(75%) width.

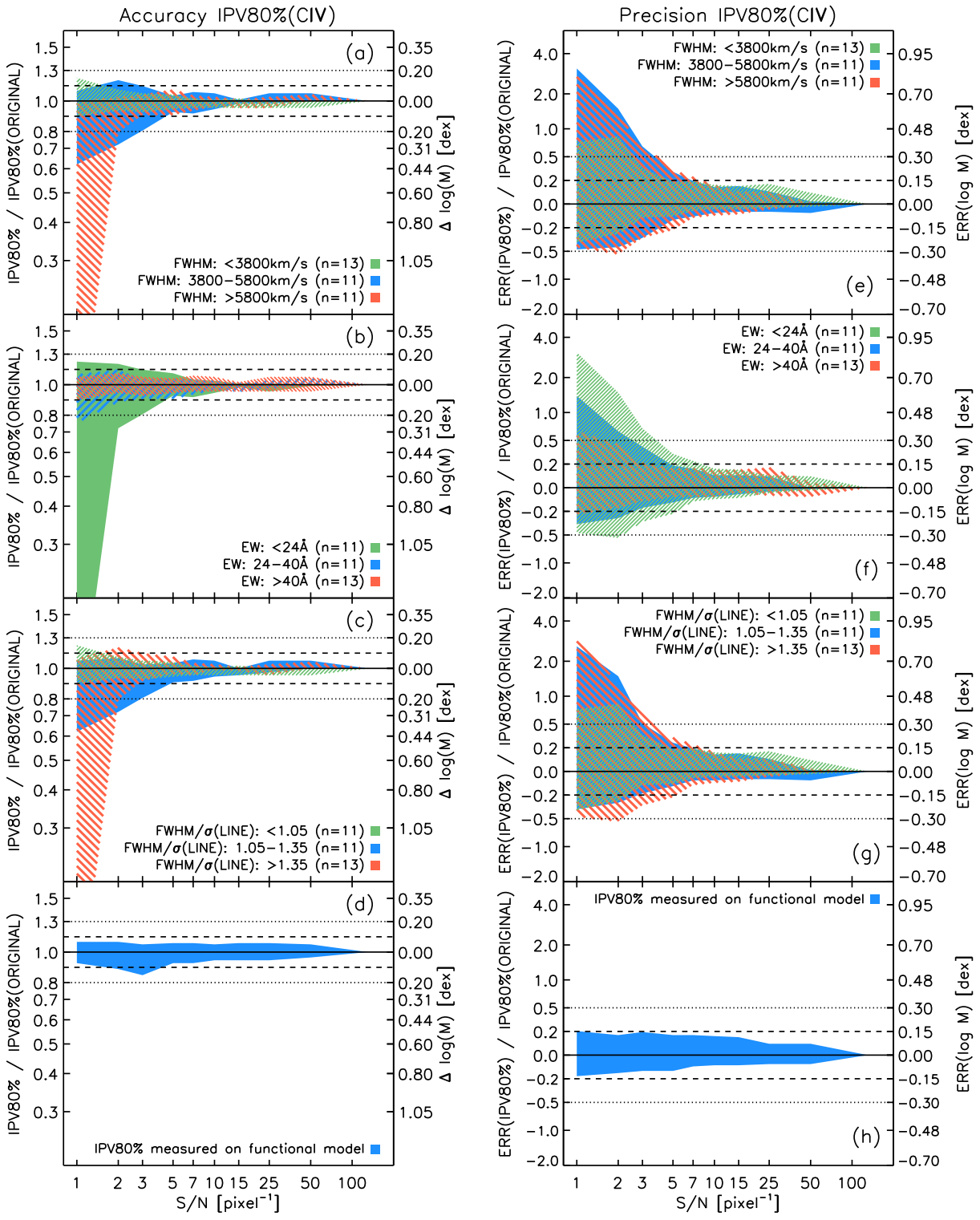

Fig. D.14 C IV IPV(80%) width.

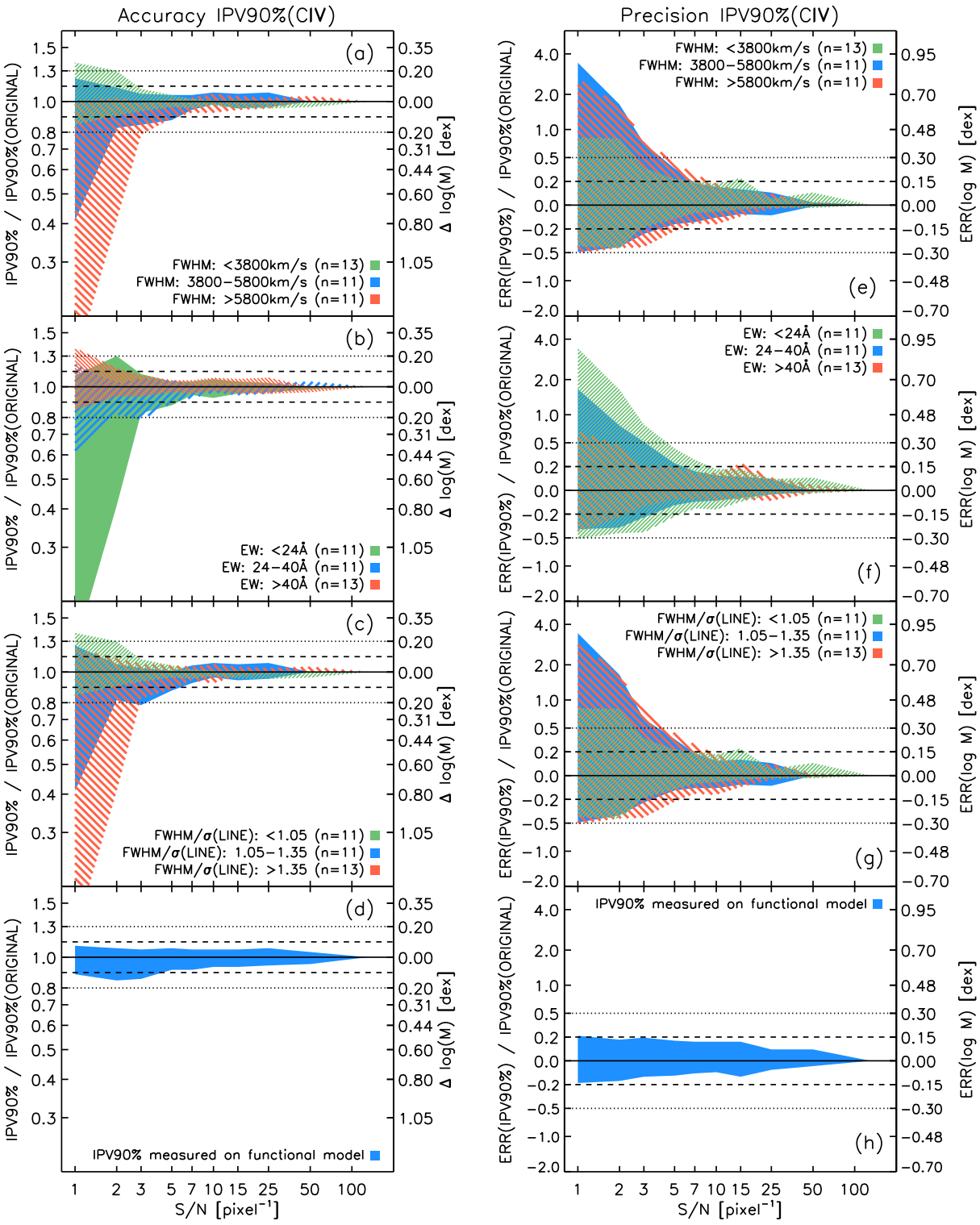

Fig. D.15 C IV IPV(90%) width.

Appendix E

X-Shooter data[1]

The X-SHOOTER data of the 15 quasars were processed using the ESO interface REFLEX (Freudling et al., 2013) with XSHOOTER pipeline version 2.6.8 (Modigliani et al., 2010; Vernet et al., 2011). The pipeline routines were used for the bias and dark subtraction, the rectification and wavelength calibration of the spectra and the absolute flux calibration. The correction for telluric absorption features in the visible and near-infrared arms was performed with the MOLECFIT (Smette et al., 2015; Kausch et al., 2015) software algorithm. The spectra covers the wavelength range of 3000 to 24 800 Å, divided into the three XSHOOTER arms: near-infrared (NIR), visible (VIS) and ultra-violet (UVB).

All spectra were binned by a factor of two, preserving a sampling of approximately three pixels per resolution element FWHM in the UVB and VIS arm and two pixels in the NIR arm. The spectral region covering the C IV line (generally the UVB arm) required no further rebinning to adhere to our demands for high S/N spectra for which we reliably could establish the line width characterisations. For our final sample of high S/N C IV spectra we exclude the spectrum of Q0317-0219 due to too low S/N and the spectrum of Q2222+0511 because the spectrum is heavily dust reddened and therefore difficult to model reliably with our decomposition method.

The Hβ line generally falls in the NIR arm where the spectral quality is adversely influenced by low S/N and residuals from the correction for telluric absorption. For this reason, we bin all the X-SHOOTER NIR spectra by a factor of up to 10 in order to increase the S/N . This level of binning results in a wavelength dispersion of no more than 140 km s^{-1} near the Hβ line which means that we are, in principle, able to resolve – at least marginally - narrow absorption lines of a few hundred km s^{-1}. We also ignore regions heavily affected by residuals after telluric absortion from the spectra. The 15 Hβ spectra in the original X-Shooter sample can be seen in Figure E.1. Even after taking these measures of rebinning and masking noisy regions, only a handful of the 15 Hβ spectra are of sufficient quality that we can perform a reliable spectral decomposition and measure the Hβ line width with high reliability. These spectra are listed in Table 2.1 and shown in Figure 2.1.

[1] Appendix to Chapter 2.

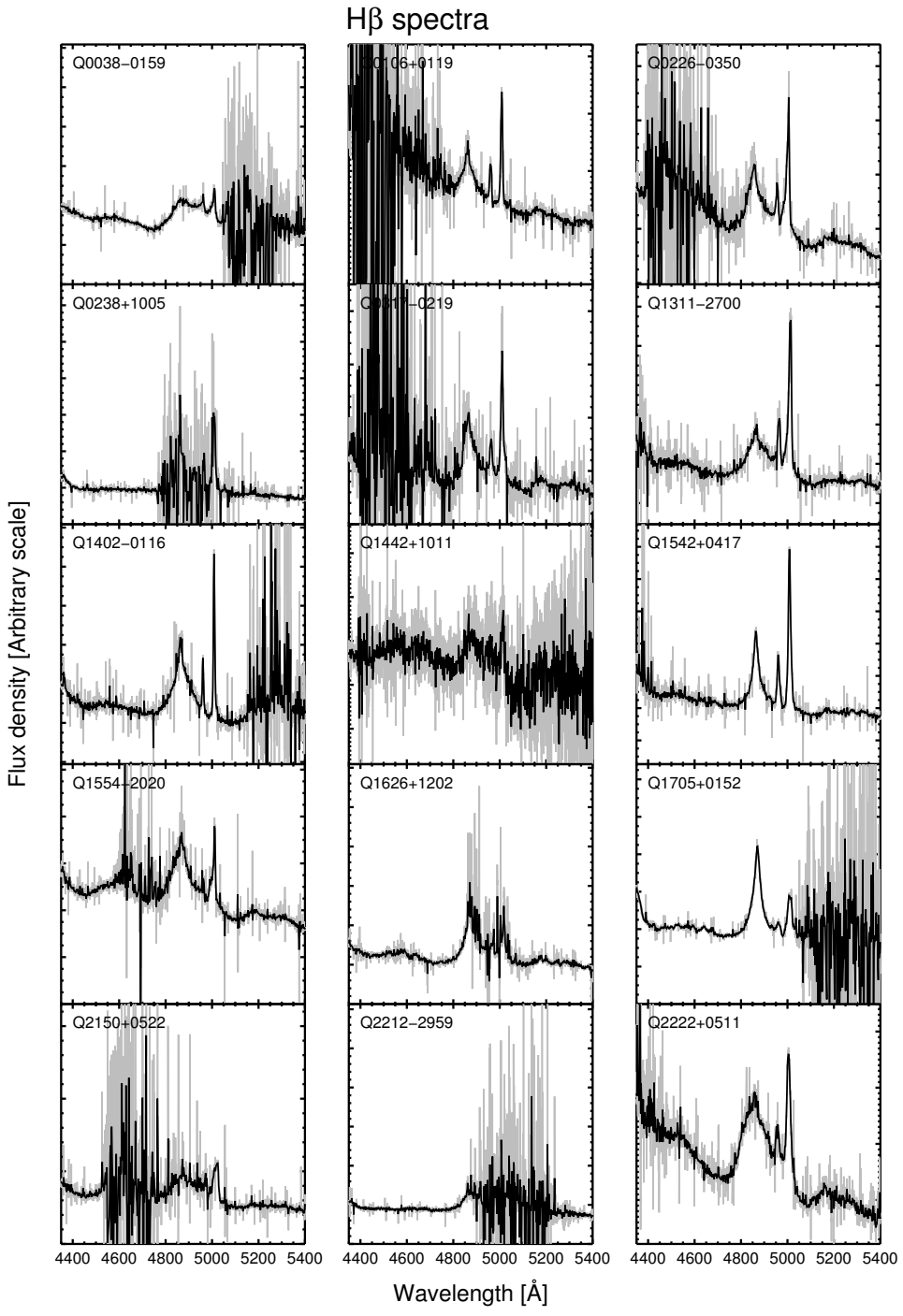

Fig. E.1 The Hβ line in the 15 X-Shooter spectra. The spectra rebinned by a factor of 10 shown in black are displayed on top of the original spectra shown in gray.

Appendix F

Variability analysis[1]

The Hβ time-delay values are listed in column 5 of Table F.1 and are adopted from the studies of Peterson et al. (2004); Bentz et al. (2007, 2009c); Denney et al. (2010), and Pei et al. (2017). We exclude data from year 12 and 19 in our analysis because in these cases the Hβ time-delay is not sufficiently constrained to be useful for our study. For year 12, the peak of the CCF is ambiguous (see Fig. 2 of Peterson et al. (2002)) while for year 19, the CCF is very broad and flat topped (see Figure 3 in Denney et al. (2010)) and indicating a broad range of Hβ time-delays between $\sim$3 to $\sim$23 light-days. This leaves us with 15 data sets, each represented by a mean and rms spectrum and a corresponding time-delay for the broad Hβ line. The construction of the mean and rms spectra is described in Peterson et al. (2004); we use an updated version of these spectra which have been re-calibrated as described in Peterson et al. (2013) and analyzed in Kilerci Eser et al. (2015).

For the year 1-13 data sets, the narrow Hβ and [O III] lines were removed by Peterson et al. (2004) from the individual spectra prior to forming the mean and rms spectra whereas for year 17, 19, and 20, both the mean and rms spectra contain the contaminating narrow-line features. We remove these components in the mean and rms spectra with the procedure described by Peterson et al. (2004), using the [O III] λ5007 line as a template for the narrow Hβ and [O III] λ4959 lines. The [O III] λ4959 / [O III] λ5007 ratio is set at 0.34 as determined by atomic physics. For the narrow Hβ/[O III] λ5007 line ratio we adopt a value of 0.110 as determined by Peterson et al. (2004) and also used by Bentz et al. (2007) and Denney et al. (2010). We note that while Bentz et al. (2009c) use a value of 0.114 as determined by Marziani et al. (2003), this difference has no effect on our results since the change in measured line widths is less than one per cent.

After removal of the narrow line features, we model the featureless nuclear continuum with a power-law function, the broad Hβ profile with three Gaussian functions, and the blend of the broad He II λ4686 emission line and nearby Fe II emission with a single Gaussian function. Due to the narrow wavelength range of the spectra – generally 4550 Å to 5200 Å – it is not possible to disentangle the Fe II and He II λ4686 emission components or to constrain the Fe II emission using a more sophisticated method using for example a template to model it (e.g., Boroson & Green,

[1] Appendix to Chapter 2.

Table F.1 Data sets for NGC 5548

Data Set[a]	Julian Date	Spectral Resolution[b]	$\tau_{cent} \pm \sigma$[c] (Å)	Reference (days)
(1)	(2)	(3)	(4)	(5)
Year 1	2447509–2447809	13.3	19.7 ± 1.5	1
Year 2	2447861–2448179	9.6	18.6 ± 2.1	1
Year 3	2448225–2448534	9.6	15.9 ± 2.9	1
Year 4	2448623–2448898	9.6	11.0 ± 1.9	1
Year 5	2448954–2449255	9.6	13.0 ± 1.6	1
Year 6	2449309–2449636	9.6	13.4 ± 3.8	1
Year 7	2449679–2450008	9.6	21.7 ± 2.6	1
Year 8	2450044–2450373	9.6	16.4 ± 1.2	1
Year 9	2450434–2450729	9.6	17.5 ± 2.0	1
Year 10	2450775–2451085	9.6	26.5 ± 4.3	1
Year 11	2451142–2451456	9.6	24.8 ± 3.2	1
Year 12	2451517–2451791	9.6	6.5 ± 5.7	1
Year 13	2451878–2452174	9.6	14.3 ± 5.9	1
Year 17	2453430–2453470	7.6	6.3 ± 2.6	2
Year 19	2454184–2454301	7.6	12.4 ± 3.8	3
Year 20	2454551–2454618	14.7	4.2 ± 1.3	4
Year 26	2456663–2456829	7.5	4.17 ± 0.36	5
Year 26 (first half)	2456663–2456747	7.5	4.99 ± 0.47	5

Note. — [(a)] All data are from the International AGN Watch program (Peterson et al., 2002) except for year 20 data which are from the LAMP project (Bentz et al., 2009c) and year 26 data from the AGN STORM collaboration (Pei et al., 2017); [(b)] Width of a spectral resolution element at the Hβ line in the wavelength restframe; [(c)] The cross-correlation function (CCF) centroid for the Hβ time-delay in the rest frame.

References. — (1)Peterson et al. (2004); (2) Bentz et al. (2007); (3) Denney et al. (2010); (4) Bentz et al. (2009c); (5) Pei et al. (2017).

1992; Vestergaard & Wilkes, 2001; Vestergaard & Peterson, 2005). For the mean spectra, we model the narrow He II λ4686 emission with a single Gaussian component. In the rms spectra we do not expect a narrow component since the timescale for narrow line variations is much longer than the observing campaigns (Peterson et al., 2013; Sergeev et al., 2017), so we model the He II λ4686 emission simply with a single (broad) Gaussian function. In general, the signal-to-noise ratio in the rms spectra is a factor of a few smaller than in their corresponding mean counterparts. The lower quality of the rms spectra forces us to perform a few extra steps to decompose these spectra. As opposed to modelling all spectral components simultaneously, as we did for the mean spectra, we first model a linear continuum model over two uncontaminated visually selected continuum regions (generally in the ranges between 4500–4600 Å and 5050–5200Å) and subtract this continuum model over the full spectral range. Subsequent to the continuum subtraction, we model the remaining spectral components simultaneously. We note that over the narrow wavelength range available in the spectra, the difference between using a power-law or linear function for the featureless nuclear continuum model is negligible. An example of a spectral decomposition of a mean and rms spectrum is shown in Figure F.1 and Figure F.2, respectively.

After subtracting the nuclear continuum component and the He II λ4686 and Fe II components from the narrow-line subtracted spectra we are left with the broad Hβ profile (shown as solid gray line profile in the inset of Figure F.1 and Figure F.2). We find, that these profiles are highly asymmetric due to what appears to be excess residual emission from the subtraction of the narrow [O III] lines in the red wing of Hβ, similar to what we found for our high S/N Hβ sample in § 2.6.1. We remove the residual emission by modelling three Gaussian profiles to the broad Hβ profile while masking the wing of the line profile redwards of 4920Å in the wavelength restframe during the fitting process (see insets in Figure F.1 and Figure F.2 for the mean and rms spectra, respectively). We then substitute the measured flux density red-wards of 4920Å with the flux density represented by the model. This procedure leads to more symmetric Hβ profiles void of the emission that appears to be residuals in the red wing of the line profile. An example of the model and the final Hβ line profile is shown in the insets of Figure F.1 (mean spectrum) and Figure F.2 (rms spectrum).

Previous studies (Peterson et al., 2004; Bentz et al., 2007, 2009c; Denney et al., 2010) calculate uncertainties in the line width measurements by doing a number of bootstrap realizations of the mean and rms spectrum for each set of observations (in this work referred to as a *year* or *data set*). Each time, N spectra is drawn from the parent sample of size N using replacement and a mean and rms spectrum is formed from the newly drawn realization. The line width is then measured for each realization and the average and standard deviation of the resulting distribution of measured line widths is used as the measured line width and its uncertainty, respectively for that data set. Generally, this results in line width uncertainties between a few and 30 per cent.

As we do not have access to the individual spectra for each data set we can not use this method. Instead, we assign a uncertainty of 5 and 15%, respectively, to the line widths measured in the mean and rms spectra. This is based on the average S/N level of the spectra and the typical uncertainties for the line width parameters at these S/N levels found in §2.8 and 2.9. This level of uncertainty

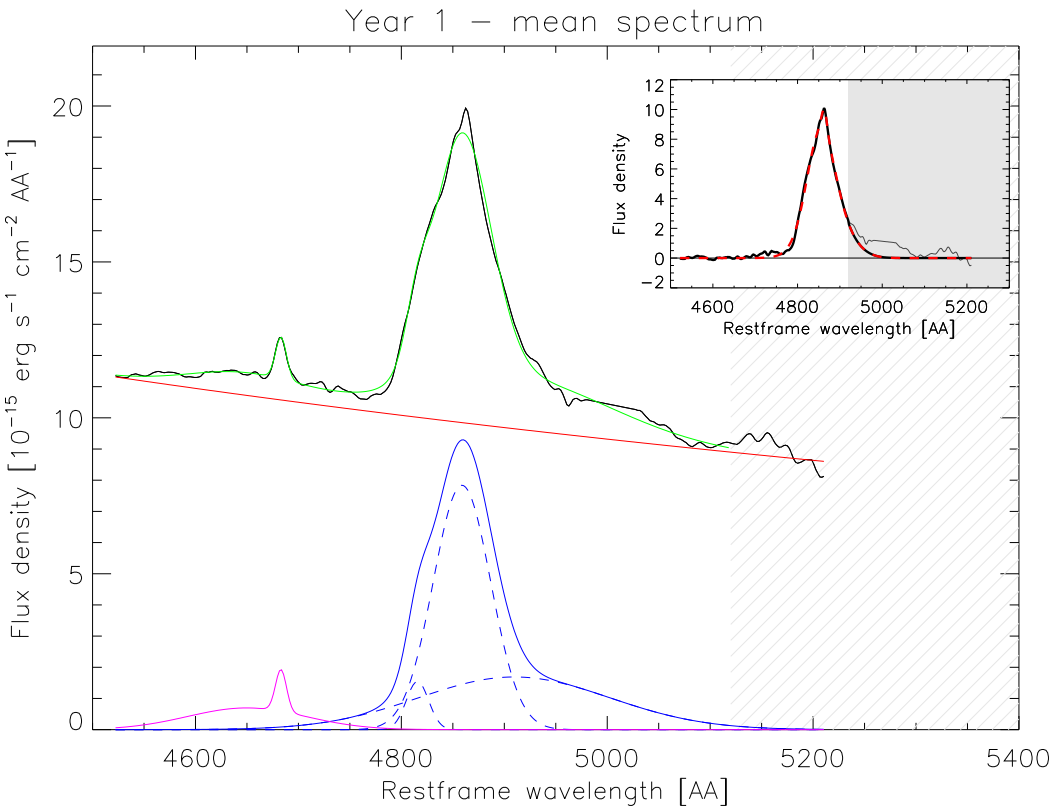

Fig. F.1 Decomposition of the narrow-line subtracted mean spectrum for Year 1, using a method similar to that described in § 2.6.1 where the broad Hβ line is modelled in two steps in order to remove residuals from the narrow line subtraction in its red wing. The spectrum is shown in solid black, the power-law continuum model is shown in red, the He II and Fe II components in magenta, the model of the broad Hβ emission line is blue (individual components shown as dashed blue lines), and the full model is shown in green. The hashed gray area is masked during the modeling as this region contains Fe II emission that the limited spectral wavelength range does not allow us to constrain. The inset shows the broad Hβ profile after subtraction of contaminating components (in this case He II and Fe II emission) in gray, the model of the broad Hβ profile (red dashed curve) when the data is masked redwards of 4920 Å (gray area), and the final cleaned Hβ line profile (solid black) after the observed flux redwards of 4920 Å has been replaced by the model.

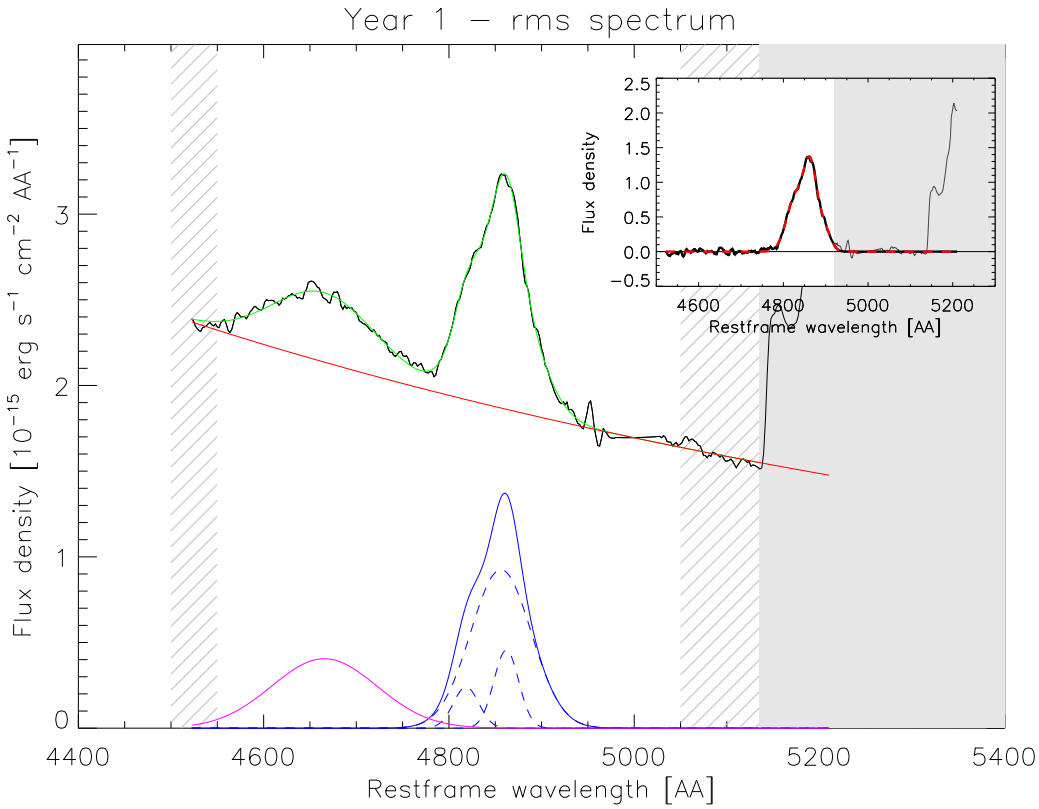

Fig. F.2 Same as Figure F.1, but now showing the decomposition of the narrow-line subtracted rms spectrum from Year 1. Colors and curves are the same as in Figure F.1, except that the hashed gray areas now show the visually selected continuum regions and the filled gray area shows the region of the spectrum that is masked during the modeling.

Table F.2 Mean and scatter of VP's

	Mean spectra		RMS spectra	
Parameter	$\log < VP >$	$\log \sigma_{VP}$	$\log < VP >$	$\log \sigma_{VP}$
(1)	(2)	(3)	(4)	(5)
VP(IPV10)	8.56	0.16	8.23	0.14
VP(IPV20)	8.28	0.13	8.02	0.12
VP(IPV30)	8.07	0.13	7.87	0.13
VP(IPV35)	7.98	0.12	7.80	0.14
VP(IPV40)	7.89	0.12	7.69	0.14
VP(IPV60)	7.49	0.13	7.35	0.17
VP(IPV70)	7.22	0.13	7.10	0.19
VP(IPV75)	7.06	0.13	6.95	0.20
VP(IPV80)	6.86	0.14	6.76	0.21
VP(IPV90)	6.26	0.14	6.20	0.23

correspond to that found by Peterson et al. (2004), Bentz et al. (2007, 2009c), and Denney et al. (2010) using their bootstrapping method.

We test for correlations between the virial products and the optical luminosity at 5100Å (L_{5100}) by bootstrapping, with replacement, each data set of corresponding VP and L_{5100} values 1000 times, each time randomly selecting N data pairs (VP, L_{5100}) from the parent sample of size N. For each of these realizations, we take the errors on both L_{5100} and the virial product into account. For L_{5100} we assume normally distributed errors in log-space and draw from a Gaussian distribution centered around the measured value and with a standard deviation equal to the error of the measurement. For the virial product, we work with asymmetric error bars and draw from an asymmetric distribution comprised of the relevant halves of two normal distributions each with a standard deviation equal to the upper and lower error, respectively. For each realization, we calculate the Spearman correlation rank ρ_s and its significance p_s.

Finally, we find the median of ρ_s and $p_s$from their respective distributions and their errors as the 15.9 and 84.1 percentiles. These values are shown in the top of each panel in Figure 2.22. Since we assign the line width error manually, we also check whether these results are changed by doubling or halving the line width errors. We find no difference between these larger og smaller errors and those results presented here and we therefore conclude that our results are robust to changes in the line width errors within at least a factor of two.

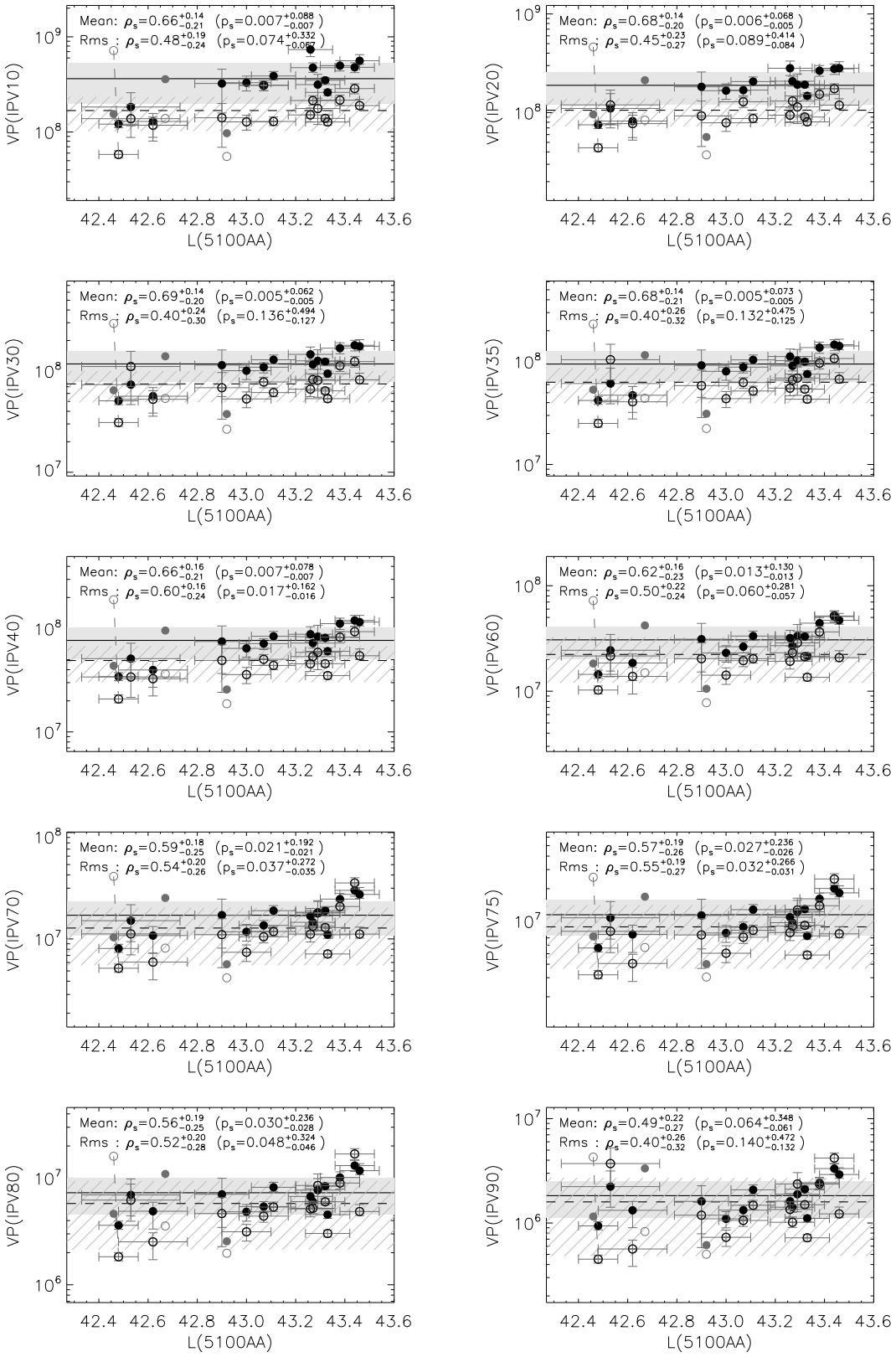

Fig. F.3 Virial products for the IPV10 - IPV90 widths. Filled circles and open circles show the virial product calculated from the line width measured in the mean and rms spectra, respectively, and solid gray and hashed areas show the corresponding scatter.

Appendix G

IPV(data) widths for Mg II[1]

[1] Appendix to Chapter 3.

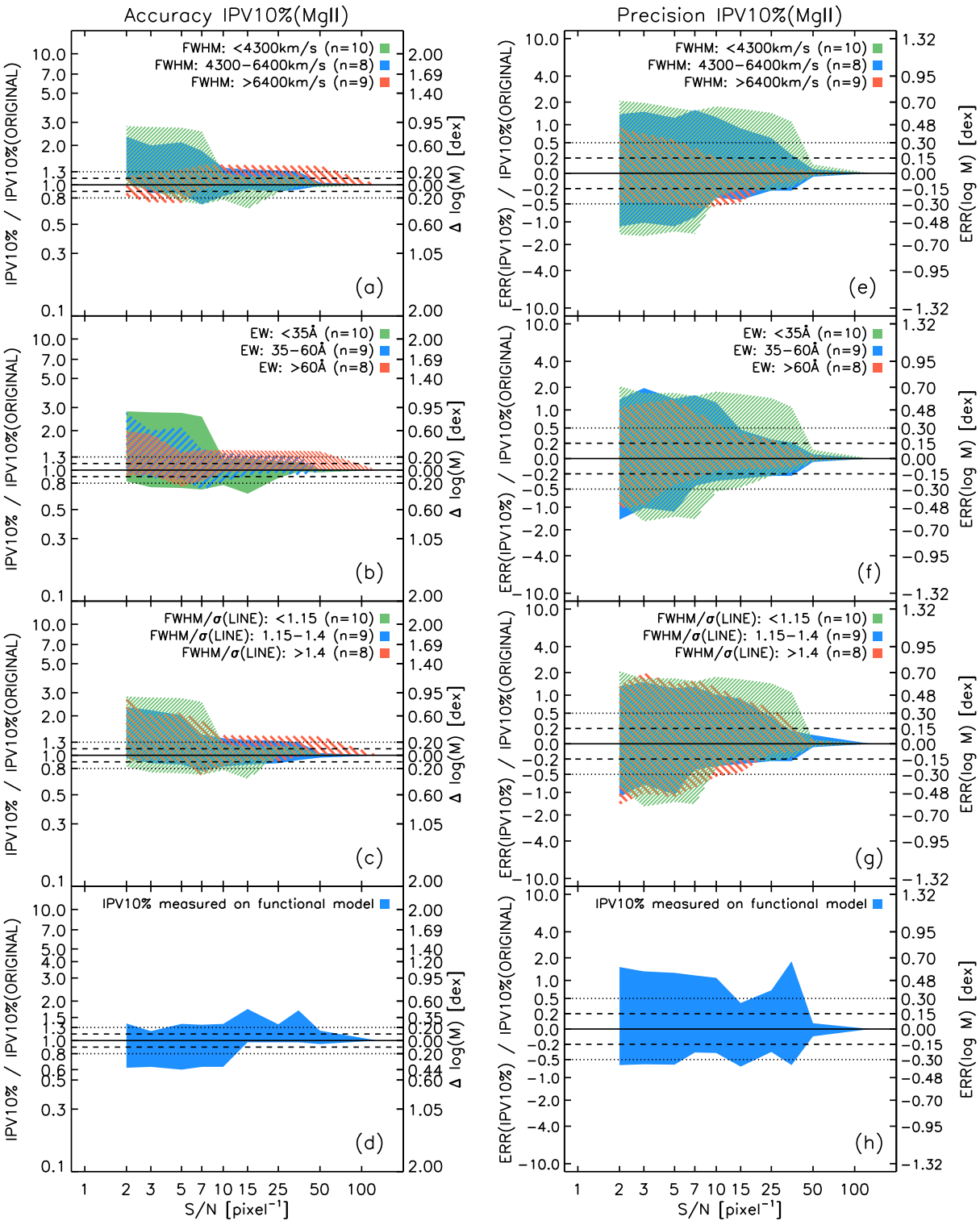

Fig. G.1 Relative accuracy (left column) and precision (right column) of the IPV10 width as a function of S/N when measured on all the spectra in our sample of degraded Mg II spectra. The figure is explained in Figure 3.3

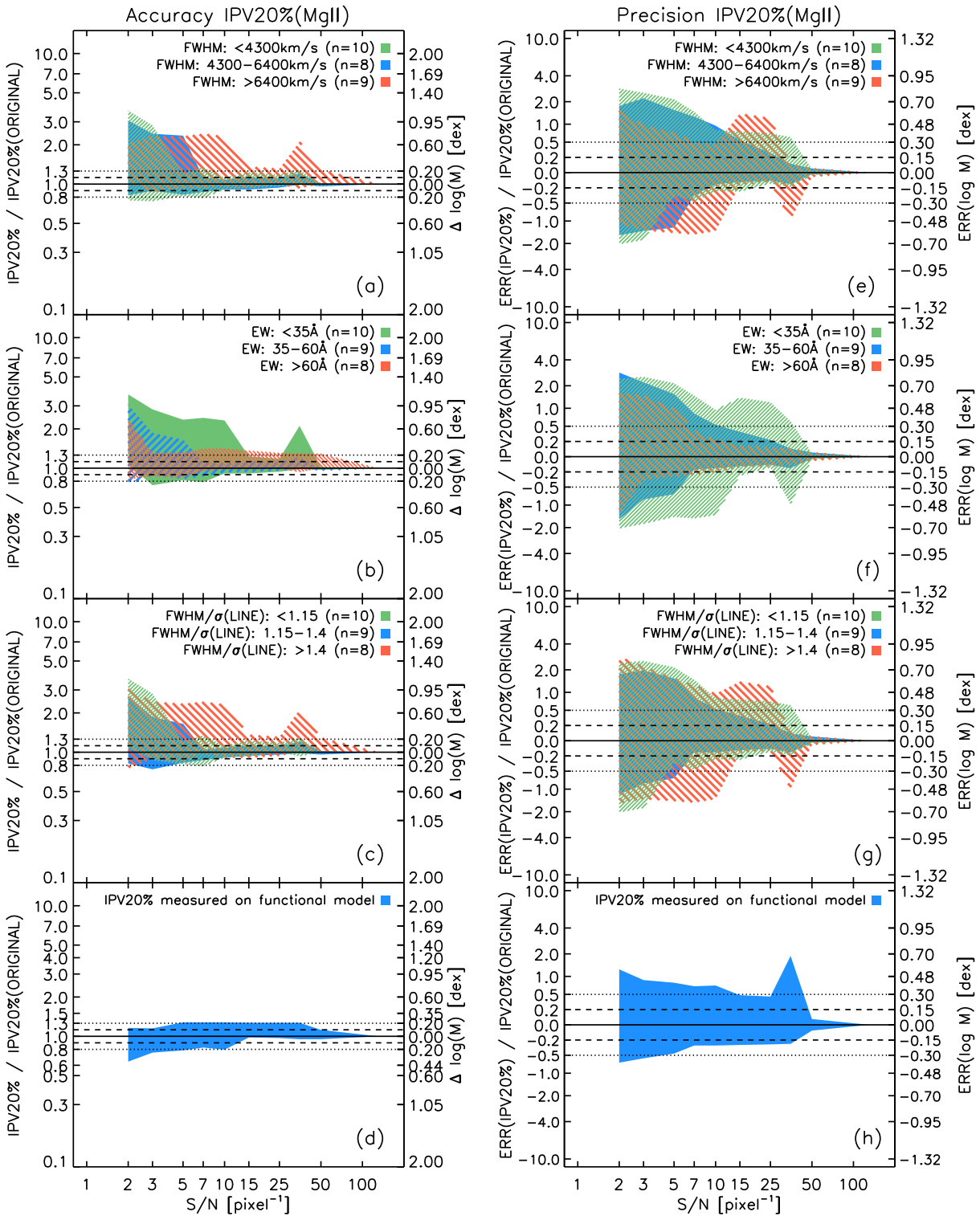

Fig. G.2 Relative accuracy (left column) and precision (right column) of the IPV20 width as a function of S/N when measured on all the spectra in our sample of degraded Mg II spectra. The figure is explained in Figure 3.3

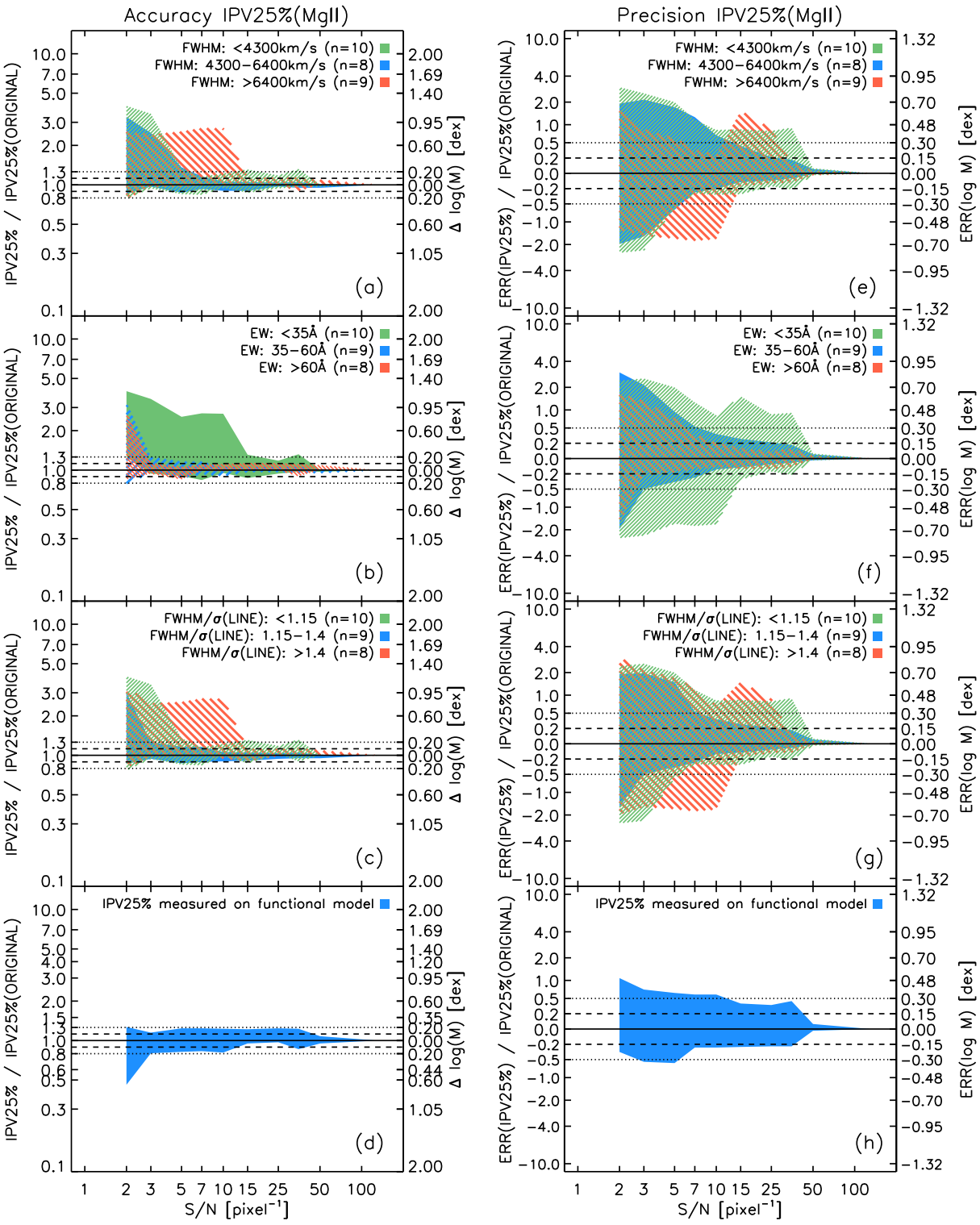

Fig. G.3 Relative accuracy (left column) and precision (right column) of the IPV25 width as a function of S/N when measured on all the spectra in our sample of degraded Mg II spectra. The figure is explained in Figure 3.3

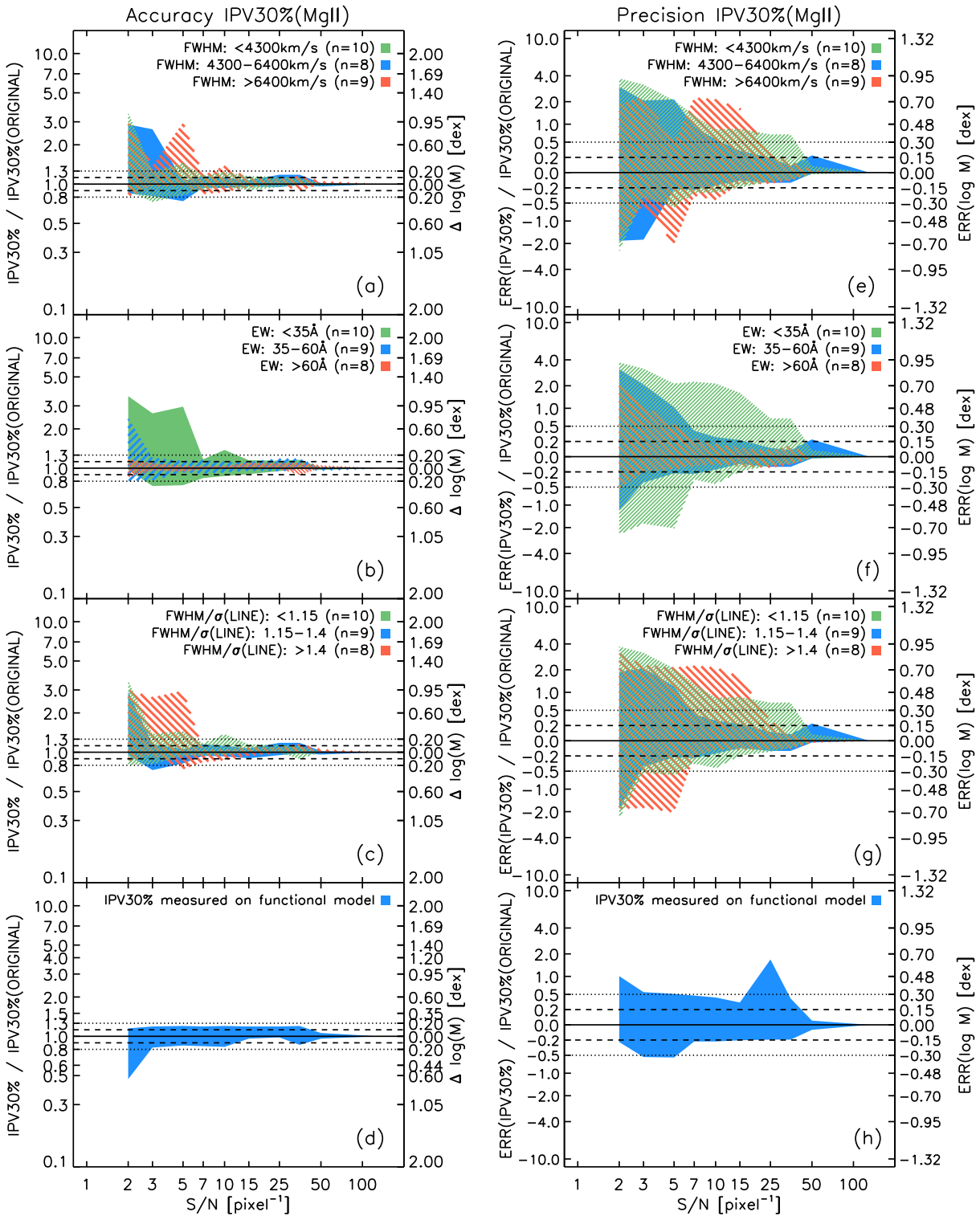

Fig. G.4 Relative accuracy (left column) and precision (right column) of the IPV30 width as a function of S/N when measured on all the spectra in our sample of degraded Mg II spectra. The figure is explained in Figure 3.3

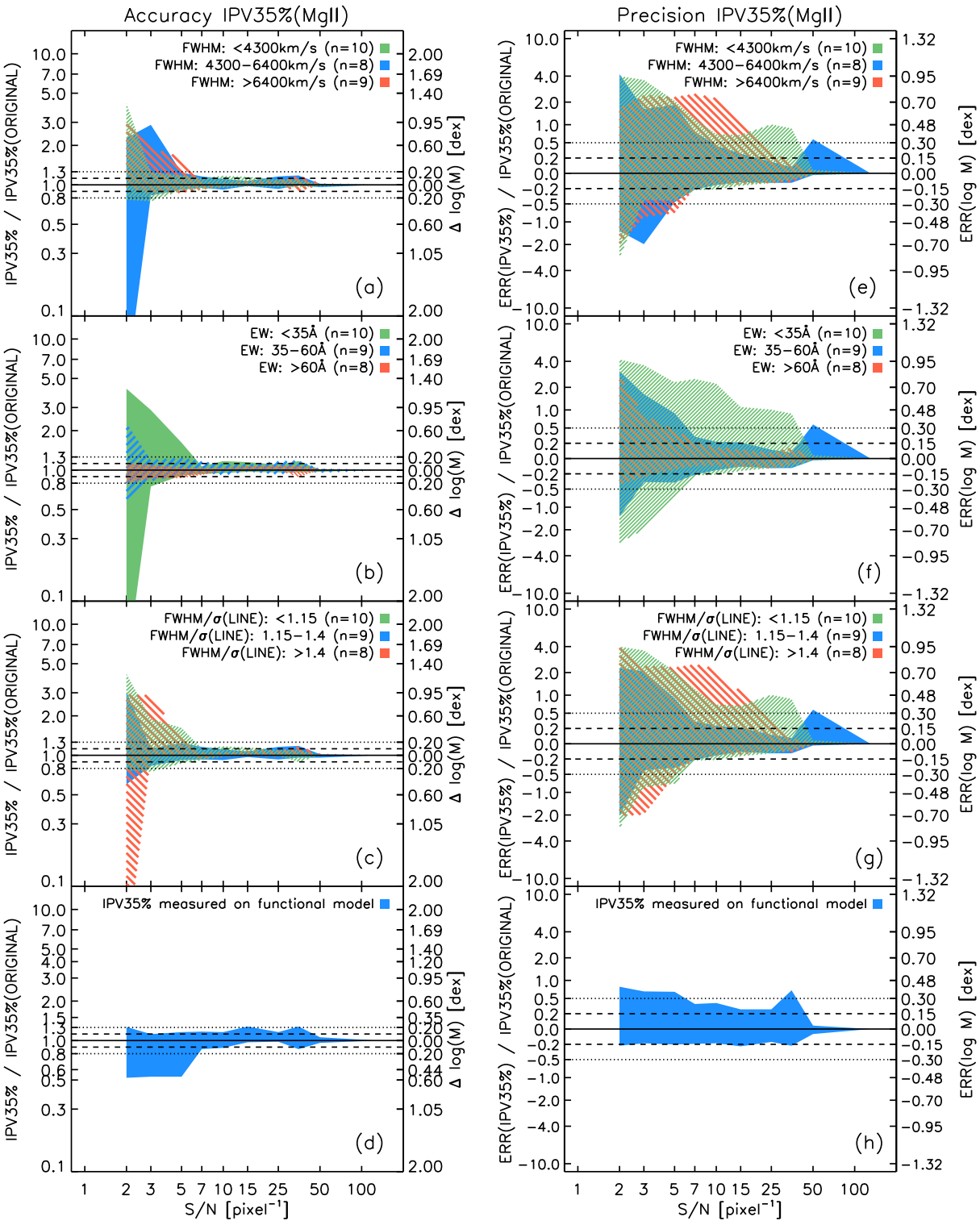

Fig. G.5 Relative accuracy (left column) and precision (right column) of the IPV35 width as a function of S/N when measured on all the spectra in our sample of degraded Mg II spectra. The figure is explained in Figure 3.3

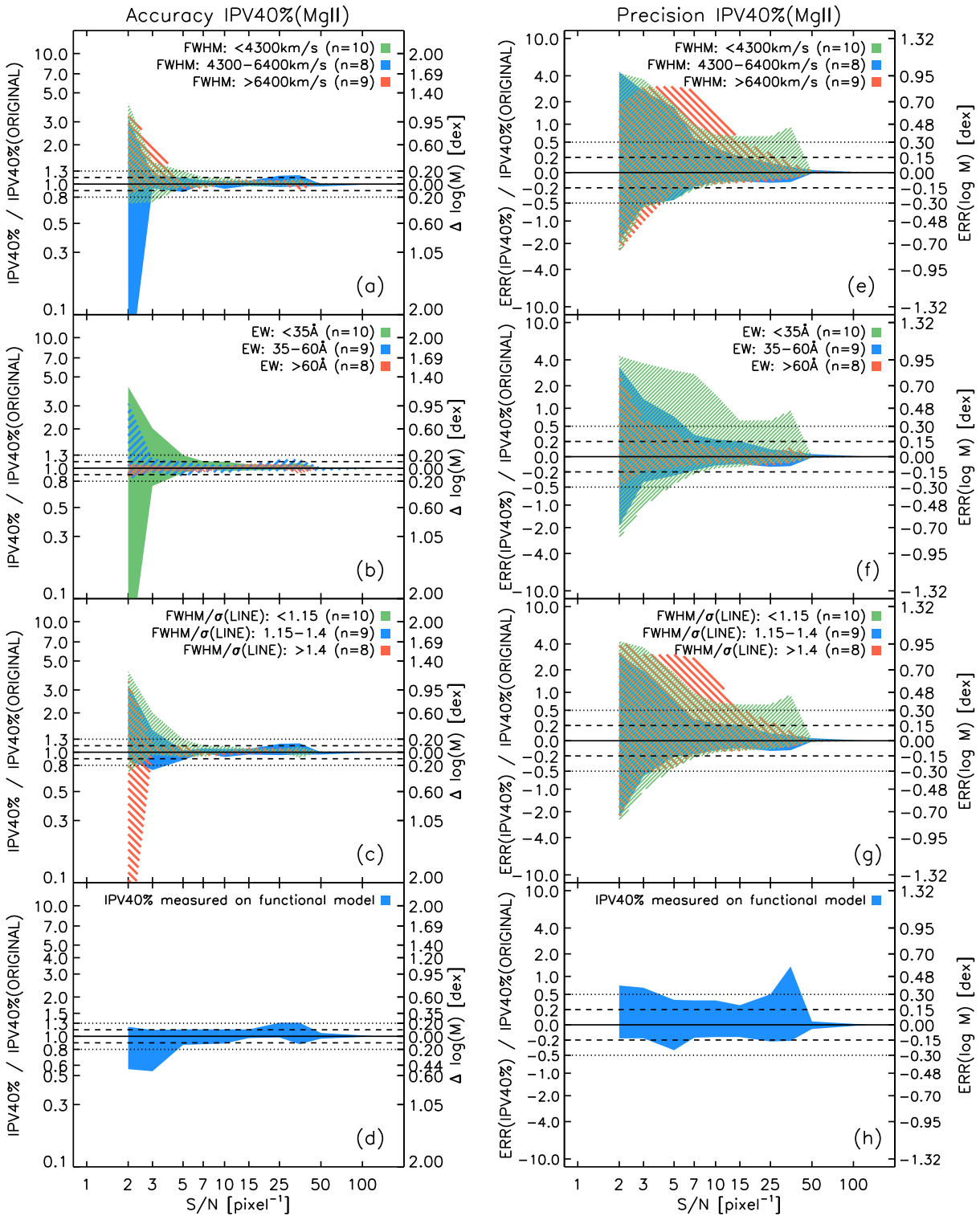

Fig. G.6 Relative accuracy (left column) and precision (right column) of the IPV40 width as a function of S/N when measured on all the spectra in our sample of degraded Mg II spectra. The figure is explained in Figure 3.3

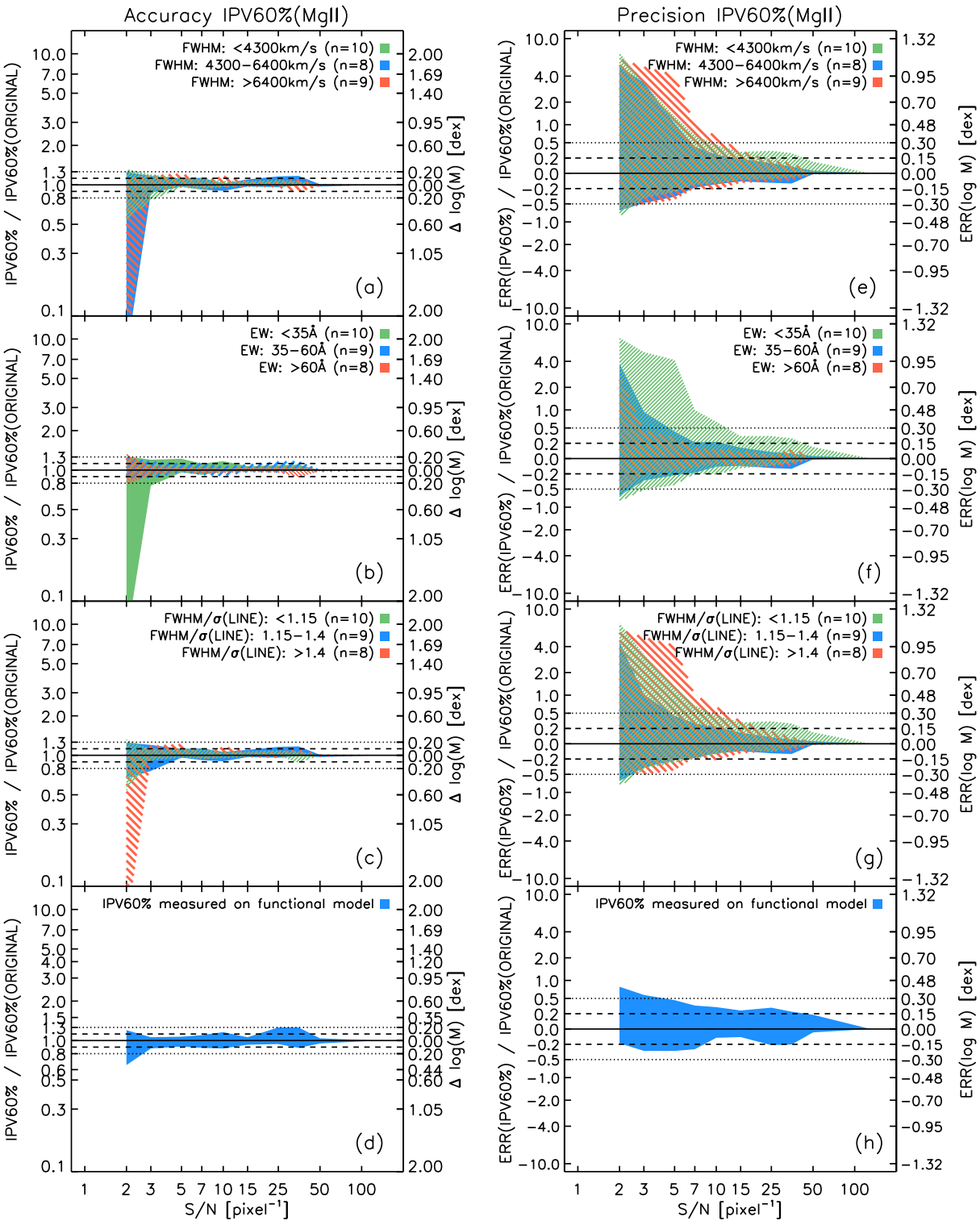

Fig. G.7 Relative accuracy (left column) and precision (right column) of the IPV60 width as a function of S/N when measured on all the spectra in our sample of degraded Mg II spectra. The figure is explained in Figure 3.3

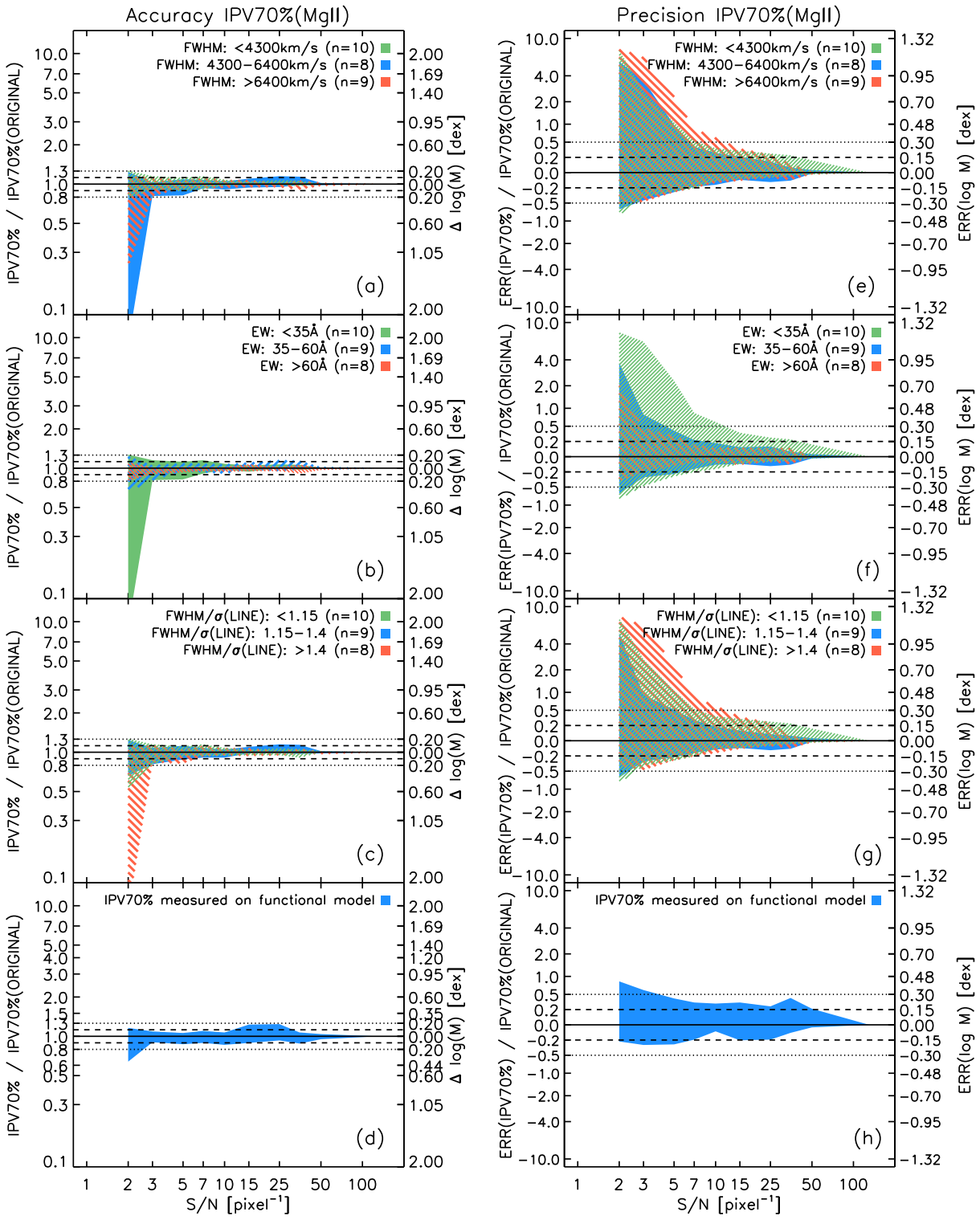

Fig. G.8 Relative accuracy (left column) and precision (right column) of the IPV70 width as a function of S/N when measured on all the spectra in our sample of degraded Mg II spectra. The figure is explained in Figure 3.3

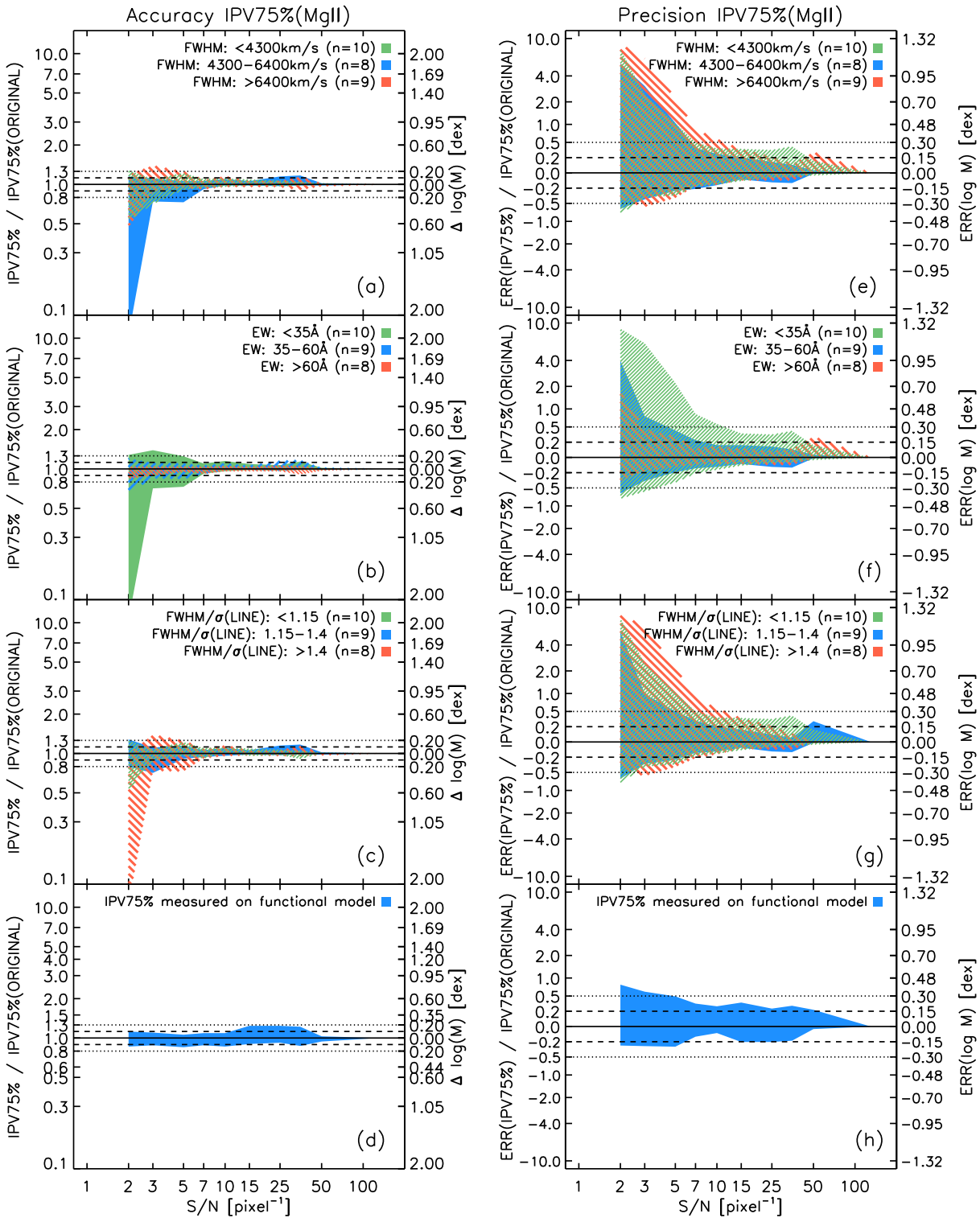

Fig. G.9 Relative accuracy (left column) and precision (right column) of the IPV75 width as a function of S/N when measured on all the spectra in our sample of degraded Mg II spectra. The figure is explained in Figure 3.3

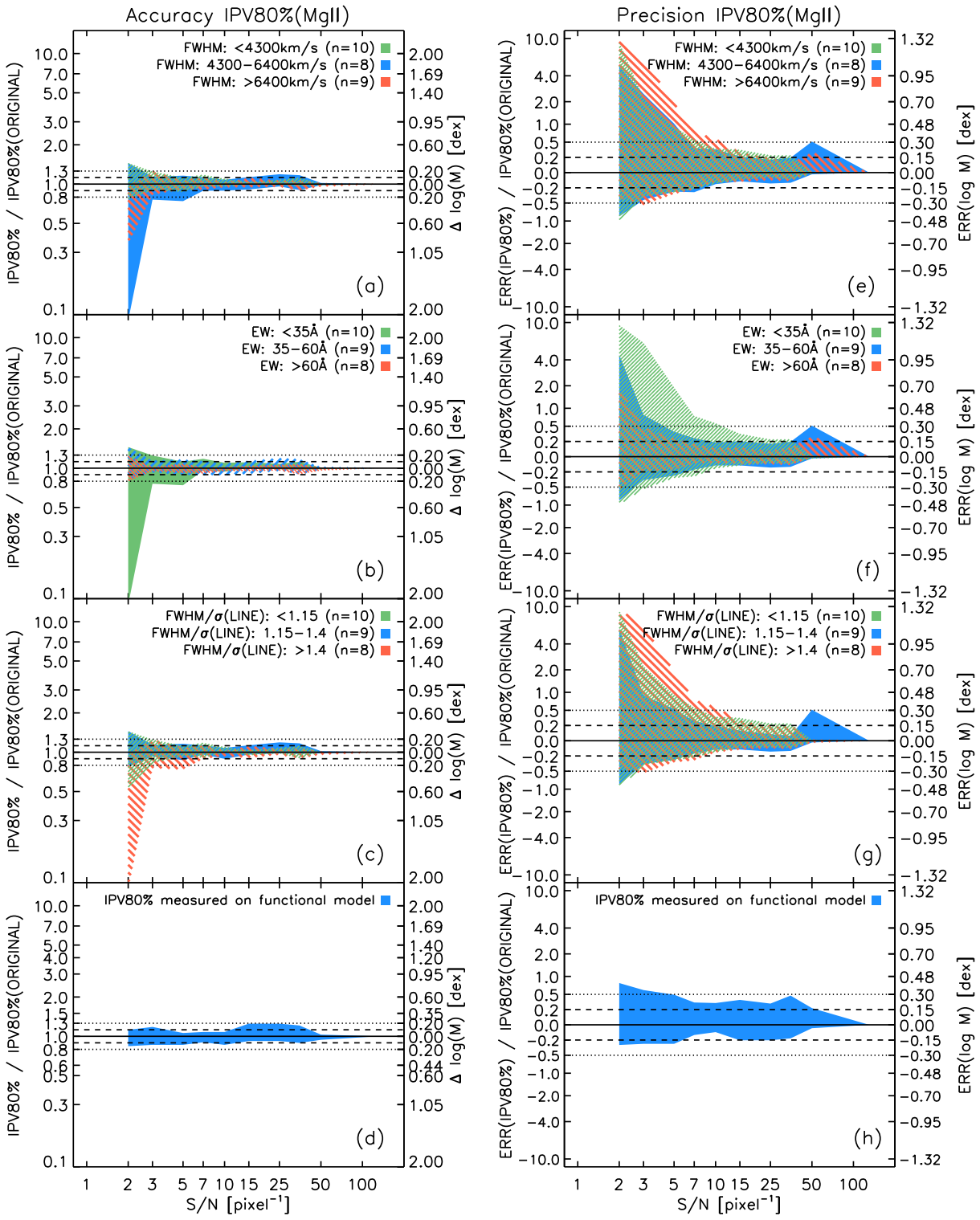

Fig. G.10 Relative accuracy (left column) and precision (right column) of the IPV80 width as a function of S/N when measured on all the spectra in our sample of degraded Mg II spectra. The figure is explained in Figure 3.3

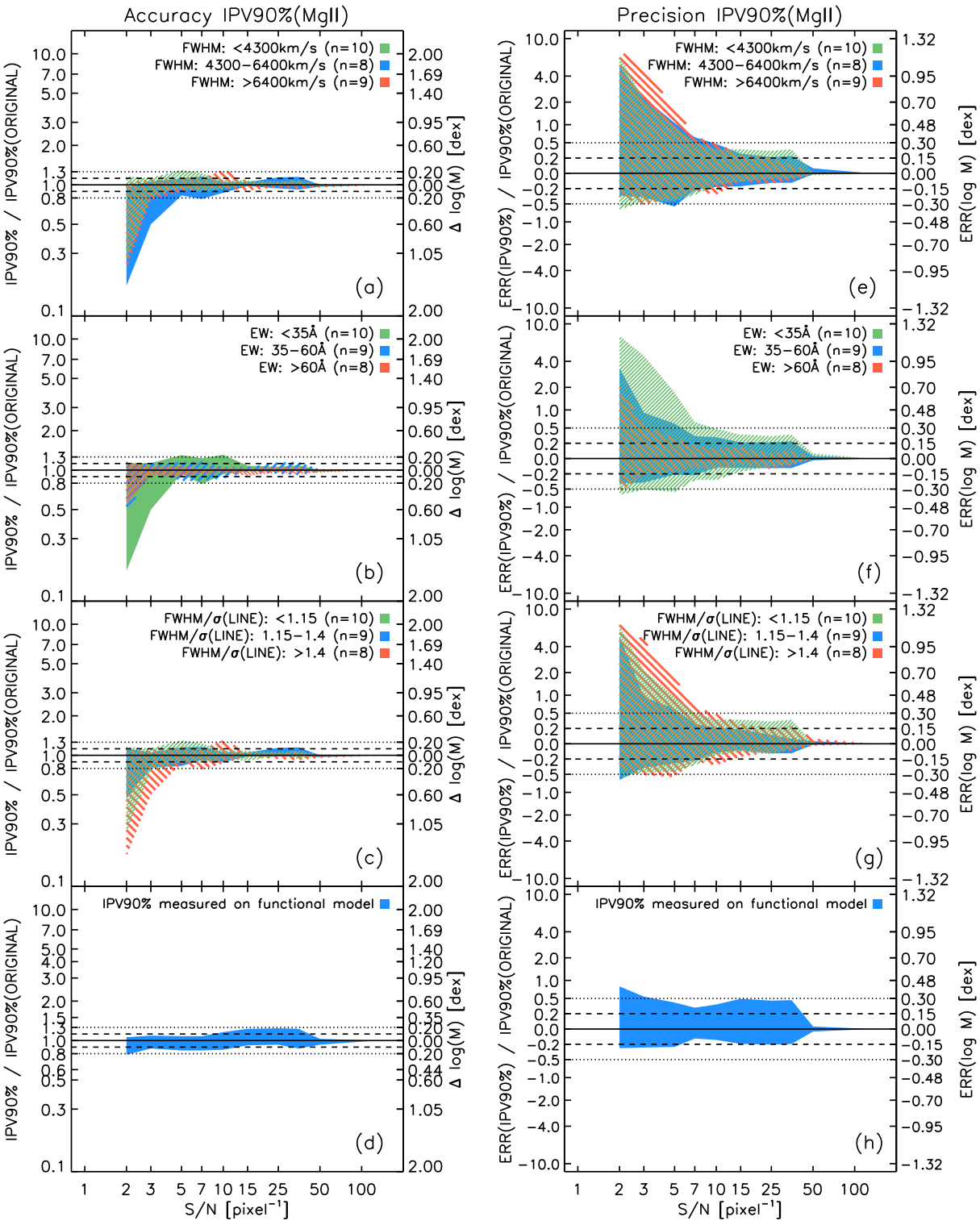

Fig. G.11 Relative accuracy (left column) and precision (right column) of the IPV90 width as a function of S/N when measured on all the spectra in our sample of degraded Mg II spectra. The figure is explained in Figure 3.3

Appendix H

FWHM with absorption[1]

[1] Appendix to Chapter 4.

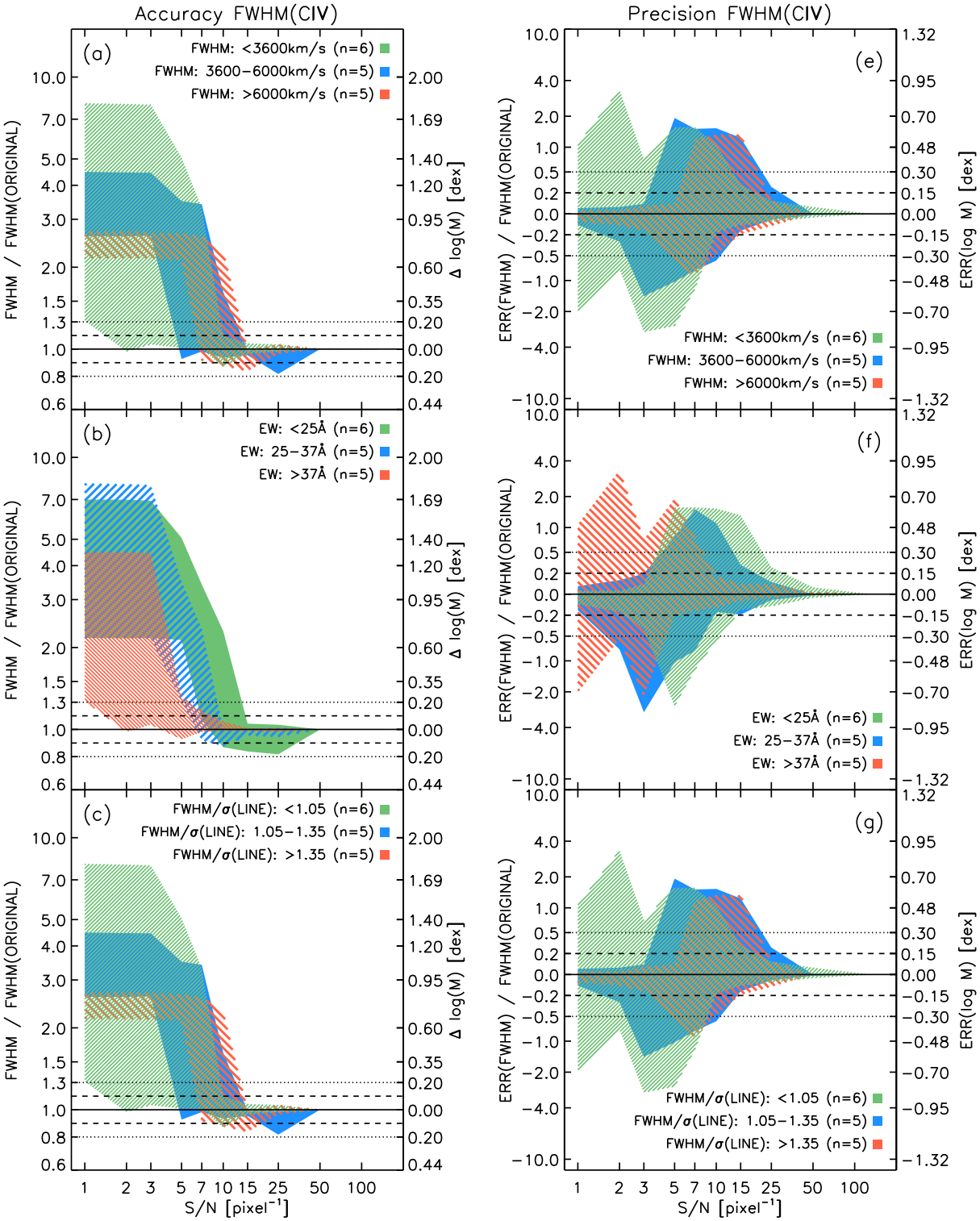

Fig. H.1 FWHM with weak absorption in the core of the emission line. The accuracy is corrected for absorption (§ 4.5), but the precision is not.

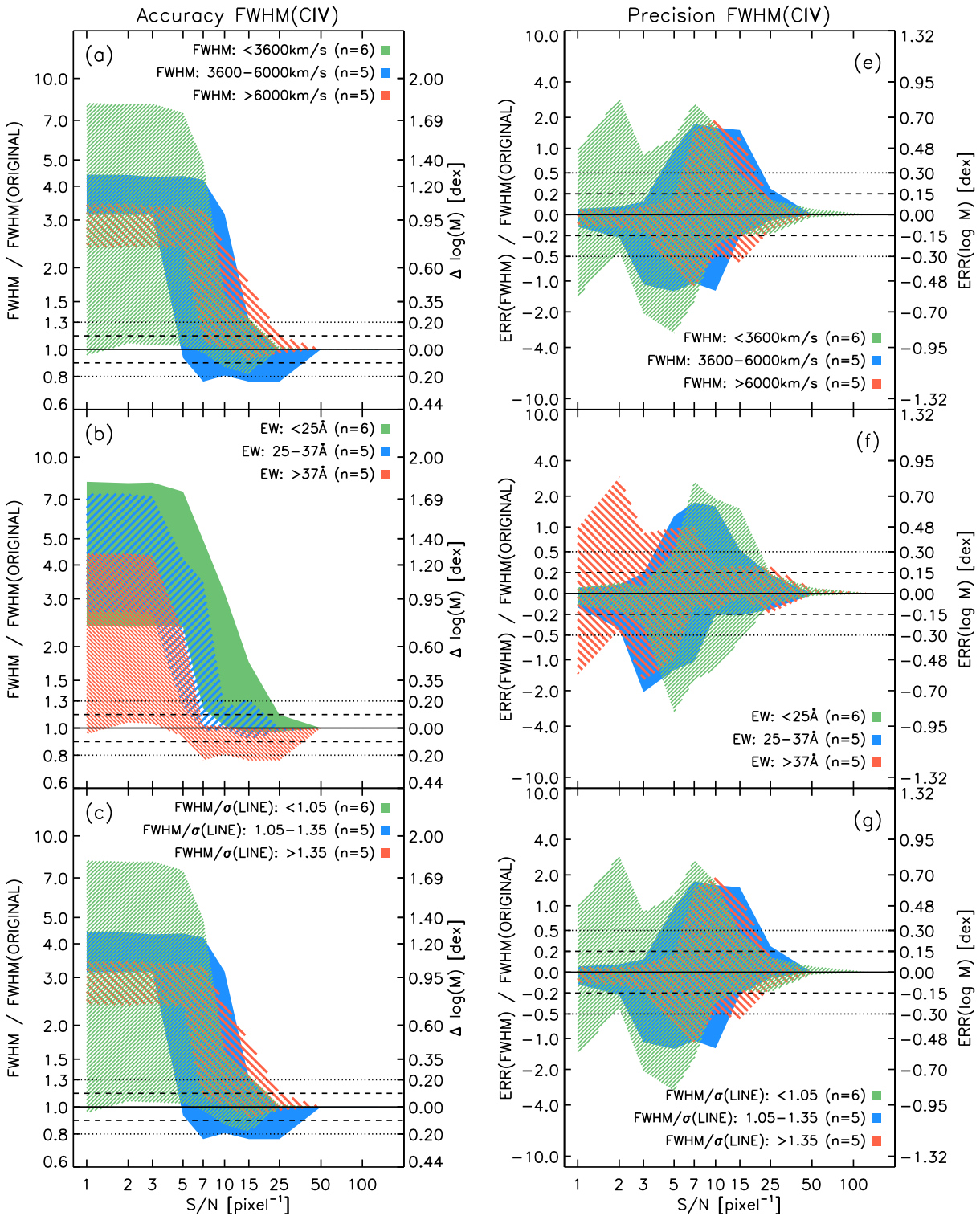

Fig. H.2 FWHM with medium strong absorption in the core of the emission line.

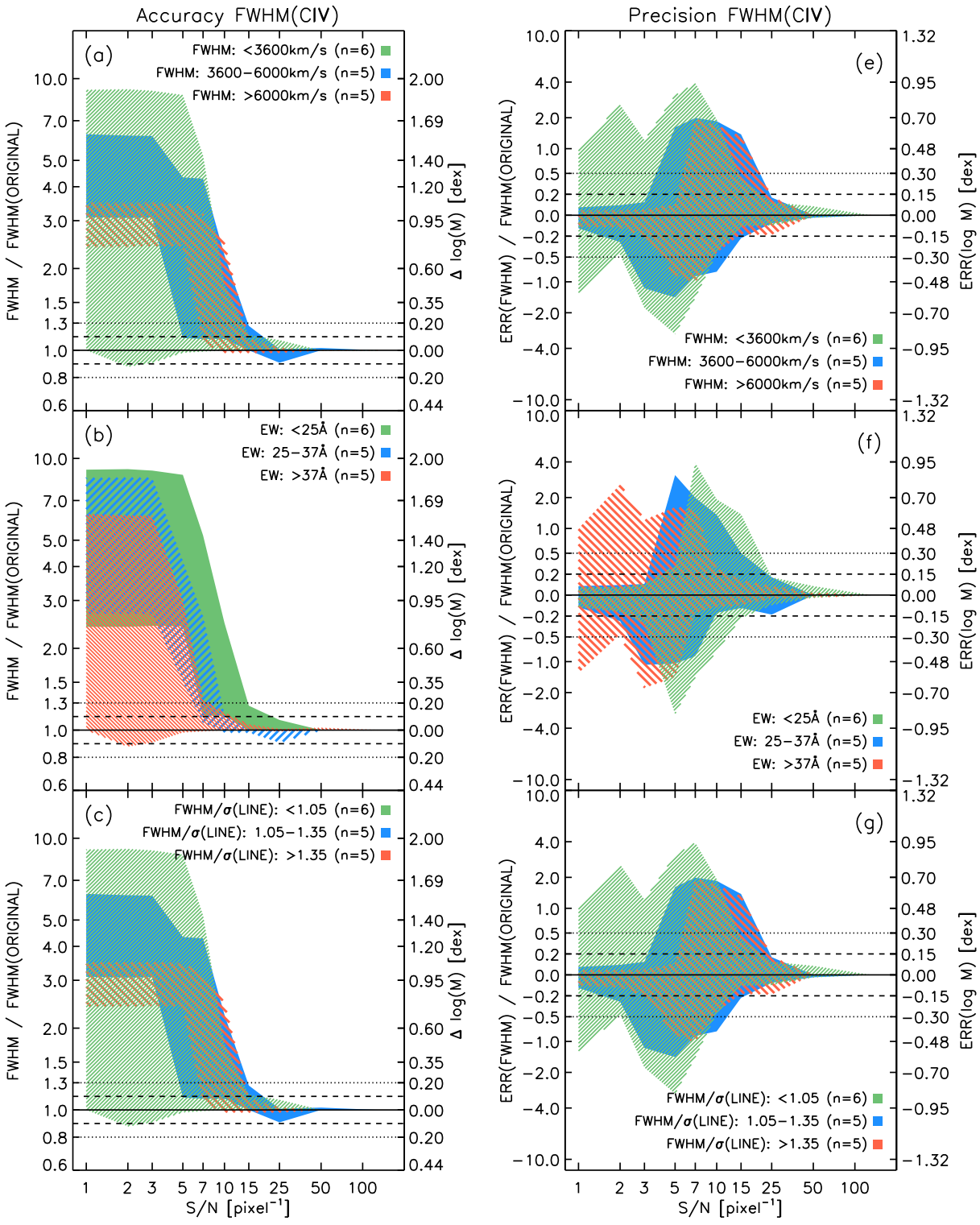

Fig. H.3 FWHM with strong absorption in the core of the emission line.

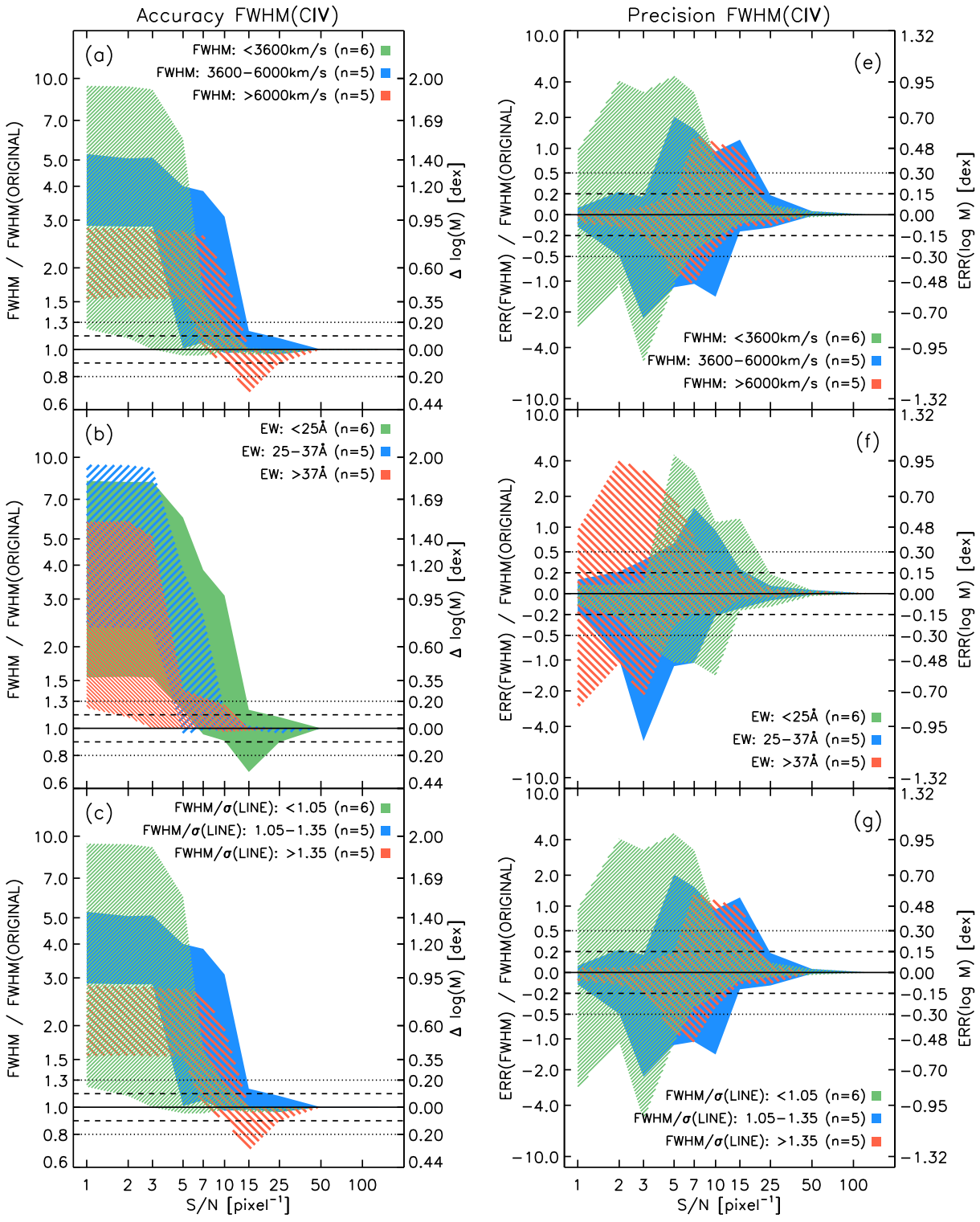

Fig. H.4 FWHM with weak abssorption in the middle of the absorption line.

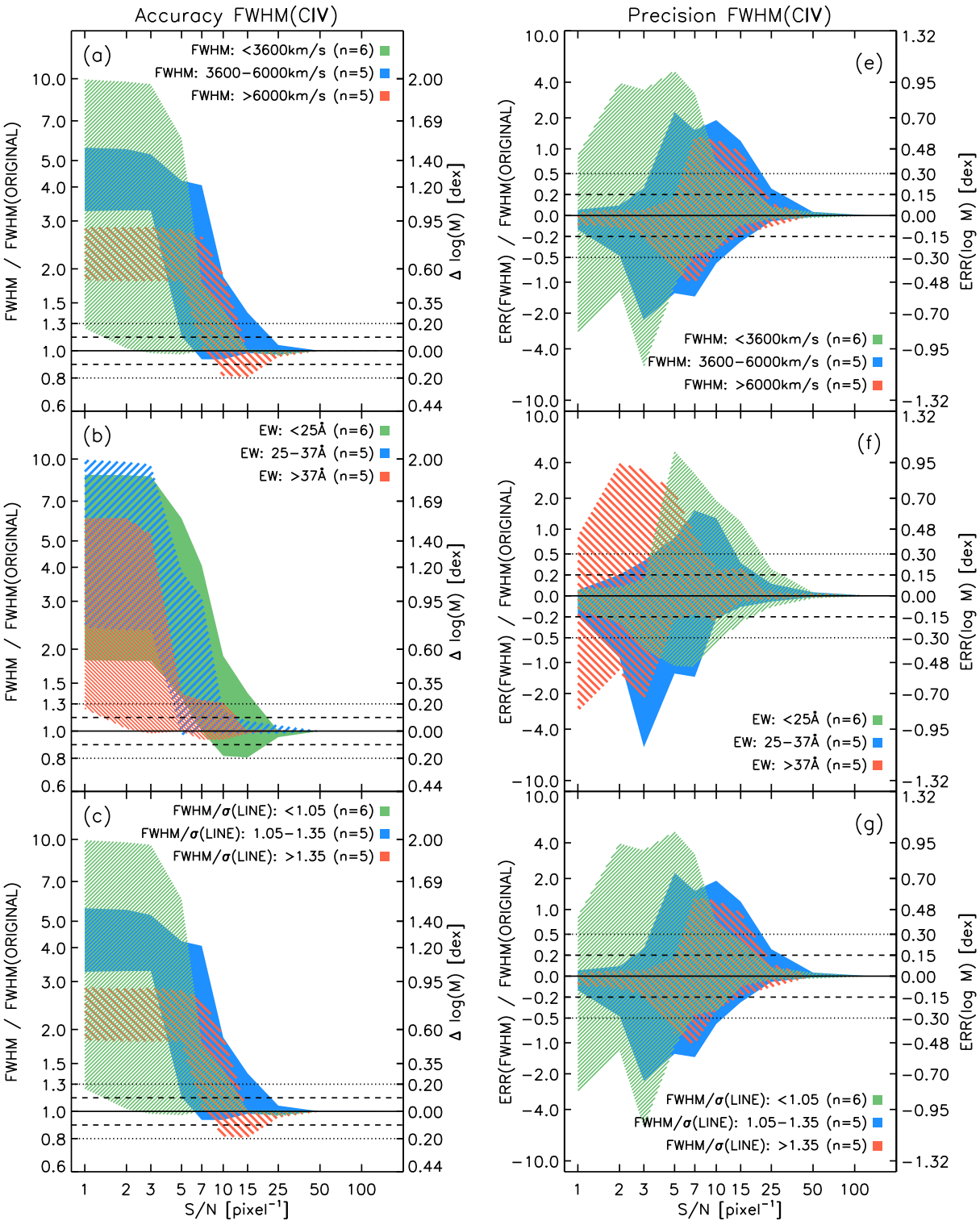

Fig. H.5 FWHM with medium strong absorption in the middle of the absorption line.

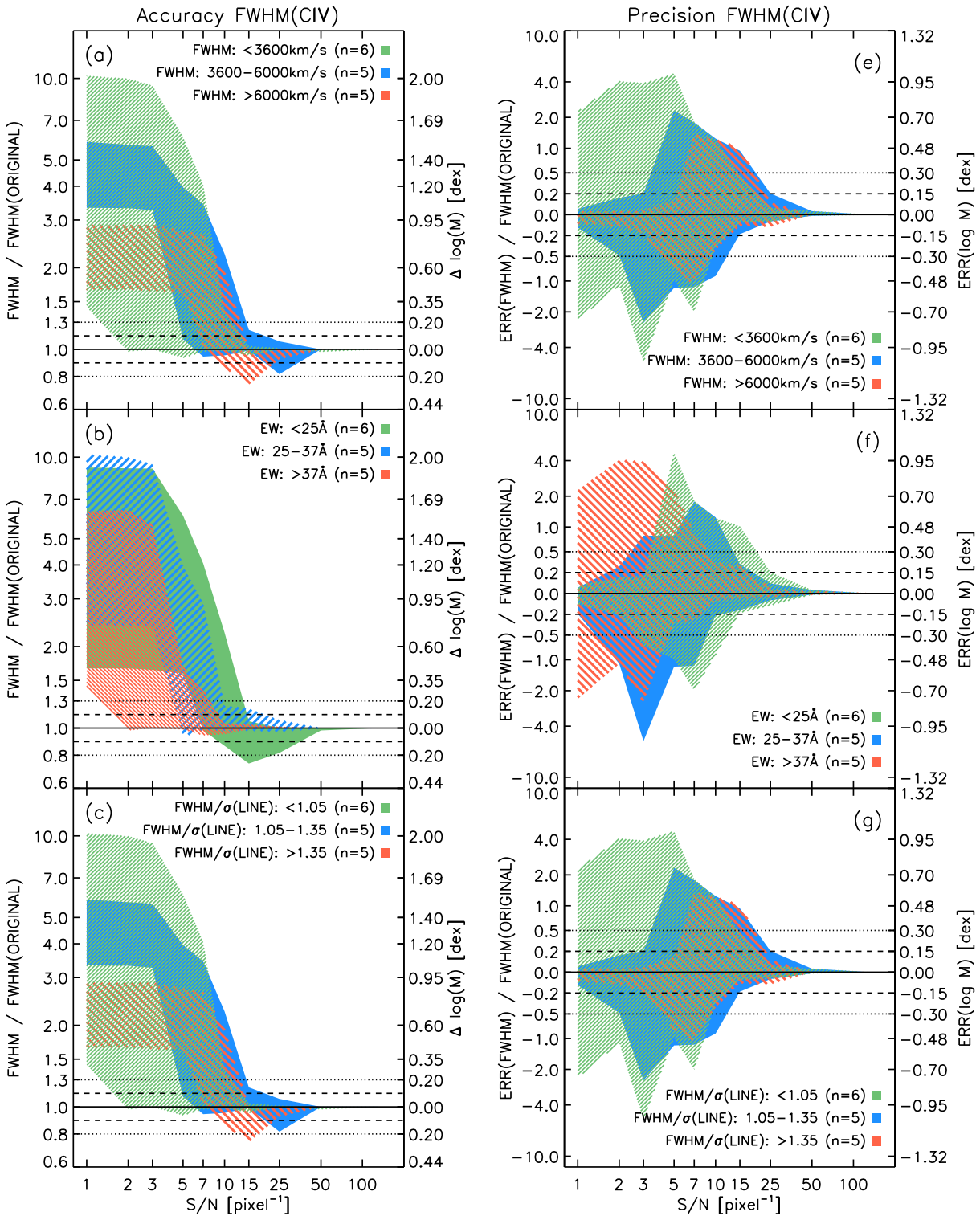

Fig. H.6 FWHM with strong absorption in the middle of the absorption line.

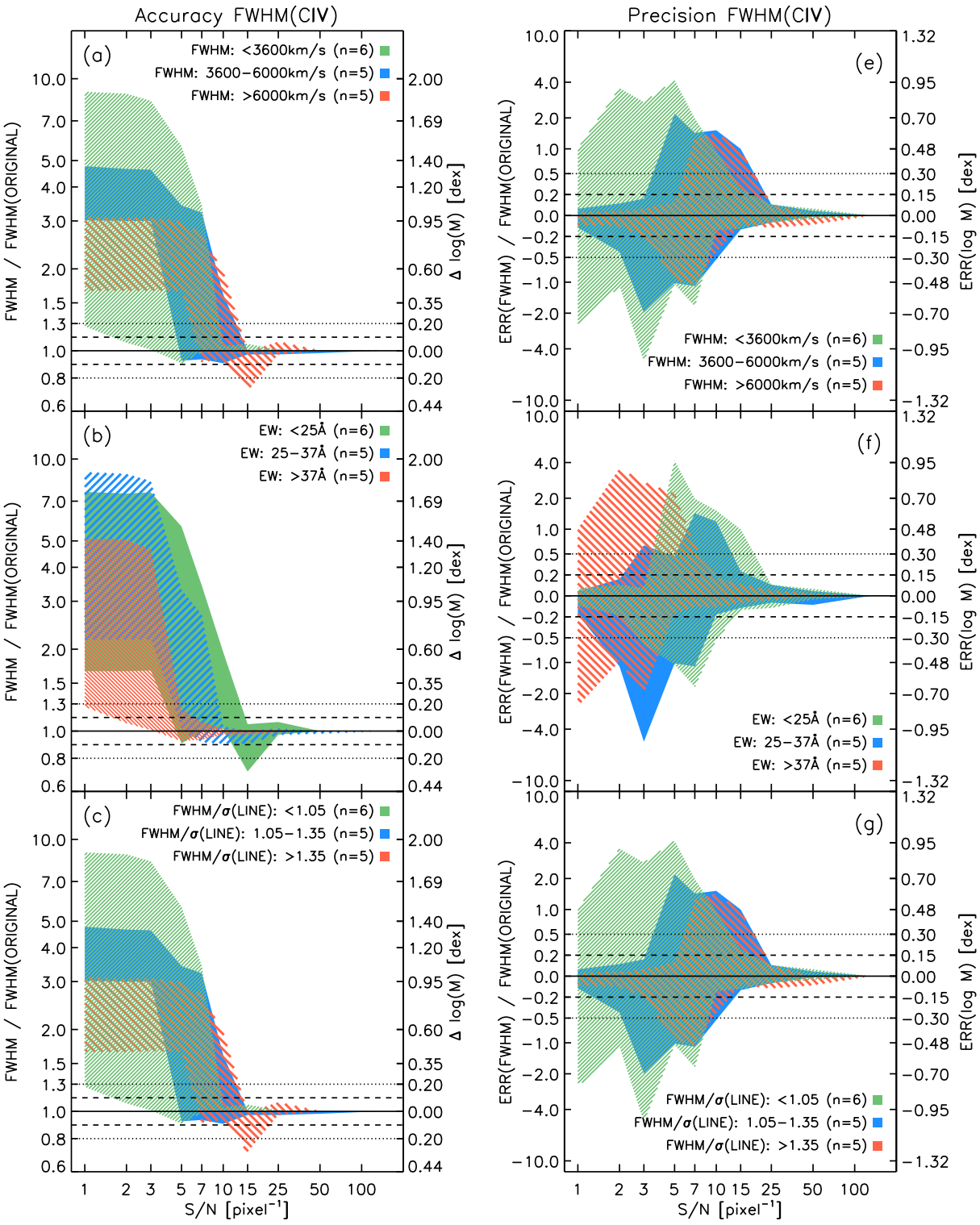

Fig. H.7 FWHM with weak absorption in the wing of the emission line.

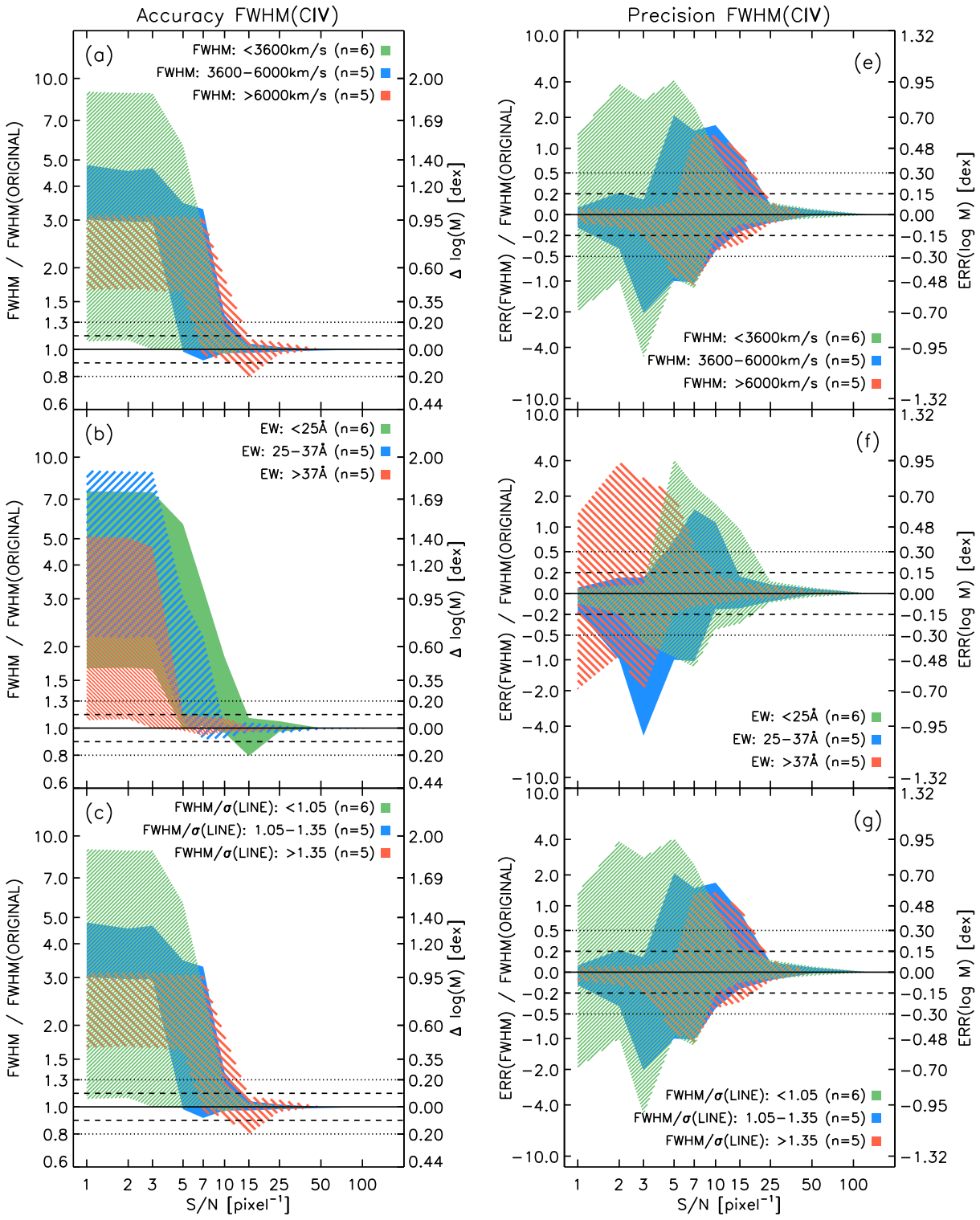

Fig. H.8 FWHM with medium strong absorption in the wing of the emission line.

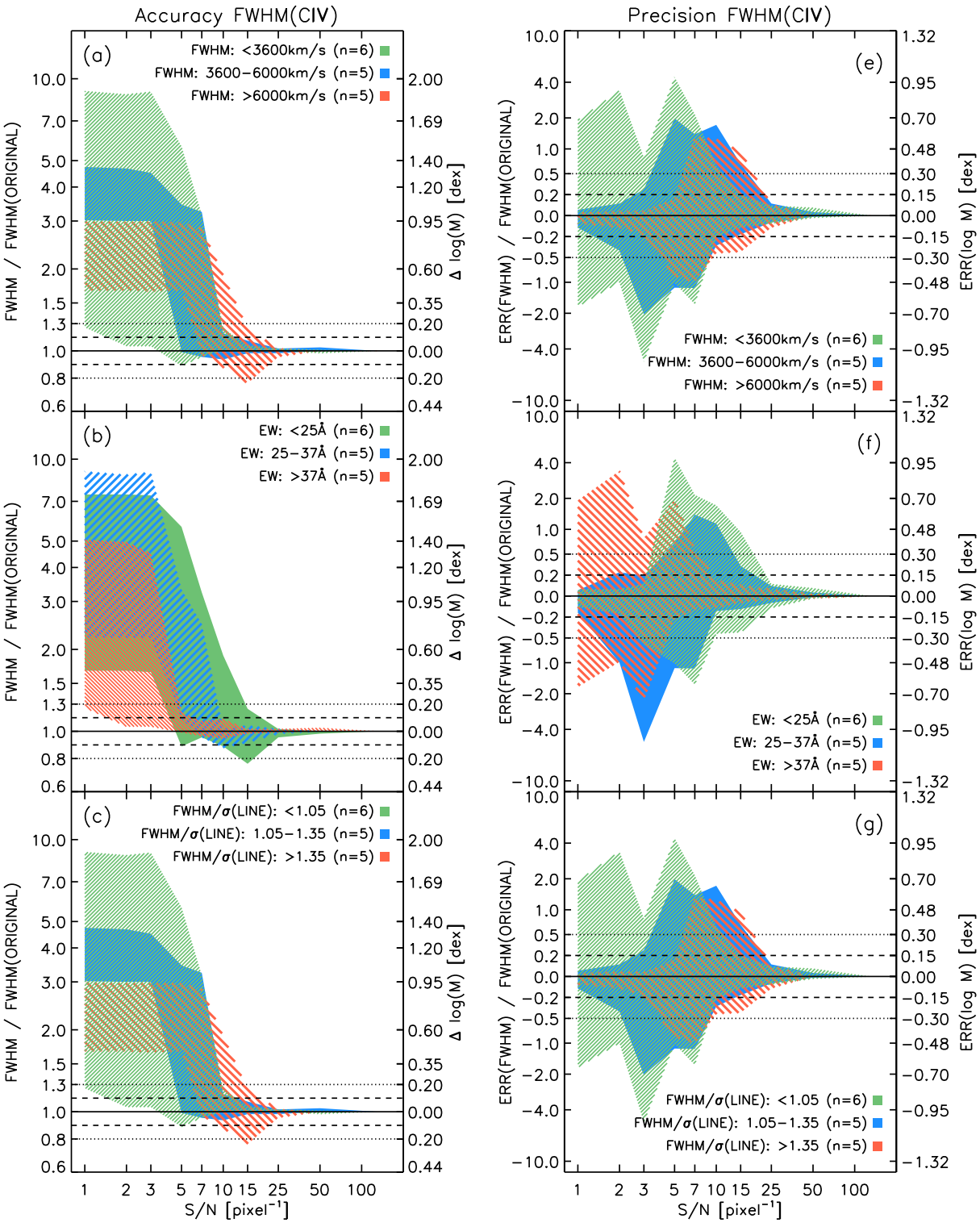

Fig. H.9 FWHM with strong absorption in the wing of the emission line.

Appendix I

σ_{line} with absorption

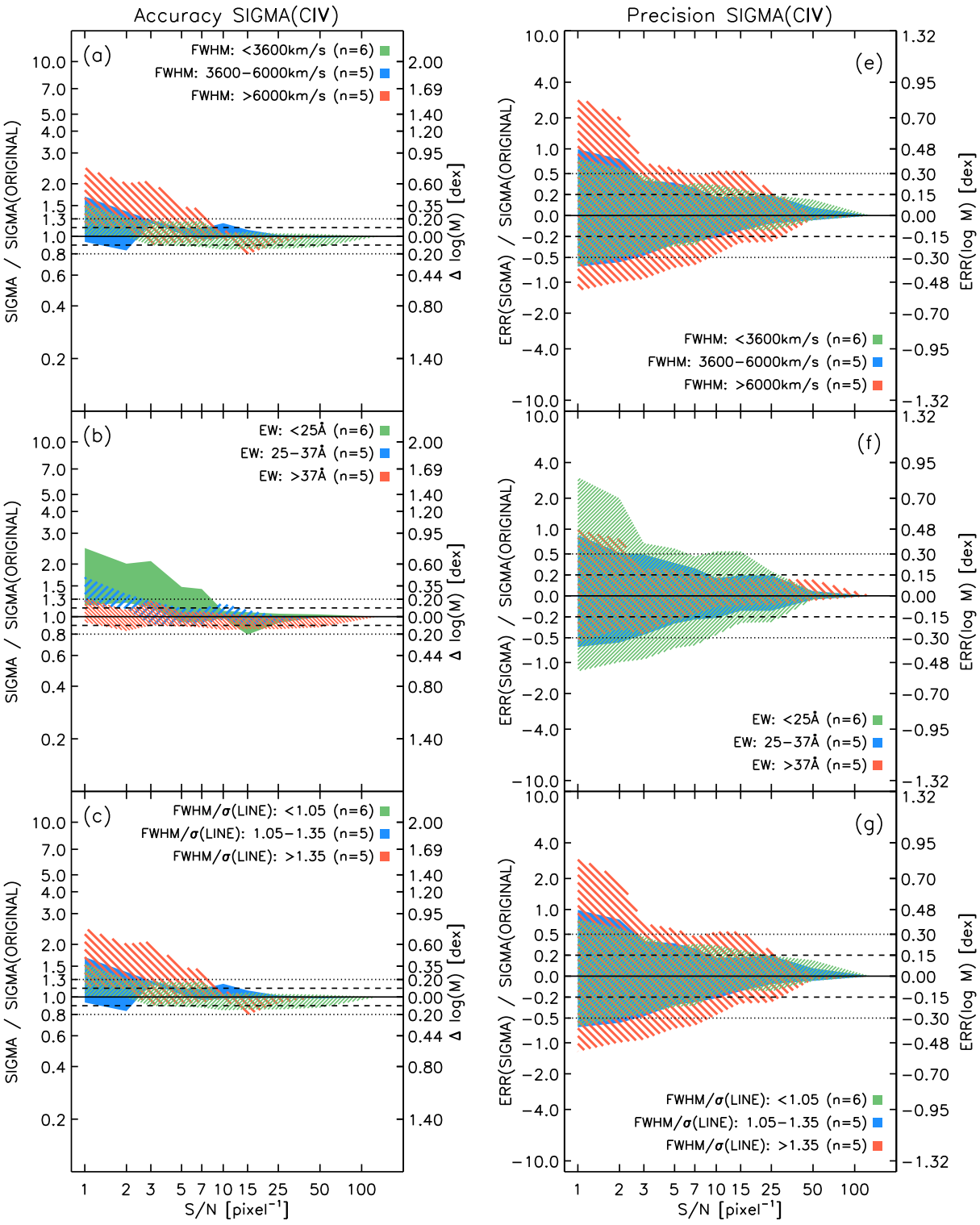

Fig. I.1 SIGMA with weak absorption in the core of the emission line.

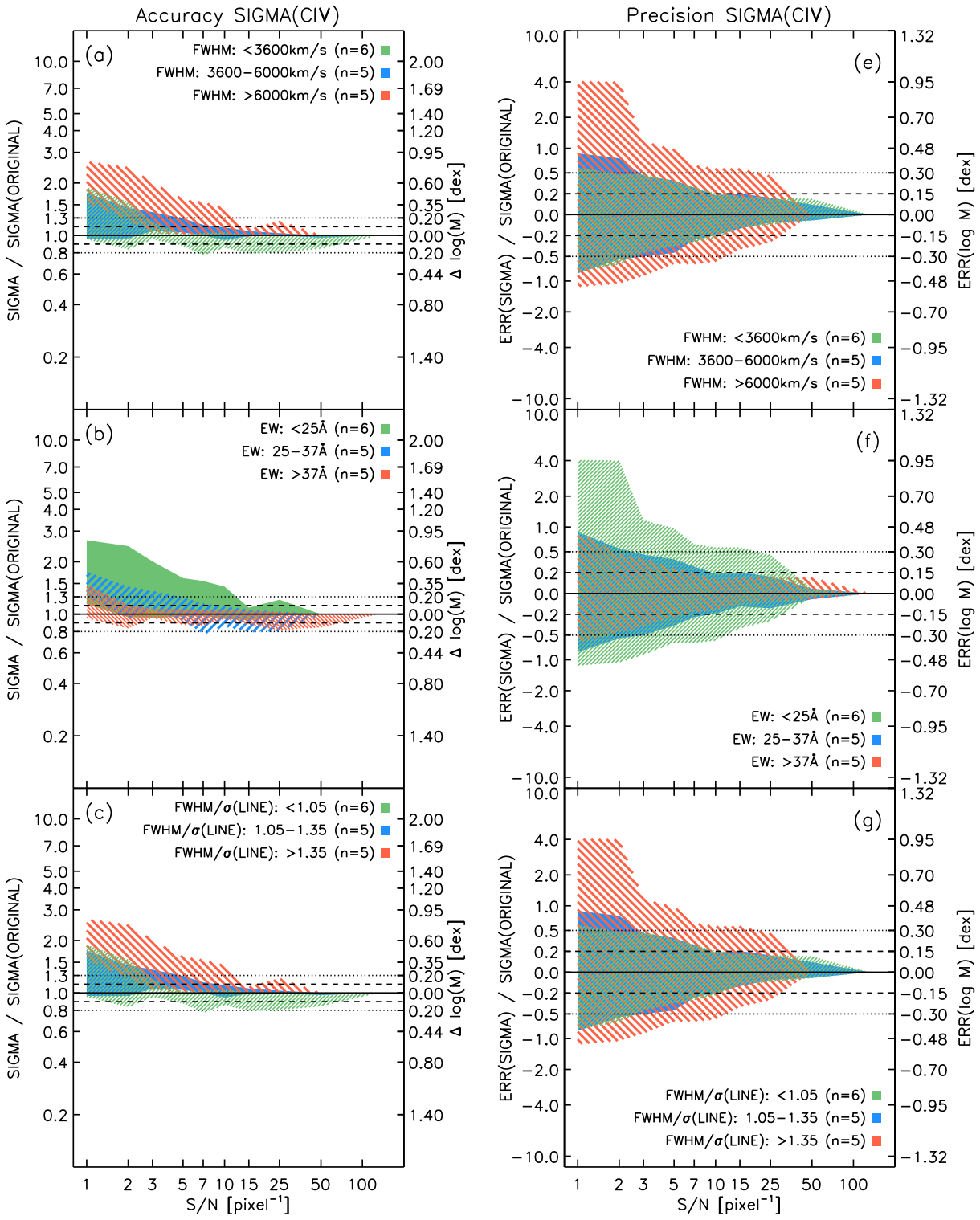

Fig. I.2 SIGMA with medium strong absorption in the core of the emission line.

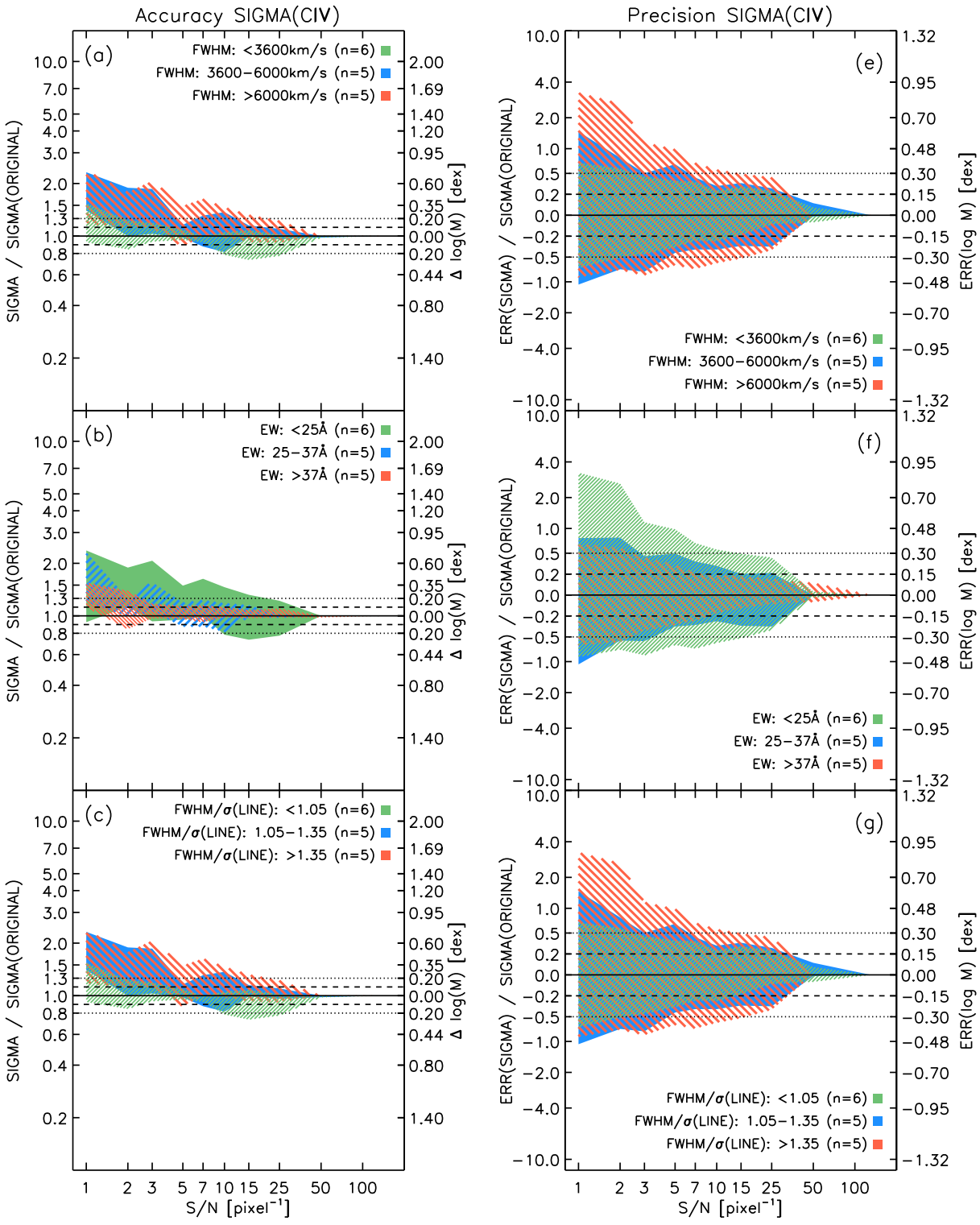

Fig. I.3 SIGMA with strong absorption in the core of the emission line.

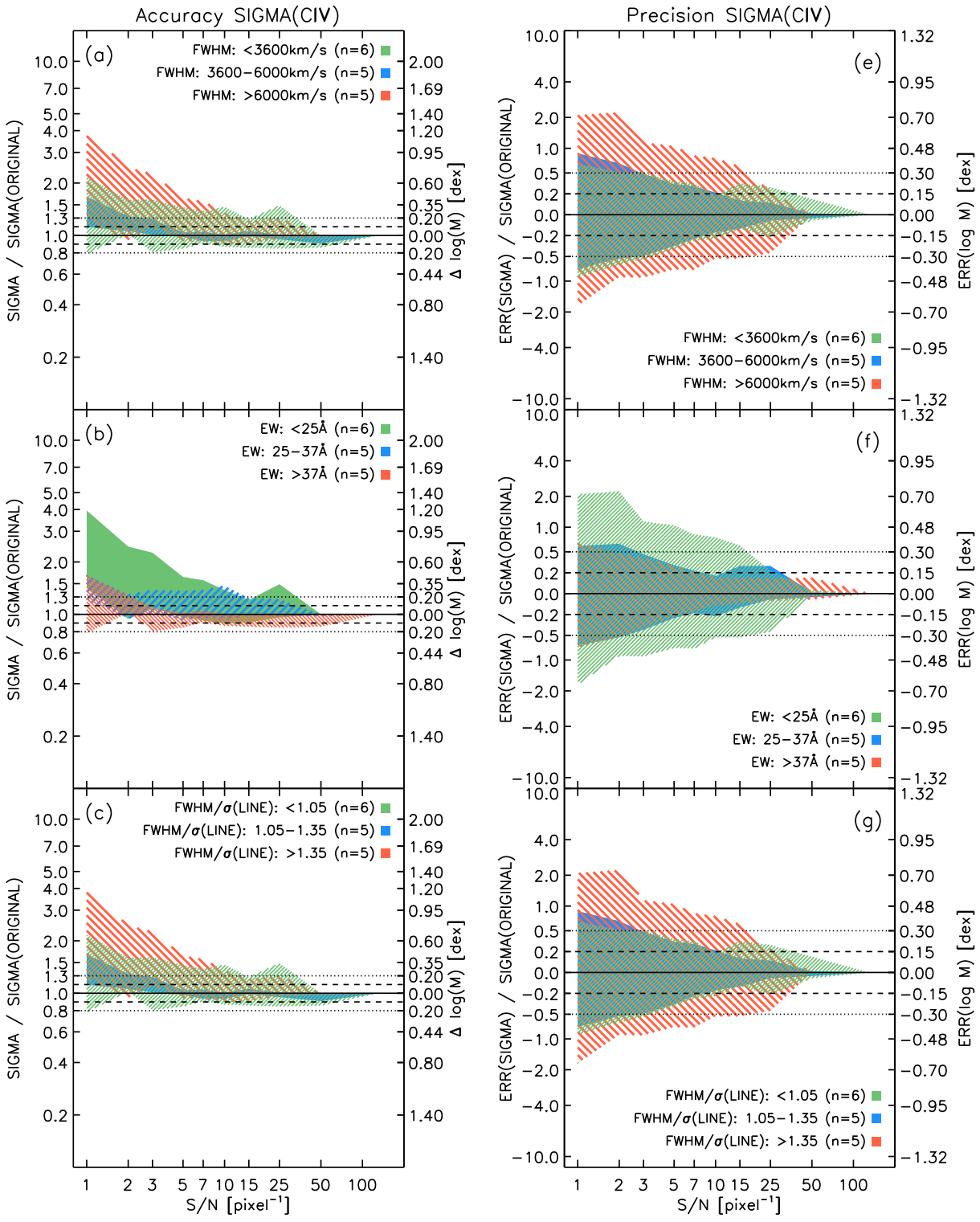

Fig. I.4 SIGMA with weak absorption in the middle of the absorption line.

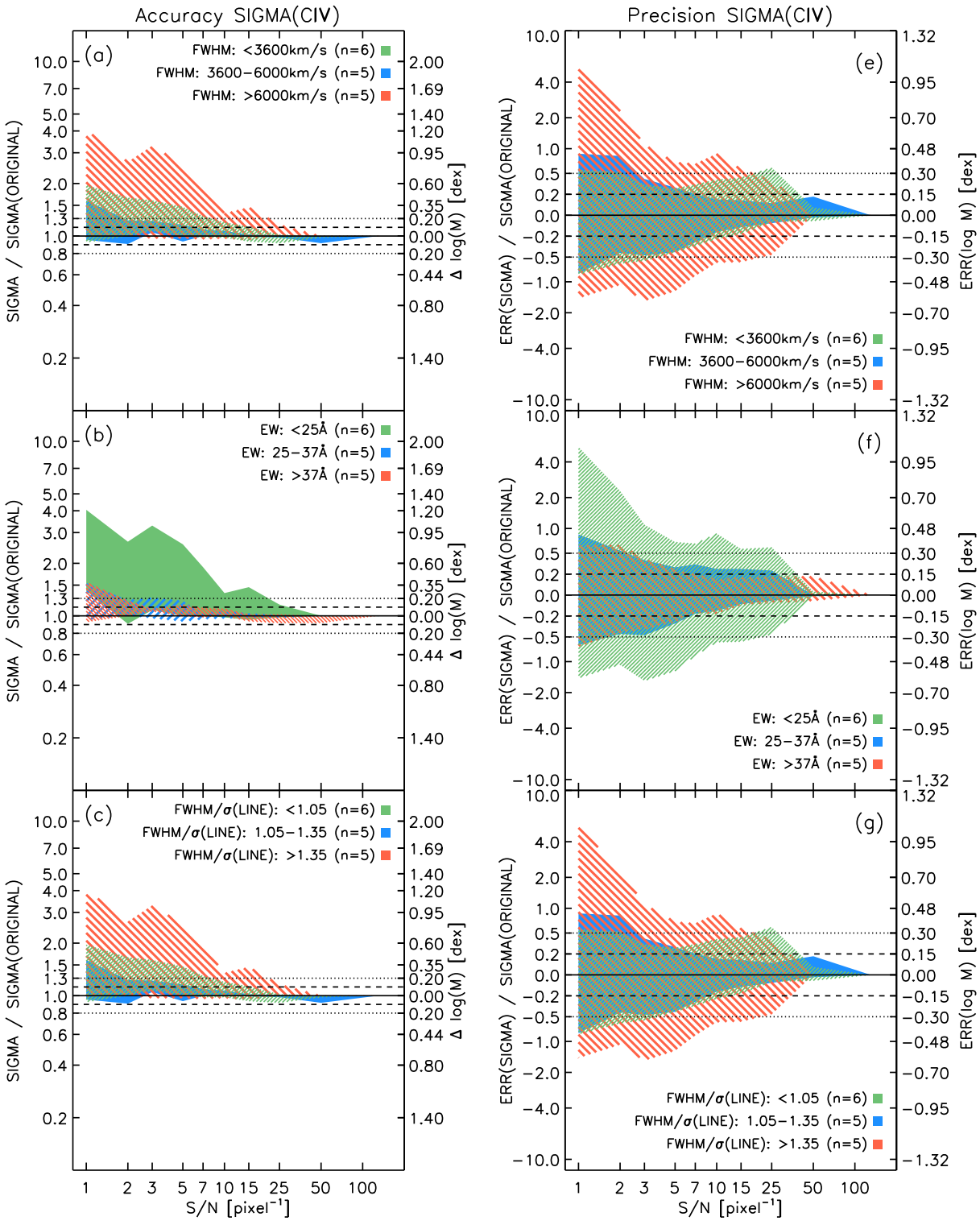

Fig. I.5 SIGMA with medium strong absorption in the middle of the absorption line.

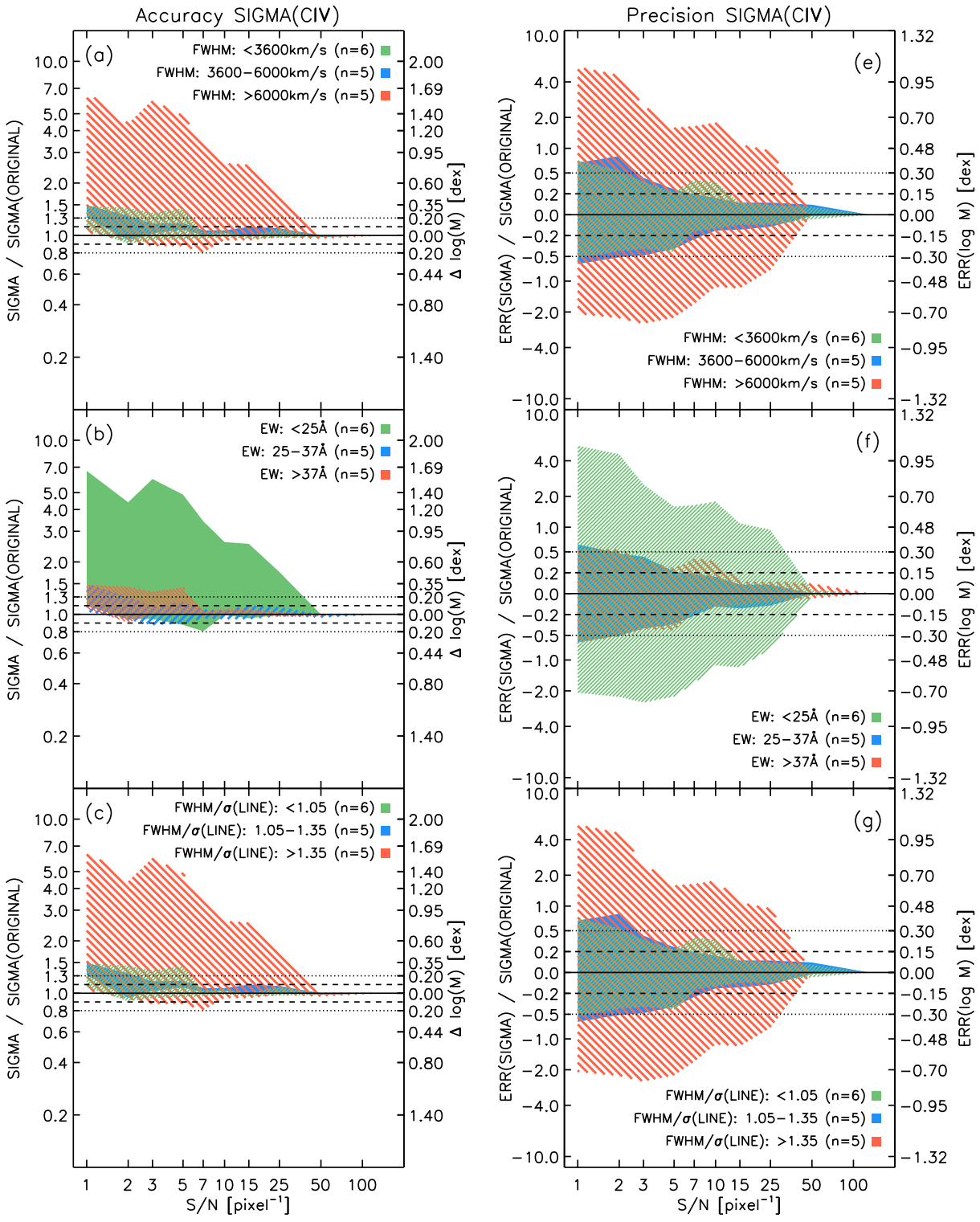

Fig. I.6 SIGMA with strong absorption in the middle of the absorption line.

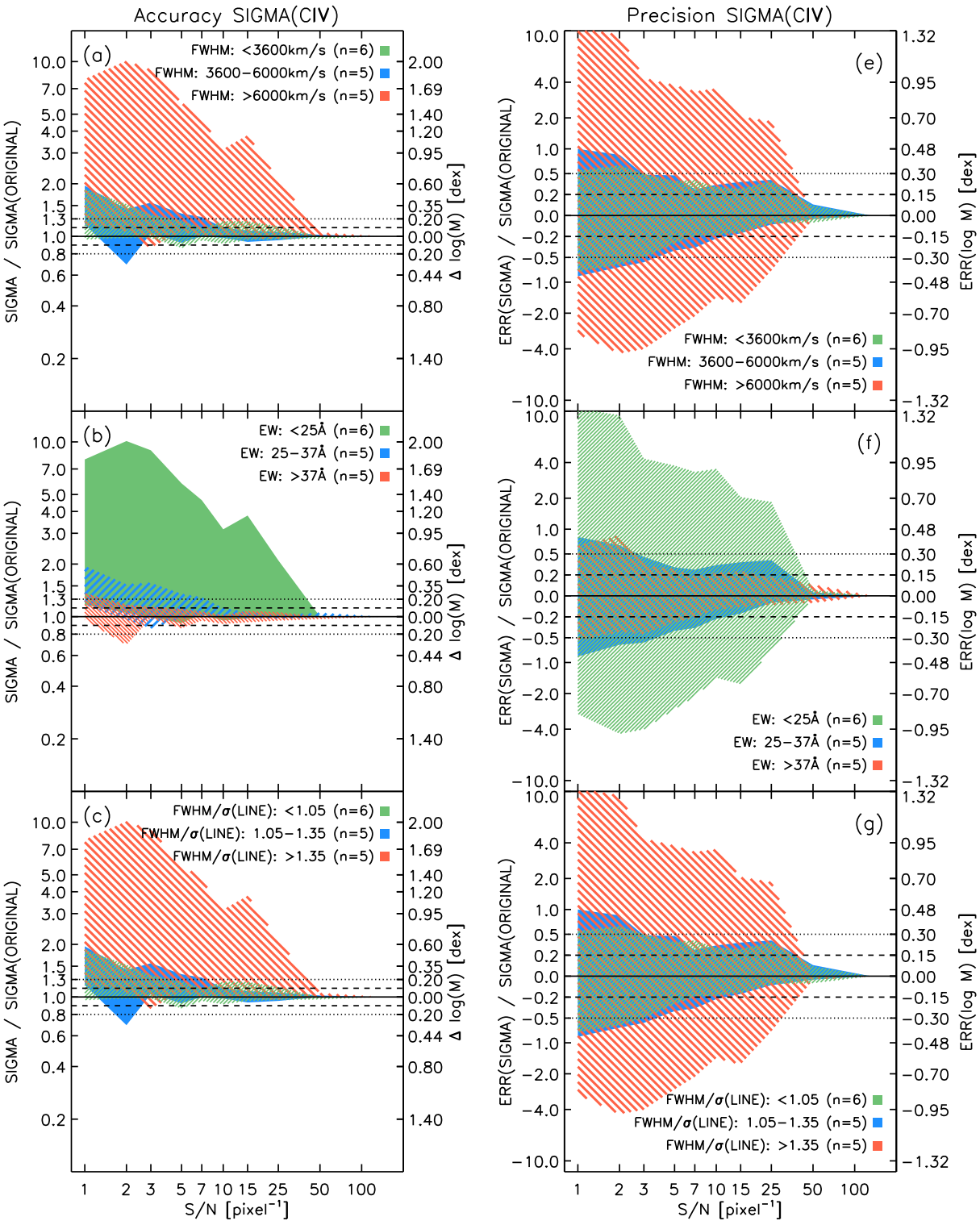

Fig. I.7 SIGMA with weak absorption in the wing of the emission line.

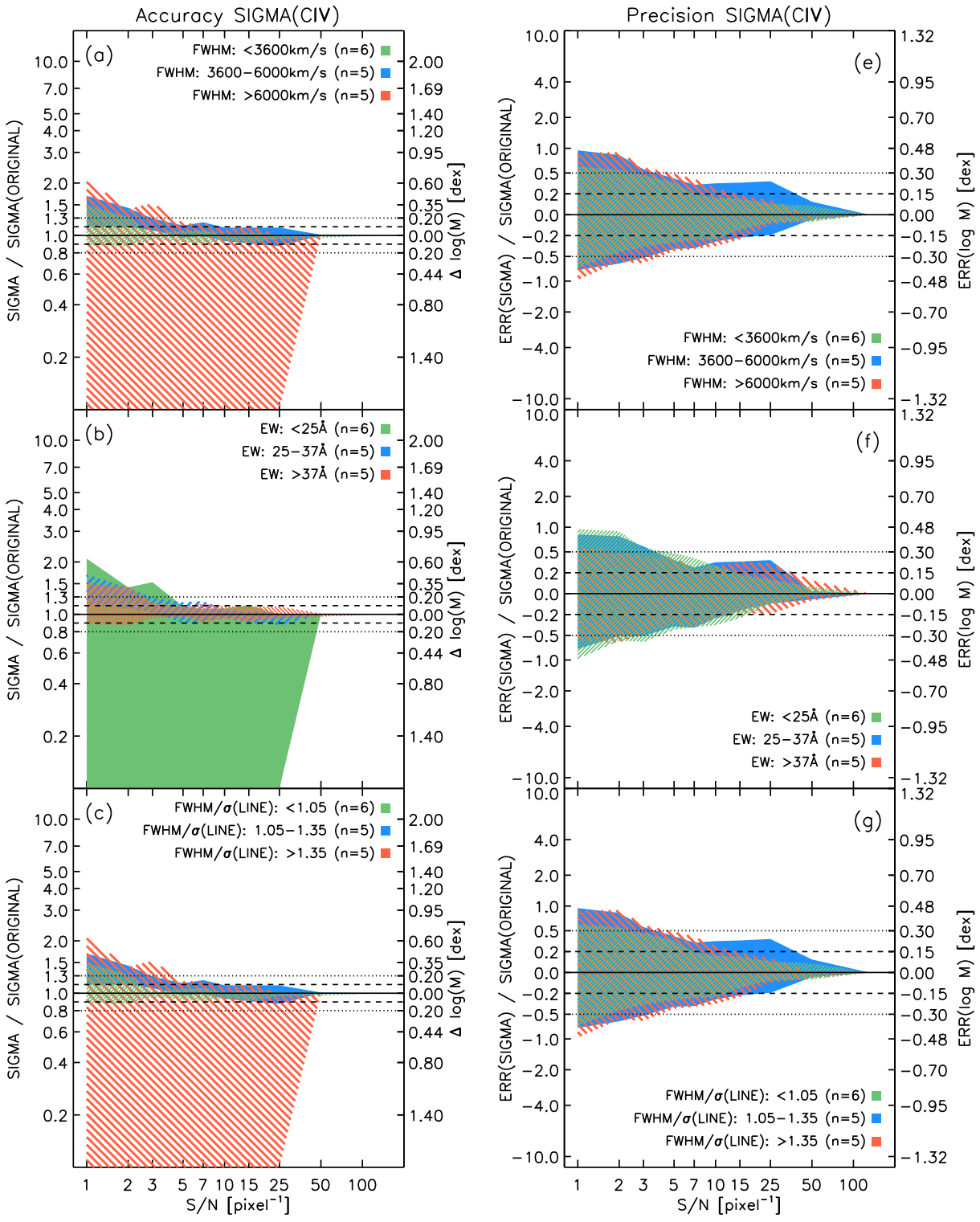

Fig. I.8 SIGMA with medium strong absorption in the wing of the emission line.

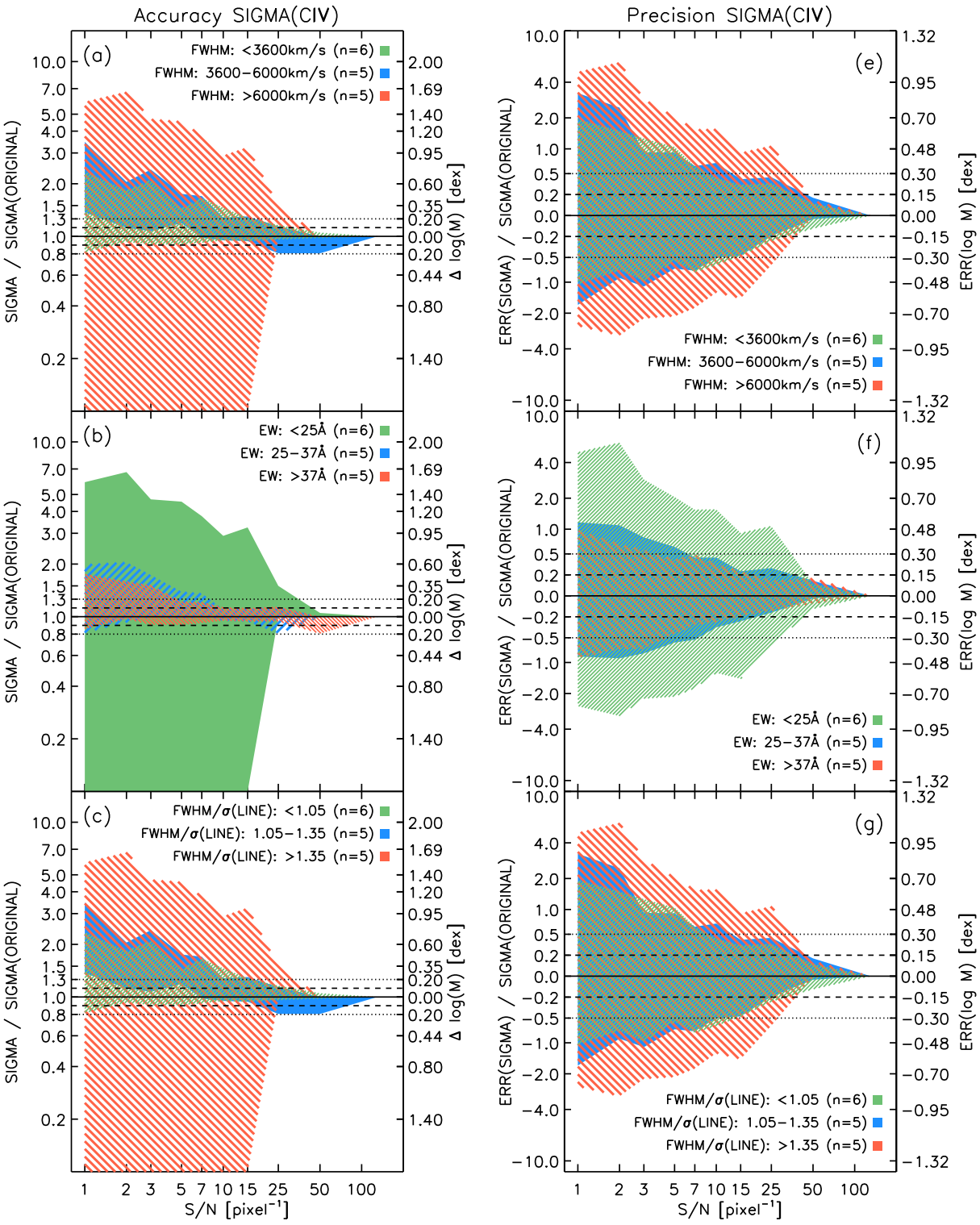

Fig. I.9 SIGMA with strong absorption in the wing of the emission line.

Appendix J

The MAD with absorption

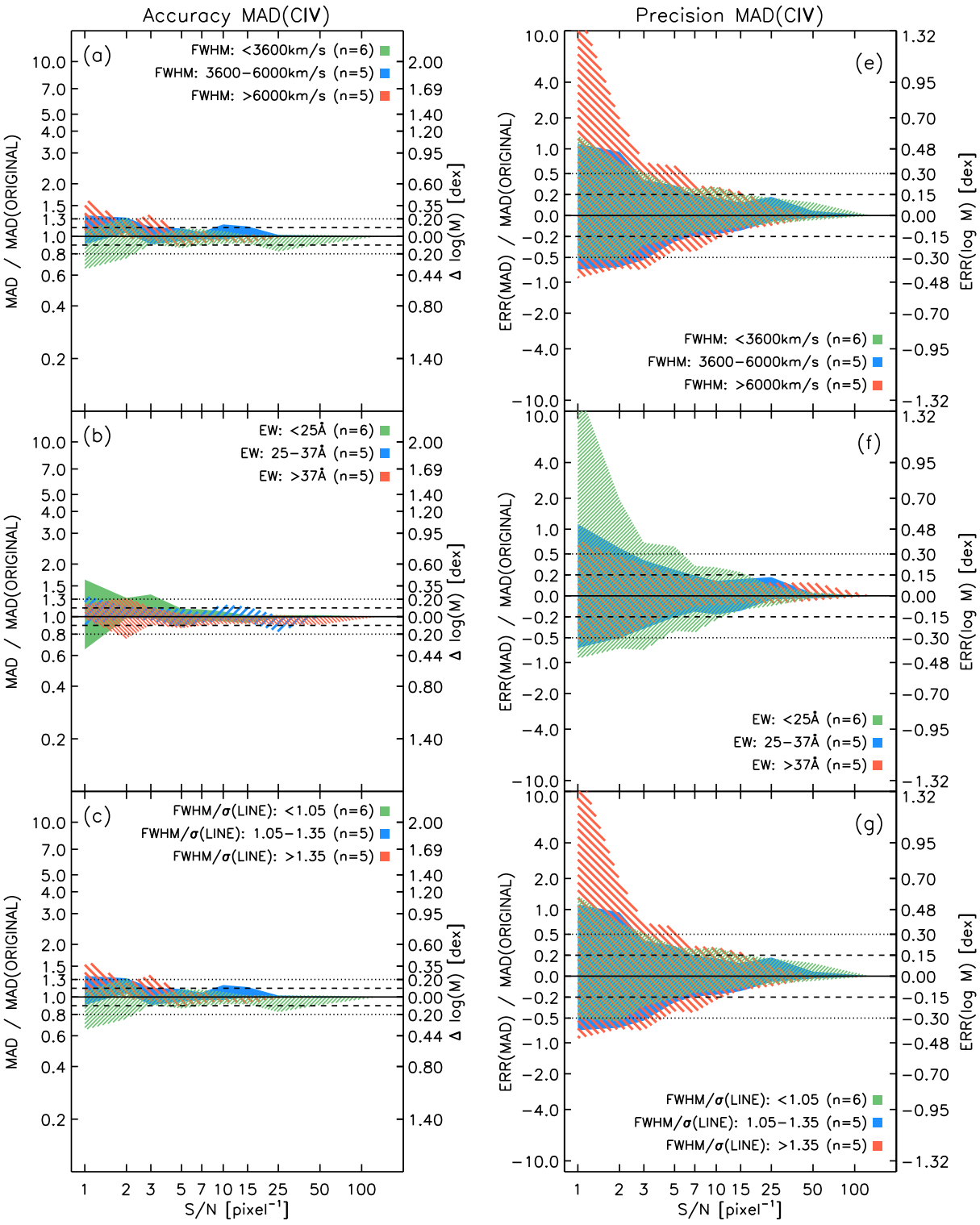

Fig. J.1 MAD with weak absorption in the core of the emission line.

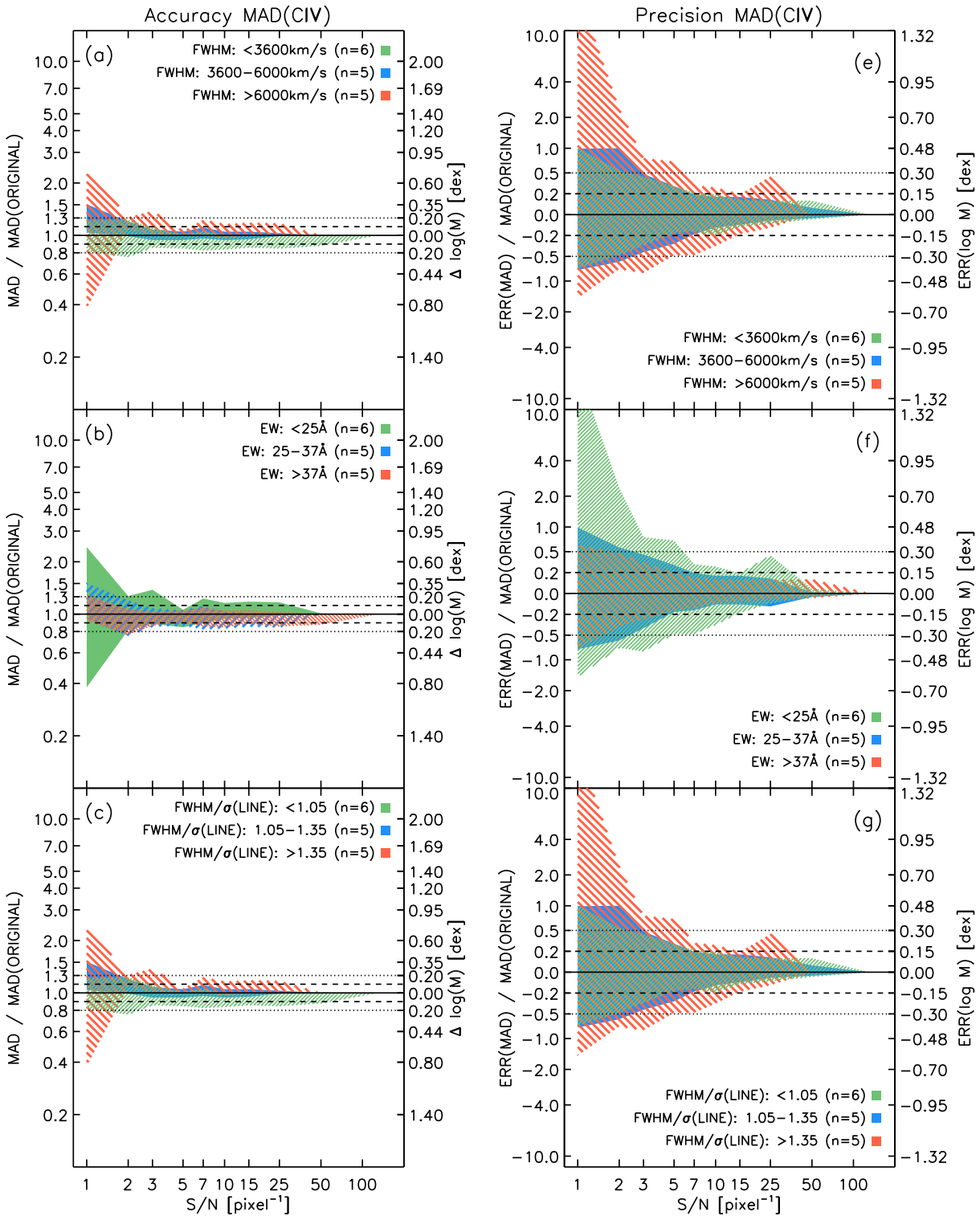

Fig. J.2 MAD with medium strong absorption in the core of the emission line.

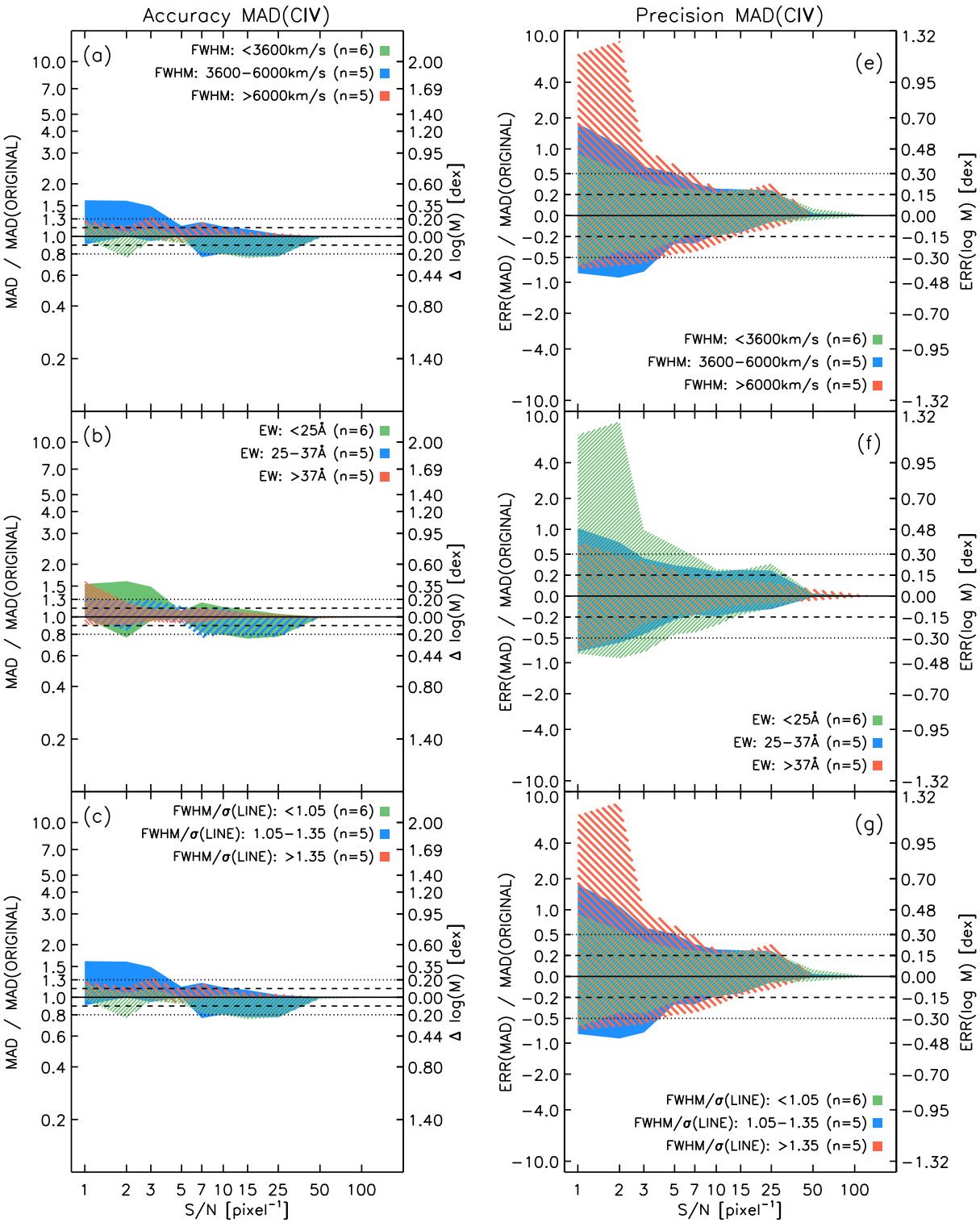

Fig. J.3 MAD with strong absorption in the core of the emission line.

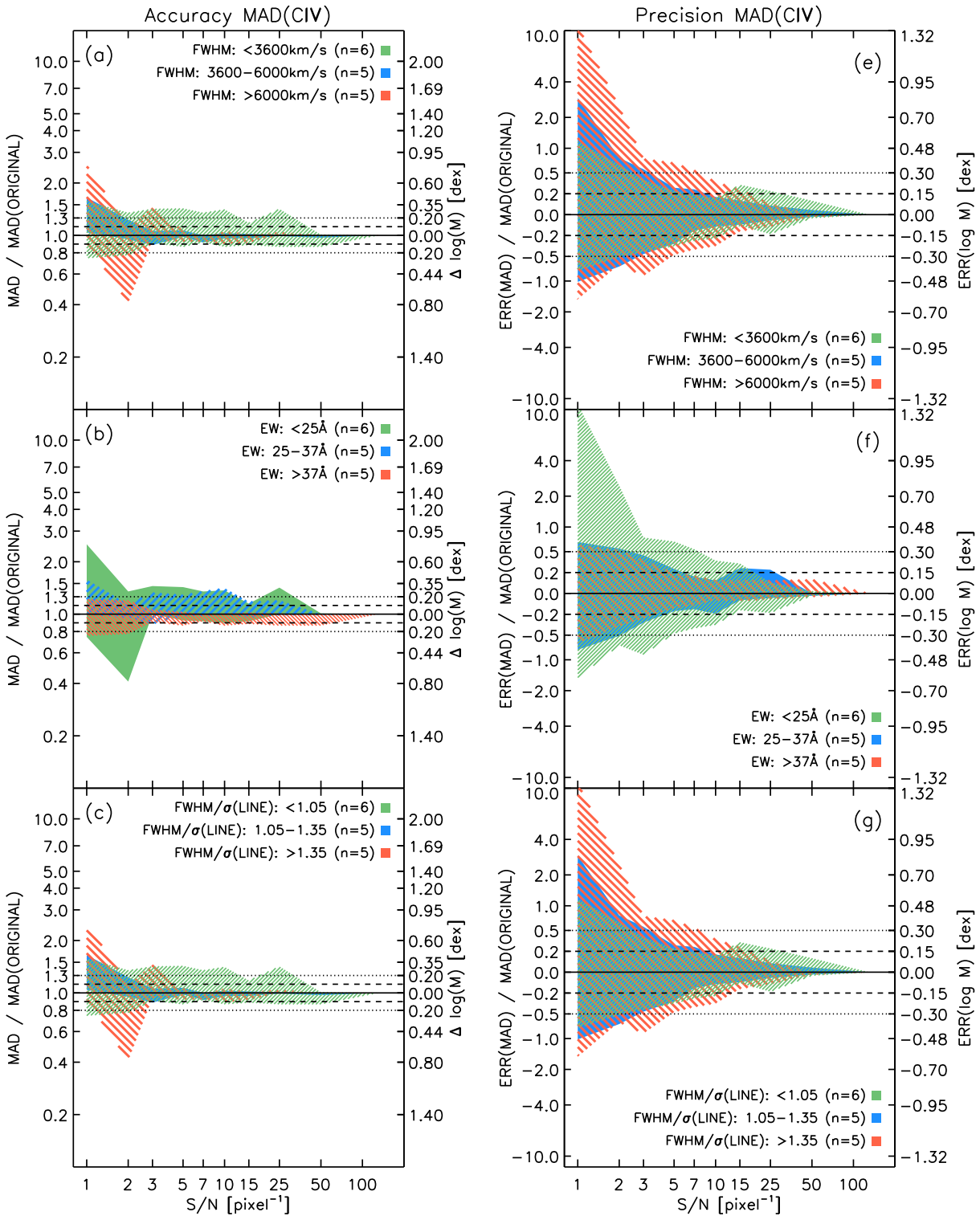

Fig. J.4 MAD with weak absorption in the middle of the absorption line.

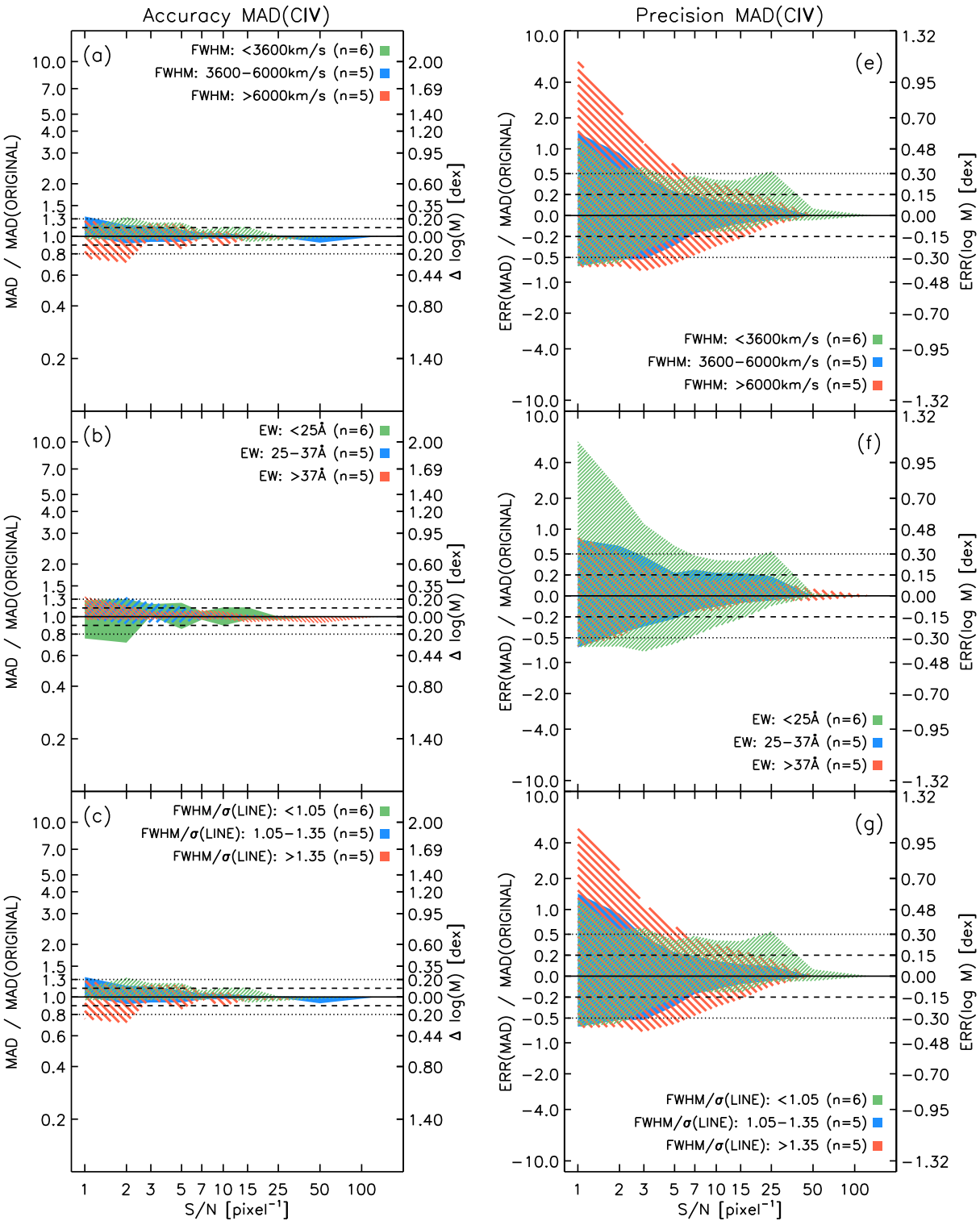

Fig. J.5 MAD with medium strong absorption in the middle of the absorption line.

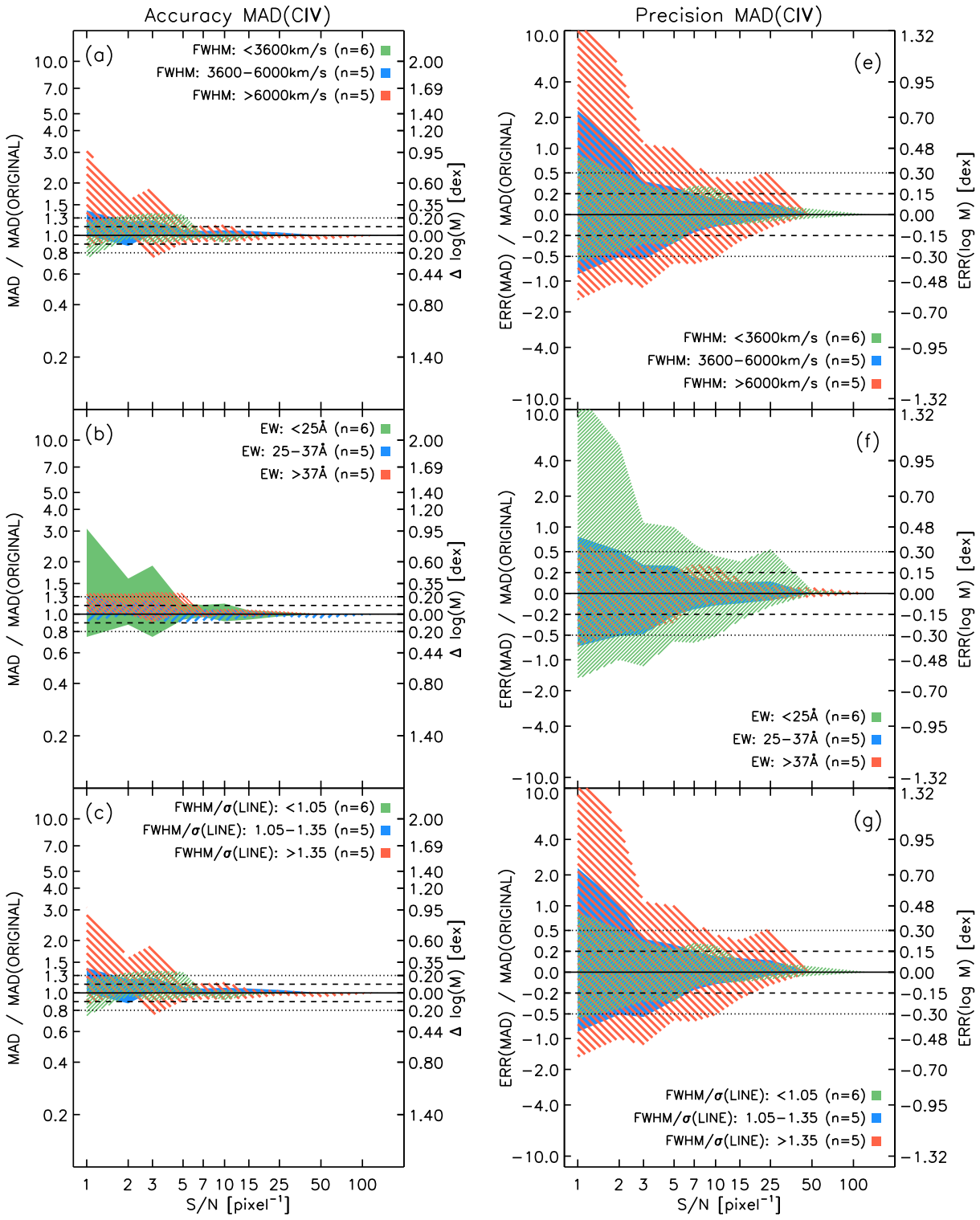

Fig. J.6 MAD with strong absorption in the middle of the absorption line.

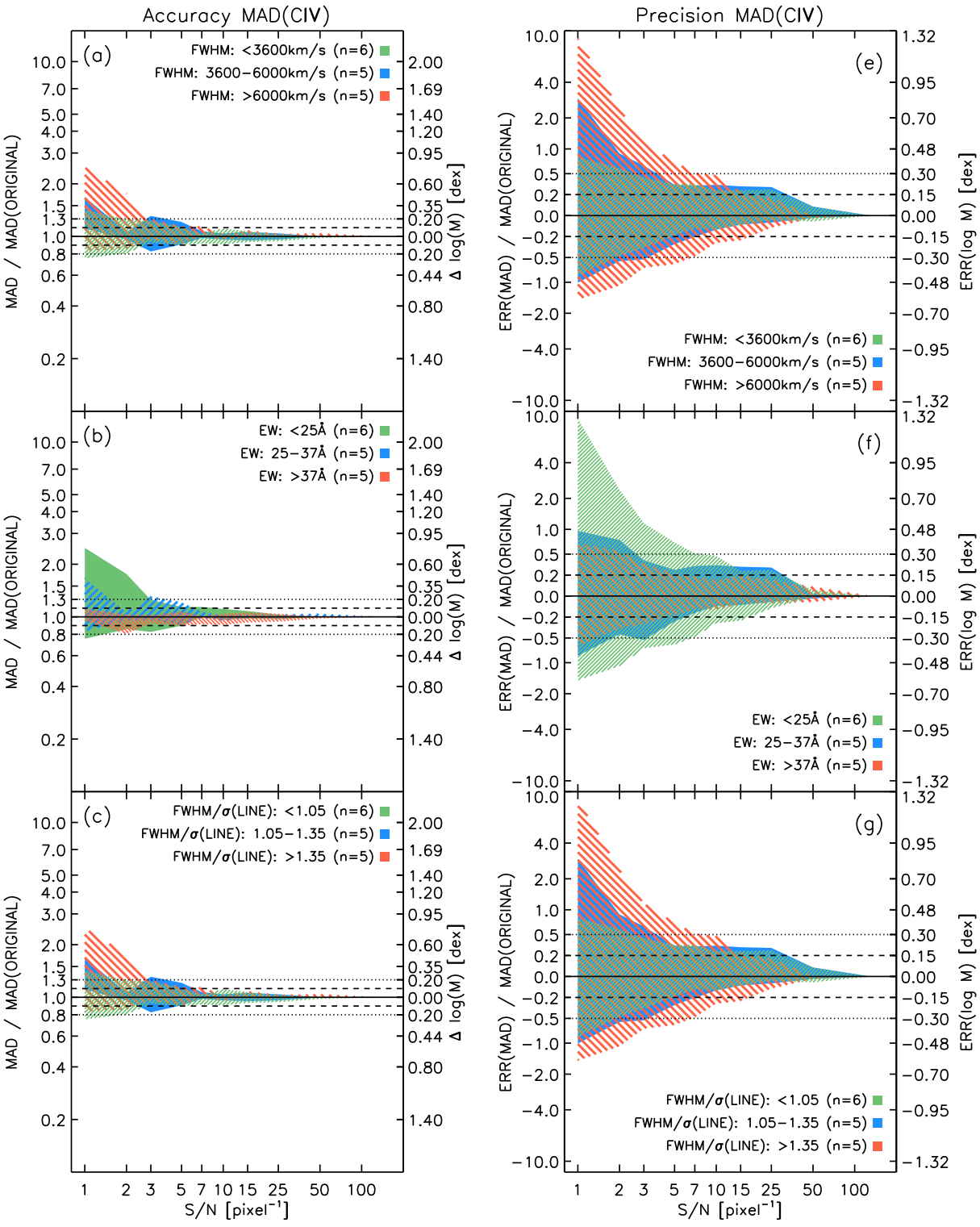

Fig. J.7 MAD with weak absorption in the wing of the emission line.

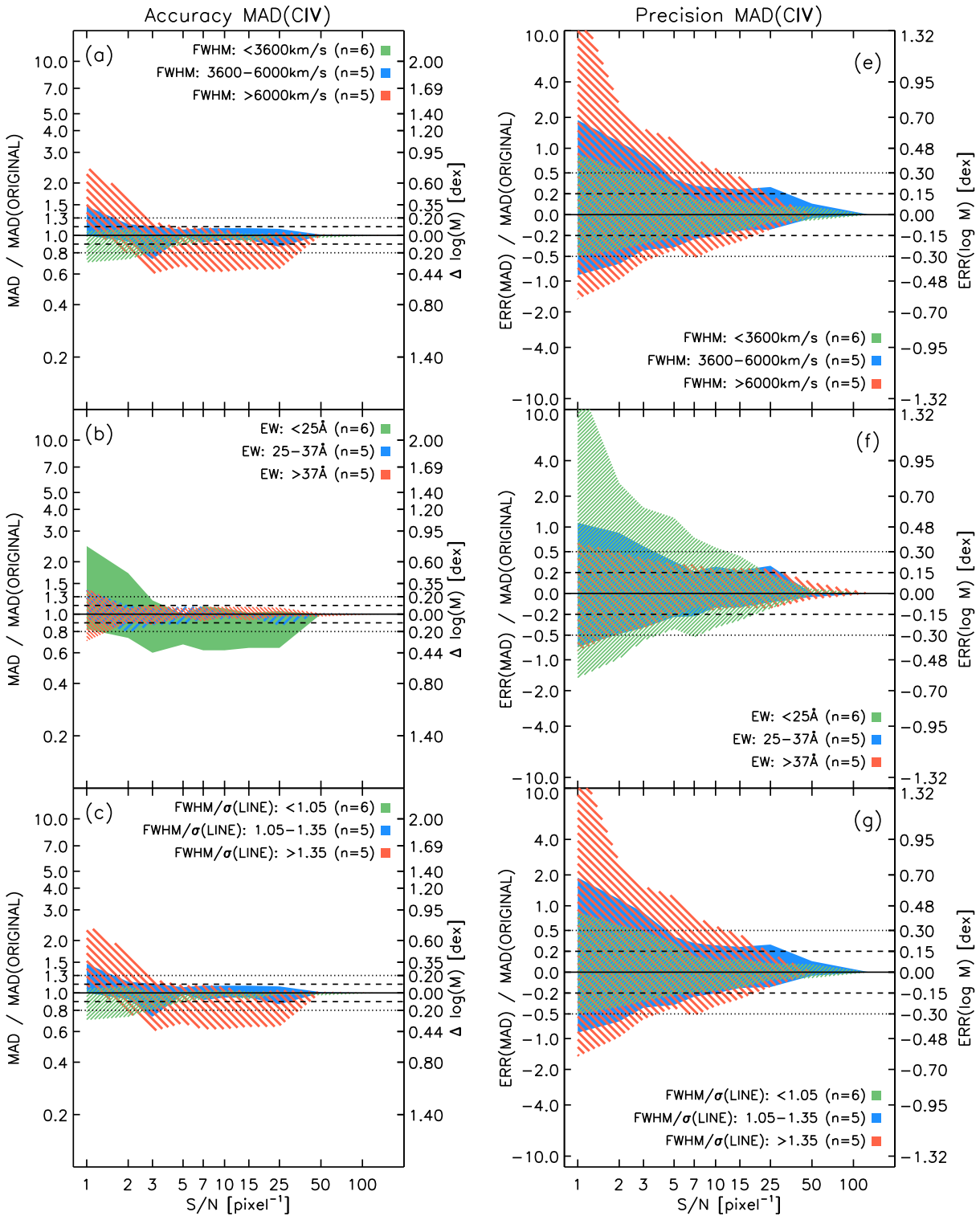

Fig. J.8 MAD with medium strong absorption in the wing of the emission line.

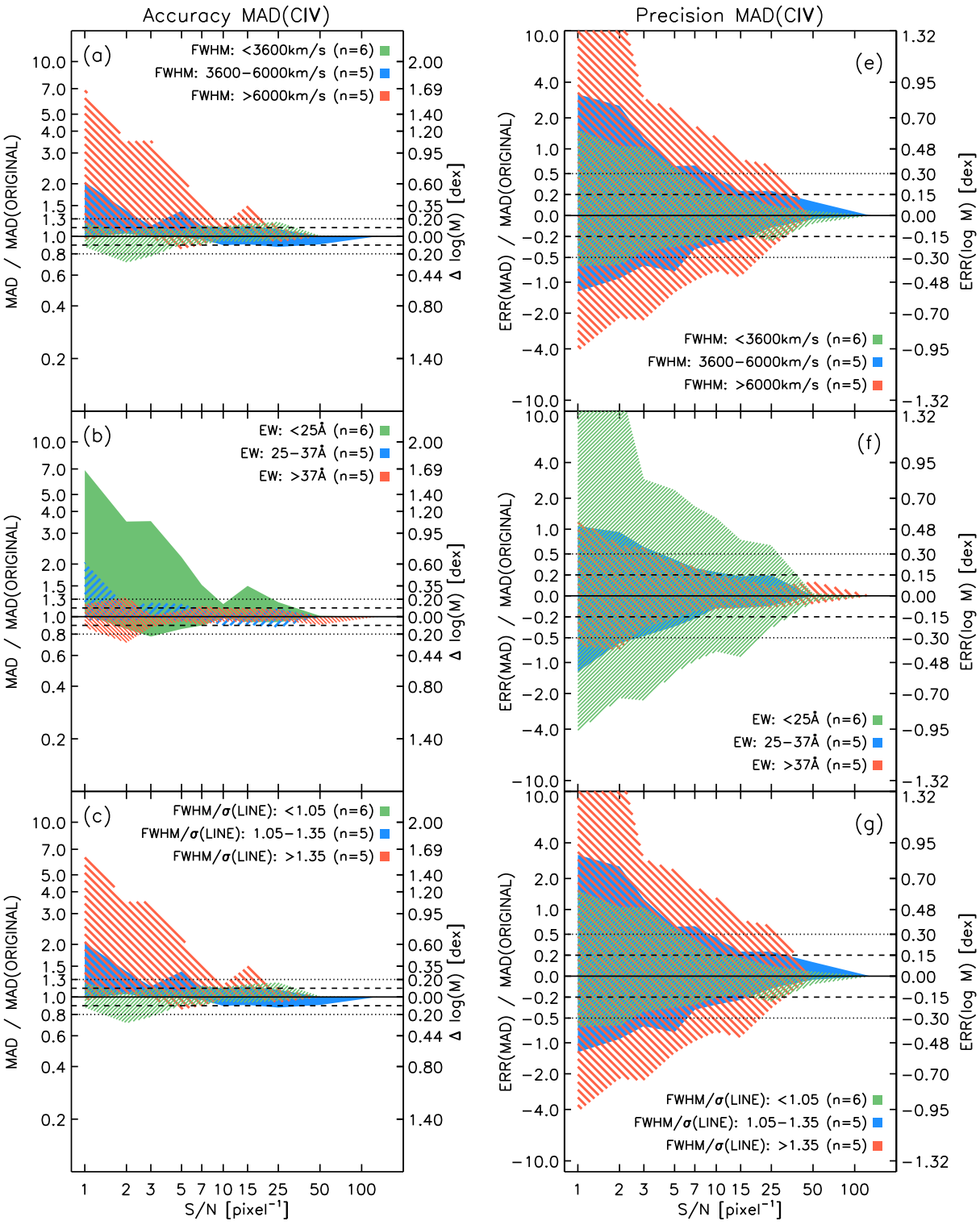

Fig. J.9 MAD with strong absorption in the wing of the emission line.

Appendix K

IPV20 with absorption

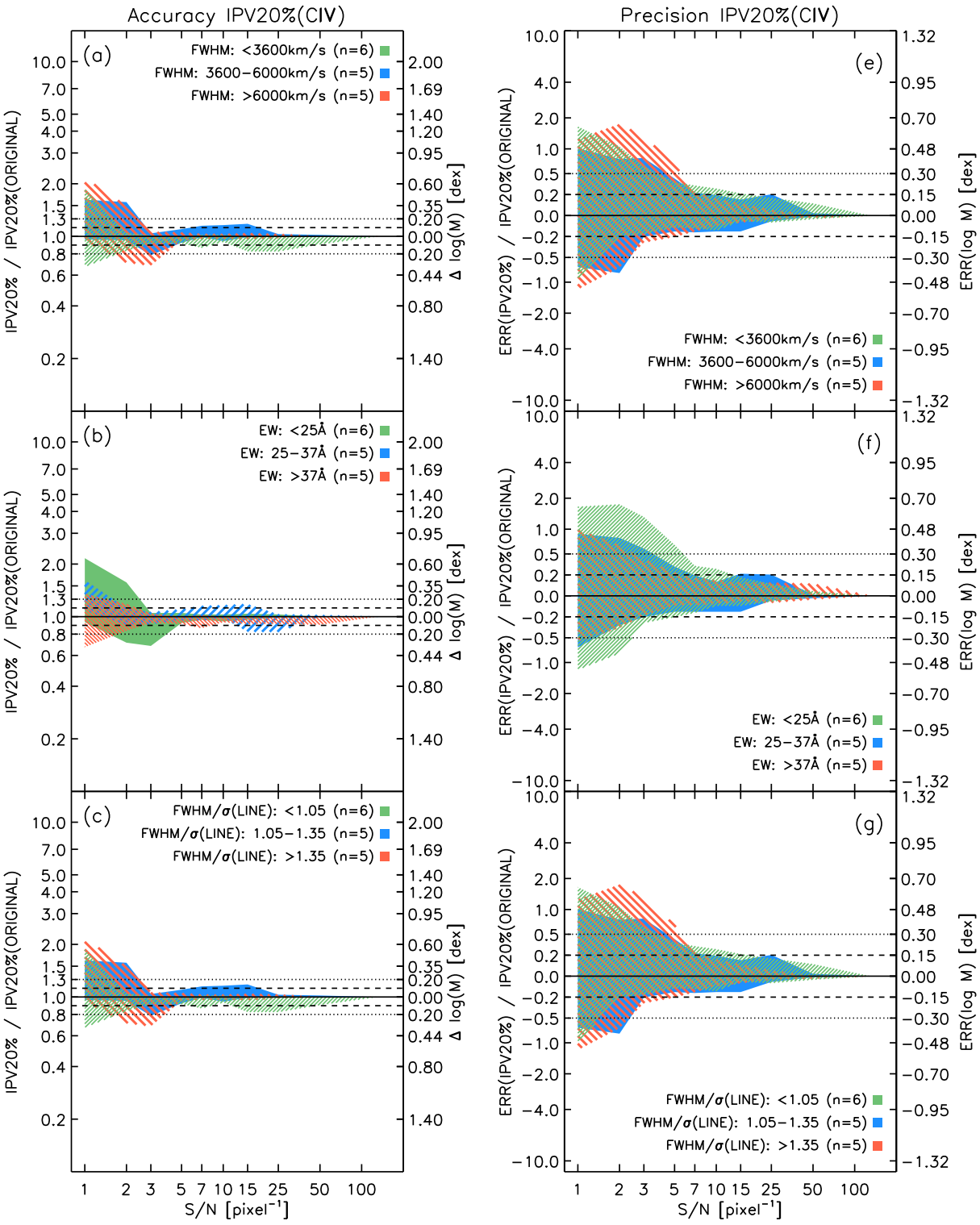

Fig. K.1 IPV20 with weak absorption in the core of the emission line.

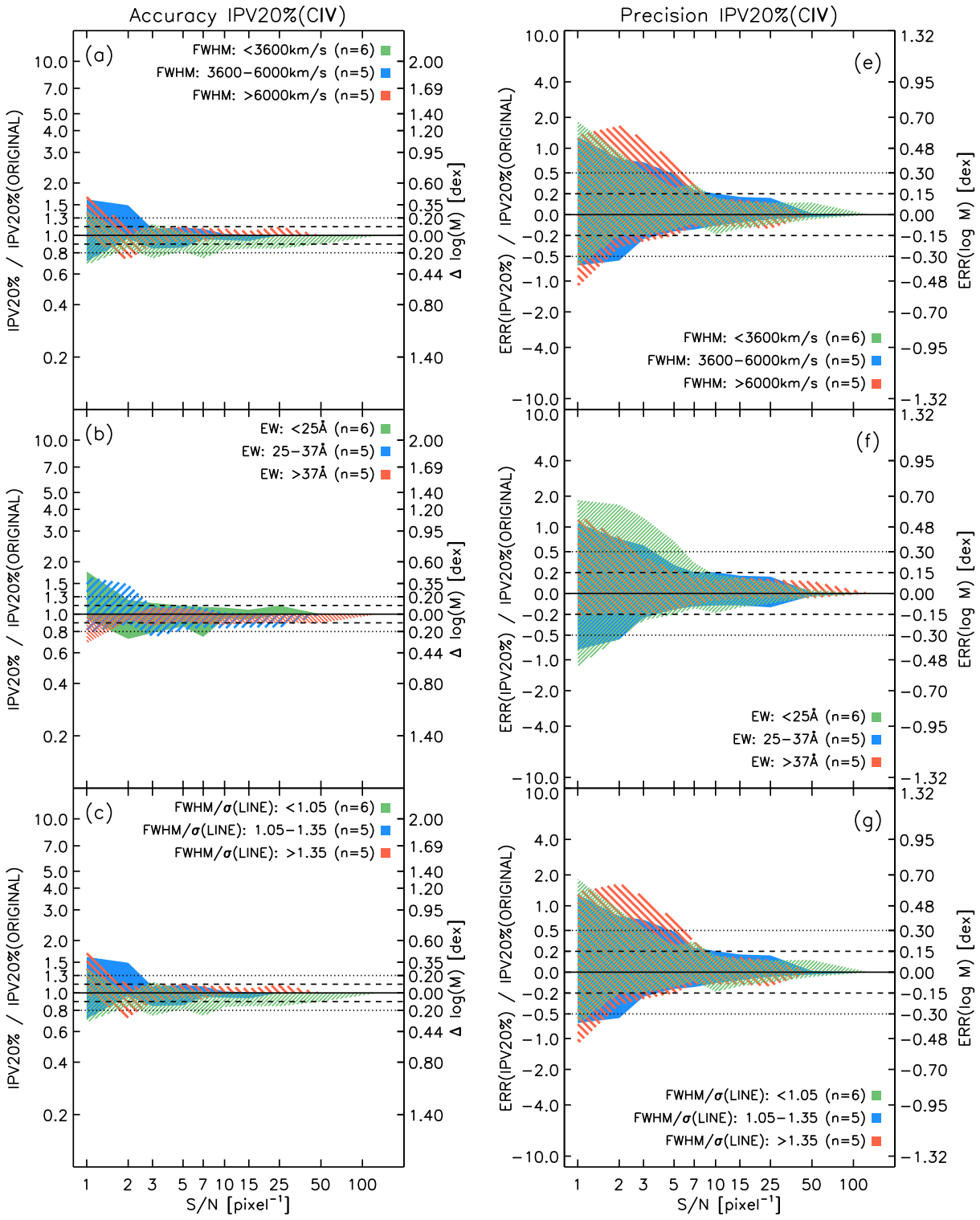

Fig. K.2 IPV20 with medium strong absorption in the core of the emission line.

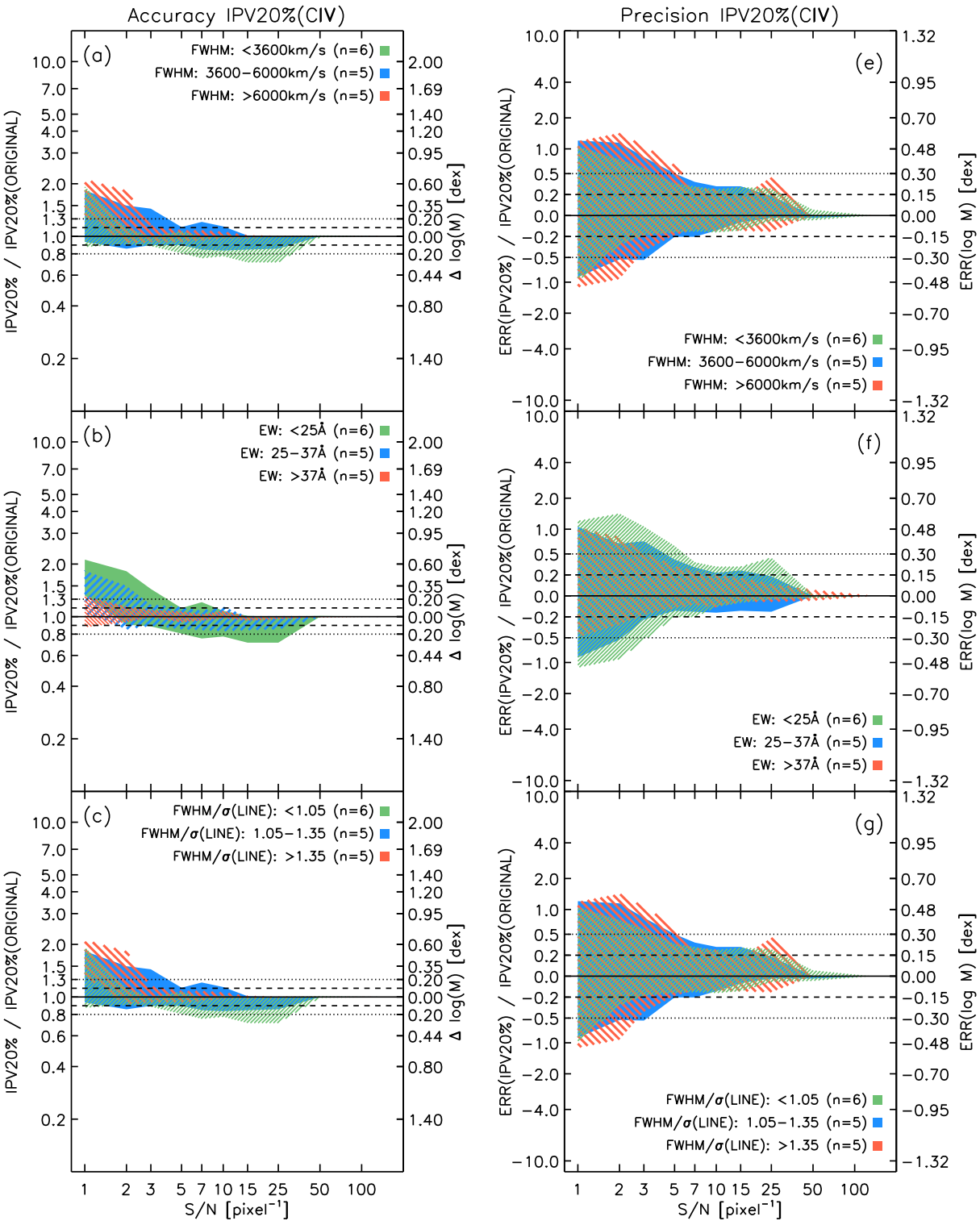

Fig. K.3 IPV20 with strong absorption in the core of the emission line.

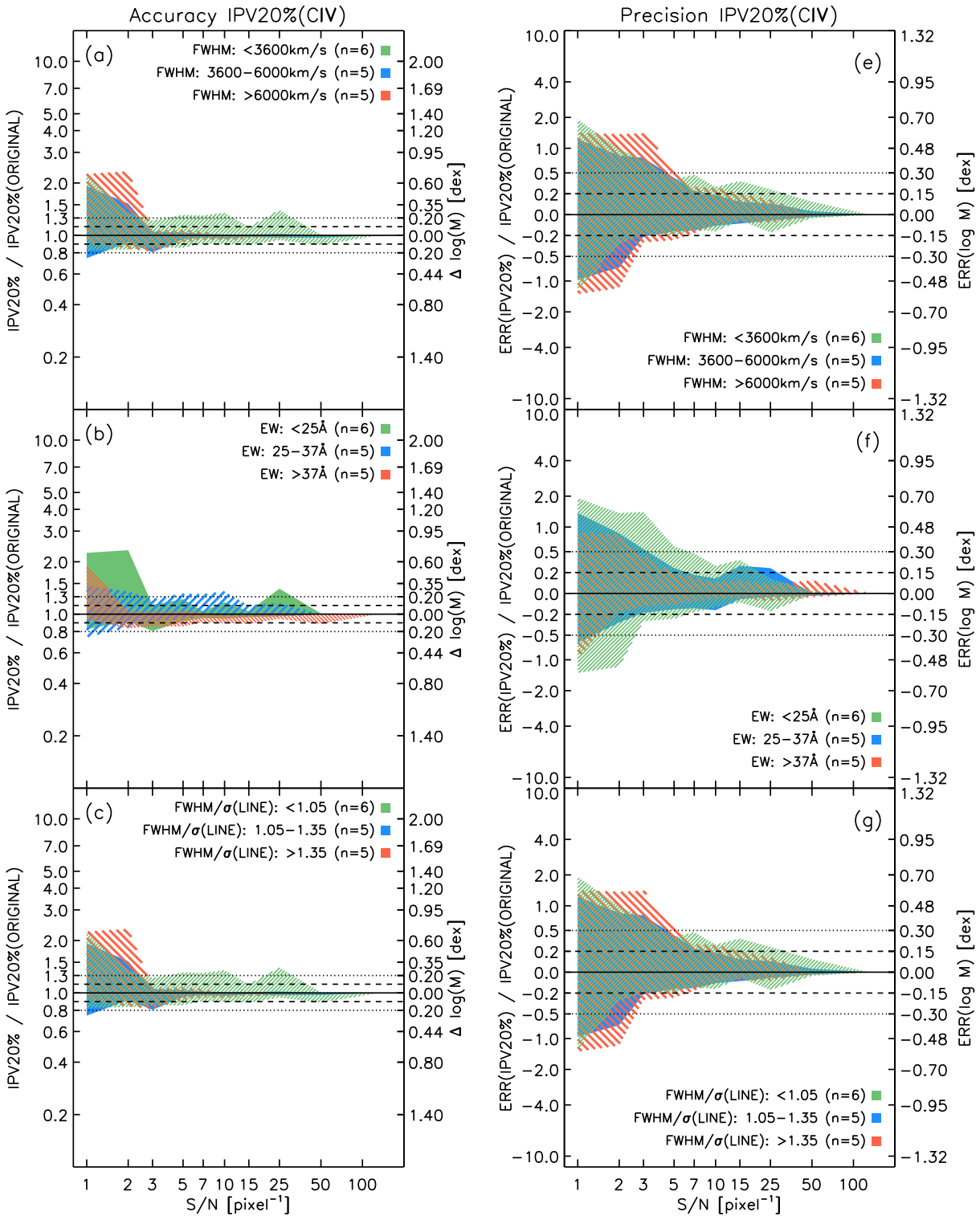

Fig. K.4 IPV20 with weak absorption in the middle of the absorption line.

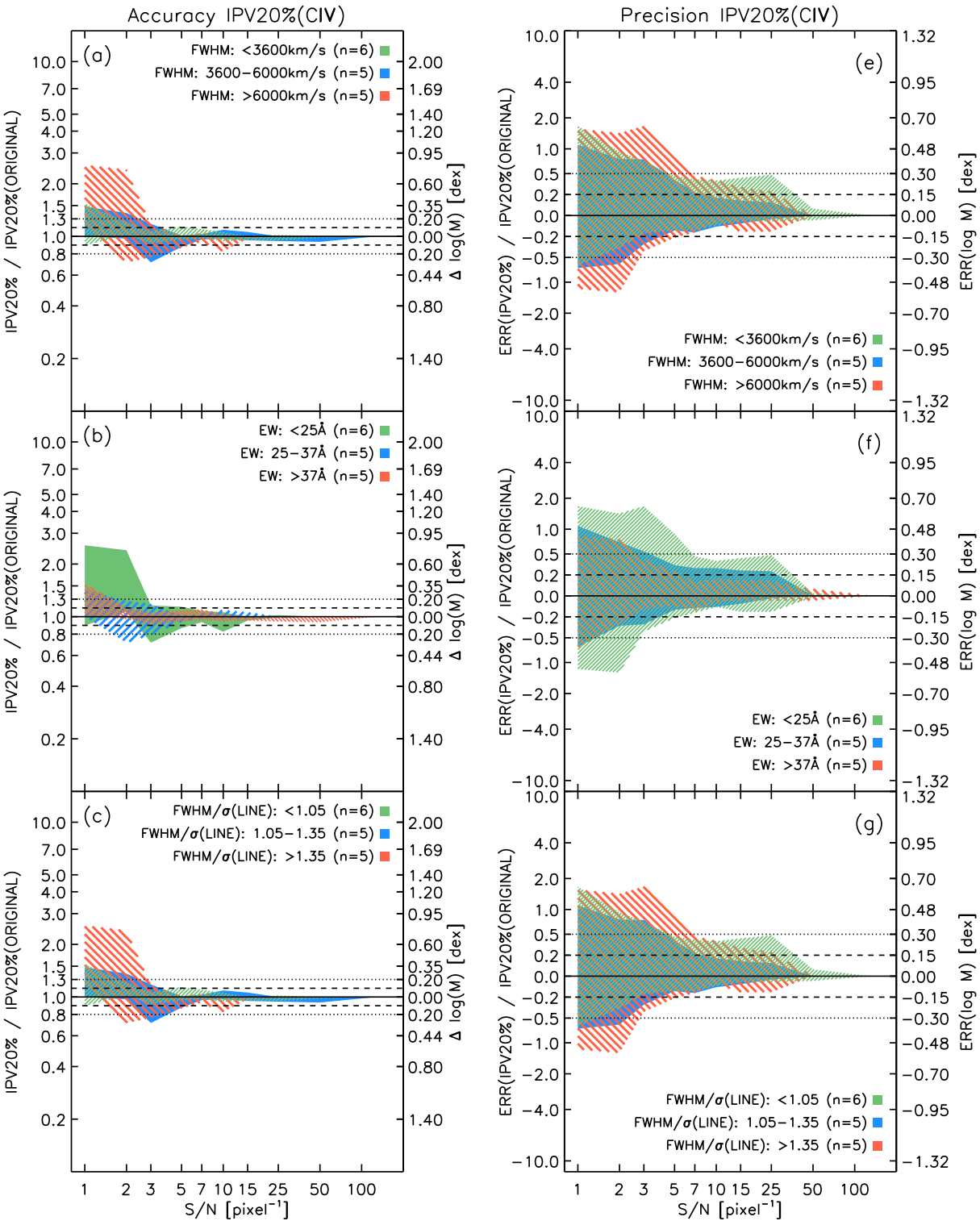

Fig. K.5 IPV20 with medium strong absorption in the middle of the absorption line.

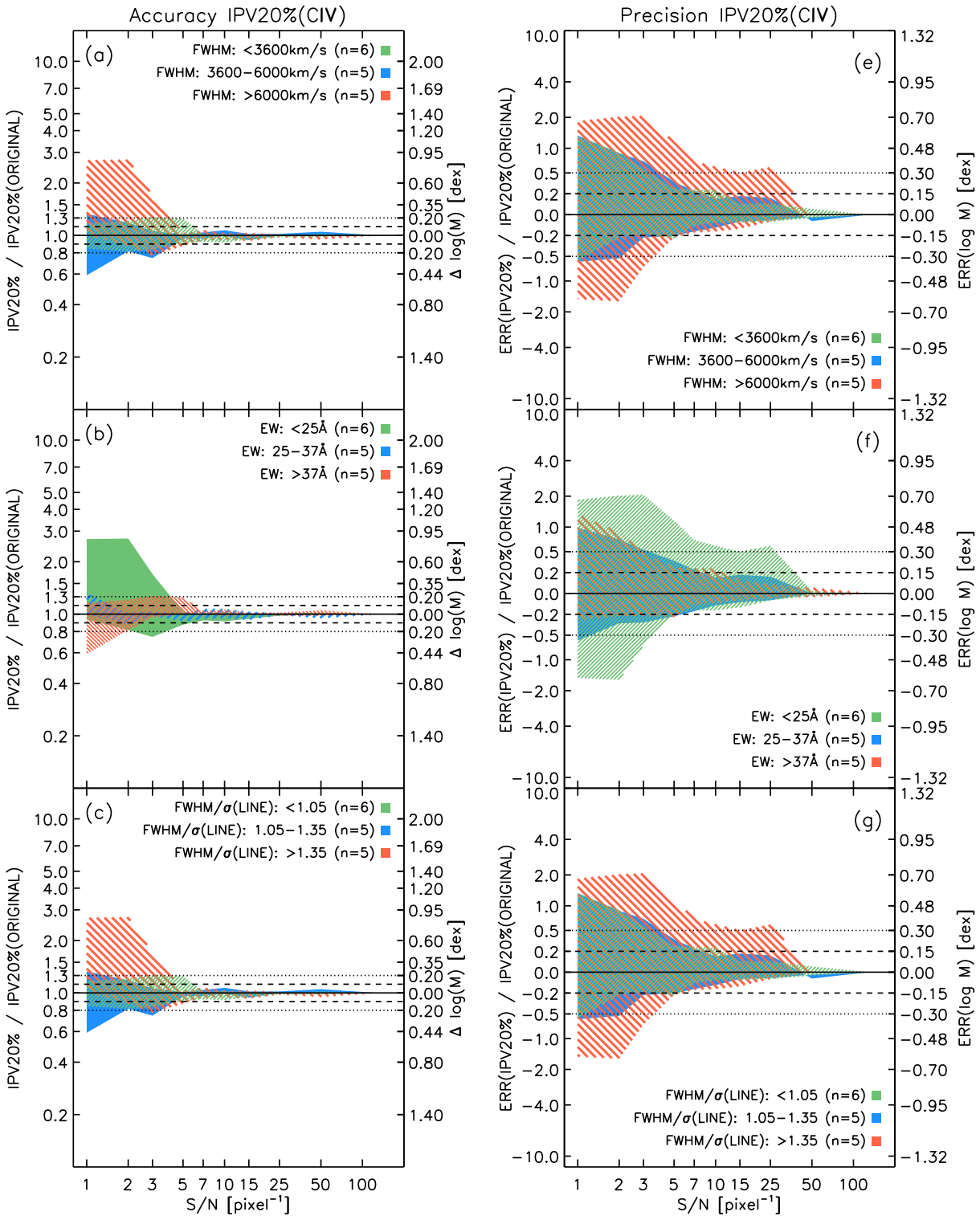

Fig. K.6 IPV20 with strong absorption in the middle of the absorption line.

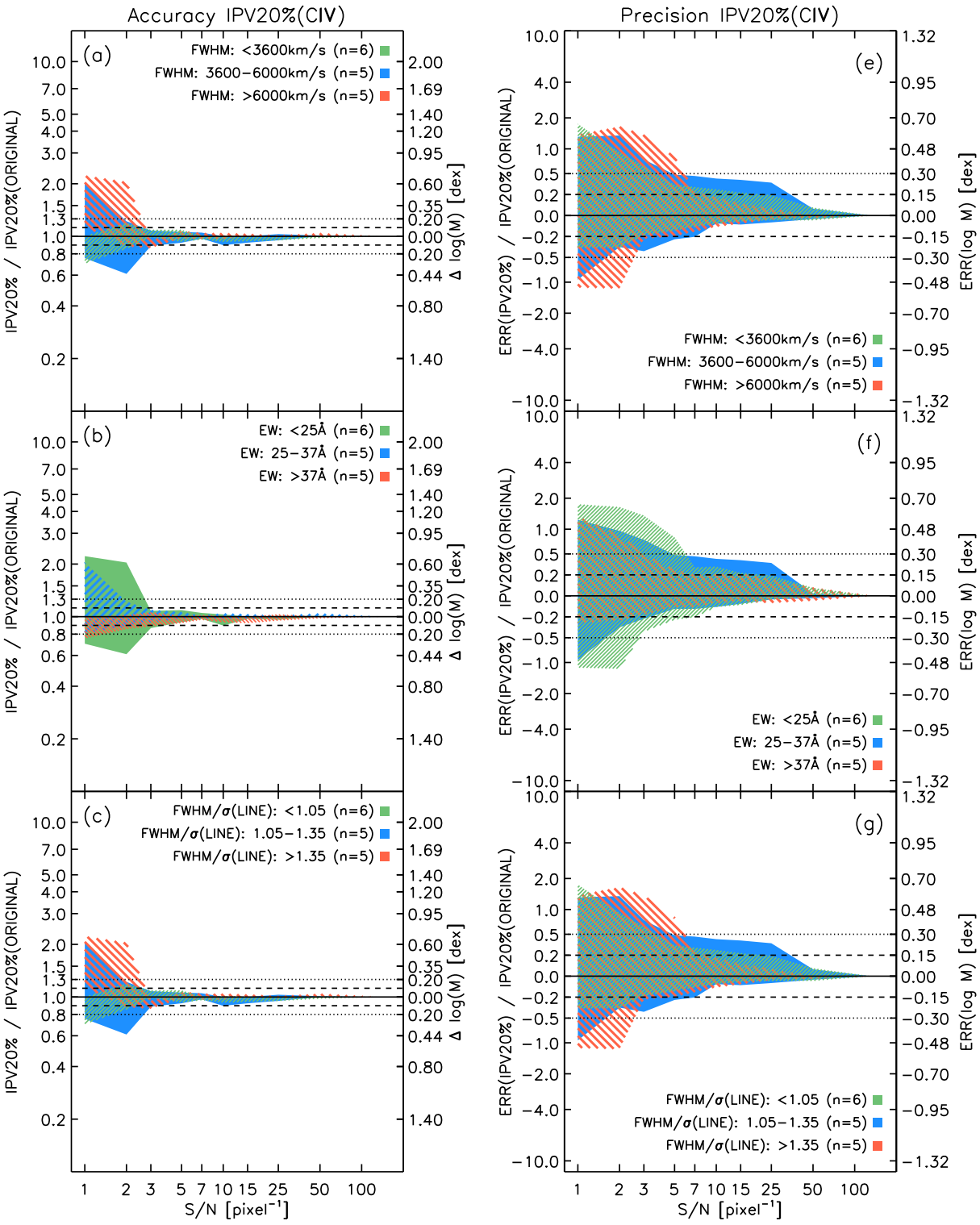

Fig. K.7 IPV20 with weak absorption in the wing of the emission line.

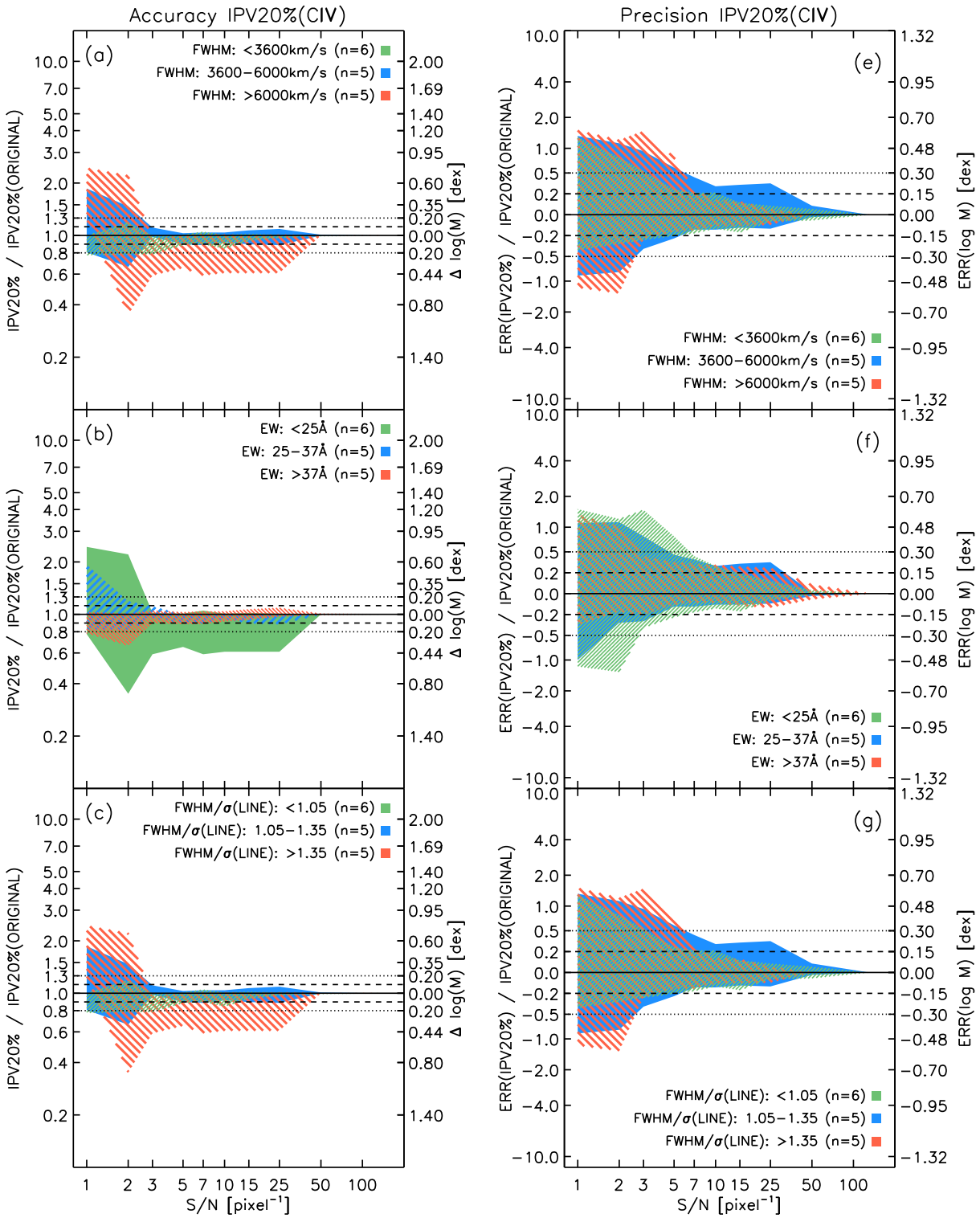

Fig. K.8 IPV20 with medium strong absorption in the wing of the emission line.

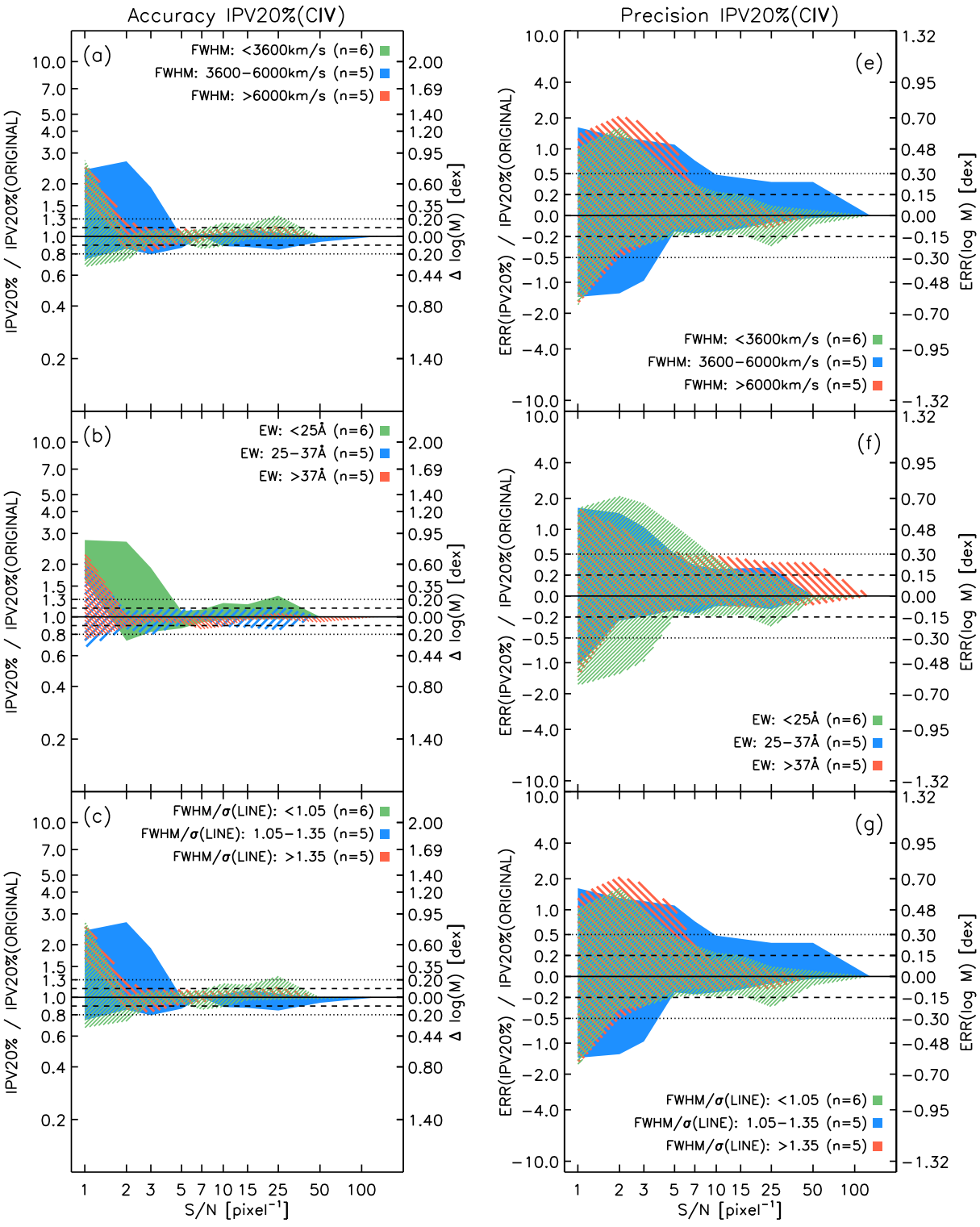

Fig. K.9 IPV20 with strong absorption in the wing of the emission line.

Appendix L

IPV50 with absorption

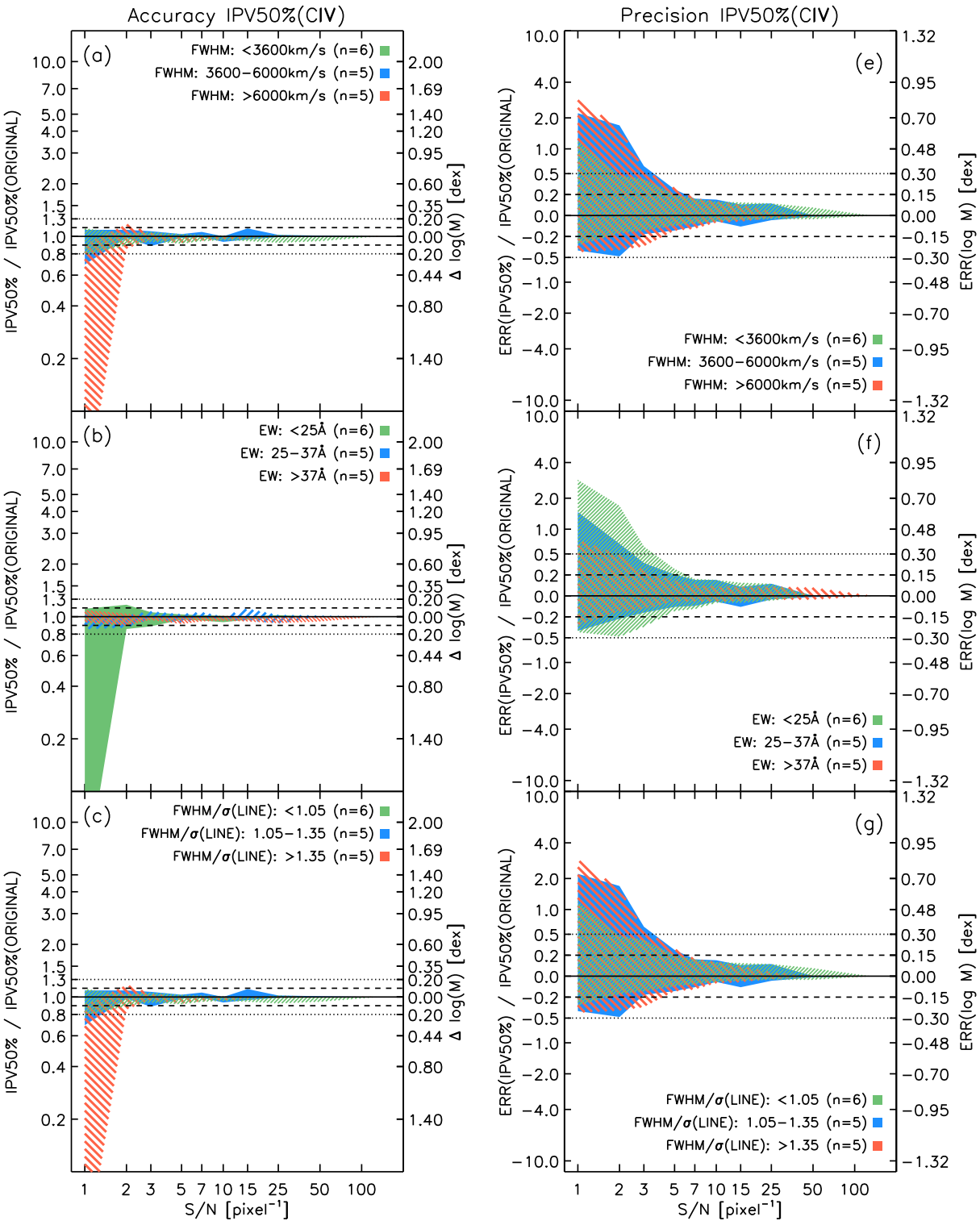

Fig. L.1 IPV50 with weak absorption in the core of the emission line.

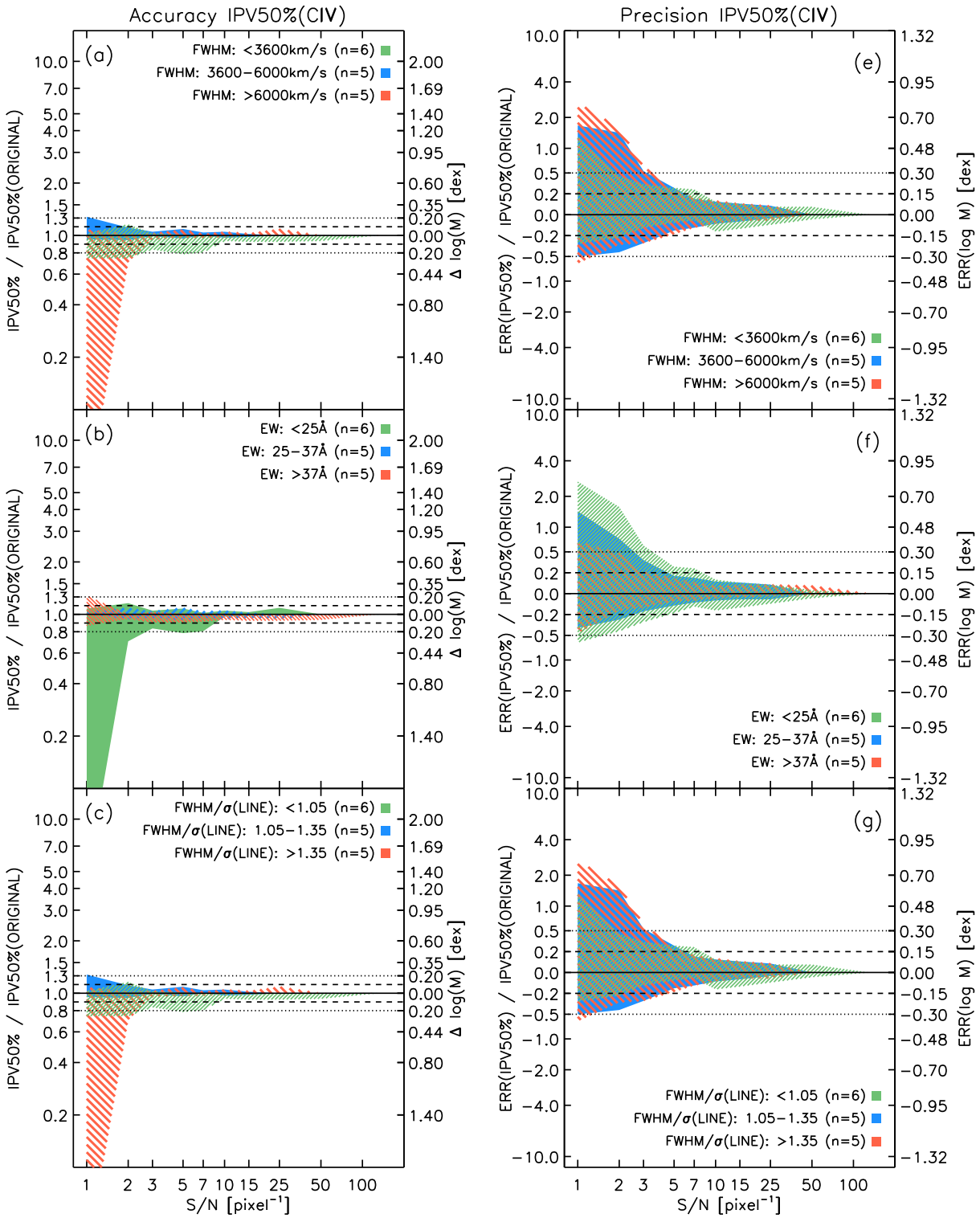

Fig. L.2 IPV50 with medium strong absorption in the core of the emission line.

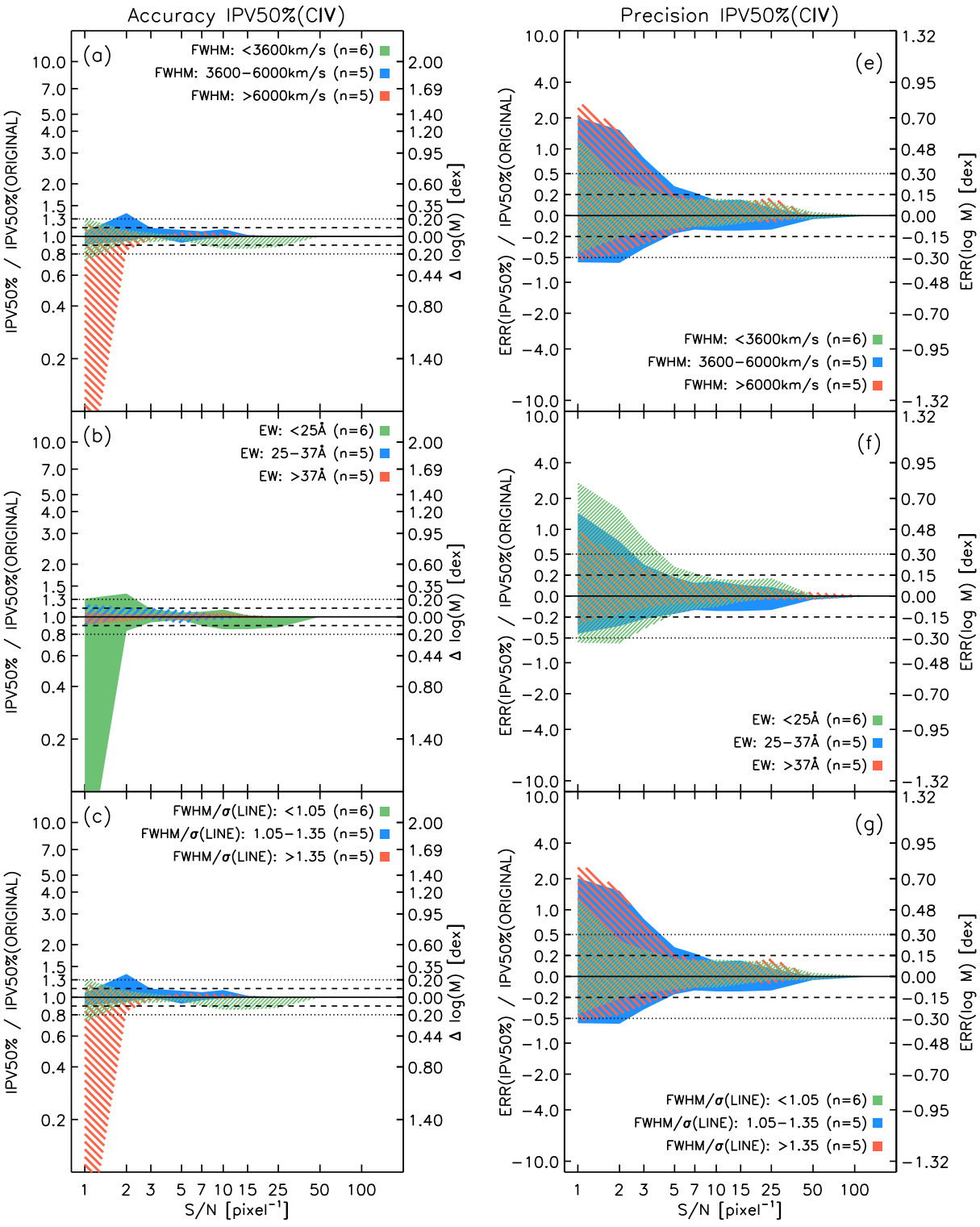

Fig. L.3 IPV50 with strong absorption in the core of the emission line.

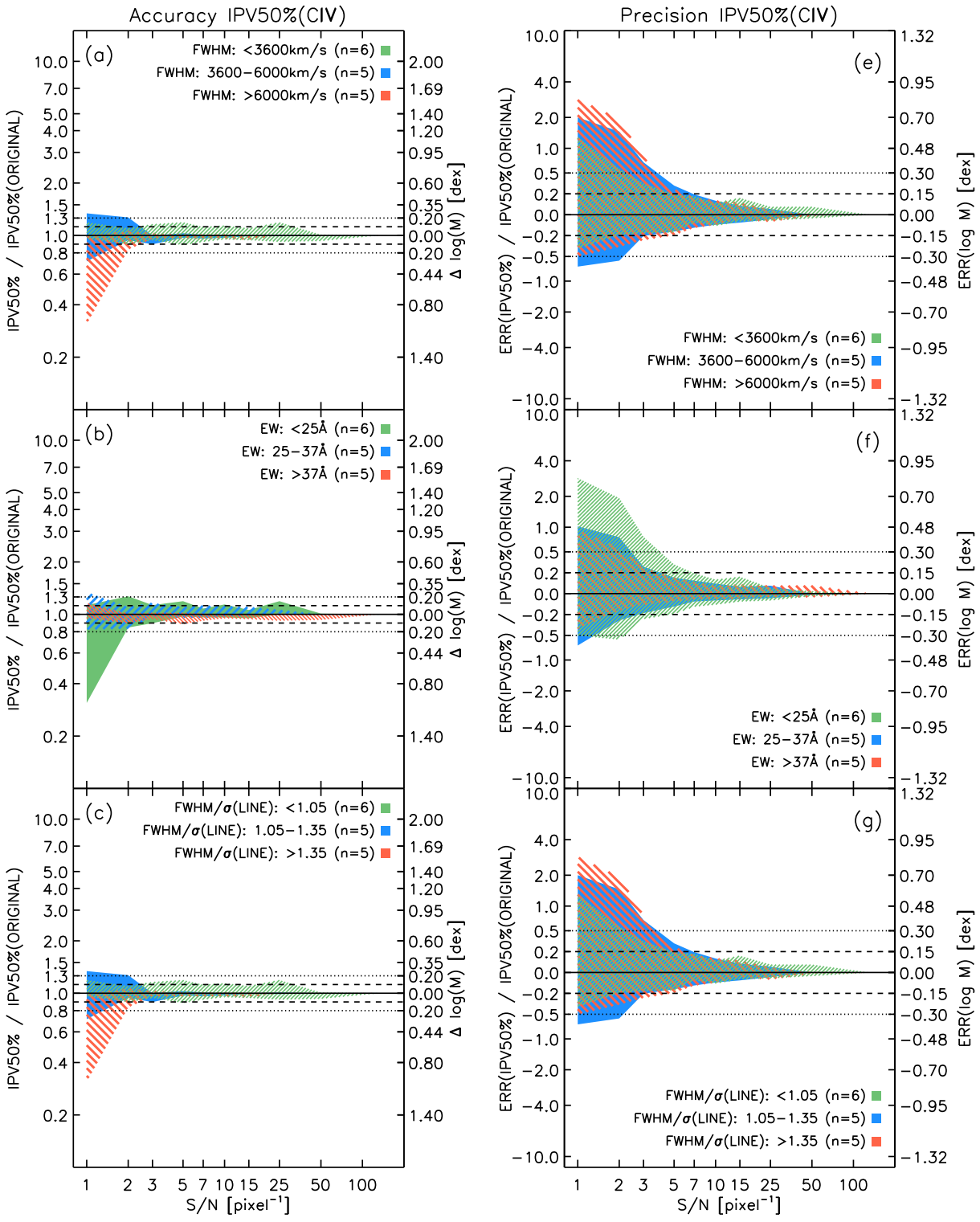

Fig. L.4 IPV50 with weak absorption in the middle of the absorption line.

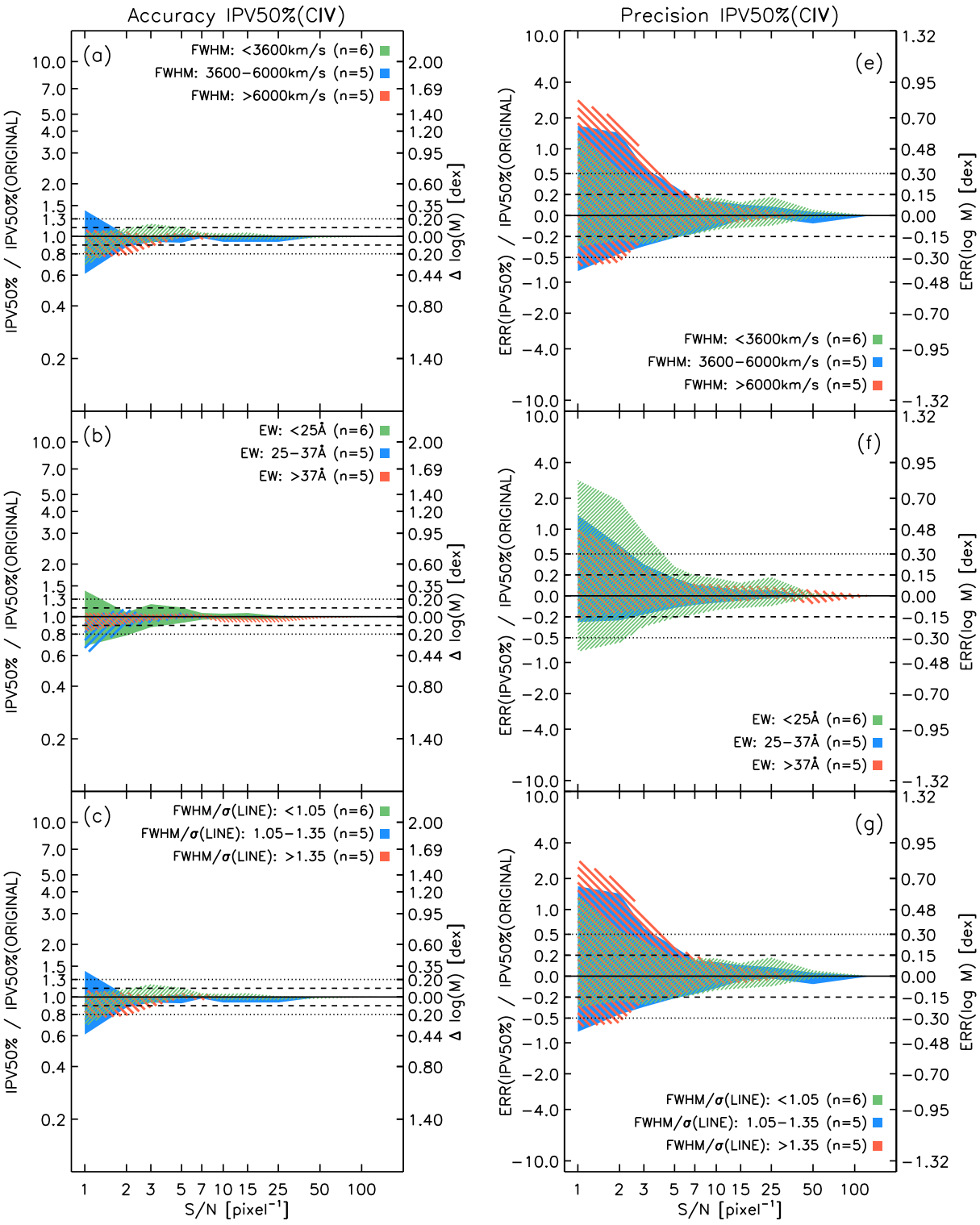

Fig. L.5 IPV50 with medium strong absorption in the middle of the absorption line.

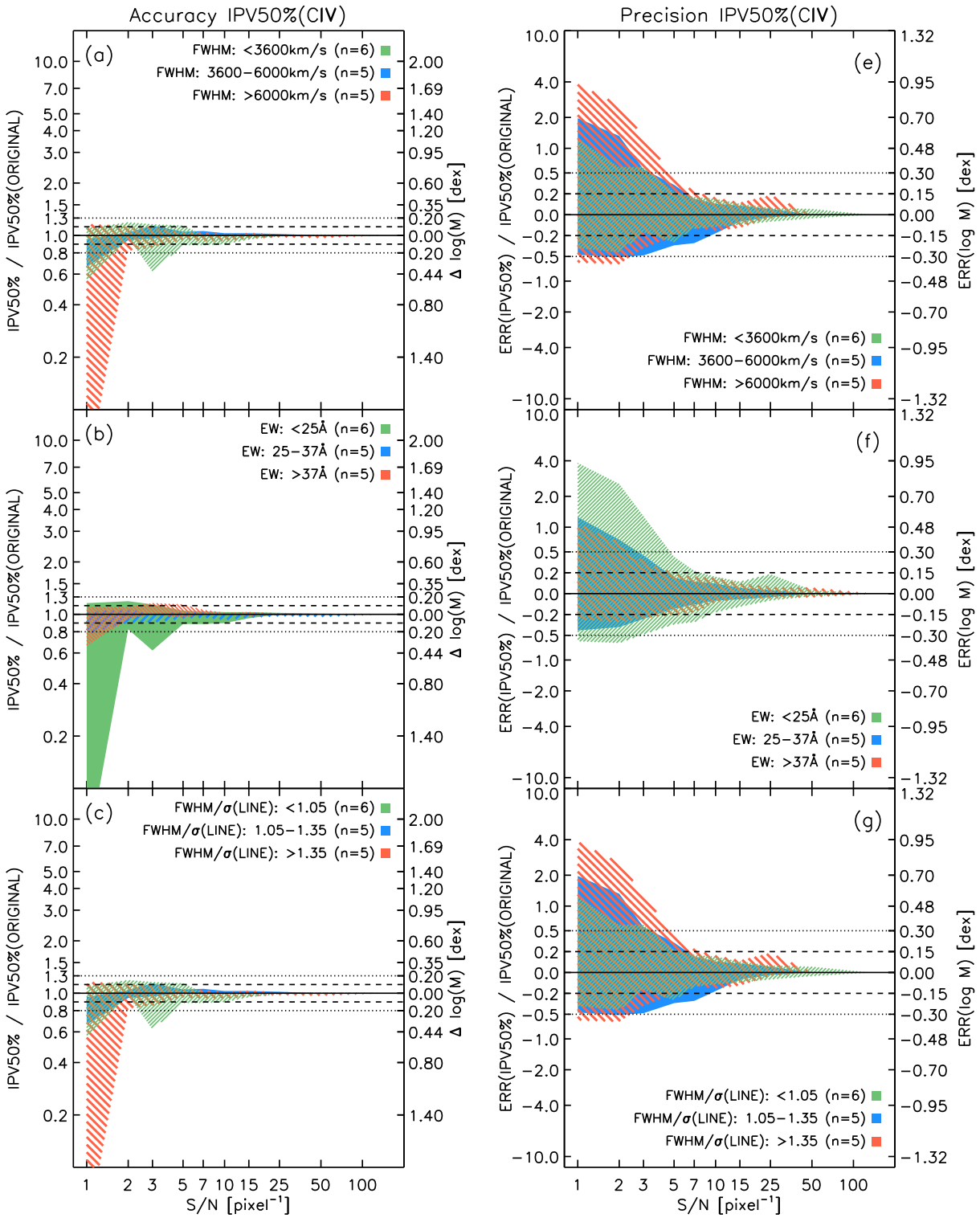

Fig. L.6 IPV50 with strong absorption in the middle of the absorption line.

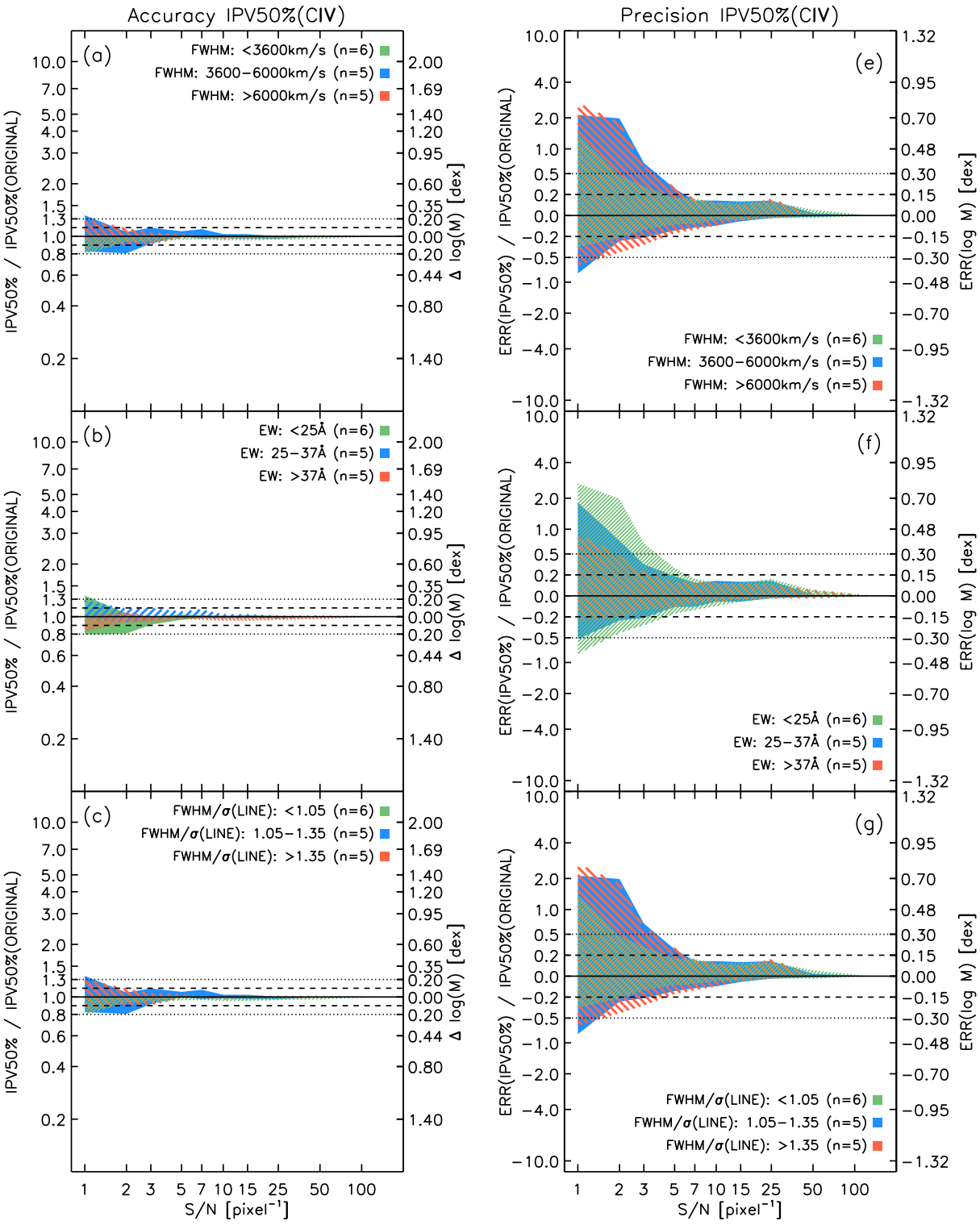

Fig. L.7 IPV50 with weak absorption in the wing of the emission line.

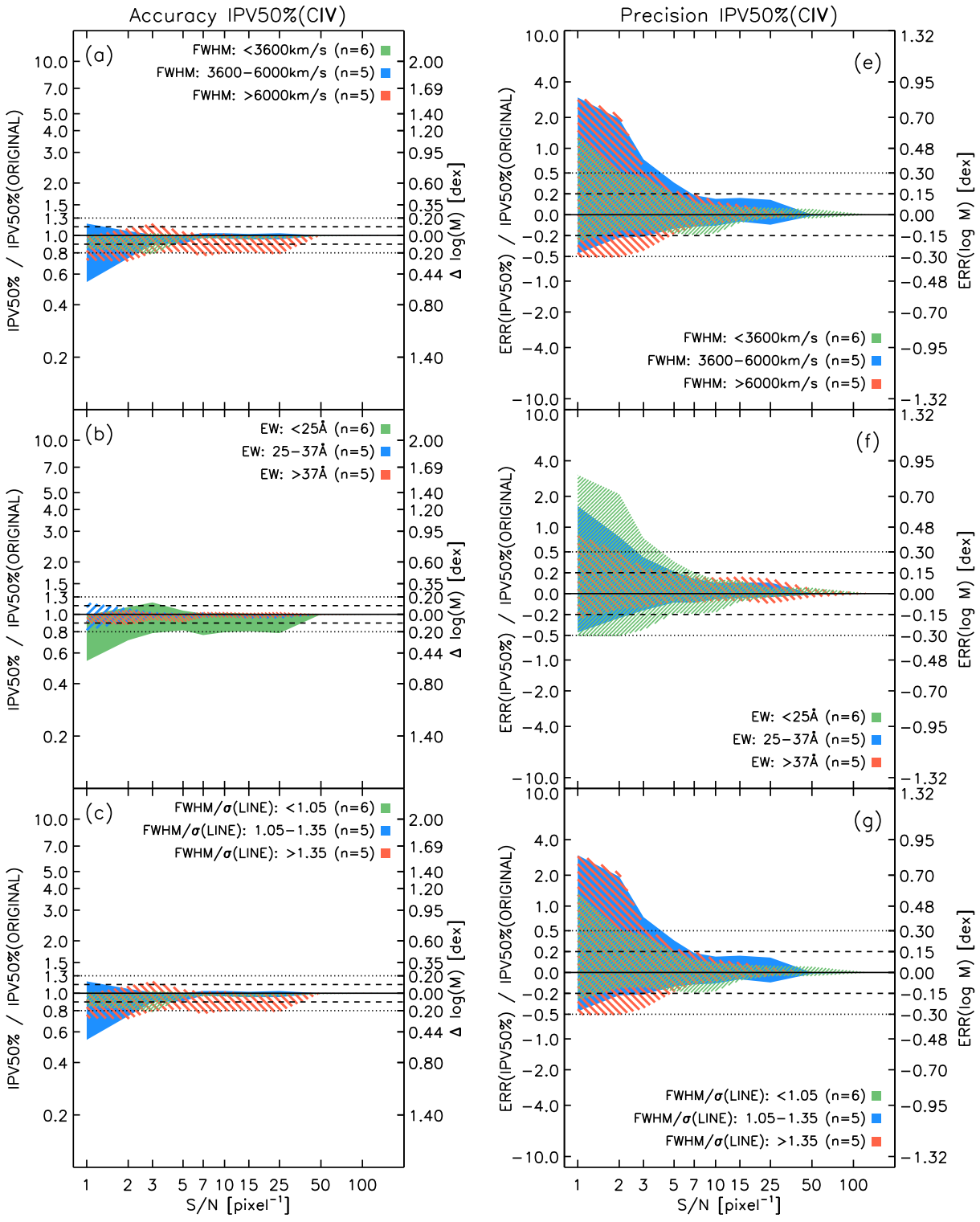

Fig. L.8 IPV50 with medium strong absorption in the wing of the emission line.

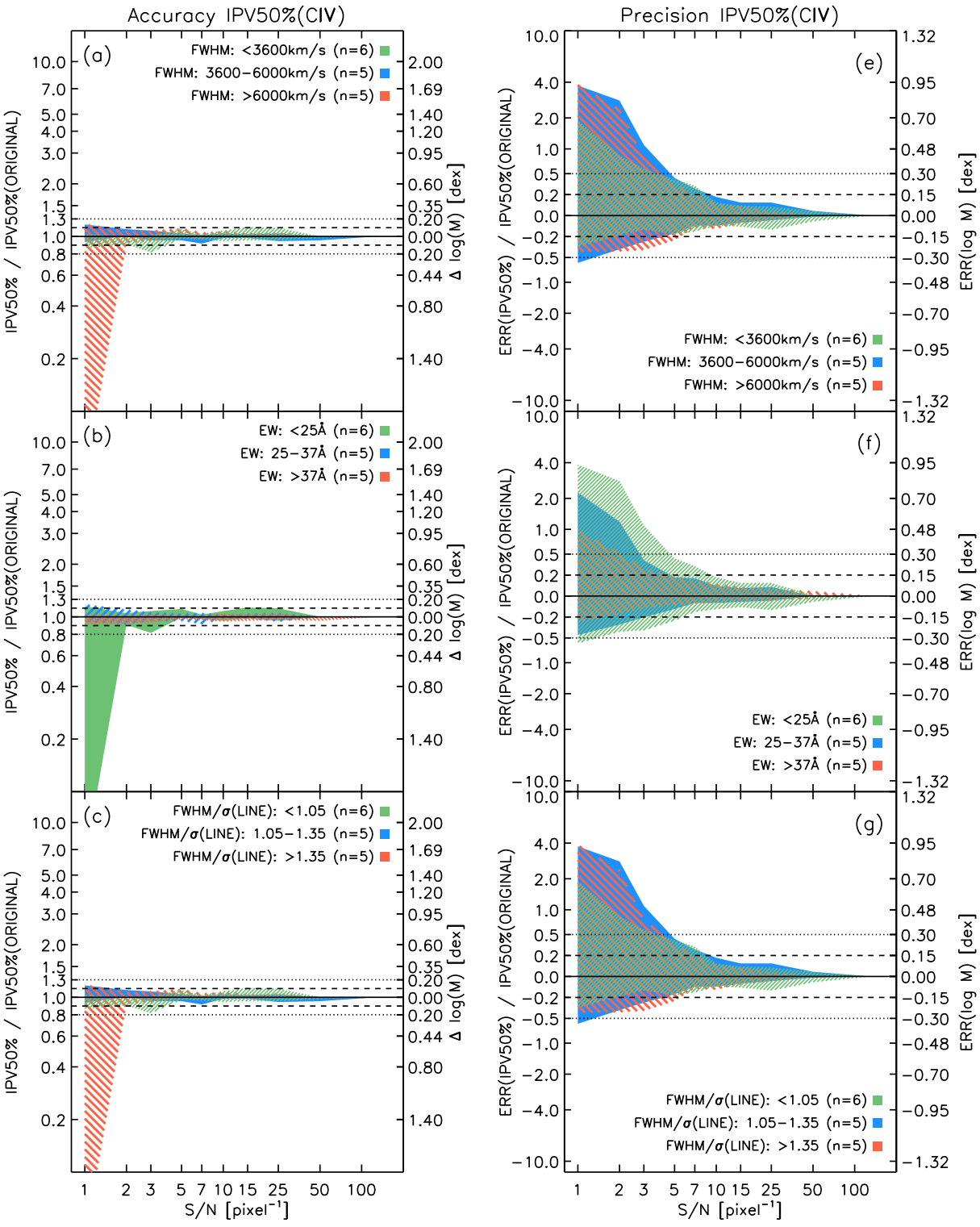

Fig. L.9 IPV50 with strong absorption in the wing of the emission line.

Appendix M

IPV90 with absorption

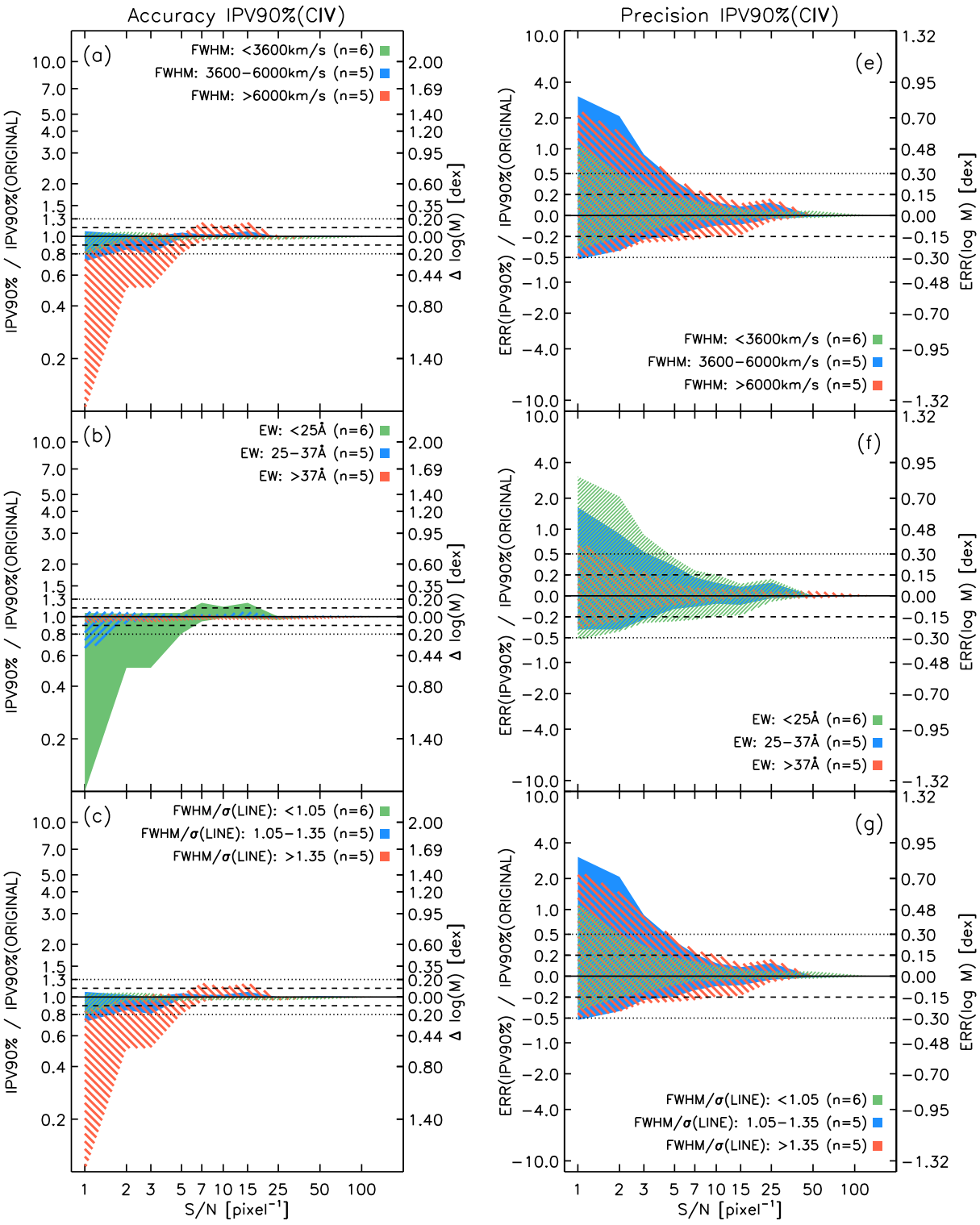

Fig. M.1 IPV90 with weak absorption in the core of the emission line.

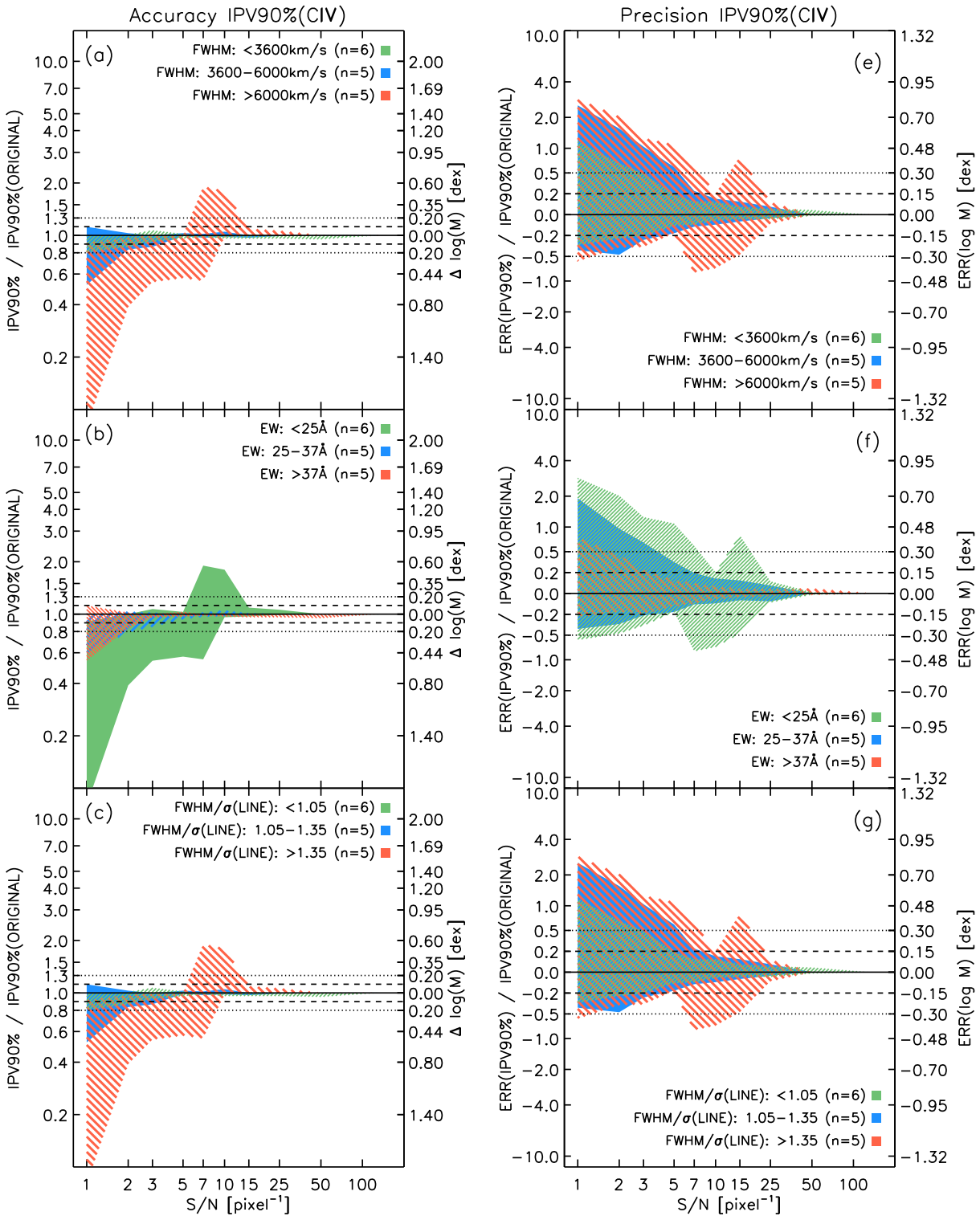

Fig. M.2 IPV90 with medium strong absorption in the core of the emission line.

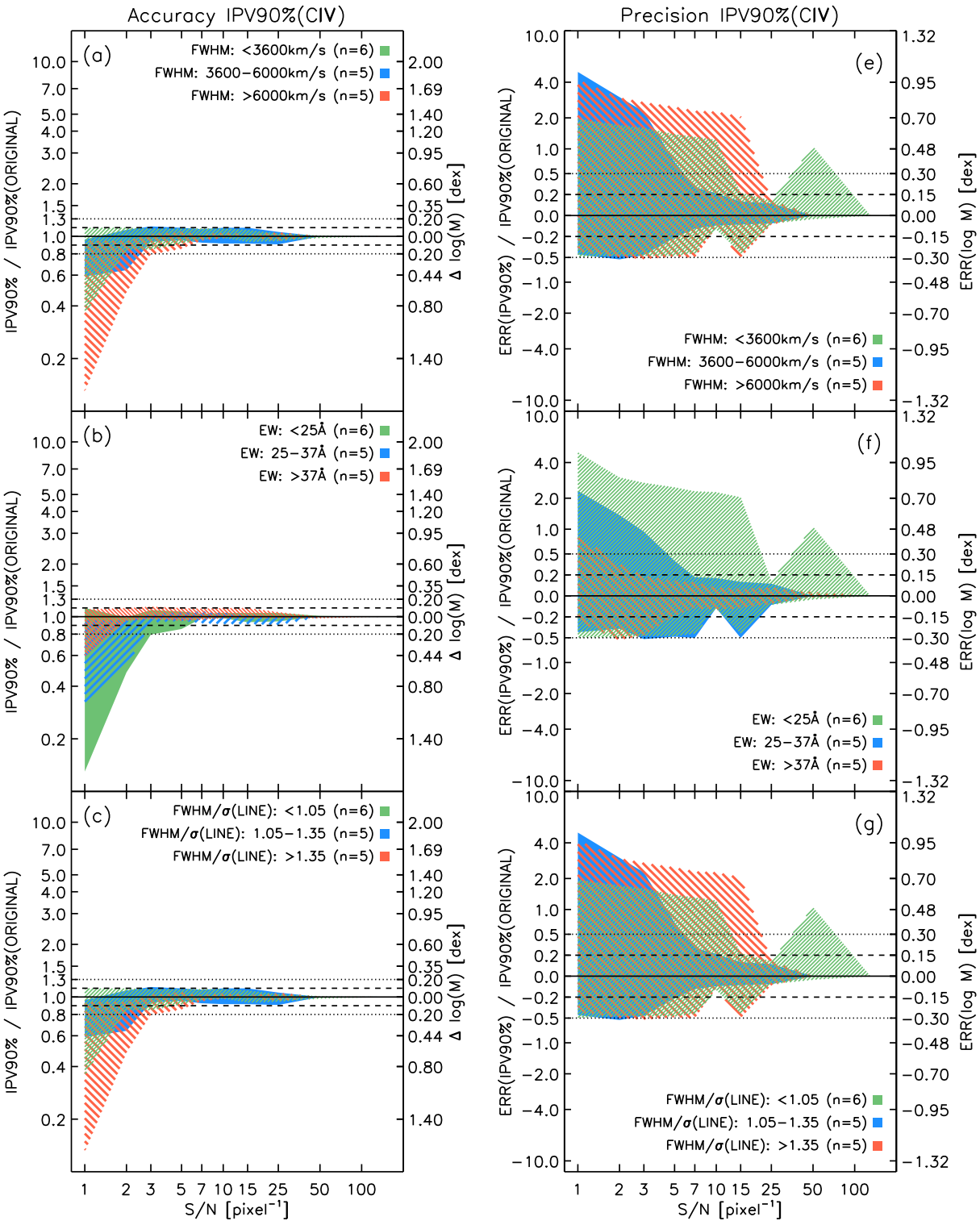

Fig. M.3 IPV90 with strong absorption in the core of the emission line.

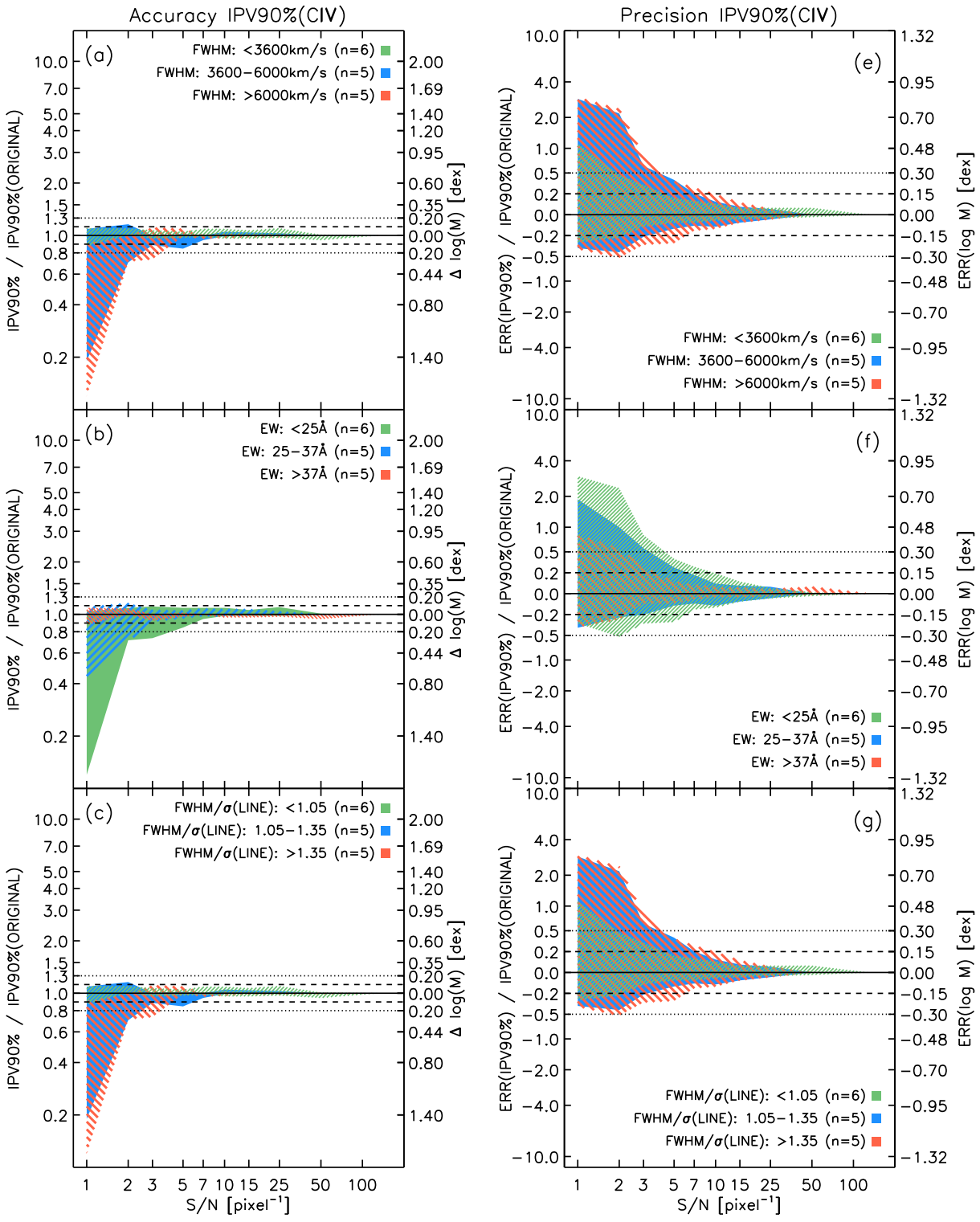

Fig. M.4 IPV90 with weak absorption in the middle of the absorption line.

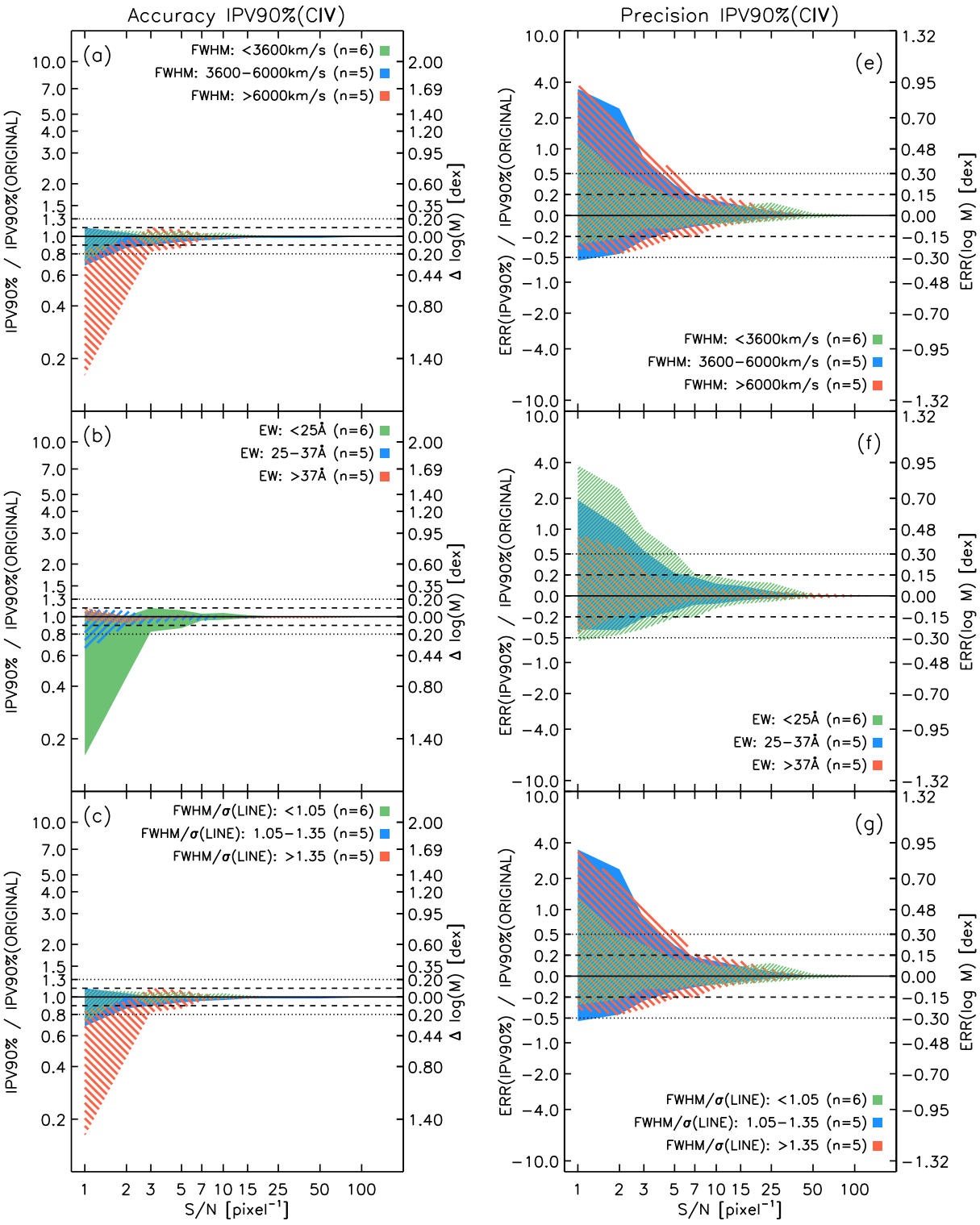

Fig. M.5 IPV90 with medium strong absorption in the middle of the absorption line.

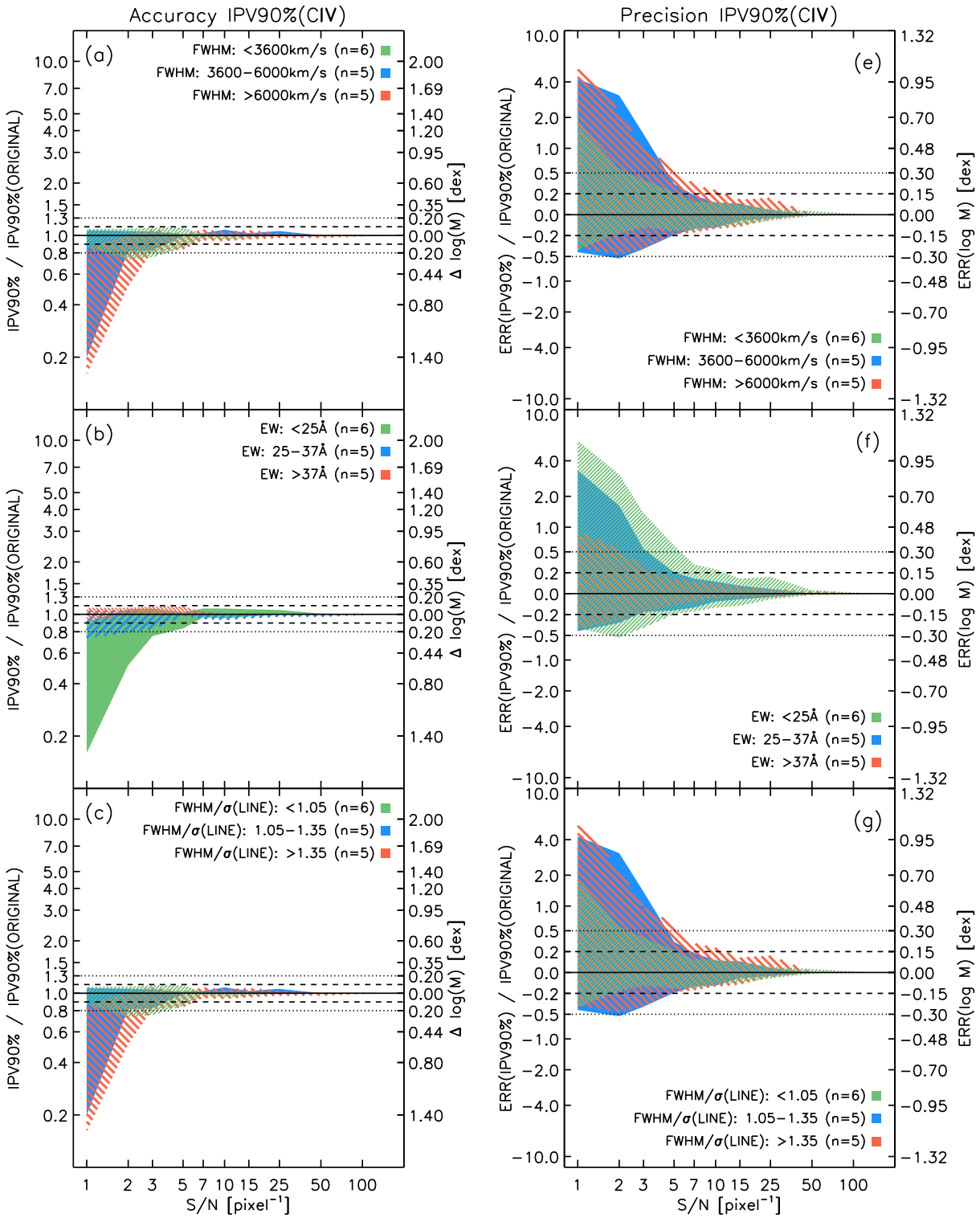

Fig. M.6 IPV90 with strong absorption in the middle of the absorption line.

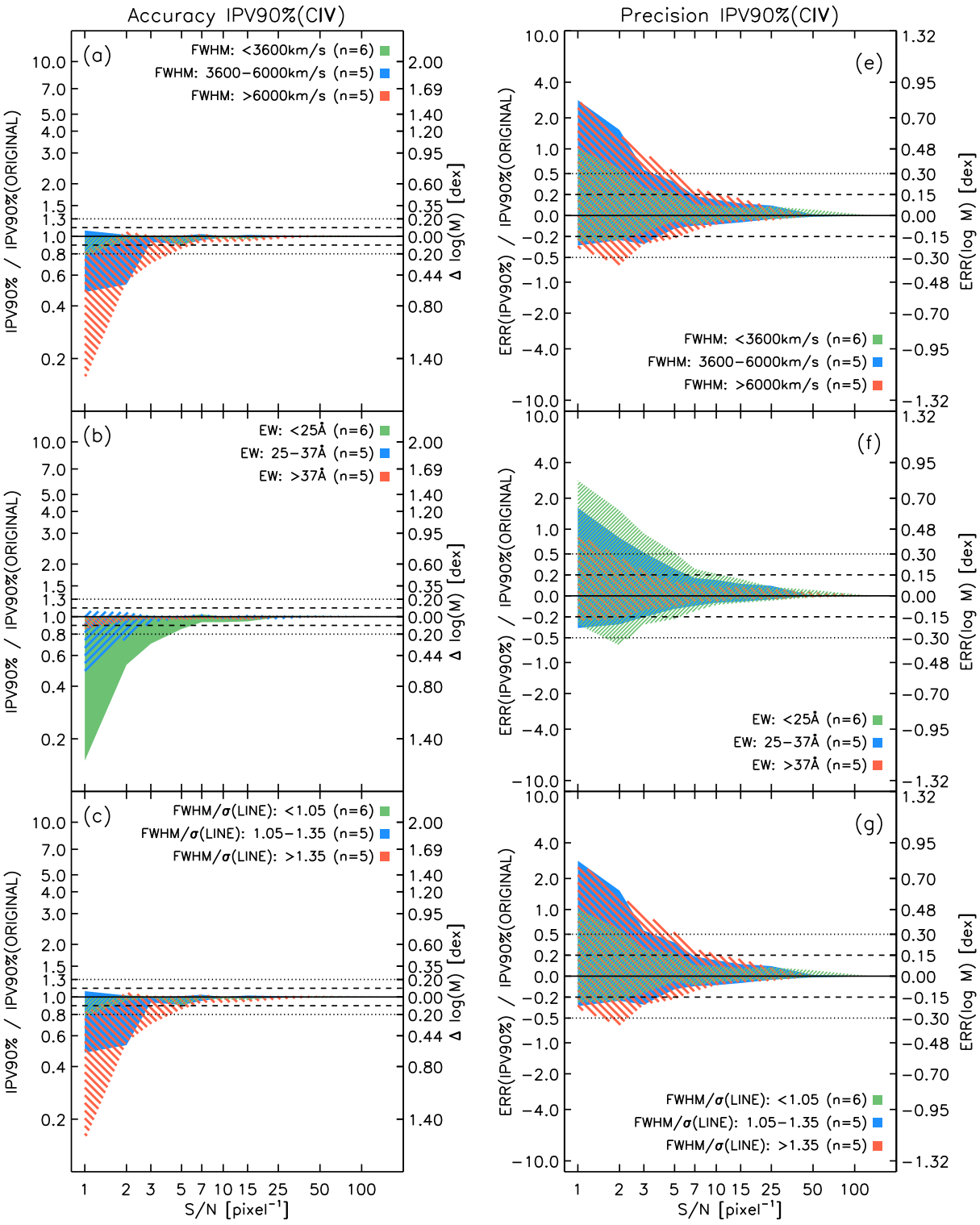

Fig. M.7 IPV90 with weak absorption in the wing of the emission line.

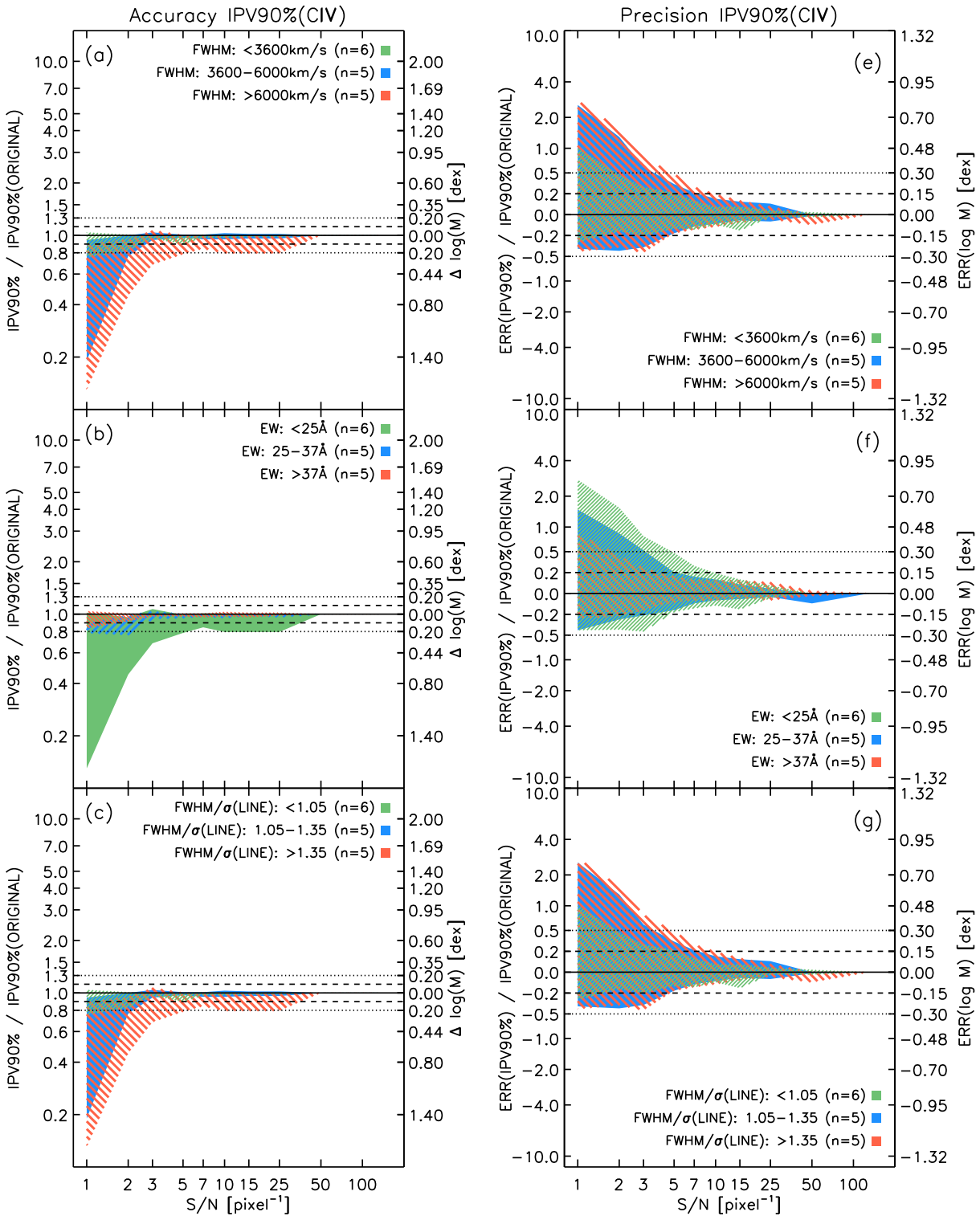

Fig. M.8 IPV90 with medium strong absorption in the wing of the emission line.

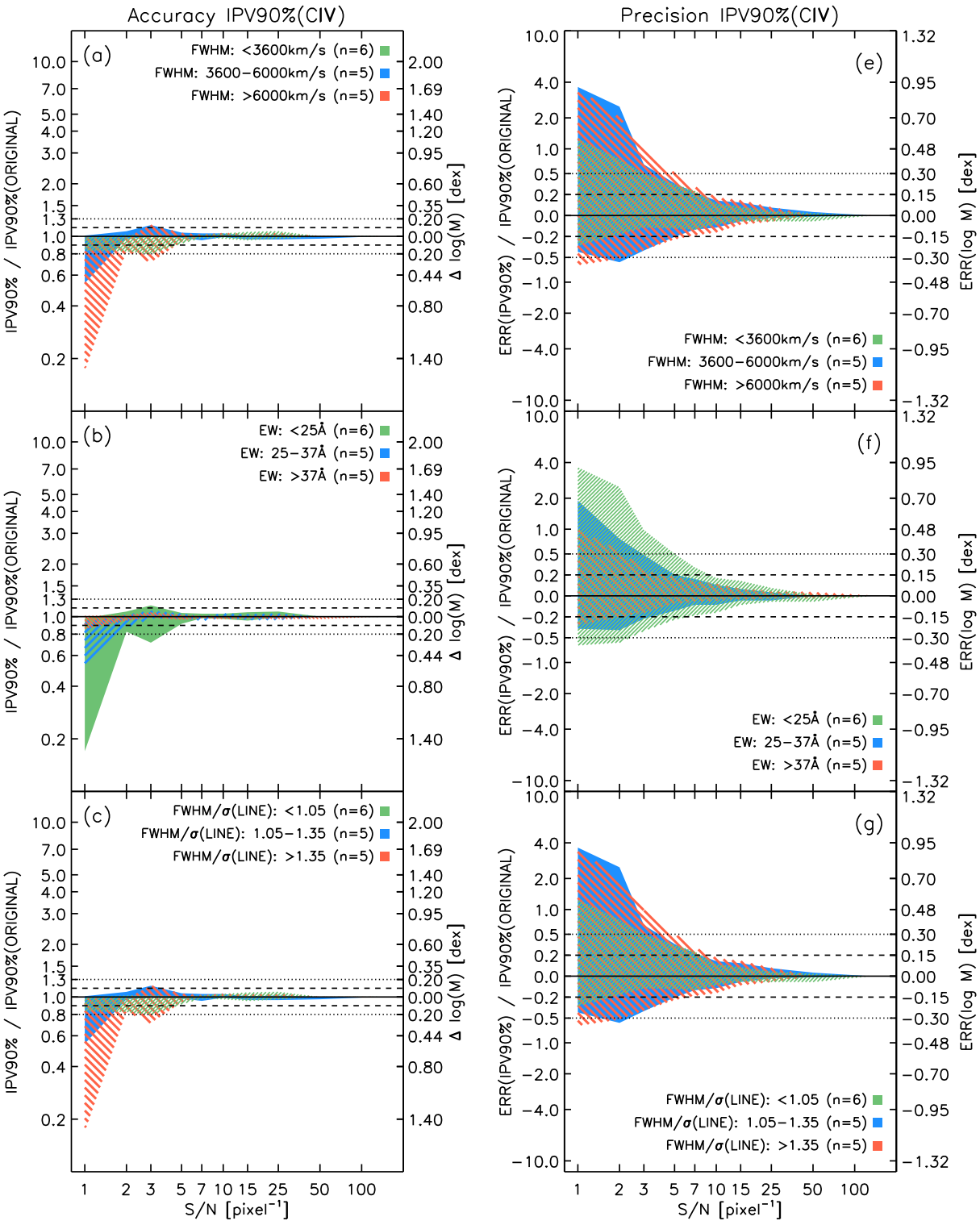

Fig. M.9 IPV90 with strong absorption in the wing of the emission line.

Appendix N

Mid-IR spectra of individual objects

Appendix to Chapter 5. Figure N.1, Figure N.2, and Figure N.3 shows the spectra extracted within the central 0.4 arcsec aperture for all the objects in our sample.

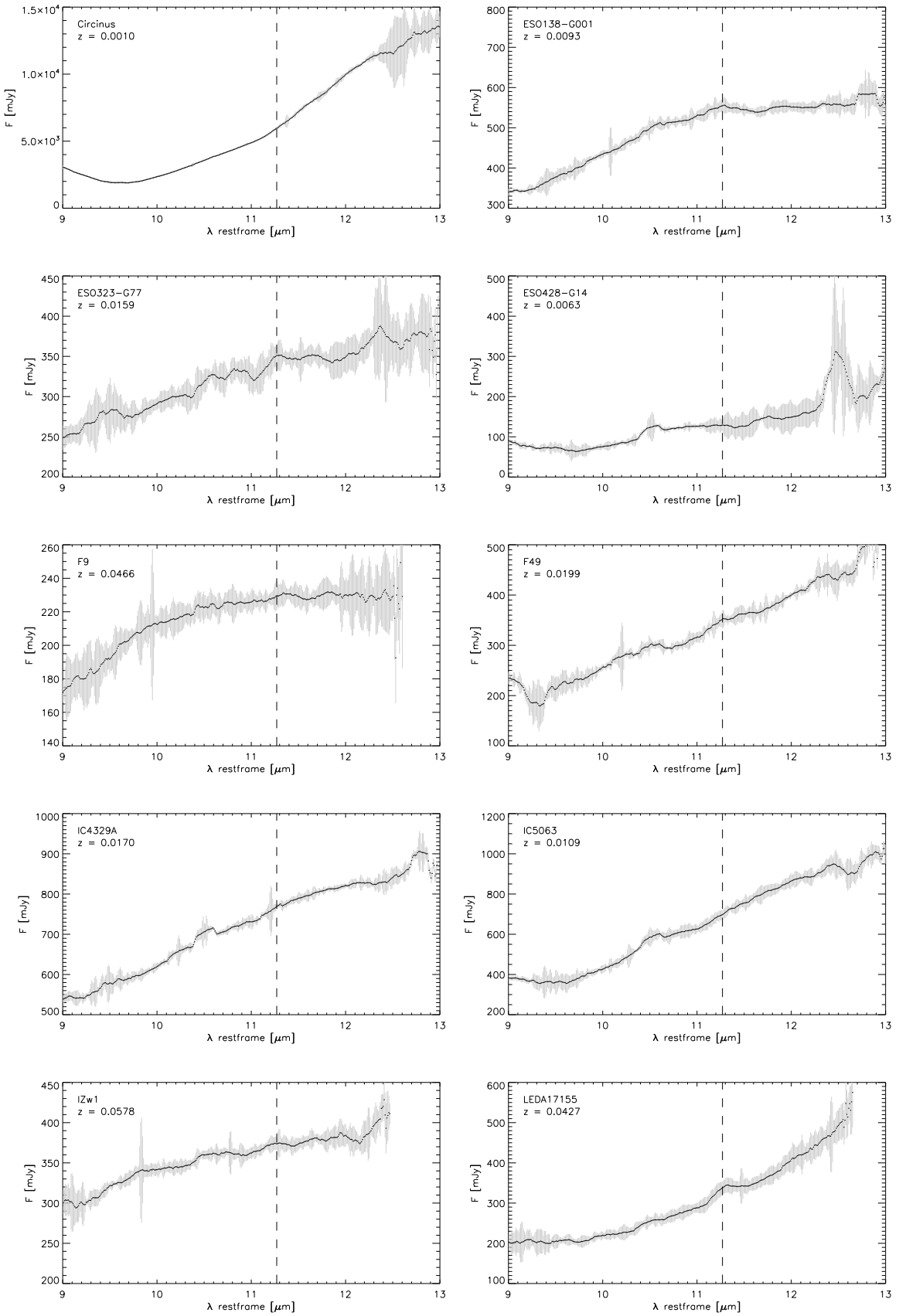

Fig. N.1 Spectra of the sample extracted within the central aperture with a width of 0.4 arcsec. The position of the 11.3 μm PAH feature is indicated by the dashed line in each plot. The data has been smoothed with a 20-pixel boxcar for display purposes.

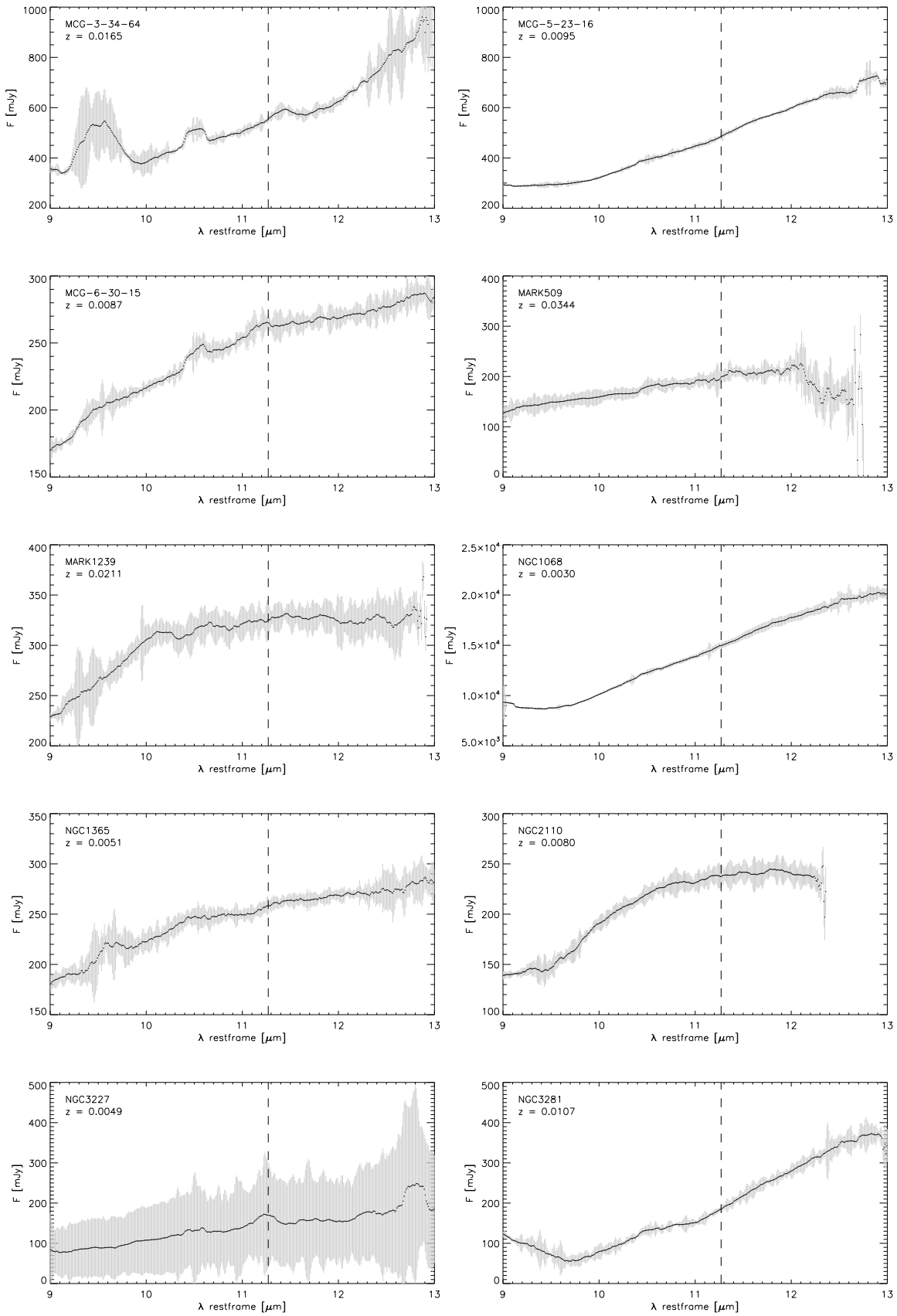

Fig. N.2 Spectra of the sample extracted within the central aperture with a width of 0.4 arcsec. The position of the 11.3 μm PAH feature is indicated by the dashed line in each plot. The data has been smoothed with a 20-pixel boxcar for display purposes.

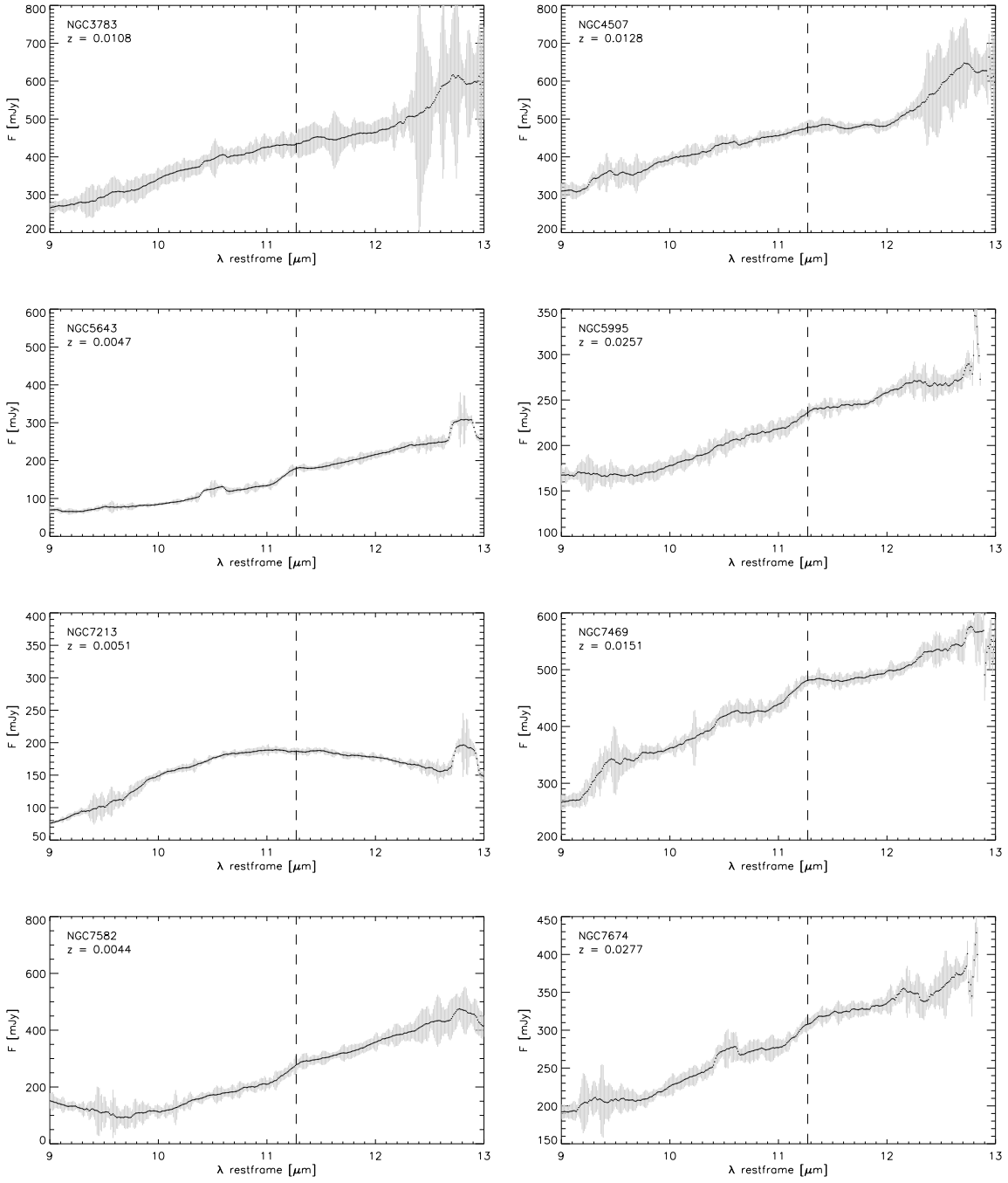

Fig. N.3 Spectra of the sample extracted within the central aperture with a width of 0.4 arcsec. The position of the 11.3 μm PAH feature is indicated by the dashed line in each plot. The data has been smoothed with a 20-pixel boxcar for display purposes.

Appendix O

Variations in PAH and continuum flux with radius for objects with 11.3 μm PAH flux measurements at three or more radii[1]

[1] Appendix for Chapter 5.

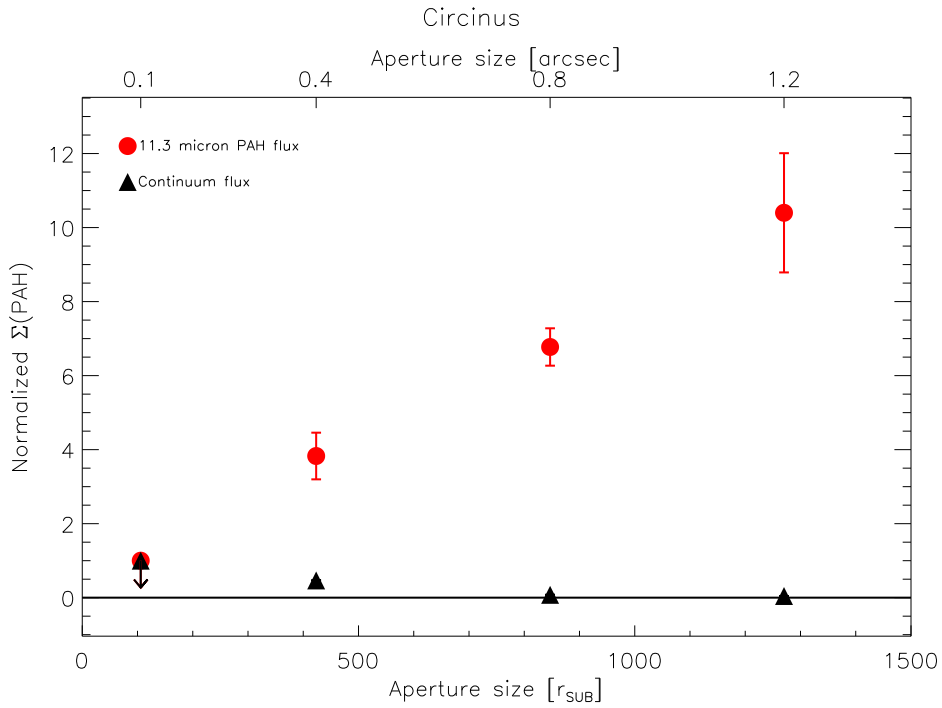

Fig. O.1 Emitted surface flux of the 11.3 μm PAH feature (red circles) and the underlying continuum flux (black triangles) as a function of sublimation radius for Circinus. Arrows denote upper limits.

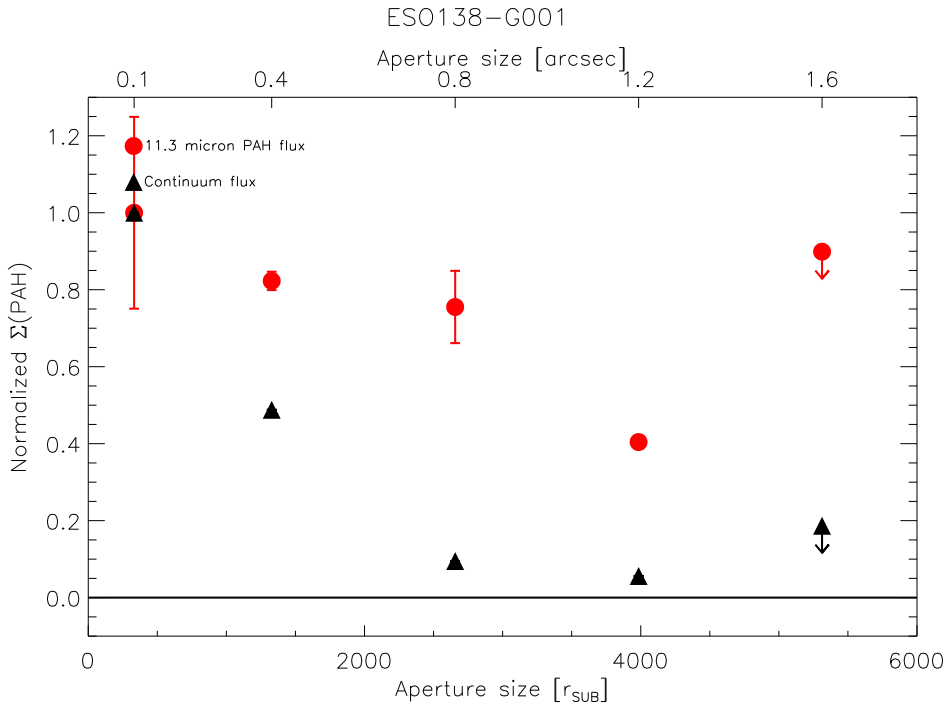

Fig. O.2 Same as Figure O.1 but for ESO138-G001.

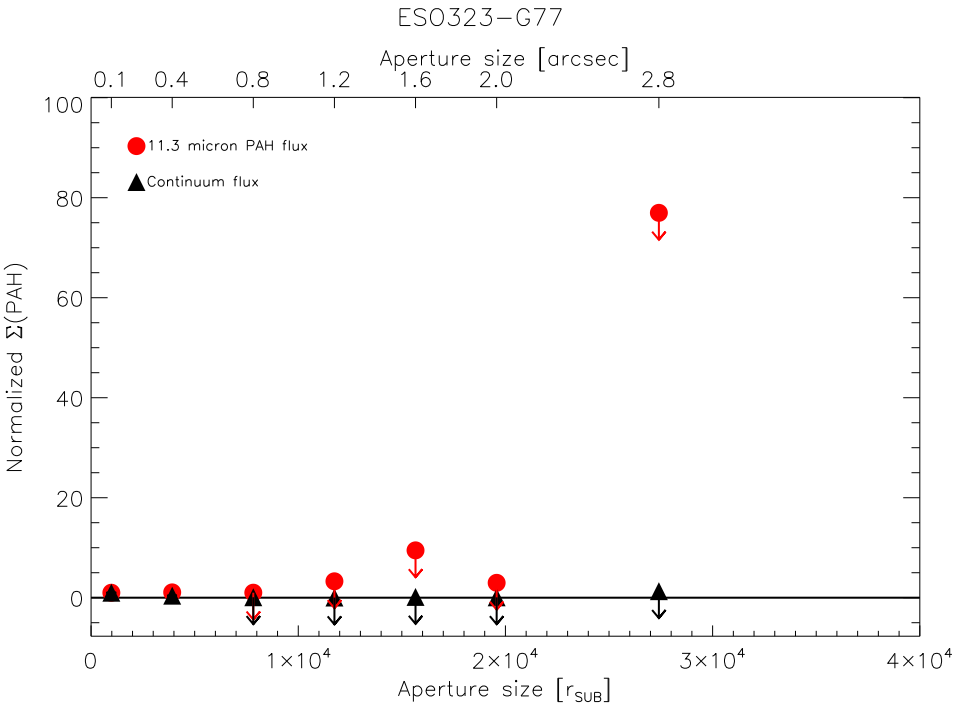

Fig. O.3 Same as Figure O.1 but for ESO323-G77.

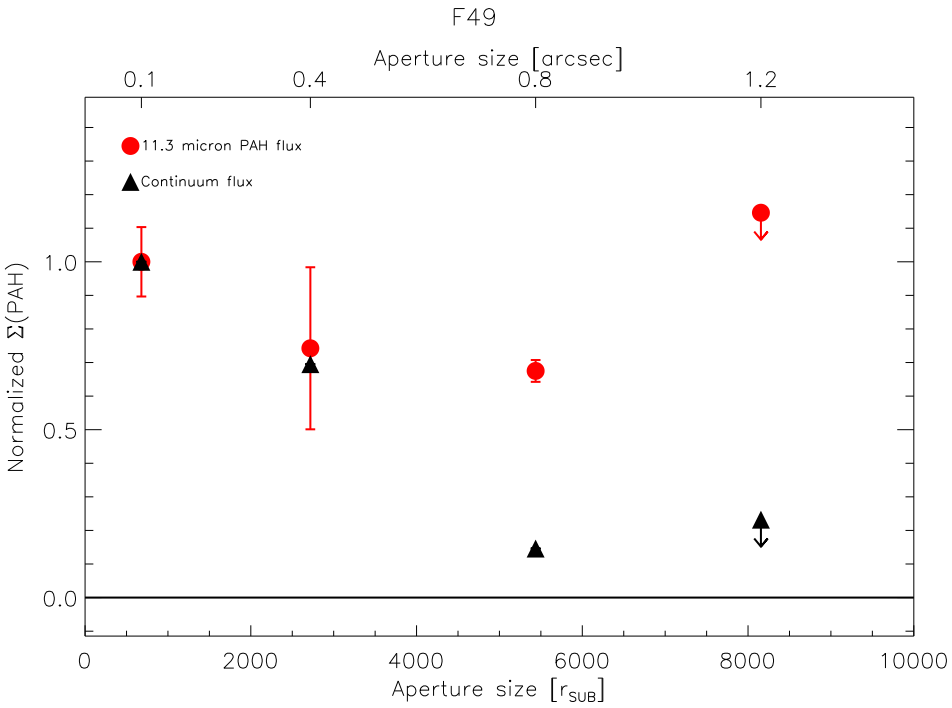

Fig. O.4 Same as Figure O.1 but for F49.

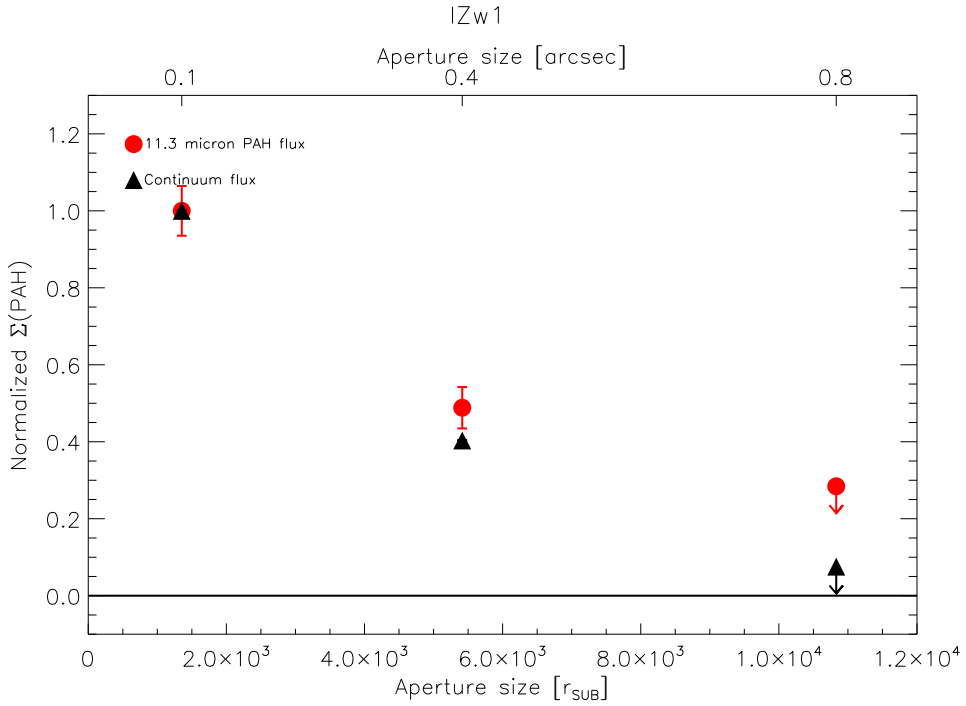

Fig. O.5 Same as Figure O.1 but for IZw1.

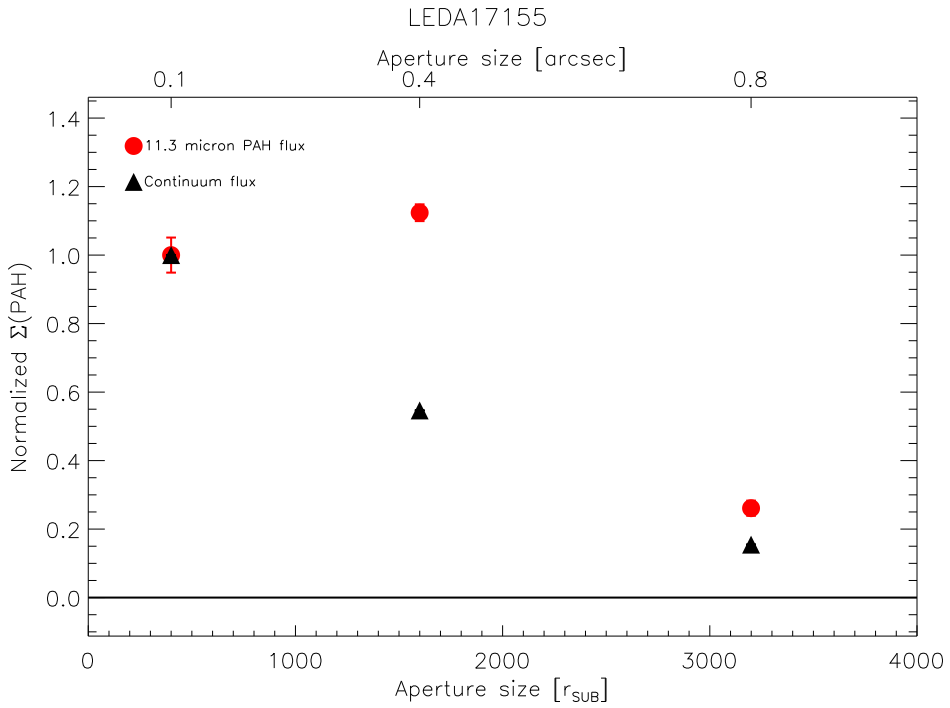

Fig. O.6 Same as Figure O.1 but for LEDA17155.

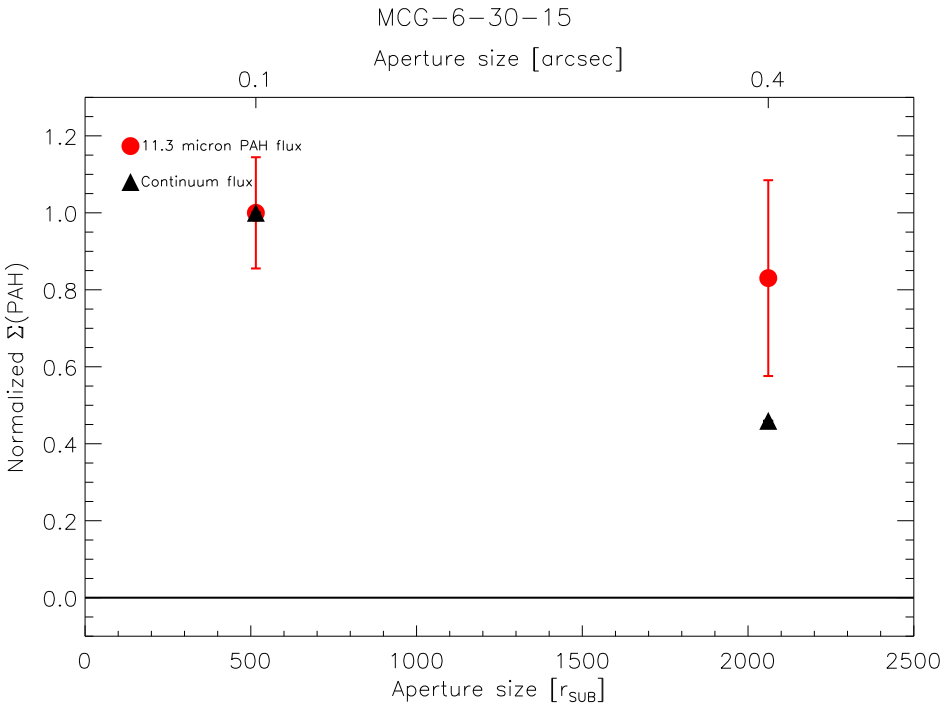

Fig. O.7 Same as Figure O.1 but for MCG-6-30-15.

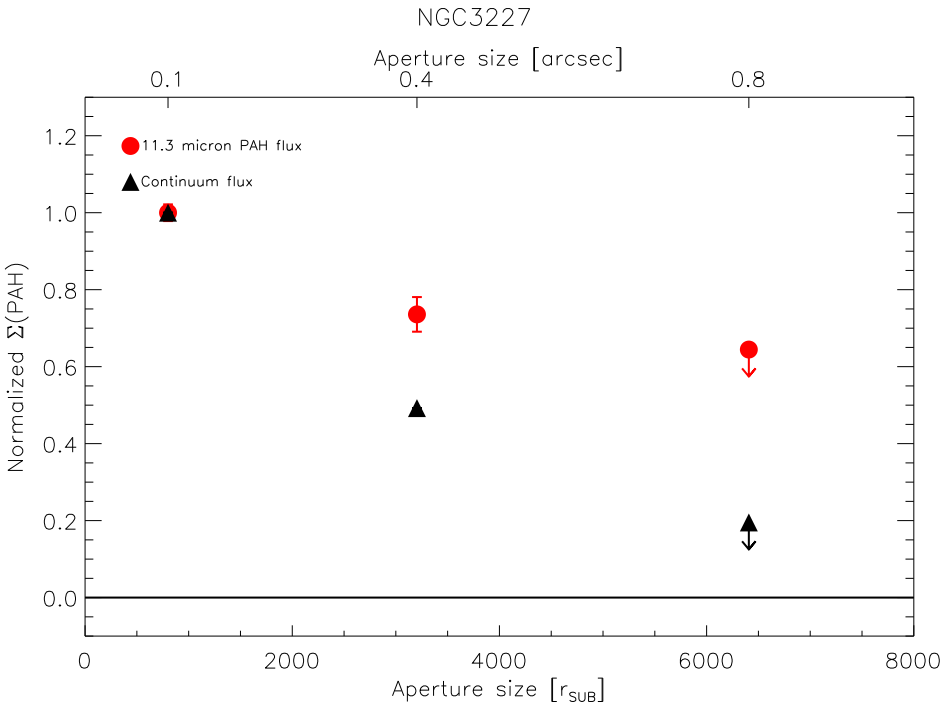

Fig. O.8 Same as Figure O.1 but for NGC3227.

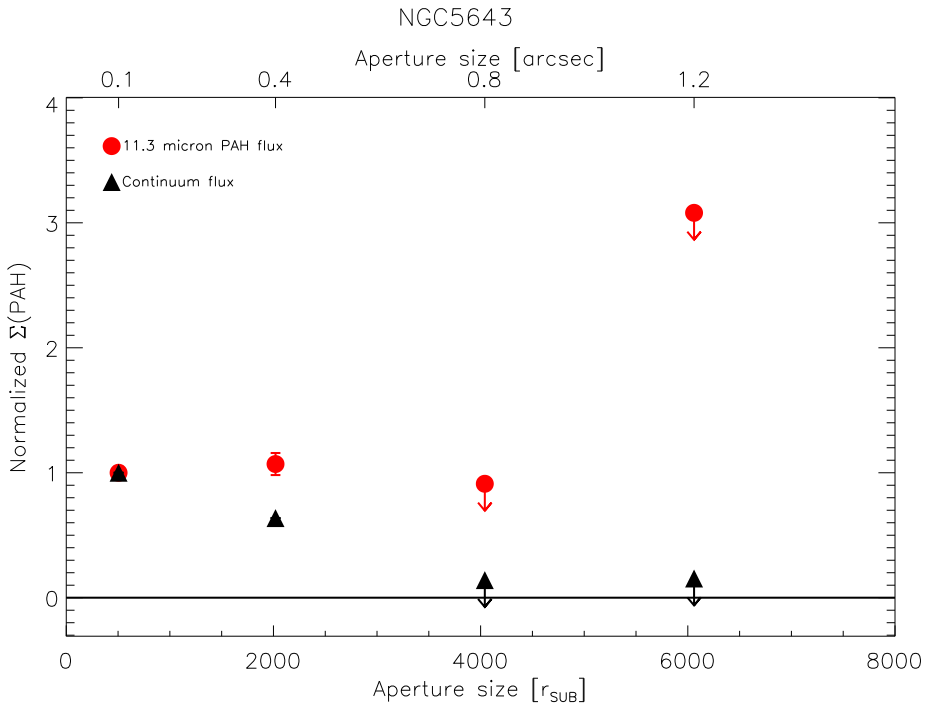

Fig. O.9 Same as Figure O.1 but for NGC5643.

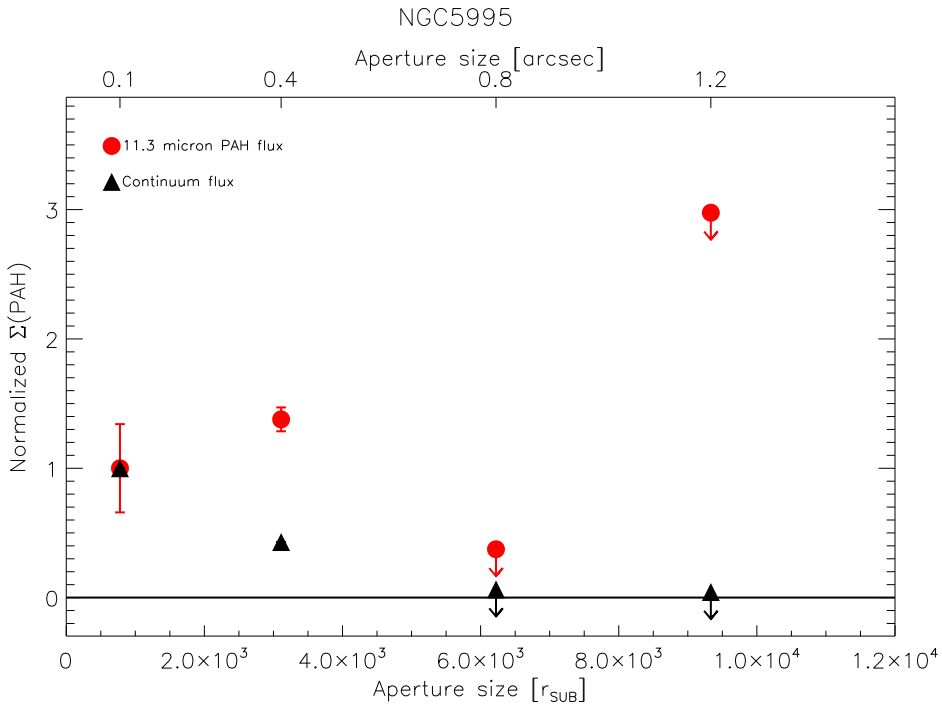

Fig. O.10 Same as Figure O.1 but for NGC5995.

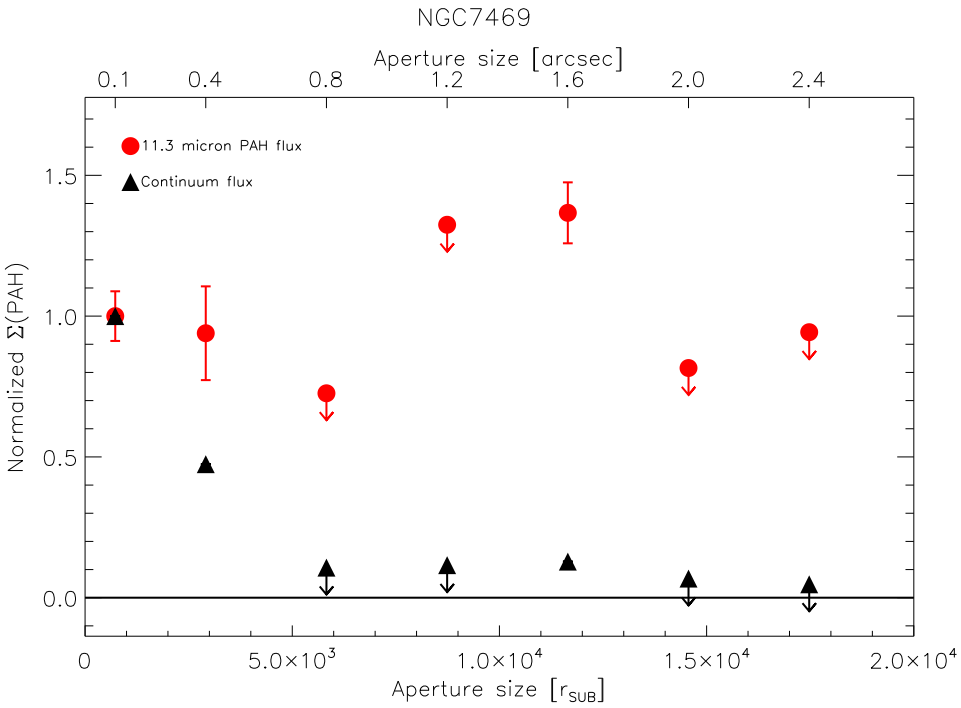

Fig. O.11 Same as Figure O.1 but for NGC7469.

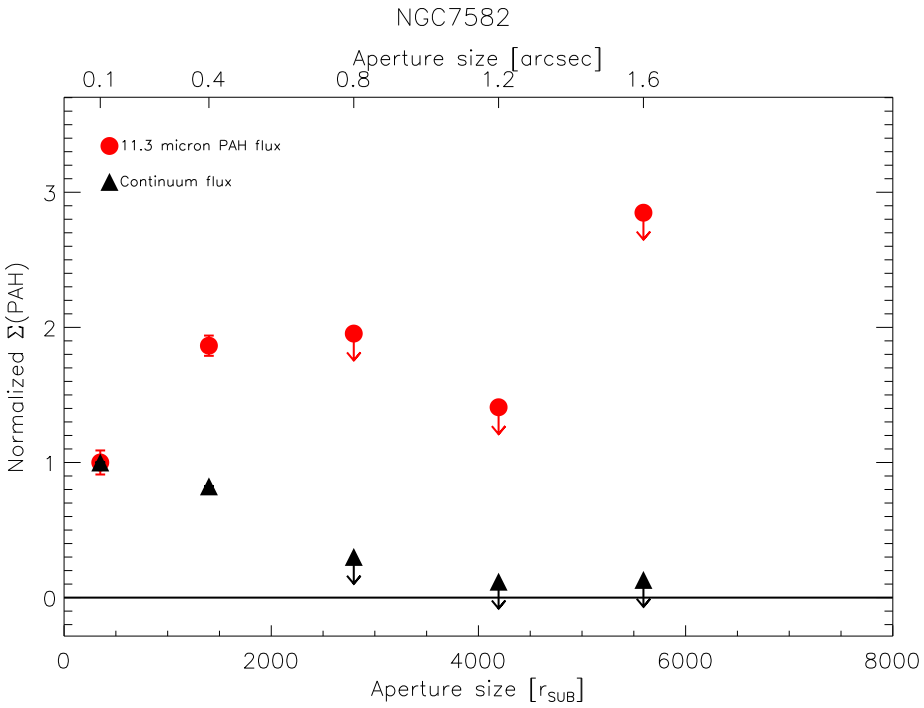

Fig. O.12 Same as Figure O.1 but for NGC7582.

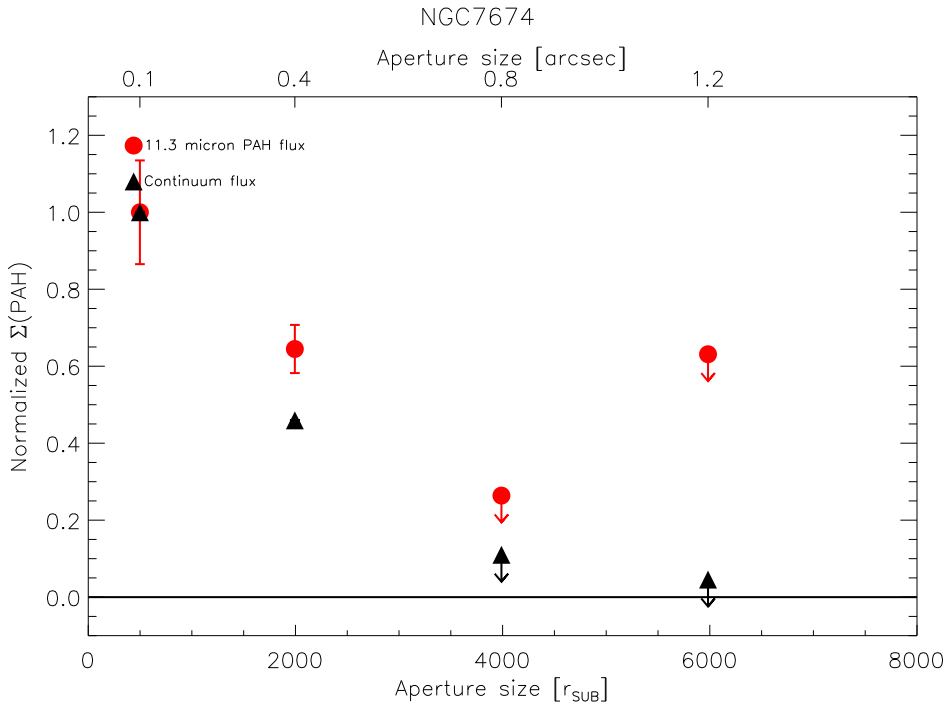

Fig. O.13 Same as Figure O.1 but for NGC7674.

Appendix P

Power-law slopes for individual objects and joint probability distribution functions for the PAH slope[1]

Figures of joint probability distribution functions for the radial PAH power-law slope.

[1] Appendix to Chapter 5.

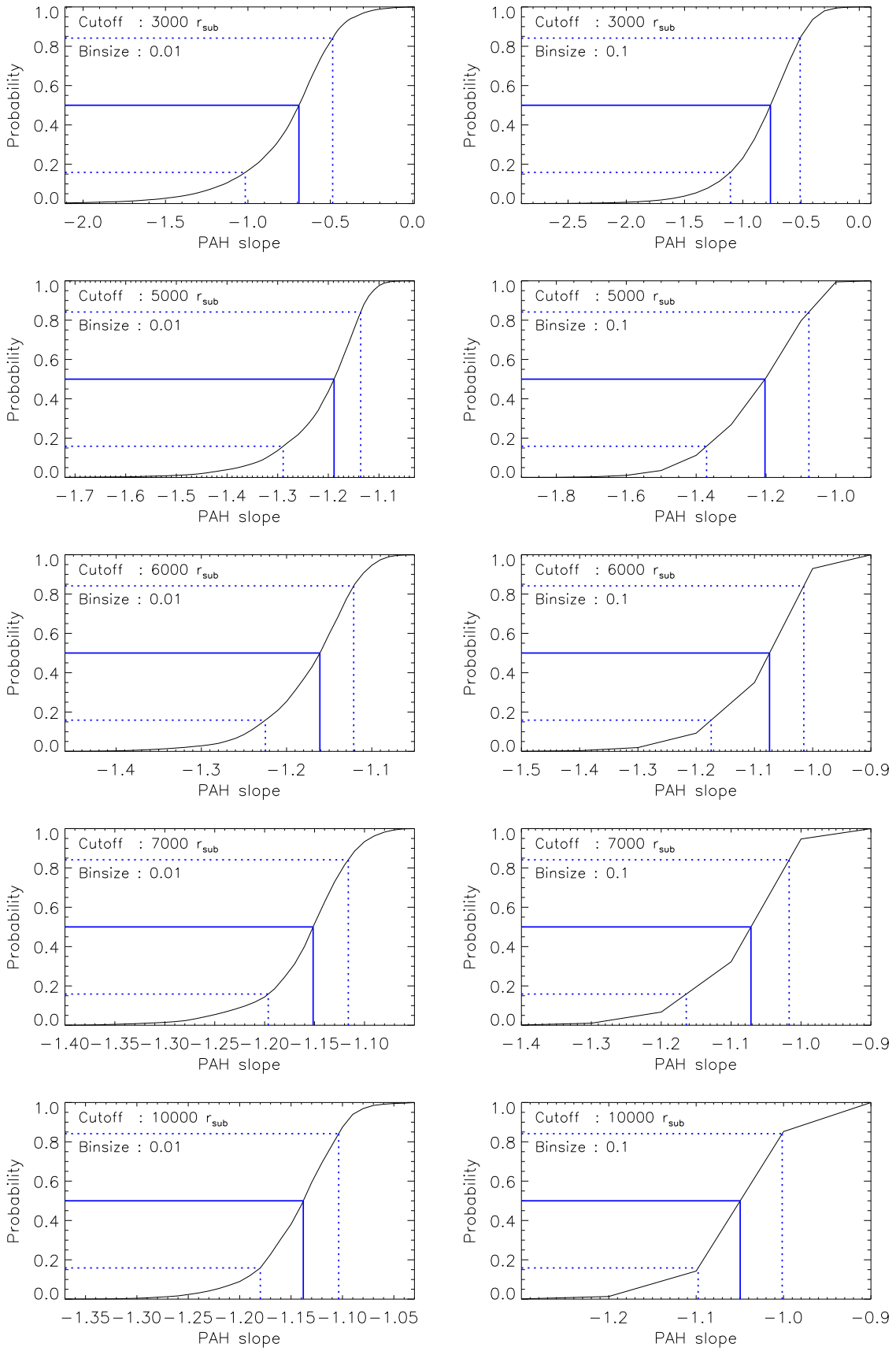

Fig. P.1 Joint cumulative distribution functions for the PAH power-law slope α for binsizes of 0.01 and 0.1, and radial cut-offs of 3000, 5000, 6000, 7000, and 10,000 sublimation radii. The solid and dashed blue lines represent the median and $\pm 1\sigma$ uncertainties, respectively.

Table P.1 Slope of the r_{sub} vs. Σ_{PAH} relation for individual objects

Object	$3000r_{sub}$	$5000r_{sub}$	$6000r_{sub}$	$7000r_{sub}$	$10000r_{sub}$
ESO138-G001	$-0.86^{+0.28}_{-0.61}$	$-0.84^{+0.19}_{-0.36}$	$-0.57^{+0.14}_{-0.25}$	$-0.58^{+0.15}_{-0.25}$	$-0.57^{+0.14}_{-0.25}$
ESO323-G77	...	...	...	...	$-0.74^{+0.29}_{-0.62}$
F49	...	...	$-0.91^{+0.27}_{-0.63}$	$-0.91^{+0.27}_{-0.62}$	$-0.50^{+0.18}_{-0.35}$
LEDA17155	...	$-1.53^{+0.31}_{-0.73}$	$-1.52^{+0.30}_{-0.72}$	$-1.52^{+0.30}_{-0.73}$	$-1.52^{+0.30}_{-0.74}$
NGC3227	...	...	...	$-0.94^{+0.27}_{-0.63}$	$-0.93^{+0.27}_{-0.60}$
NGC5643	...	$-0.79^{+0.27}_{-0.62}$	$-0.80^{+0.28}_{-0.62}$	$-0.35^{+0.25}_{-0.40}$	$-0.35^{+0.25}_{-0.41}$
NGC5995	...	...	...	$-1.35^{+0.34}_{-0.72}$	$-0.55^{+0.29}_{-0.41}$
NGC7582	$-0.41^{+0.30}_{-0.68}$	$-0.55^{+0.25}_{-0.41}$	$-0.38^{+0.21}_{-0.33}$	$-0.39^{+0.21}_{-0.32}$	$-0.38^{+0.21}_{-0.32}$
NGC7674	...	$-1.40^{+0.28}_{-0.67}$	$-1.00^{+0.23}_{-0.38}$	$-1.00^{+0.23}_{-0.38}$	$-1.00^{+0.23}_{-0.38}$
NGC7469	...	...	$-0.90^{+0.27}_{-0.60}$	$-0.90^{+0.28}_{-0.62}$	$-0.66^{+0.25}_{-0.40}$

Note. — Median power-law slope and $\pm 1\sigma$ uncertainty for the individual objects at radial cut-offs of 3000, 5000, 6000, 7000, and 10,000 sublimation radii. For a radial cutoff between 5000 and 7000 r_{sub}, the spearman rank significance for most objects is < -0.8.